# Development of a Novel Composite Bioink for Cartilage Tissue Engineering

## Mr Thomas Harry Jovic

*MA MB BChir PGCert MRCS*

Submitted to Swansea University in fulfilment of the requirements for the
Degree of Doctor of Philosophy

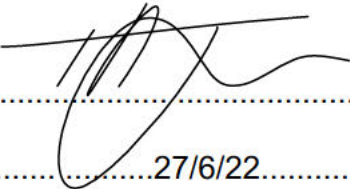## Swansea University

## 2022

## Summary

**Introduction and aims**: Nanocellulose bioinks have promising biological and mechanical properties for 3D bioprinting. The aim of this thesis was to develop a novel natural composite biomaterial derived of nanocellulose to bioprint with cartilage derived cells for ear reconstruction.

**Methods**: Cartilage derived cells were extracted from nasoseptal cartilage and chondroprogenitor cells were isolated using fibronectin adhesion assay. Different combinations of progenitor cells and chondrocytes were created to determine the most chondrogenic combination for 3D bioprinting cartilage. Nanocellulose blend, crystal and fibrils were blended with alginate and compared for printability and chondrogenicity profiles. The most chondrogenic and printable formulation was then mixed with varying proportions of hyaluronic acid to produce composite bioinks. Human nasoseptal chondrocytes from at least 3 separate patients were cultured in the composite biomaterial, and crosslinking with low dose hydrogen peroxide was optimised. Chondrogenicity was determined with PCR, quantitative protein assays and histology. Printability was assessed using rheology and printing assays. Mechanical properties were examined using atomic force microscopy and compression testing. Biocompatibility was demonstrated with Live-Dead, lactate dehydrogenase and alamarBlue assays.

**Conclusions**: There were no benefits to combining cells isolated with the fibronectin assay compared to using native cartilage cell populations, indicating an inadequacy with the validity of this assay in nasoseptal cartilage. All nanocellulose materials demonstrated superior printability and bicompatibilty to alginate, with crystals and blend varieties offering superior biological properties. Instant crosslinking of the nanocellulose-hyaluronic acid bioinks were achievable with no detriment to cell survival. Nanocellulose-hyaluronic acid bioink was more chondrogenic than nanocellulose-alginate and hyaluronic acid alone. Cell viability and proliferation was sustained over 21 days. Nanocellulose-hyaluronic acid bioinks demonstrate superior chondrogenicity, favourable mechanical properties and excellent biocompatibility for bioprinting cartilage for reconstructive surgery. These inks hold promise for in vivo testing and eventually clinical translation.
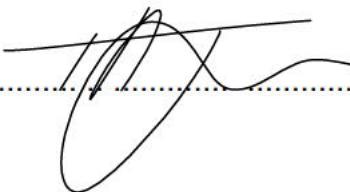
## Declarations and Statements

This work has not previously been accepted in substance for any degree and is not being concurrently submitted in candidature for any degree.

Signed ........................................................................... (candidate)

Date .............................27/6/22.............................................
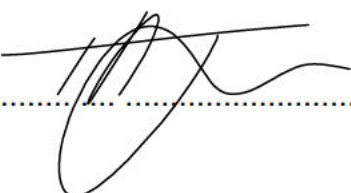
## STATEMENT 1

This thesis is the result of my own investigations, except where otherwise stated. Where correction services have been used, the extent and nature of the correction is clearly marked in a footnote(s).

Other sources are acknowledged by footnotes giving explicit references. A bibliography is appended.

Signed ........................................................................... (candidate)

Date ............................27/6/22.........................................

## STATEMENT 2

I hereby give consent for my thesis, to be available for photocopying and for inter-library loan, and for the title and summary to be made available to outside organisations following an restricted access embargo period of 1 year to enable publication.

Signed ........................................................................... (candidate)

Date ............................27/6/22.........................................

# Contents

# Acknowledgements

This thesis is dedicated to my father, Alek Jovic, who sadly passed away in April 2021. Your resilience and determination will inspire me for a lifetime.

**<u>List of tables, illustrations and figures</u>**

**<u>Figures</u>**

**Chapter 1:**

**Chapter 4:**

**Chapter 5:**

**<u>Tables</u>**

**Chapter 1:**

Table 1.1: Ordinal regression analysis of variables that may influence SATs scores at Key Stage 2.

Table 1.2: Results of binary logistic regression showing proportional odds of anxiety and depression based on a diagnosis of microtia and microtia surgery as a child.

Table 1.3: 3D bioprinting technologies, their key features, cellular compatibility, advantages and disadvantages.

Table 1.4: Commonly used cell sources for cartilage tissue engineering, and their advantages and disadvantages.

Table 1.5: Natural bioinks used in 3D printing cartilage tissue, their sources, advantages and disadvantages.

Table 1.6: Plant-derived biomaterials used in 3D bioprinting, their printability characteristics and tissue engineering applications.

Table 1.7: Growth factors, cytokines and non-proteinaceous additives and their role in enhancing chondrogenesis in culture.


**Chapter 2:**

Table 2.1: Nasoseptal cartilage donor demographics.

Table 2.2: Chondrogenic media formulation.

Table 2.3: Positive cartilage and chondroprogenitor cell surface markers, their associated fluorophores, detection channels and excitation and emission spectra.

Table 2.4: Negative stem cell and chondrogenic cell surface markers their associated fluorophores, detection channels and excitation and emission spectra.

Table 2.5: Nanocellulose-hyaluronic acid composite bioinks and their associated nomenclature.

Table 2.6: Crosslinking dose recommendations for 5% tyramine substituted hyaluronic acid hydrogel.

**Chapter 3:**

## Abbreviations

### 1. Symbols

| | |
|---|---|
| % | Percentage |
| < | Less Than |
| = | Equal To |
| > | More Than |
| ± | Plus/Minus |
| α | Alpha |
| β | Beta |
| Δ | Delta |
| ΔΔCt | Double Delta Threshold Cycle (Relative Gene Expression) |

### 2. Units of measurement

| Prefix | | Suffix | |
|---|---|---|---|
| p | Pico | g | Grams |
| n | Nano | l | Litres |
| μ | Micro | m | Metres |
| m | Milli | M | Moles |
| k | Kilo | N | Newtons |
| M | Mega | Pa | Pascals |
| G | Giga | s | Seconds |
| | | V | Volts |
| | | W | Watts |

| | |
|---|---|
| °C | Degrees Celsius |
| IU, U | International Units, Units |
| g | Relative Centrifugal (or g-) Force |
| G | Gauge (of needle/nozzle) |
| N | Normality (number of equivalents of solute dissolved in 1L of solution) |
| rpm | Revolutions Per Minute |

## 3. General Abbreviations

| | |
|---|---|
| 2D | Two Dimensional |
| 3D | Three Dimensional |
| 20HA | 20% Hyaluronic Acid: 80% Nanocellulose |
| 40HA | 40% Hyaluronic Acid: 60% Nanocellulose |
| 60HA | 60% Hyaluronic Acid: 40% Nanocellulose |
| 80HA | 80% Hyaluronic Acid: 20% Nanocellulose |
| 100HA | 100% Hyaluronic Acid |
| 20N80F | 20% Non Fibronectin Adherent Cells: 80% Fibronectin Adherent Cells |
| 40N60F | 40% Non Fibronectin Adherent Cells: 60% Fibronectin Adherent Cells |
| 60N20F | 60% Non Fibronectin Adherent Cells: 40% Fibronectin Adherent Cells |
| 80N20F | 80% Non Fibronectin Adherent Cells: 20% Fibronectin Adherent Cells |
| | |
| AAPS | American Association of Plastic Surgeons |
| ACAN1 | Aggrecan Type 1 |
| ADSC | Adipose Derived Stem Cell |

| | |
|---|---|
| AFM | Atomic Force Microscopy |
| ALP | Alkaline Phosphatase |
| Am Cy | Amicyanin |
| ANOVA | Analysis of Variance |
| APC | Allophycocyanin |
| ATMP | Advanced Therapy Medicinal Products |
| AVAP | American Value Additive Processing |
| BC | Before Christ |
| BCA | Bicinchoninic Acid |
| BCL-2 | B Cell Lymphoma 2 |
| BMP | Bone Morphogenetic Protein |
| BMSC | Bone Marrow Derived Stem Cell |
| BSA | Bovine Serum Albumin |
| BV | Brilliant Violet |
| $^\circ$C | Degrees Celsius |
| CA | California |
| $CaCl_2$ | Calcium Chloride |
| CAD | Computer Aided Design |
| calcein AM | Calcein Acetoxymethyl Ester |
| CAM | Cell Adhesion Molecule |
| CD | Cluster of Differentiation |
| CDC | Cartilage Derived Cells |
| cDNA | Complementary DNA |
| CFD | Computational Fluid Dynamics |

| | |
|---|---|
| $CO_2$ | Carbon Dioxide |
| COL2A1 | Type 2 Collagen A1 |
| CPC | Chondroprogenitor Cell |
| CS-AEMA | Chondroitin Sulfate Amino Ethyl Methacrylate |
| Ct Value | Cycle Threshold Value |
| DAPI | 4,6-diamidino-2-phenylindole |
| DE | Delaware |
| DMAB | p-Dimethylaminobenzaldehyde |
| DMMB | Dimethylmethylene Blue |
| DMSO | Dimethylsulfoxide |
| DNA | Deoxyribonucleic Acid |
| DNAse | Deoxyribonuclease |
| dNTP | Deoxynucleoside Triphosphate |
| DPBS | Dulbecco's Phosphate Buffered Saline |
| EC | European Commission |
| ECM | Extracellular Matrix |
| EDTA | Ethylenediaminetetraacetic Acid |
| EU | European Union |
| EURAPS | European Association of Plastic Surgeons |
| EUROCAT | European Network of Population-Based Registries for the Epidemiological Surveillance Of Congenital Anomalies |
| FACs | Fibronectin Adherent Chondrocytes |
| FACS | Flow Assisted Cell Sorting |
| FBS | Fetal Bovine Serum |

| | |
|---|---|
| FDA | Food and Drug Administration |
| FGF | Fibroblast Growth Factor |
| FITC | Fluoroscein-5-isothiocyanate |
| G' | Storage Modulus |
| G" | Loss Modulus |
| G* | Complex Modulus |
| GAG | Glycosaminoglycan |
| GAPDH | Glyceraldehyde 3-phosphate dehydrogenase |
| GelMA | Gelatin Methacrylate |
| GMP | Good Manufacturing Practice |
| gpIIa | Glycoprotein IIa |
| H+E | Haematoxylin and Eosin |
| $H_2O_2$ | Hydrogen Peroxide |
| HA | Hyaluronic Acid |
| HEMA | Hyaluronic Acid Methacrylate |
| HLA | Human Leukocyte Antigen |
| hNCs | Human Nasoseptal Chondrocytes |
| HPMAm-lac-PEM | Poly(n-(2-hydroxypropyl)methacrylamide lactate)-polyethylene glycol methacrylate |
| HRP | Horseradish Peroxidase |
| ID | Identification |
| IGF | Insulin-like Growth Factor |
| IgG | Immunoglobulin G |
| IL | Interleukin |

| | |
|---|---|
| iPSC | Induced Pluripotent Stem Cell |
| IQR | Interquartile Range |
| IRAS | Integrated Research Application System |
| ISO | International Organisation for Standardisation |
| LDH | Lactate Dehydrogenase |
| m | Mass |
| MA | Massacheussetts |
| MFI | Median Fluorescence Index |
| $MgCl_2$ | Magnesium Chloride |
| MN | Minnesota |
| MO | Missouri |
| mRNA | messenger RNA |
| n | Number (of Repeats) |
| n/a | Not Applicable |
| NaCl | Sodium Chloride |
| NaOH | Sodium Hydroxide |
| NCA | Nanocellulose Alginate |
| NCAM | Neural Cell Adhesion Molecule |
| NCBI BLAST | National Centre for Biotechnology Information Basic Local Alignment Search Tool |
| NCC | Nanocellulose Crystals |
| NCF | Nanocellulose Fibrils |
| NCHA | Nanocellulose-Hyaluronic Acid |
| NFAC | Non-Fibronectin Adherent Cells |

| | |
|---|---|
| NHS | National Health Service |
| NIH | National Institute of Health |
| NY | New York |
| OCN | Osteocalcin |
| OCT | Optimum Cutting Temperature |
| OR | Oregon |
| P0 | Passage 0 |
| P1 | Passage 1 |
| P2 | Passage 2 |
| P5 | Passage 5 |
| P8 | Passage 8 |
| PA | Pennsylvania |
| PBS | Phosphate Buffered Saline |
| PBS-T | Phosphate Buffered Saline - Tween |
| PBT | Polybutylene Terephalate |
| PCL | Polycaprolactone |
| PDLLA | Poly (D, L) - Lactic Acid |
| PE | Phycoerythrin |
| PEG | Polyethylene Glycol |
| PEGDA | Polyethylene Glycol Diacrylate |
| PEGTA | Polyethylene Glycol Tetracrylate |
| PEOT | Polyethylene Oxide Terephthalate |
| Per CP | Peridinin Chlorophyll Protein |
| PEU | Poly-ether urethane |

| | |
|---|---|
| PFA | Paraformaldehyde |
| PGE2 | Prostaglandin E2 |
| PGS | Pyrolytic Graphite Sheet |
| pH | Potential of Hydrogen |
| PLA | Poly-lactic Acid |
| PLGA | Poly-lactic-co-glycolic Acid |
| PLLA | Poly-L-Lactic Acid |
| pMHMGCL | Phenyl Magnesium Chloride |
| PPF | Polypropylene fumarate |
| PTFE | Polytetrafluoroethylene |
| PU | Polyurethane |
| RIPA | Radioimmunoprecipitation Assay |
| RNA | Ribonucleic Acid |
| RNAse | Ribonuclease |
| RPL | Ribosomal Protein L |
| RPM | Revolutions Per Minute |
| RT-qPCR | Real time Quantitative Polymerase Chain Reaction |
| RUNX2 | Runt-related Transcription Factor 2 |
| S:N Ratio | Signal:Noise Ratio |
| SD Card | Secure Digital Card |
| SD | Standard Deviation |
| SEM | Scanning Electron Microscopy |
| SOX9 | SRY-Box Transcription Factor 9 |
| STL | Stereolithography |

# Chapter 1: Introduction

# Chapter 1: Introduction

## 1. Introduction

### 1.1 General overview

Approximately 1 in 5 individuals in the United Kingdom (UK) are affected by a visible difference, and over 500,000 people in the UK are believed to have facial disfigurement (Changing Faces, 2019). Many of these patients would benefit from reconstructive surgery to restore the form and function of the face. Auricular anomalies fall under this spectrum of anomalies and may be associated with significant psychosocial burden for patients (Jiamei *et al.*, 2008). The current gold standard is autologous auricular reconstruction, which despite offering excellent results in many cases, does require extensive donor tissue to be harvested from the rib cage, and multiple lengthy operations for patients (Truong and Maricevich, 2017). As such there have been attempts to tissue engineer auricles for use in reconstructive surgery for over 25 years (Cao *et al.*, 1997). In particular, 3D bioprinting has gained significant traction owing to the ability to have greater control over macroscopic and microscopic structures and cellular placement, offering true personalisation for the intended recipient (Jovic *et al.*, 2020). However, owing to a suboptimal combination of cells, biomaterials and culture conditions, attempts to date have been hindered by complications such as construct degradation, immunological reactions, resorption and calcification (Jessop *et al.*, 2015). In particular, whilst synthetic scaffolds may possess excellent printability and stiffness this may be at the expense of biomimicry and biocompatibility, whereas natural materials such as collagen offer superior biomimicry but are inherently unstable for long term use (Kyle *et al.*, 2017)  This thesis explores the development of a novel, natural biomaterial combination that seeks to meet both the mechanical and biological needs of a substitute auricular construct for facial reconstructive surgery.

## 1.2    The auricle

### 1.2.1  Anatomy of the auricle

The auricle is a complex 3-dimensional (3D) structure comprising a thin layer of elastic cartilage covered in a layer of perichondrium and closely adherent skin. The cartilage provides structural support to the auricle and is shaped into a series of cavities, ridges and grooves that are believed to have evolved to funnel sound waves towards the external acoustic meatus (Szymanski and Bhimji, 2021). The anatomy of the ear is structurally unique to an individual (much like the fingerprint): it differs so widely between individuals that it has been considered a form of forensic identity (Purkait and Singh, 2008). The pinna comprises an outer rim known as the helix, and an inner fold known as the antihelix, the latter of which bifurcates into superior and inferior crura, producing a triangular shaped fossa between them. Between the antihelix and helix sits a deep groove: the scapha. The external auditory meatus is surrounded by two cartilaginous projections: the tragus and antitragus, and a deep bowl comprising most of the concavity of the inferior pinna: the concha, which itself comprises the cymba and cavum concha (Figure 1.1).
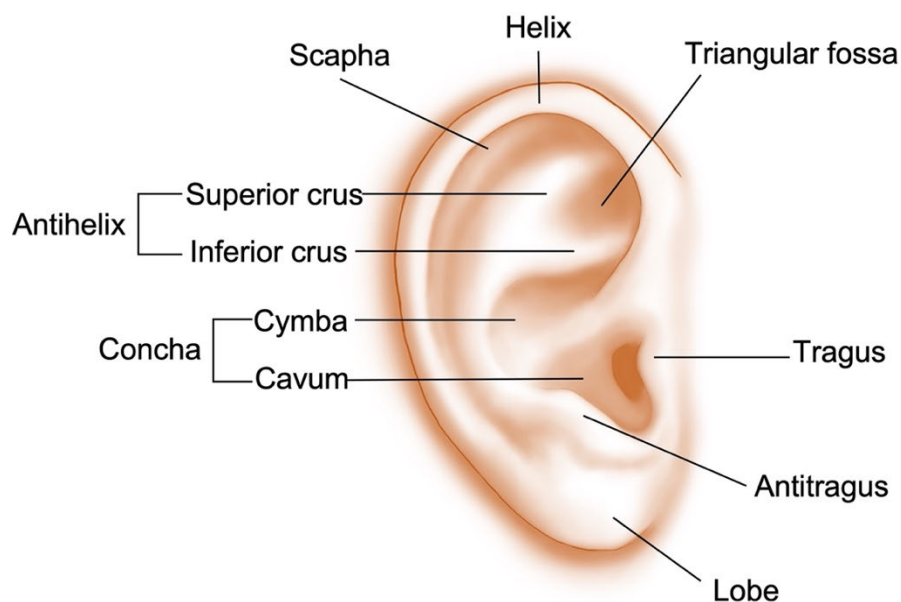


*Figure 1.1: An illustration of the surface anatomy of the auricle (right ear) with labelled surface anatomy. Image kindly provided by Steve Atherton, Medical Illustration, Swansea Bay University Healthboard.*

### 1.2.2 Auricular development

The external ear, or auricle, is a derivative of the branchial (or pharyngeal) arches. At four to five weeks of gestation, pharyngeal pouches emerge in the developing embryo, with recesses that regress further into the mesenchyme during the early stages of gestation. In parallel, recesses known as branchial clefts also develop on the surface of the embryo, separating the mesenchymal tissue into bulging segments that form between the pharyngeal pouches and branchial clefts, known as branchial arches. These arches are filled with neural crest cells containing a core of mesoderm. By the fifth week of gestation, there are five discrete branchial arches, each of which develops a cartilaginous skeleton, an artery, nerve and set of muscles (Helwany and Tadi, 2021). By week six, six mesenchymal thickenings known as hillocks arise on the first and second branchial arches. The external auditory meatus arises from the first pharyngeal cleft, and on each side, lies three auricular hillocks. The first three arise from the first pharyngeal arch and produce the tragus, helix and cymba concha. The second three arise from the second pharyngeal arch and yield the concha, antihelix and antitragus (Helwany and Tadi, 2021). As a result, the auricle is a composite structure derived from neural crest, endoderm, mesoderm and ectoderm (Anthwal and Thompson, 2016). In the context of cartilage tissue development, embryonic mesenchymal stem cells are believed to aggregate into clusters, known as condensation and thereafter differentiate into chondroblasts (Figure 1.2). These cells give rise to the typical, rounded chondrocytes that produce the extracellular matrix (ECM) of cartilage tissue (Quintana, Zur Nieden and Semino, 2009).

MESENCHYMAL STEM CELLS

CHONDROBLASTS

CHONDROCYTES

↓

**CARTILAGE**
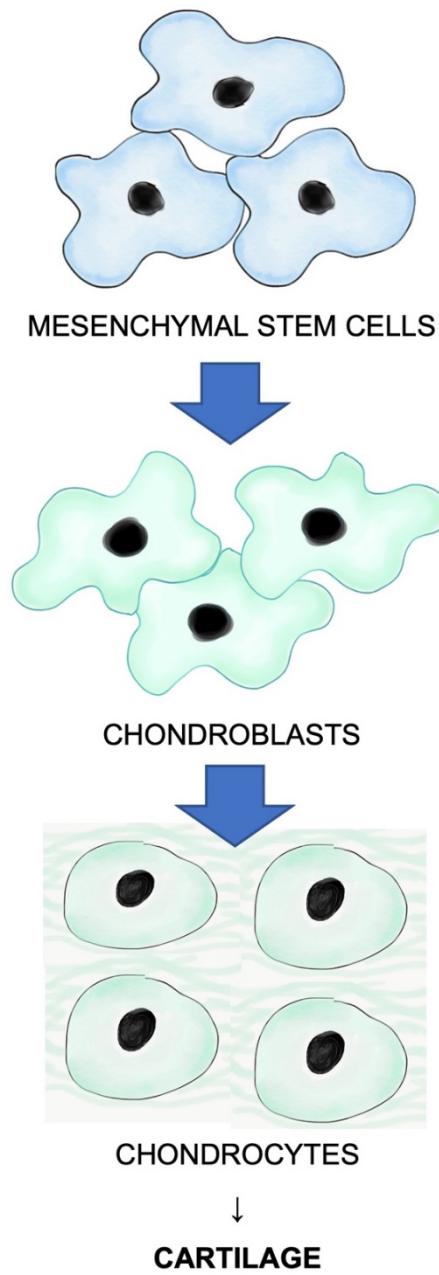
*Figure 1.2: The process of chondrogenic differentiation from mesenchymal stem cells. Mesenchymal stem cells committed to a chondrogenic lineage differentiate into chondroblasts and then mature chondrocytes capable of depositing extracellular matrix.*

### 1.2.3  Auricular cartilage composition

### 1.2.3.1  General morphology

Cartilage tissue is structurally unique in its elasticity, flexibility and strength (Fung, 1981). These unique properties enable this tissue to protect and cushion joint surfaces whilst offering a stiff yet pliable composition to facial cartilages, the rib cage and airways.

The three main types of cartilage tissue are: elastic cartilage, hyaline cartilage and fibrocartilage, of which each comprises different proportions of ECM constituents such as proteoglycans, elastin and collagen fibres in order to meet its biological and mechanical requirements (Zambrano *et al.*, 1982). Osteoarthritis is one of the most significant degenerative diseases of cartilage, and as such, the majority of structural and functional characterisation is derived from studies of articular hyaline cartilage (Eyre, 2002; Gelse, Pöschl and Aigner, 2003).

Auricular cartilage is an elastic fibrocartilage with a histological structure similar to hyaline cartilage lining the surface of joints and nasoseptal cartilage, but with a greater abundance of elastic fibres. The ECM of cartilage tissue dominates structural composition, with chondrocytes comprising a mere 2% of the structure of cartilage, embedded in cavities known as lacunae. Cartilage is unique in the sense that it is avascular, aneural, alymphatic and relatively immunoprivileged, which simplifies the process of tissue engineering but conversely means that inherent regeneration and repair is restricted (Vinatier *et al.*, 2009; Jessop *et al.*, 2016).

### 1.2.3.2  Cellular morphology

Chondrocytes are the primary cell type of cartilage, and adopt a rounded, spheroidal morphology. They exist largely in isolation, but occasionally in pairs or small clusters within a bed of pericellular matrix, known as a 'chondron' (Poole, 1997). Chondrocytes are highly differentiated quiescent cells responsible for maintaining the extracellular matrix (Hall, 2019) and are around 13 microns in diameter. They occur at a density of approximately 10,000 cells

per mm$^3$ (Hunziker, Quinn and Häuselmann, 2002) equating to 25 million cells per gram of tissue in nasoseptal cartilage (Homicz *et al.*, 2003).

Chondrocytes in culture conditions are phenotypically unstable, and easily dedifferentiate away from their normal spheroidal phenotype, characterised by collagen II and aggrecan production to a fibroblastic phenotype (Hunziker *et al.*, 2015). The fibroblastic phenotype is characterised by the production of greater amounts of collagen I and decorin: constituents of a weaker, fibrous cartilage (Hunziker *et al.*, 2015). Another potential route of phenotypic divergence is towards the formation of hypertrophic chondrocytes, typically seen in growth plates (Figure 1.3). These cells are characterised by the expression of Type X collagen and alkaline phosphatase (ALP), and are prone to making an unstable mineralised matrix (Pitsillides and Beier, 2011). Many of these changes are seen in diseases like osteoarthritis but may also occur in 2D tissue culture environments, albeit with a greater degree of reversibility (Pitsillides and Beier, 2011; Hall, 2019).
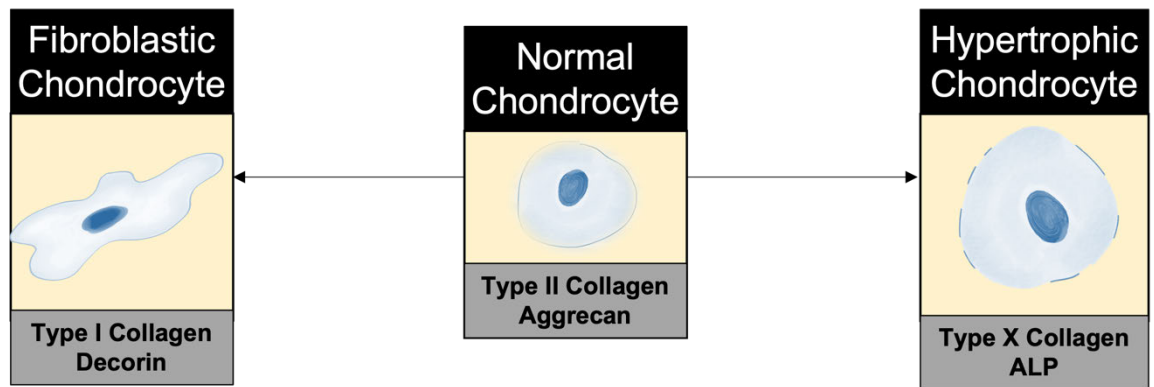


*Figure 1.3: Schematic to demonstrate the deviation of cellular morphology from typical spheroidal chondrocyte to fibroblastic and hypertrophic phenotypes and the key molecules that underpin these phenotypic changes.*

### 1.2.3.3 Extracellular matrix

The ECM lends structural and biochemical support to tissues and surrounding cells, facilitating cell adhesion, cell-cell interactions and differentiation (Gao *et al.*, 2014). Cartilaginous ECM comprises mostly type II collagen, large

amounts of glycoproteins, and proteoglycans of which aggrecan is the dominant subtype.

Collagens form the major structural components of ECM, and have a tertiary structure comprised of three intertwining polypeptide chains formed into a right handed helix (Prockop and Kivirikko, 1995). Type II collagen comprises over 90% of all collagens in adult cartilage, and forms complexes with type XI and IX collagen, chondroitin and aggrecan (Eyre, 2004; Bächinger *et al.*, 2010). These aggregations produce fibrils of which collagen II forms the backbone, and to which type IX and XI collagens are covalently linked, with bonds between collagen IX chains contributing to matrix stabilisation (Gelse, Pöschl and Aigner, 2003). Collagen VI is also present to a lesser degree and mediates the attachment of chondrocytes to Type II collagen and other ECM components (Eyre, 2004). The expression of type II collagen and aggrecan are characteristic of cartilage tissue and chondrogenic differentiation, and mediated by the transcription factor SRY-Box Transcription Factor-9 (SOX9) (Hardingham, Oldershaw and Tew, 2006). As such, these genes are commonly investigated as markers of chondrogenesis (Yi *et al.*, 2018), particularly in contrast to markers of osteogenic differentiation (Runt-related Transcription Factor-2: RUNX2) or mineralisation (ALP, Osteocalcin) (Figure 1.4).

Proteoglycans are another component of ECM, comprising a core protein to which glycosaminoglycans (GAGs) are covalently bonded. The glycosaminoglycans contained within proteoglycans are linear polymers of repeating disaccharide units. There are four main types of GAG in the extracellular matrix: heparan sulphate/heparin, chondroitin/dermatan sulphate, keratan sulphate and hyaluronic acid (HA). Of these, hyaluronic acid is the only non-sulphated GAG (Casale and Crane, 2021) and demonstrates a high degree of polarity and hydrophilicity, enabling the molecule to bind up to 10000 times its own weight in water. This property underpins many of the structural roles of HA in the ECM (Casale and Crane, 2021). Of the non-sulphated GAGs, chondroitin sulphate is the most abundant in nasoseptal cartilage ECM, comprising roughly 2.9% of the wet mass of the tissue.
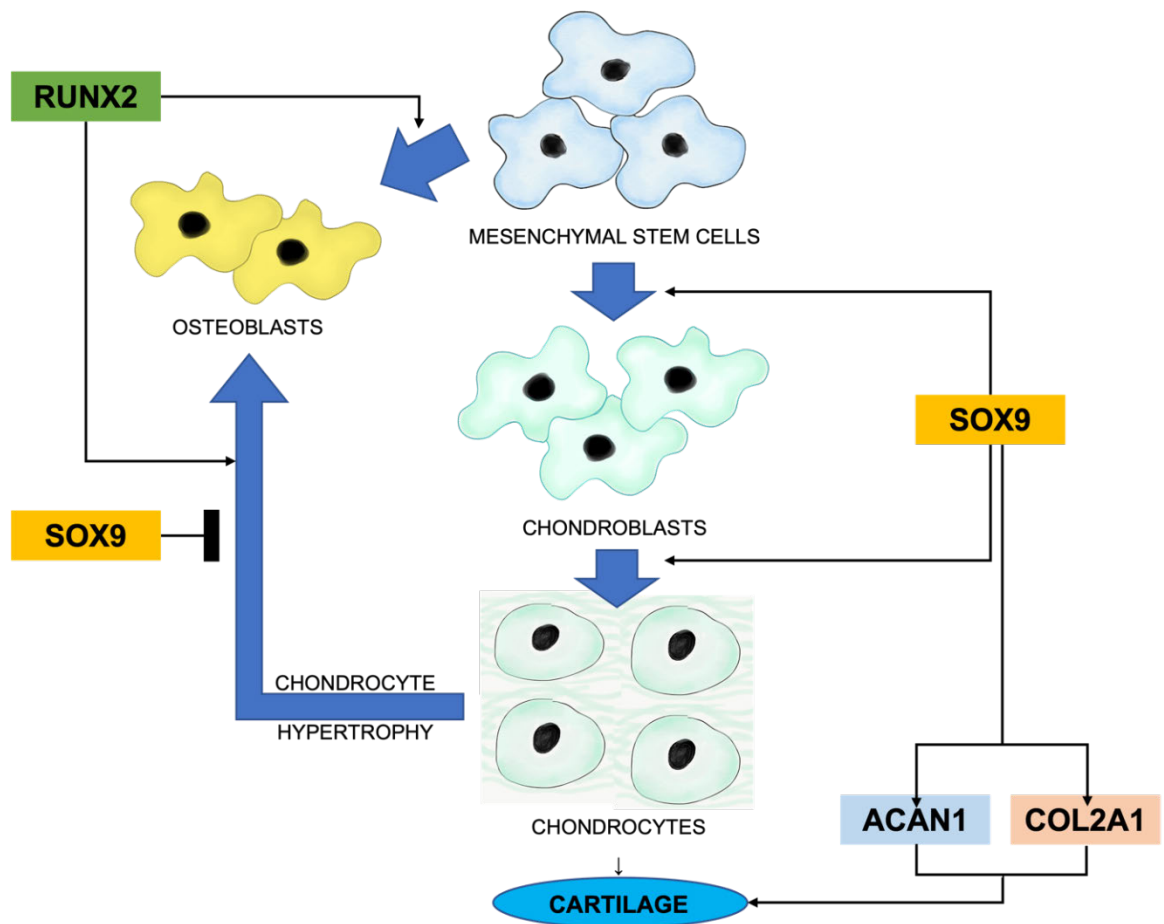
*Figure 1.4: Schematic of the relationship of key genes explored in this thesis; their role in chondrogenic differentiation and cartilage extracellular matrix production. SOX9 is an early mediator of chondrogenic differentiation and upstream regulator of Aggrecan (ACAN1) and Type 2 Collagen (COL2A1). SOX9 additionally protects against chondrocyte hypertrophy and osteoblastic differentiation: a process mediated by RUNX2.*

### 1.2.3.4 Biomechanical properties

The properties of auricular cartilage have been characterised biomechanically and there are noted to be subtle differences in elastic modulus (also known as Young's modulus, a measure of material stiffness) and elastin content within the different anatomical subunits of the auricle. The highest Young's modulus was found to be in the concha (2.08 MPa) and the lowest in the helix (1.41 MPa), but this did not correlate with any differences in elastin content (Griffin, Premakumar, Seifalian, Szarko and Butler, 2016), suggesting this may relate to the shape and thickness of the cartilage rather than the histological features. The Young's modulus of nasoseptal cartilage for comparison is higher than

that of auricular cartilage with a mean of 2.72 MPa across the different cartilages (Griffin, Premakumar, Seifalian, Szarko and Butler, 2016). Articular cartilage in comparison has a Young's modulus of up to 36 MPa reported in the literature (Kerin, Wisnom and Adams, 1998).

## 1.3 The epidemiology of auricular anomalies

Approximately 1 in 100 individuals experience some form of impairment to the form or function of the face. In particular, cartilaginous structures such as the external ear bear an underappreciated functional and social significance in modern culture: supporting glasses, masking hearing aids and displaying jewellery are all examples of the wider function of the auricle in modern society. Modifications of the aesthetic of the ear are intertwined with its cultural history in that it is a part of the body to which attention can be both drawn and detracted, playing a pivotal role in identity (Pitts-Taylor, 2008). In light of the sociocultural importance of the ear, it is clear as to why ear anomalies may be stigmatising and a source of significant conscious and subconscious psychological burden (Li *et al.*, 2010).

Abnormalities of the auricle encompass a spectrum of partial to complete defects, resulting from both congenital and acquired aetiologies. Congenital causes of ear anomalies are common, affecting approximately 1 in 20 of the population (Guyuron and DeLuca, 1997; Ma *et al.*, 2019), ranging from prominent ears to a congenital absence of a part of, or the entirety of, the external ear: microtia. Microtia can occur as an isolated phenotype or as part of a syndrome such as Goldenhar Syndrome or Treacher Collins. Nagata classified the ear anomalies in microtia into four distinct types: lobular type, small concha type, concha type and anotia, which is a reflection of both the severity of the abnormality and the reconstructive needs (Figure 1.5).

| Normal Ear | Lobular Type | Small Concha Type | Concha Type |
|---|---|---|---|
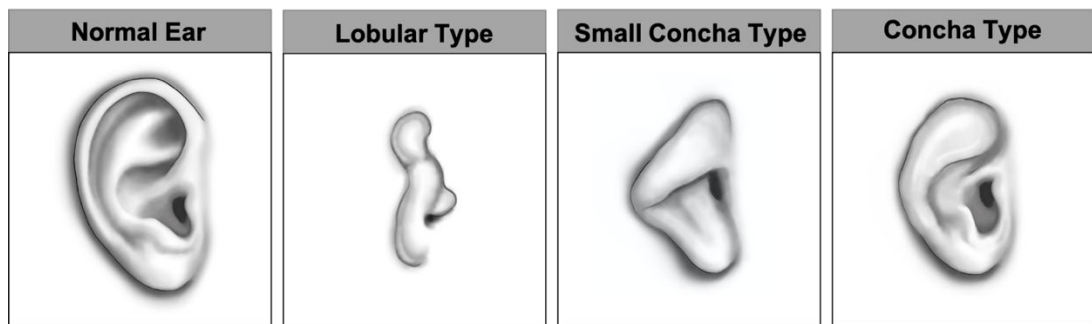
*Figure 1.5: Nagata classification of auricular anomalies in microtia: A normal ear is presented next to a lobular type, small concha type and concha type microtia. The fourth type: anotia, being complete absence of the auricle is not shown.*

Global studies of microtia epidemiology have demonstrated significant geographical and ethnic variation (Luquetti, Leoncini and Mastroiacovo, 2011). Microtia is loosely cited as affecting approximately 3-5 in 10,000 live births (Luquetti *et al.*, 2012), though markedly higher incidences have been observed in a few ethnic groups including the Navajo population (12 per 10,000 births) (Jaffe, 1969) and 8.8 per 10,000 births in Chile (Julio Nazer, Guillermo Lay-Son and Lucía Cifuentes, 2006). Anonymised data linkage has been used to interrogate several clinical data sets encompassing primary and secondary care records to determine the incidence of microtia between 2000 and 2018 in Wales (Figure 1.6). This approach demonstrated both annual and geographic variation but determined a mean incidence of 2.13 cases per 10,000 live births (range 0.3 -2.96) (Jovic *et al.*, 2021).
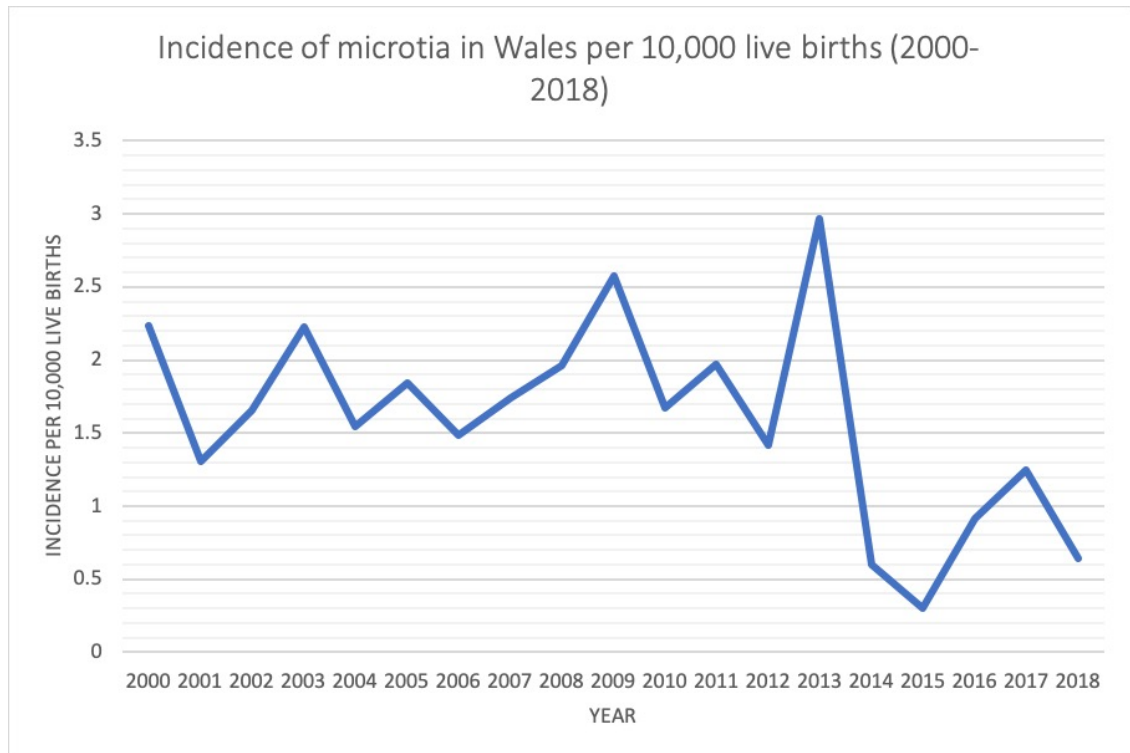
*Figure 1.6: Annual incidence of microtia in Wales from 2000-2018 inclusive. The incidence is plotted per 10,000 live births that year.*

This data suggests there is a significantly higher incidence rate than previously reported (1.11 per 10,000 births) based on data acquired solely from the "European network of population-based registries for the epidemiological surveillance of congenital anomalies (EUROCAT)", and is also higher than the average rate for Western Europe (0.88 per 10,000 births) (Luquetti, Leoncini and Mastroiacovo, 2011). As such, the clinical burden of this condition in the UK may be higher than initially anticipated, perhaps attributable to superior data capture with a data linkage approach.
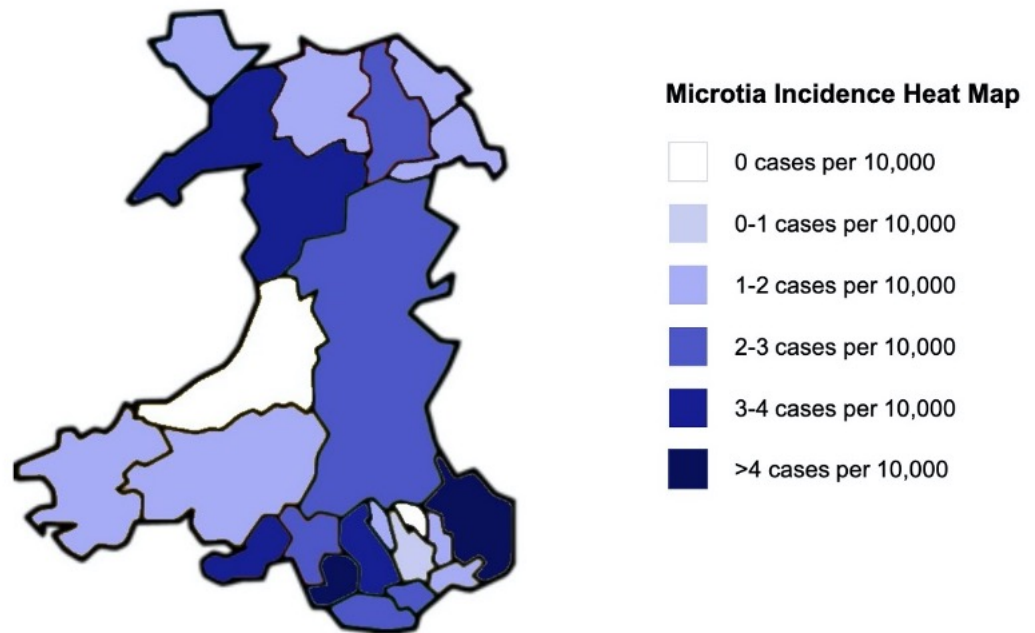
*Figure 1.7: Graphical representation of the regional epidemiology of microtia in Wales. County districts are colour coded according to the legend (right) with incidence per 10,000 live births expressed between 2000-2015 (Jovic et al., 2021).*

### 1.3.1 Psychosocial implications of auricular anomalies

The presence of facial disfigurement is associated with negative psychological behaviours. They may manifest as reduced self-confidence, poorer quality of life and an increased risk of affective disorders, and this has been suggested to be stark in auricular anomalies such as microtia (Jiamei *et al.*, 2008). The psychosocial effects may also manifest as bullying and social exclusion or depression, anxiety, poor academic performance and behavioural problems (Gasques, Pereira de Godoy and Cruz, 2008; Niemelä *et al.*, 2008; Songu and Kutlu, 2014) which present psychological implications for both the patient (Li *et al.*, 2010) and their carers (Johns, Im and Lewin, 2018).

As such, microtia surgery is usually sought around the ages of 8 -10, as the ear has grown to be sufficiently comparable to its adult size, but early enough to hopefully evade the adverse psychosocial impacts associated with an auricular abnormality (Bulstrode, Stewart and Moffat, 2015). In Wales, of the patients that undergo reconstructive surgery, 72.9% opt for autologous

reconstruction with the remainder receiving prosthetic ears (Jovic *et al.*, 2021). Through an analysis of the Welsh microtia cohort using data-linkage, a diagnosis of microtia was not associated with increased rates of anxiety and depression (Table 1.2), or a predictor of poorer school performance (Table 1.1) (unpublished, in preparation).

| ORDINAL REGRESSION | ENGLISH | | MATHS | | SCIENCE | |
|---|---|---|---|---|---|---|
| **VARIABLE** | P value | Odds | P value | Odds | P value | Odds |
| **AGE** | 0.01 | 0.93 | 0.09 | 0.95 | 0.50 | 0.98 |
| **DEPRESSION** | 0.65 | 0.87 | 0.91 | 0.97 | 0.83 | 1.07 |
| **ANXIETY** | 0.70 | 0.88 | 0.98 | 1.01 | 0.66 | 0.86 |
| **MICROTIA** | 0.89 | 0.96 | 0.67 | 1.12 | 0.73 | 1.10 |
| **GENDER (MALE)** | 0.02 | 0.65 | 0.64 | 0.92 | 0.07 | 0.71 |

*Table 1.1: Ordinal regression analysis of variables that may influence SATs scores at Key Stage 2. Proportional odds are expressed with a 95% confidence interval (CI) and p values, with statistically significant findings highlighted in bold.*

| ANXIETY | | | DEPRESSION | | |
|---|---|---|---|---|---|
| **VARIABLE** | P value | Odds | Variable | P value | Odds |
| **OPERATION** | 0.661 | 1.73 | Operation | 0.787 | 1.292 |
| **MICROTIA** | 0.404 | 0.601 | Microtia | 0.821 | 0.896 |

*Table 1.2: Results of binary logistic regression showing proportional odds of anxiety and depression based on a diagnosis of microtia and microtia surgery as a child. Proportional odds are expressed with a 95% confidence interval (CI) and p values*

This finding indicates that the support available for patients with microtia and the timing of ear reconstruction may be protective against the development of adverse psychosocial outcomes.

## 1.4 Auricular reconstruction

### 1.4.1 The history of auricular reconstruction

The concept of ear reconstruction is recorded as early the ancient Egyptian times, as noted in the Edwin Smith Surgical Papyrus (approximately 3000 BC), in which 'Case 23: The management of trauma to an ear' is presented (Myres, 1933).

Thereafter, there have been additional attempts to reconstruct the partially or totally amputated auricle from texts as early as the Sushruta Samhita (5th Century BC) (Loukas *et al.*, 2010). Herein, Sushruta presents the use of a pedicled cheek flap to reconstruct split ear lobes as a result of ear piercing and gauging: an act believed to have deterred evil spirits.

In 1597, Tagliacozzi published his text 'De Curtorum Chirurgia' using local posterior auricular flaps to restore both upper and lower ear defects (Truong and Maricevich, 2017). Thereafter, John Dieffenbach (1792-1847) reported the post-traumatic correction of the auricle and an attempt to correct prominent ears through the combination of postauricular skin excision and conchomastoidal fixation (Nazarian and Eshraghi, 2011).

Ear reconstruction was revolutionised by the emergence of general anaesthetics in the mid-19th century. In 1870, Szymanowski (von Szymanowski, 1870) described the concept of total auricular reconstruction using a bilobed scalp flap which prompted an attempt to restore auricular form through subcutaneous petroleum jelly injections in 1901 (Hacker, 1901). Just prior to this, in 1890, a legitimate attempt at total auricular reconstruction was reported by Schanz and Kuhnt in Germany, using ipsilateral cartilage remnants to restore auricular form for a patient with a subtotal auricular avulsion injury (Schanz, 1890). This inspired attempts to recreate an auricular structure from cartilage borrowed from rabbits in 1893 (Randall, 1893) the contralateral ear (Korte, 1905), autologous mastoid bone (Gillies, 1937; Cotin *et al.*, 1983), tibial bone (Joseph, 1916), iliac bone (Gillies, 1937), nasoseptal cartilage (Graham, 1927), allogenic conserved auricular cartilage (Kirkham, 1940; Campbell, 1983), ivory (Joseph, 1931) and maternal auricular cartilage (Gillies, 1937; Peet, 1971), culminating in over 40 different approaches in the

20th century. There were also numerous attempts to reconstruct the auricle without the use of a supporting frame (Beck, 1925; de River, 1927; Sarig *et al.*, 1982).

Tanzer, an early adopter of autologous costochondral grafts, described a six-stage auricular reconstruction procedure in 1959 (Tanzer, 1983). These earlier attempts using autologous cartilage highlighted the potential complications of this approach including graft resorption, extrusion and skin necrosis (Berghaus and Toplak, 1986). After the 1980s, autologous costal cartilage, polyethylene and silicone became the mainstays of auricular reconstruction (Papacharalampous *et al.*, 2007). The main operative risks of skin necrosis, erosion and extrusion of the framework, spreading and contracture, cartilage resorption, pneumothorax and infection remained prevalent in reconstructions (Berghaus and Toplak, 1986). Silicone frames were considered briefly as a replacement for autologous cartilage, bypassing the need for, and morbidity associated with, graft harvest from a donor site but similarly displayed high rates of infection and failure (Berghaus and Toplak, 1986).
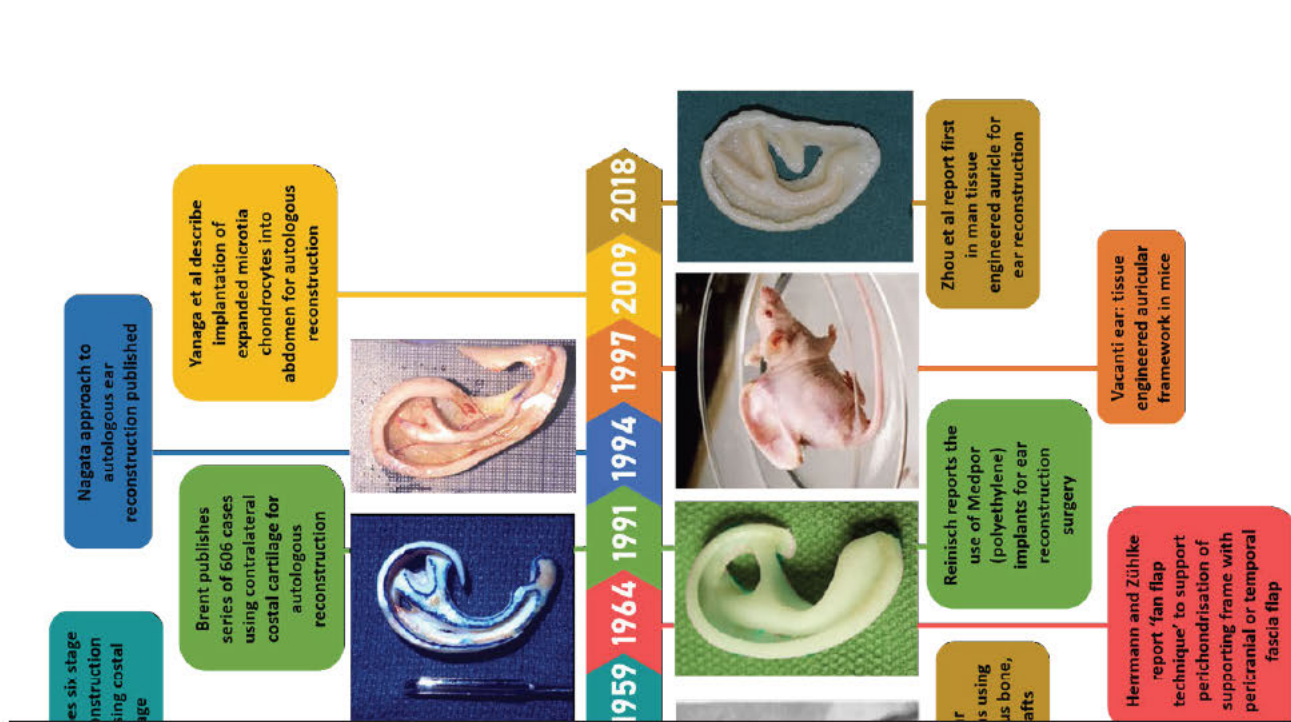
Figure 1.8: Timeline of major milestones in au[ricular reconstruction ...] BC to the present day. As published in Jovic et al, 2020.

### 1.4.2 Current approaches to auricular reconstruction

Contemporary reconstructive approaches use autologous, synthetic or prosthetic materials dependent on patient factors and the experience and preference of the surgeon (Figure 1.9). Modern auricular reconstruction was first described by Brent in 1992 (Brent *et al.*, 1992) and comprises the removal of rib cartilage of the 6th to 8th ribs. Rib 8 yields the helix, and the synchondrotic 6th and 7th rib produce the body of the auricle. The assembled framework was placed under skin with a silicon drain to apply vacuum to the pocket. In the 2nd stage, the earlobe was transposed, followed by a third stage to elevate the ear and a fourth stage to reconstruct the tragus using contralateral conchal cartilage.

Significant modifications to this approach were by Satoru Nagata (Nagata, 1994a, 1994b) and Francoise Firmin (Firmin, 2010). Nagata takes cartilage of ribs 6 to 9, leaving the perichondrium intact at the donor site. Crucially he divides the auricle into three layers: the base layer of the cymba and cavum conchae; the middle comprising the fossa triangularis and scapha and the top comprising the helix, antihelix, tragus and antitragus (Figure 1.1) (Nagata, 1994a). Any residual cartilage is diced, returned to the perichondrial pouch and after six months, the auricle is elevated using a graft from the fifth rib (Nagata, 1994b) and covered in a temporoparietal fascia (TPF) flap and a thin skin graft from the occipital scalp (Nagata, 1994b).

Firmin (Firmin, 2010) described a classification of skin approaches, framework classifications and methods of improving projection using projection pieces without the use of TPF flaps, minimising scarring in the temporal hair bearing area. This in part was due to the differences in the patients in Europe and South-East Asia. In the European population, ear prominence is deemed less desirable than in Asia, and hair is typically lighter and less dense, meaning the TPF flap is less suitable due to the scar burden.

The main alternatives to autologous reconstruction at present are synthetic materials such as Medpor®, Su-Por® and auricular prosthetics (Figure 1.9) (Lewin, 2015). Medpor® and Su-Por® are a prefabricated synthetic porous polyethylene mould customised to the shape of the auricle. The material is

placed under a temporoparietal fascia flap with skin graft coverage. This approach evades rib donor site morbidity, and can be done as a single-stage procedure at a younger age than autologous reconstruction (Reinisch and Tahiri, 2018). Despite the use of the TPF flap for implant coverage, a significant risk of extrusion remains (7%) (Reinisch and Lewin, 2009). Medpor® also conveys an increased risk of fracture, immune reactions and infection compared to autologous tissue (Constantine *et al.*, 2014) and does not possess the elasticity of native auricular cartilage.

In 1977 Branemark described an osseointegration approach for prosthesis retention (Parel *et al.*, 1986). Bone anchors enable magnetic bars to be affixed over the temporal skin linked to a prosthetic ear. The ability to replicate the shape, colour and dimensions of the contralateral ear using silicone is an attractive alternative for some patients in particular where adequate skin coverage is lacking (Thorne *et al.*, 2001). Limitations of this approach include that the patient must detach and reattach the prosthesis at regular intervals and the ear lacks many components of autologous auricular reconstruction such as temperature, texture and quality of actual human ear tissue (Thorne *et al.*, 2001).
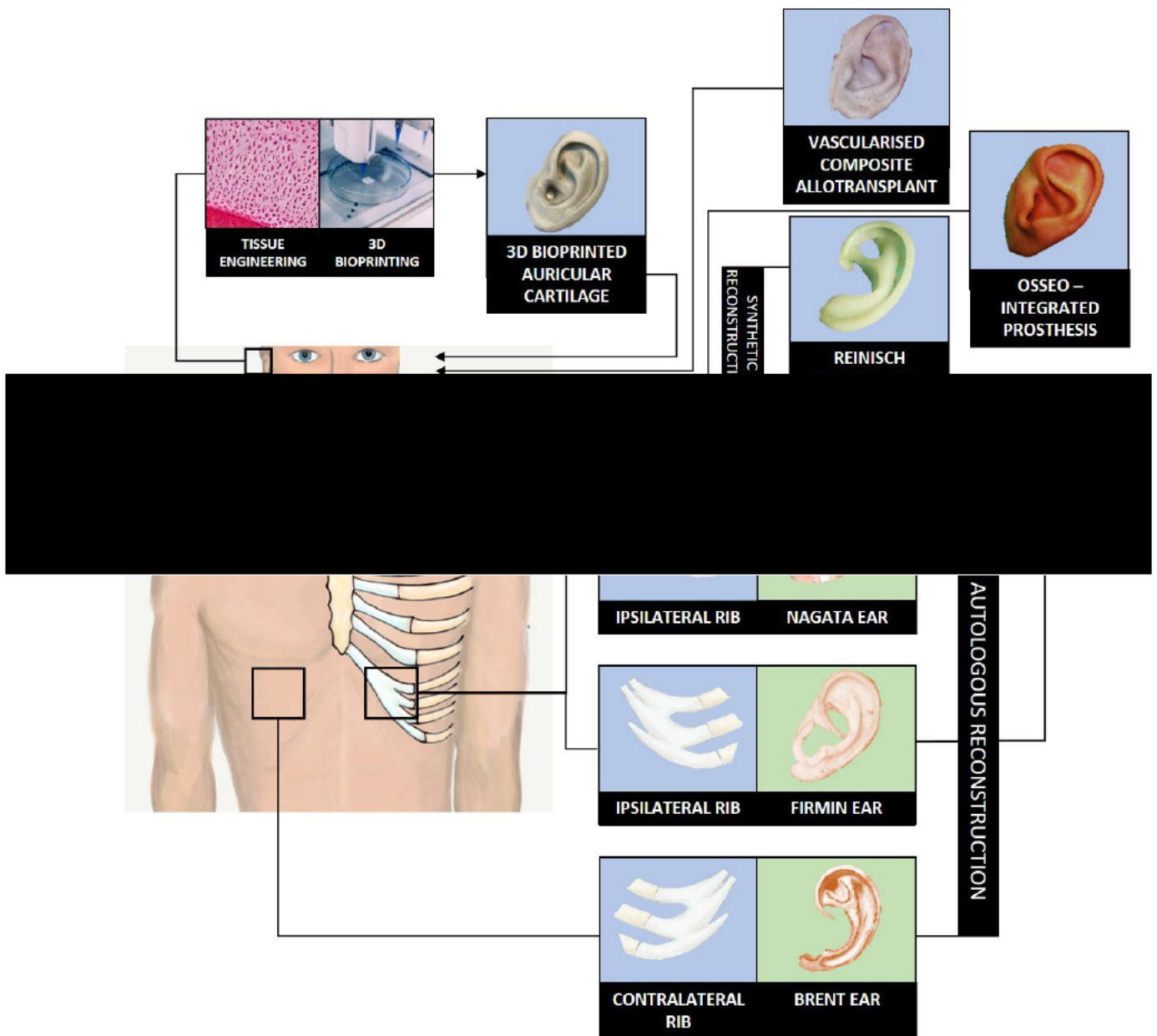
*Figure 1.9: Approaches to reconstruction of the external ear and the potential role of novel technologies such as tissue engineering. Current reconstructive options include prosthetics or synthetic reconstruction and autologous reconstruction of which there are three principle types in use. Future directions include Vascularised Composite Allotransplantation and 3D bioprinting. As published in (Jovic et al., 2020)*

### 1.4.3 Limitations of autologous ear reconstruction surgery

There is significant amount of cartilage required from the donor site in auricular reconstruction: particularly where Nagata's technique is used. Costochondral harvest may lead to donor site complications (Figure 1.10) (Ohara, Nakamura and Ohta, 1997; Wallace *et al.*, 2014) and often comprises two procedures,

55

six months apart to firstly create and then project the auricle (Nagata, 1994b). Both the act of removing autologous rib cartilage, and the length of the surgeries needed to carve a new auricular framework, present risks to patients, the most common being pain (6.92%) but the most severe being injury to the lung tissue (2.8%), resulting in a potential pneumothorax (Figure 1.10).
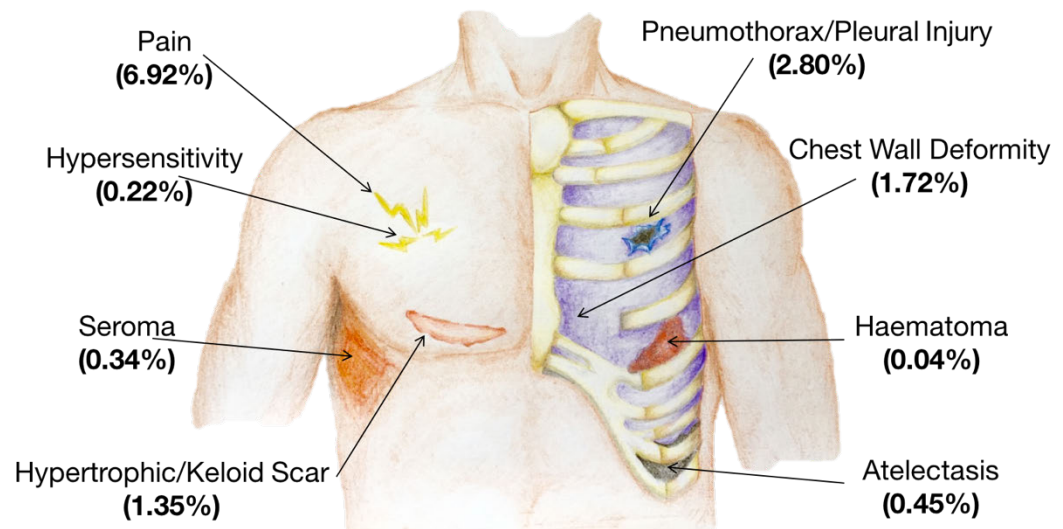


*Figure 1.10: Schematic to demonstrate complications of harvesting costochondral rib grafts for head and neck reconstruction and their reported frequencies from the available literature. Original image produced for a systematic review of donor site complications in costochondral rib harvest (unpublished).*

Post-operatively, the results may vary as a result of patient factors such as healing, scarring, skin and cartilage quality and in light of construct longevity owing to reabsorption and ossification of the cartilage grafts. Some also criticise the mechanical properties of rib cartilage, which although robust for reconstructive purposes, fails to emulate the elasticity of native auricular cartilage (Bos *et al.*, 2018).

### 1.4.4 Future directions in auricular reconstruction

Autologous ear reconstruction provides excellent results with minimal donor site morbidity for many patients (Stewart and Wikström, 2008). The ultimate ambition of reconstructive surgery would be to offer surgery without the need for donor sites. The two approaches by which this could be achieved are tissue engineering – in which 3D bioprinting is included, or Vascularised Composite Allotransplantation (VCA) (Figure 1.9).

Tissue engineering and 3D Printing have been highlighted as one of the Royal College of Surgeons 'Futures of Surgery' (Alderson, 2019) and one of the UK's '8 Great Technologies' (European Commission, 2013). Towards the end of the 20th century, the concept of bioengineering a human ear took the world by storm, sensationalised by the media through an iconic image of an ear on the back of a mouse in 1997. The ear comprised chondrocytes cultured in a polyglycolic acid scaffold, previously demonstrated to produce extracellular matrix and retain viability *in vitro* (Cao *et al.*, 1998). The images of the 'Vacanti mouse' portray a preserved three-dimensional structure *in vivo* (Langer and Vacanti, 1993) however the reality is that these ears collapsed and deformed upon removal of the supporting metal stents (Cao *et al.*, 1997).

This initial case summarises the paradigm of auricular bioengineering: there is copious public interest but an abundance of components to optimise prior to clinical translation. Construct degradation, calcification and instability impair most efforts to biofabricate auricular cartilage, along with immunological reactions including fibrosis and inflammation (Jessop *et al.*, 2016). There have only been two reported cases of clinical translation of bioengineered cartilage for ear reconstruction to date, neither of which directly use the technology of bioprinting.

Firstly, Yanaga et al (Yanaga *et al.*, 2009) expanded microtic auricular chondrocytes *in vitro*, to the point at which immature cartilage was formed. This cartilaginous mass was surgically implanted into the abdomen for six months, during which time it formed neocartilage and neoperichondrium. This cartilage was subsequently harvested from the abdomen and carved into an auricle as per conventional ear reconstructive practice (Yanaga *et al.*, 2009).

Secondly, the first clinical study of an *in vitro* engineered auricular cartilage was published in 2018 (Zhou *et al.*, 2018a). This study describes a 3D printed resin mould used to cast an auricular scaffold of polyglycolic acid, polylactic acid and polycaprolactone. Microtic cartilage remnants were used to isolate and expanded chondrocytes to seed onto the scaffold and mature over 12 weeks. This auricle was then implanted under an expanded skin flap for five patients. At 2.5 years follow-up, some of the implanted ears demonstrated histological appearances of cartilage formation and elastin production, but scaffold resorption and construct distortion occurred in two patients (40%) with no cartilage seen in one patient (20%) (Zhou *et al.*, 2018a).

3D bioprinting offers the advantage of controlled cellular and structural deposition, ultimately facilitating microscopic biological mimicry, whilst enabling control over the macroscopic structure of the construct by printing the 3D shape directly from patient images (Jessop *et al.*, 2015).

VCA has gained traction since the advent of facial transplantation and has potential to be an additional long-term, viable option for ear reconstruction, if in the first instance, the side effect profile of immunosuppressants can be improved (Whitaker *et al.*, 2008; Diaz-Siso *et al.*, 2018). VCA demands not only a need for antigenic matching, but aesthetic matching: variability in auricular size, skin tone and cartilage structure are so extensive, it has been considered a form of forensic identification (Purkait and Singh, 2008). Auricular replants have offered some insight into the approach and challenges that may underpin the feasibility of ear transplantation. Ensuring adequate blood supply is the primary operative challenge, and reports to date have used the posterior auricular artery and superficial temporal artery to achieve arterial inflow (Jung *et al.*, 2012), though venous congestion is as a major limiting factor (Jung *et al.*, 2012). Although donor selection and availability are issues in all transplantation cases, previous successful VCAs of the hand (Jones *et al.*, 2000) and face (Barret *et al.*, 2011) demonstrate that cosmesis is secondary to function in the hands whereas the appearance of soft tissue in the face is largely influenced by the patient's underlying bone structure.

## 1.5 3D Bioprinting in reconstructive surgery

### 1.5.1  The clinical need for 3D bioprinting

The clinical translation of 3D bioprinting technology has the potential to yield novel and personalised surgical options for patients (Li et al., 2017; Rana, Kumar and Ramalingam, 2017). As outlined above, the current gold standard approaches to reconstructing tissue defects such as the ear depend largely on the use of autologous tissue transfer to restore form and function, or the use of synthetic materials or prosthetics which lack the properties of native tissue. 3D bioprinting has the potential to obviate the need for tissue transplantation and to offer the restoration of form and function whilst lessening the burden of destructive, painful or disfiguring donor sites (Orlando et al., 2013).

Additional advantages of 3D bioprinting in surgery include the potential to replicate the anisotropy of biological tissues through tailoring structure at the macro- to nano-scale in order to optimise ECM composition, cellular interactions and topography. This could prove highly beneficial in reconstructive surgery, in particular where extensive or inaccessible donor sites are required (Jovic *et al.*, 2018). Specifically, in auricular reconstruction where costal cartilage harvest may limit construct formation and lead to donor site complications, 3D bioprinting could offer a more reliable and less disruptive option for patients.

### 1.5.2  Translational obstacles

Bioprinting combines cells, bioinks and bioprinters, of which, each presents a set of biological, technical and ethical challenges, in addition to questions surrounding clinical and cost-effectiveness (Gardner *et al.*, 2017). The main challenges associated with translation of 3D bioprinting into mainstream clinical practice are summarised in Figure 1.11.
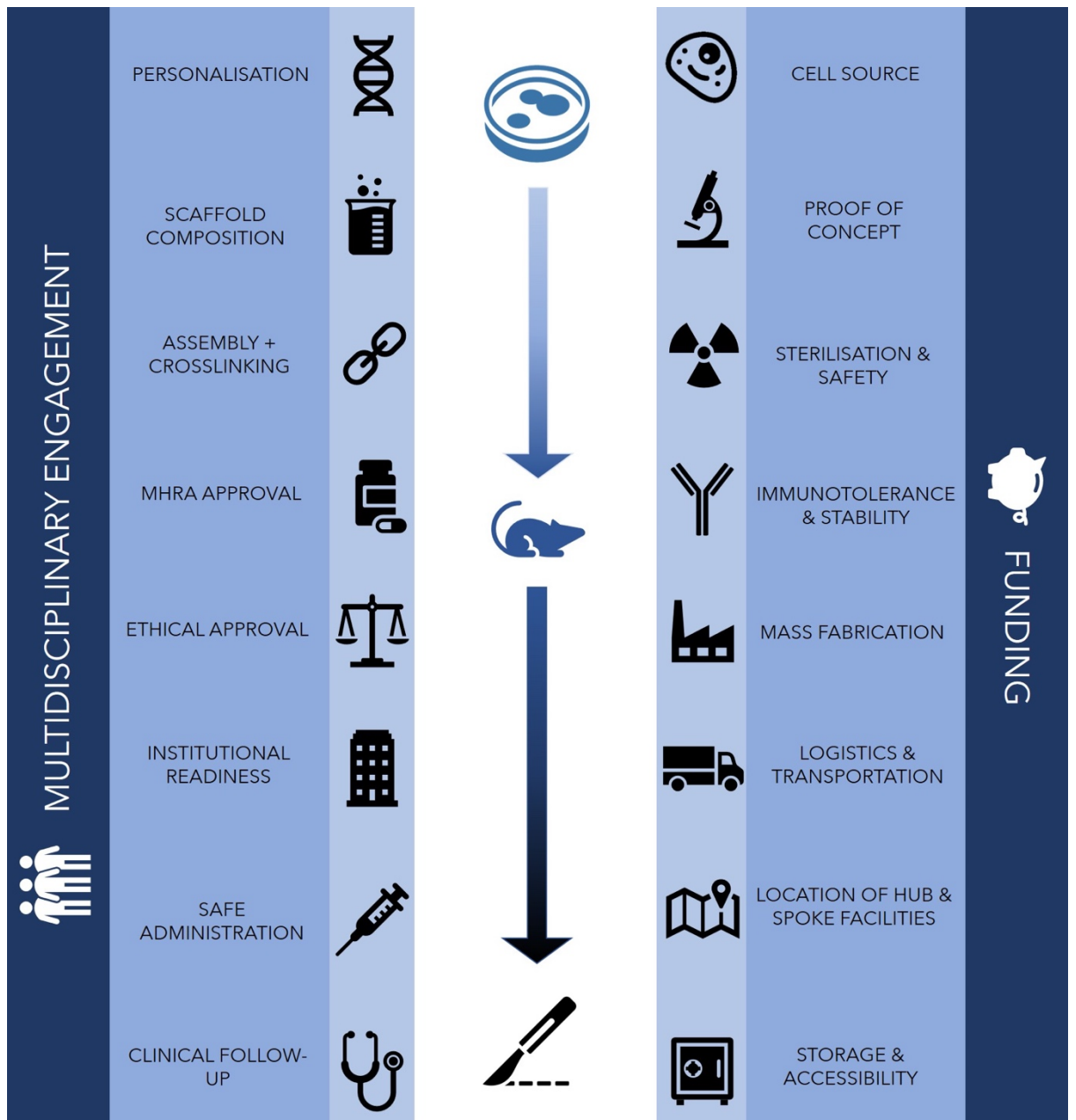
*Figure 1.11: Diagram depicting the key translational obstacles for 3D Bioprinted and Tissue engineered materials in order to progress to clinical translation (as published in (Jovic et al., 2020))*

### 1.5.2.1 Challenges of cell and tissue sourcing

In current clinical practice, cells and tissues may be acquired from the patient (autograft), donors (allograft) or from animal sources (xenograft) in the treatment of disease. When extrapolated to 3D bioprinting, each approach has its own advantages and caveats.

Animal sources are currently used for surgical procedures such as heart valve replacement and owing to their availability, are likely to enable greater mass production of tissue for surgical use. The main caveat of animal tissue is a risk of disease xenotransmission (Yoon *et al.*, 2015).

Cell and tissue derived from human subjects convey the advantages of increased biocompatibility and the possibility of autologous personalisation, but their use is likely to be fraught with tighter regulation, lengthier production times and higher costs. The anatomical inaccessibility of some cell types may render autologous cell sourcing a challenge for certain tissues. Similarly, if the tissue in question is defective owing to genetic diseases, cells harvested from this tissue may not be suitable for tissue engineering (Gilbert *et al.*, 2018). Due to limited clinical studies of tissue engineered constructs at present, the behaviour of autologous cells in tissue engineered constructs remains largely unknown. Introducing a biological component in the form of cells or tissue, makes implants more unpredictable when inserted into hosts than currently used implantable medical devices in the form of artificial joints, stents or pacemakers. Patient variability will affect processes such as cell migration, phenotypic behaviours, neoplastic potential and impaired differentiation: adipose derived stem cells producing ectopic bone is a recorded example of this phenomenon (Thirabanjasak, Tantiwongse and Thorner, 2010; Jabr, 2012). The formation of teratomas or neoplasia from the use of stem cells remains a significant concern: a human trial of induced pluripotent stem cells in Japan was terminated owing to the genetic mutations that occurred (Nakano-Okuno, Borah and Nakano, 2014; Kimbrel and Lanza, 2015). As discussed in Section 1.6.2, there has been significant heterogeneity in cell selection for cartilage tissue engineering, which may in part underpin successes and failures to date.

### 1.5.2.2 Regulatory challenges

An additional challenge is the regulation of tissue engineered and bioprinted products. Owing to the high levels of personalisation: biological and structural, bioprinted tissue is a 'custom made device'. Governing bodies worldwide such

as the Food and Drug Administration (FDA) are struggling to categorise the rapidly developing field of bioprinting, with currently unclear guidance and regulations for such technology (Gilbert *et al.*, 2018). The classification of complex and novel regenerative and gene medicinal products was expanded to include tissue engineered constructs which sought to define Advanced therapy medicinal products (ATMPs) (European Medicines Agency, 2016). These therapies are a distinct and novel set of therapies differing from those currently licenced and available on the European market (Carvalho, Martins and Sepodes, 2019). In an effort to standardise market availability within the European Union (EU) the European Commission (EC) established the ATMP Regulation (EC 1394/2007) alongside directive 2009/120 which created definitions for these novel technologies alongside marketing authorisation guidance (European Commission, 2007). Tissue engineered products are one of the four product types covered by the ATMP umbrella, but have shown limited progression in the last decade, with relatively few transitioning from bench to bedside. International regulation, and regional challenges regarding safety, scalability and production present challenges for both regulators and applicants. Currently, the majority of these innovations are being produced within academic institutions rather than commercial enterprises (Ferreira *et al.*, 2017). The EU regulatory committees recognise the challenges of these novel technologies and need for development of bespoke guidance as new challenges arise. In the UK, early engagement with the MHRA would ensure standards required for both clinical trials and commercial manufacture are adhered to. Outside of healthcare, advancements in 3D printing technology are exponential, with more affordable, efficient and compact systems emerging each year (Roots Analysis Private Limited, 2017). It has even been predicted that 3D printers may become commonplace household appliances, similar to conventional inkjet printers (Neely, 2016). With these ambitious aspirations, come fears of the power of such technology being widely accessible. Unregulated and personal use of such technology may facilitate bioterrorism (Mattox, 2013) and unregulated clinical practices, much like the current epidemic of unregulated injectables such as botulinum toxin and fillers (Browne *et al.*, 2021).

### 1.5.2.3 Ethical challenges

Designing clinical trials for 3D bioprinted products will be extremely challenging: a trial of tissue engineered organ transplantation on healthy volunteers would be unethical, and if a patient's own cellular material is used, the patient would need to act as their own control, presenting challenges in assessing treatment efficacy owing to the heterogeneity between participants (Gilbert *et al.*, 2018). A means of evaluating the effect of bioprinted interventions need to be defined for clinical trials in this area. In the UK, trials using tissue engineered material have been exclusively in patients with terminal disease: a 'last resort' option. This is usually considered 'more ethical', in the face of uncertain complications, an example of which is seeding a patient's mesenchymal stem cells on to a skeletonised cadaveric trachea (Macchiarini *et al.*, 2008). Here, ethical approval was granted as a 'last resort option' secondary to the patients' clinical urgency (Adams, Arruda and Larkin, 2012; Gardner and Webster, 2016), but resulted in uncontrolled and unethical practices (Delaere, 2013).

### 1.5.2.4 Technological and institutional challenges

The 'Technology Readiness Scale' (Mankins, 1995) is a useful means of mapping the pathway from conception to patient implementation, in particular understanding the challenges associated with widespread uptake of the technology (Figure 1.12). In the field of bioprinting, most technology exists in the Technology Readiness Level (TRL) 1-4 stages, with extensive research efforts involved in optimising cell and scaffold combinations and methods of 3D bioprinting, though a few groups have reported 3D bioprinted tissues such as vessels, bone, skin and cartilage in animal models (Jessop *et al.*, 2017) and even some traversing into human use (Probst *et al.*, 2010; Zhou *et al.*, 2018b). Institutional readiness is a concept describing the "capacity and willingness of organisations and inter-organisational structures to adopt, respond to and utilise novel technologies" (Gardner, Webster and Barry, 2018). In a healthcare setting, this encompasses logistical considerations such as Good Manufacturing Practice (GMP) licenced manufacturing, storage and

transport infrastructure, which may involve integration within the blood and transplant services owing to their expertise in handling tissues and preparing recipients for the receipt of tissues (Lowdell and Thomas, 2017; Gardner, Webster and Barry, 2018).
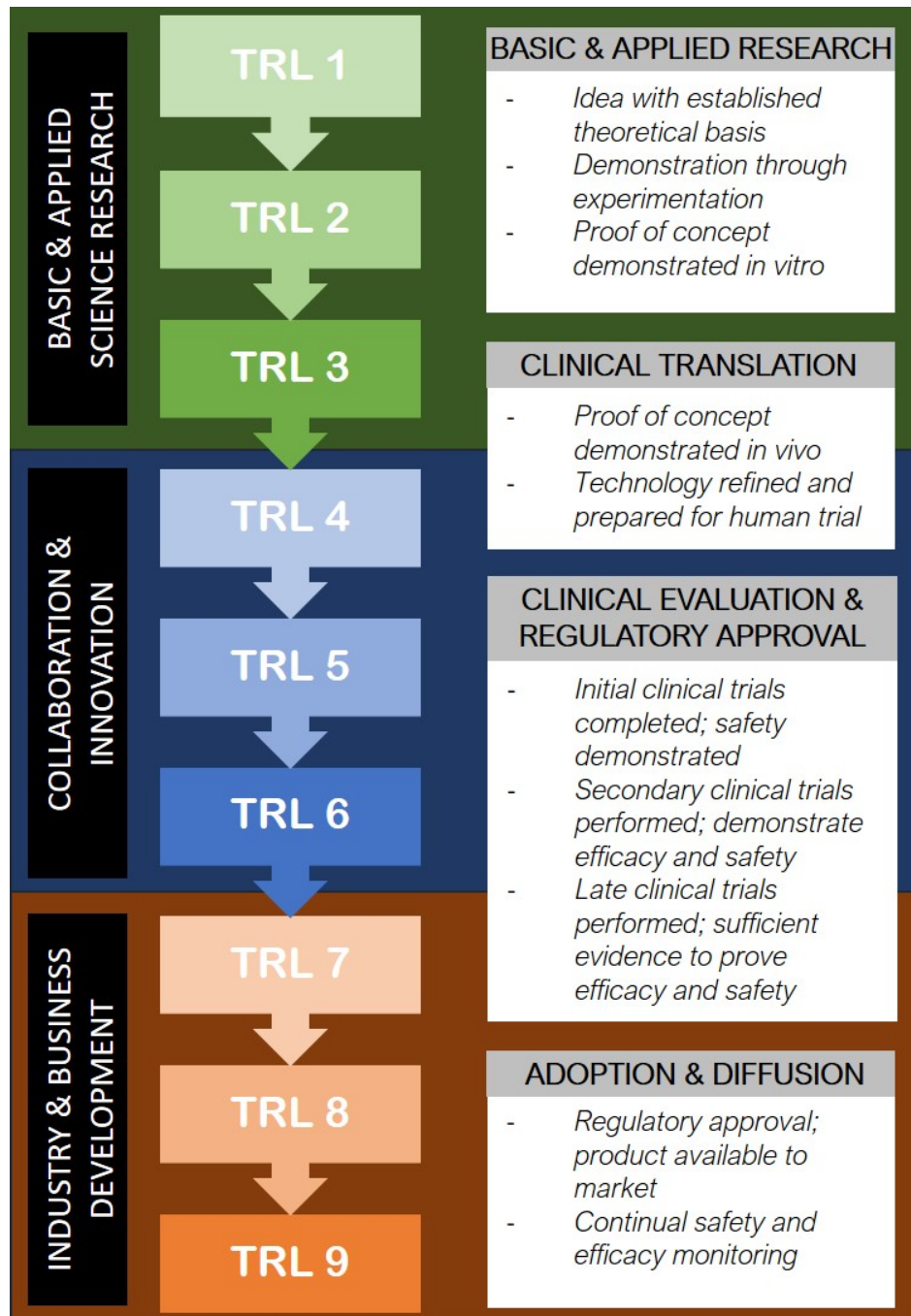


*Figure 1.12: Technology Readiness Level Scale for 3D Bioprinted tissues (as published in (Jovic et al., 2020)) demonstrating transition of technologies such as bioprinted tissue from basic science research to clinical trials and widespread clinical implementation.*

## 1.6 3D Bioprinting cartilage tissue

Cartilage is an ideal tissue to bioengineer as it is avascular, aneural and devoid of extensive cell-cell connections (Perera, Jaiswal and Khan, 2012). Research in this area has been a focus of translational regenerative medicine research, in particular due to the increasing burden of degenerative diseases like osteoarthritis in the ageing population (Vinatier and Guicheux, 2016) and the fact that cartilage becomes prone to ossification with age, becoming too stiff and brittle a material to reproduce the elastic function of nasal and auricular cartilage when harvested for use in reconstructive surgery (McCormick, 1980; Jovic *et al.*, 2018).

### 1.6.1 Principles of bioprinting

3D bioprinting is a rapidly evolving field, merging the allied disciplines of tissue engineering, materials science and 3D printing in the pursuit of customisable biological mimicry.

Bioprinting has its appeal in facilitating the precise placement of cells in a biomaterial using computer-aided designs and manufacture. This divergence from mainstream 3D printing to include biological components has increased demands on the technology to serve biological roles such as cell adhesion and proliferation in addition to the mechanical roles such as tissue support and durability (Thomas, Jessop and Whitaker, 2018). In contrast to 3D printing, some elements of the 3D bioprinting process must be refined to enable interaction with cellular material, including printing temperatures and mild, non-cytotoxic crosslinking methods to preserve cellular integrity (Malda *et al.*, 2013).

There are broadly four classes of 3D bioprinting technology: inkjet, laser-assisted, stereolithography and extrusion bioprinting (Table 1.3) (Agarwal *et al.*, 2020). Inkjet bioprinting typically uses low viscosity solutions, such as cell suspensions that are deposited at high shear rates as droplets of approximately 50 µm diameter (Hölzl *et al.*, 2016). In contrast, laser assisted bioprinting focuses a laser towards a laser-absorbing biomaterial layer which in turn produces a local pressure to enable ink deposition (Derakhshanfar *et*

*al.*, 2018). Stereolithography, typically involves a layer of photopolymer resin that is crosslinked through ultraviolet lasers in a layer-by-layer manner, enabling the formation of 3D structures (Grigoryan *et al.*, 2021). Extrusion based bioprinting, or bioplotting, is the most common type of bioprinting, and is essentially the deposition of cells embedded in a bioink through a nozzle driven by pneumatic, piston or screw forces (Landers *et al.*, 2002; Jakab *et al.*, 2008). This process may be slower than laser, stereolithography or inkjet bioprinting, but extrusion bioprinting conveys the advantages of tunability, good cell viability and the potential for multiple nozzles to incorporate different materials and cell types (Smith *et al.*, 2004; Derakhshanfar *et al.*, 2018).

| Bioprinting Technology | Key features | Ink Viscosity | Cell density | Cell viability | Pros | Cons |
|---|---|---|---|---|---|---|
| Inkjet-based | - Liquified droplets deposited onto solid platform<br>- Droplets must solidify before next layer added<br>- Droplet size 1-300 pL; rates 1-10000 droplets per second | 3.5 – 12 mPas/s | Low ($<10^6$ cells/ml) | >85% | - High printing speeds<br>- Cheap<br>- Readily available<br>- High resolution (adjustable to approx. 10 μm = one cell) | - Low viscosity liquid needed<br>- Heat ultrasound and shear stress may impair cell viability<br>- Risk of nozzle clogging with biomaterial use<br>- Low cell numbers only<br>- Finite printing height |
| Laser-based | - Uses laser pulse to heat and deposit energy-absorbing biomaterial<br>- Nozzle-free high precision deposition of cells and material | 1 – 300 mPa/s | Moderate ($<10^8$ cells/ml) | <85% | - Multiple cell types can be simultaneously deposited for composite tissue engineering<br>- Wide range of viscosities and cell laden solutions with high cell density can be printed | - Slow process<br>- Laser induced cell damage<br>- Low cell deposition accuracy<br>- Metal contamination<br>- Restrictive in use of suitable biomaterials |
| Extrusion based | - Materials deposited through a nozzle/syringe<br>- High, ambient and low temperature settings available | 30-6x10$^7$ mPa/s | High (cell spheroids) | ~90% | - Cheap<br>- Modifiable platform, nozzles and environmental controls permit large range of biomaterials<br>- High cell density and cell viability demonstrable<br>- Largely open access hardware and software | - Slower than other technologies<br>- High temperature settings may be unsuitable for cellular material |
| References | (Xiong et al., 2002; Wang et al., 2016; Thomas, Jessop and Whitaker, 2018) | (Bertassoni et al., 2014; Aljohani et al., 2018) | (Murphy and Atala, 2014; Mandrycky et al., 2016; Aljohani et al., 2018) | (Catros et al., 2010; Hopp et al., 2012; Mandrycky et al., 2016; Aljohani et al., 2018) | (Landers et al., 2002; Smith et al., 2004; Jakab et al., 2008; Schuurman et al., 2013; Murphy and Atala, 2014; Groll et al., 2016; Derakhshanfar et al., 2018) | |

*Table 1.3: Table outlining 3D Bioprinting technologies, their key features, cellular compatibility, advantages and disadvantages*

### 1.6.2 Cell selection

### 1.6.2.1    Stem cells for tissue engineering

Unsuccessful attempts to engineer tracheal tissue for human use has highlighted that merely combining stem cells derived from unrelated tissue types into a synthetic scaffold is insufficient to effectively regenerate cartilage (Delaere, 2013; Gonfiotti *et al.*, 2014). Successful tissue engineering demands that the optimum cell source is selected to ensure the bioengineered tissue emulates the form and function of the intended tissue (Jessop *et al.*, 2016). Stem cells: cells capable of differentiation and self-renewal offer obvious appeal for tissue engineering, promising the ability to populate scaffolds with numerous cells directed towards a target lineage. There is debate surrounding the optimum source of stem cells for cartilage tissue engineering: conflicting demands such as ease of access, potency and tissue specificity supporting arguments for one type over the other (Kuo *et al.*, 2006; Park and Cho, 2010). Stem cells are ranked according to potency: according to which totipotent cells are the only stem cells capable of producing all tissue types and are found exclusively in the early stages of embryogenesis, whereas pluripotent stem cells offer the capacity for differentiation down multiple diverse lineages. These are characteristic of embryonic stem cells after the cells have split down trophoblastic or somatic lineages however induced pluripotent stem cells: cells forced down a dedifferentiation pathway to acquire pluripotency are becoming increasingly explored as potential sources of stem cell (Medvedev, Shevchenko and Zakian, 2010). Less potent stem cells include those of multipotency such as bone marrow derived stem cells, comprising haematopoetic stem cells capable of yielding all mature lineages of blood cell and mesenchymal stem cells capable of generating adipose, cartilage and bone. Progenitor cells are generally considered to be multipotent, possessing the ability to replace and repair cells lost through age or injury (Dowthwaite *et al.*, 2004).

Where cartilage tissue engineering is concerned, commonly used cell sources have included induced pluripotent stem cells, bone marrow derived stem cells, adipose derived stem cells, chondroprogenitor cells and chondrocytes (Al-Himdani *et al.*, 2017). The advantages and drawbacks of each cell type are outlined in Table 1.4.

| Cell type | Advantages | Disadvantages | References |
|---|---|---|---|
| **iPSC** | Can use easily accessible cells<br>Potential to yield all cell types within tissue | Genetic instability<br>Immunogenicity<br>Low throughput | (Check Hayden, 2011; Zhao *et al.*, 2011; Gorecka *et al.*, 2019) |
| **ADSC** | Accessible, well-defined cell source<br>Large quantities available | Poor capacity for mature cartilage development | (Baptista *et al.*, 2013) |
| **BMSC** | Produce cartilage matrix when differentiated | High cell seeding density needed for chondrogenesis<br>Prone to hypertrophy and ossification<br>Requires growth factor supplementation to sustain chondrogenesis | (Afizah *et al.*, 2007; Koga *et al.*, 2008; Diekman *et al.*, 2010) |
| **CPC** | Produce cartilage without need for growth factors/cytokines in culture<br>Higher proliferation potential than terminally differentiated cells | Controversy surrounding their isolation and characterisation | (Baptista *et al.*, 2013; Vinod, Boopalan and Sathishkumar, 2018; Zita M. Jessop *et al.*, 2019) |
| **Chondrocytes** | Naturally produce appropriate cartilage tissue<br>Greatest tissue specificity | Restricted differentiation potential<br>Difficulty acquiring sufficient cells<br>Dedifferentiation | (Darling and Athanasiou, 2005; Hamada *et al.*, 2013) |

*Table 1.4: Table outlining the commonly used cell sources for cartilage tissue engineering, and their advantages and disadvantages. IPSC = Induced Pluripotent Stem Cell; ADSC = Adipose Derived Stem Cell; BMSC = Bone Marrow Derived Stem Cell; CPC = Chondroprogenitor Cell.*

### 1.6.2.2 Cartilage-specific stem/progenitor cells

First described in articular cartilage, cartilage specific stem cells have now been isolated from cartilage tissue of the intervertebral disks, auricle, nasoseptum, trachea and costal cartilages (Jessop *et al.*, 2019). Believed to have a key role in mediating tissue homeostasis, this elusive stem cell population has been speculated to possess the properties of a mesenchymal stem cell as defined by the International Society of Cellular Therapy (Dominici *et al.*, 2006):

- Plastic adherence in standard culture conditions
- Expression of CD105, CD73, CD90
- No expression of CD45, CD34, CD14 or 11b, CD79α or CD19, HLA-DR
- Differentiation into osteoblasts, adipocytes and chondrocytes in vitro

A number of different techniques have been described regarding chondroprogenitor isolation, with some studies adopting flow cytometric cell sorting based on key surface markers (Hattori, Oxford and Reddi, 2007; Grogan *et al.*, 2009), some using fibronectin adherence (Dowthwaite *et al.*, 2004; Anderson *et al.*, 2018; Jessop *et al.*, 2020) and others identifying migratory cells from perichondrial tissue where the stem cells were thought most likely to be located (Koelling *et al.*, 2009; Seol *et al.*, 2012). Irrespective of the methods of isolation, most of the chondroprogenitor cells isolated from cartilage tissue express comparable cell surface markers: CD90, 105, 44, 166, 73 and 29 plus an absence of CD34 and 45 expression (Jessop *et al.*, 2019). The exception to this pattern was found to be intervertebral disks which arise from different embryological origins: the primitive notochord (Risbud and Shapiro, 2011). Additionally, most of the chondroprogenitor cells isolated demonstrate multi-lineage potential, in particular down osteogenic as well as chondrogenic lineages and to a lesser reported degree, adipogenic lineages (Jessop *et al.*, 2019).

Despite these behaviours and overlapping characteristics with mesenchymal stem cells, there has been some controversy about the behaviour of the proposed chondroprogenitor population, the reliability of the fibronectin assay in isolating said population and the distinction between chondroprogenitor cells and cells that have simply dedifferentiated in culture conditions (Vinod, Boopalan and Sathishkumar, 2018; Vinod *et al.*, 2020, 2021). Furthermore, there is some

evidence to suggest that mixing stem cells (such as mesenchymal stem cells (Cohen *et al.*, 2018) or ADSCs (Xie *et al.*, 2012) with chondrocytes would yield superior bioengineered cartilage, offering better mimicry of the mixture of cells *in vivo*.

### 1.6.3  Biological inks

A major challenge in bioprinting research, in particular where clinical translation is the end goal, is the pursuit of appropriate, biocompatible materials to serve as bioinks (Malkoc, 2018). Historically, a variety of materials have contributed towards the advancement of biomedicine, with the most noteworthy candidates including alloys, ceramics, metals and composites (Le May, Lappi and White, 1975). Although the desired properties for biomedical application may vary between materials, the fundamental requirements for *in-vivo* implementation remain universal. Successful tissue engineering demands that an optimal scaffold should interface with biological systems to support cell growth whilst displaying biocompatibility, non-toxicity and providing the mechanical support to emulate natural tissue macro and microarchitecture (Drury and Mooney, 2003; Gungor-Ozkerim *et al.*, 2018). The requirement to refine a biomaterial into a bioink places additional demands on the criteria for candidate biomaterials. Mechanically, the material must enable extrusion as a liquid bioink through a thin nozzle (shear thinning) and yet be capable of maintaining its shape in the post-printing phase (elasticity) to yield viable tissues, organs and biological materials. Biologically, the material should be cytocompatible, encourage differentiation into the intended tissue type and be non-toxic *in vivo* (Drury and Mooney, 2003; Gungor-Ozkerim *et al.*, 2018). Kyle *et al* further delineated the properties of an ideal bioink to include the following (Kyle *et al.*, 2017):

- Ability to maintain post-printing shape fidelity
- Tunable gelation to enable extrusion
- Mimicry of the native cellular microenvironment
- Biocompatibility
- Amenable to chemical modification or functionalisation
- Consistency in large scale synthesis

Often these demands on a material are conflicting (Chimene *et al.*, 2016), and the needs on a biomaterial have been summarised as the 'biofabrication window': an ideal balance struck between shape fidelity and polymer stiffness and the ability for cells to migrate, grow and differentiate (Malda *et al.*, 2013). This paradigm is visually depicted in Figure 1.13.
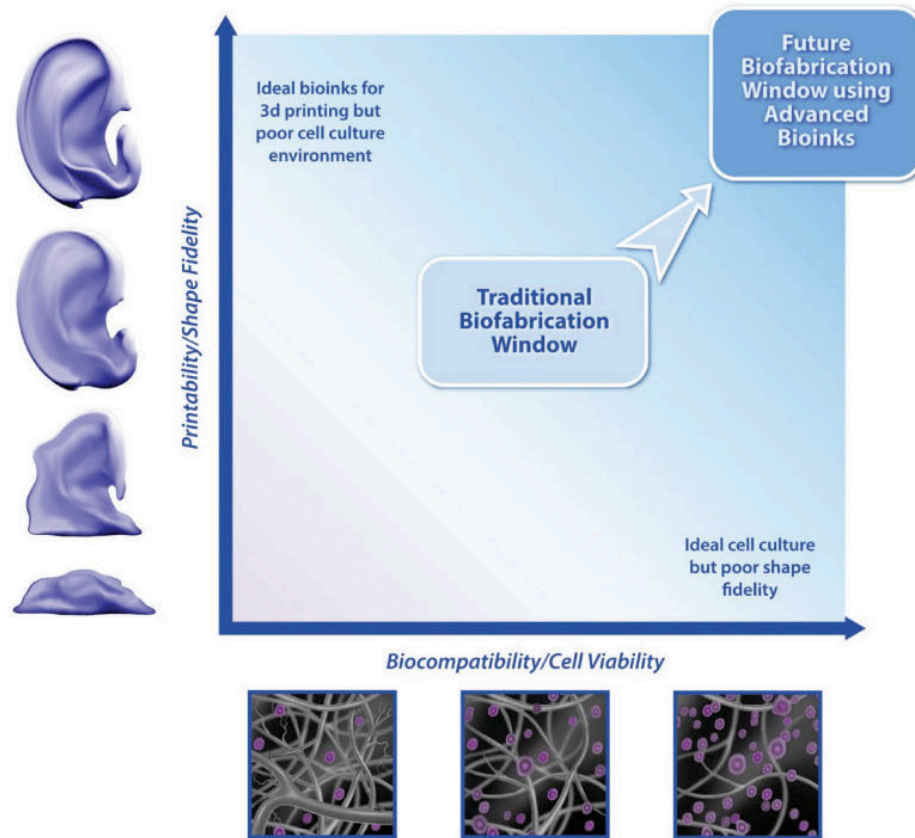
*Figure 1.13: The Biofabrication Window. A paradigm shift has seen more conventional biomaterials in which there is compromise between shape fidelity and biocompatibility being superseded by more printable and biocompatible materials. From (Kyle et al., 2017) with permission.*

As such, the practice of blending multiple biomaterials together to achieve the desired properties is commonplace, but as such yields an enormous range of potential bioinks that warrant exploration (Tarassoli *et al.*, 2021).

### 1.6.3.1 Synthetic and natural polymers for extrusion bioprinting

Synthetic materials such as plastic offer greater tunability in structural properties and the potential to convey predictable printability and stiffness behaviours, albeit at the expense of biocompatibility: cell adhesion and extracellular mimicry are usually more of a challenge (O'Brien, 2011). An additional limitation of synthetic materials is their degradation profiles, which convey a risk of extrusion, immunogenicity, and impedance of *de novo* tissue formation (Sarkar, Xue and

Sant, 2017). Degradation itself may release toxic by-products, presenting a risk of harm when implanted into humans (Athanasiou, Niederauer and Agrawal, 1996).

In light of these limitations, there has been an increasing shift towards the pursuit of natural materials, offering the advantages of reduced ecological and environmental burden, enhanced bioactivity, biodegradability, stability and cell interactivity (Gershlak *et al.*, 2017; Yegappan *et al.*, 2018; Jovic *et al.*, 2019). These materials also offer the advantages of facile hydrogel formation and an affinity for chemical modification to enhance crosslinking behaviours (Jovic *et al.*, 2019).
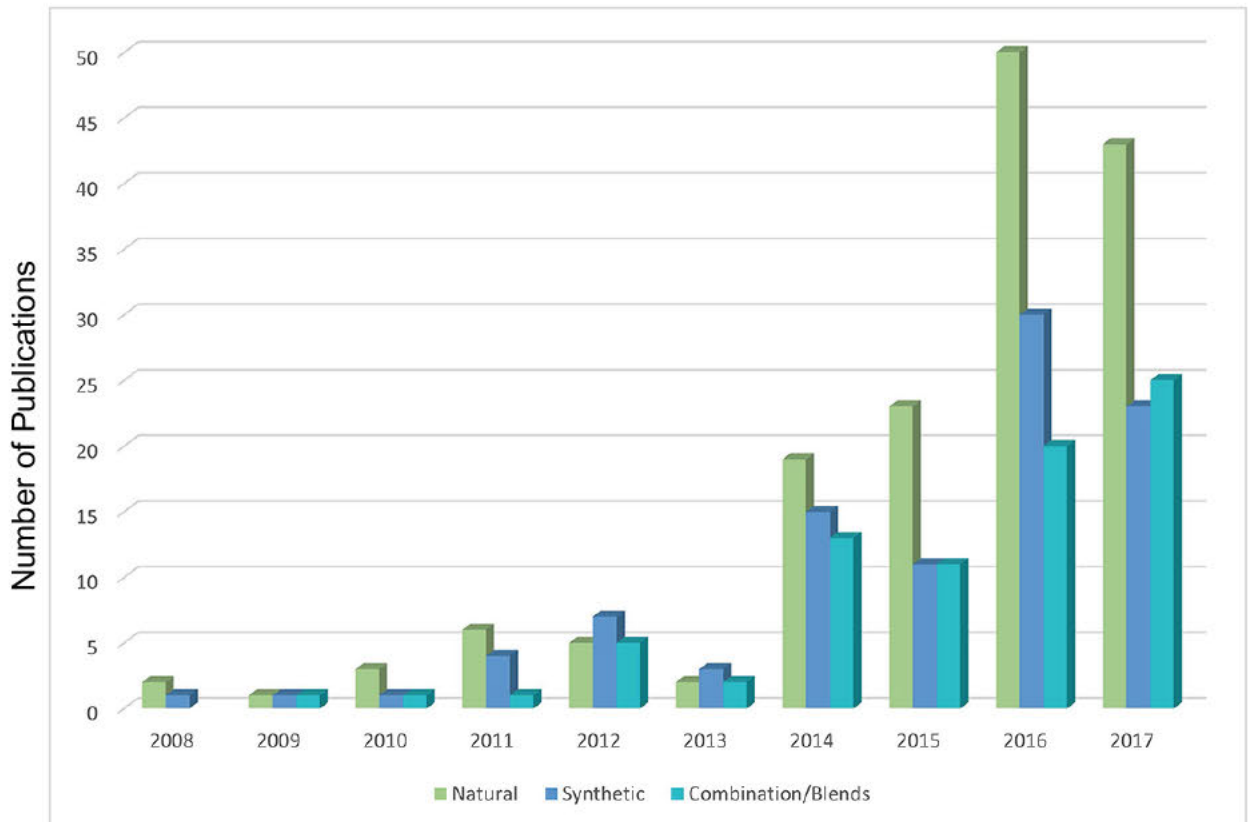


*Figure 1.14: Natural, synthetic and combination/blend materials used for extrusion bioprinting classified according to year of publication. Natural biomaterials are becoming the dominant bioinks of research interest. From previously published work (Tarassoli et al., 2021)*

Within each class of biomaterial, there are certain materials that have dominated research, the most commonly researched synthetic material being polycaprolactone (PCL), followed by polylactic acid (PLA) and polyethylene glycol diacrylate (PEGDA) whereas the most common natural material is alginate, followed by gelatin/ gelatin methacrylate (Figure 1.15). With regard to cartilage tissue engineering specifically, alginate and gelatin composite bioinks are the most popular materials investigated for 3D bioprinting, demonstrating a shift towards natural materials for bioengineering this tissue type (Tarassoli *et al.*, 2021).

### 1.6.3.2 Natural materials for 3D bioprinting cartilage tissue

The topography and architecture of natural scaffolds determines the cell-biomaterial interactions and consequently influences cellular behaviour (Jorfi and Foster, 2015). A range of natural materials have been explored for cartilage extrusion bioprinting and encompasses materials from plants, algae, bacterially synthesised, marine and animal products (Tarassoli *et al.*, 2021). The advantages and limitations of natural bioinks identified in (Tarassoli *et al.*, 2021) are further explored in Table 1.5.

Whilst many natural bioinks offer the advantages of cytocompatibility and biocompatibility, Table 1.5 highlights that many of the shortcomings of these materials lie in their structural and printability properties, consistent with the previously described biofabrication window (Figure 1.13). In order to surpass these limitations, interest in plant derived biomaterials has sought to address this conflict: namely land plants and marine algae such as seaweed have been explored for a variety of biomedical applications (Figure 1.16), harnessing the structural benefits of plant matter coupled to their natural biological interactions with eukaryotic cells (Jovic *et al.*, 2019).
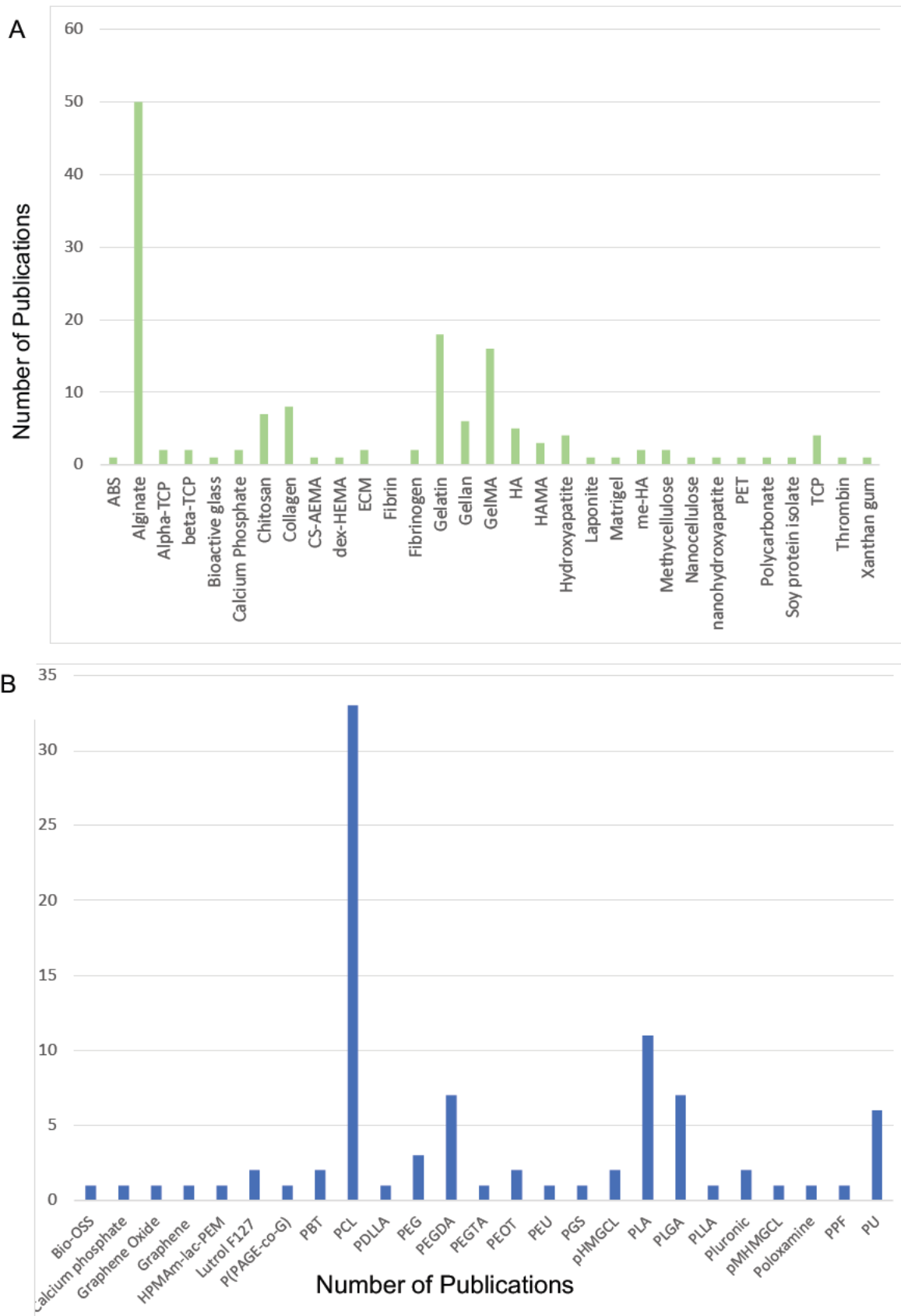
*Figure 1.15: Numbers of research papers focussing on the development or use of natural (A) and synthetic (B) materials for extrusion-based 3D bioprinting. As published previously in (Tarassoli et al., 2021)*

| Material | Source | Advantages | Disadvantages | References |
|----------|--------|------------|---------------|------------|
| **Alginate** | Algae | • Extensively researched<br>• Biocompatible<br>• Low cost | • Poor printability<br>• Low stability post-crosslinking<br>• Restricts cell migration | (Jovic *et al.*, 2019) |
| **Chitosan** | Marine | • Naturally anti-microbial<br>• Polycationic<br>• Affinity for modification | • Weak mechanical strength<br>• Poor rheological properties | (Ye *et al.*, 2014; Li *et al.*, 2019) |
| **Collagen** | Marine, animal | • Extracellular matrix mimicry<br>• High biocompatibility | • Rapid *in vivo* hydrolysis<br>• High production cost<br>• Poor printability and mechanical properties | (Osidak *et al.*, 2020) |
| **Fibrin** | Animal blood | • Rapid physiological crosslinking<br>• Cell adherence | • Rapid degradation<br>• Limited printability<br>• Weak mechanical properties | (Shpichka *et al.*, 2020) |
| **Gelatin** | Animal | • Functionalisation with methacrylate<br>• ECM mimicry | • Thermosensitive<br>• Poor printability properties | (Van Hoorick *et al.*, 2019) |
| **Hyaluronic acid** | Animal, microbial | • ECM component<br>• Biocompatible<br>• Modifiable for crosslinking<br>• Reasonable rheological properties | • Degradation *in vivo*<br>• Poor post-printing fidelity | (Petta *et al.*, 2020) |
| **Nanocellulose** | Plant, microbial | • ECM mimicry<br>• Excellent rheology and printability<br>• Biocompatible | • High production cost (especially bacterial)<br>• Often blended with other materials for crosslinking | (Wang, Wang and Xu, 2020) |

*Table 1.5: Natural bioinks used in 3D printing cartilage tissue, their sources, advantages and disadvantages.*

### 1.6.3.3        Plant-derived materials for 3D bioprinting

Plant derived biomaterials have been explored as bioinks in their pure form (Figure 1.16) but more commonly as blended or composite scaffolds, with evidence of 3D bioprinting blood vessels, bone, cartilage and skeletal muscle (Table 1.6). As with natural bioinks, there are some limitations of plant derived biomaterials that pertain to structural and printability characteristics, for example, nanocellulose is hindered by poor cross-linking potential, whereas alginate alone has only a moderate affinity for cell-adhesion or proliferation (Lee and Mooney, 2012). Nanocellulose and alginate are the most explored materials for the purposes of cartilage tissue engineering, and are commonly combined with materials that augment the desired characteristics for enhanced 3D bioprinting (Jovic *et al.*, 2019).
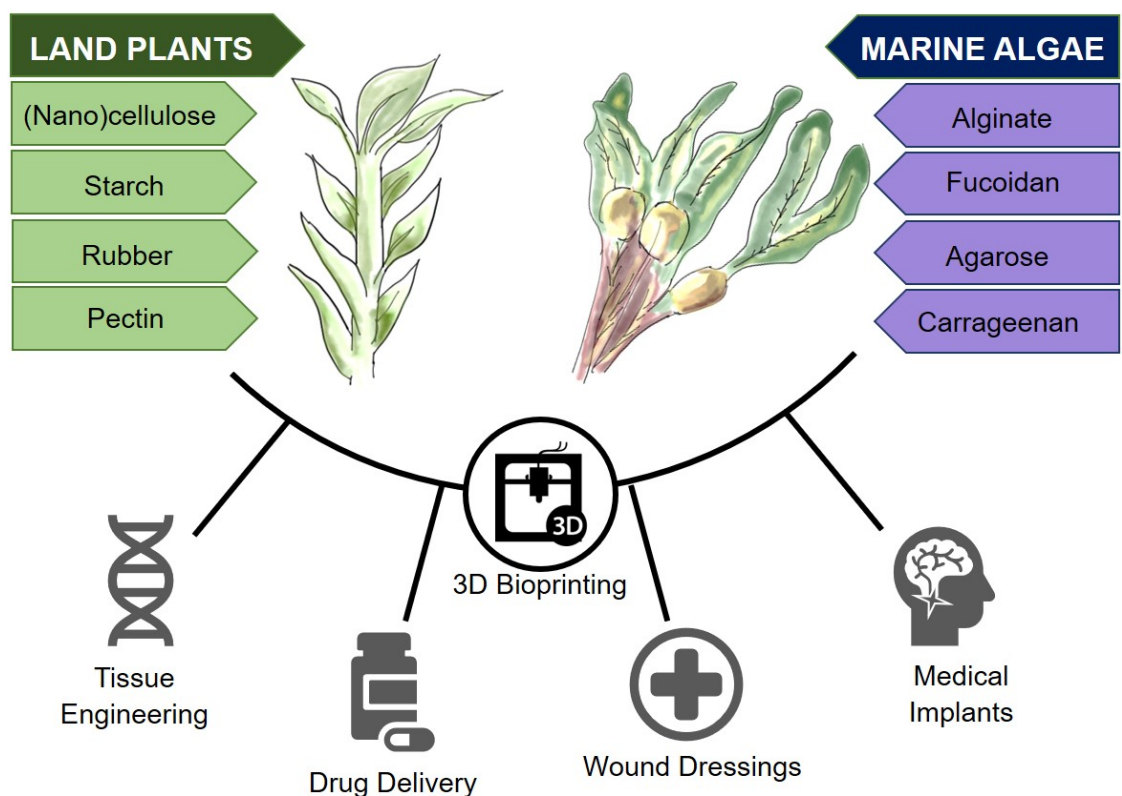


*Figure 1.16: Plant-derived biomaterials of land and marine sources and their role in biomedical applications and 3D bioprinting*

Other plant derived materials such as agarose and carrageenan have also been used for cartilage bioprinting purposes but in a limited number of studies to date

(Table 1.6). Agarose is a red seaweed derivative capable of thermoreversible gelling in the absence of any crosslinking chemicals or additives (Zarrintaj *et al.*, 2018). Its mechanical properties when crosslinked are limiting factors of its use, which is weakened further following the addition of cells owing to disrupted hydrogen bonding (Shoichet *et al.*, 1996; Ahearne *et al.*, 2005). Carrageenan is another seaweed derivative capable of thermal and ionic crosslinking, and displaying extracellular matrix mimicry that may render it suitable for cartilage bioprinting (Bakarich *et al.*, 2014; Popa *et al.*, 2015) however there are some concerns about its biocompatibility that require further clarification if the intended use is ultimately clinical (McKim, 2014).

| Material | Reported Viscosities | Mechanical Properties | Printing methods used | Tissue engineering applications | References |
|---|---|---|---|---|---|
| *Alginate* | 300-30000 mPas<br>2% w/v = 0.9 Pa.s<br>3% w/v = 2 Pa.s<br>5% w/v = 6.4 Pa.s | Young's modulus 12.9 MPa Tensile strength 25.8mPa | Extrusion | • Bone<br>• Cartilage<br>• Cardiac<br>• Muscle<br>• Neural<br>• Skin<br>• Vasculature | (Malda *et al.*, 2013)(He *et al.*, 2016; Zhu *et al.*, 2018)(Park *et al.*, 2018)(Daly *et al.*, 2016)(Duan *et al.*, 2013; Dolati *et al.*, 2014; Kundu *et al.*, 2015; Markstedt *et al.*, 2015a; Wenyan Li *et al.*, 2015; Zhang *et al.*, 2015; Ansari *et al.*, 2016; Nishimura *et al.*, 2018; Solovieva *et al.*, 2018) |
| *Nanocellulose* | Measurements recorded for shear rates $10^{-1} - 10^{3}$ $(s^{-1})$ at temperature 25 °C.<br><br>CNF (Concentration 0.7 wt%): 100 - > 10000 mPas<br><br>CNC (Concentration 1 wt%): 10 – 100 mPas | Young's modulus 167.5 GPa | Extrusion | • Bone<br>• Cartilage<br>• Adipose<br>• Hepatic<br>• Vasculature<br>• Neural | (Rees *et al.*, 2015; Moberg *et al.*, 2017)(Bhattacharya *et al.*, 2012; Lou *et al.*, 2014; Malinen *et al.*, 2014; Markstedt *et al.*, 2015a; Torres-Rendon *et al.*, 2015; Weichang Li *et al.*, 2015; Toivonen *et al.*, 2016; Ao *et al.*, 2017; Gorgieva, Girandon and Kokol, 2017; Kuzmenko *et al.*, 2018) |
| *Agarose* | >257 mPas as 4% solution | Young's modulus 5.6Kpa to 3000kPa Tensile strength ~31MPa | Inkjet | • Cartilage<br>• Mesenchymal stem cells<br>• Gastrointestinal<br>• Neural | (Balgude *et al.*, 2001; Chen, Suki and An, 2003; Ahearne *et al.*, 2005; Lewitus *et al.*, 2011; Walker *et al.*, 2011; Bhatnagar, Simon and Rafailovich, 2016; Fan *et al.*, 2016; Gu *et al.*, 2016; Forget *et al.*, 2017; Zarrintaj *et al.*, 2018; Benning *et al.*, 2018) |
| *Carrageenan* | 1.5% w/v at 75 °C: 5-800 mPa.s | Young's modulus 0.1-0.66MPa Tensile strength 39.34 MPa | Extrusion | • Bone<br>• Cartilage | (Iglauer *et al.*, 2011; Rhim, 2012; In, Naguib and Haider, 2014; J. Li *et al.*, 2015; Popa *et al.*, 2015; Cunha and Grenha, 2016; Feng *et al.*, 2017; |

| | | | | | |
|---|---|---|---|---|---|
| | | | | | Kelder *et al.*, 2018; Diañez *et al.*, 2019) |
| *Starch* | Measurements recorded at shear rates 0.1 – 100 (s$^{-1}$) at temperatures 70 °C (Potato Starch), 75 °C (Corn Starch) & 80 °C (Rice Starch).<br><br>Potato Starch (5 – 30%, w/w): 10 – 10000 Pa.s<br>Corn Starch (5 – 30%, w/w): 1 – 10000 Pa.s<br>Rice Starch (5 – 30% w/w): 1 – 100000 Pa.s | Tensile strength 2.26 MPa Young's modulus 25.4 MPa | Extrusion | • Bone | (Gomes *et al.*, 2002; Salgado, Coutinho and Reis, 2004; Martins *et al.*, 2009; de Moraes, Müller and Laurindo, 2012; Chen *et al.*, 2019) |
| *Pectin* | At room temperature, 1.5 w/v%:<br><br>Pectin + CaCl$_2$ (0 Mm): < 0.01 Pas<br>Pectin + CaCl$_2$ (1 Mm): 0.01 – 0.1 Pas<br>Pectin + CaCl$_2$ (3 Mm): 0.01 – 1 Pas<br>Pectin + CaCl$_2$ (5 Mm): 0.01 – 10 Pas | Tensile strength 0.5 MPa Young's Modulus 6 – 100 KPa | Extrusion | • Bone<br>• Skin | (Mishra, Datt and Banthia, 2008; Coimbra *et al.*, 2011; Markov *et al.*, 2017; Pereira, Barrias, *et al.*, 2018; Pereira, Sousa, *et al.*, 2018; Türkkan *et al.*, 2018) |
| *Fucoidan* | As a 0.25% - 2% w/v solution:<br>1.8 – 34.8 mPa.s | n/a | n/a | • Bone<br>• Vasculature | (Thébaud *et al.*, 2007; Park *et al.*, 2012; Jeong, Venkatesan and Kim, 2013; Venkatesan, Bhatnagar and Kim, 2014; Monsur *et al.*, 2016) |

*Table 1.6: Plant-derived biomaterials used in 3D Bioprinting, their printability characteristics and tissue engineering applications. As published in (Jovic et al., 2019)*

### 1.6.3.3.1 Nanocellulose

There are three main types of nanocellulose used in biomedical applications: nanocellulose crystals (NCC), nanocellulose fibrils (NCF) and bacterial cellulose. The plant-derived NCC and NCF are commonly extracted from natural biomass such as wood, hemp, cotton, potato tuber and algae (Lin and Dufresne, 2014) using acidic hydrolysis processes: a top-down approach that typically separates the crystals and fibrils out during the extraction process (Phanthong *et al.*, 2018). The extraction process is not necessarily 'clean' and may include other plant matter such as hemicelluloses, xylan and lignin as by-products of extraction (Jovic *et al.*, 2019). Bacterial cellulose is produced using a bottom-up approach in which a more pure nanocellulose is produced, although structurally the fibres sizes are far greater than that achieved through plant-derived extraction processes and this process may attract significant processing costs (Thomas *et al.*, 2020).

Nanocellulose is an abundant natural polymer, with low degradation and toxicity yet excellent mechanical strength making it a desirable material for cartilage tissue engineering (Lin and Dufresne, 2014). Nanocellulose is arranged into a hierarchy of polymeric cellulose chains (~1 nm) that combine into fibrillar structures of approximately 5-20 µm in diameter and highly organised crystalline regions with alternating amorphous domains (Gumrah Dumanli, 2017). These components influence the mechanical behaviour of cellulose, with the disordered (amorphous) regions providing flexibility and plasticity and the ordered (crystalline) fraction yielding the strength and elasticity of the material (Lin and Dufresne, 2014).

This material has attracted attention in the realm of 3D bioprinting owing to its unique balance of extracellular matrix mimicry and unrivalled shear thinning behaviour, making it a promising candidate for 3D bioprinting cartilage tissue (Markstedt *et al.*, 2015a; Martínez Ávila *et al.*, 2015; Müller *et al.*, 2017)

### 1.6.3.3.2 Alginate

Alginate is the most commonly used natural hydrogel in 3D bioprinting (Tarassoli *et al.*, 2021) and derived from brown algae (Lee and Mooney, 2012). Structurally, this material comprises polymers of the polysaccharides β-D-Mannuronic acid and α-L-Gluloronic acid arranged in residues that confer rigidity, gelation and flexibility (Axpe and Oyen, 2016; Stößlein *et al.*, 2019). Similarly to nanocellulose, alginate is typically acquired using acidic hydrolysis to yield alginic acid, precipitated as a sodium or calcium salt (Fawzy *et al.*, 2017). Their appeal for cell encapsulation arises from their facile hydration into hydrogel suspensions and readiness to crosslink in the presence of divalent cations (Wee and Gombotz, 1998). Crosslinked alginate can add structural strength to bioinks making it an attractive material for cartilage tissue engineering purposes (Park *et al.*, 2018), however its printability characteristics prior to crosslinking are hindered by its viscosity and subsequent poor post-printing shape fidelity (Axpe and Oyen, 2016).

### 1.6.4 Assessing the printability of bioinks

Printability is a term used to describe the suitability of biological inks for extrusion bioprinting processes which according to Kyle et al, can be divided into the following key components (Kyle *et al.*, 2017):

- Rheological properties
- Bioink composition, concentration and crosslinking
- Grid geometry
- Ability to print angles

These key characteristics underpin many of the tests that are performed on candidate biomaterials to determine their potential and suitability for extrusion 3D bioprinting: to become a valid bioink.

### 1.6.4.1     Rheology

Rheology is the study of flow of matter and offers important information about the properties of a candidate bioink in its uncrosslinked hydrogel phase. Specifically,

materials should demonstrate shear thinning or 'pseudoplastic' behaviour: a reduction in viscosity when placed under shear strain. This property ensures that the biomaterial will flow through an extrusion printer nozzle when the extrusion pressure is applied (Paxton *et al.*, 2017).

Other important properties are the storage and loss modulus of the bioinks. These characterise the dominance of viscous and elastic components of the bioink. Ideally, there should be a dominance of elasticity to ensure that after printing, the material is able to 'recover' from the printing process and is able to retain its shape in the intended design, however cells prefer viscosity to enable growth in the low pressure environment, so a delicate balance must be struck (Khatiwala *et al.*, 2013; Kyle *et al.*, 2017; Paxton *et al.*, 2017).

### 1.6.4.2 Gelation

Gelation is a multifactorial feature of bioinks that reflects its composition, concentration and also its ability to be crosslinked post-printing. The degree of gelation has an effect on how the bioinks are extruded from a printer and how the printed filaments behave after printing (Kyle *et al.*, 2017). Under-gelation of the bioink causes the ink to pool as a droplet rather than a long filament, and upon deposition, the filaments may converge and lose fidelity (Figure 1.17). Over-gelation causes the filaments to extrude in a non-linear fashion and deposit as uneven filaments post-printing (Ouyang *et al.*, 2016).
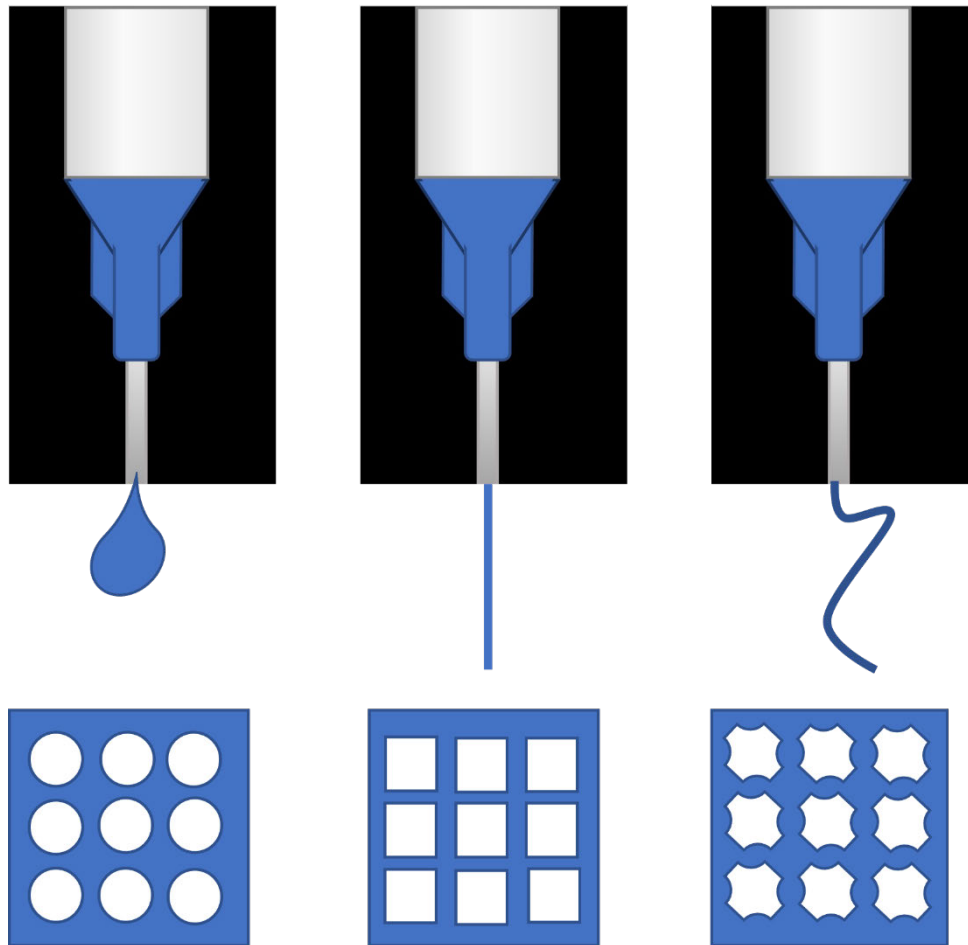
*Figure 1.17: Schematic to demonstrate the effects of gelation on filament deposition and shape fidelity. Undergelated inks dispense as droplets with poor post-printing shape fidelity (left) whereas overgelated inks have a tendency to coil on extrusion with an adverse effect on resolution (right). Appropriately gelated inks offer the best chance of reproducing shape fidelity and resolution (centre).*

### 1.6.4.3 Grids and angles

Another commonly used printability assay is the printing of grids and lines at different angles (as demonstrated in Figure 1.17). Lattices or grids are commonly used to assess accuracy and print fidelity and are useful means of assessing the interactions between dispensed filaments, their spreading ratios and ability to stack in 3D dimensions (Schwab *et al.*, 2020). The uniformity of grids also enables spacing between filaments to be measured for print consistency. Angles in grids are at $90^\circ$ between filaments and are useful to observe for gelling and uniformity of bioink deposition at points of interface, however, more commonly issues regarding filament spread are encountered at acute angles, making these an additional useful measure of filament characteristics (Kyle *et al.*, 2017).

### 1.6.4.4 Crosslinking

In order to retain their shape post-printing, hydrogels intended for use as a bioink should be able to be crosslinked: the formation of bonds between two or more polymer chains to render the structure more rigid (Kyle *et al.*, 2017).

Crosslinking is typically categorised according to the mechanism by which gelation occurs, specifically this is by chemical, physical or enzymatic means (Reddy, Reddy and Jiang, 2015). Naturally, for cartilage tissue engineering, crosslinking must be of adequate strength to provide structural integrity to the printed construct to offer structural and functional biomimicry.

Chemical crosslinking involves the use of additives such as glutaraldehyde, genipin or isocyanates that bind covalently to sites within the polymers to enable bridging bonds to be formed between them (Reddy, Reddy and Jiang, 2015). These additional covalent bonds yield a stiffer material and facilitates shape retention. Physical crosslinking methods include the use of temperature, pH, ultraviolet (UV) light or ions to make bonds between polymer chains (Hu *et al.*, 2019). Methods such as temperature typically disrupts pre-existing bonds in the material and enables these to reform, setting the material in a new gelled state. This approach is a common crosslinking method for gelatin and carrageenan but may require temperatures above physiological levels, rendering it unsuitable for use with cells (Wilson *et al.*, 2017). UV however, promotes the formation of new covalent bonds between additives such as hydroxyethyl methacrylate via a free radical polymerisation reaction (Huang *et al.*, 2020). Ionic bonding is another popular crosslinking mechanism, particularly in negatively charged hydrogels such as alginate, that readily assemble into complexes with divalent cations to stiffness and solidify the construct, but may be disrupted in culture conditions where media containing ionic solutes is used (Naghieh *et al.*, 2018).

An additional type of crosslinking reaction is enzymatic, whereby a covalent bond between polymers is encouraged through the use of peroxidase or transferase enzymes: an approach that is believed to offer the superior mechanical strength of covalent bonds with greater control over cytotoxicity than UV-mediated crosslinking (Moreira Teixeira *et al.*, 2012). Many of the crosslinking methods

described have a potential for cytotoxicity or poor biocompatibility however, which imposes some restrictions over the crosslinking methods used when cells are present during the crosslinking process (Reddy, Reddy and Jiang, 2015).

## 1.7 Environmental factors

In addition to cells and scaffold, the environment is an essential component to optimise for cartilage tissue engineering and 3D bioprinting. There is significant heterogeneity in the use of growth factors, cytokines, hormones and physical culture conditions in the literature pertaining to cartilage bioprinting, making this a challenging field to navigate (Heng, Cao and Lee, 2004; Sharifi and Gharravi, 2019). Furthermore, the parameters of the printing process itself give rise to environmental cues that may direct cell lineage, behaviour and viability (Liu *et al.*, 2016).

### 1.7.1 Growth factors and additives

A multitude of growth factors, cytokines and non-proteinaceous compounds have been described for culturing chondrocytes and promoting chondrogenic differentiation (Heng, Cao and Lee, 2004) and are outlined in Table 1.7.

.

| Additive | Role | References |
|---|---|---|
| **Growth Factors/Cytokines** | | |
| **TGFβ1** | Increased proliferation Accelerated chondrogenesis | (Iwasaki *et al.*, 1993) |
| **IGF-1** | Retained chondrogenic phenotype, increased matrix production | (Fortier, Nixon and Lust, 2002) |
| **FGF-2** | Promotes redifferentiation in monolayer culture | (Martin *et al.*, 1999) |
| **Prolactin** | Induces proteoglycan synthesis Promotes proliferation Chondrogenic differentiation | (Ogueta *et al.*, 2002) |
| **IL-1β** | Enhances cartilage catabolism & proliferation | (Tonon and D'Andrea, 2000) |
| **BMP4** | Increased chondrogenic differentiation | (Chen *et al.*, 1991) |
| **Non-proteinaceous** | | |
| **Dexamethasone** | Chondrogenic differentiation and ECM production | (Johnstone *et al.*, 1998) |
| **Ascorbic acid** | Terminal differentiation, ECM production | (Farquharson *et al.*, 1998) |
| **Insulin** | Chondrogenic differentiation | (Quarto *et al.*, 1997) |
| **PGE2** | Chondrogenic differentiation | (Miyamoto *et al.*, 2003) |
| **Vitamin D3** | Chondrogenic differentiation | (Tsonis, 1991) |

*Table 1.7: Growth factors, cytokines and non-proteinaceous additives and their role in enhancing chondrogenesis in culture. TGF= Transforming Growth Factor; IGF = Insulin-like Growth factor; FGF= fibroblast growth factor; IL-1B=Interleukin 1B; BMP4 = Bone Morphogenetic Protein-4; PGE2 = Prostaglandin E2.*

The majority of these factors induce chondrogenic differentiation or promote proliferation and cell condensation implicated in the earlier stages of cartilage formation in limb bud embryogenesis, and as such can be exploited to augment cell culture conditions (Heng, Cao and Lee, 2004). Whilst supplementation with

growth factors and additives may prove essential to maturing 3D bioprinted cartilage tissue, their use in all stages of *in vitro* research may distract from the inherent ability or inability of scaffold materials to direct chondrogenesis and cell proliferation *in vitro*. The use of platelet-rich plasma and fetal bovine serum also contain a number of the aforementioned additives, although the composition may be inconsistent between donors (Mollon *et al.*, 2013).

### 1.7.2  Mechanical forces and bioreactors

Chondrocytes are known to respond to mechanical stimuli, particularly in articular cartilage, and these stimuli may be converted into a mechanotransduction signal to increase chondrogenesis and/or proliferation which can be exploited *in vitro* (Lane Smith *et al.*, 2000; Millward-Sadler and Salter, 2004; Shahin and Doran, 2015). Mechanical stresses play a role at all stages of cartilage development: from chondrogenesis, maturation and homeostasis, but abnormal mechanical stresses can evoke hypoplasia, differentiation disorders and degradation (Zhao *et al.*, 2020). The reactions to mechanical cues are detected by deformation of the pericellular matrix and cell surface receptors, such as integrins, channelomes and the primary cilium, leading to the induction of gene expression that directs extracellular matrix production. The nature of the stress may evoke cartilaginous or mineralised matrix as a response highlighting the importance of appropriate biomechanical signals to the chondrocyte and pericellular matrix (Gao *et al.*, 2014; Zhao *et al.*, 2020). There are numerous different mechanical forces to which cartilage may be subjected, some of which have been shown to have advantageous effects whilst others have deleterious effects. Specifically, these forces can be broadly classified as:

- Hydrostatic pressure – pressure exerted by fluid in a confined space
- Shear stress – force from deformation of a material parallel to the direction of stress
- Tensile stress – forces pertaining to stretch or pulling of a material
- Compressive stress – forces that cause a material to occupy a smaller area

These stresses can be applied continuously, intermittently or cyclically to emulate a large range of forces that may be endured *in vivo* (Heath, 2000). Studies of articular cartilage have demonstrated that cyclic compressive loading as seen on load bearing joints is an important contributor to cartilage homeostasis, but can have deleterious effects when excessive, leading to osteoarthritic changes (Havaldar, Pilli and Putti, 2014; Young *et al.*, 2017; Takeda *et al.*, 2021). Similarly, tensile and hydrostatic forces have been demonstrated to be important contributors to cartilage ECM production at physiological levels, which in excess can drive osteogenic changes and mineralisation of matrix (Elder and Athanasiou, 2009; Bleuel *et al.*, 2015; Zhong *et al.*, 2018; Maki *et al.*, 2021).

Whilst most research has focussed on articular cartilage, there are a limited number of studies that indicate facial cartilages also have the capacity to respond favourably to hydrostatic pressure and compressive loading, but that these responses may differ between different facial cartilages such as temporomandibular and nasoseptal cartilage (Takano-Yamamoto *et al.*, 1991; Correro-Shahgaldian *et al.*, 2016). Shear stress in contrast, has the potential to evoke apoptotic and osteogenic changes in cartilage at levels in excess of 1 Pa, and is believed to contribute to osteoarthritic changes *in vivo*, making this an important force to modulate during tissue engineering and bioprinting processes (Lane Smith *et al.*, 2000; Smith, Carter and Schurman, 2004; Sharifi and Gharravi, 2019). The ability to control the environment in regard to mechanical forces has as such promoted the development of dynamic culture conditions in the form of bioreactor systems that attempt to maximise extracellular matrix production in tissue engineered cartilage (K. Li *et al.*, 2017; Sharifi and Gharravi, 2019; Fu *et al.*, 2021).


## 1.8 Opportunities for development

This chapter has highlighted the clinical need for 3D bioprinted auricular tissues and has highlighted the controversies and drawbacks of previous attempts to bioengineer auricular prostheses for reconstructive surgery. There is an unmet need to identify and refine a natural biomaterial with properties that enable 3D printing but support a chondrogenic environment. The demands on this material

are extensive, as any material designed for human implantation must fulfil the eligibility criteria from a mechanical perspective (adequate mechanical strength, resistance to degradation) and a biological perspective (non-immunogenic, non-toxic, biocompatible with relevant cell types). Additional demands on this material are enforced through the intention to use extrusion bioprinting: extrudability, satisfactory printability and a capacity for crosslinking. These demands are exhaustive and often conflicting, which has presented challenges in progression to clinical implementation. These demands must be explored within the context of cells, biomaterials and the pre-, intra- and post-printing environment to fully explore the suitability of the bioink for clinical translation.

## 1.9 Thesis aims and objectives

The primary objective of this thesis is to use a clinically applicable chondrocyte cell source to develop a novel nanocellulose biomaterial for bioprinting facial cartilage. The unique focus of this work is on the development of a natural, clinically-oriented bioink capable of not only printability but also chondrogenicity, biocompatibility and structural biomimicry.

Specifically, the hypothesis is that combining a novel plant-derived nanocellulose material with a crosslinkable hyaluronic acid bioink will offer a more chondrogenic, printable and mechanically robust bioink than conventional alginate-based bioinks. In order to suitably investigate this hypothesis, consideration must be applied to each of the key components of successful tissue engineering: cells, scaffold and environment. As such, the aims and objectives are subdivided as follows:

### 1.9.1 Characterise & optimise cartilage-derived cells for cartilage tissue engineering

Whilst the ultimate goal of the project is to produce 3D printed auricular constructs for reconstructive surgery, nasoseptal cartilage cells will be used owing to previous work in identifying and characterising this cell population, the stiffer matrix it produces being more suitable for reconstructive surgery and the

availability of nasoseptal tissue samples from surgical procedures. Specifically, the objectives are:

i. Confirm whether a chondroprogenitor population can be reliably isolated from nasoseptal cartilage

ii. Confirm this population meets the criteria to be defined as a mesenchymal stem cell

iii. Assess which combination of chondroprogenitors and/or chondrocytes is most suitable for 3D bioprinting cartilage

### 1.9.2 Optimise pulp-derived nanocellulose for 3D bioprinting

The base material of this bioink will be nanocellulose, using previously optimised nanocellulose-alginate bioinks, comprising nanocellulose crystals, fibrils or nanocellulose blend (NCB). The objectives within this aim are to:

i. Determine which nanocellulose subtype has the best printability profile

ii. Determine which nanocellulose is the most chondrogenic relative to alginate as a control

iii. Explore whether 3D bioprinted cartilage in nanocellulose-alginate can be optimised through dynamic culture conditions

### 1.9.3 Develop & optimise a nanocellulose-hyaluronic acid bioink

In order to offer superior biomimicry, the alginate in the nanocellulose bioink will thereafter be replaced with hyaluronic acid as a natural, crosslinkable component of cartilage extracellular matrix. This thesis will therefore aim to address the following objectives:

i. Explore the optimum combination of hyaluronic acid and nanocellulose for extrusion bioprinting

ii. Explore the optimum combination of hyaluronic acid and nanocellulose for chondrogenicity

iii. Explore a suitable dose of crosslinking agent that is structurally and biologically compatible

### 1.9.4 Compare the suitability of the nanocellulose-based bioinks for bioprinting human facial cartilage tissue

Once suitable nanocellulose based bioinks have been optimised, confirmation of their suitability in terms of 3D printing, biocompatibility and chondrogenicity needs to be verified and compared across formulations. As such, the last part of the thesis addresses the following objectives:

i. Explore the relative printability of nanocellulose-alginate and nanocellulose-hyaluronic acid bioinks

ii. Determine the relative chondrogenicity and structural properties of these optimised bioinks

iii. Confirm biocompatibility of the bioinks and 3D printing process

# Chapter 2: Materials and Methods

## Chapter 2: Materials and Methods

## 2. Methods

### 2.1 Consumables and chemicals

Plastic consumables, cell culture flasks and multi-well plates for tissue culture were purchased from Greiner Bio-One GmbH (UK) unless otherwise stated. The RTCA iCELLigence multi-well plates were purchased from ACEA Bioscience (UK) until September 2020 at which point the company merged with Agilent (UK). All the plasticware, pipette tips and molecular biology reagents were verified to be DNase and RNAse free prior to use. Chambered borosilicate cover-glass systems used for confocal microscopy were purchased from ThermoFisher Scientific (Massachusetts, USA). Countess™ slides and Trypan blue for use with the automated cell counter were purchased from Life Technologies (UK). Polymerase Chain Reaction (PCR) 96 well plates were purchased from Bio-Rad (CA, USA). All 3D printing plasticware was purchased from CELLINK (Gothenburg, Sweden).

### 2.2 Buffers, chemicals and reagents

All standard reagents were purchased from Sigma Aldrich, now Merck (Darmstadt, Germany), unless otherwise specified and were selected on the basis of being analytical grade or superior.

All cell culture media and supplements including Dulbecco's Modified Eagle Medium (DMEM), Fetal Bovine Serum (FBS), L-Glutamine, Penicillin/Streptomycin were all purchased from Gibco, Life Technologies, ThermoFisher Scientific (MA, USA). Flow cytometry antibodies for confirming isolation optimisation and monitoring stem cell phenotype and characterisation were all purchased from BioLegend (San Diego, USA). Ribonucleic acid (RNA) extraction kits were all purchased from Qiagen (Hilden, Germany). PCR reagents were purchased from Thermofisher Scientific (MA, USA) with the exception of random primers (Promega, UK). Nanocellulose was provided by GranBio (Brazil), Hyaluronic Acid hydrogel was purchased from LifeCore Biosciences (Chaska,

MN, USA) and alginate was purchased from Sigma Aldrich (now Merck, Darmstadt, Germany).

## 2.3 Cell isolation and culture

The cells used in this thesis are entirely human nasoseptal cartilage derived primary cells acquired from a range of patients undergoing elective NHS procedures within the Swansea Bay University Health Board (formerly Abertawe Bro Morgannwg) as outlined below (Section 2.3.1). No other cell sources or cell lines have been used to generate the data in this thesis.

### 2.3.1 Acquisition of human nasoseptal cartilage

Human nasoseptal cartilage was collected from healthy donors undergoing septorhinoplasty procedures in which the cartilage would normally be discarded. All samples were taken following the acquisition of informed patient consent and after having received approval by the South Wales Research and Ethics Committee (IRAS ID 99202) for regenerative medicine research. The demographics of the population are outlined in Table 2.1.

| Sample ID | Age at surgery | Gender |
|-----------|----------------|--------|
| HN31 | 22 | F |
| HN32 | 31 | M |
| HN33 | 35 | F |
| HN34 | 17 | M |
| HN35 | 25 | M |
| HN36 | 28 | F |
| HN37 | 27 | M |
| HN38 | 26 | M |
| HN39 | 40 | M |
| HN40 | 20 | M |
| HN41 | 34 | F |
| HN42 | 39 | M |
| HN43 | 29 | F |
| HN44 | 18 | M |
| HN45 | 29 | F |
| HN46 | 30 | F |
| HN47 | 38 | F |
| HN48 | 28 | F |
| HN49 | 32 | M |
| HN50 | 32 | F |
| HN51 | 32 | F |

*Table 2.1: Nasoseptal cartilage donor demographics. The Study ID number, age and gender of the patients from whom the nasoseptal cartilage was acquired are outlined for reference.*

On the day of surgery, patients were approached and counselled on the use of any residual, non-essential nasoseptal cartilage remnants for this research project and offered a written information leaflet on the intended research study. If amenable, patients signed a consent form verified by the Ethics Committee as part of Study ID 99202. Immediately after acquisition, samples were stored in a universal container containing sterile, normal saline (0.9% NaCl) and transported

on ice. Samples were processed immediately for enzymatic digestion upon arrival in the laboratory.

### 2.3.2 Isolation of cartilage derived cells from nasoseptal cartilage tissue

In a laminar flow hood, macroscopic fibrous tissue, perichondrium and bone remnants were removed from the sample with a sterile 15 blade scalpel (Swann Morton, Sheffield, UK) and discarded. The cartilaginous specimens were washed in PBS and divided into approximately 1 mm cubes using a sterile scalpel.

Enzymatic digestion was performed sequentially using 2 mg/ml Pronase (Roche, Basel, Switzerland) solution for 40 minutes and 2.4 mg/ml Collagenase solution (Sigma Aldrich, Germany) for 16 hours. All enzymatic solutions were made by dissolving the enzyme in pre-warmed (37°C, to prevent denaturation of the enzymes) Chondrogenic media "Chondromedia" (Table 2.2) and digests were performed in an incubator at 37°C, 5% $CO_2$ with gentle agitation on a plate shaker set at 300 rpm.

| Constituent | Quantity | Source |
|---|---|---|
| Dulbecco's Modified Eagle Medium, no glucose | 500 ml | Gibco |
| D-glucose solution | 500 µl (1 mM) | Gibco |
| Penicillin-Streptomycin | 5 ml | Gibco |
| Minimum non-essential amino acids | 500 µl | Gibco |
| Fetal Bovine Serum (FBS) | 50 ml | Gibco |
|  |  |  |

*Table 2.2: Chondrogenic media formulation*

Digested tissue was thereafter filtered using a 40 µm cell strainer (Corning, NY, USA) and centrifuged for 5 minutes at 350 g. The supernatant was discarded and the cell pellet resuspended in 1 ml chondromedia (dilutions of up to 5 ml media were performed depending on the size of the centrifuged cell pellet). Cells were counted using a trypan blue exclusion assay in which a 10 µl solution of cell suspension was mixed with 10 µl trypan blue stain (Invitrogen, Thermofisher, MA,

USA). 10 µl of the stained cell suspension mixture was added to a chamber slide (Invitrogen, Thermofisher, MA, USA) and a cell count was performed using an automated cell counter (Invitrogen Countess, Thermofisher, MA, USA) to calculate the total number of cells per ml and estimate the number of viable cells per ml. For standard culture, cells were seeded in sterile tissue culture (T75, T175) flasks (CELLSTAR, Greiner Bio-one, Württemberg, Germany) at a density of 7,000 cells/cm$^2$ in line with the range of chondrocyte seeding densities reported in previous literature (Das *et al.*, 2008; Solchaga, Penick and Welter, 2011).

### 2.3.3  Isolation of fibronectin adherent chondrocytes (FACs)

It has been previously suggested that fibronectin adherent cells may constitute a native stem cell population within nasoseptal cartilage, so called 'chondroprogenitor cells', and as such a differential fibronectin adhesion assay was used to separate adherent cells from non-adherent cells as previously described (Williams *et al.*, 2010; Jessop *et al.*, 2019). T75 flasks were coated with a mixture of fibronectin (10 µg/ml) in Dulbecco's PBS (Gibco, Thermofisher, MA, USA) containing 0.5 mM MgCl$_2$ and 0.9 mM CaCl$_2$. The solution was left to coat the flask 24 hours prior to use at 4°C and the residual solution discarded.

The cell suspension acquired was diluted in 9 ml chondromedia to make 10 ml, added to the flask and left in an incubator for 20 mins at 37°C. The non-adherent cells in the solution were extracted, counted and seeded separately. 10 ml fresh chondromedia was added to the fibronectin-coated flask for ongoing culture.

### 2.3.4  Calculation of cell ratios

Cell counts were performed by using a 10 µl solution of cell suspension which was mixed with 10 µl trypan blue stain (Invitrogen, Thermofisher, MA, USA). 10 µl of this mixture was added to a chamber slide (Invitrogen, Thermofisher, MA, USA) and a cell count was performed using an automated cell counter (Invitrogen Countess, Thermofisher, MA, USA) to calculate the total number of cells per ml and the number of viable cells per ml. Following enzymatic digestion, cell counts were performed at the cell isolation stage to give the total number of cartilage

derived cells (CDCs) harvested from the nasoseptal cartilage sample. After the fibronectin adhesion stage, the non-fibronectin adherent cell population (NFACs) was removed from the T75 flask and also counted. The number of fibronectin-adherent cells (FACs) could as such be calculated through subtracting the total number of NFACs from the total cell count (Equation 1)

**Equation 1:** FACs = CDCs – NFACs

### 2.3.5  Cell culture and passage

Cell populations were seeded using 7000 cells per $cm^2$ in a T175 flask with 20 ml chondromedia or a T75 flask with 10 ml. All cell culture was carried out under sterile conditions in a ScanLaf Mars Class II hood (Denmark) which was thoroughly decontaminated with 70% (v/v) ethanol prior to use. Cells were cultured in a humidified Memmert $CO_2$ incubator ICO (Memmert GmbH, Germany) at 37°C and 5% $CO_2$ in air until 70% confluent. Cells were incubated in standard culture conditions (37°C, 5% $CO_2$) with media changes performed twice per week. At each culture change, cells were examined under Brightfield microscopy (CKX53 Microscope, Olympus, Japan) at 4x and 10x magnification to visualise morphology, for the presence of infection and for the degree of cell confluence. Cells were passaged at 70% confluence. Media was discarded and flasks were washed in warm PBS solution. 0.05% trypsin-EDTA solution (Gibco, Thermofisher, MA, USA) was added to the flasks (6 ml for T75, 12 ml for T175) which were transferred to an incubator for 5-7 minutes in standard culture conditions. Flasks were then visualised under light microscopy to confirm cellular detachment, and returned to the incubator for additional 2 minute intervals if required, repeated until complete cellular detachment had occurred. Trypsin was next neutralised by adding an equal volume of chondromedia and the resultant mixture was centrifuged at 500 g for 7 minutes at room temperature. The supernatant was discarded and the cell pellet resuspended in chondromedia for cell counting using Trypan Blue exclusion as previously described (above, Section 2.3.2).

### 2.3.6 Cryopreservation and storage of cells

For long term storage, cells were stored in liquid nitrogen in a state of senescence in a liquid nitrogen dewar (Locator 6 Dewar storage system, Thermofisher Scientific, MA, USA). Cells were trypsinised from culture vessels as described in Section 2.3.5. The cells were counted and aliquoted into samples of approximately $1 \times 10^6$ cells. The cells were then centrifuged as previously described to separate out the supernatant. The residual cells were prepared for cryopreservation through immersing the cells in 1 ml of a mixture of one part Dimethyl Sulfoxide (DMSO, Merck, Darmstadt, Germany) and 9 parts FBS (Gibco, Thermofisher, MA, USA). The cells were mixed in the solution using a pipette and transferred to a 2 ml cryovial. The cryovials were transferred to a Mr Frosty™ Freezing container (Thermofisher, MA, USA) containing isopropanol solution (Merck, Darmstadt, Germany) and added to a -80°C freezer for at least 48 hours. The frozen cells were then transferred to a Locator™ liquid nitrogen dewar (Thermofisher, MA, USA) for long term storage.

### 2.3.7 Thawing of cryopreserved cells

The cryovials containing frozen cells were removed from liquid nitrogen and immediately transferred to a water bath maintained at 37°C. The cells were observed for thawing over the course of approximately one minute whilst gently swirling the vial in the water bath until only a small amount of ice remained. At this point the cryovial was cleaned with 70% ethanol and transferred to a class 2 cabinet, where the suspended cells were transferred to a 50 ml centrifugation tube (Falcon, Corning, NY, USA) with 5 ml of pre-warmed chondromedia added dropwise to the cells. The mixture was then centrifuged at 220 g for 5 minutes, after which the supernatant was removed and replaced with warm chondromedia, into which the pellet was dissolved. The suspension was then transferred to an appropriate culture vessel (T75, T175) and allowed to grow for 2 passages or at least 14 days prior to use in any further experiments.

## 2.4 Verification of Stem Cell Characteristics

To determine the stem cell properties of the fibronectin adherent population, cells were assessed according to the minimum criteria for mesenchymal stem cells (Dominici *et al.*, 2006) as outlined in Section 1.6.2.2.

### 2.4.1  Trilineage differentiation

The ability of cells to undergo trilineage differentiation was investigated through the use of StemPro$^{TM}$ differentiation kits (Gibco, Thermofisher Scientific, MA, USA), to direct cells down osteogenic, chondrogenic and adipogenic lineages.

#### 2.4.1.1       Osteogenic Differentiation

Cells were seeded at a density of $5x10^3$ cells per $cm^2$ on to the wells of a 12 well plate. The cells were cultured in chondromedia for 24 hours in standard culture conditions to allow adherence to occur. The media was then replaced with StemPro Osteogenesis Differentiation Media (Gibco, Thermofisher Scientific, MA, USA) and changed every 3-4 days for a total of 21 days.

At 21 days, media was discarded and the cells were washed with Dulbecco's PBS (DPBS). 4% paraformaldehyde solution (VWR, PA, USA) was then added to the wells and left for 30 minutes. This was then removed and the wells were washed 3 times further with DPBS. A 2% (w/v) Alizarin Red solution (Sigma Aldrich, Darmstadt, Germany) was added to the wells for 3 minutes, after which point excess dye was washed off with distilled water. Cells were visualised under light microscopy and images acquired at 4, 10 and 20x magnification.

#### 2.4.1.2       Chondrogenic differentiation

Cells were diluted in chondromedia to give a concentration of $1.6x10^7$ viable cells per ml. 5 µl droplets of the cell suspension were added to the base of a 12 well plate to generate a micromass culture. Micromasses were allowed to adhere for 2 hours, after which point, StemProTM Chondrogenesis Differentiation Media (Gibco, Thermofisher Scientific, MA, USA) was added to the cells and changed every 2-3 days for 14 days.

At 14 days, media was discarded and the cells were washed with DPBS. 4% paraformaldehyde solution (VWR, PA, USA) was then added to the wells and left for 30 minutes. This was then removed and the wells were washed 3 times further with DPBS. Cells were stained with a 1% (w/v) alcian blue solution (Sigma Aldrich, Darmstadt, Germany) prepared in 0.1N hydrochloric acid for 30 minutes. After 30 minutes, excess stain was removed by washing three times with 0.1N hydrochloric acid and thereafter distilled water until clear. Cells were visualised under light microscopy and images acquired at 4, 10 and 20x magnification.

### 2.4.1.3    Adipogenic differentiation

Cells were seeded into the wells of a 12-well plate at a density of $1x10^4$ cells/cm$^2$. The cells were incubated in chondromedia for 24 hours to facilitate adhesion, at which point, the media was replaced with StemPro$^{TM}$ Adipogenesis Differentiation Media (Gibco, Thermofisher Scientific, MA, USA), changed every 3-4 days for 14 days.

At 14 days, media was discarded and the cells were washed with DPBS. 4% paraformaldehyde (PFA) solution (VWR, PA, USA) was then added to the wells and left for 30 minutes. This was then removed and the wells were washed 3 times further with DPBS. A 5% (w/v) stock solution of Oil Red O stain was made through dissolution in 100% isopropanol, of which a 60% working solution was made with distilled water and filtered using Whatman's grade 1 filter paper (Merck, Darmstadt, Germany). Cells were pre-rinsed with 60% isopropanol and the working solution of Oil red O was applied the cells for 10 minutes and washed thereafter with distilled water until clear. Cells were visualised under light microscopy and images acquired at 4, 10 and 20x magnification.

### 2.4.2  Flow cytometry

Human nasoseptal cartilage cells were trypsinised from passages 0 to 8 and used for immunophenotypic characterisation using flow cytometry. Cell populations were phenotyped for the presence of tentative positive (Table 2.3) and negative

cartilage and mesenchymal stem cell markers (Table 2.4) as previously published and characterised for this cell population (Jessop *et al.*, 2020).

| CD Marker | Other names | Fluorophore | Detection Channel | Excitation wavelength (nm) | Emission wavelength (nm) |
|---|---|---|---|---|---|
| **CD 29** | Integrin β1, VLA-β, gpIIa | PE | PE | 565 | 575 |
| **CD 44** | Hermes, Pgp1, H-CAM, HUTCH | Per CP | APC | 488 | 675 |
| **CD 56** | NCAM, Leu-19, NKH1 | BV 605 | Q dot 605 | 405 | 605 |
| **CD 73** | Ecto-5'-nucleotidase | APC / Cy 7 | APC Cy7 | 650 | 774 |
| **CD 90** | Thy-1 | BV 510 | Am Cy | 405 | 510 |
| **CD49e** | α5 integrin, VLA-5α | FITC | FITC | 493 | 525 |

*Table 2.3: Positive cartilage and chondroprogenitor cell surface markers, their associated fluorophores, detection channels and excitation and emission spectra.*

| CD Marker | Other names | Fluorophore | Detection Channel | Excitation wavelength (nm) | Emission wavelength (nm) |
|---|---|---|---|---|---|
| **CD 24** | HAS, Ly-52, Nectadrin | BV 421 | Pacific Blue | 405 | 421 |
| **CD 34** | Gp105-120 | APC/Cy7 | APC Cy 7 | 650 | 774 |
| **CD 45** | LCA, T200 | BV 570 | PE | 405 | 570 |
| **Stro-1** | - | AF 647 | APC | 650 | 668 |

*Table 2.4: Negative stem cell and chondrogenic cell surface markers their associated fluorophores, detection channels and excitation and emission spectra.*

Positive markers, negative markers, CD24, CD49e and CD90 were processed in separate tubes owing to the degree of overlap in fluorescence spectra as identified by the Biolegend Fluorescence Spectra Analyser (Figure 2.1, Figure 2.2). 100,000 cells per condition were extracted and centrifuged at 500 g for 7 minutes at 4°C. The resultant cell pellet was suspended in 100 µl of Flow Assisted Cell Sorting (FACS) buffer consisting of 0.2% bovine serum albumin (Sigma Aldrich) and 0.05% sodium azide in PBS solution (Gibco, Thermofisher Scientific, MA, USA). 5 µl of each antibody (all acquired from Biolegend, CA, USA) was added to the corresponding flow tube, vortexed and incubated in darkness on ice for 30 minutes. Note, owing to excessive fluorescence using 5 µl of antibody, 4 µl was used for CD73 and CD24 antibodies. Centrifugation and washing steps were repeated twice using FACS buffer, with a final solution of cells in 100 µl FACS buffer.
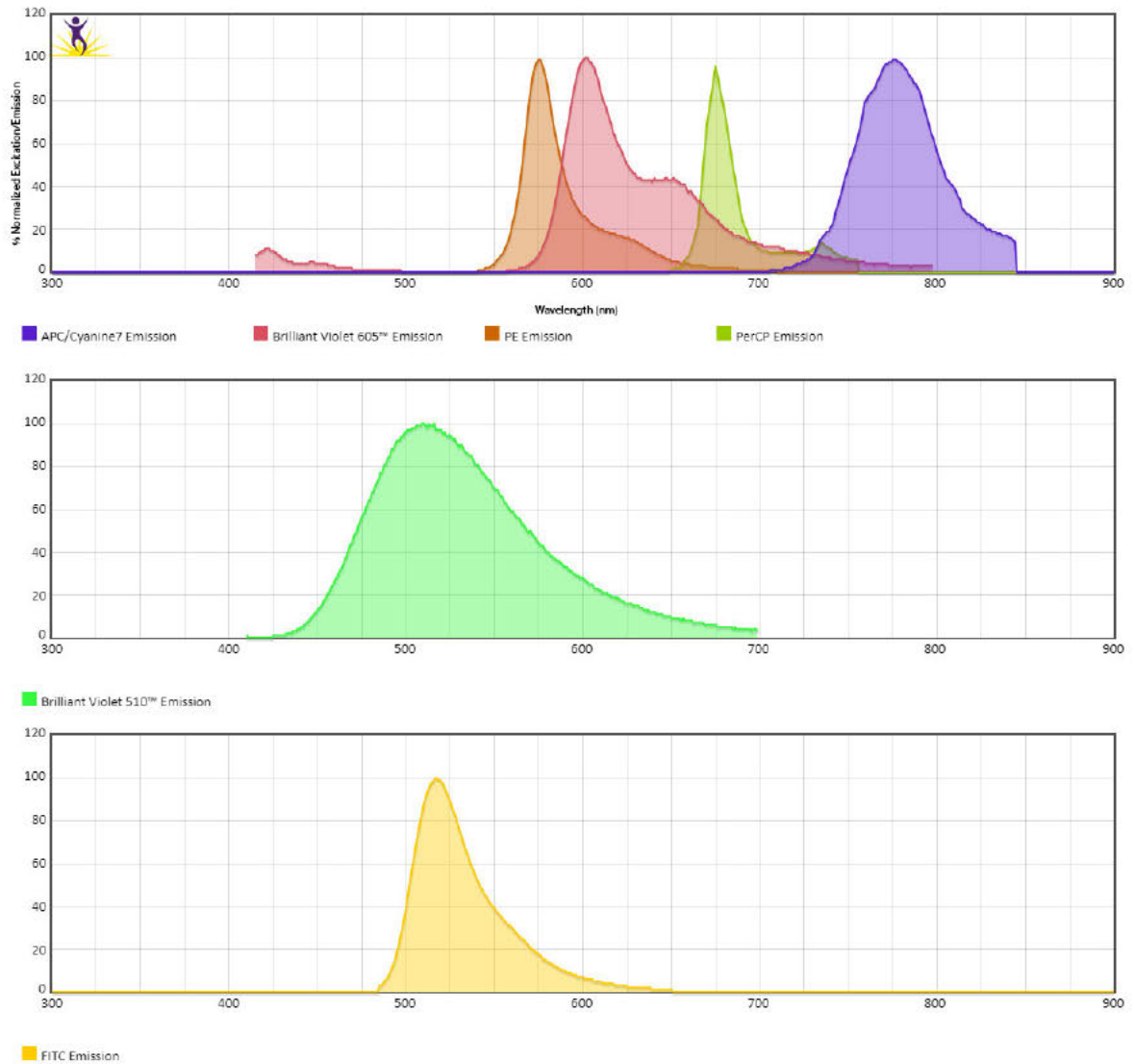
*Figure 2.1: Emission spectra of fluorophores associated with positive markers. Fluorophores with significant overlap in their emission spectra were stained in separate tubes to minimise artefact between fluorophores. Graphs generated from Biolegend (CA, USA).*

Cell suspensions were run immediately on the NovoCyte Flow Cytometer (ACEA Biosciences, Agilent, CA, USA). Gating was performed whilst visualising the cells under Forward Scatter plotted against Side Scatter logarithmic axes to isolate a viable, homogeneous population in each unstained sample. This gating was thereafter applied to the stained cell tubes from the same cell populations. The flow cytometer was allowed to run for a minimum of 10,000 events and the result

of each stain was compared to a control, unstained matched population of that cell type processed in parallel to enable correction for autofluorescence.
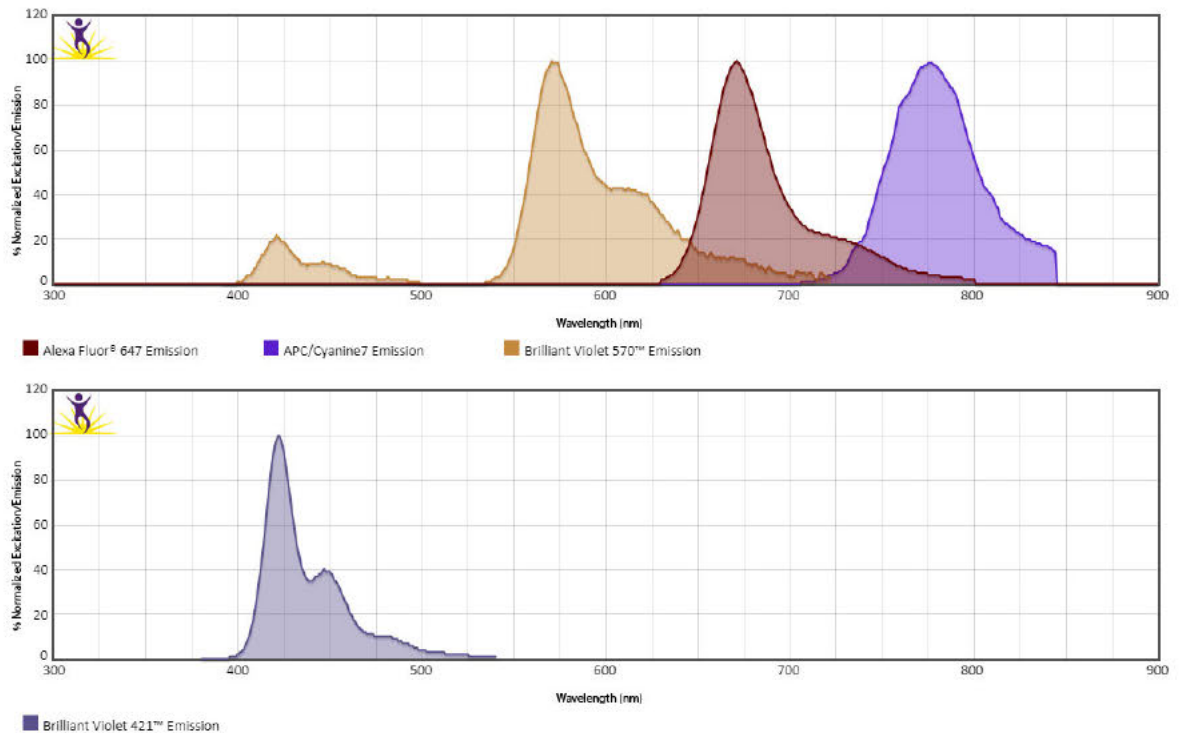


*Figure 2.2: Emission spectra of negative cell surface markers. Separate tubes were used where there was noted to be overlap in the spectra to minimise artefact.*

To adjust for artefact and non-specific staining, a compensation matrix was generated using Versacomp antibody capture beads (Life Technologies, Thermofisher). Each antibody was added to a flow tube with one drop of positive and negative beads, incubated, washed and centrifuged with FACS buffer as per cellular samples. The resultant fluorescence was used to generate a compensation matrix using FlowJo software (FlowJo, LLC, OR, USA), which was applied to all resultant flow cytometry data.

All data analysis was performed using FlowJo software, with the Median Fluoresence Index (MFI) calculated for each marker compared to the unstained control population. These values were compared to calculate the number of positive staining cells for each fluorophore and the signal:noise ratio of each

fluorophore (the median fluorescence index of the stained cells/median fluorescence index of the unstained cells).

## 2.5 Bioink preparation

### 2.5.1 Nanocellulose production

The nanocellulose used in this research is derived from softwood biomass acquired through American Value Added Pulping (AVAP) biorefinery technology: a process of fractionation using ethanol and sulphur dioxide. The final nanocellulose formulations are available in 3 types: hydrophilic nanocellulose crystals (NCC, pure crystals); hydrophilic nanocellulose fibrils (NCF, a combination of cellulose, xylans and mannans) and a hydrophilic blend (NCB, containing components of both NCC and NCF). Each formulation comprises 5% w/v nanocellulose powder in distilled water (BioPlus, GranBio, GA, USA).

### 2.5.2 Neutralisation and sterilisation

Upon receipt, nanocellulose has a pH of approximately 2 and as such were adjusted to pH 7 with 4 M NaOH added dropwise to 100 ml of nanocellulose hydrogel. The mixture was decanted into 50ml tubes and centrifuged at 1000 g for 10 minutes. The volume of supernatant comprising excess water content was measured and discarded from the hydrogel. The nanocellulose hydrogel was transferred into an autoclavable screw-top container and steam autoclaved at 126°C for 20 minutes using a desktop autoclave (Prestige Medical, Blackburn, UK) as previously described (Al-Sabah *et al.*, 2019). Once autoclaved, the volume of water removed through centrifugation was replaced with tissue culture grade distilled water to reconstitute the hydrogel.

### 2.5.3 Alginate production

Alginic acid sodium salt (Sigma Aldrich, 80,000–120,000 Da, 1.56 mannuronate/guluronate ratio) was sterilised under ultraviolet light (UV-C 254nm) for one hour in a laminar flow hood and dissolved in sterile tissue-culture grade water (Gibco, Thermofisher Scientific, MA, USA) to make a 2.5% (w/v) hydrogel

solution. 2.5% alginate was chosen as the hydrogel concentration used in this study owing to data from previous optimisation studies in which it was reported that this concentration offered the best compromise between ease of admixture with nanocelluloses and post printing shape stability (Jessop *et al.*, 2019b). The alginate hydrogel was sealed in a 50 ml tube and vortexed to encourage dissolution. The preparation was left to settle for 48 hours at room temperature to allow complete dissolution into a hydrogel and thereafter was stored at 4°C until further use.

### 2.5.4  Hyaluronic acid hydrogel

Hyaluronic acid powder with a 5% tyramine substitution (HA) was purchased from LifeCore Biomedical (Corgel 5%; Chaska, MN, USA) and maintained at -20°C until further use. The HA powder was dissolved in sterile horseradish peroxidase in PBS (10 U/mL; LifeCore, MN, USA) to produce a hydrogel with concentration of 30 mg/ml as per manufacturer guidance. The Corgel hydrogel has been tested against ISO10993 safety and toxicity standards and is deemed biocompatible by the manufacturers.

### 2.5.5  Biomaterial blending

#### 2.5.5.1        Nanocellulose-alginate bioinks

Composite bioinks were produced consisting of the different formulations of nanocellulose (NCC, NCF and NCB) with 2.5% (w/v) alginate to yield composite nanocellulose-alginate bioinks of 75% nanocellulose (v/v) and 25% alginate (v/v) composition as previously described (Markstedt *et al.*, 2015; Al-Sabah *et al.*, 2019a; Jessop *et al.*, 2019a).

#### 2.5.5.2        Nanocellulose-hyaluronic acid bioinks

Composite nanocellulose-hyaluronic acid (NCHA) bioinks were produced using NCB and the 5% Tyramine-substituted HA hydrogel described in 2.4.4. NCHA bioinks were produced in a series of formulations as outlined in Table 2.5.

| Bioink Name | % Volume Nanocellulose Blend | % Volume Tyramine-substituted HA |
|---|---|---|
| **100HA** | 0 | 100 |
| **80HA** | 20 | 80 |
| **60HA** | 40 | 60 |
| **40HA** | 60 | 40 |
| **20HA** | 80 | 20 |

*Table 2.5: Nanocellulose-hyaluronic acid composite bioinks with percentage v/v of each constituent and their associated nomenclature*

### 2.5.5.3 Crosslinking of Nanocellulose-alginate and alginate bioinks

Alginate is a polysaccharide polymer comprising two main monosaccharide components: D-mannuronic acid and L-guluronic acid. Each possesses a side chain containing carboxyl groups and an ether component in which exposed electrons from the oxygen atoms enable ionic bonds to form between components in the presence of divalent cations such as calcium ions ($Ca^{2+}$). The alginate in NCA was crosslinked post-printing using 0.5 M $CaCl_2$ solution (made from anhydrous $CaCl_2$ powder, Sigma-Aldrich, MO, USA). The anhydrous powder was UV sterilised for 1 hour prior to dissolution in tissue culture grade ultrapure water as previously described (Al-Sabah *et al.*, 2019). All solutions were then filtered in a linear flow hood using a sterile 0.22 µm filter (Merck, MO, USA). When applied to biomaterials, equal volumes of crosslinking agent and biomaterial were used and where cells were also used, the crosslinking agent was first preheated to 37°C in a water bath.

### 2.5.5.4 Crosslinking of hyaluronic acid and nanocellulose-hyaluronic acid composite bioinks

The Tyramine substitution of HA side chains renders it amenable to covalent crosslinking mediated through a peroxidation reaction catalysed enzymatically using horseradish peroxidase enzyme (HRP) and low dose hydrogen peroxide.

Manufacturer recommendations for crosslinking are reproduced in Table 2.6.

| Tyramine Substitution (%) | 5.5 | 5.5 | 5.5 |
|---|---|---|---|
| Gel concentration (mg/mL) | 30 | 40 | 50 |
| $H_2O_2$ recommended for crosslinking (%) | 0.391 | 0.522 | 0.652 |

*Table 2.6: Crosslinking dose recommendations for 5% tyramine substituted hyaluronic acid hydrogel. Reproduced from LifeCore Biomedical product information leaflet.*

As the lowest dose of crosslinking agent was indicated for a 30 mg/ml gel, this was selected for the formulation of the HA hydrogel for these experiments. The hydrogen peroxide solution (LifeCore Biomedical, MN, USA) was diluted further in PBS (Sigma Aldrich, MO, USA) to provide a range of concentrations that were more appropriate for use with cells according to doses deemed suitable for cartilage biocompatibility reported in the literature (Martin *et al.*, 2005; Khan *et al.*, 2008). Specifically, solutions of 5, 10, 15, 20 and 25 µM were used and compared to 0.391% (115 mM).

### 2.5.6  Rheology

Rheological analysis of the materials in their uncrosslinked, hydrogel states was performed to determine properties of significance to 3D printing in collaboration with Prof Karl Hawkins and Bethan Morgan, Centre for Nanohealth, Swansea University. Specifically, parameters such as viscosity, shear thinning, and viscoelastic properties were interrogated using an AR-G2 Controlled Stress Rheometer (TA instruments, New Castle, DE, USA). The rheometer is fitted with 40 mm diameter parallel plates, and for the purposes of this experiment the bottom plate was set at a temperature of 22°C.

Samples of each hydrogel of interest (100HA – 20HA) were mixed to encourage homogenisation prior to loading 700 µl onto the centre of the lower plate using a 1 ml syringe. The upper plate of the rheometer was lowered onto the sample, to remove air, set at a maximum pressure of 0.1 N. The sample was surrounded by

a low viscosity silicon oil to minimise evaporation during analysis. Samples were left to equilibrate for 2 minutes.

An initial frequency sweep was performed using a range of 0.1 to 10 Hz maintained at 0.5 Pa stress throughout. All measurements were noted to be within the linear viscoelastic range of the samples during this sweep. The values of storage modulus (G'), loss modulus (G") and complex modulus (G*) were also recorded throughout this frequency range. The loss tangent (tanδ), is tangent of the phase angle (δ) between stress and strain and was calculated as a ratio of loss and storage modulus (**Equation 2**), with values greater than 1 indicating dominance of the viscous component of the complex modulus.

**Equation 2:**

$\tan\delta = G''/G'$

The sample was allowed to equilibrate for 10 seconds prior to commencing a shear flow ramp analysis, in which logarithmically increasing shear rates of 0.1-100 s[1] were exerted over a two-minute period. Each hydrogel was tested by using separate samples in triplicate with measurements repeated in triplicate for each new sample used.


## 2.6 3D Bioprinting

### 2.6.1  3D Bioprinter assembly and calibration

A CELLINK INKREDIBLE (CELLINK, Gothenburg, Sweden) 3D printer was used for bioprinting the constructs. The syringes were fitted with 22 G conical nozzles as standard to enable the bioink deposition to be performed with both accuracy and resolution.

The 3D bioprinter components were each sterilised with 70% ethanol and transferred to a Class II cabinet (Scanlaf, Denmark). Within the cabinet, further sterilisation was performed under UV light for 60 minutes.

Prior to initiating a print, the print bed is levelled according to X, Y and Z axes and homed in a neutral position. The printer is connected to an air compressor and set to 300 kPa. The printheads are reset to 0 kPa and the nozzles opened through

the printer control system. The minimum extrusion pressure is determined by slowly increasing the pressure of each printhead until bioink is extruded through the nozzle.

Prior to commencing a print, the extrusion nozzles are primed with bioink to remove the air in the system which could impair print quality.

### 2.6.2 Computer Aided Design (CAD)

Cellink Heartware software (Version 2.4.1, CELLINK, Gothenburg, Sweden) was used to design the 3D shapes for extrusion bioprinting within the parameters of the print bed area. 3D shapes for printing were designed *ab initio* using the software and saved as .STL (stereolithography) files, or 3D design software packages including Autodesk (Autodesk, CA, USA) and Windows 3D Viewer (Microsoft, WA, USA). The 3D shapes created then converted into vertical layer by layer instructions in the form of .gcode files through the use of Slic3r software (v3, GitHub, CA, USA). This software was also used to refine the printer settings including infill pattern, density, print speed, layer height and supporting frameworks. The G-code file was transferred to the 3D printer directly through a USB connection to the printer or via upload onto an SD card.

### 2.6.3 Bioink resolution assays

### 2.6.3.1　　　Straight line resolution assay

Resolution was determined using the CELLINK F600 Resolution Assay (CELLINK, Gothenberg, Sweden), in which 4 parallel straight lines of 1 mm thickness are bioprinted on to the base of a petri dish. This assay enables both filament spreading (a marker of fidelity) and line resolution to be determined for each bioink.

To calculate filament spreading, the intended width of each line was compared to the actual width of each bioprinted line. The lines were inspected for continuity and then visualised under 4x magnification and the width of each line measured at 3 separate points using Image J (NIH, USA) to check for linear uniformity. The mean line width and mean line width variation were calculated for each bioink.
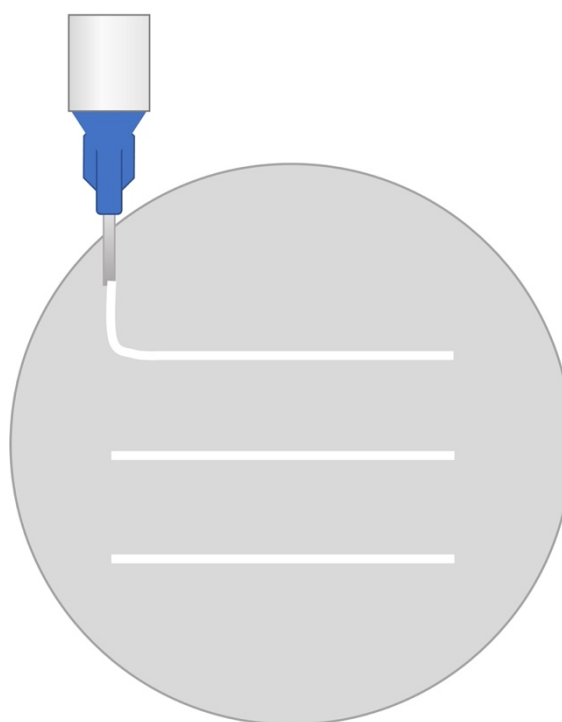
*Figure 2.3: Schematic of Line fidelity assay test in a petri dish. Three straight lines of equal length and width are printed on to the base of a petri dish.*

Bioink resolution and filament spreading was determined for 2.5% (w/v) alginate (A), 30 mg/ml Tyr-substituted Hyaluronic acid (Corgel, USA) (HA), Nanocellulose-Alginate composite bioinks (NCA) and NCHA.

### 2.6.3.2 Grid Assay

Square grids of one layer height (0.7mm) were designed using TinkerCAD software (Autodesk, CA, USA) and printed using each biomaterial (Figure 2.4). A grid of 5x5 small squares was designed each with an area of 9mm$^2$. The grids were measured at several points using digital callipers, photographed and inspected under 4x magnification. The line thickness was measured using Image J software and the angles between the crossing points were measured and compared to the intended angle of 90 degrees. The area of each of the empty square spaces between the lines of the grid were measured and compared within the same grid for consistency.
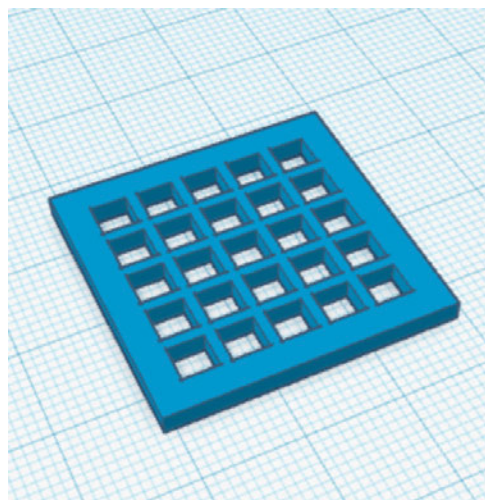
*Figure 2.4: Computer aided design (STL file) image of the grid used in the grid assay*

### 2.6.4 Bioink fidelity and accuracy assays

To determine the fidelity and accuracy of the bioprinted constructs compared to the intended design, anatomical structures comprising a tracheal ring and an auricular antihelix were designed using TinkerCAD software (Autodesk, CA, USA).

The tracheal ring was measured using digital callipers at set points to determine the minimum and maximum thicknesses and the degree of deviation from the original design (ring width 3mm). The antihelix was measured at a series of fixed points pertaining to the key anatomical components of the structure: namely the superior and inferior crura, the length, width and body of the construct (Figure 2.5).
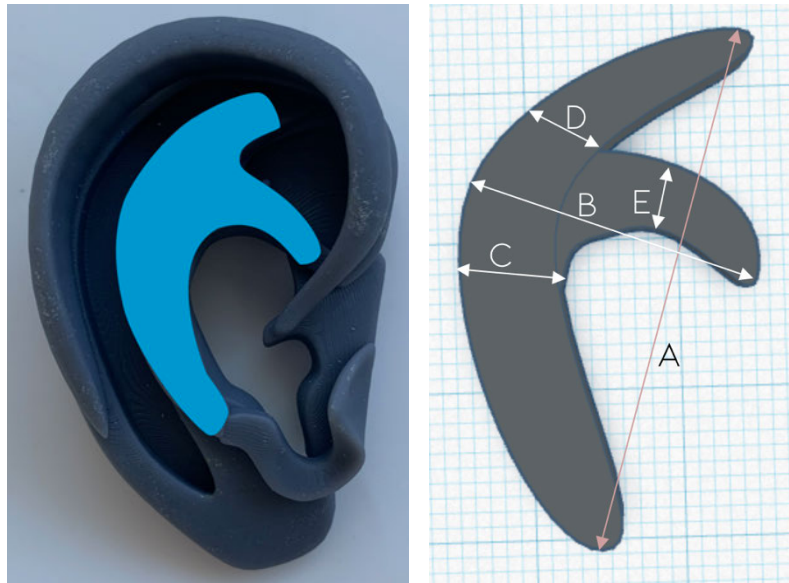
*Figure 2.5: Auricular antihelix and associated measurements taken. A= length, B = width, C= body, D= superior crux; E= inferior crux.*

### 2.6.5 Bioink flow and drop test assays

To determine bioink flow, a flow assay was performed in which the print nozzle was opened and the extrusion pressure gradually increased from 0 kPa until the ink flows through the nozzle continuously. The mean of at least 3 separate batches of bioink were tested. An ideal bioink should be able to be extruded as a continuous filament and retain its continuity upon deposition: this can be tested using a filament drop test (Figure 2.6). The printer nozzle was opened at the minimum extrusion pressure and the bioink was gently purged through the printer nozzle. Photographs were acquired of each filament to inspect for under or overgelation.
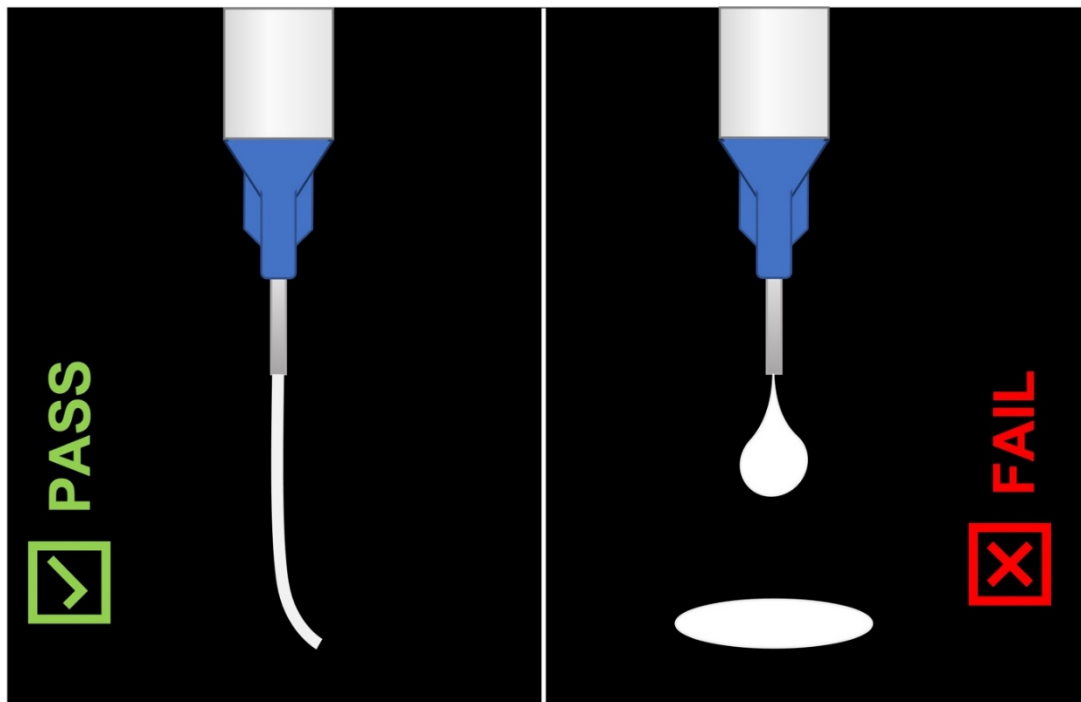
*Figure 2.6: Filament drop test. A bioink of adequate gelation should be able to hold its shape as a continuous filament when extruded from a printer nozzle. Inks that simply drop out of the nozzle are deemed to fail this test and lack the desired tensile strength.*

### 2.6.6   Cell encapsulation

Human nasoseptal chondrocytes were suspended in 1 ml of chondromedia and added to a 1 ml syringe. The biological ink was added to a 10 ml syringe and combined with the cells using the CELLINK CELLMIXER (CELLINK, Sweden). This apparatus merges up to 1 ml syringe of cell suspension with up to 10 ml of biological ink into a new filling cartridge through a two-way Luer-lock connector (Figure 2.7). The volume ratios of cell:bioink can be adjusted according to the amount of biomaterial or cells required, but were maintained at a seeding density of $3 \times 10^6$ cells/ml unless otherwise stated.

*Figure 2.7: CELLINK CELLMIXER apparatus demonstrating simultaneous extrusion of cells in media and bioink through a Luer lock system used to prime a printing syringe.*

### 2.6.7 3D bioprinting cellular constructs

The cell-bioink formulations were printed into semispheres using 22 G precision nozzles into the wells of a 48 well plate. Each semisphere had a volume of 100 µl, and was immersed in 100 µl of crosslinking agent immediately post-printing.

Alginate-containing bioinks were crosslinked with sterile 0.5 M $CaCl_2$ and HA based bioinks with 5 µM $H_2O_2$ unless otherwise specified. The crosslinking agent was left for 10 minutes for calcium chloride and 5 minutes for hydrogen peroxide, after which point, the bioprinted constructs were washed three times with warm PBS and immersed in 750 µl of chondromedia, preheated in a water bath to 37°C. The semispheres were kept in standard culture conditions with media changes every 3 days. The semispheres were harvested and analysed at serial time points to assess chondrogenicity, cell viability and metabolic activity.

### 2.6.8 Dynamic cell culture using orbital shaking

Dynamic cell culture conditions were produced to investigate the effect of increased media perfusion, pressure gradients and shear stress on the chondrogenicity of chondrocytes cultured in crosslinked bioinks. 100 µl of a bioink comprised of nanocellulose blend (75% v/v) and sodium alginate (25% v/v) were produced containing 300,000 cells. The bioink was crosslinked through the

118

addition of 0.5 M $CaCl_2$. 48 well plates containing 100 µl semispheres of cell-laden material and media were produced as outlined above. One plate was added to an orbital shaker, calibrated to 37°C and 5% $CO_2$ in the cell incubator and set at 500 rpm. The plate was secured to the orbital shaker with autoclave tape (dynamic condition). Another plate was added to a standard shelf of the same incubator but not subjected to any movement or shaking (static condition).

### 2.6.9 *In silico* simulation of orbital cell shaking system

The *in silico* modelling of the orbital cell shaking system was conducted by Dr Feihu Zhao (Swansea University College of Engineering) through a collaborative research endeavour based on the parameters provided below. To simulate the micro-mechanical environment generated within a crosslinked, cell-laden hydrogel (in this case nanocellulose-alginate) a multiphasic computational fluid dynamics (CFD) approach was used in this study. In the CFD model, a semisphere with a volume of 100 µl was created to represent the cell-laden hydrogel droplet (Figure 2.8). The medium volume in each well was 0.75 ml, mirroring the experimental condition. In the CFD model, the cell-laden construct is modelled as porous media, of which the permeability was determined using Equation 3 (Nabovati, Llewellin and Sousa, 2009).

**Equation 3**:

$$\kappa = 0.491 \cdot \delta^2 \left( \frac{1-\psi_c}{1-\psi} - 1 \right)^{1.155}$$

where, $\Psi_c$ is the percolation threshold, $\Psi_c = 0$ (Guyot *et al.*, 2015); $\Psi_c$ is the porosity of the cell-laden hydrogel, $\Psi = 42\%$ (Al-Sabah *et al.*, 2019); average pore size $\delta = 0.8$ µm (Al-Sabah *et al.*, 2019); therefore, $\kappa = 2.1645 \times 10^{13}$ $m^2$.

The medium in this model is assumed to be a Newtonian fluid with the density and dynamic viscosity of 1000 $kg/m^3$ and 1 mPa/s, respectively. The top surface of the 48 plate well was defined as open boundary with the relative pressure of 0 Pa, and the side and bottom walls are defined as non-slip walls (Figure 2.8). The 48 well plate, in the coordinates of (X, Y, Z) was loaded with an orbital shaking speed of 500 rpm with reference to the coordinate of ($X_0$, $Y_0$, $Z_0$). The Volume of

Fluid technique was used in this CFD model for tracking the medium-air interface during shaking. For each element at the interface, the continuity and momentum equations were solved on the modified definition of the fluid properties ($P$) as per Equation 4 (Salek, Sattari and Martinuzzi, 2012).

**Equation 4**:

$$\begin{cases} P = \alpha_M \cdot P_M + \alpha_A \cdot P_A \\ \quad \alpha_M + \alpha_A = 1 \end{cases}$$

where, $P_M$ and $P_A$ are the properties of medium and air that are density and dynamic viscosity); while $\alpha_M$ and $\alpha_A$ are the volume fraction of medium and air, respectively.

Both mixed fluid-air domain and porous media domain were meshed by a tetrahedron method with a patch-conforming algorithm. Transient analysis was used in the simulation with a time step of 0.006 seconds for 5 periods. Finally, the CFD model was solved by finite volume method using ANSYS CFX under the convergence criteria of root-mean-square residual of the mass and momentum < $10^{-4}$.
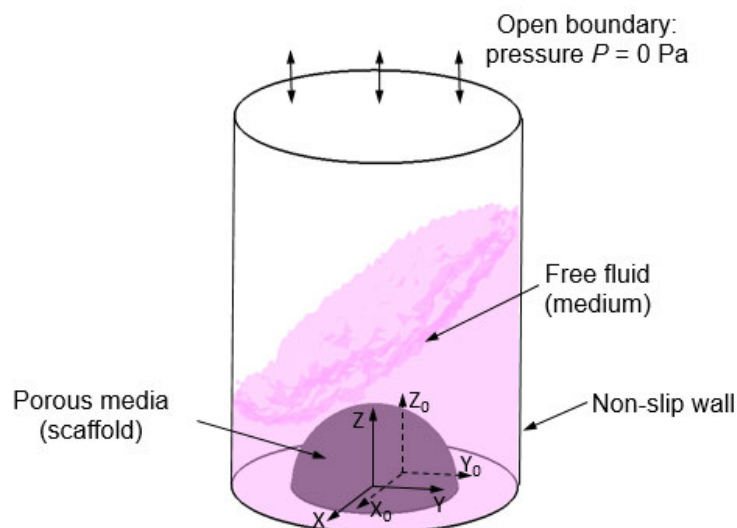


*Figure 2.8: Illustration of CFD model setting and boundary conditions, (X, Y, Z) is the local coordinate and ($X_0$, $Y_0$, $Z_0$) is the original coordinates.*

### 2.6.10 Shear stress calculations

Computational fluid dynamics was used in collaboration with Dr Feihu Zhao and Josh Roberts (Swansea University College of Engineering) to model the amount of shear stress the cells experience during the 3D printing process at the pressure and nozzle size used for 3D printing. The nozzle (22 G) and syringe used in the CELLINK INKREDIBLE printer, were measured using digital callipers and from the Product Information Sheet (CELLINK, Gothenburg, Sweden). These measurements were translated into a 3D model of the nozzles and syringes used in SolidWorks software (MA, USA) which were subsequently exported as a .stl file to TetGen software (Berlin, Germany) to undergo mesh mapping for modelling purposes. The boundary conditions of the internal surface of the nozzle were set as non-slip walls with the outlet pressure set at atmospheric values (zero fluid dilatation).

A range of extrusion pressures from 20 to 40 kPa were used to model the fluid velocity and shear stress in increments of 10 kPa within the bioink at these printing pressures, plotted against increasing extrusion time.


## 2.7 Cell growth and proliferation

### 2.7.1 alamarBlue assay

The alamarBlue dye (ThermoFisher Scientific, MA, USA) was used to provide an indication of cell number and metabolic activity. A 10% (v/v) alamarBlue solution was made by adding the solution to chondromedia, which was added to the cells or cell-laden biomaterials for 4 hours in standard culture conditions. To enable a representative colorimetric change to occur, and for the solution to permeate the biomaterial, this duration of time was demonstrated to be appropriate for cells laden in biomaterials to produce a colorimetric change. The dye contains an active ingredient, resazurin, that relies upon the reducing environment of growing cells to evoke a redox reaction, in which they take the dye from its oxidised, blue, non-fluorescent form to a reduced, red and weakly fluorescent form. To demonstrate cell proliferative activity over a 24 hour period within the biomaterial, the dye was left *in situ* in standard culture conditions at 37°C, 5% $CO_2$ with serial readings of 100 µl taken at 4, 12 and 24 hour time points. For longer time periods

(up to 21 days of culture), a new volume of 10% solution was added at days 0, 7, 14 and 21, with washes in PBS to remove any excess alamarBlue media followed by standard media changes using chondromedia performed twice weekly between alamarBlue measurements. In each case, 100 μl of the alamarBlue media was added to at least three wells per condition and sampled in at least duplicate from each well. The samples were added to separate wells of a 96 well plate with unreacted alamarBlue media added in triplicate to serve as control values. The colorimetric change was quantified using a plate reader (POLARstar Omega spectrophotometer, BMG LABTECH, Ortenberg, Germany) in which absorbency readings were taken at 570 nm (reduced form) and 600 nm (oxidised form) wavelengths.

All biomaterials used were tested without cells for cross-reactivity with the alamarBlue media and verified through comparing the readings to media alone.

To determine the degree to which the resazurin within the dye was reduced to the red form, Equation 5 was used.

**Equation 5:**

% reduction of alamarBlue = $\dfrac{(\varepsilon_{ox})\lambda_2 A\lambda_1 - (\varepsilon_{ox})\lambda_1 A\lambda_2}{(\varepsilon_{red})\lambda_1 A\prime\lambda_2 - (\varepsilon_{red})\lambda_2 A\prime\lambda_1}$

Where,

$\varepsilon_{ox}$ = molar extinction coefficient of alamarBlue oxidized form (BLUE)

$\varepsilon_{red}$ = molar extinction coefficient of alamarBlue reduced form (RED)

A = absorbance of test wells

A' = absorbance of negative control well. The negative control well should contain media + alamarBlue but no cells.

$\lambda_1$ = 570 nm value

$\lambda_2$ = 600 nm value

### 2.7.2 iCELLigence impedance-based cell assay

### 2.7.2.1    Cell proliferation

Cell proliferation of CDCs, FACs and NFACs and ratios of these cell types were compared using the RTCA iCELLigence apparatus (ACEA Biosciences, San Diego, CA, USA). The apparatus allows for the insertion of two 8-well E8 plates (Figure 2.9), in which 17500 cells per well were seeded.
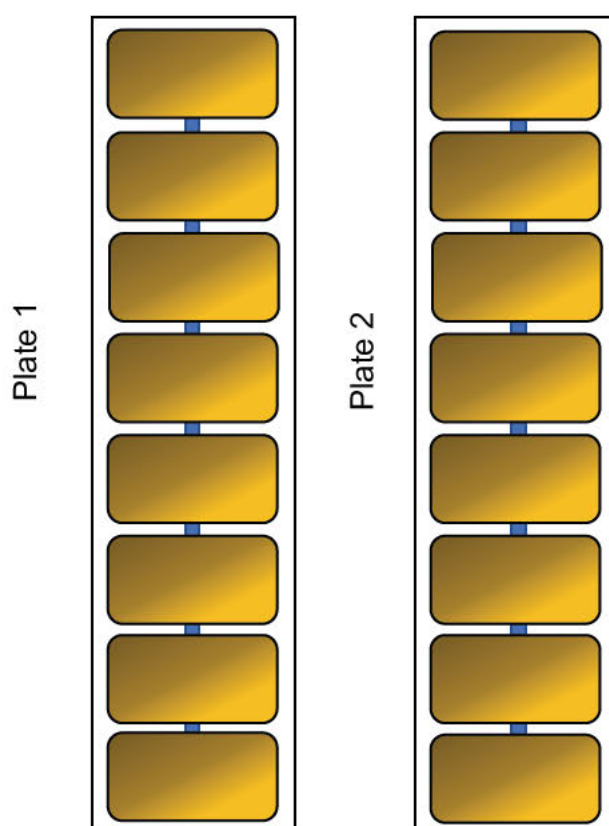


*Figure 2.9: Schematic of the pair of E8 plates that can be inserted into the iCELLigence apparatus. A total of 16 wells are available for cell seeding.*

The iCELLigence E8 plates (ACEA Biosciences) contain 8 wells per plate each made of polystyrene with a base area of $64mm^2$. These plates have low current electrodes at the base of their wells (Figure 2.9) which enable measurements of cell index, growth and death through electrical impedance. As cells proliferate upon the electrode, and increase in number, the amount of electrical impedance on the plate increases, which is converted to a cell index using RTCA software

(ACEA Biosciences, San Diego, CA, USA) and can be visualised in real-time throughout the course of the experiment.

Prior to use the machine was left for 2 hours to calibrate to $37^{\circ C}$ after which point background measurements were taken using 150 µl media only. Next, 17500 cells were added to each well in 350 µl media to make a total volume of 500 µl per well. 2 wells were filled with only media and no cells to act as negative controls. Measurements were taken once per minute for the first 2 hours to capture cell adhesion and then every hour for 70 hours to measure proliferation.

### 2.7.2.2 Cell cytotoxicity

The iCELLigence apparatus was also used to measure cell death and toxicity following exposure to potentially cytotoxic agents, in this instance, hydrogen peroxide. Cells were seeded into the wells of an E8 plate as described in Section 2.7.2.1; and allowed to adhere to the plate for 18 hours. After this time point the impedance readings were paused, the media was removed from the cells, and 200 µl of warm PBS or warm hydrogen peroxide diluted in PBS (doses as reported in Section 2.5.5.4), was added to each well and left at room temperature for 5 minutes. The hydrogen peroxide was thereafter discarded and the wells were washed three times with warm PBS, after which fresh 500 µl chondromedia was added to the wells. The experiment was resumed, with measurements taken every minute for 2 hours to accurately capture the immediate cytotoxic window, and then hourly until a total experimental time of 70 hours was attained.

### 2.8 Gene expression analysis

### 2.8.1 RNA extraction of cells only

Total RNA was extracted using a modified protocol of the Qiagen RNEasy Mini kits (Qiagen, Hilden, Germany). 500 µl of TRIzol (Thermofisher Scientific, MA, USA) was added to cells on the base of a 6 well plate and immediately frozen at -80°C to promote cell lysis. After at least 24 hours, the TRIzol-cell suspension was defrosted, transferred to a 2 ml microcentrifugation tube and 150 µl of chloroform was added to the mixture. The samples were vortexed for 15 seconds

and left for 10 minutes at room temperature. The mixture was then centrifuged for 15 minutes at 14500 g, 4°C. After this point, the mixture had separated into a phenol phase, a debris phase and a supernatant phase, the latter of which contained the RNA of interest (Figure 2.10).



RNA rich supernatant
Cellular/biomaterial debris
Phenol
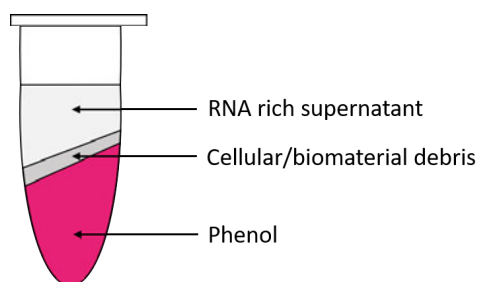
*Figure 2.10: Schematic to demonstrate appearance of RNA extracts after high speed centrifugation with TRIzol and chloroform.*

The RNA rich supernatant phase was extracted and added to a separate microcentrifugation tube with an equal volume of 70% ethanol (v/v; in nuclease free water) and mixed gently. The mixture was transferred to the top of an RNEasy column. The columns were then centrifuged at 8000 g using a Hereaus Biofuge Pico (Thermofisher. MA, USA) for 15 seconds. The flow through was discarded and 700 µl of RW1 buffer was added to the column and centrifuged for 15 seconds at 8000 g. The flow through was discarded and the columns were then washed twice with 500 µl of RPE buffer for 15 seconds for the first wash and then 2 minutes at the second wash at 8000 g. The collection tube was then replaced, and 30 µl of nuclease free water was added to the column membrane. This was left for 2 minutes and then centrifuged for 1 minute at full speed. The resultant RNA was added to the membrane once again and the centrifugation step repeated to increase yield. The RNA eluted through the column was stored at -80°C for subsequent analysis.

### 2.8.2 RNA extraction of cells in biomaterials

In order to extract cells within biomaterials, a modified protocol of the above RNA extraction protocol was performed. The biomaterial-cell pellets were immersed in

500 µl TRIzol with either 100 µl 0.1% (w/v) EDTA (for alginate-based biomaterials) or 100 µl RLT buffer (for all other biomaterials) and the materials were diced using a sterile scalpel. The mixture was then frozen at -80°C for at least 24 hours to facilitate material degradation. The samples were then homogenised using a TissueRuptor II probe (Qiagen, Hilden, Germany) for 30 seconds and centrifuged for two minutes through a QIAshredder column at 8000 g for 2 minutes. The flow through was then mixed with 150 µl of chloroform and processed as per Section 2.7.1.

### 2.8.3   RNA quantification and purity assessment

The RNA concentration and quality was determined using a Nanodrop 2000 Spectrophotometer (Thermofisher Scientific, MA, USA). The machine was calibrated to zero using the same nuclease free water used to prepare the RNA elutes and wiped with clean tissue between measurements. 1 µl of each RNA sample was measured for RNA concentration (ng/µl) and purity, as indicated by the absorbance values at 260/280 and 260/230. Elutes with 260/280 and 260/230 values close to 2 (>1.6 as a minimum) were selected for subsequent processing.

### 2.8.4   cDNA synthesis

For use in polymerase chain reaction, cDNA was produced through reverse transcription using the RNA elutes acquired in the steps above. In order to compare equal amounts of RNA across samples, RNA samples were diluted with nuclease free water to produce 11 µl of RNA of a consistent concentration for each set of experiments. This concentration ranged from 200 ng to 800 µg depending on the source of the RNA (higher concentrations were achievable from cell only isolates). Each concentration-corrected RNA sample was mixed with 1 µl of dNTP mix (Thermofisher Scientific, MA, USA) and 1 µl random primers (Promega, Southampton, UK). The samples were added to a T100 Thermal Cycler (BioRad, CA, USA) for 5 minutes at 65°C and 1 minute at 4$^{°C}$. The samples were then each combined with a mixture of 1 µl of SuperScript IV Reverse Transcriptase enzyme (Thermofisher Scientific, MA, USA), 1 µl of dithiothreitol (DTT, Thermofisher Scientific, MA, USA), 1 µl of RNase inhibitor (Promega) and

4 µl of 5x First Strand Buffer (Thermofisher Scientific, MA, USA) to bring the sample volume to 20 µl. The samples were then added to the T100 thermal cycler and incubated at 23°C for 10 minutes, followed by 53°C for 10 minutes and 80°C for 10 minutes. Samples were then maintained on ice or at 4 °C or frozen at either -20 °C for short term use or -80 °C for long term storage.

### 2.8.5 Chondrogenicity primer design

Primers were designed using Primer-BLAST software (NIH, USA) with a view to yield primers specific for human genes, spanning exon-exon boundaries. The primers selected were purchased from Sigma Aldrich (now Merck) or Eurofins genomics (Ebersberg, Germany) and initially screened against the NCBI BLAST database to ensure homology to other genes was avoided.

| Gene | | Primer sequence | Accession number | Product size (base pairs) |
|------|------|-----------------|------------------|---------------------------|
| TBP | Forward | 5'-GCCAAGAGTGAAGAACAG | NM_001172085.2 | 90 |
| | Reverse | 5'-GAAGTCCAAGAACTTAGCTG | | |
| RPL13A | Forward | 5'-GTCTGAAGCCTACAAGAAAG | NM_012423.4 | 189 |
| | Reverse | 5'-TGTCAATTTTCTTCTCCACG | | |
| ACAN1 | Forward | 5'-CACCCCATGCAATTTGAG | NM_001135.4 | 82 |
| | Reverse | 5'-AGATCATCACCACACAGTC | | |
| COL2A1 | Forward | 5'-GAAGAGTGGAGACTACTGG | NM_001844.5 | 165 |
| | Reverse | 5'-CAGATGTGTTTCTTCTCCTT | | |
| SOX9 | Forward | 5'-CTCTGGAGACTTCTGAACG | NM_000346.4 | 172 |
| | Reverse | 5'-AGATGTGCGTCTGCTC | | |
| RUNX2 | Forward | 5'-AAGCTTGATGACTCTAAACC | NM_001015051.4 | 164 |
| | Reverse | 5'-TCTGTAATCTGACTCTGTCC | | |
| ALP | Forward | 5'-CTTTATAAGGCGGCGGGGG | NM_000478.6 | 942 |
| | Reverse | 5'-AACTGATGTTCCAATCCTGCG | | |
| OSC/ BGLAP | Forward | 5'-CTCACACTCCTCGCCCTATTG | NM_199173.6 | 109 |
| | Reverse | 5'-GCTTGGACACAAAGGCTGCAC | | |

*Table 2.7: Primers used in this thesis according to their gene, sequence, accession number and product size*

The following genes were selected for chondrogenicity analysis: Type 2 Collagen, Aggrecan and SOX9, as these are recognised and specific markers of cartilage tissue formation and differentiation (Yi *et al.*, 2018). Whereas for osteogenic gene expression, OSC, ALP and RUNX2 were selected, as these are well established markers of osteogenic differentiation and mineralisation (Granéli *et al.*, 2014).

### 2.8.6  Housekeeping genes

Housekeeping genes were selected according to the most stable combination for human nasoseptal cartilage. Three biological repeats were tested for the stability of candidate housekeeping genes and ranked according to RefFinder. This programme generates a geometric mean of gene stability from three separate, commonly used computer programmes: BestKeeper, geNorm and NormFinder (Table 2.8). The most consistent housekeeping genes were found to be Tatabox Protein (TBP) with a stability value of 1.00; Ribosomal Protein L (RPL) with a value of 2.21 and Glyceraldehyde 3-phosphate dehydrogenase (GAPDH) with a value of 2.45 (Figure 2.11). As such TBP and RPL were selected as the reference housekeeping genes for PCR in this thesis.

| Method | 1 | 2 | 3 | 4 | 5 | 6 | 7 |
|---|---|---|---|---|---|---|---|
| Delta CT | TBP | GAPDH | RPL13A | YWHAZ | SDHA | HPRT | 18S |
| BestKeeper | TBP | RPL13A | GAPDH | YWHAZ | 18S | SDHA | HPRT |
| Normfinder | TBP | GAPDH | YWHAZ | RPL13A | SDHA | HPRT | 18S |
| Genorm | RPL13A | TBP | GAPDH | YWHAZ | SDHA | HPRT | 18S |
| Recommended Comprehensive ranking | TBP | RPL13A | GAPDH | YWHAZ | SDHA | HPRT | 18S |

*Table 2.8: Rankings of housekeeping gene stability based on 4 different analyses of gene stability.*

## Comprehensive gene stability
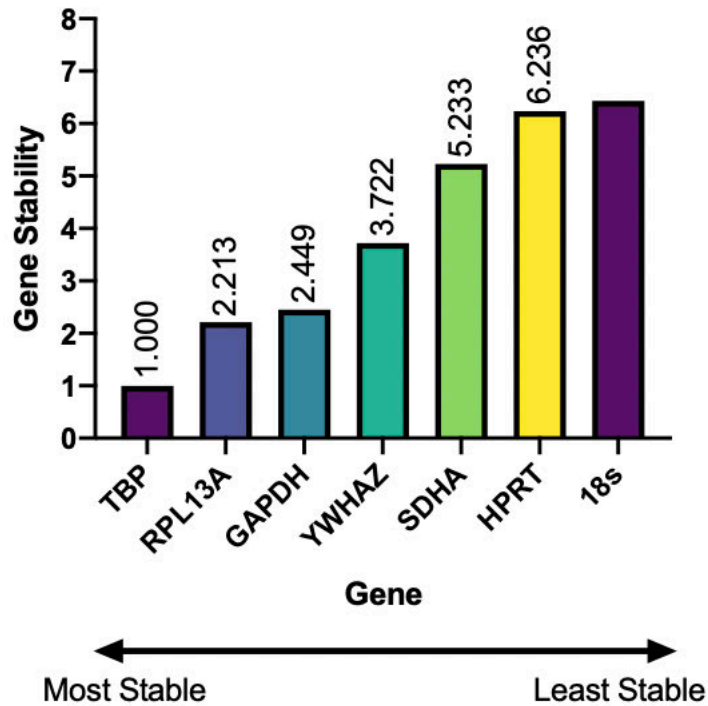


*Figure 2.11: Comprehensive gene expression according to RefFinder in nasoseptal cartilage cells. The most stable genes (TBP) are located on the left of the x axis and least stable (18s) on the right.*

### 2.8.7   Quantitative reverse transcription polymerase chain reaction

Transcript levels of the genes of interest were quantified using real time quantitative polymerase chain reaction (RT-qPCR). 1 µl of each cDNA sample was added to the well of a clear 96 well plate alongside 10 µl of Brilliant III Ultra-Fast SYBR Green qPCR Master Mix (Agilent Technologies, CA, USA), 0.4 µl of the primer for the target gene of interest (containing equal volumes of forward and reverse primers for each gene at a concentration of 0.2 µM) and 8.6 µl of Ambion™ nuclease free water (Thermofisher, MA, USA), bringing the total volume per well to 20 µl. The Brilliant III mixture importantly contains Taq DNA polymerase, and a SYBR Green fluorescent dye that binds to double stranded DNA yielding a fluorescent signal in proportion to the amount of DNA present. The plate was protected from light throughout and sealed with a clear adhesive

129

film (Thermofisher, MA, USA). The plate was briefly centrifuged to eliminate bubbles and encourage mixing and inserted into a CFX Connect RT-PCR machine (Bio-Rad, CA, USA).

A protocol was established to run the plate as follows:

| Step | Temperature (°C) | Duration | Notes |
|------|------------------|----------|-------|
| 1 | 95 | 3 mins | Activation of DNA polymerase |
| 2 | 95 | 5 seconds | |
| 3 | 60 | 10 seconds | Annealing & extension; Ct Data Captured |
| 4 | Repeat Steps 2 &3 a further 39x | | |
| 5 | 55 | 5 seconds | Melt Curve Captured |
| 6 | 95 | 5 seconds | |

Table 2.9: Stages of real time quantitative PCR process used to generate Ct values in the CFX connect apparatus

Standard curves over a linear range of amplification were generated for each primer, according to Table 2.9. The point at which the fluorescent value surpasses a threshold (baseline) set is known as the threshold cycle (Ct) value. Only values in which the Ct values acquired were under 30 and where a single clear melt curve for each primer was available, were used in subsequent analysis. All samples were repeated in at least triplicate readings.

## 2.8.8 Double delta Ct analysis

The geometric mean of Ct values from the gene of interest and housekeeping genes from each sample were calculated. The Ct value of the baseline housekeeping genes for each sample was subtracted from the gene of interest (ΔCt) and repeated for the control and test conditions. The difference in gene expression between the test and control condition was normalised by subtracting the arithmetic mean of the ΔCt values in the control group from the test population ΔCt values to provide a ΔΔCt value. This value was then converted to a relative 'fold-change' in gene expression compared to the control population by

expressing this as $2^{\Delta\Delta Ct}$. This is known as the double delta Ct analysis method (ΔΔCt, or Livak method) and is a well reported means of yielding a fold change in gene expression between two conditions, normalised to the baseline expression of the most stable housekeeping genes (Section 2.7.6) (Livak and Schmittgen, 2001). The control and test conditions were compared statistically using t-tests (or Mann-Whitney).

## 2.9 Protein analysis

### 2.9.1 Protein extraction

Biomaterial samples were harvested into 2 ml microcentrifugation tubes containing RIPA buffer (Thermofisher Scientific, MA, USA) supplemented with 100x Protease and Phosphatase inhibitor (Thermofisher Scientific, MA, USA). Samples were frozen at -80°C and after at least 24 hours were subsequently disrupted using a Qiagen TissueRuptor II (Qiagen, Darmstadt, Germany) fitted with a homogenising probe for 30 seconds, on ice. The lysate was then centrifuged at 14500 g for 15 minutes and the liquid supernatant was decanted into a new microcentrifugation tube. Thereafter, the protein rich supernatant was maintained on ice for further processing or stored at -20 °C for short term use.

### 2.9.2 Bicinchoninic Acid (BCA) assay

The BCA assay was used as a means of quantifying the amount of protein within lysates extracted in Section 2.9.1. A BCA assay kit (Pierce™, Thermofisher Scientific, USA) was used to generate a set of standards using a stock of 2 mg/ml bovine serum albumin (BSA) ranging from 0 to 2 mg/ml (Table 2.10).

| µg/ml | BSA (µl) | Water (µl) |
|---|---|---|
| **2000** | 200 | 0 |
| **1800** | 180 | 20 |
| **1500** | 150 | 50 |
| **1000** | 100 | 100 |
| **800** | 80 | 120 |
| **600** | 60 | 140 |
| **400** | 40 | 160 |
| **200** | 20 | 180 |
| **0** | 0 | 200 |

*Table 2.10: BSA standards used in the BCA assay to generate a standard curve*

10 µl of the samples of interest (diluted in distilled water up to 1/100 where necessary), 80 µl of a solution comprising 50 parts bicinchoninic acid and 1 part copper (II) sulphate pentahydrate 4% solution was added to the wells of a 96 well plate. The samples were incubated at 37°C for 30 minutes and then read on a plate reader at 562 nm (POLARstar Omega spectrophotometer, BMG LABTECH, Ortenberg, Germany). The absorbency values from the BSA standards in Table 2.10 were used to generate a standard curve from which the protein content of each sample could be acquired, corrected according to the initial dilution.

### 2.9.3   Dimethylmethylene blue assay

A stock solution of dimethylmethylene blue (DMMB) was made by dissolving 32 mg of 1,9-DMMB in 20 ml of pure ethanol overnight on an orbital shaker at room temperature. This stock solution was added to a mixture of 1.5 L distilled water, 59 ml 1 M NaOH and 7 ml 98% formic acid and left to mix for 2 hours. To verify adequate DMMB dissolution, the mixture was then verified for absorbance at 525 nm and 592 nm compared to distilled water alone. This solution was protected from light until use.

Protein lysates were prepared according to Section 2.9.1, and in experiments in which hyaluronic acid was used as a component of one of the bioinks, all samples

were treated with prior hyaluronidase digestion (a 10 mg/ml solution of Type I hyaluronidase powder, Merck, MO, USA) at 37°C for 1 hour to eliminate this glycosaminoglycan from the analysis. 40 µl of each protein lysate was added into the wells of a 96 well plate in triplicate, and in triplicate serial dilutions of 1/20, 1/50 and 1/100 owing to the narrow linear standard curve of the assay. Standards were produced using chondroitin sulphate C (Merck, MO, USA) in concentrations of 0, 10, 20, 30, 40 and 50 µg/ml in distilled water. 40 µl of standards were added to each plate in duplicate or triplicate.

To each well, 200 µl of DMMB solution was added and the plate read immediately at an absorbency of 525 nm. The total concentration of glycosaminoglycan in each sample was acquired using the standard curve of chondroitin samples.

### 2.9.4  Hydroxyproline assay

10 mg of each cell-laden material was weighed and added to a PTFE-lined screw cap microcentrifugation tube with 100 µl of ultrapure water. The mixture was homogenised using a Qiagen TissueRuptor II probe (Qiagen, Germany) for up to 30 seconds at full speed. To this lysate, 100 µl of 12 M hydrochloric acid (Merck, MO, USA) was then added and allowed to hydrolyse at 120°C for 3 hours on a heating block. The hydrolysed lysate acquired was then mixed using a vortex and centrifuged at 10,000 g for 3 minutes. 10 µl of the supernatant was then transferred to a 96 well plate in triplicate along with one spiked sample containing 0.4 µg of hydroxyproline sample, and a set of hydroxyproline standards ranging from 0 to 1 µg. The plate was then allowed to evaporate in a 60°C oven until dry. 100 µl of a solution of Chloramine T and oxidation buffer was added to each well and left for 5 minutes, with a further 100 µl mixture of DMAB reagent diluted in perchloric acid and isopropanol added thereafter for 90 minutes at 60°C. The plates were then read at 560 nm absorbance using a plate reader (POLARstar Omega spectrophotometer, BMG LABTECH, Ortenberg, Germany). The concentration of hydroxyproline was calculated using the following formula (Equation 6).

**Equation 6:**

$$\text{Concentration} = \frac{(A_{560})\text{sample} \times 0.4 \text{ } \mu\text{g}}{(A_{560})\text{spiked control} - (A_{560})\text{sample}}$$

### 2.9.5 Immunofluorescence
### 2.9.5.1 Cells in chamber slides

30,000 cells (FAC, NFAC, CDC) of three biological repeats were added to the chambers of an 8 well chamber slide (Nunc™ Lab-Tek™ II, Thermofisher Scientific, MA, USA) with 250 µl chondromedia. The cells were left to adhere for 72 hours, after which, the media was discarded and the chambers irrigated with three washes of PBS. The cells were fixed with 250 µl of 4% PFA for a total of 20 minutes, after which point, three further PBS washes were performed. A 0.2% solution of TritonX (Merck, MO, USA), in distilled water was added to the chambers for 15 minutes to permeabilise the cell membranes and washed again with PBS three times. 250 µl of 1% BSA solution (Merck, MO, USA) was then added to each chamber for 1 hour to block non-specific binding. After further washes with PBS, a 1 in 200 solution of phalloidin rhodamine stain (Invitrogen™, Thermofisher Scientific, MA, USA) in PBS was prepared, protected from light and added to the chamber in the dark for one hour. The phalloidin stain binds to F-actin and is conjugated with tetramethylrhodamine (TRITC) dye with an excitation/emission spectrum of 540/565. After one hour, the stain was discarded and three further washes with PBS were performed. A 1 in 10,000 solution of 4,6-diamidino-2-phenylindole (DAPI; Invitrogen™, Thermofisher Scientific, MA, USA) stain was made in PBS, protected from light and added to the chambers for 15 minutes. DAPI has an excitation and emission wavelength of 359/457nm. The chambers were washed again with PBS and the chambers removed from the slides once dry. A small drop of VectaShield (Vectorlabs, CA, USA) was added to each well area and a glass coverslip affixed to the slide. The slides were protected from light and visualised using fluorescent microscopy with a confocal microscope (Zeiss Laser Scanning Microscope 710, Thornwood, NY, USA) at 4x and 20x magnification at the aforementioned spectral ranges for each fluorophore.

## 2.10  Histology

### 2.10.1 Fixation and preservation

In order to preserve the cell-laden biomaterials, or native cartilage tissue, the constructs were immersed in 4% paraformaldehyde (PFA) for 30 minutes in a 1:10 volume:PFA ratio (i.e. 1 ml PFA for a 100 µl biomaterial construct) on ice. The PFA was removed using three washes with PBS.

### 2.10.2 Cryopreservation and sectioning

The fixed biomaterial constructs were immersed in 1 ml of 30% (w/v) sucrose solution (Sigma Aldrich). The sucrose was removed once the constructs had sunk to the bottom of the vial, indicating sucrose had penetrated throughout porous network of the constructs. The sucrose embedding step was omitted for native cartilage tissue sections. The specimens were then immersed in Optimum Cutting Temperature (OCT) compound for 30 minutes and snap frozen in liquid nitrogen to minimise ice crystal formation. Cryopreserved samples were mounted onto the plates of a Cryostat (Leica Biosystems, Wetzlar, Germany) using OCT and sectioned into 8-10µm thick slices. The slices were then mounted on to poly-L-lysine coated slides and stored at -20°C. Prior to staining the slides were heated in a dry oven at 37°C for 30 minutes to allow the specimens to stick to the slides. The specimens were demarcated with a hydrophobic peroxidase-antiperoxidase (PAP) pen (Sigma) and washed with PBS. The stains were then added on to the specimens within the PAP rings dropwise as per Section 2.10.3.

### 2.10.3 Histological staining

Samples were stained following fixation with paraformaldehyde or after cryosectioning. Where stained on slides, all stained specimens were covered in mounting medium (Histochoice, VWR, Pennsylvania, USA) and protected with a clear coverslip, sealed with clear nail varnish.

### 2.10.3.1 Haematoxylin and Eosin (H&E) staining

H&E staining was conducted to enable differentiation between the nuclear and cytoplasmic components of cells and extracellular matrix. Haematoxylin is a violet, basophilic stain with an affinity for negatively charged cellular components such as nucleic acids whereas eosin is a red acidophilic dye that preferentially binds positive charges found on amino acid side chains, such as proteins and extracellular matrix. Liquid haematoxylin stain (TCS Biosciences, UK) was added to the preserved specimens for 20 minutes. The specimens were thereafter washed with acid alcohol for 30 seconds, a solution comprising a solution of 3% (w/v) hydrochloric acid in 70% (v/v) ethanol solution. The specimens were then washed gently with distilled water until the run off was clear. Next, a 5% (w/v) aqueous eosin stain (TCS Biosciences) was added to the specimens and left for 30 seconds. The specimens were once again irrigated thereafter with distilled water until the water run off was clear. Specimens and slides were viewed under brightfield microscopy and stored at room temperature.

### 2.10.3.2 Alcian Blue staining

Alcian blue stain is used primarily to detect mucins and sulphated glycosaminoglycans, rendering it a useful adjunct in histological staining of cartilage extracellular matrix. A 1% (w/v) alcian blue solution (Sigma Aldrich) was prepared in 0.1 N hydrochloric acid (Sigma Aldrich) and added to the samples for 30 minutes. After 30 minutes, excess stain was removed by washing three times with 0.1 N hydrochloric acid and thereafter distilled water until the water remained clear of excess stain.

### 2.10.3.3 Toluidine blue staining

Toluidine blue is a basic metachromatic dye primarily used for staining sulphated glycoproteins in cartilage extracellular matrix such as aggrecan. A 0.1% (w/v) toluidine blue solution (TCS Biosciences, UK) was prepared in distilled water. The solution was then added to samples for 10 minutes. Excess stain was removed by washing the samples with distilled water.

### 2.10.3.4    Safranin O staining

Sulphated glycosaminoglycans also stain positively with Safranin O, whereas bone matrix stains green with Fast Green. In order to attain this staining and to determine whether cartilage and/or bone matrix was produced, first a solution of 0.1% (w/v) Fast Green (TCS Biosciences, UK) was prepared in distilled water and added to the specimens for 20 minutes. Thereafter, the specimens were washed with 1% (w/v) acetic acid solution (Sigma Aldrich) for 20 seconds before adding 0.1% (w/v) safranin O solution (TCS Biosciences, UK) to the cells for a total of 40 minutes duration. The specimens were then washed with distilled water until the runoff was clear.

### 2.10.3.5    Brightfield microscopy

Fixed and stained specimens were visualised under brightfield microscopy at 4, 10 20 and 40x magnification using an inverted tissue culture microscope (Olympus CKX53 with a DP23 digital camera, Olympus Keymed, Essex, UK) and processed using Olympus cellSens Software (Olympus, Tokyo, Japan).

### 2.11   Structural and mechanical characterisation

### 2.11.1  Atomic force microscopy (AFM)

AFM was performed in collaboration with Dr Andrea Gazze, Swansea University and used to characterise the properties of each biomaterial, effect of crosslinking agents and to compare changes in biomaterial properties following 21 days of culture with cells. 100 µl disks of crosslinked biomaterial were produced without cells and immersed in media for 24 hours in standard culture conditions. After 24 hours of incubation, the biomaterial discs were removed and washed with PBS. The discs were then secured onto the base of a microscope cover slip with a single drop of mounting medium (VWR, PA, USA). This minimised movement artefact during subsequent analysis.

The surface topography and elastic modulus of each biomaterial was investigated using a Bruker BioScope Catalyst Atomic Force Microscope (Bruker, MA, USA) and MikroMasch cantilevers CSC37 (Mikromasch, Tallinn, Estonia), with a

nominal radius of 8 nm, a nominal resonance frequency of 20 kHz and a nominal spring constant of 0.3 N/m. Prior to measurements, the cantilevers were calibrated on a glass slide to determine the experimental deflection sensitivity and spring constant.

The elastic modulus of the biomaterials (with and without cells) was extracted from force curves acquired on each scaffold type using a maximum force of 4 nN. The contact regimen of the retract part of each force curve was fitted with the equation of the Sneddon model in the Nanoscope Analysis software (v1.50, Bruker, MA, USA) to extract the elastic modulus (Equation 7).

**Equation 7:**

$$F = \frac{2E}{\pi(1 - v^2)} \tan(\alpha)\delta^2$$

Where F is the force applied, E is the elastic modulus, v is the Poisson ratio (0.5), R is the radius of the indenter (8 nm), δ is the indentation depth and α the half-angle of the indenter (18°).

Only data with a goodness-of-fit of at least 0.8 was considered and a minimum of 50 data points was collected for each sample type. Sample topography was acquired in PeakForce Quantitative NanoMechanics (QNM) mode (Bruker, MA, USA). Data distribution, analysis and plotting was performed using Mathematica 12 (Wolfram, Champaign, IL, USA).


## 2.11.2 Biomechanical testing

A 3D printed mould was used to produce 200 μl biomaterial cylinders of equal volume and dimensions (Figure 2.12).
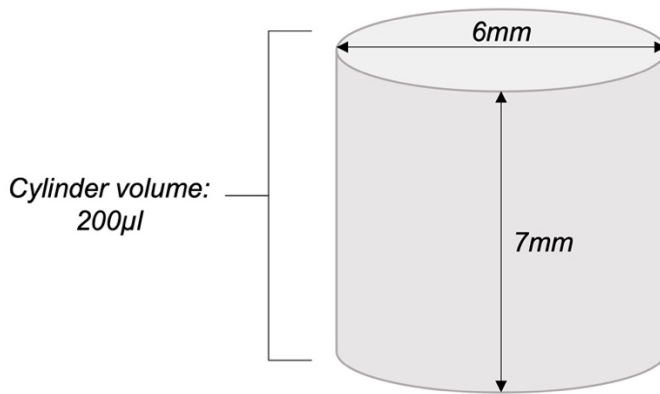
*Figure 2.12: Schematic to represent the dimensions of the cylinders made for mechanical testing using a 3D printed mould*

The material cylinders were transferred in PBS to a $1^{ST}$ Mechanical compression machine (Tinius Olsen, Redhill, UK). The device was set up for compression testing using a 25 N load cell and parallel compression plates. The machine enables capture of strain, position, time, stress, force and position rate. Each material was placed in the centre of the bottom plate and the upper plate was lowered to within 2 mm of the upper border of the specimen. The compression test was commenced thereafter at a rate of 2 mm/min until even contact with the surface has been attained, defined as a force equal to 0.01 N. The machine was then paused for 10 seconds to allow for equilibration and the material was gradually compressed at a rate of 5mm/minute for a maximum distance of 7 mm, or sooner following complete failure (disintegration) of the material. The Tinius Olsen Horizon software collects values for the break force, ultimate force, break stress and break distance based on initial values of length and cross-sectional area. From these values, data pertaining to the maximum compressive strength of the material, its break force and the percentage strain to failure were calculated using at least three separate repeat samples.
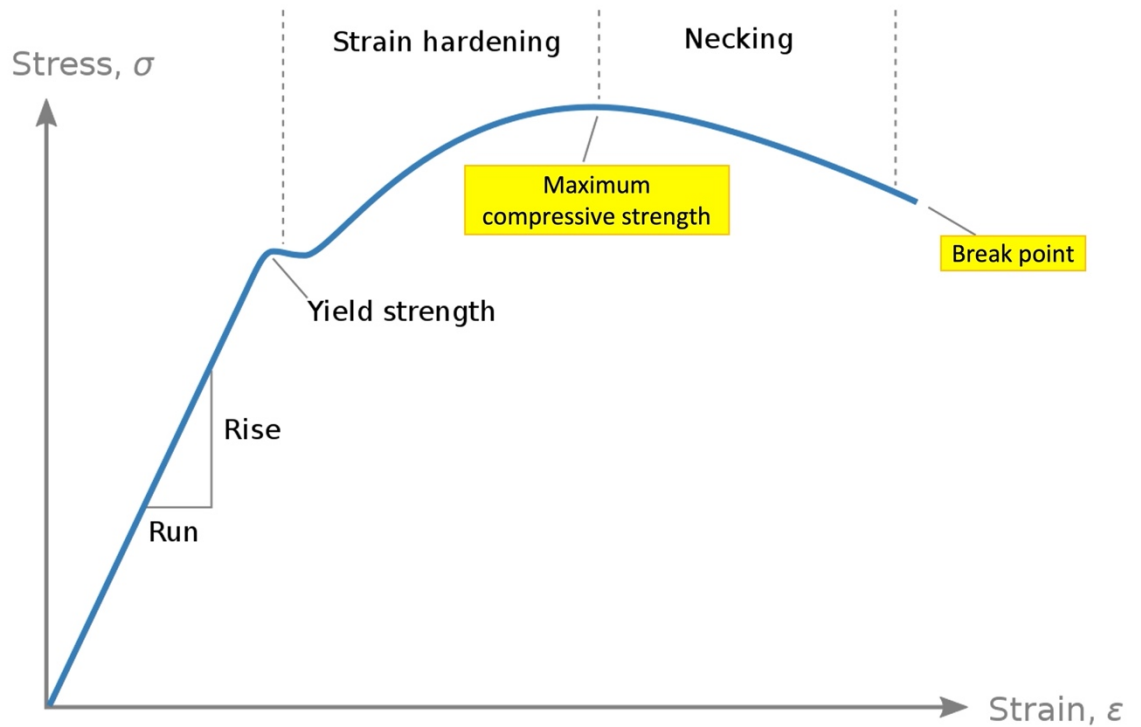
*Figure 2.13: Stress-strain curve of mechanical compression testing, highlighting the points of maximum compressive strength and the material breaking point*

It is documented that alginate based bioinks crosslinked with divalent cations have a predisposition to degrade and disintegrate in culture media, as rapidly as within 21 days (Shoichet *et al.*, 1996; Freeman and Kelly, 2017), secondary in part to the degradation of the ionic bonds when immersed in liquid and due to being subject to higher temperatures of cell culture conditions. As such, re-crosslinking was done as per the methods described for initial crosslinking in Section 2.5.5.3 prior to attempting mechanical tests.

### 2.11.3 Swelling assay

100 µl discs of biomaterial were produced and crosslinked using 100 µl of crosslinking agent. Excess crosslinking agent was blotted away using tissue paper and the discs were weighed ($m_{wet}$). Triplicates of each condition were produced. The discs were transferred to a 48 well plate with 1 ml PBS added to each well. The 48 well plate was transferred to an incubator set at 37°C and 5%

$CO_2$ for 24 hours. The discs were weighed to attain the fully hydrated weight ($m_{fully\ hydrated}$). The swelling was calculated using Equation 8.

**Equation 8:**

$$Swelling\ \% = \frac{m_{fully\ hydrated} - m_{wet}}{m_{wet}}\ x\ 100$$

### 2.11.4 Porosity assay

100 µl discs of biomaterial were produced and crosslinked using 100 µl of crosslinking agent, reproduced in triplicate. The discs were transferred to 48 well plates and left for 24 hours in 1 ml PBS at room temperature. The discs were removed from their wells and the excess PBS was removed through blotting using tissue paper. Each disc was weighed after blotting and recorded as $m_{wet}$. The discs were returned to the 48 well plate and transferred to a non-humid 37°C chamber for 72 hours. The discs were weighed again at the end of this period and recorded as $m_{dry}$. Porosity (%) was calculated using Equation 9.

**Equation 9:**

$$Porosity = \frac{m_{wet} - m_{dry}}{\rho_{PBS}\ x\ V_{pellet\ fully\ swollen}}\ x100$$

Where $\rho$ = is the density of PBS at 20°C (1.0723 g/cm$^3$).

### 2.11.5 Crosslinking size changes

To determine the change in construct size after crosslinking, 100 µl discs of biomaterial were produced in triplicate. The construct diameter of the discs was measured using digital callipers at 3 separate points and recorded as the initial diameters. Next, each disc was crosslinked using 100 µl of crosslinking agent as outlined in Sections 2.4.5.3-4. Excess crosslinking agent was blotted away using tissue paper. Once crosslinking had been achieved (5 or 10 minutes), the constructs were measured again at 3 separate points and these were recorded as post-crosslinking diameters. In order to calculate the % change in diameter post-crosslinking Equation 10 was used.

**Equation 10:**

% change in diameter post crosslinking $= \frac{\emptyset_{post} - \emptyset_{pre}}{\emptyset_{pre}} \, x \, 100$

Where $\emptyset_{post}$ = post-crosslinking diameter and $\emptyset_{pre}$ = pre-crosslinking diameter.

## 2.12    Biocompatibility

### 2.12.1 Live dead assay

A live dead mammalian cell viability assay kit (Thermofisher Scientific, MA, USA) was used to visualise live and dead cells within biomaterials and in cell culture conditions. Media was discarded from the cells and pellets and washed three times with warm PBS. A solution of PBS containing 1:1000 Calcein-AM dye and 1:500 Ethidium homodimer-1 was produced and protected from light. The solution was added to the wells of interest, protected from light and left to incubate in standard culture conditions for 45 minutes. The staining mixture was discarded and the wells were washed three times with warm PBS. The cells and pellets of interest were visualised under fluorescent microscopy using an inverted microscope (Olympus Ixplore, Olympus, Tokyo, Japan). The FITC channel for live cells (Calcein AM has an excitation of 488nm and emission of 520nm wavelength) and TRITC channel for dead cells with ethidium homodimer (a stain which emits fluorescence when able to traverse damaged membranes and bind to nuclear DNA at an excitation wavelength of 528 nm and 617 nm emission). 3 to 4 representative points were visualised for each sample, and at different depths where 3D structures were visualised at 10x magnification. The live and dead images acquired at each focal point were combined to enable live and dead cells to be counted using ImageJ. The mean proportion of live cells was calculated for each condition and expressed as a percentage of the total cells visualised.

### 2.12.2 Lactate dehydrogenase assay

A lactate dehydrogenase (LDH) assay kit (Thermofisher Scientific, MA, USA) was used to determine cytotoxicity in the biomaterials of interest. Cell-laden biomaterials (300,000 cells per pellet) were incubated in standard culture

conditions overnight alongside wells containing cell only controls (300,000 cells per well). Lysis buffer solution was added to 3 of the cell only wells and left to incubate for 45 minutes. 50 µl of media from each well was transferred to a 96 well plate alongside the provided LDH positive control samples. An equal volume of reaction mixture was added to each well for 30 minutes at room temperature and protected from light. After 30 minutes, 50 µl of stop solution was added to each well and mixed by tapping. The plate was thereafter read at 490 nm and 680 nm absorbance using a plate reader (POLARstar Omega spectrophotometer, BMG LABTECH, Ortenberg, Germany). The 680 nm value (background signal) was subtracted from the 490 nm value and used to calculate the degree of cytotoxicity in each sample using Equation 11.

**Equation 11:**

$$\% \text{ cytotoxicity} = \frac{\text{Treated LDH activity} - \text{spontaneous LDH activity}}{\text{Maximum LDH activity (lysed cells)} - \text{spontaneous LDH activity}} \times 100$$

### 2.13  Statistical analysis

Results are expressed as mean values with standard deviation unless otherwise stated. Data was assessed for Gaussian distributions and normality using Anderson Darling tests to guide the selection of an appropriate statistical test. The statistical test chosen was based upon the number and nature of independent variables and the normality of the datasets, and the equality of the standard deviations. Detailed descriptions of statistical methods used in each dataset are outlined in each results chapter. The most commonly used tests and examples of their use are outlined in Table 2.11.

| Independent variables | Dependent variables | Gaussian distribution? | Test selected | Multiple comparison test | Example use |
|---|---|---|---|---|---|
| 2 | 1 | Yes<br>No | T-test<br>Mann Whitney | n/a | qPCR $\Delta\Delta CT$ data |
| Greater than 2 | 1 | Yes<br><br>No | 1-way ANOVA<br>Kruskal Wallis | Tukey's<br><br>Dunn's | LDH assay of $H_2O_2$ crosslinking doses |
| Greater than 2 (two categories or time points) | 1 | Yes<br>No | 2-way ANOVA | Tukey's<br>Dunn's | iCELLigence growth curves |

*Table 2.11: Commonly used statistical tests and their conditions and applications*

All data is conducted in repeats of at least three for technical repeats, and where possible at least three biological repeats; where this has not been the case, or indeed if a larger number of repeats have been performed, this is outlined with the results and/or figure legend where appropriate. The statistical significance is indicated on graphical representations of the data and displayed according to the following: * $p<0.05$; ** $p<0.01$; *** $p<0.001$; **** $p <0.0001$. A p value of less than 0.05 was deemed statistically significant. Where qPCR data is concerned, a relative gene expression of over 2-fold difference, or less than 0.5-fold difference was deemed biologically significant. Statistical software used in this thesis were a combination of SPSS (IBM, NY, USA) and GraphPad Prism (version 9, San Diego, CA, USA).

# Chapter 3: Cellular Optimisation for 3D Bioprinting Cartilage

# Chapter 3: Cellular Optimisation for 3D Bioprinting

## 3.1 Introduction

### 3.1.1 Background

The success of tissue engineering is determined by the combination of cells, scaffold and environment (Almouemen, Kelly and O'Leary, 2019). With regard to optimal cell selection for cartilage tissue engineering, there have been competing strategies employed to generate cartilage *in vitro* (Jessop *et al.*, 2016). Mesenchymal stem cells such as bone marrow derived stem cells and adipose derived stem cells have gained traction owing to their multipotency and accessibility for harvest (Raghunath *et al.*, 2005; Xie *et al.*, 2012; Veronesi *et al.*, 2014; Yamasaki *et al.*, 2014; Rosadi *et al.*, 2019). However, stem cells acquired from unrelated tissue sources have proven problematic in clinical translation, resulting in poor quality cartilage formation prone to degradation, calcification, and mechanical instability (Cao *et al.*, 1997; Kusuhara *et al.*, 2009; Bichara *et al.*, 2012). The use of induced pluripotent stem cells has been explored for tissue engineering, but concerns remain about the efficiency of redifferentiation and the potential for neoplastic development owing to the genetic reprogramming of pluripotency (Medvedev, Shevchenko and Zakian, 2010; Yamashita *et al.*, 2013).

Cartilage is a tissue of very limited regenerative capacity, owing to its avascularity, as evidenced by degenerating diseases of cartilage such as osteoarthritis (Tuan, Chen and Klatt, 2013). In light of the limitations of non-cartilaginous stem cell sources, the pursuit of a chondroprogenitor cell population within cartilage has been a highly sought solution, offering not only the potential to regenerate defective cartilage but also to lend itself to exploitation for tissue engineering applications (Williams, *et al.*, 2010; Jessop *et al.*, 2016; Jessop *et al.*, 2019). Chondroprogenitor cells were first described in the context of articular cartilage, and are believed to offer clonal expansion and renewability: a panacea for cartilage tissue regeneration (Khan *et al.*, 2009; Williams *et al.*, 2010; Otto *et al.*, 2018). Dowthwaite et al discovered a small population of cells on the articular surface, believed to be chondroprogenitor cells owing to their high colony forming efficiency, adhesion to fibronectin and Notch1 expression (Dowthwaite *et al.*, 2004). Based on their high levels of cell surface adhesion proteins: integrins, such

as α5β1 integrin, it has been proposed that chondroprogenitor cells can be isolated through their capacity to bind fibronectin: a glycoprotein involved in organising extracellular matrix components such as collagen and fibrin (Grogan *et al.*, 2007; Williams *et al.*, 2010) and mediating cell adhesion (Pankov and Yamada, 2002).

Whilst an important finding, the isolation and behaviour of chondroprogenitor cells is controversial. Firstly, there remains controversy regarding the key cell surface markers that reliably differentiate chondoprogenitors from chondrocytes in cartilage (Jessop *et al.*, 2019), and secondly, the chondrogenic potential of chondroprogenitor cells appears to be attenuated when these cells are grown alone in isolation (Marcus *et al.*, 2014; Vinod *et al.*, 2019). Until recently, they have been most extensively characterised in the context of articular cartilage, however a population of fibronectin adherent cells in nasoseptal cartilage believed to represent chondroprogenitor cells have been identified that appear capable of trilineage differentiation, expressed recognised mesenchymal stem cell surface markers and displayed expression of key cartilage-specific genes (Jessop *et al.*, 2020).

In the context of native cartilage, the proposed chondroprogenitor population is believed to comprise a very small number of the total cell population (0.7% of cells in articular cartilage (Williams *et al.*, 2010)), in keeping with a tissue capable of limited regeneration such as cartilage. However, in the context of tissue engineering, in which the cells are required not only to populate a scaffold but thereafter to deposit copious extracellular matrix, it is uncertain whether mimicry of the native proportions of stem cell and mature cell populations should be emulated or whether the balance should be exploited to maximise tissue growth and maturation *in vitro* (Vinod *et al.*, 2019).

### 3.1.2  Aims

This chapter aims to identify the most suitable cell population derived from human nasoseptal cartilage for cartilage tissue engineering. This chapter must first identify the different cell populations within human nasoseptal cartilage and thereafter verify their ability to populate a scaffold and produce extracellular

matrix. In order to address the aim of this chapter, the following objectives will be explored:

- To evaluate the validity of the fibronectin adhesion assay in isolating a stem cell "chondroprogenitor" population from nasoseptal cartilage
- To determine the proportion of fibronectin adherent and non-adherent cells in native nasoseptal cartilage tissue samples
- To elucidate the growth kinetics and chondrogenic properties of the cell populations
- To determine whether different proportions of fibronectin-adherent and non-adherent cells can be manipulated to enhance chondrogenesis (chondrogenic gene expression, ECM production and cell number) in 2D and 3D culture.

## 3.2 Experimental methods

### 3.2.1 Isolation of cartilage derived cells and fibronectin adherent cells

Human nasoseptal chondrocytes were isolated from nasoseptal cartilage remnants following septorhinoplasty procedures through pronase and collagenase digestion as described in Sections 2.3.1-2.3.2. The mixed population of cells acquired from enzymatic digest should contain a mixture of chondroprogenitor cells and chondrocytes and this heterogeneous population is referred to in this thesis as Cartilage Derived Cells (CDCs). Isolation of a suspected chondroprogenitor cell population has been previously described using a fibronectin adhesion assay (Section 2.3.3). In brief, culture vessels are coated with a mixture of 10 µg/ml fibronectin solution at least 24 hours prior to the addition of cells. The CDC mixture, suspended in media, is added to the fibronectin-coated plate immediately post-digest and the chondroprogenitor cells are believed to adhere to the cells within 20 minutes. The cells that adhere to the fibronectin within this period are referred to in this thesis as fibronectin-adherent cells (FACs): a presumed chondroprogenitor population. The remaining media contains cartilage derived cells that are not adherent to fibronectin within the 20-minute period and are referred to as non-fibronectin adherent cells (NFACs). These cells should theoretically represent a chondrocyte population free from chondroprogenitors.

### 3.2.2 Generation of "cell ratio" populations

Artificially generated populations of FAC and NFAC cells were combined after first passage in the ratios outlined in Table 3.1.

149

| Cell ratio | Proportion of NFAC cells | Proportion of FAC cells |
|---|---|---|
| CDC | Native proportion | Native proportion |
| 100NFAC | 100 | 0 |
| 80N:20F | 80 | 20 |
| 60N:40F | 60 | 40 |
| 40N:60F | 40 | 60 |
| 20N:80F | 20 | 80 |
| 100FAC | 0 | 100 |

*Table 3.1: Cell ratio populations, their nomenclature and constituents*

Cell ratio populations were achieved using cell counting as described in Section 2.3.4, and a total of 50,000 cells were plated onto the wells of a 6 well plate to determine gene expression in monolayer culture conditions and to observe for cell morphology upon reaching confluence. To determine the chondrogenic potential of the different cell ratios in 3D culture, cells from each population were combined in a microcentrifugation tube in the proportions outlined in Table 3.1 and assessed for their chondrogenic potential in 2D and 3D as described in Section 3.2.7. The cell suspension was thereafter added to a 2.5% w/v alginate hydrogel at a density of $3x10^6$ cells per ml and dispersed into 100 µl beads using a 1ml syringe. The beads were crosslinked through the addition of 0.5M $CaCl_2$ for 5 minutes and cultured in chondromedia for up to 21 days. Technical triplicates of each condition were performed in biological triplicates.

### 3.2.3  Flow cytometric characterisation of cell populations

The three cell populations were characterised using flow cytometry to examine for mesenchymal stem cell surface markers and chondrogenic cell surface markers and to ensure that negative markers (i.e. haematopoietic and non-mesenchymal lineages) were not present on the cells. Automated cell counting

(as described in Section 2.3.2) was used to determine the concentration of each cell population, and using this information, 100000 cells were added to flow tubes and centrifuged to remove media as described in Section 2.3.2. CDCs were taken immediately post-harvest and characterised for the surface expression of a panel of mesenchymal and chondrogenic stem cell markers as previously optimised (Jessop *et al.*, 2020). After splitting and separately culturing the cells to first passage, the individual cell populations: CDC, NFAC and FAC cells were then characterised using the same flow cytometry panel. As reported in Section 2.4.2, cells from each population were transferred to 6 separate flow tubes to be processed as unstained, stained for CD29, CD44, CD56 and CD73; CD90; CD49e; CD24, CD34 and CD 45, or Stro-1 to minimise overlap in emission spectra. The cell pellet was then resuspended in FACS buffer with 5μl of fluorophore conjugated antibody (Section 2.4.2) and allowed to adhere for 30 minutes protected from light. The unbound antibody was washed away using further washes and centrifugation with FACS buffer as described in Section 2.4.2. The fluorescent-labelled cells were then run through a NovoCyte Flow Cytometer (ACEA Biosciences, Agilent, CA, USA) for a minimum of 10,000 events and compared to a control, unstained sample from the same cell population. The percentage of cells positive for each fluorophore (and thus cell surface marker) were ascertained relative to the unstained population (% cells positive). The median fluorescence index (MFI) of the stained populations for each fluorophore were expressed relative to the unstained MFI and expressed as a signal:noise (S:N) ratio. A compensation control matrix was generated and applied to the data to negate artefactual fluorescence (Appendix 1). Each experiment was performed in biological triplicates for each passage and fluorophore specified (n=3).

### 3.2.4  Trilineage differentiation of cartilage cell populations

The potential of each cell population to differentiate into osteogenic, adipogenic and chondrogenic lineages was determined using StemPro trilineage differentiation kits (Thermofisher, MA, USA) as outlined in Section 2.4.1. In brief, cells from each of the FAC, NFAC and CDC populations were seeded into 12 well plates and cultured until adherent using standard chondromedia (the constituents

of which are described in Section 2.3.2). Thereafter, the cells were cultured using chondrogenic, adipogenic or osteogenic media for up to 21 days. The cells were then fixed with 4% paraformaldehyde solution for 30 minutes and stained with lineage specific stains: Alizarin Red (bone), Alcian blue (cartilage) or Oil Red O stain (adipose). All populations were also stained with haematoxylin and eosin to facilitate the characterisation of cell morphology. Duplicate wells were seeded using biological triplicates (n=6).

### 3.2.5  Characterisation of tissue morphology

Small pieces of nasoseptal cartilage were taken immediately after acquisition from surgery and immersed in 4% paraformaldehyde for 30 minutes. The tissue was washed in PBS three times and embedded in OCT compound for 30 minutes and snap frozen in liquid nitrogen. Tissue was sectioned as per Section 2.10.2 and mounted on to slides for staining. The cartilage tissue was stained with Haematoxylin and eosin (Section 2.10.3.1), alcian blue (Section 2.10.3.2) and toluidine blue (Section 2.10.3.3) stains as described and washed until clear runoff was achieved. A coverslip was mounted onto the slides using mounting medium and the stained specimens were then examined under brightfield microscopy using an Olympus CKX53 microscope as described in Section 2.10.3.5. Samples were taken from one biological repeat and processed in triplicate (n=3).

### 3.2.6  Characterisation of cell morphology

Cell morphology was visualised using brightfield microscopy and immunofluorescence. For brightfield microscopic analysis of cell morphology, 50,000 cells were cultured in separate wells of a 6 well plate until confluent (72 hours). Cells from the CDC, NFAC and FAC populations were visualised under Brightfield microscopy immediately after separation to assess for morphological differences. After reaching confluence, media was discarded from the plates and washed with PBS three times. 500 µl of 4% paraformaldehyde solution was added to each plate and left for 30 minutes, after which it was removed and the plates washed with PBS. 500 µl of 1% Alcian blue stain was added to each well and left for 20 minutes. The plate was then washed with distilled water until the

runoff was clear. Cells were visualised at 10 and 40x magnification using an Olympus CKX53 microscope, and captured using cellSens software (Olympus, Tokyo, Japan) as outlined in Section 2.10.3.5. Images were compared for disparities in cell morphology, size and Alcian blue staining intensity in the different populations. Three representative images were taken from biological triplicates.

To further characterise morphological differences, the CDC, FNAC and FAC populations were cultured separately on the wells of an 8 well chamber slide (Thermofisher, MA, USA) in duplicate from three biological repeats (n=6). The cell populations were allowed to adhere and proliferate for 72 hours after which the slides were fixed with 4% PFA for 20 minutes. The cells were permeabilised using 0.2% TritonX solution (Merck, MO, USA) and blocked with 1% BSA solution. Cells were stained sequentially with phalloidin rhodamine stain for F-actin and DAPI for nuclear staining, protected from light and a coverslip mounted using Vectashield (Vectorlabs, CA, USA). The cells were visualised using confocal microscopy at 4 and 20x magnification (Zeiss Laser Scanning Microscope 710, NY, USA).

### 3.2.7    Assessing chondrogenic potential of cell populations

### 3.2.7.1        Chondrogenic gene expression

The cell populations from 3 biological repeats were harvested at first passage using TRIzol reagent (Thermofisher, MA, USA) and frozen at -80C. The RNA from the lysate was extracted through the addition of chloroform and centrifuged at 14500 g for 15 minutes to separate out the phenol, cell debris and RNA rich supernatant as described in Section 2.8.1. The supernatant was purified using a Qiagen RNEasy Mini Kit (Qiagen, Germany) and the purified RNA extract was then assessed for RNA content and purity using a Nanodrop Spectrophotometer (Thermofisher, MA, USA) as described in Section 2.8.3.

The purified mRNA was reverse transcribed into cDNA as described in Section 2.8.4 using the superscript IV reverse transcriptase enzyme (Thermofisher, MA, USA) and associated reagents catalysed using sequential temperature changes in the T100 thermal cycler (BioRad, CA, USA). 1 µl of the cDNA was added to

the wells of a 96 well PCR plate with 10 µl Brilliant III Ultra-fast SYBR Green PCR Master Mix (Agilent Technologies, CA, USA), 8.6 µl nuclease free water and 0.4 µl of the target gene primer (reverse and forward). The target genes used were Type 2 collagen, aggrecan and SOX9 alongside the housekeeping genes RPL13A and TBP as justified and described in Sections 2.8.5-2.8.6. The loaded 96 well plate was run in a CFX connect machine (BioRad, CA, USA) using the protocol described in Section 2.8.7, generating Ct values that were subsequently analysed for relative gene expression as described in Section 2.8.8. The control population was the CDC population in all gene expression analyses reported in this chapter, and relative gene expression values were therefore expressed relative to the control CDC population. Four technical repeats were performed per biological sample (n=12).

### 3.2.7.2    Chondrogenic extracellular matrix production

To determine the production of cartilage extracellular matrix components, a dimethylmethylene blue assay (Section 2.9.3) was conducted, on 3 separate alginate beads per cell population in biological triplicate (n=9), using 40 µl of protein lysate prepared as per Section 2.9.1, using RIPA buffer and protease inhibitor solution to extract intra- and extracellular protein. Each lysate was reacted with 200 µl of DMMB solution and read at an absorbency of 525 nm along with a series of chondroitin sulphate standards ranging from 0 to 50 µg/ml. A standard curve generated from the chondroitin samples was used to calculate the glycosaminoglycan content of each sample.

### 3.2.8  Cell adhesion and proliferation

The iCELLigence impedance-based assay was used to determine the adhesion and growth trajectories of the different cell populations and cell ratio populations over a 72-hour period. 17500 cells were seeded per well, containing the mixture of cells described in Table 3.1 in duplicate per biological repeat. A total of 6 biological repeats were performed (therefore n=12 per condition). During the first 2 hours of the iCELLigence protocol, impedance readings were acquired every minute to record adhesion rates on to the polystyrene wells as a marker of plastic

adherence. Thereafter, hourly readings were acquired to capture changes in electrical impedance as a measure of cell proliferation. The different populations were pooled across biological repeats and used to calculate growth curves, adhesion rates and population doubling times.

### 3.2.9  Statistical analysis

Data sets were assessed for normality (Gaussian distribution) visually and where needed using an Anderson-Darling test. Statistical analyses were thereafter selected accordingly. All data presented is the mean value of technical +/- biological replicates which is presented graphically with error bars depicting standard deviation unless otherwise stated.

For statistical comparisons between two dependent variables, either a t-test (+/- Welch's correction; where standard deviations were not equal) or Mann Whitney test (where data was not normally distributed) was used. In this chapter, the following data sets were analysed using unpaired, two tailed t-tests: comparison of ratio of FAC:NFAC cells in human nasoseptal cartilage samples (Figure 3.1) and for PCR analyses comparing relative gene expression to a reference population using the ΔΔCt method (Figure 3.12). Whereas Mann Whitney tests were used to assess differences in male and female cohorts of FAC and NFAC cells (Figure 3.2). For this data set, median and interquartile range (IQR) values are also presented.

For statistically analysing multiple dependent (>2) variables, typically a one-way ANOVA was used with a Tukey's post hoc test for multiple comparisons. In this chapter this analysis was used for comparing flow cytometry data for each CD marker between cell populations (Figure 3.7, Figure 3.8, Figure 3.10) and for comparing population doubling times (Figure 3.16) and ECM production between cell populations (Figure 3.18).

A 2-way repeated measures ANOVA was used when multiple dependent variables (>2) were used across multiple different time points, with a Tukey's post hoc test. In this chapter, this analysis was used for comparing differences in growth curves between cell populations (Figure 3.13, Figure 3.14).

## 3.3 Results

This section addresses the primary aim of this chapter: to identify the most suitable combination of cells derived from nasoseptal cartilage for bioengineering cartilage. First, native human nasoseptal cartilage is examined at the level of the tissue architecture and cellular constituents: FACs and NFACs extracted from all cartilage derived cells (CDCs). The cellular populations are examined in terms of their morphological and chondrogenic characteristics and mesenchymal stem cell properties. Thereafter, the cell populations are combined in different proportions to determine whether a particular ratio of NFAC to FAC cells is superior to naturally occurring CDCs in terms of growth kinetics and chondrogenicity.

### 3.3.1 Determination of native proportions of fibronectin adherent and non-fibronectin adherent cells in adult nasoseptal cartilage

Firstly, the relative proportions of FAC and NFACs was determined from human nasoseptal cartilage samples. Cell counting was used to determine the number of cartilage derived cells that were fibronectin adherent and those that were non-adherent after 20 mins of incubation on a fibronectin plate. The results were separated on the basis of gender (Figure 3.1). The number of NFAC cells was lower than the number of FACs in both male (47.4%, n=10) and female patients (42.3%, n=10), though this was only a statistically significant difference in female patients (p=0.001).
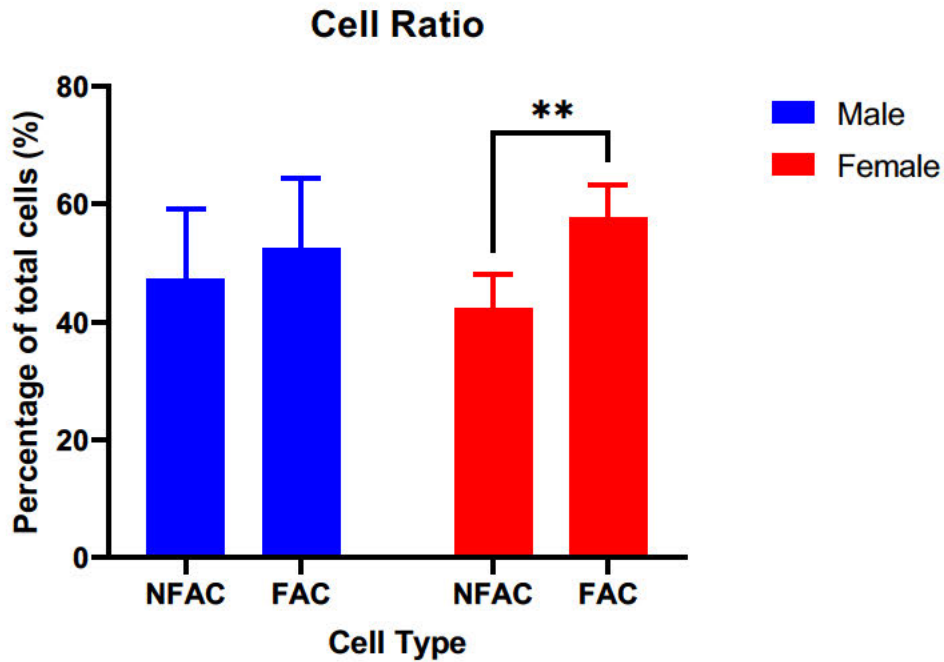
*Figure 3.1: Proportion of fibronectin-adherent (FAC) and non-adherent chondrocytes (NFAC) from donor patients. Mean values from a set of 10 male and 10 female patients are presented with standard deviation (SD) error bars. There were no significant differences noted in the male cell populations. \*=p<0.05; \*\*=p<0.01.*

Of the patients studied, the female cohort were significantly older than the male cohort studied (p=0.02) with a median age of 29.5 in the female cohort (IQR=7.75, range 28) and 25.5 in the male cohort (IQR 9.5, range 23) (Figure 3.2A). The proportion of FACs did not appear to differ significantly between male (median 51.5, IQR 18.25) and female (median 57, IQR 5.75) subjects, though a much broader range of FAC cells were observed in the male cohort (range 34) compared to females (range 19) (Figure 3.2B). The trend in the proportion of FAC cells appeared to display minimal correlation with age in both male (y=-0.51x + 65.5; $R^2$=0.0834) and female (y=-0.14x+ 62.4; $R^2$= 0.0382) patients using Spearman's rank correlation coefficient (Figure 3.2C). The correlation was so weak in both gender cohorts, that no significant changes to the FAC:NFAC ratio were observed with increasing age in either gender (Males: p=0.418; Females: p=0.589). As such, age and gender were not significantly associated with the proportion of FACs in human nasoseptal cartilage.
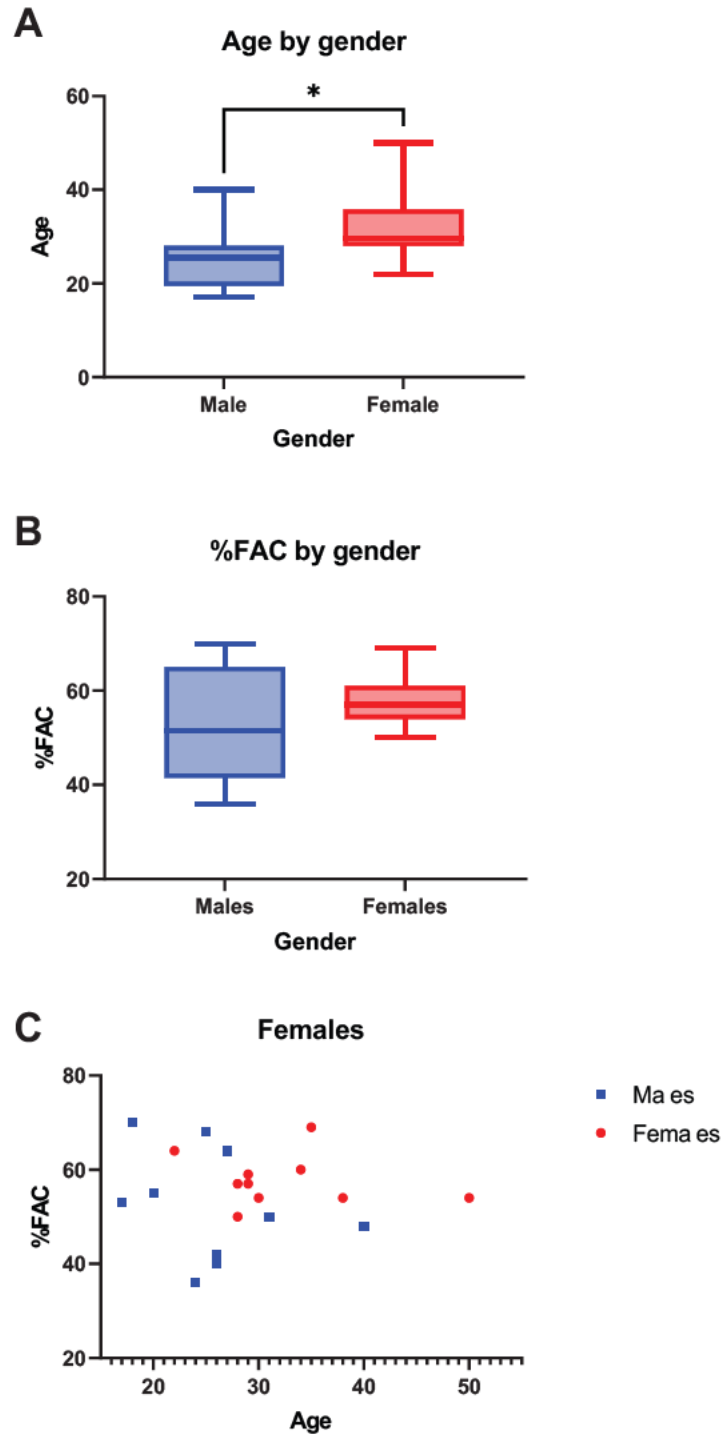
*Figure 3.2: Characteristics of male and female patient cohorts. A) Box and whisker plot of age (years) in male and female cohorts with boxes depicting IQR and median and whiskers depicting the range. \*=p<0.05. B) Percentage of FAC cells (as a percentage of total cells) in male and female cohorts with boxes depicting IQR and median and whiskers depicting the range. C) Scatterplot of age in years (x axis) compared to percentage of FAC cells (y axis) of total cell numbers. A biological n of 20 is presented (n=10 female; n=10 male subjects).*

### 3.3.2 Characterisation of adult nasoseptal cartilage, NFACs and FACs

### 3.3.2.1 Histological appearance of native cartilage tissue

It is important to appreciate the native structure of nasoseptal cartilage and the cells that reside therein in order to achieve suitable biomimicry in cartilage tissue engineering. Figure 3.3 depicts the appearance of nasoseptal cartilage taken immediately post acquisition from surgery and stained with H&E, Alcian Blue and Toluidine blue stains to highlight cell morphology, arrangement and the presence of extracellular matrix components such as glycoasminoglycans and proteoglycans. In nasoseptal cartilage, the cells exist singly or in small clusters in lacunae, as seen clearly in the H&E stain. Here, small cavities surrounded by layers of extracellular matrix are evident, with cells appearing to adopt a rounded morphology with centrally located nuclei. The extracellular matrix comprises a mixture of collagen, proteoglycans (stained with Toluidine blue) and glycoasminoglycans such as hyaluronic acid as visualised with Alcian blue stain. This appears to stain less intensely at the edge of cell lacunae but is largely homogeneous in staining intensity elsewhere in the tissue matrix.
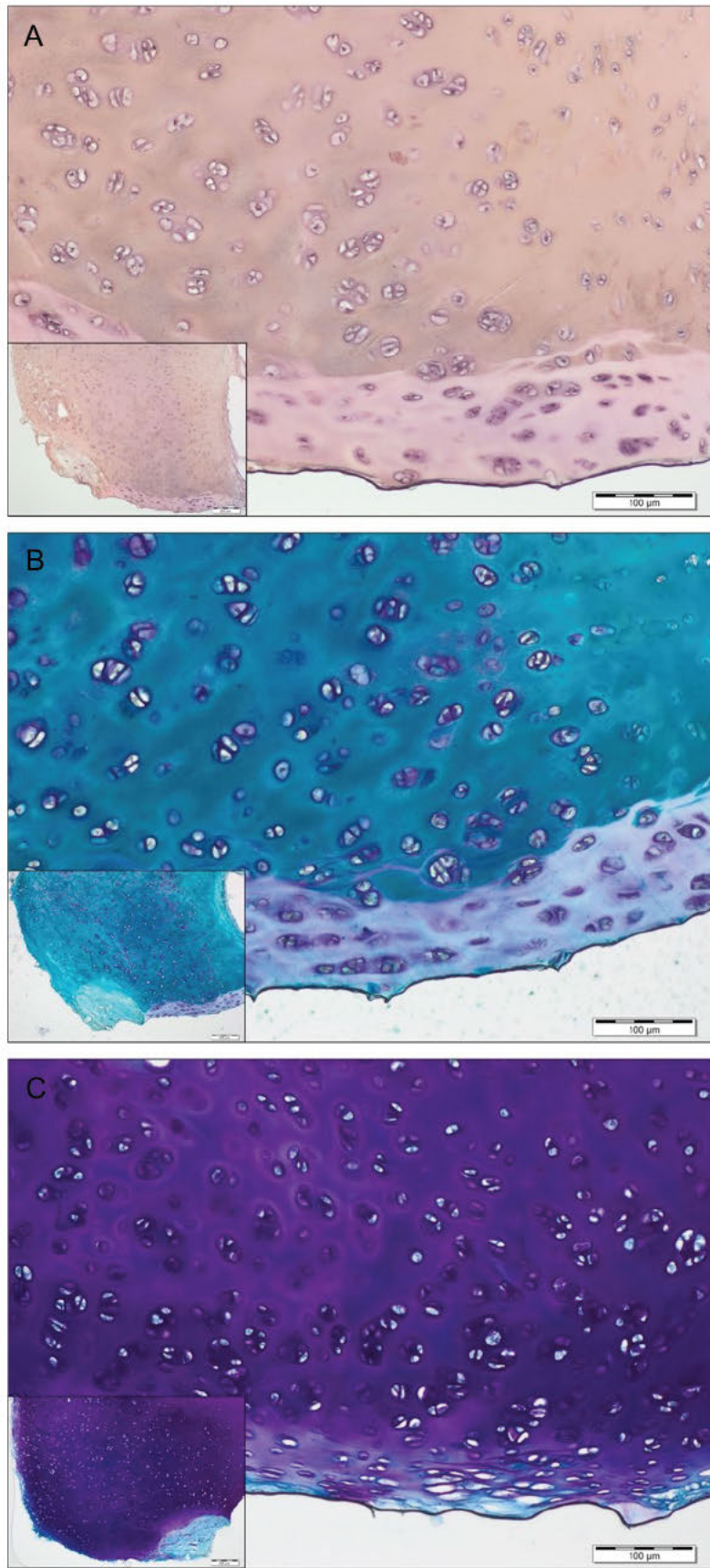
*Figure 3.3: Histological sectioning and staining of native nasoseptal cartilage tissue with H&E (A), Alcian Blue (B) and Toluidine blue (C). Images are taken at 10x and 4x magnification for each stain (n=1).*

### 3.3.2.2    Cell morphology

Cells were imaged to ascertain whether there were any structural or morphological differences between FAC and NFACs. Each cell population was imaged microscopically immediately after digest and after 7 days in culture with Alcian blue stain for extracellular matrix production (Figure 3.4). The cells initially displayed a rounded phenotype after digest, irrespective of adhesion to fibronectin. Thereafter, cells demonstrated a bipolar or multipolar morphology with elongated shapes and 2-3 cytoplasmic processes along with evidence of attachment to the underlying plastic material. All the cell types demonstrated an ability to produce glycosaminoglycans as demonstrated by Alcian blue staining at 7 days, irrespective of fibronectin adherence (Figure 3.4).
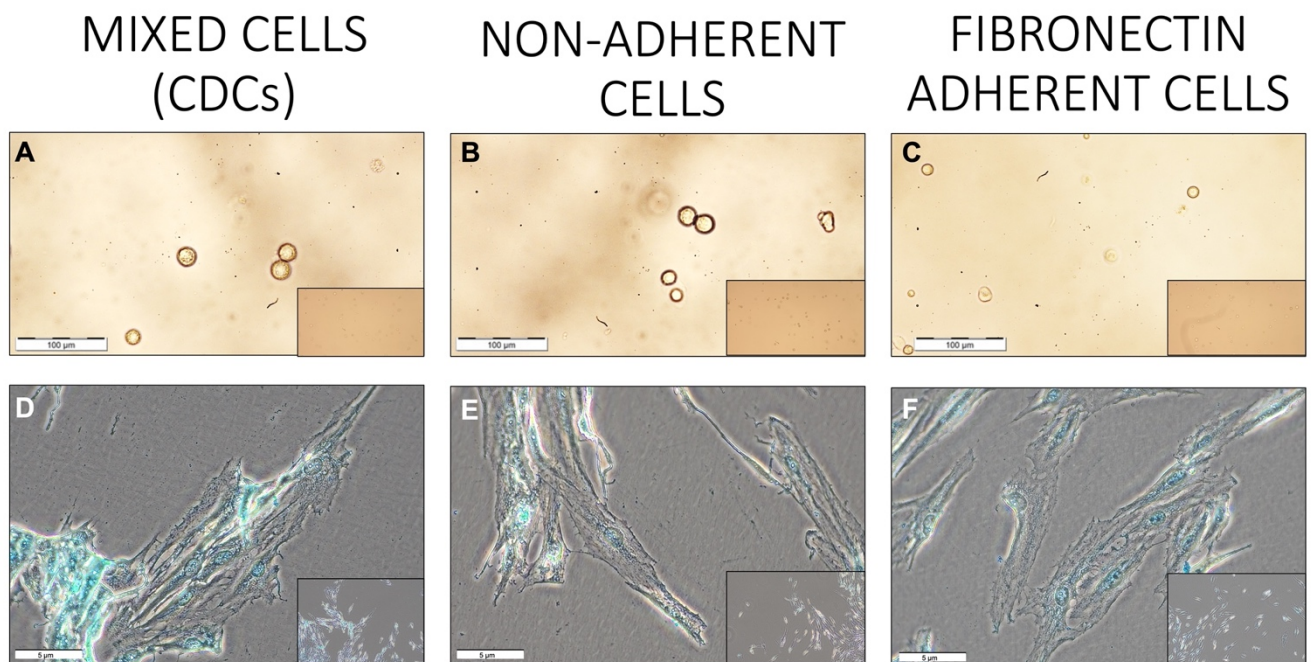


*Figure 3.4: CDC (A+D); NFAC (B+E) and FAC (C+F) taken using brightfield microscopy at Day 0 (A-C) and after staining with alcian blue after 7 days of culture (D-F). All cells demonstrate similar morphology and cell sizes and are capable of extracellular matrix production (stained blue in D-F). Images are taken at 4x and 10x magnification (A-C), scale bars equate to 100 μm and 10x and 40x magnification (D-F), scale bars equate to 5 μm.*

Cells from each source were cultured separately on chamber slides and stained with DAPI for nuclei and phalloidin for cytoskeletal components and visualised at 20x magnification (Figure 3.5). All cells demonstrated an ability to form confluent

cell populations over a 48-hour time period and all demonstrated evidence of cytoplasmic processes with the actin stain. The cells appeared generally to have a greater number of rounded morphologies in the non-adherent cell population than the mixed cell and fibronectin adherent populations, where cytoplasmic extensions and multipolar morphologies dominate cell appearance. In summary, there were minimal morphological differences observed between cell populations.
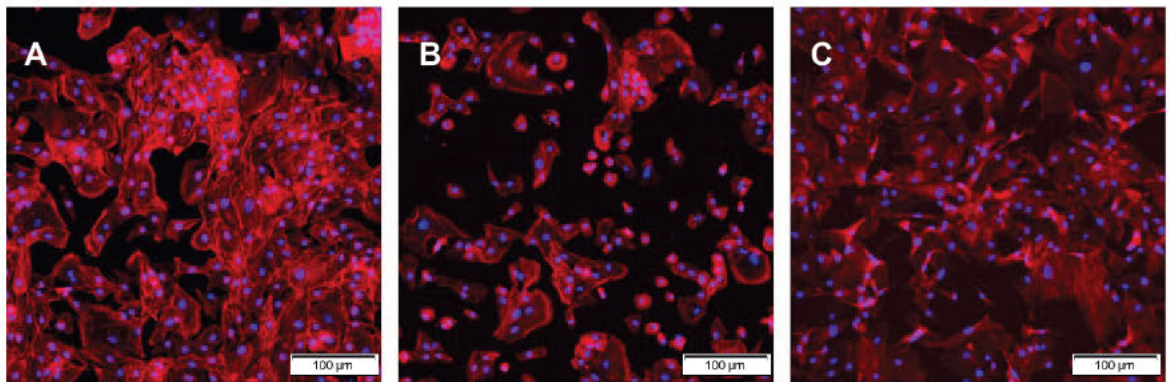


*Figure 3.5: Immunofluorescence of cell populations viewed at 20x magnification. All cell populations were stained for nuclei with DAPI and actin cytoskeletal proteins with Rhodamine Phalloidin stain. A) Mixed cell populations (CDCs) forming confluent cell populations with spindle shaped morphology B) NFACs showing rounded morphologies with limited evidence of confluence C) FACs demonstrating spindle shaped confluent morphologies. Representative images from a single biological replicate are presented based on a total biological n of 3.*

### 3.3.2.3    Characterisation using flow cytometry

Immediately after digest, CDCs were collected for flow cytometric analysis prior to fibronectin adhesion, to determine the proportion of cells expressing CD49e: the marker believed to characterise the chondroprogenitor phenotype and enable adhesion to fibronectin, in addition to acquiring baseline cell surface markers.
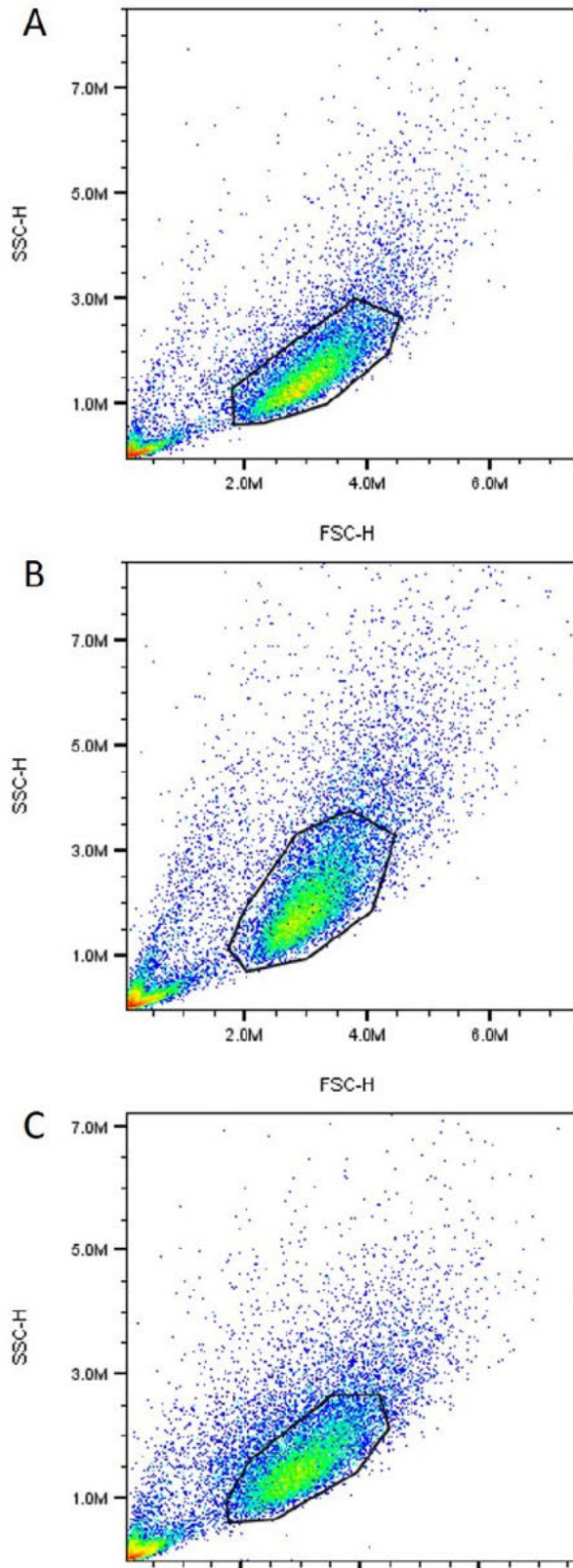
*Figure 3.6: Flow cytometry scattergrams plotted using forward (FSC-H) and side scatter (SSC-H) for identifying and gating cell populations. CDC populations (A), NFAC populations (B) and FAC populations (C) were each gated for the most homogeneous, viable cell population as drawn. The 100,000 cells gated in each sample were used in subsequent analysis for cell surface markers. Representative images are shown from a single biological sample for illustrative purposes.*

163

The proportion of cells displaying positivity for each cell marker were expressed as percentage of the total cell population (Table 3.2) and as a signal:noise (S:N) ratio based on the median fluorescence index.

CDCs, FACs and NFACs were cultured in separate containers up to 70% confluence (10-14 days), at which point flow cytometric analysis of the same cell surface markers was repeated. The expression of cell surface markers was compared between the three different cell populations and the original cell population post digest.

|  | CDC P0 | | CDC P1 | | NFAC P1 | | FAC P1 | |
|---|---|---|---|---|---|---|---|---|
|  | Mean | SD | Mean | SD | Mean | SD | Mean | SD |
| CD29 | 65.03 | 15.80 | 99.07 | 1.05 | 100.00 | 0.00 | 99.93 | 0.05 |
| Cd44 | 6.05 | 3.28 | 97.33 | 2.10 | 95.20 | 4.37 | 88.40 | 15.06 |
| CD56 | 0.28 | 0.01 | 32.60 | 45.68 | 17.49 | 24.62 | 0.67 | 0.60 |
| CD73 | 97.13 | 0.66 | 100.00 | 0.00 | 100.00 | 0.00 | 99.97 | 0.05 |
| CD90 | 21.07 | 5.55 | 97.50 | 2.01 | 97.57 | 1.44 | 84.60 | 12.92 |
| CD49e | 0.19 | 0.17 | 21.38 | 9.87 | 8.50 | 4.19 | 21.80 | 6.53 |
| CD34 | 6.38 | 1.61 | 3.09 | 1.67 | 2.35 | 1.46 | 1.61 | 1.22 |
| CD45 | 0.14 | 0.06 | 0.15 | 0.04 | 0.17 | 0.04 | 0.09 | 0.01 |
| Stro-1 | 1.13 | 0.30 | 5.51 | 2.91 | 9.67 | 8.96 | 3.84 | 2.68 |
| CD24 | 3.63 | 2.54 | 27.40 | 20.37 | 27.57 | 4.80 | 21.13 | 10.70 |

*Table 3.2: Mean percentage of cells (+Standard Deviation (SD)) expressing cell surface markers immediately post-digest (CDC P0) and in the separately cultured populations (CDC, NFAC and FAC) at Passage 1 (P1)*

There were highly significant differences in cell surface markers between cell populations with an ANOVA analysis ($p < 0.0001$). Tukey's multiple comparison test did not demonstrate any significant differences between the CDC, NFAC or FAC cell surface markers after separate culture (Figure 3.7). However, there were noted to be a greater proportion of cells expressing positive stem cell markers (CD29, CD44, CD56, CD73, CD90, CD49e) and CD24 after 10-14 days of culture

to 70% confluence. Furthermore, these were statistically significant increases for CD29 (p=0.006 for P0 vs P1 cells), CD44 (p<0.0001 for P0 vs all P1 cells) and CD90 (p<0.0001 for P0 vs P1 cells) and a statistically significant reduction in cells with CD34 expression was observed in the FAC and NFAC population at first passage. Notably, 100% of cells expressed stem cell marker CD73 by the first passage in all cell populations, and greater than 99% expressed CD29. CD90 was also expressed in >97.5% of cells in the CDC and NFAC population, and 84.6% in the FAC population (Table 3.2). CD56 was higher in the CDC population at P1 (32.6%) vs P0 (0.3%, p=0.01) and higher at P1 in the CDC population compared to the FAC population (0.7%, p=0.01). There were no other significant differences noted between the P1 cell populations.
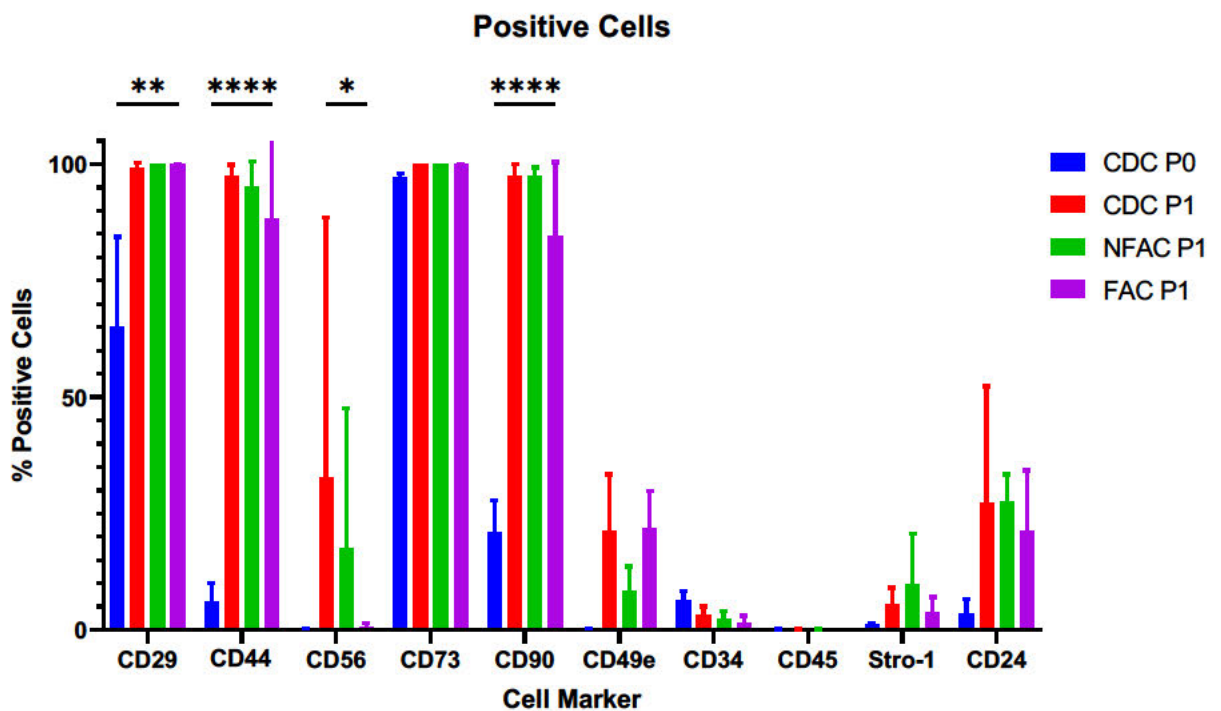


Figure 3.7: Mean percentage of total cells expressing cell surface markers at P0 (blue) and P1 (CDC = red, NFAC=green, FAC=purple). *=p<0.05; **=p<0.01; ***=p<0.001; ****=p<0.0001. The mean of a biological n of 3 is presented with error bars depicting standard deviation.

Similar trends were observed with the S:N ratios for cell surface markers (Figure 3.8): a normalised value indicating the median fluorescence intensity for the fluorophores affixed to each cell surface marker, corrected for background fluorescence from unstained cells from the same population, in which a ratio of 1 indicates an absence of a fluorescent signal.

Highly significant differences between the cells immediately post-digest (P0) and at first passage (P1) ($p<0.0001$) were identified, there was also noted to be significant variation between patient samples ($p=0.008$). However, no significant differences were observed between the different cell populations at P1. Particularly stark was the increase in the CD49e signal at first passage from a mean SN ratio of 1.26 to greater than 3 in the CDC and FAC populations ($p=0.004$, $p=0.02$ respectively). Similarly, there was a large rise in the SN ratio of CD29 from a mean of 10.9 at P0 to 90 (CDC, $p=0.03$), 209 (NFAC, $p<0.0001$) and 154 (FAC, $p<0.0001$) in the cell populations at P1. CD73 increased from P0 to all P1 cell populations ($p<0.0001$ for all comparisons) and stark rises were also observed in CD44 and CD90 between P0 and P1 but his was not significant. Similarly notable is the absence of CD56, also known as NCAM-1, staining relative to the other stem cell markers, though this was noted to be higher (albeit not significant) in the FAC population at P1.

In summary, there appeared to be significant differences in the presence of cell surface markers between P0 and P1, particularly increases in mesenchymal stem cell markers such as CD29, CD44, CD73 and CD90. However, there were fewer differences between cell types, indicating the main changes are associated is with increasing time in cell culture rather than fibronectin adherence.
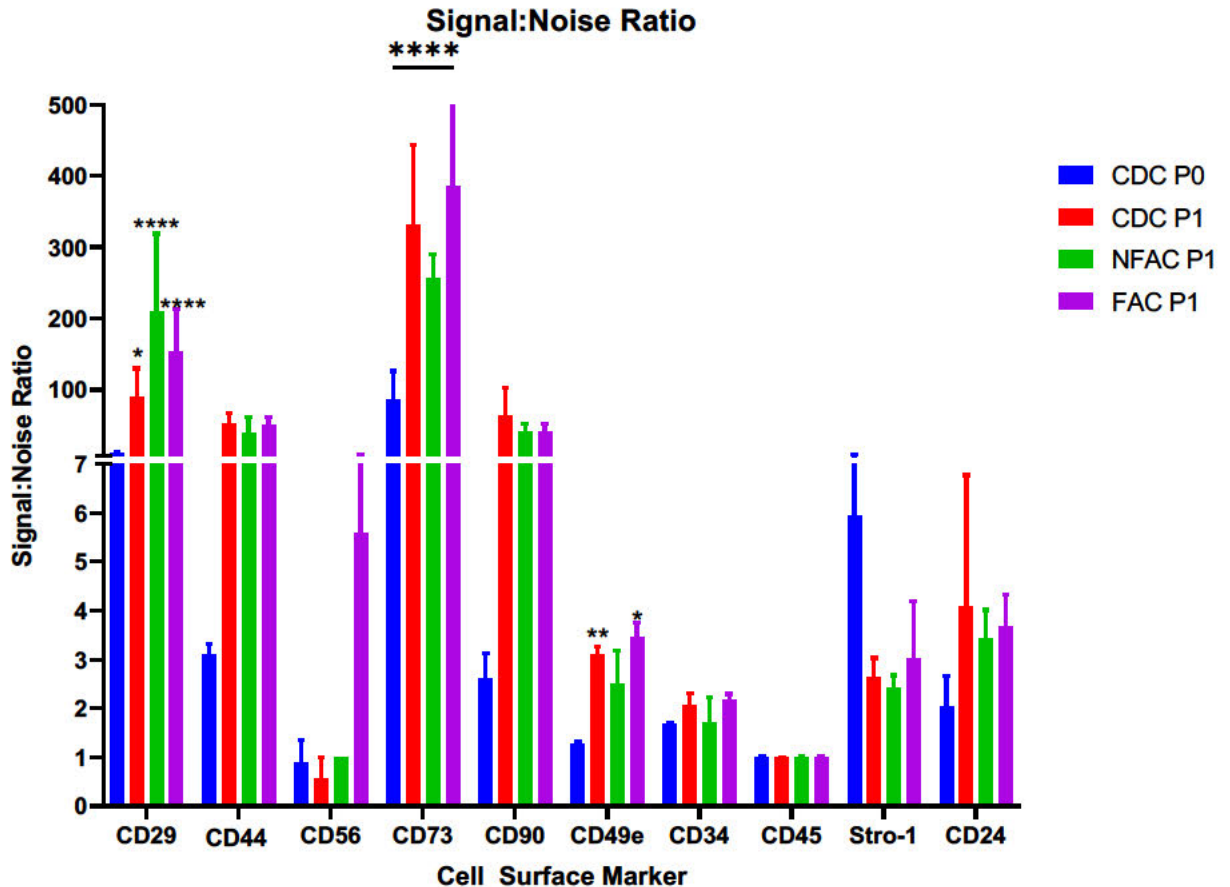
*Figure 3.8: Signal:Noise ratios derived from median fluorescence index (MFI) of stained populations corrected for the MFI of the unstained population. A S:N ratio of 1 is therefore equivalent to no fluoresence. Each cell surface marker is examined in the full cell population immediately post-digest at P0 (blue, CDC only) and then in the three populations at P1 (CDC = red, NFAC=green, FAC=purple).The mean S:N ratio of 3 biological replicates are presented with SD error bars. \*=p<0.05; \*\*=p<0.01.*

For the majority of stem cell markers, there were minimal further changes observed between second (P2) and eighth (P8) passage, particularly those that changed starkly been P0 and P1 such as CD29, CD44 and CD90 demonstrated no further changes (Figure 3.9). Stro-1 expression did rise between P2 (4.3%), P5 (16.2%, p=0.38) and P8 (48.9%, p=0.0001), with almost half of the cartilage derived cells expressing Stro-1 by P8. Furthermore, CD24 continued to rise between P2 (30.5%), P5 (71.1%, p<0.0001) and P8 (93.1%, p<0.0001 compared to P2, p=0.039 compared to P5) with essentially all cells expressing CD24 by P8. The signal to noise ratio however (Figure 3.10) did demonstrate that CD29 and CD73 continued to rise in signal, implying the cells upregulated their surface

expression of these markers with increasing passage. Specifically, CD29 rose from 259.3 at P2 to 517.7 at P5 (p<0.0001) and 473.5 at P8 (p=0.0005, relative to P2) and CD73 rose from 191.0 at P2 to 407.1 at P8 (p=0.0004). Prolonged cell culture therefore not only increases some mesenchymal stem cell markers (CD29, CD73) but also some markers associated with 'immature' cell markers such as CD24 and Stro-1.

**P2, P5, P8 Data**
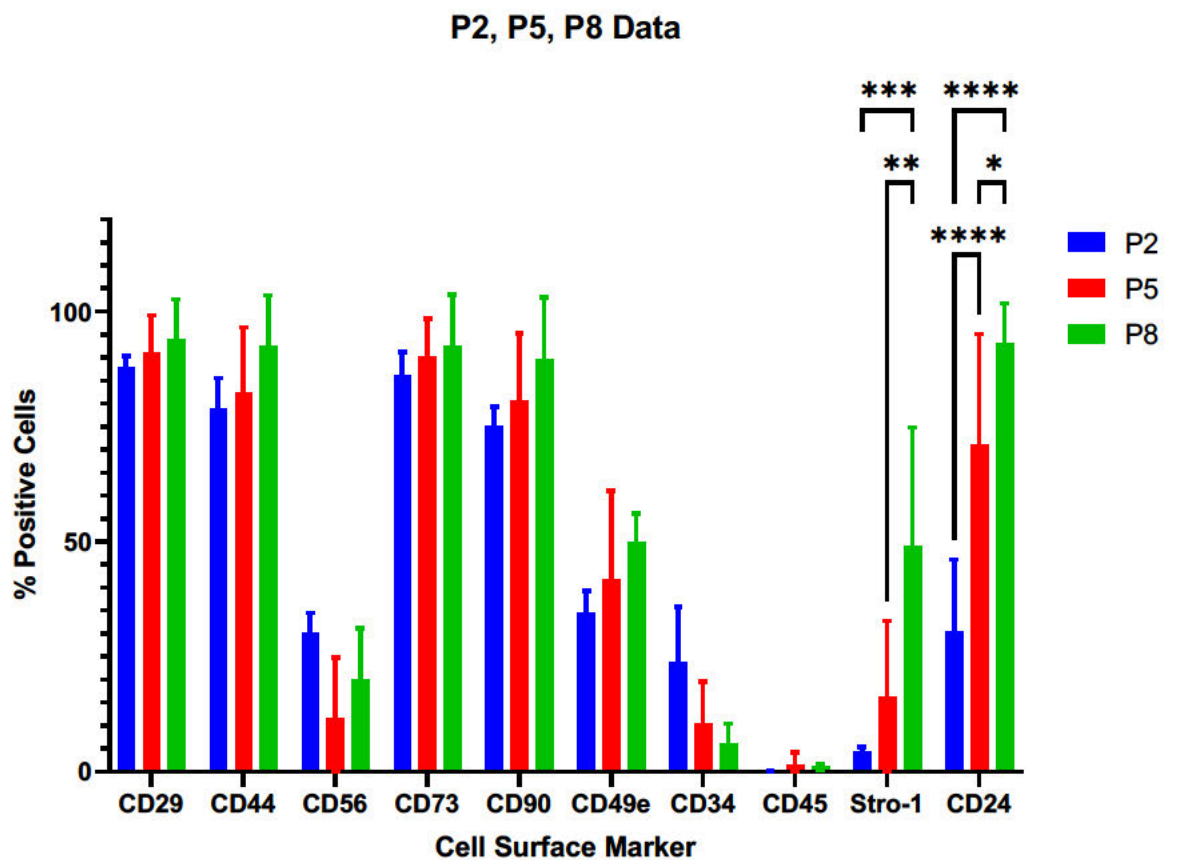


Figure 3.9: Changes in cell surface markers between passages. The percentage of cells positive for each cell surface marker are presented for CDCs with SD (error bars). Mean values from 3 biological repeats are presented at Passages 2 (P2), 5 (P5) and 8 (P8). *=p<0.05; **=p<0.01; ***=p<0.001; ****=p<0.0001.

**P2, P5, P8 Data**
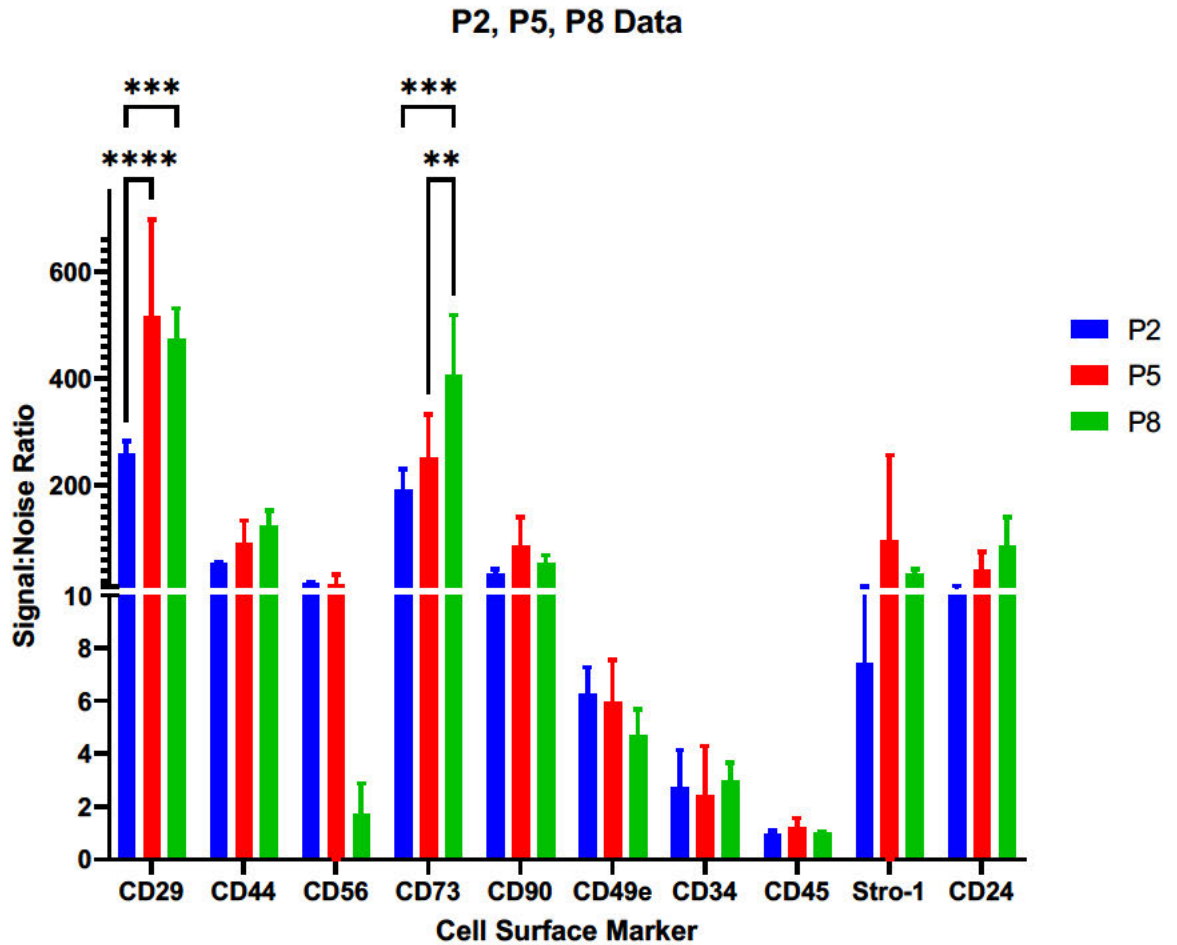
*Figure 3.10: Changes in cell surface marker fluorescence intensity between passages. Signal:Noise ratios at P2, P5 and P8 for each CD marker are presented for CDCs. Mean values with standard deviation from 3 biological repeats are presented. \*=p<0.05; \*\*=p<0.01; \*\*\*=p<0.001; \*\*\*\*=p<0.0001*

### 3.3.2.4 Histological Evidence of Trilineage Differentiation

The Dominici criteria also decree that mesenchymal stem cells should possess the ability to undergo trilineage differentiation. It was noted that at P1, all cell populations, not just those displaying fibronectin adherence, were capable of trilineage differentiation into osteogenic, chondrogenic and adipogenic lineages, indicating multipotency.

Staining with haematoxylin and eosin demonstrated cellular morphology consistent with a chondrocytic phenotype in all cell populations, confirmed with characteristic staining of glycosaminoglycan production with alcian blue (Figure 3.11). In the presence of osteogenic medium, all populations also demonstrated

169

an arrangement into an osteoblastic phenotype and demonstrated an ability to produce calcium deposits, as visualised with Alizarin red stain, consistent with successful osteogenic differentiation (Figure 3.11). Additionally, all cell types similarly demonstrated an affinity for adipogenic differentiation, evidenced by large, round cells with cytoplasmic droplets on H&E staining, which when stained with Oil Red O stain, verified these as lipid droplets confirming adipogenic differentiation had occurred (Figure 3.11). As such, all cell types displayed an affinity for trilineage differentiation in culture at P1.

CHONDROGENIC   ADIPOGENIC   OSTEOGENIC
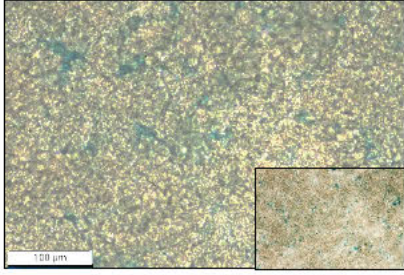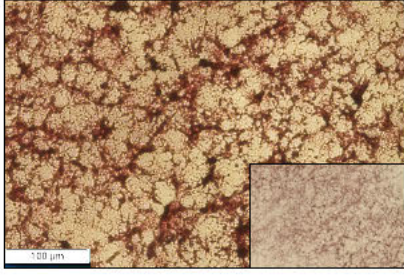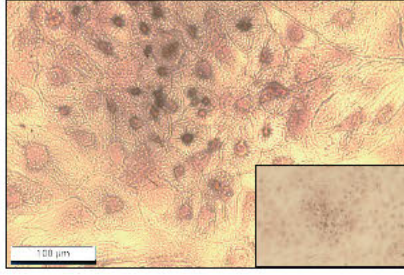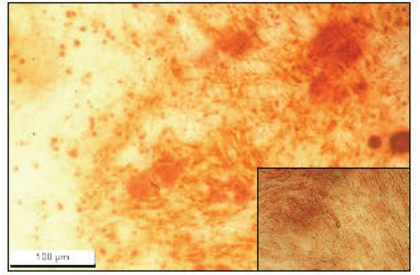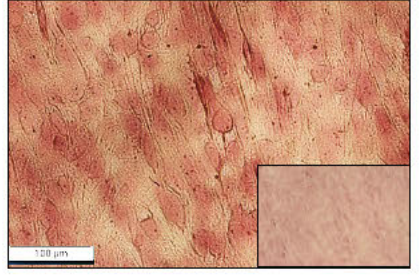
FIBRONECTIN ADHERENT (FAC) — H&E Stain / Lineage Stain
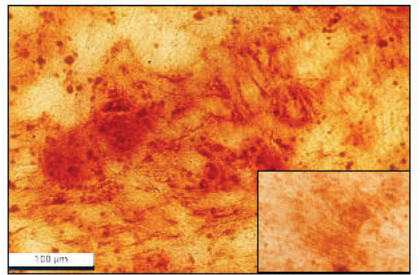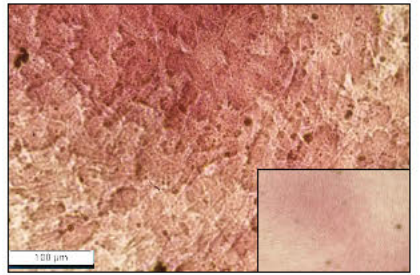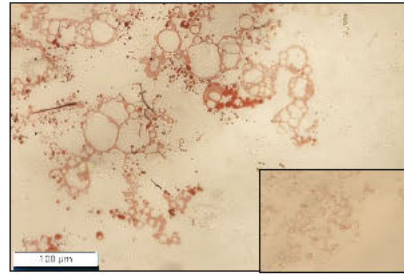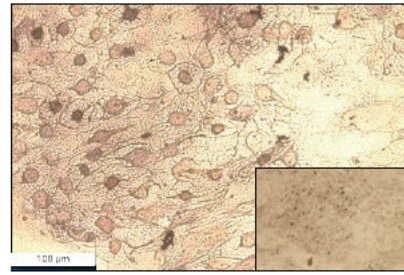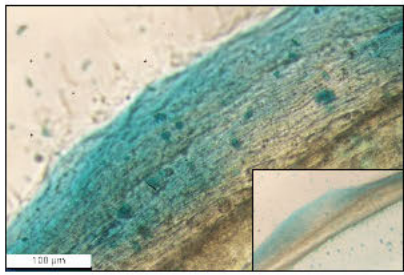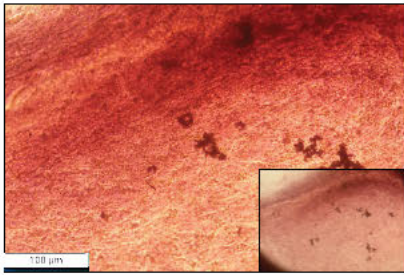
NON-ADHERENT (NFACs) — H&E Stain / Lineage Stain
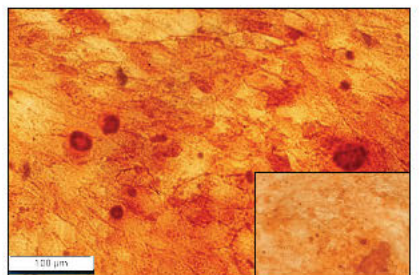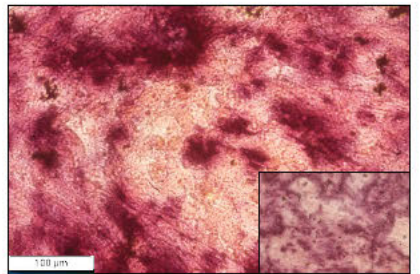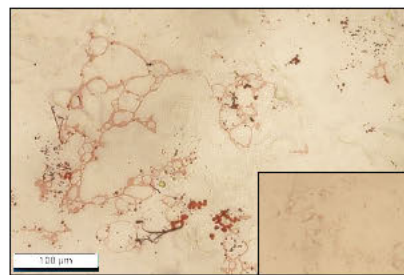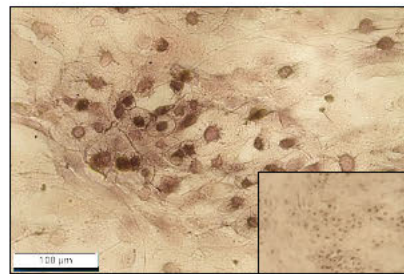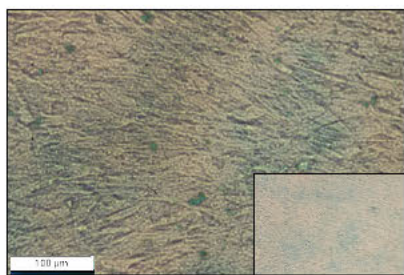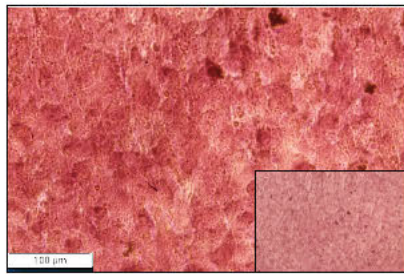
MIXED CELLS (CDCs) — H&E Stain / Lineage Stain

*Figure 3.11: Histological analysis of FAC, NFAC and CDC cell populations directed down chondrogenic (left column), adipogenic (central column) and osteogenic (right column) lineages. All cells were stained for lineage specific stains (bottom row): Alcian blue for cartilage, Alizarin red for bone and Oil red O for adipose tissue in addition to H+E staining (top row) for cell morphology. All images presented depict cells taken at 20x magnification (large image) and 4x magnification (small image, bottom left).*

### 3.3.2.5 Chondrogenic gene expression of nasoseptal cartilage cell populations

Cell populations were next examined for differences at the level of chondrogenic gene expression. Cells were harvested at the first passage following separation into the three distinct populations (CDC, FAC, NFAC) and the baseline gene expression of chondrogenic markers SOX9, COL2A1 and ACAN1 were determined relative to housekeeping genes TBP and RPL13A (Figure 3.12).

Using a T-test with Welch's correction, there were no significant differences observed in the gene expression observed between the FAC, NFAC and CDC populations for SOX9 (p=0.18) expression. However, there was noted to be a statistically significant difference in the expression of aggrecan between the cell populations: the FAC population had significantly higher ACAN1 expression than CDCs (1.7-fold increase, p=0.0082) whereas no difference was observed between the CDC and NFAC population (p=0.72). When comparing COL2A1 expression across these cell populations, there were differences observed between the CDC population and FAC cell population (2.0-fold higher; p=0.012) but not the CDC and NFAC population (1.5-fold higher, p=0.29). In summary, at first passage, the FAC population appears to possess superior ECM gene expression (ACAN1 and COL2A1) compared to the CDC population, whilst the NFAC population was comparable in all gene expression to the CDC population.

In summary, fibronectin adherence is associated with greater expression of ECM genes: ACAN1 and COL2A1.
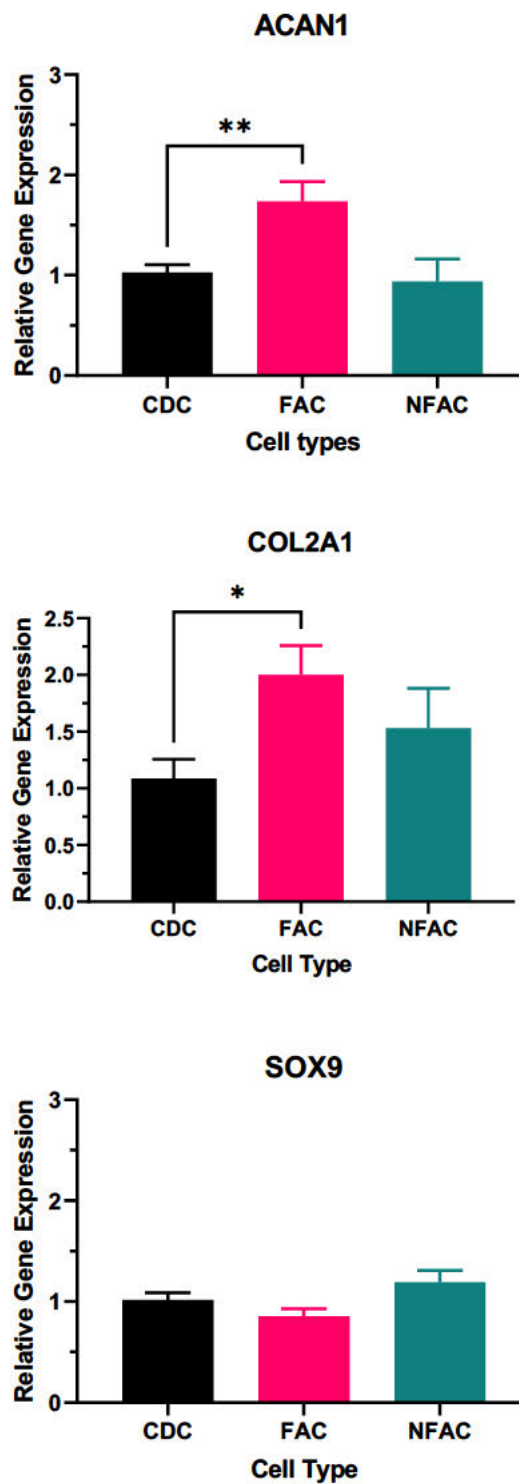
Figure 3.12: RT-PCR analysis of chondrogenic gene markers Type 2 Collagen (COL2); Aggrecan (ACAN1) and SOX9. Mean FAC and NFAC gene expression is reported relative to CDC at P1 from 3 biological repeats (in technical triplicates, total n=9). Statistical comparisons made using unpaired T-tests with Welch's correction are displayed. *=p<0.05, **=p<0.01.

### 3.3.2.6 Adherence and proliferation of nasoseptal cartilage populations

All cells must also demonstrate plastic adherence in order to be considered as mesenchymal stem cells (Dominici *et al.*, 2006): this was confirmed in all cell populations through microscopy (Figure 3.4) and objectively through the iCELLigence apparatus (Figure 3.13).

The iCELLigence impedance-based apparatus was used to measure cellular plastic adherence in the different cell populations and to characterise their growth characteristics over a 72-hour period.

A 2-way repeated measures ANOVA with Tukey's post-hoc test was performed and demonstrated there were no statistically significant differences between cell populations or compared to media in terms of adherence at 1 or 2 hours post seeding (Figure 3.13). Statistically significant changes were seen in the ANOVA model across the three time points ($p<0.0001$). However, the FAC and CDC cell population demonstrated a statistically significant difference compared to media at 2 hours, indicating cell adhesion had occurred (CDC $p=0.007$; NFAC $p=0.4$; FAC $p=0.03$).

Therefore, all cells demonstrated an ability to adhere to plastic but this appeared to occur more readily in the CDC and FAC populations.
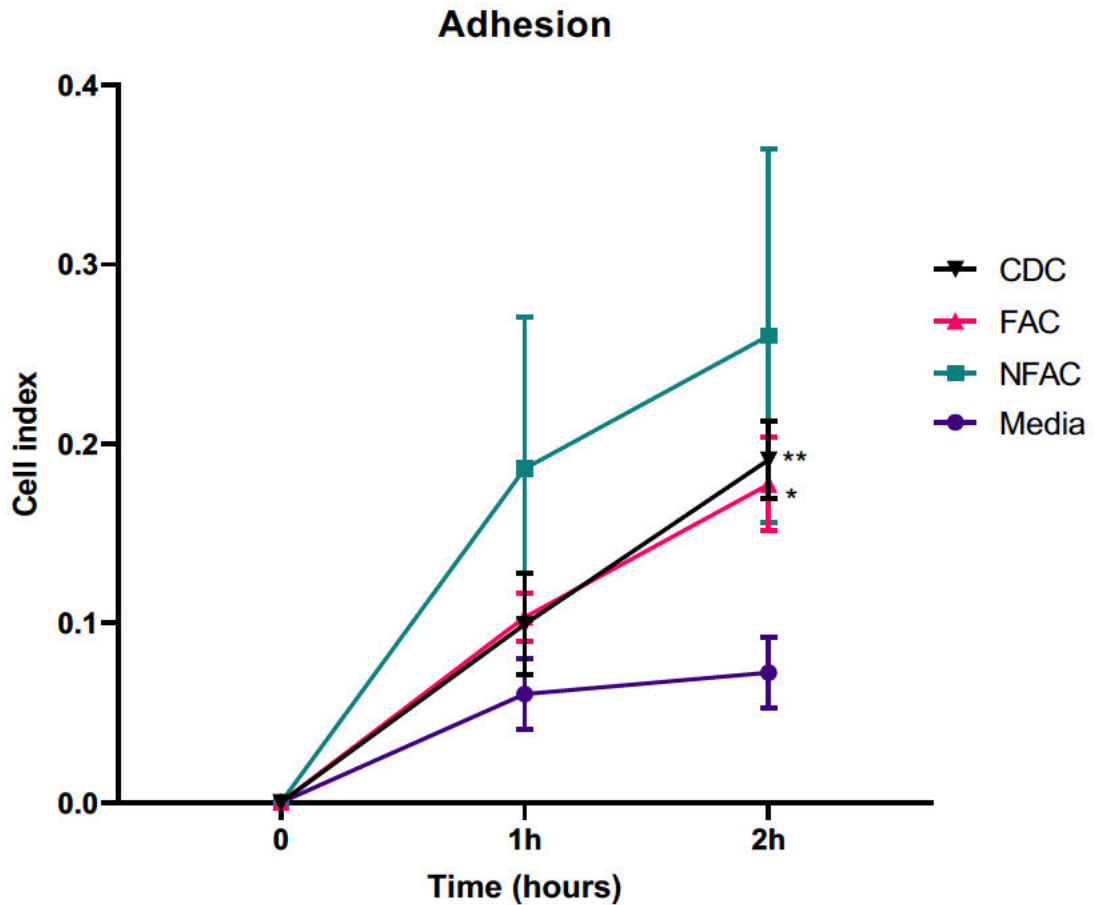
**Adhesion**



*Figure 3.13: Adhesion rates in different cell populations at 0, 1 and 2 hour time points compared to media. Mean values of 7 biological repeats are provided performed in technical duplicates with standard error of the mean. Statistical significance was observed at 2 hours in the CDC and FAC populations. *=p<0.05, **=p<0.01.*

### 3.3.3  Comparison of cell ratio populations

Combining different proportions of NFAC and FAC cells was performed to determine the effect on adhesion, growth kinetics and chondrogenicity in 2D and 3D culture, to determine whether superior combinations of cells could be produced for cartilage tissue engineering.

### 3.3.3.1     Cell Adhesion

To determine the affinity for adhesion, all cell ratio populations were found to have evoked statistically significant changes in electrical impedance (indicative of plastic adherence) compared to media controls by 6 hours (Figure 3.14) with

175

mean cell indices of 0.46 (100NFAC, p=0.02), 0.41 (80N20F, p=0.02), 0.40 (60N40F, p=0.04), 0.34 (40N60F, p=0.0002), 0.30 (20N80F, p=0.006), 0.35 (100FAC, p=0.02) and 0.44 (CDC, p=0.007). However, at 6 hours there were no statistically significant differences between cell ratio populations. Statistically significant differences compared to media alone were observed as early as at 2 hours in the 40N60F population (p=0.02), the 100FAC population (p=0.04) and the CDC population (p=0.008). This data indicates that all cell types were capable of adhesion, and that the rate of adhesion was not significantly different between cell populations.
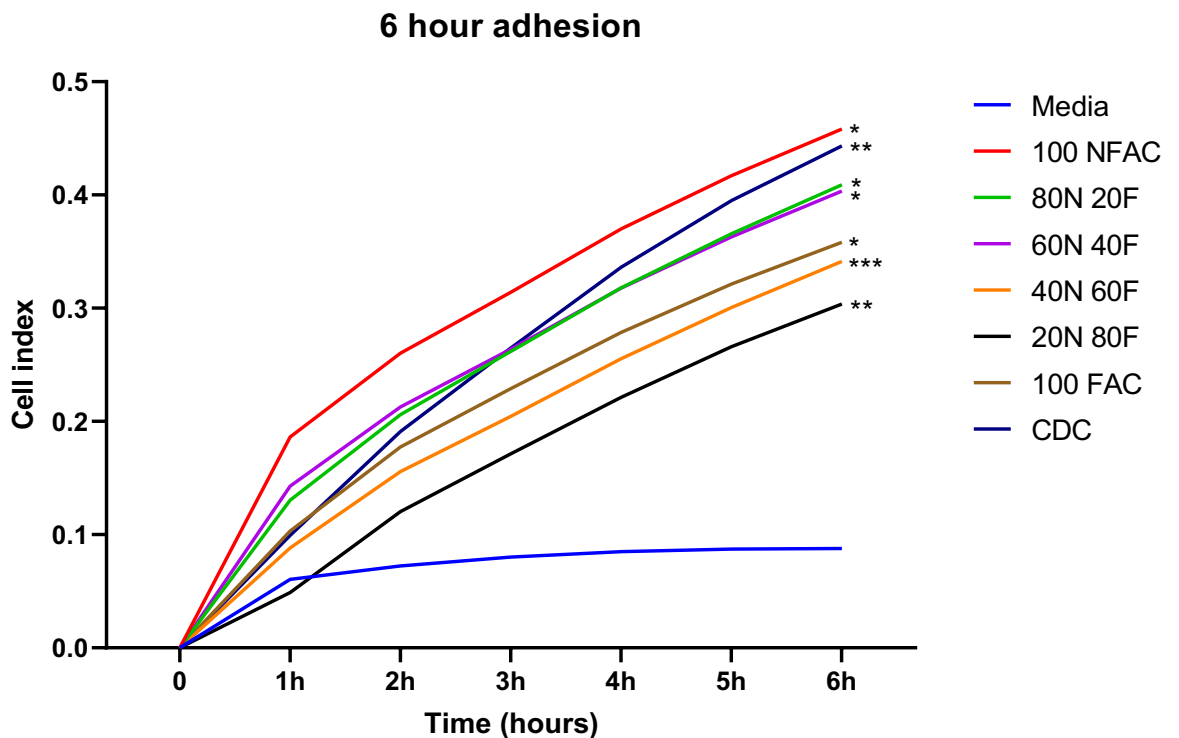


*Figure 3.14: Mean cell adhesion observed using the iCELLigence apparatus for the first 6 hours of culture from a biological n of 7 (technical duplicates). Cells of differing ratios of FAC and NFAC were compared to CDC populations and media only controls. Time is plotted on the x axis against cell index as a marker of cellular adhesion on the y axis. Significance at the 6 hour timepoint is demonstrated compared to media. \*=p<0.05, \*\*=p<0.01, \*\*\*\*=p<0.0001*

### 3.3.3.2    Cell growth

To predict the ability of the cell populations to populate a bioengineered scaffold, cell growth was measured in the different cell populations over the course of 72 hours (Figure 3.15). A two-way repeated measures ANOVA indicated that time (p<0.0001), cell population (p<0.0001) and patient (p<0.0001) were all statistically significant sources of variation. However, a Tukey's multiple comparison post hoc test was performed at each hour across populations and demonstrated significant differences only between cell populations and media only. All cell populations displayed comparable growth curves with no statistically significant differences observed.
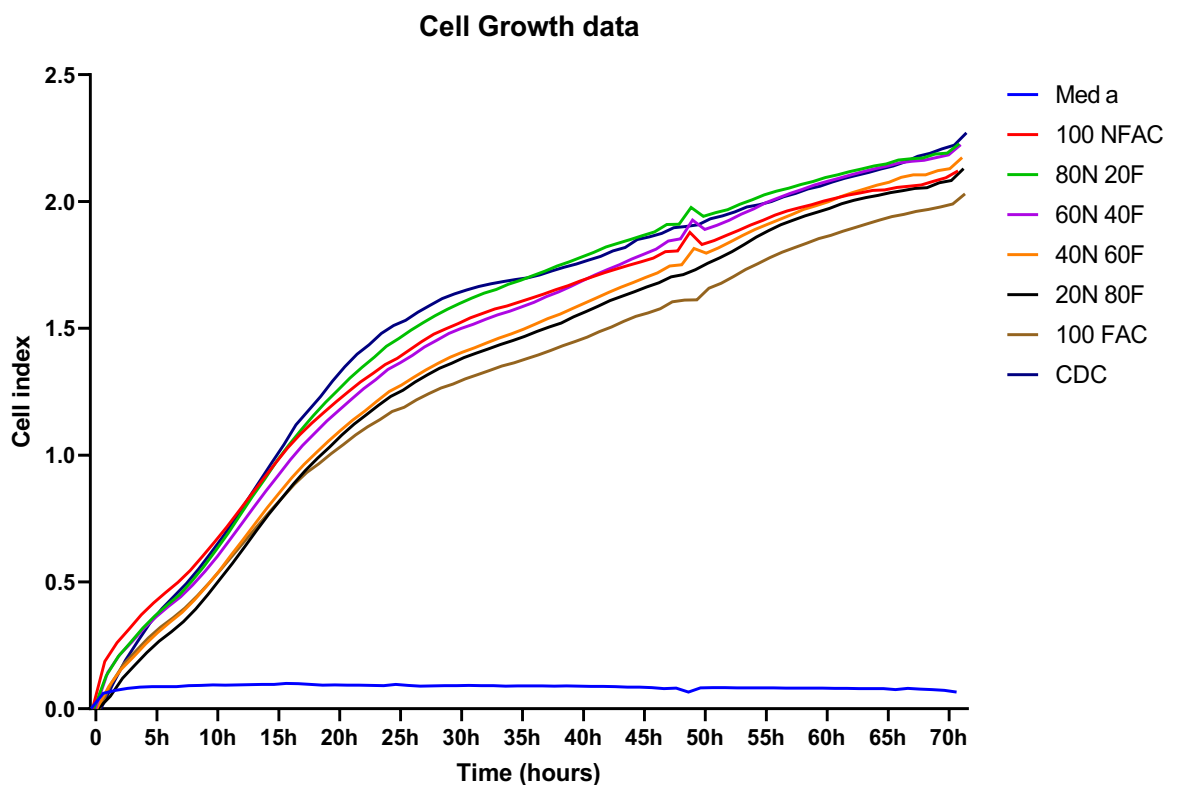


*Figure 3.15: iCELLigence-acquired cell growth data over a 72-hour time period for the different ratios of cell populations compared to media only controls (blue). Mean values from a biological n of 7 is presented, performed each in technical duplicates.*

To determine the rate of growth over 24-hour and 72-hour periods, population doubling times were calculated for each cell population (Figure 3.16). There were no statistically significant differences observed between any cell populations at either 24 or 72 hours of culture (p>0.999 for all comparisons).

**A**

**24 hour Population doubling**



**B**

**72 hour Population doubling**
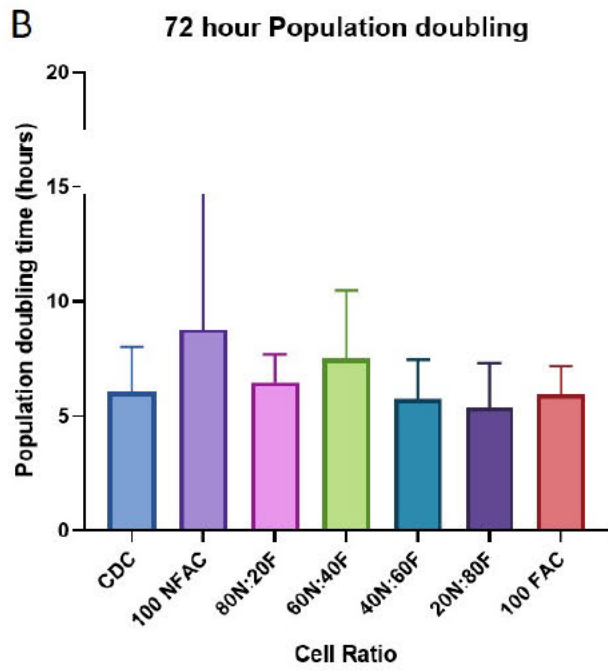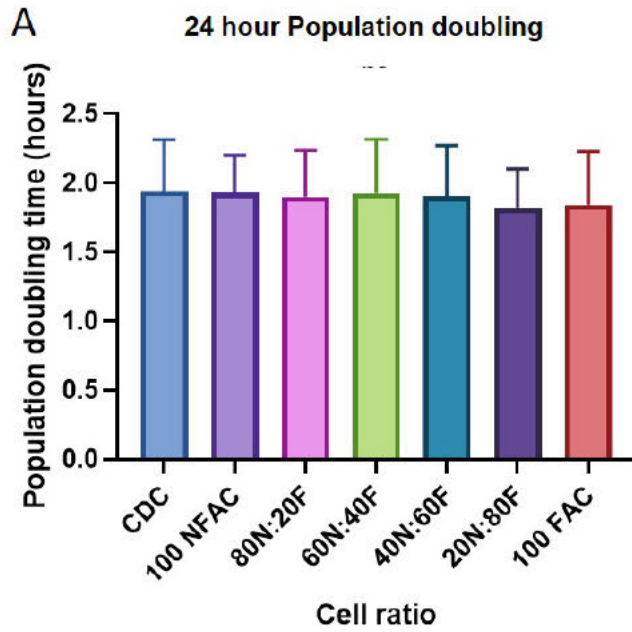
*Figure 3.16: Mean population doubling times taken at A) 24 hours of culture on iCELLigence device and at B) 72 hours after culture. Mean values of 7 biological repeats are presented with error bars depicting the standard deviation.*

### 3.3.3.3    Chondrogenic potential of cell ratio populations in 2D culture

To determine whether any combination of cells offered superior chondrogenic potential, the chondrogenic gene expression profiles of the different cell ratio populations were compared across 3 biological repeats in monolayer culture on a 6 well plate and expressed relative to the NFAC population (Figure 3.17 A-C).

Signficant variation amongst means was observed across all cell populations for ACAN1 (p=0.002), SOX9 (p=0.0035) and COL2A1 (p=0.0058). Post-hoc multiple comparisons between the cell populations demonstrated further significant differences. Specifically, there was a trend towards lower ACAN1 expression in the FAC weighted populations (20N:80F= 0.26-fold change, p=0.012; 100FAC =0.20-fold change, p=0.008), whereas the inverse was seen of COL2 expression, whereby 100FAC had the greatest (6.8-fold) relative gene expression compared to 100NFAC. SOX9 expression was signifcantly higher in 80N:20F (1.4-fold, p=0.002) and lower in 40N:60F (0.68-fold, p=0.036).

### 3.3.3.4    Chondrogenic gene expression in 3D culture

To negate the impact of 2D culture on gene expression, cells were cultured in 3D alginate beads and the gene expression analysed at 21 days relative to the CDC population (Figure 3.17 D-F). The gene expression profiles of the different cell combinations was significant across cell populations for SOX9 expression (p=0.035) and COL2A1 (p=0.0059). Multiple comparisons were conducted using t-tests against the CDC population as a control, to which the relative gene expression was calculated. SOX9 expression was largely uniform across cell populations, but with significantly lower expression in the 100NFAC (0.39-fold difference, p=0.0001) and 40N:60F populations (0.55-fold difference, p=0.013). ACAN1 similarly demonstrated minimal signficant difference between cell populations, but a signifcant reduction of 0.47-fold was noted in the 40N:60F cell mixture in alginate (p=0.02). Whereas COL2 was the gene in which the largest variation was seen, with many populations having lower gene expression than CDCs: 100NFAC (0.25-fold, p<0.0001), 40N:60F (0.31-fold, p<0.0001), 20N:80F (0.42-fold, p=0.0005).

In both 2D and 3D culture, the expression of Type 2 collagen appeared to display the most variability across cell populations, however between the two experiments, there was no consistently superior cell combination noted. In 3D in fact, no cell combination was superior to CDCs.
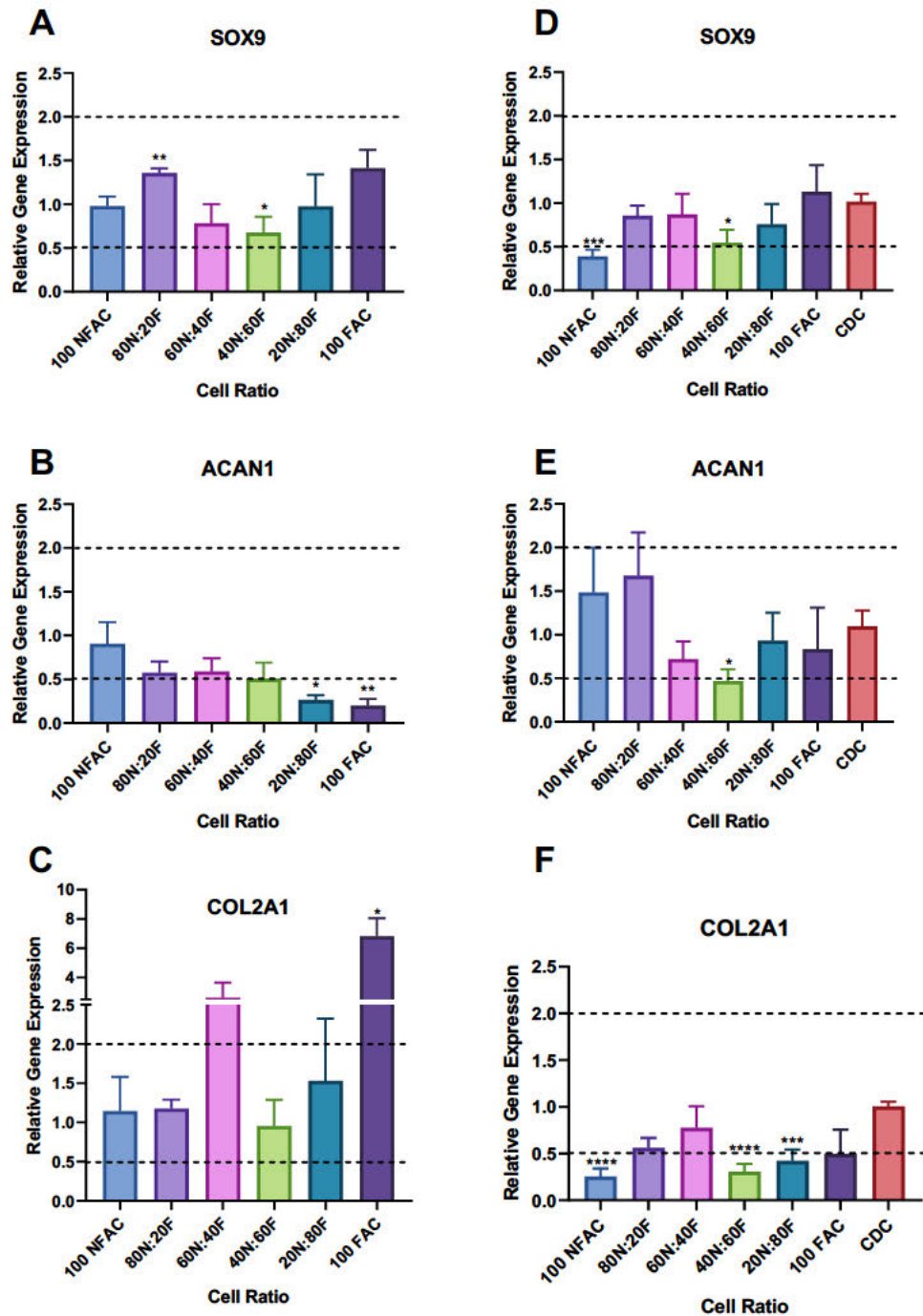
Figure 3.17: Mean relative gene expression of chondrogenic markers in cell ratios cultured in 2D (A-C) and 3D culture (D-F) (n=12, from biological triplicates). SOX9 gene expression at 21 days in 2D culture (A) and in 3D culture (D); Aggrecan gene expression at 21 days in 2D culture (B) and 3D culture (E); Type 2 Collagen expression at 21 days in 2D culture (C) and 3D culture (F). All gene expression values are expressed relative to 100NFAC (A-C) and relative to CDC (D-F); biological thresholds of significance are taken as <0.5 and >2 as demarcated using a dotted line perpendicular to the y axis. NFAC =N; FAC=F for brevity. *=p<0.05, **=p<0.01, ***=p<0.001; ****=p<0.0001.

### 3.3.3.5 Extracellular matrix production in 3D culture

A DMMB assay was performed to determine the differences in glycosaminoglycan content in different ratios of cells grown in 3D alginate culture. Over 3 mg/ml of glycosaminoglycan was detected in all cell ratio protein lysates however no statistically significant differences were observed between cell populations after 21 days of culture (Figure 3.18). This was also indicated by staining the cells grown in monolayer with alcian blue (Figure 3.19): cells demonstrated comparable elongated, spindle-like morphology and had mild pericellular staining with the alcian blue stain.
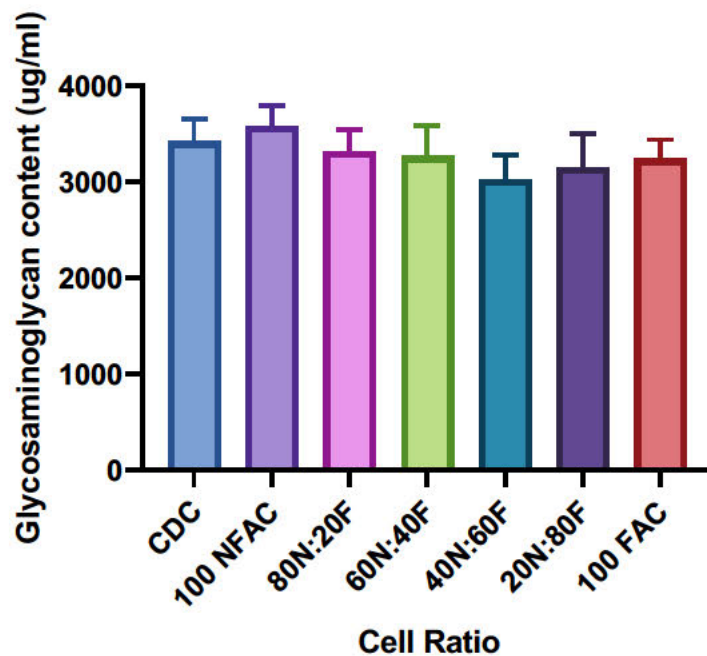


*Figure 3.18: Dimethylmethylene blue assay to quantify glycosaminoglycan content in different cell ratio populations cultured in alginate beads over 21 days. GAG content is expressed as a mean value of 3 technical and 3 biological repeats + standard deviation.*
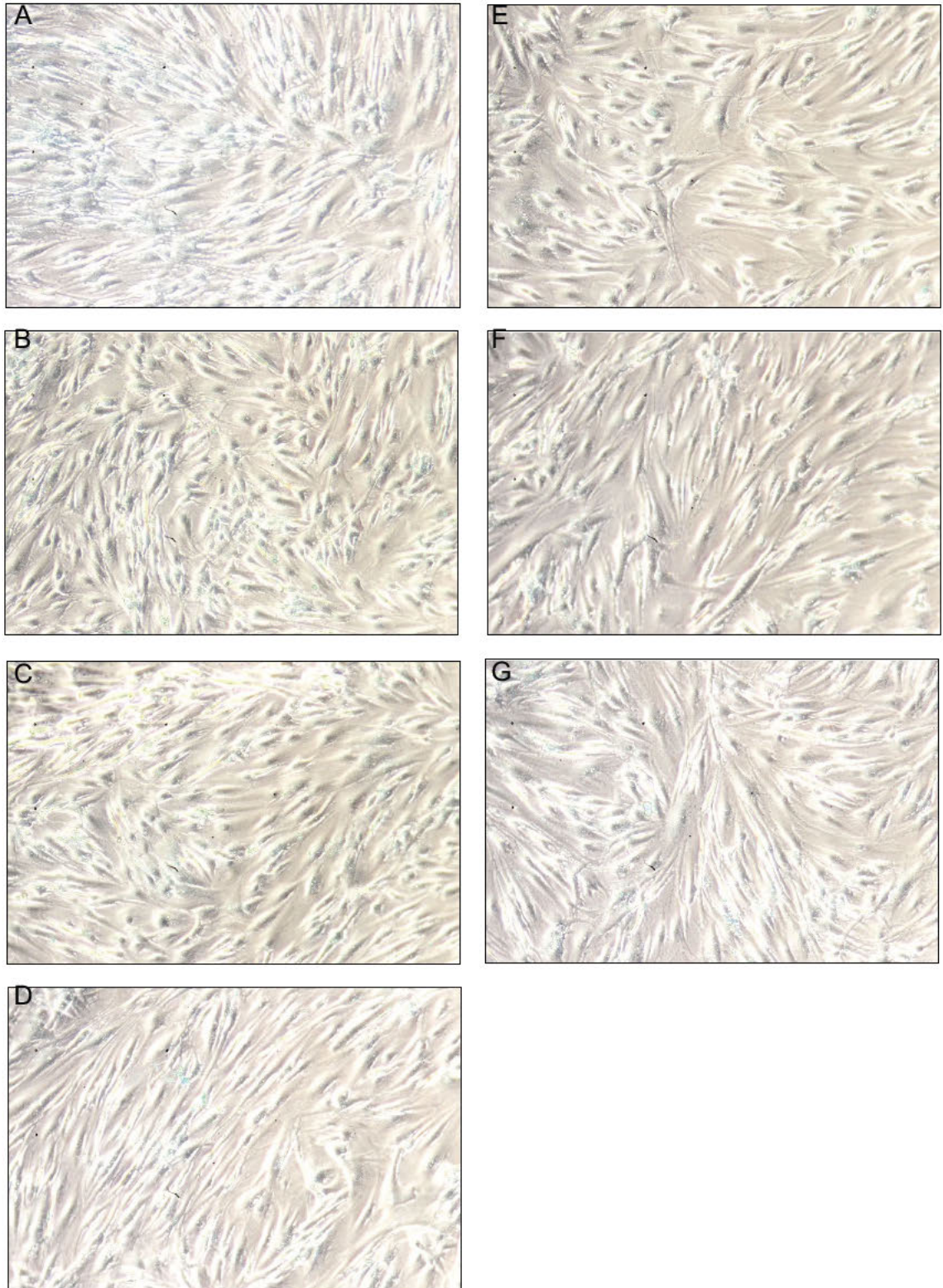
*Figure 3.19: Histological analysis of different cell ratio populations grown from a single biological repeat to confluence over 72 hours, fixed with formalin and stained with Alcian Blue. A) CDC cell population B) 100FAC cell population C) 80F:20N cell population D) 60F:40N cell population E) 40F:60N cell population F) 20F:80N population G) 100NFAC cell population. All images are taken at 10x magnification. Cells demonstrate comparable morphology and evidence of mild intra- and extracellular staining with Alcian blue in all populations studied.*

## 3.4 Discussion

This chapter aimed to characterise the populations of cells available in nasoseptal cartilage and to explore means of optimising cell combinations and culture conditions for exploitation in cartilage tissue engineering. The results firstly evaluate the validity of the fibronectin adhesion assay in isolating chondroprogenitor cells from nasoseptal cartilage. The results then consider the effects of combining different proportions of fibronectin adherent and non-adherent cells to determine whether the ratios of these cell populations can be exploited for enhancing cell growth or chondrogenicity in tissue engineering applications.

### 3.4.1 The fibronectin adhesion assay does not convincingly isolate chondroprogenitor cells from nasoseptal cartilage

Cartilage tissue is notorious for its poor ability to renew and regenerate, underpinning cartilage specific pathologies such as osteoarthritis (Hunziker *et al.*, 2015). As such, attention has been focussed towards isolating a population of stem cells within cartilage tissue, which could be manipulated to facilitate repair and regeneration (Williams *et al.*, 2010). It is also in the interest of tissue engineers to identify and exploit the ability of stem cell populations to proliferate, differentiate and self-renew, particularly in the context of populating a scaffold.

There has been significant interest in isolating and characterising chondroprogenitor cells from articular cartilage, and in 2010, a small population of CD49e positive cells were identified within articular cartilage that possessed the ability to clonally proliferate, expressed Notch1, retained stem cell surface markers CD90 and Stro-1 and were capable of trilineage differentiation (Williams *et al.*, 2010). In Williams et al's study, the proportion of CD49e positive cells deemed to be the fibronectin adherent population constituted only 0.7% of the total cells analysed. Other studies of articular and auricular cartilage indicate that values as high as 2-3% of the total cells may be chondroprogenitor cells (Jessop *et al.*, 2019).

In this chapter, the data indicates that there are a proportion of cells that preferentially adhere to fibronectin within 20 minutes of coculture: FACs, which might draw parallels to the previously reported chondroprogenitor population described in articular cartilage. Indeed, this cell population does appear to meet many of the mesenchymal stem cell characteristics defined by Dominici et al (Dominici *et al.*, 2006): specifically expressing key stem cell markers such as CD73 and CD90, but lacking the expression of CD45 and CD34; demonstrating an affinity for plastic adherence and a capacity for trilineage differentiation. However, the FAC population in nasoseptal cartilage appears to constitute a much higher proportion of the total cell population than previously reported. In both male and female subjects, over 50% of the cells adhered to fibronectin, thereby being the dominant cell population in nasoseptal cartilage. However, only 0.19% of all CDCs liberated from nasoseptal cartilage were found to be CD49e positive prior to commencing culture (P0): a value that increased to greater than 21% of cells by first passage in the CDC and FAC populations. These findings indicate that the cell surface expression of CD49e is therefore unlikely to be solely accountable for fibronectin adherence. As such, it can be hypothesised that either CD49e is not a valid chondroprogenitor stem cell marker in nasoseptal chondrocytes, or that the fibronectin adherent cells isolated here are not, in fact, chondroprogenitor cells.

The overt disparity in CD49e expression (0.19%) and fibronectin adherence (>50%) indicates another cell surface marker may be attributable for enabling fibronectin adherence. CD49e comprises part of the $\alpha 5\beta 1$ integrin receptor: also known as the fibronectin receptor. Integrins are heterodimeric membrane proteins, whereby CD49e comprises the integrin $\alpha 5$ chain. The $\beta 1$ subunit with which $\alpha 5$ (CD49e) dimerises, is also known as CD29, and in this study, the expression of CD29 in CDCs at P0 is approximately 65%. This more closely aligns to the numbers of cells adhering to fibronectin than CD49e, which indicates that the $\beta 1$ subunit may be expressed on CDCs with an alternative alpha subunit capable of fibronectin adherence. Integrin $\beta 1$ is one of the most widely expressed beta integrins and associates with at least 10 different alpha integrins (Hynes, 1992). Candidate fibronectin adherent alpha subunits include alpha 4 integrins (CD49d), however this has been demonstrated to not be expressed at any higher

level in candidate progenitor populations than in nasal chondrocytes (Elsaesser *et al.*, 2016).

Other integrins capable of fibronectin adherence include αVβ3, αVβ6 and αVβ8. However, αV (CD51) and its associated beta integrins are typically seen on endothelial, epithelial and neural cells respectively. One study has noted that dimerization of αV with β1 also served as a fibronectin receptor but with a four-fold lower affinity for fibronectin than α5β1 (Zhang *et al.*, 1993) making this an unlikely receptor to enable fibronectin adherence within 20 minutes.

### 3.4.2 Cartilage derived cells display evidence of early 'stem cell' phenotypic changes when grown in 2D cell culture

Where FAC cells were able to demonstrate the main Dominici criteria in being plastic adherent, expressing key MSC markers and being capable of trilineage differentiation (Dominici *et al.*, 2006), so too were CDC and FAC cell populations. At P1, all cells demonstrated an ability to differentiate into osteogenic, chondrogenic and adipogenic lineages, suggestive of multipotent stem cell characteristics. Furthermore, although upon immediate isolation of CDCs from nasoseptal cartilage, the expression of key stem cell markers was relatively low with 6% of cells expressing CD44, 97% expressing CD73 and 21% expressing CD90.

However by P1, CD44, CD73, CD90 and CD29 were expressed in almost all cells regardless of ability to adhere to fibronectin. Of note, many of these markers (CD44, CD29 and perhaps CD90) are all involved in mediating cell-matrix and cell-cell adhesion. The levels of CD49e expression also demonstrated a significant rise, particularly in CDC and FAC populations at P1. The fact that essentially all cells upregulate their expression of these markers in 2D culture may therefore reflect adherence to the plastic of tissue culture vessels, or perhaps to neighbouring cells as they approach confluence. Indeed, CD49e expression in particular has been shown to increase within 24 hours in culture conditions, which is argued to be neither a product of plastic adherence nor cell overgrowth, as the expression of CD49e also increased in non-adherent cell cultures (Kachroo, Ramasamy and Vinod, 2020). The authors also observed the

186

phenomenon of increasing CD29 expression by as early as 24 hours in culture, drawing parallel to the findings of this thesis.

With the exception of aggrecan, there were no statistically significant differences in the expression of chondrogenic genes in these populations. In cartilage, stem cell populations would be expected to direct cell growth and proliferation, whereas the mature chondrocytes would be the more likely candidates for depositing extracellular matrix (Lefebvre, Angelozzi and Haseeb, 2019). With regard to aggrecan however, the inverse was observed: the expression of this gene was higher in the FAC population. This might suggest that cells capable of fibronectin adherence have a greater role in extracellular matrix production. Fibronectin is only present in small amounts in cartilage tissue but is believed to have a role in organising the extracellular matrix and has been implicated in promoting chondrogenic differentiation (Casanova *et al.*, 2020). Whilst there were no significant differences in the gene expression of SOX9 at first passage, ACAN1 was noted to be significantly higher in the fibronectin adherent population at P1, and COL2A1 was higher in the FAC populations relative to CDCs. However, it is not possible to determine whether the differences in gene expression are a result of the FACs being inherently more chondrogenic than NFAC and CDC populations, or whether the increase in aggrecan and COL2 gene expression is a result of the cells being exposed to fibronectin (Singh and Schwarzbauer, 2014; Casanova *et al.*, 2020).

It has been reported previously that prolonged culture evokes dedifferentiation of chondrocytes with a loss of phenotype and reduction in the expression of chondrogenic gene markers: specifically a fall in type II collagen and a rise in type I collagen expression (Hamada *et al.*, 2013). Hamada et al also indicate that increases in cell surfaces markers CD44, CD49c and CD151 characterise dedifferentiation, whereas CD14, CD49d and CD54 downregulation occurs (Hamada *et al.*, 2013). In contrast, Grogan et al report CD44 amongst the genes that associated with a higher expression of enhanced chondrogenicity, associated with greater GAG production and Collagen II expression (Grogan *et al.*, 2007). Other studies indicate that upregulation of CD10, CD90, CD105 and CD166 occur (Diaz-Romero *et al.*, 2005), and that in particular, CD14, CD90 and

CD105 are the best differentiators between MSCs and dedifferentiated chondrocytes: dedifferentiated chondrocytes express high levels of CD90, are CD14 positive and weakly positive for CD105 in contrast to MSCs which display the inverse (Diaz-Romero *et al.*, 2008). As such, future work should aim to clarify and refine a reliable set of cell surface markers to distinguish progenitor cells and dedifferentiated cells.

### 3.4.3 Heterogeneous FAC and NFAC cell populations confer no additional advantage for cartilage tissue engineering

It was apparent that there were no overtly superior ratios of FAC and NFAC relative to CDC populations in either 2D or 3D culture in this study. There were some significant differences in gene expression noted, but these were always significantly lower levels of relative gene expression in the FAC:NFAC mixed populations relative to the CDC populations and there were no significant differences observed in the growth kinetics of these cells in any combination. At the level of ECM production, there were no overt differences in cell morphology or ECM staining with alcian blue and no significant differences in GAG content with the DMMB assay. These findings mirror the findings of Vinod *et al*, in which articular cartilage chondroprogenitor cells were combined with chondrocytes in ratios of 80:20, 65:35, 50:50, 35:65 and 20:80 (Vinod *et al.*, 2019). Similarly, this study did not reveal any differences in population doubling times, cell surface markers, or chondrogenic gene expression (COL2, ACAN1 and SOX9) between any of the cell populations (Vinod *et al.*, 2019). The cells used in Vinod et al's study were however, cultured in monolayer until P2 prior to combining, whereas cells were used at P1 in this study. This methodological difference may have further increased the similarities between the cell populations, in light of the convergence in phenotype seen in this chapter as early as P1. The fact that the gene expression of chondrogenic markers such as COL2A1 was higher in the CDC cell population than any artificial cell ratio combination may indicate an ongoing interaction between the FAC and NFAC cells, which in the separate populations has been lost prior to reconstitution.

It has been previously reported in a number of studies that chondrocytes cultured in 2D may dedifferentiate (Diaz-Romero *et al.*, 2005, 2008; Grogan *et al.*, 2007; Hamada *et al.*, 2013), which could be an explanation for a more uniform stem cell like behaviour seen across the cell populations in this study. However, Vinod et al have shown that the phenomenon exists in pellet culture as well as 2D (Vinod *et al.*, 2019), and similarly in this study, the FAC and NFAC cell populations did not appear to differ in GAG production when cultured in 3D alginate beads. It has also been reported previously that chondrocytes will redifferentiate when returned to a 3D environment such as a hydrogel (Caron *et al.*, 2012; Aurich *et al.*, 2018; Kisiday, 2019). As such, it would be expected that significant differences between the cell populations would be observed in 3D culture settings. The homogeneity of the GAG content and gene expression profiles in the different cell ratios is therefore unlikely to be attributable purely to dedifferentiation of cell populations.

Previous studies have used mesenchymal stem cells derived from adipose, bone marrow and synovium combined with chondrocytes to successfully promote chondrogenesis (Chang, Cui and Fan, 2011; Kubosch *et al.*, 2016; Arora *et al.*, 2017). This phenomenon did not appear to be replicated in this instance with fibronectin adherent cells, again suggesting that the fibronectin adherent population is not representative of a true mesenchymal stem cell population.


### 3.4.4  Summary

This chapter aimed to emulate, or improve upon, the relationship between native cartilage derived cells: chondroprogenitor cells and chondrocytes, for exploitation in cartilage tissue engineering. The data acquired highlighted that a large proportion of cartilage derived cells demonstrate an affinity for fibronectin, and that by first passage, all cells demonstrate multipotency, expression of stem cell markers and plastic adherence. Phenotypic drift was stark when expanded for even brief periods in 2D culture and combining fibronectin adherent (proposed chondroprogenitor cells) with non-adherent cells did not confer any chondrogenic benefit compared to culturing these cells separately. This chapter highlights the importance of finding a reliable and reproducible means of identifying and isolating chondroprogenitor cells in nasoseptal cartilage: the fibronectin adhesion

assay does not appear to be an adequate means of isolating the very small number of chondroprogenitor cells that exist within a senescent tissue like cartilage. Furthermore, additional work is warranted to identify a more robust means of distinguishing true mesenchymal stem cells from cells that have dedifferentiated in a tissue culture environment and establishing superior means of culturing chondrocytes *in vitro* to retain properties that better mimic *in vivo* behaviours.

# Chapter 4: The Chondrogenic Potential of Pulp-derived Nanocellulose for 3D Bioprinting Cartilage

# Chapter 4: The Chondrogenic Potential of Pulp-derived Nanocellulose for 3D Bioprinting Cartilage

## 4.1 Introduction

### 4.1.1 Background

An optimal biomaterial for 3D printing cartilage tissue through an extrusion bioprinter should be balanced in terms of its biological and mechanical factors. Facilitating cell proliferation, differentiation and extracellular matrix production are desirable criteria, in addition to possessing properties in liquid form to allow extrusion through a bioprinter nozzle and solidification into the desired shape and structure post-printing (Tarassoli *et al.*, 2021). However, achieving this balance is often fraught with conflict (Chimene *et al.*, 2016) and the pursuit of advanced biomaterials possessing both these properties is known as the 'biofabrication window', first described in 2013 (Malda *et al.*, 2013). Synthetic materials, such as plastics, traditionally convey superiority in addressing the mechanical properties required to support tissue growth and can be easily modified to augment their printability, viscosity and strength (Jovic *et al.*, 2019). A major drawback of these materials is their limited bioactivity: poor cell adhesion and lack of extracellular matrix mimicry translate to a limited capacity to support the biological components of cell growth (O'Brien, 2011). In addition, many synthetic materials are often non-degradable which presents the risks of extrusion, immunogenicity and impedance of *de novo* tissue formation (Sarkar, Xue and Sant, 2017). Of those that are degradable, toxic by-products may be released during the degradation process, presenting a risk of harm when implanted into humans (Taylor *et al.*, 1994; Athanasiou, Niederauer and Agrawal, 1996).

As such, there has been a progressive shift in focus towards developing natural materials for a variety of biomedical applications (Tarassoli *et al.*, 2021). Plant-derived biomaterials offer the benefits of harnessing the structural strength of plant microarchitecture combined with their inherent bioactivity as supporters of cell growth (Gershlak *et al.*, 2017). A number of plant materials have been found to possess ECM mimicry and offer biodegradability and mechanical stability (Yegappan *et al.*, 2018). Their use as potential bioinks is strengthened by the potential for chemical modification and hydrogel formation. The abundance of

these materials, from natural and renewable sources has therefore garnered significant attention in the field of 3D bioprinting, and have dominated 3D bioprinting research over the last decade (Tarassoli *et al.*, 2021).

Alginate is the most researched bioink in extrusion based 3D bioprinting (Tarassoli *et al.*, 2021) and has been prevalent in cartilage tissue engineering research (Axpe and Oyen, 2016). For extrusion bioprinting, low weight alginate hydrogels are required, which translates to poorer mechanical properties (Axpe and Oyen, 2016). Alginate bioinks vary in their printability characteristics depending on the molecular weight, viscosity and concentration of the bioinks but research to date has highlighted poor post printing shape fidelity as a recurring and persistent issue with inks based in this material, particularly at low concentrations (<3% w/v) (Piras and Smith, 2020). Despite this, lower concentration alginate bioinks have been demonstrated to augment chondrogenic gene expression in 3D culture, to a greater degree than higher concentration formulations (Ewa-Choy *et al.*, 2017).

In order to augment the printability, strength and bioactive potential of alginate bioinks for 3D bioprinting, previous research has examined the role of blending alginate with nanocelluloses (Aarstad *et al.*, 2017; Siqueira *et al.*, 2019). Specifically, this has been investigated for cartilage bioprinting using a combination of alginate and tree pulp-derived nanocellulose fibrils, now known commercially as "CELLINK", developed by researchers in Sweden (Pääkko *et al.*, 2007; Markstedt *et al.*, 2015a; Martínez Ávila *et al.*, 2016). The combination of the two materials was felt to offer superior shear thinning, rapid crosslinking and printability with evidence of satisfactory cell survival in the material (Markstedt *et al.*, 2015a). Furthermore, chondrocytes cultured in the material demonstrate proliferation and cartilage specific gene expression (Type 2 Collagen) over time indicating an inherent chondrogenicity of this material combination (Müller *et al.*, 2017).

Nanocellulose has attracted significant attention in the field of 3D bioprinting owing to its excellent printability characteristics and biocompatibility and is derived primarily from two sources: plant matter and bacterial biosynthesis (Lin and Dufresne, 2014). Of the plant derived types, the material is topographically

nanostructured into nanocrystals or nanofibrils, though a blended morphology has been described, comprising a natural combination of the two (Kyle *et al.*, 2018a; Al-Sabah *et al.*, 2019a; Jessop *et al.*, 2019a).

Plant derived nanocellulose fibrils, crystals and blend have been characterised structurally using scanning electron microscopy, transmission electron microscopy, atomic force microscopy and rheology. Each material demonstrates extensive porosity at the micro and nanoscale, in addition to excellent thermal stability comprised of pure cellulose I components using X-ray diffraction (Kyle *et al.*, 2018).

The nanocelluloses used in this research are derived through AVAP technology, which yields nanocelluloses with enhanced thermal stability, owing to the absence of sulphate substitution to functional side chains that occurs with conventional sulphuric acid hydrolytic processing (Nelson and Restina, 2014). As such, the nanocelluloses remain suitable for use at physiological temperatures and indeed for autoclaving at 121°C (Al-Sabah *et al.*, 2019). Rheologically, all the nanocellulose formulations demonstrate shear thinning behaviour rendering them suitable for extrusion-based 3D printing, and a dominance of elastic type behaviour with a G' greater than G" (Kyle *et al.*, 2018b; Jessop *et al.*, 2019b). Hierarchically, the rigidity of the nanocellulose is greatest for the blend variant, followed by the fibrils and then the crystals, and the blend also demonstrated the highest viscosity for printing. Regarding pore sizes, it was noted that NCF possessed the highest diameter pores in between fibrillar entanglements of 750 to 5000 nm size, whereas the crystals were much more compact, with pore sizes of 100-500 nm (Kyle *et al.*, 2018). The blend variant had a higher range of pores depending on the prevalence of fibrillar and crystalline components (ranging from 55 to 1200 nm) but averaging approximately 934 nm (Kyle *et al.*, 2018).

Despite their similar origins, the variation in the nanoarchitecture of nanocellulose variants appears significant, which may have implications at a cellular level especially considering the micro- and nanoscale at which cell-material interactions may be occurring (Al-Sabah *et al.*, 2019). As such, further

investigation into the printability and chondrogenic potential of these structurally disparate variants is warranted.

In addition to the cell source and scaffold, the environment in which the cells are cultured is an additional consideration in tissue engineering. *In vitro*, the environment incorporates culture conditions such as media constituents, growth factors and exposure to mechanical stimuli. Whilst it is accepted that cartilage cells demonstrate superior phenotypic retention when cultured in 3D compared to 2D (Caron *et al.*, 2012), growth can be further optimised according to a number of extrinsic factors such as perfusion with growth media, exposure to certain types of mechanical stimulation and supplementation with growth factors: many of these concepts underpin the design of bioreactors for enhancing tissue engineering (Concaro, Gustavson and Gatenholm, 2009; K. Li *et al.*, 2017). As such, bioreactors are an attractive means of maximising environmental control, particularly in the realm of *de novo* tissue engineering (Martin, Wendt and Heberer, 2004). In particular, culturing cells in dynamic conditions may replicate biomechanical signals such as compression and perfusion, normally encountered in the development of cartilage tissue, and as such facilitate cell growth and matrix production (Concaro, Gustavson and Gatenholm, 2009; Fu *et al.*, 2021). However, the effect of simple perfusion-based bioreactors for nasoseptal cartilage tissue engineering is less well explored than its articular counterpart (K. Li *et al.*, 2017).

### 4.1.2  Aims

As three different structural subtypes of plant derived nanocellulose have been identified previously, it is essential that the most chondrogenic and printable derivative is used for the production of nanocellulose composite bioinks for bioprinting cartilage. As such this chapter aims to determine the suitability of pulp-derived nanocellulose formulations (NCC, NCF and NCB) as a nanocellulose-alginate composite bioink for 3D bioprinting nasoseptal cartilage. In order to address this aim, the following objectives will be explored:

- To determine the suitability of the different nanocellulose formulations for 3D printing

- To assess and compare key 3D printing resolution and shape fidelity tests for each nanocellulose material

- To determine the chondrogenic potential of crosslinked nanocellulose-alginate composite bioinks relative to pure alginate

- To verify whether the conditions in which crosslinked nanocellulose-alginate materials are cultured can be optimised through the use of an orbital shaking system

## 4.2 Experimental Methods

### 4.2.1 Nanocellulose preparation

Nanocellulose bioinks ("BioPlus ® Nanocellulose") were derived from softwood pulp biomass using American Value Added Processing (AVAP®) technology as described in Section 2.5.1 and gifted from GranBio (Sao Paolo, Brazil). Three separate structural types of nanocellulose were used: nanocellulose crystals, nanocellulose fibrils and nanocellulose blend. Each biomaterial type was decanted separately in a class II cabinet into 50 ml tubes and centrifuged at 1000 g for 10 minutes. The supernatant volume was recorded and then discarded. The residual biomaterial was then autoclaved at 126°C for 40 minutes and reconstituted with tissue culture grade sterile water (Gibco, Thermofisher Scientific) to match the pre-centrifugation volume. The pH of the material was neutralised to 7 using 4 M NaOH added dropwise (Sigma Aldrich, MO, USA).

### 4.2.2 Nanocellulose-alginate bioink formulation

75 ml of each nanocellulose biomaterial was made into a composite bioink through the addition of 25 ml of 2.5% (w/v) sodium alginate solution (Sigma-Aldrich, MO, USA). The composite bioink was homogenised using a stirrer and syringe until a homogenous appearance was achieved. For simplicity, the resultant 75% (v/v) nanocellulose: 25% alginate (v/v) composite bioinks are reported as following in the remainder of this chapter: nanocellulose crystals + alginate (NCC); nanocellulose fibrils + alginate (NCF) and nanocellulose blend + alginate (NCB).

After printing, each nanocellulose:alginate composite bioink was crosslinked using 100 µl of 0.5 M $CaCl_2$ added dropwise until the construct was coated in crosslinking solution.

### 4.2.3  Nanocellulose-alginate bioink printability assessments

A CELLINK INKREDIBLE printer was used to determine the minimum extrusion pressure, line fidelity and shape fidelity of each nanocellulose:alginate composite bioink. Specifically, a line assay (n=3), grid assay (n=3) and shape fidelity tests comprising a circular ring (n=3) and auricular antihelix (n=5) were used to compare printing accuracy, resolution and subsequent shape fidelity. Measurements were taken at a minimum of three fixed points as outlined in Section 2.6.3 using digital callipers and repeated in at least 3 separate 3D printed samples per condition.

### 4.2.4  Production and culture of cell laden-biomaterial constructs

Semispheres comprising 100 µl of each biomaterial (Alginate, NCB, NCC or NCF) were seeded with human nasoseptal chondrocytes from one of three separate patient cell lines (HN48, HN49, HN50) at a seeding density of $3\times10^6$ cells per ml. Semispheres were produced using a 1 ml syringe and decanted onto a sterile 96 well plate lid as a template. The semispheres were immersed in 100 µl of 0.5M $CaCl_2$ (Sigma Aldrich, as per Section 2.5.5.3) crosslinking solution, preheated to 37°C and allowed to crosslink for 10 minutes. The crosslinked semispheres were then immersed in warm PBS solution to remove any excess crosslinking agent and transferred to individual wells of a 48 well plate. Chondromedia (Section 2.3.2) was preheated to 37°C, and 750 µl was added to each well containing a biomaterial semisphere. The 48 well plates containing cells and biomaterials were thereafter transferred to a 170 L incubator (GS Biotech Limited,) set at 37°C and 5% $CO_2$ for up to 21 days. Media changes were performed twice per week.

### 4.2.5 Biocompatibility of nanocellulose bioinks

Biocompatibility of each of the nanocellulose materials was determined through a combination of live-dead assays (Section 2.12.1) and alamarBlue assays (Section 2.7.1) to determine cell viability and proliferation over a course of 21 days.

The alamarBlue assay was performed using a 10% (v/v) alamarBlue solution (Thermofisher) mixed in 90% chondromedia (Section 2.3.2) to generate alamarBlue media. 500 µl of the solution was added to the wells of a 48 well plate with a cell laden semisphere produced as per Section 2.6.6. The alamarBlue media was also added to cell only control wells and to blank wells to serve as cell only and media only controls. The alamarBlue was allowed to react for 4 hours in culture conditions, enabling sufficient time for the media to perfuse the biomaterial and evoke a colour change. Thereafter, triplicate samples of 100 µl of the reacted alamarBlue media were added to the wells of a 96 well plate and read at 570 nm and 600 nm on a plate reader. The percentage of reacted media was calculated compared to media only control values as described in Section 2.7.1. Measurements were taken immediately (0-4 hours), and at Day 7, 14 and 21 of culture. Biological triplicates were used and 4 samples taken per condition (n=12).

The live-dead assay was conducted after 24 hours of cellular encapsulation within the crosslinked biomaterial, and thereafter at 21 days of culture. A mixture of PBS containing Calcein-AM (1:1000) and Ethidium homodimer-1 (1:500) was produced, protected from light and added to the cell-laden semispheres for 45 minutes in standard culture conditions to stain live and dead cells respectively (as outlined in 2.12.1). The live cells were visualised using a FITC channel and the dead cells using the TRITC channel on an Olympus inverted fluorescent microscope. Representative images were taken in at least triplicate and at 4 and 10x magnification to provide an overview of overall cell viability.

### 4.2.6 Chondrogenic assessment of nanocellulose bioinks

Chondrogenicity of each bioink was determined at the level of gene expression through RT-qPCR, and at the level of extracellular matrix production using a

quantitative dimethylmethylene blue (DMMB) assay and histological staining of glycosaminoglycans with alcian blue.

In order to quantify gene expression, triplicates of each biomaterial were mixed with 0.1% (w/v) EDTA solution (Sigma Aldrich) and TRIzol (Invitrogen, Thermofisher) and subsequently degraded with a TissueRuptor II probe for 30 seconds. The lysate was processed using Qiagen QIAshredder and RNeasy Mini Extraction kits (Qiagen, Germany; as described in Sections 2.8.2) to yield RNA for reverse transcription. The RNA was quantified and assessed for purity using a Nanodrop Spectrophotometer. The concentrations of RNA in each sample were diluted with ultrapure nuclease free water across repeats to yield 11 µl samples each containing 200 ng RNA. The RNA was converted to cDNA through reverse transcription as described in Section 2.8.4, and quantified for the expression of COL2A1, SOX9 and ACAN1 relative to housekeeping gene expression (RPL13A and TBP) as per section 2.8.7. Each material was harvested for RNA extraction and PCR analysis at 4 hours, 7 days, 14 days and 21 days of culture. All relative gene expression values were expressed as fold-changes using the ΔΔCT method compared to a control value (Section 2.8.8): in this case alginate at the 4-hour time point. The gene expression of each material at each timepoint was compared statistically to the alginate 4 hour value for the same gene using an unpaired, two-tailed t-test.

The DMMB assay was used to quantify glycosaminoglycan (GAG) content in each material at 7 days and 21 days of culture. The cell-laden biomaterial semispheres of each bioink were lysed according to Section 2.9.1 to yield protein isolates for GAG quantification. Isolates were diluted 1 in 50 with distilled water and added to the wells of a 96 well plate in triplicate with 200 µl DMMB reagent. The plates were read immediately at 525 nm compared to a series of chondroitin standards ranging from 0 to 50 µg/ml as outlined in Section 2.9.3.

To determine the arrangement of extracellular matrix relative to the cells within the biomaterials, histological analysis was performed. Cell-laden biomaterial semispheres were immersed in 4% paraformaldehyde solution for 30 minutes and then washed three times in PBS (Section 2.10.1). The constructs were then immersed in 1% (w/v) Alcian Blue stain as described in Section 2.10.3.2 for 30

minutes and washed sequentially with hydrochloric acid and distilled water until no further stain was released. The semispheres were viewed under brightfield microscopy at 4, 10 and 20x magnification using an CKX53 Microscope (Olympus, Japan). Images were taken throughout the construct (in x, y and z axes) using CellSens Software (Olympus, Tokyo, Japan) to ensure the images captured were representative of the whole material.

### 4.2.7 Biomechanical testing of nanocellulose bioinks

200 µl cylindrical disks of each biomaterial were produced using the 3D printed mould described in Section 2.11.2 to produce equal cylinders of 6 mm diameter and 7 mm length. The materials were crosslinked within the moulds using 0.5 M $CaCl_2$ for 10 minutes and transferred to the 1$^{ST}$ Mechanical Compression Device (Tinus Olsen, Redhill, UK) in PBS for compression testing. Each material was compressed using a 25 N load cell as outlined in Section 2.11.2, to determine the break distance, break force and ultimate compressive force. These values were used to calculate the ultimate mechanical stress, break stress and strain to failure of each material. Materials were examined without cells, and then after culture with cells for 21 days to determine whether the cells amended the mechanical properties of the material over this time course.

### 4.2.8 Orbital shaking system for cell culture

48 well plates containing 100 µl semispheres of cell-laden material and media were produced as outlined above (Section 4.2.4). One plate was added to an orbital shaker, calibrated to 37°C and 5% $CO_2$ in the cell incubator and set at 500 rpm. The plate was secured to the orbital shaker with autoclave tape (dynamic condition). Another plate was added to a standard shelf of the same incubator but not subjected to any movement or shaking (static condition). The plates were cultured for a total of 14 days and analysed at 4 hours, 24 hours, 7- and 14-day timepoints for gene expression of COL2A1, SOX9 and ACAN1 as described in Section 4.2.6, for 3 biological repeats. The 14 day time point PCR was repeated with 6 biological repeats as this was the point at which the greatest differences in gene expression were observed between conditions. At 7 and 14 days, DMMB

assays were conducted on semispheres from the static and dynamic conditions as described in Section 4.2.5 using the same three biological repeats used for the PCR time point series.

### 4.2.9 *In silico* modelling of orbital shaking

Computational fluid dynamics was conducted in collaboration with Dr Feihu Zhao of the College of Engineering, Swansea University as described in Section 2.6.9. CFX software (ANSYS) was used to simulate the stress, perfusion and pressure gradient exerted upon the cell-laden biomaterial semispheres in dynamic culture. The model was built using the dimensions of a 48-well plate containing a 100 µl semisphere of crosslinked nanocellulose-alginate (NCB) biomaterial, with a porosity of 42% and a pore size of 0.8 µm and 750 µl of media, set at an orbital rotation speed of 500 rpm.

### 4.2.10 Statistical analysis

Data sets were assessed for normality (Gaussian distribution) visually and where needed using an Anderson-Darling test. Statistical analysis were thereafter selected accordingly. All data presented is the mean value of technical +/- biological replicates which is presented graphically with error bars depicting standard deviation unless otherwise stated.

For statistical comparisons between two dependent variables, either a t-test (+/- Welch's correction; where standard deviations were not equal). In this chapter, the relative gene expression data sets were analysed using unpaired, two tailed t-tests to compare gene expression relative to a control population using the ΔΔCt method (Figure 4.12, Figure 4.14).

For statistically analysing multiple dependent (>2) variables, typically a one-way ANOVA was used with a Tukey's post hoc test for multiple comparisons. In this chapter this analysis was used for comparing swelling characteristics (Figure 4.5) and the biomechanical compression data between the bioinks without cells (Figure 4.6). To account for unequal variances, Brown Forsythe ANOVA and

Welch ANOVA with Dunnett's multiple comparison test were used for the printability assays (Figure 4.1, Figure 4.2, Figure 4.3, Figure 4.4).

A 2-way ANOVA was used when multiple dependent variables (>2) were used across two separate series (such as different time points), with a Tukey's post hoc test. In this chapter, this analysis was used for comparing alamarBlue assays between materials and timepoints (Figure 4.8), for comparing DMMB assays between materials and timepoints (Figure 4.9, Figure 4.15) and for mechanical compression testing before and after the addition of cells in different nanocelluloses (Figure 4.11).

## 4.3 Results

In this section, experiments are conducted to compare the nanocellulose formulations: NCB, NCC and NCF in a composite bioink with alginate. Specifically, printability, mechanical characteristics, chondrogenicity and biocompatibility will be investigated to determine which nanocellulose is the most suitable base ink for a chondrogenic bioink.

### 4.3.1 Comparison of printability characteristics using different nanocellulose subtypes

#### 4.3.1.1 Extrudability and resolution of nanocellulose bioinks for 3D printing

Two important features of bioink printability are extrusion and resolution. It is essential for a candidate bioink to be able to flow through a bioprinter nozzle upon the application of an extrusion pressure, and an ideal criterion for bioinks to be dispersed in a way that enables fine detail to be preserved after extrusion (resolution). The inclusion of all formulations of nanocellulose in the bioinks was found to significantly improve printability compared to alginate alone in this regard. Despite having the lowest extrusion printing pressure (3 kPa), the alginate demonstrated poor fidelity and post-printing stability rendering it unsuitable for 3D printing at the viscosity (2.5% w/v) used in this study. Of the nanocelluloses used, the NCF had the lowest extrusion pressure (5 kPa), followed by the NCB (7 kPa)

and lastly the NCC (10 kPa). There were no significant differences in the mean line diameter generated by the biomaterials when printed (p=0.57) with a Brown-Forsythe ANOVA test. However, a much greater range of values was observed in the NCC lines (SD=0.46mm) than NCB (0.27mm) and NCF (0.13mm) indicating a greater degree of line width consistency was achieved in the NCF prints.

All nanocellulose materials displayed satisfactory printing resolution using the straight-line assay (Figure 4.1), with NCF capable of the greatest resolution (0.6mm +-0.13) compared to NCB (0.68mm+-0.27) and NCC (0.84mm+-0.46).
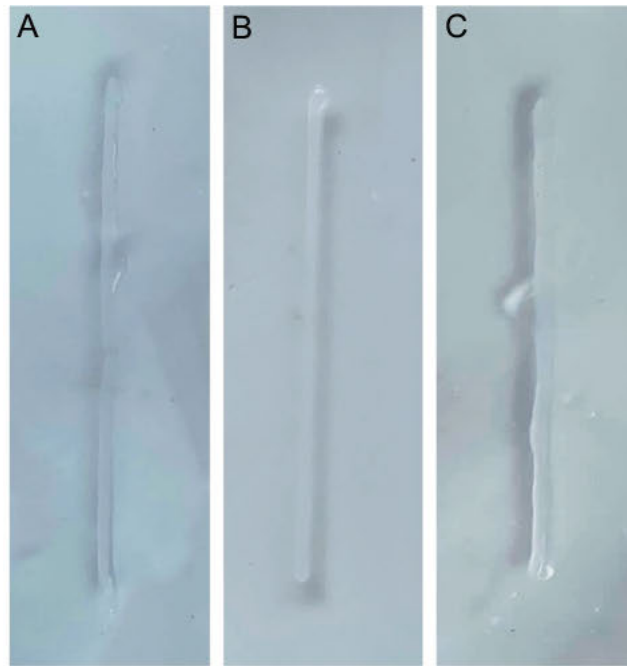
| | NCB | NCC | NCF |
|---|---|---|---|
| Mean line width (mm) | 0.68 | 0.84 | 0.60 |
| Std dev | 0.27 | 0.46 | 0.13 |
| Range | 0.64 | 0.83 | 0.28 |
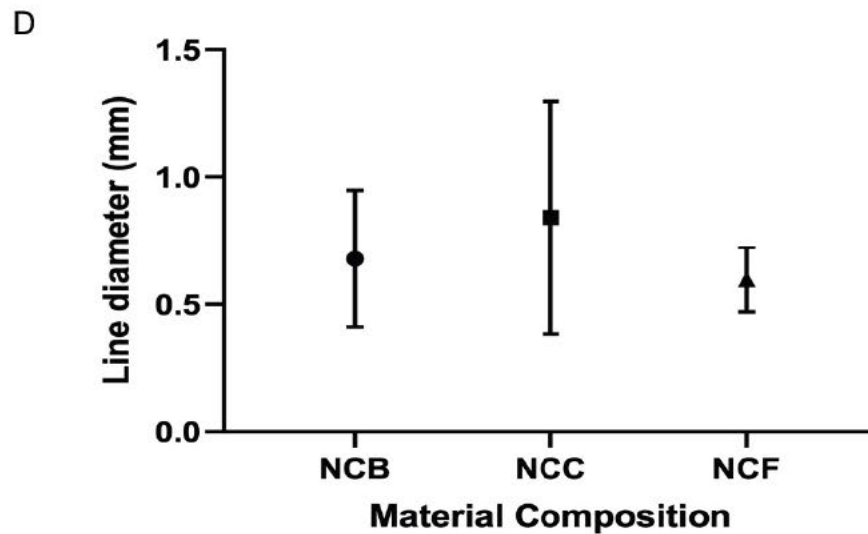


*Figure 4.1: Line resolution assay comparing NCB (A), NCC (B) and NCF (C). Representative images of each line are displayed (A-C) with the mean measurements (n=3) of each line, the standard deviation and range displayed beneath. The mean line width values plus range (in mm) are depicted graphically in (D), demonstrating a smaller range and narrower line in NCF compared to NCB and NCC. No statistically significant differences were observed between the mean line thicknesses.*

### 4.3.1.2    Grid Assays

Repeated linear assays such as a grid assay are useful indicators of both print resolution and print consistency. Each nanocellulose bioink was used to print a simple grid or lattice comprising 5 horizontal and 5 vertical lines, yielding 25 square spaces for measurement. The NCF displayed the tightest range of peripheral border sizes (0.5mm), compared to NCB (1.04mm) and NCC (1.49mm) but the NCB had the best reproducibility in grid sizes with a more consistent mean grid area (7.2mm$^2$) compared to the plastic control (9mm$^2$) when compared to NCF (12.4mm$^2$) and NCC (11.1mm$^2$). Statistical analyses (as per Section 4.2.9) revealed that none of the differences in grid resolution were significant (p=0.94).

| | NCB | NCC | NCF |
|---|---|---|---|
| Intended line width (mm) | 3 | 3 | 3 |
| Mean line width (mm) | 2.79 | 2.83 | 2.72 |
| Range of line widths (mm) | 0.89 | 0.63 | 0.19 |
| Intended grid area (mm²) | 9 | 9 | 9 |
| Mean grid area (mm²) | 7.2 | 11.1 | 12.4 |
| Mean Area Discrepancy (mm²) | -1.8 | 2.1 | 3.4 |
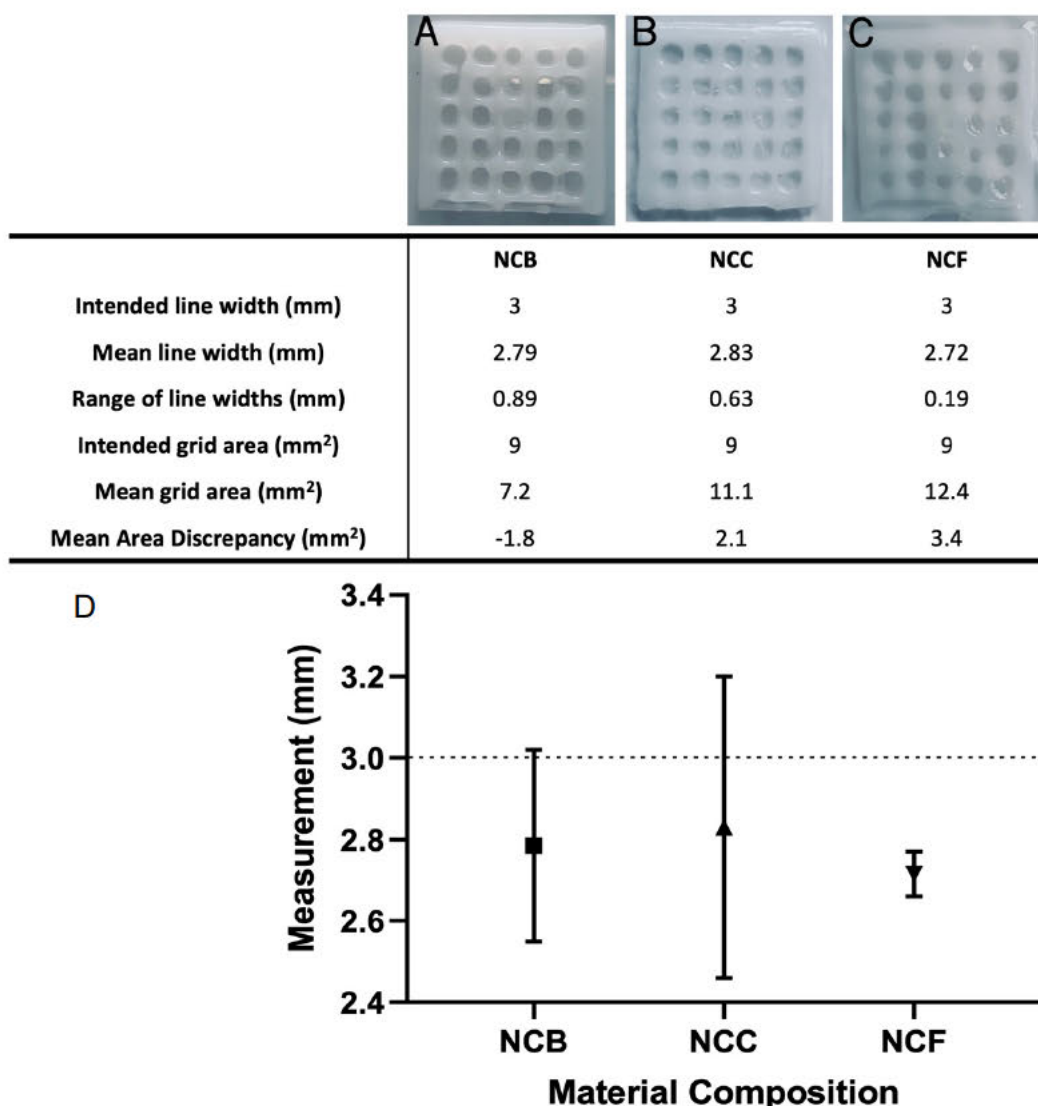


*Figure 4.2: Grid Assays and their measurements printed with representative images of NCB (A), NCC (B) and NCF (C). Three grids per material were printed and the mean line width taken from a minimum of 3 lines per grid. The range and deviation from the intended grid geometry is presented in the table and graphically depicted in (D). The mean plus range is displayed with a dotted line to represent the intended line width of 3mm for reference.*

### 4.3.1.3    Ring assay

The ability to print curves and arcs is an essential test of 3D print resolution and post-printing shape fidelity, particularly where anatomical structures such as ears are the intended design. All nanocellulose materials were able to produce rings consistent with the 3D design (Figure 4.3). All constructs were thicker at their minimum and maximum widths than the 3D design by a mean of 1.775 (NCB),

0.725 (NCF) and 1.205mm (NCC) but this was not statistically significant (p=0.5). As with the other assays, there was a greater range of thicknesses observed in the NCC (range=1.33mm) and NCB (range=1.03mm) prints than the NCF (range=0.09mm), the latter of which displayed greater uniformity and consistency throughout the prints.



|  | NCB | NCC | NCF |
|---|---|---|---|
| Intended width (mm) | 3 | 3 | 3 |
| Maximum width (mm) | 5.29 | 4.87 | 3.77 |
| Minimum width (mm) | 4.26 | 3.54 | 3.68 |
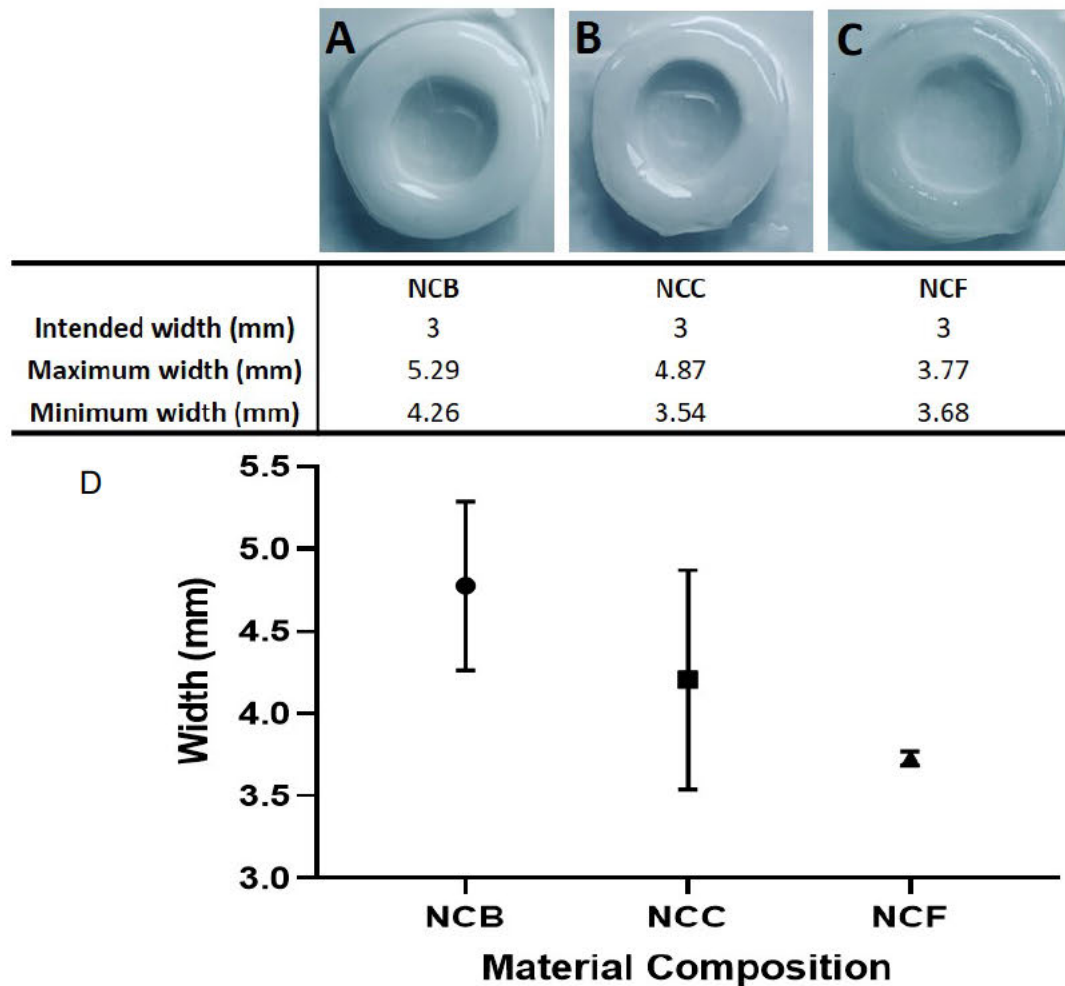
Figure 4.3: Representative images of circular rings printed using NCB (A), NCC (B) and NCF (C) are displayed with mean measurements of tracheal ring thickness taken from least 3 points per ring (D). Error bars depicting the range are displayed. No signifcant differences were observed between mean ring thicknesses (p=0.5).

### 4.3.1.4       Auricular antihelix

Reproduction of a human auricular antihelix was achieved with each nanocellulose-alginate bioink, however the NCB offered the most consistent measurements in this test compared to the plastic control (mean difference = 0.424mm +-1.68), followed by NCF (0.526mm +-2.17) and NCC (-1.234mm +-3.44). No material was found to be significantly different to the plastic control measurements however (p>0.99 for all comparisons) and there were no statistically significant differences between the NC bioinks (p=0.52). Therefore, with regard to producing anatomical structures such as an anthelix, all bioinks possess the necessary resolution but NCB offers the most consistency and reproducibility.

| | Intended size (mm) | NCB (mm) | NCC (mm) | NCF (mm) |
|---|---|---|---|---|
| Length | 33.29 | 31.72 | 27.61 | 30.72 |
| Width | 18.32 | 17.36 | 14.13 | 17.42 |
| Body | 5.64 | 6.66 | 7.5 | 8.22 |
| Superior crus | 5.77 | 6.82 | 6.89 | 7.59 |
| Inferior crus | 3.6 | 6.18 | 4.32 | 5.3 |
| Mean deviation | - | 0.424 | -1.234 | 0.526 |
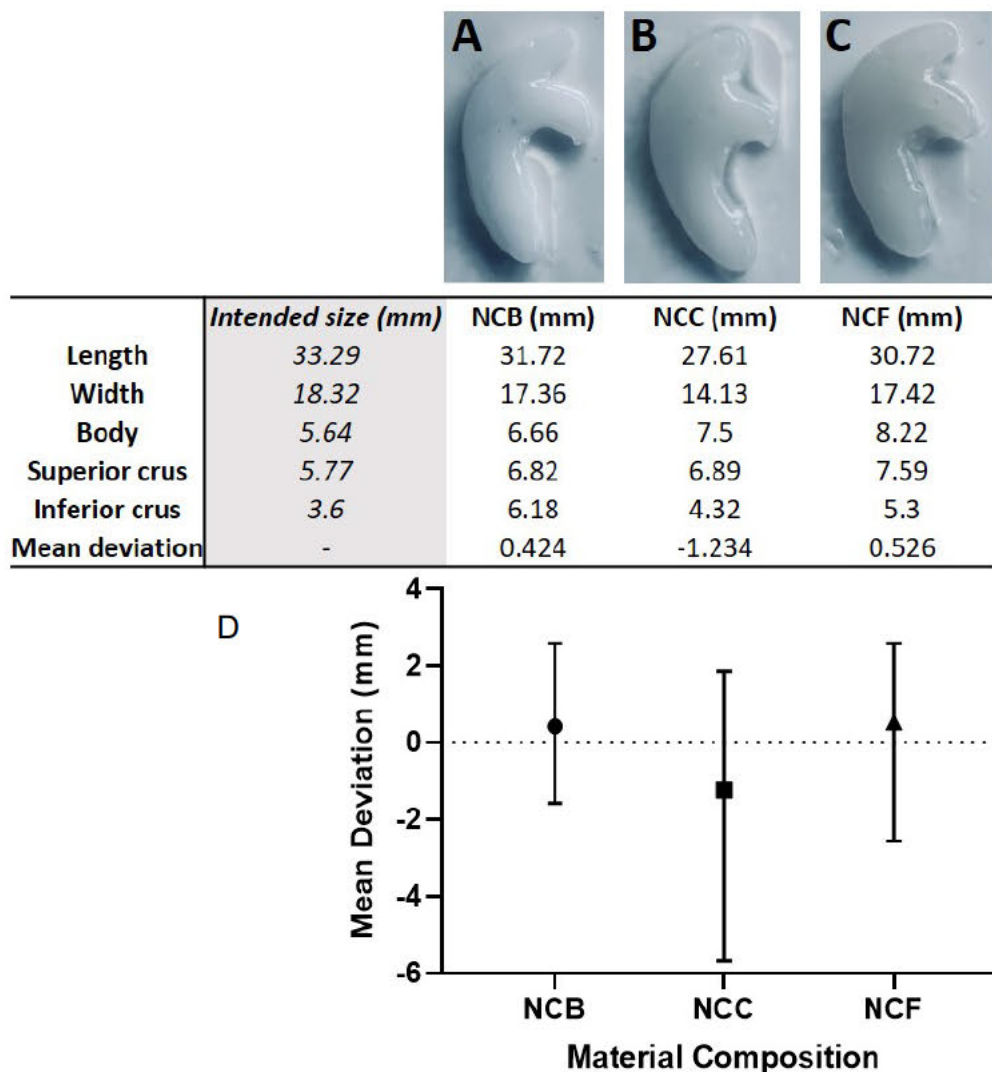
*Figure 4.4: Representative images of antihelices printed with NCB (A), NCC (B) and NCF (C). A recognisable antihelix was producible with all nanocellulose subtypes but NCB had the lowest amount of deviation from the intended parameters of the antihelical design as demonstrated in the table and graphically in (D). A dotted line on (D) is used to depict the point of no deviation in size from printing in plastic; mean values of 3 repeats with error bars depicting the range are presented. No statistically significant differences were noted between bioinks or compared to plastic.*

## 4.3.2 Effect of crosslinking on size of 3D printed constructs

Despite demonstrating good post-printing fidelity, some bioinks may distort or change in size following the application of a crosslinking agent owing to the formation of new bonds between polymers. The swelling of the nanocellulose materials was compared before and after immersion in crosslinking agent to determine changes in construct size as a result of the crosslinking process.

209

Comparable swelling properties were observed with each of the nanocellulose materials, with a lowest mean swelling in the NCC (3.2%) and NCB materials (6.6%) and highest in the NCF (9.9%) (Figure 4.5). However the differences between these materials was not significant (p=0.13, n=6). The degree of enlargement following crosslinker application should be considered in the context of future construct design, in particular when using NCF and fine resolution prints.
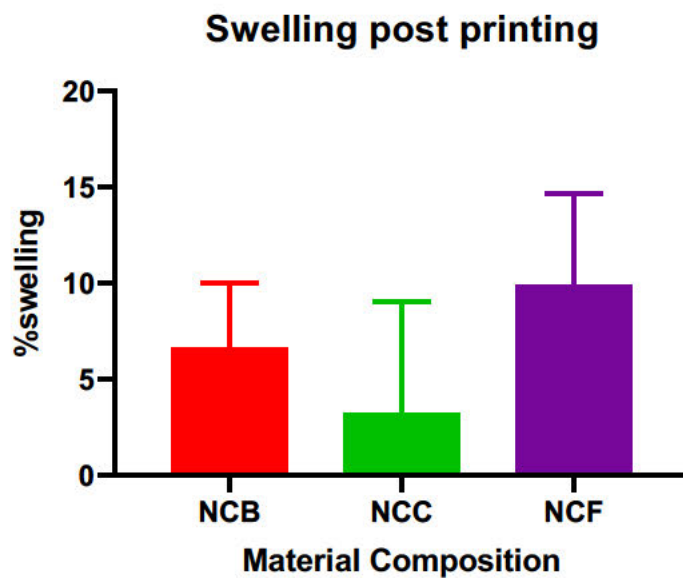


Figure 4.5: Swelling of nanocellulose bioinks after printing and crosslinking application expressed as a percentage of the original size post-printing. The mean values of each material are presented with error bars depicting standard deviation (n=6). No statistically significant differences were observed between materials.

### 4.3.3 Biomechanical properties of nanocellulose materials

In order to withstand biomechanical forces when implanted *in vivo*, crosslinked bioinks must demonstrate sufficient resistance to compressive forces without significant distortion or disintegration. Each of the biomaterials was tested mechanically for the ultimate compressive stress, break force and strain to failure experienced by the biomaterial when subjected to compressive forces (Figure 4.6, Appendix 2). It was noted that NCF was able to withstand a significantly lower ultimate compressive stress (0.14 MPa, p=0.029) than alginate alone (0.76 MPa),

but that there were no significant differences between alginate and NCC (0.20 MPa, p=0.45) or NCB (0.24 MPa, p=0.99).

With regard to strain to failure, there were comparable levels of strain noted across all biomaterials: Alginate (75.5%), NCB (78.7%), NCC (69.7%) and NCF (68.2%). These were not statistically significant differences (p=0.35). A higher break force was achieved with alginate (4.99 N) than the other nanocellulose materials, of which NCB had the highest break force (1.49 N, p=0.34 vs alginate) and NCF was significantly lower than alginate (0.59 N, p=0.006), no other significant differences were observed between the nanocellulose biomaterials. In summary, the compression testing has identified that the alginate alone has the most robust mechanical compression properties compared to the nanocellulose-alginate composite bioinks. Of the composite bioinks, the NCF appeared to be structurally weaker than NCB and NCC, raising some doubts over its relative suitability for clinical translation.
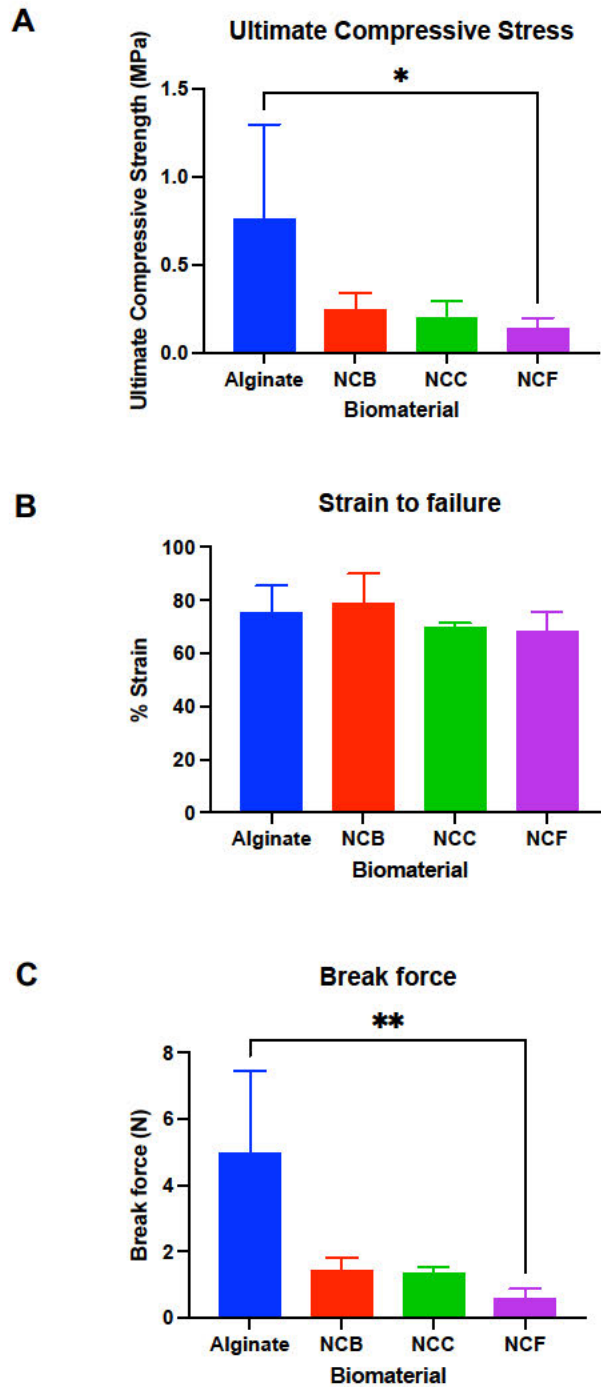
**Figure 4.6: Mechanical compression testing of alginate and nanocellulose-alginate composite bioinks. A) The mean ultimate compressive stress (UCS or strength) of each material is displayed with error bars depicting standard deviation (n=4). Significant differences in mean UCS was seen only between alginate and NCF. B) The mean strain to failure of each material when compressed is demonstrated with standard deviation (n=4) in which no statistically significant differences were observed. C) The mean break force required for each biomaterial is presented with standard deviation (n=4), significant differences were observed between NCF and alginate only. \*=p<0.05; \*\*=p<0.01**

### 4.3.4 Assessment of nanocellulose biocompatibility

Viability of cells in the biomaterials of interest post-printing is paramount for subsequent cell proliferation and cartilage formation. Immediately post-bioprinting, all materials demonstrated excellent cell viability with no significant differences noted between material types (Figure 4.7, Figure 4.8). Highly significant differences were observed between timepoints ($p < 0.0001$) and materials ($p < 0.0001$) with the alamarBlue assay using a 2-way ANOVA. Initial alamarBlue assays at 4 hours demonstrated a higher degree of metabolism in the alginate material compared to the nanocellulose materials (Alginate vs NCB, $p < 0.0001$; vs NCC $p = 0.0007$, vs NCF $p = 0.0336$). However, by 7 days there were no longer significant differences between the alginate, NCB and NCC materials but a significant rise in metabolic activity was noted in the NCF group (67.5%; vs alginate $p = 0.0323$; vs NCB $p = 0.0384$). By 14 and 21 days, the highest mean value of metabolic activity was observed in the NCB (63% at 14 days, vs Alginate $p = 0.012$, vs NCF $p = 0.0001$; 68% at 21 days, vs alginate $p < 0.0001$, vs NCF $p = 0.0004$) and NCC materials (64.8% at 14 days vs Alginate $p = 0.0076$, vs NCF $p = 0.0001$; 67.1% at 21d vs Alginate $p < 0.0001$, vs NCF $p = 0.0007$), which had both increased significantly from 4 hours implying an increase in cell number (NCB 4h vs 7d, $p = 0.001$, vs 14d $p = 0.017$, vs 21 days $< 0.0001$), NCC (vs 21d $p = 0.0024$). There were no significant changes noted between NCB and NCC at any timepoint, meaning a comparable and favourable biocompatibility profile exists for both materials.

Live dead assays were conducted at 1 and 21 days and demonstrated evidence of chondrocyte proliferation within all biomaterials (Figure 4.7). The viability was noted to be greatest in the NCB and lowest in the NCF, consistent with the findings observed in the AlamarBlue Assay (Figure 4.8). On the basis of these experiments, the NCB and NCC appear to be the most conducive bioinks of cell proliferation and viability, making them the most suitable for cartilage tissue engineering.
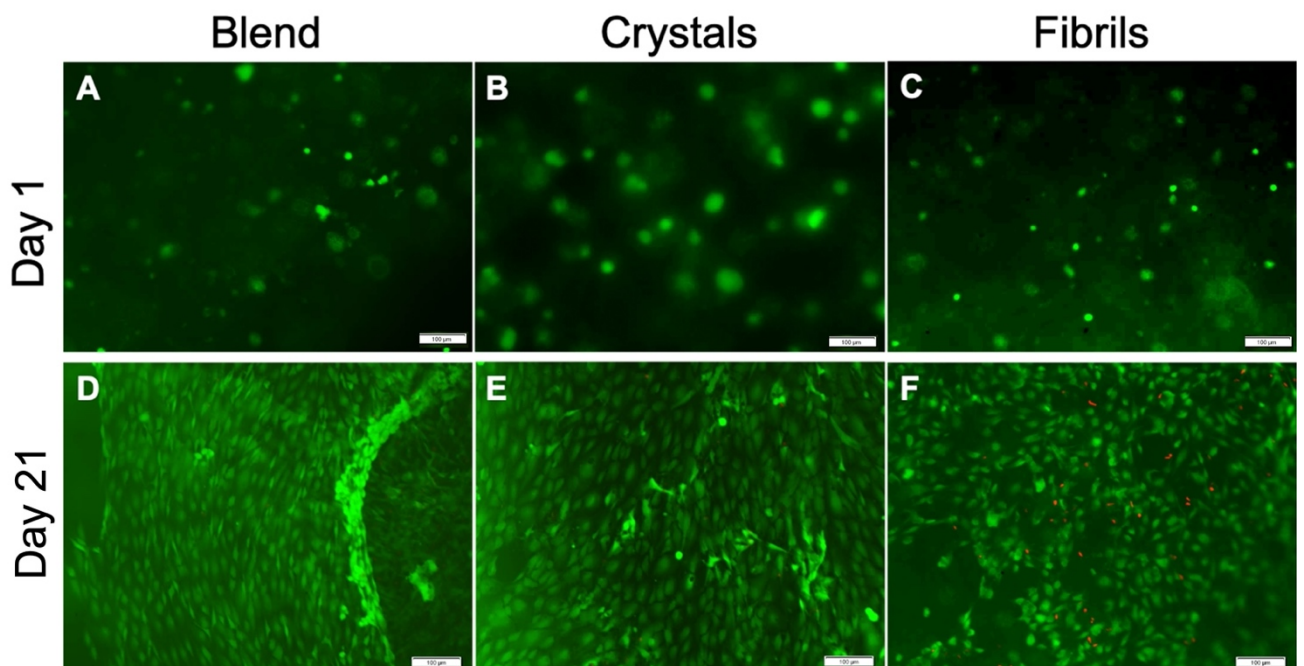


*Figure 4.7: Live-dead assay of cell-laden biomaterials at Day 1 (A-C) and Day 28 (D-F). NCB (A, D) demonstrated the highest cell number and viability at 21 days, followed by NCC (B, E) and NCF (C, F). Representative images (as displayed) were taken in at least triplicate at 4x magnification from 3 biological repeats, scale bars denote 100µm.*
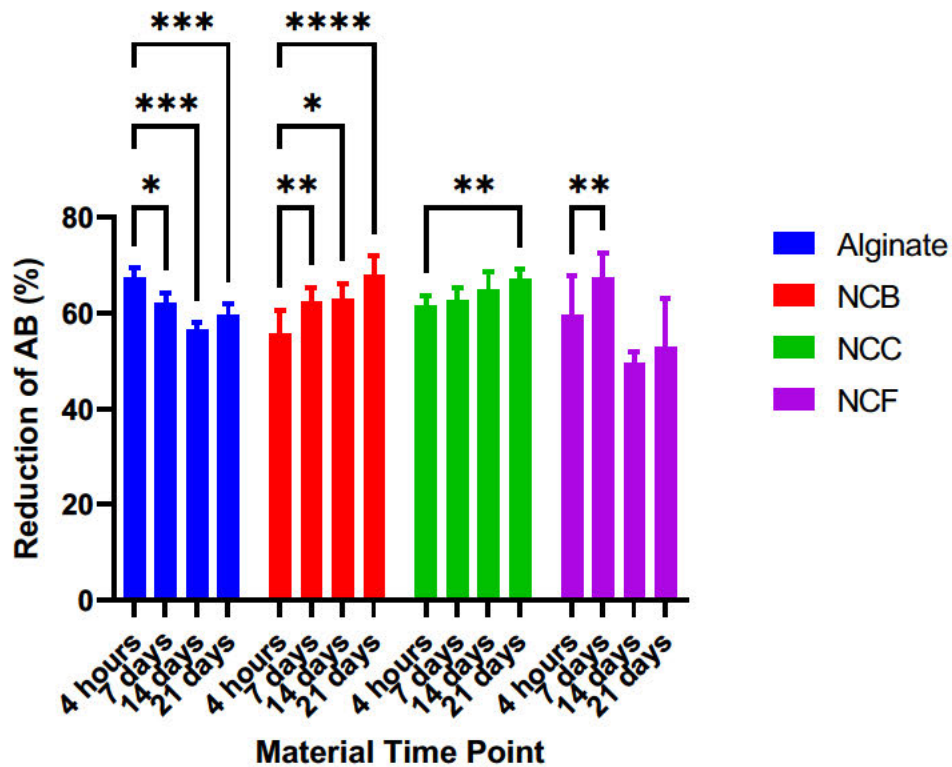
*Figure 4.8: AlamarBlue (AB) Assay demonstrating degree of metabolic activity (as a marker of cell number) in different biomaterials over 21 days. The mean percentage of AB that had been reduced by cells is expressed relative to negative controls (media and AB only) with error bars depicting standard deviation. Pairwise comparisons were performed using a 2 Way ANOVA and Tukey's multiple comparison test with each material compared to baseline values at 4 hours. A total n of 12 is presented (4 repeats from biological triplicates). \*=p<0.05; \*\*=p<0.01; \*\*\*=p<0.001, \*\*\*\*=p<0.0001*

### 4.3.5 Chondrogenic potential of nanocellulose biomaterials

### 4.3.5.1       Extracellular matrix production in nanocellulose materials

Glycosaminoglycan (GAG) content was quantified using the DMMB assay at 7 and 21 days of culture in each biomaterial (Figure 4.9). All of the biomaterials studied demonstrated a statistically significant increase in GAG content from 7 to 21 days (p<0.0001) with a mean increase of 832.1 µg/ml (±46.39). At 21 days the highest GAG content was observed in the NCC material (1434 µg/ml) though no statistically significant differences were observed between biomaterials (p=0.091).
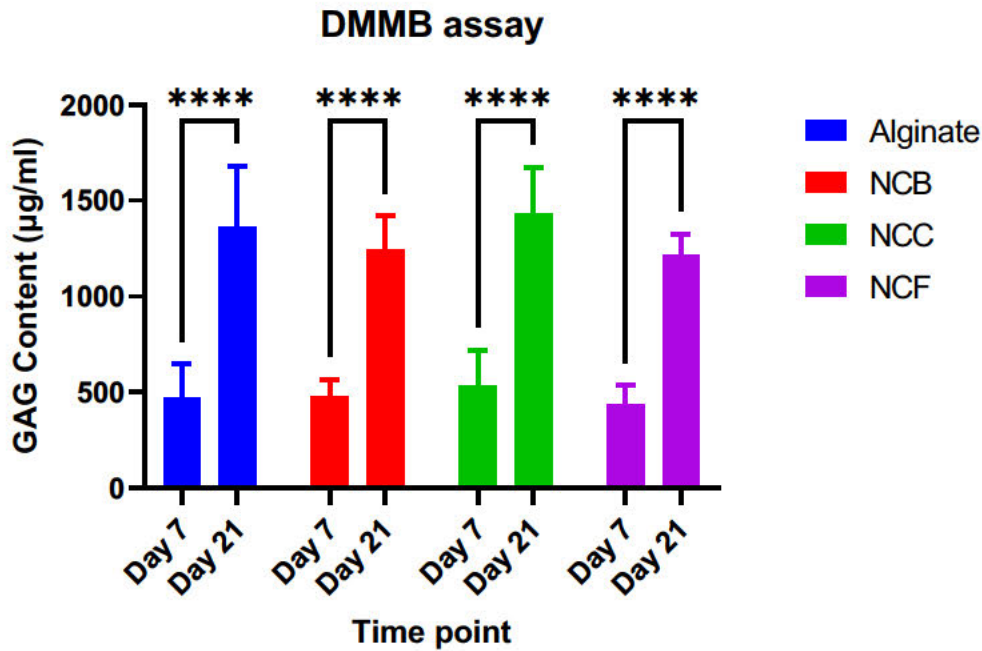
*Figure 4.9: Dimethylmethylene Blue (DMMB) Assay to quantify glycoasminoglycan (GAG) content in biomaterials of interest at 7 and 21 days of culture. The mean value of 9 repeats (technical n=3, biological n=3) is presented with error bars of standard deviation. Significant increases were observed in all biomaterials between the two time points, however no statistically significant differences in GAG content were observed between the materials at Day 7 or Day 21. \*\*\*\*=p<0.0001*

### 4.3.5.2 Histological visualisation of extracellular matrix production in nanocellulose biomaterials

The cell-laden biomaterials were stained with Alcian Blue stain to visualise cell density, arrangement, pericellular and extracellular matrix production. Extracellular matrix was readily stained in each of the biomaterials studied. The greatest number of cells could be visualised in the NCB material in which there was also evidence of intense extracellular matrix staining. This indicates the matrix has been deposited by cells within the material rather than non-specific staining to the material as evidenced in Figure 4.10C. The cells appear to exist in isolation surrounded by matrix as in native cartilage lacunae. This phenomenon was also observed albeit to a lesser degree in the NCC, NCF and Alginate materials (Figure 4.10A, C & D) however there was variable uptake of stain around cells in the alginate material, with many not staining for GAG production (Figure 4.10A). Histologically, it would therefore appear that NCB appears to offer

the greatest degree of biomimicry in ECM production and cellular density, however objectively, there is no significant difference in the quantity of GAG content in any of the bioinks at 21 days of culture using the DMMB assay.
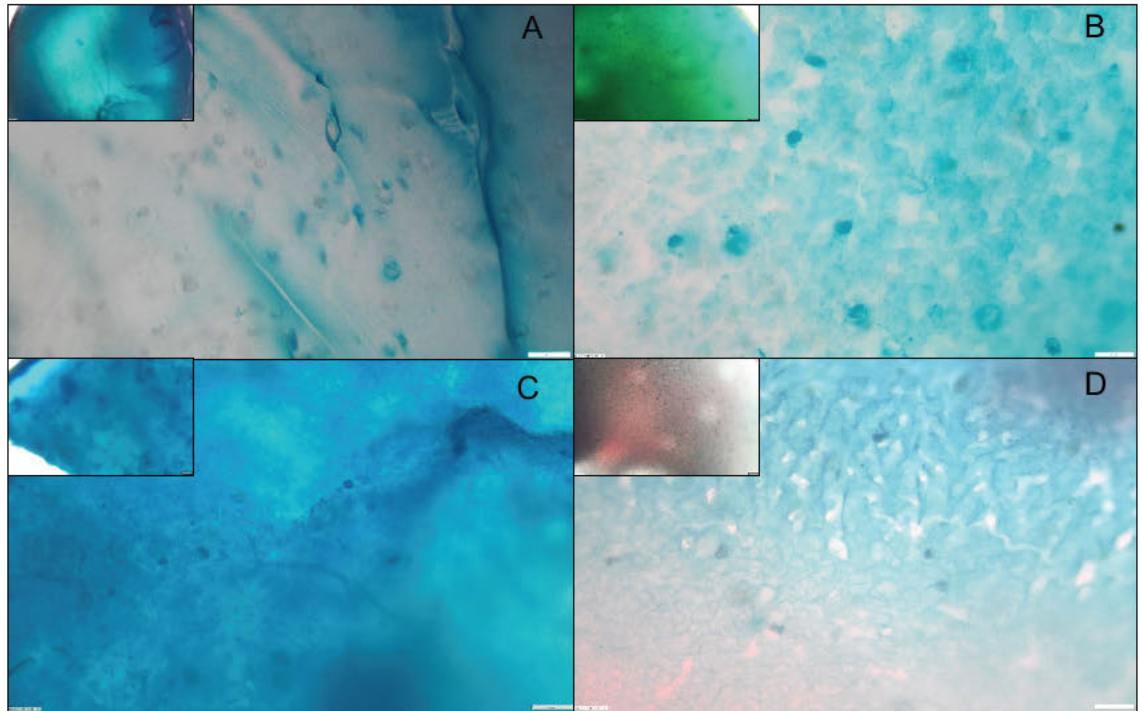


Figure 4.10: Histological analysis of nanocellulose Blend (B), Fibrils (C) and Crystals (D) compared to Alginate (A) at 4x (small images, top left) and 20x (large images) magnification. All materials demonstrate staining with alcian blue with pericellular staining noted most prominently in B, C and D. Scale bars (bottom right) depict 50µm.

### 4.3.5.3 The effect of cell-biomaterial interaction on biomechanical properties of nanocellulose-alginate bioinks

It is important to determine whether embedding the material with cells in culture conditions influences the mechanical properties of the candidate biomaterials. In the compression testing with and without cells, the alginate material was consistently stronger than the nanocellulose-alginate composite bioinks in terms of UCS (Figure 4.11A), achieving a maximum value of 1.49 MPa with cells. However, this was not significantly different than the strength without cells (0.76 MPa, p=0.07). The NCB demonstrated the most significant increase in UCS from

217

0.24 to 0.53 MPa (p=0.004), but NCC (0.49 MPa, p=0.02) and NCF (0.27 MPa, p=0.02) also demonstrated significant increases after culture with cells.

The degree of strain to failure experienced by the materials was found to generally be higher after culture with cells than without cells (Figure 4.11B), but this was only a significant difference in the alginate material (p=0.009). Between materials, the alginate with cells had a significantly higher degree of strain to failure than the NCF (71.9%, p=0.006) but was not significantly different to the other material with cells. This indicates that despite a higher compressive strength, the alginate with cells became more prone to deformation under compressive loading after culture with cells unlike the nanocellulose based materials.

The break force of the materials expectedly mirrored the UCS (Figure 4.11C), showing that the alginate material had the highest break force both without cells (5MPa) and with cells (9.5MPa) and that this difference between the two conditions was statistically significant (p=0.0001). The break force with cells was also significantly higher than NCB (1.4N, p<0.0001), NCC (1.4N, p<0.0001) and NCF (0.6N, p<0.0001). There were no significant differences noted between the nanocellulose-based inks with cells. The alginate is the component of the biomaterial capable of crosslinking meaning this finding is not unexpected, but emphasises the importance of robust crosslinking to enhance compressive strength.
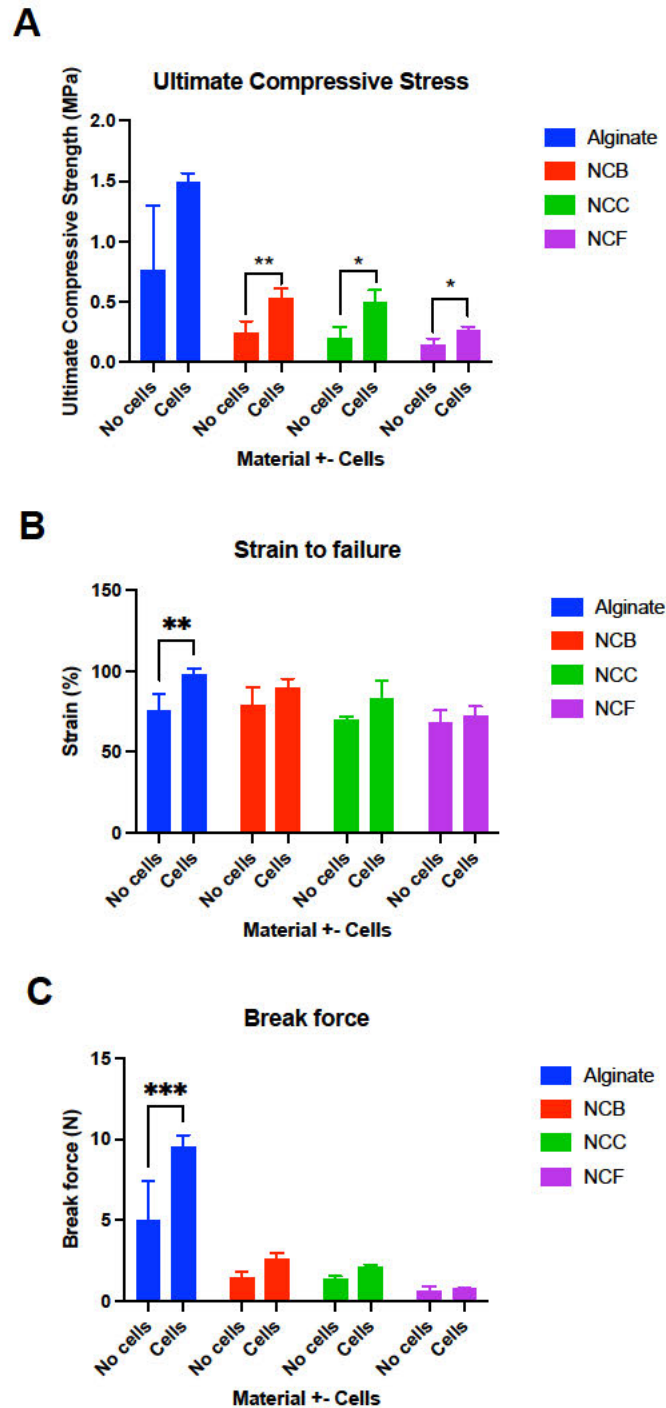
Figure 4.11: Mechanical compression testing of materials with and without cells after 21 days of culture. A) The mean UCS of the biomaterials is presented in MPa with error bars depicting standard deviation (n=4). All nanocellulose based materials demonstrated a significant increase in UCS after co-culture with cells. B) The mean strain to failure of the materials (expressed as a percentage) when compressed is presented with and without cells with error bars of standard deviation (n=4). The strain of alginate was the only material to significantly increase after 21 days of culture with cells. C) The mean break force (Newtons) of each material is presented with standard deviation (n=4). Increases were observed in all materials after culture with cells but this was only significant for alginate. *=p<0.05; **=p<0.01; ***=p<0.001.

### 4.3.5.4 Chondrogenic gene expression profile in nanocelluloses

To determine the ability of the materials to evoke a chondrogenic environment, gene expression changes can offer a reliable and comparative assessment of the effect of the biomaterials on the cells of interest at various time points. Chondrogenic gene expression was observed over a 21-day time course to determine expression of the chondrogenic hypertrophy gene (SOX9) and the expression of cartilage-specific extracellular matrix genes: type 2 collagen (COL2A1) and aggrecan (ACAN1). All results were compared to alginate at 4 hours as a control to determine the temporal relationship in relative gene expression (Figure 4.12). All materials demonstrated biologically relevant (>2x) increases in COL2A1 expression beyond 4 hours compared to alginate alone, with statistical significance achieved in the NCC (405.7-fold increase, $p<0.0001$) and NCF (302.1-fold increase, $p=0.0003$)) materials at 14 days. The gene expression of COL2A1 had risen by 1580-fold greater expression ($p<0.0001$) in NCC by 21 days. Aggrecan expression demonstrated a similar temporal relationship, increasing in NCC at all time points, with statistically significant increases in gene expression seen at 14 days (31-fold, $p=0.0002$) and 21 days (36.7-fold, $p<0.0001$). NCF had a significantly higher expression of ACAN1 at 14 days ($p=0.0006$) but no other time points. With regards to SOX9, a statistically significant elevation of expression was observed in NCB (1.7-fold, $p<0.0001$) and NCC (1.4-fold, $p=0.0005$) as early as 4 hours and at 14 days in NCC (4.9-fold, $p=0.0041$). In summary, the NCC appeared to be the most chondrogenic bioink across the timepoints studied, however biologically relevant increases in gene expression were seen in all biomaterials.

**A** ACAN1

**B** SOX9

**C** COL2A1
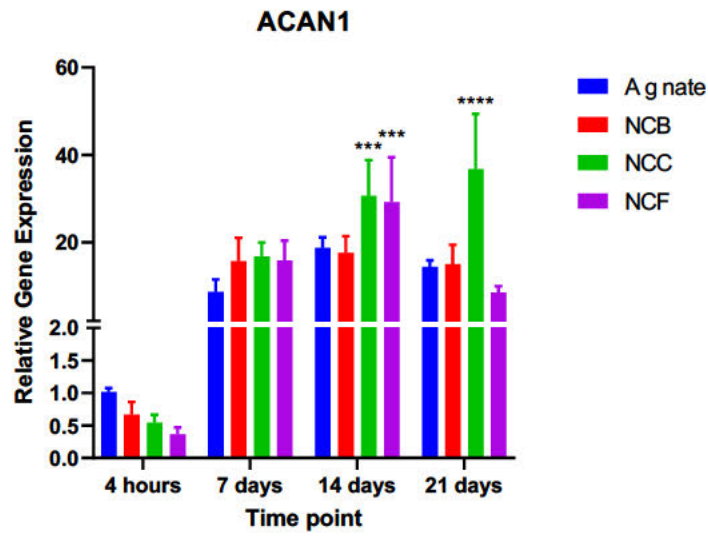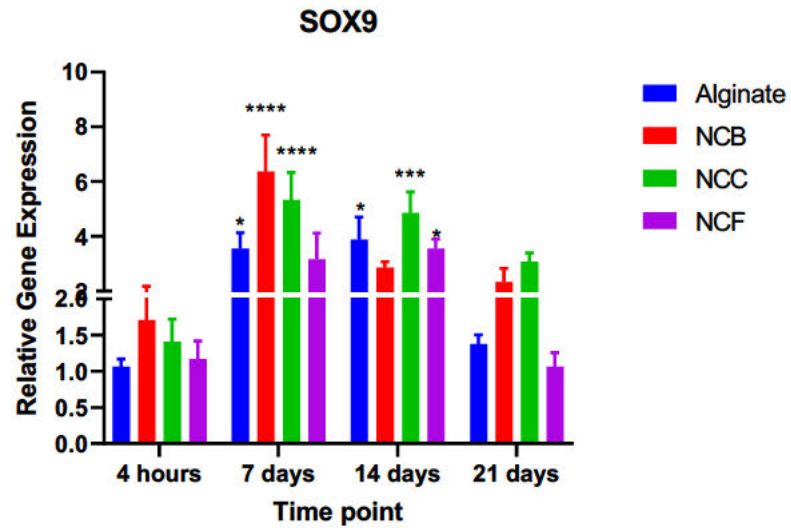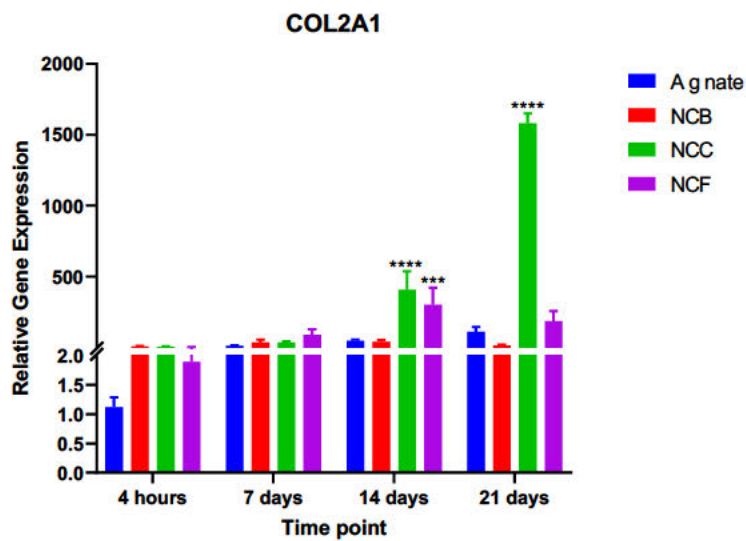
*Figure 4.12: Chondrogenic gene expression profile over 21-day time course. All relative gene expression values displayed represent a mean of three biological repeats (performed in at least technical triplicates) with standard error, relative to alginate at 4 hours. A) Aggrecan gene expression profile at 4 hours, 7 days, 14 days and 21 days in culture. All values were biologically significant (>2) after 7 days but only statistically significant in NCC (14 days, 21 days) and NCF (14 days). B) SOX9 gene expression profile over 21 day time series. All bioinks produced biologically significant differences in SOX9 expression relative to 4 hours at 7 and 14 days with the highest peak achieved in NCB at day 7. C) Type 2  collagen gene expression profile over 21 days. Biologically significant increase in type 2 collagen were observed after 7 days but significant in NCC (14, 21 days) and NCF (14 days) only. \*=p<0.05; \*\*=p<0.01; \*\*\*=p<0.001; \*\*\*\*=p<0.0001.*

### 4.3.6  Optimisation of cell culture conditions to enhance chondrogenesis in nanocellulose blend with alginate

The cell-laden biomaterial semispheres were subjected to dynamic orbital shaking at 500 rpm over the course of 14 days to determine the effects on chondrogenesis and to model the degree of mechanical stress this model exerted on the material and cells.

Computational modelling identified that the maximum fluid velocity experienced by the material-cell combination was under 3 μm/second with a maximum pressure range of 48 Pa and shear stress less than 0.02 mPa, with the most intense shear stress predicted at the base of the semisphere.
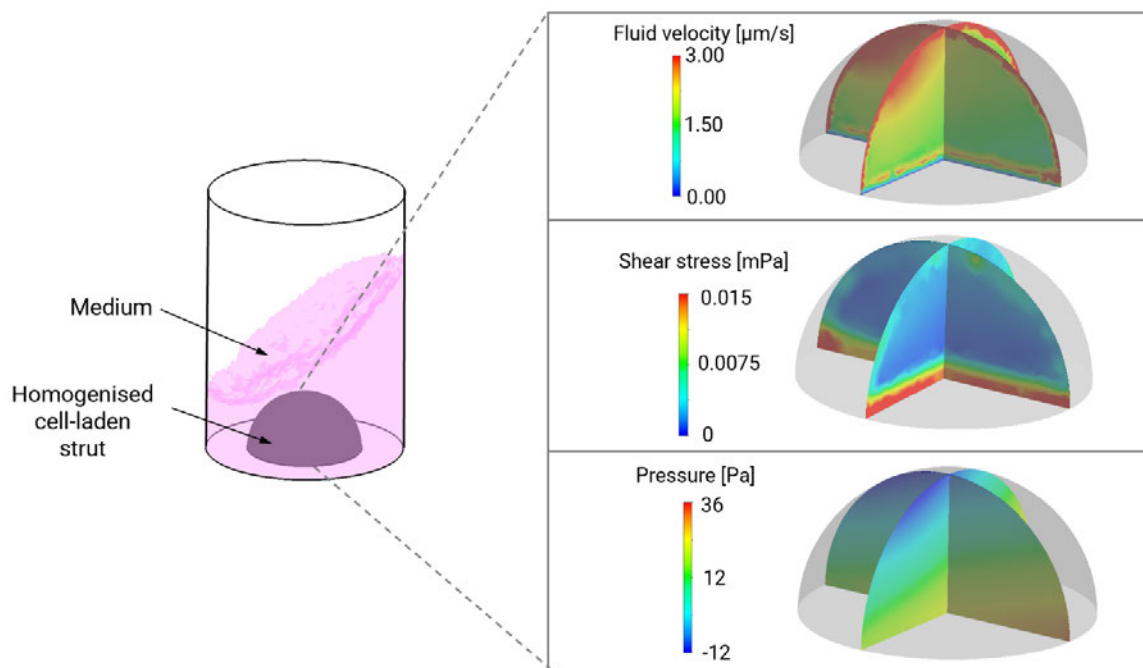
*Figure 4.13: Computation modelling of shear stress, pressure and fluid velocity in NCB biomaterials with chondrocytes in dynamic culture conditions in a 48 well plate. Maximum fluid velocity was predicted in the upper poles of the material, with the greatest amount of shear stress at the base. Produced in collaboration with Dr Feihu Zhao.*

Despite the low levels of pressure and shear stress exerted in this model, there were enhancements in chondrogenesis observed with the dynamic culture environment. This trend was visualised through observing the gene expression profile over a 14-day timepoint series in dynamic and static culture conditions (Figure 4.14). Specifically, at 4 and 24 hours, 7 and 14 days, the relative gene expression of ACAN1, SOX9 and COL2A1 were compared to baseline gene expression values (static, 4 hours). Aggrecan expression rose significantly as early as 24 hours in both static conditions (14.3-fold increase, p<0.0001) and dynamic conditions (17.8-fold increase, p=0.02). This trend continued in the static condition to a time point of 7 days (85.4-fold increase, p=0.03) compared to 4 hours but began to decrease by 14 days in the static culture conditions (25.9-fold increase, p=0.02). Conversely, in the dynamic conditions ACAN1 expression remained elevated at both 7 days (123.5-fold increase, p<0.0001) and 14 days (184.5-fold increase, p<0.0001). In the dynamic conditions, a transient rise in SOX9 expression was observed at 4 hours (2.2-fold increase, p=0.009), 24 hours (5.6-fold increase, p=0.03) and 7 days (5.7-fold increase, p=0.05) but fell

thereafter at 14 days (2.4-fold increase, p=0.1). Conversely, a more gradual increase in SOX9 expression was observed over 14 days in the static conditions, increasing to 1.8-fold at 24 hours (p=0.02), 6.1-fold at 7 days (p=0.03) and 6.7-fold at 14 days (p=0.02). Conversely, with regard to COL2A1, there was a marked increase in expression at 4 hours (1.49-fold, p=0.049), 24 hours (2.5-fold, p=0.01), 7 days (226.3-fold increase, p=0.049) and 14 days (546.6-fold increase, p=0.06) in the dynamic culture conditions relative to static conditions at 4 hours. Although increases in COL2 gene expression were also observed in the static conditions this was only statistically significant at 24 hours (1.6-fold, p=0.009).

This data indicates that dynamic culture conditions evoke a transient statistically significant increase in SOX9, followed by sustained increases in ACAN1 and COL2A1 expression which appear to outweigh the magnitude of temporal gene expression changes seen in static conditions. These effects may be attributable to the increased media flow as depicted by the enhanced fluid velocity through the scaffold as visualised in Figure 4.13.
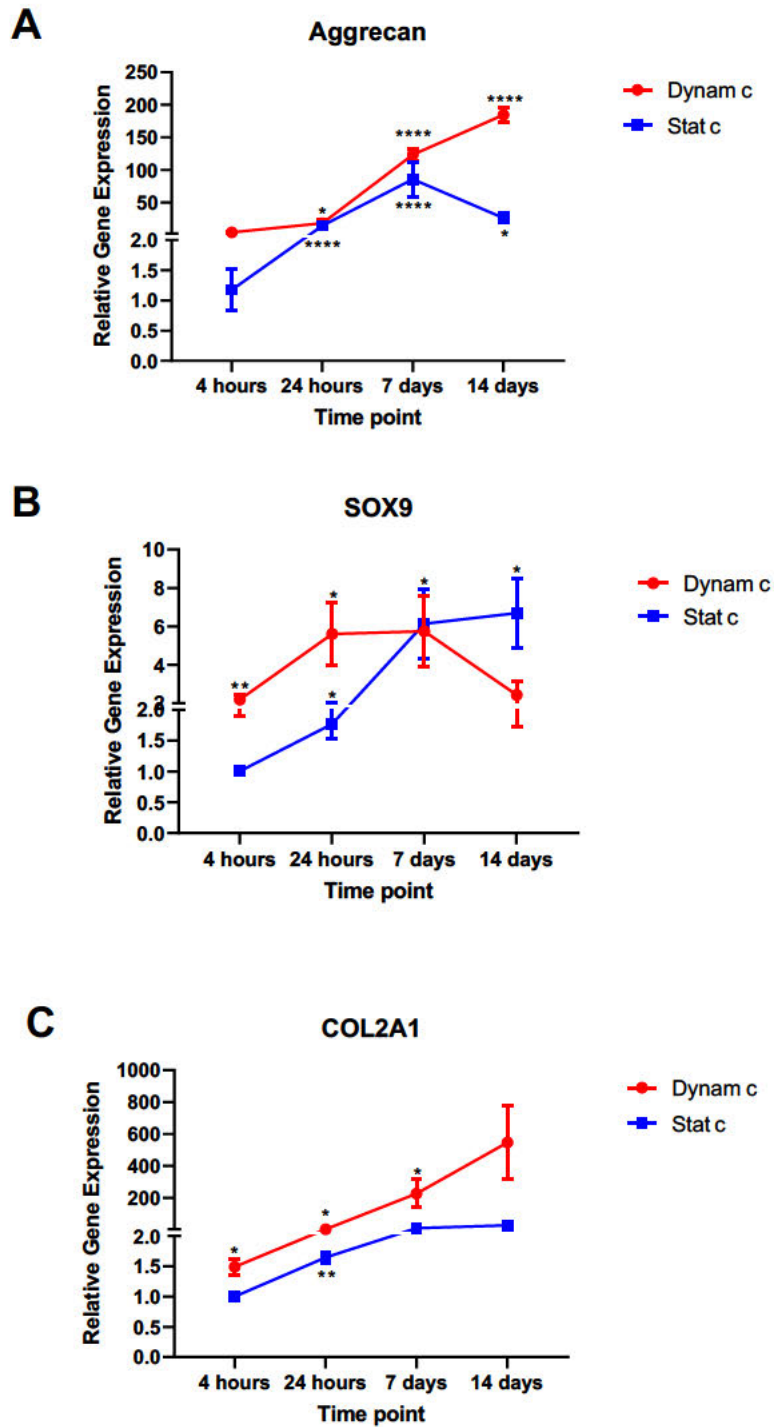
*Figure 4.14: Aggrecan, SOX9 and COL2A1 gene expression over 14-day time period in dynamic and static culture conditions (n=6 per condition and time point). Values of the mean gene expression of the chondrogenic gene markers A) Aggrecan, B) SOX9, C) COL2A1 are expressed relative to static conditions at 4 hours (as control) with standard error. Pairwise comparisons of each condition relative to the 4-hour static time point are displayed using an unpaired t-test. \*=p<0.05; \*\*=p<0.01; \*\*\*=p<0.001; \*\*\*\*=p<0.0001.*

With regard to the production of extracellular matrix (Figure 4.15), there were no significant differences in the quantity of glycosaminoglycan produced either within the two culture conditions at 14 days (p=0.8), but significant differences were noted between the static conditions at Day 7 (513.3 µg/ml) and the dynamic conditions at day 7 (639.7 µg/ml, p=0.04) and day 14 (661.9 µg/ml, p=0.01).
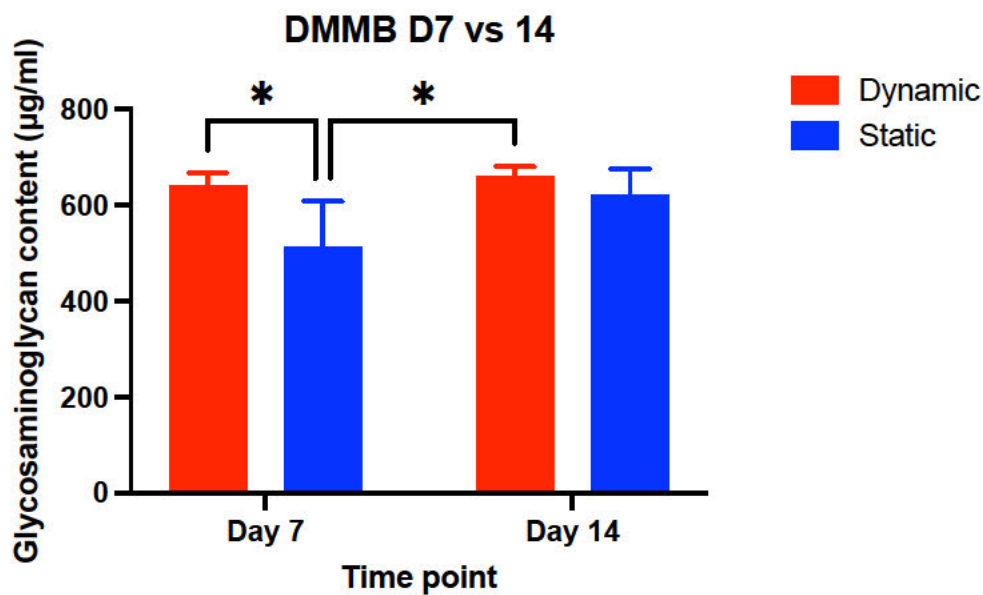


Figure 4.15: DMMB Assay comparing mean GAG content of static and dynamic culture conditions at day 7 and day 14 of culture. Mean values at each time point are presented with standard deviation and pairwise comparisons from a 2-way ANOVA (n=4). *=p<0.05

Whilst differences between the dynamic and static conditions are noted at the level of gene expression, this has manifested in differences in protein expression at Day 7 and between Day 14 dynamic and Day 7 static conditions. This reinforces the fact that one of the mechanical stimuli in the dynamic culture conditions detected in Figure 4.13 may have contributed to enhanced chondrogenesis.

226

## 4.4 Discussion

### 4.4.1 Nanocellulose improves printability of bioinks

2.5% alginate was deemed unsuitable for standard extrusion based bioprinting as used in this study owing to poor post-printing shape fidelity and high viscosity, mirroring the findings of previous assessments of alginate printability (Freeman and Kelly, 2017; Jessop *et al.*, 2019; Hazur *et al.*, 2020). A benefit of low viscosity bioinks is the low extrusion pressures needed to facilitate flow through a nozzle (Kyle *et al.*, 2017), which is likely to offer superior cell viability during the printing process owing to lower amounts of shear stress exerted upon the cells (Axpe and Oyen, 2016). Previous work by Jessop *et al*, demonstrated that whilst 2.5% (w/v) alginate demonstrates almost Newtonian-type fluid behaviour, there was limited shear thinning at 5% (w/v) and above, with all alginate bioinks demonstrating a dominance of viscosity (G") over elasticity (G') (Jessop *et al.*, 2019). In this study, extrusion pressures as low as 1-2 kPa were sufficient to enable the flow of 2.5% alginate through a 22 G printer nozzle. The caveat to low viscosity inks is their tendency to have inadequate tensile strength to hold their shapes after printing (Freeman and Kelly, 2017), which was indeed consistent with the alginate hydrogel used in this study, in which the surface tension of the plastic petri dish into which they were printed appeared to exert more of an influence over the shape geometry than the printing process itself. All attempts to print grids, rings and antihelical structures were unsuccessful and unsuitable for further analysis. However, when blended with nanocellulose, the printability of 2.5% alginate was found to be markedly improved, consistent with previous studies of nanocellulose-alginate printability assessments (Müller *et al.*, 2017; Jessop *et al.*, 2019). All nanocellulose subtypes: NCC, NCF and NCB demonstrated satisfactory post-printing shape fidelity as demonstrated by successful prints for lines, grids, rings and antihelices. Expectedly, the extrusion pressure to enable extrusion bioprinting was higher than pure alginate hydrogels, with a range of 5-12 kPa needed to extrude nanocellulose-alginate composite bioinks. This mirrors the rheological properties of nanocellulose-alginate bioinks, which demonstrate shear thinning, non-Newtonian type viscoelastic behaviour in contrast to pure alginate bioinks (Jessop *et al.*, 2019). In particular, it was suggested that the nanocellulose fibrils and blend variants demonstrated superior printability owing

to higher viscosity than nanocellulose crystals. Indeed, the fibrils and blend nanocelluloses performed more consistently in every printability study tested in this chapter than NCC, with the NCF demonstrating the lowest degree of intra-print variation in the line fidelity and ring assays, whilst the NCB demonstrated measurements closest to the intended construct size in the antihelix and grid assays. Based on previous transmission electron microscopy analysis of the nanocellulose variants, this superior post-printing shape fidelity may reflect the nanostructure of the fibrils, in which a greater degree of entanglement between long nanofibrils was observed compared to the crystalline variants (Kyle *et al.*, 2018b; Jessop *et al.*, 2019).

### 4.4.2 Nanocellulose is more chondrogenic than alginate

Nanocellulose augments printability through enhancing the rheological properties of the material as previously shown (Jessop *et al.*, 2019) and confirmed in this chapter. Furthermore, the structure of nanocellulose has been speculated to mirror collagen fibre bundles in extracellular matrix, promoting a pro-chondrogenic environment (Nguyen *et al.*, 2017). In light of these advantageous structural changes and a closer mimicry of the properties of cartilage extracellular matrix, this thesis hypothesised that chondrocytes should proliferate and produce extracellular matrix to a greater degree in nanocellulose-based inks compared to pure alginate.

Indeed, that was the observation in this study: nanocellulose blend and crystals demonstrated an increase in metabolic activity over the course of 21 days: a phenomenon that was not observed in the nanocellulose fibrils or alginate materials. Furthermore, although extracellular matrix production was observed in all materials over 21 days, the nanocellulose materials demonstrated greater pericellular staining with alcian blue than the alginate material, indicating the cells in these materials were producing and depositing glycosaminoglycans into the material. This finding was supported by the ultimate compressive strength of the material, which was noted to increase significantly in the nanocellulose biomaterials but not the alginate material over 21 days. It is notable that in terms of mechanical properties, alginate was considerably stronger in terms of break

force and ultimate compressive stress than any of the nanocellulose-alginate composite bioinks. This pertains to the fact that the nanocellulose itself is not crosslinked in these bioinks, and that the strength post-printing is derived from the ionic bonds formed between alginate in the presence of divalent cations such as calcium. Naturally in a material that is fully crosslinked, it would be expected that the strength and break force would be higher than one in which only 25% of the material is involved in crosslinking. The maximum compressive strength of the nanocellulose-alginate materials with cells, was in the region of 0.3-0.6 MPa. For reference, this is comparable to previous studies of alginate-hydroxyapatite composite bioinks for bone tissue engineering (0.2-0.9 MPa for 0-40% hydroxyapatite substitution (Presbítero-Espinosa *et al.*, 2021)) and superior to a bacterial nanocellulose with alginate formulation (in an 80:20 nanocellulose:alginate composition) which had a compressive strength of 33 kPa (Markstedt *et al.*, 2015a). The pulp derived nanocellulose-alginate materials developed in this chapter, although superior in strength to Markstedt et al, remain notably less strong than porcine nasoseptal cartilage which has an ultimate compressive stress of 1.4-3.3 MPa (Al Dayeh and Herring, 2014) and markedly lower than costal cartilage (11.4 MPa) and articular cartilage, which has a compressive strength of approximately 36 MPa (Kerin, Wisnom and Adams, 1998; Griffin *et al.*, 2020).

At the level of gene expression, all the materials demonstrated increases in chondrogenic gene expression over the course of 21 days, but the most marked rises were in NCC for all genes, with NCB and NCF also demonstrating significant rises in SOX9 and ACAN1/COL2A1 gene expression respectively. Whilst increases in the relative gene expression of alginate were observed over the 21 days, none of these changes were statistically significant. Previous studies of alginate chondrogenicity have been explored using MSCs and demonstrated significant rises in type 2 collagen, SOX9 and ACAN1 over 21 days relative to cells cultured in 3D pellet or 2D monolayer conditions (Yang *et al.*, 2004; Dashtdar *et al.*, 2016). This demonstrates the advantageous nature of hydrogels for chondrocyte cell culture, attributable to superior mimicry of the *in vivo* environment (Tibbitt and Anseth, 2009). Structurally, nanocellulose may promote a more chondrogenic environment than alginate owing to ECM mimicry, and both

nano- and micro-roughness, which may evoke superior cell adhesion and chondrogenic differentiation (Kyle *et al.*, 2018).

Bacterial nanocellulose-alginate scaffolds have been demonstrated to offer chondrogenicity with human nasoseptal chondrocytes previously, with increases in ACAN1, COL2A1 and COL1A1 gene expression seen over a course of 6 weeks (however this was not a statistically significant rise in this study) (Martínez Ávila *et al.*, 2015). There was not a comparison made with pure alginate in this article however, and indeed none of the previous studies of nanocellulose-alginate include a comparison of chondrogenic gene expression relative to pure alginate (Martínez Ávila *et al.*, 2015, 2016; Möller *et al.*, 2017; Müller *et al.*, 2017).

This comparative gene expression analysis indicates that not only is nanocellulose superior in printability, but it additionally confers a biological advantage of enhanced chondrogenicity over alginate. The main caveat relative to pure alginate is the lower mechanical compressive strength owing to the lower amount of crosslinking in nanocellulose-alginate composite materials.

### 4.4.3 Nanocellulose subtypes each confer different strengths for cartilage tissue bioprinting

Whilst studies of nanocellulose-alginate bioinks for cartilage tissue engineering have been explored previously, there are currently none that have sought to explore how the effects of different structural types of pulp-derived nanocelluloses translate to their chondrogenic potential.

Previous studies have explored the chondrogenic potential of bacterially derived nanocellulose fibrils, which owing to their fibril size of approximately 100nm are speculated to be comparable in size to collagen fibrils (Fink *et al.*, 1997; Bäckdahl *et al.*, 2006). Previous SEM and TEM analysis of the nanocellulose formulations used in this study revealed that the nanocellulose crystals demonstrated a nano-surface of approximately 100 nm, corelating with the size of collagen fibrils whereas the fibrillar structures had a mixture of nano and micro surfaces ranging from 100 nm to 100 μm, which lend themselves more favourably to facilitate cell migration and distribution (Smith *et al.*, 2009; Kyle *et al.*, 2018). Furthermore, the

network of NCC demonstrates compact nanorods packed together with relatively low porosity, in contrast to the fibrils which form complex entanglements in the micro to nano scale, and NCB which contains both porous fibrillar elements and compact nanorods that more closely resemble bacterial nanocellulose (Kyle *et al.*, 2018).

It was interesting to note that the crystals were the formulation evoking the most favourable gene expression profile for chondrogenesis, with significant elevations in COL2A1 and ACAN1 relative to alginate at 4 hours and higher fold-changes than the other formulations. The compact, homogeneous nature of the crystalline subtype may offer a more close structural mimic of the compact and regular arrangement of glyocsaminoglycans such as hyaluronic acid and chondroitin sulphate, whereas the fibrillar arrangement may match the anisotropy of the collagen bundles found in cartilage tissue ECM (Han, Grodzinsky and Ortiz, 2011). This could certainly explain why the NCC and NCF appeared to have high increases in ACAN1 and COL2 expression over 21 days. It might be expected however, that the NCB, containing both the crystalline and fibrillar elements, may therefore even better emulate the structure of cartilage ECM. The NCB did cause the highest fold-change in SOX9 expression at the 7-day time point but this did not otherwise translate to advantageous gene expression profiles. SOX9 is a marker of chondrocyte differentiation, survival and an upregulator of extracellular matrix genes (Lefebvre, Angelozzi and Haseeb, 2019). However, in this study, the rise in SOX9 failed to translate to a subsequent rise in the expression of ACAN1 and COL2A1. An understanding of the full expression profiles of these ECM genes could be hindered by the duration of the experimental period.

### 4.4.4 Orbital shaking improves chondrogenicity in NC-alginate bioinks

The final component of this chapter was an exploration of the role of an orbital shaking system for culturing tissue engineered cartilage. This set up sought to recreate and simplify bioreactors used in a laboratory environment coupled to *in silico* modelling of the degree of shear stress and pressure the cells experience in these conditions. There were significant enhancements in chondrogenic gene

expression achieved through the orbital shaking system, but this effect appeared to be independent of the effects of shear stress and pressure, which were relatively low when modelled through *in silico* computational fluid dynamics. In articular cartilage tissue, intermittent hydrostatic pressures of as high as 10 MPa have been required to evoke increases in cartilage gene expression (SOX9, COL2, ACAN1) (Fahy, Alini and Stoddart, 2018) or shear stresses of 0.1 Pa (approx. 1000-fold greater than the shear stress in this model) (Gemmiti and Guldberg, 2009). As a load bearing cartilage, the effects of compressive loading, hydrostatic pressure and shear on chondrogenic gene expression in articular cartilage have been well explored but this mechanotransducive threshold has not been as extensively explored in the facial cartilages (Takano-Yamamoto *et al.*, 1991). It is unlikely, but not impossible, that pressure gradients of 48 Pa evoked by the orbital shaking system would be sufficient to evoke a mechanotransductive signal, as this is in the region of 200,000-fold lower than that of articular cartilage. A more likely explanation of the enhanced chondrogenesis is attributable to the porosity of the scaffold and the augmented perfusion of media throughout the scaffold. This phenomenon was also observed in a comparison of chondrogenesis in static conditions and dynamic conditions (a perfused bioreactor), where flow rates of 1 µm/s demonstrated significant elevations in DNA content, GAG content and hydroxyproline content compared to static conditions (Pazzano *et al.*, 2000). It is possible therefore that flow speeds of 3 µm/s were sufficient to evoke an elevation in chondrogenesis in this study. Similarly, previously investigated models include the use of a linear "see-saw" plate shaker, which has been shown to promote chondrogenic differentiation of induced pluripotent stem cells with increased toluidine blue staining, cell clustering and augmented expression of chondrogenic genes COL2A1, Aggrecan and SOX9 at frequencies of 0.3-0.5 Hz (Limraksasin *et al.*, 2020). In addition to increasing the delivery of nutrients through enhanced media perfusion, it has been previously reported that fluid flow has a key role in chondrocyte biosynthesis (Zhao *et al.*, 2020), with postulated mechanisms being attributed to mechanosensitivity sensed by PIEZO calcium channel receptors (Lee *et al.*, 2014), the primary cilium (Yuan and Yang, 2015) and integrins (Zhang *et al.*, 2008). The impact of orbital shaking on chondrogenesis is therefore potentially

multifactorial and may be attributable to flow-mediated mechanotransductive signals that warrant further investigation in nasoseptal cartilage. There is potential to exploit these mechanotransductive pathways for the purposes of tissue engineering and bioreactor design.

### 4.4.5  Summary

This chapter highlights the potential of nanocellulose-based bioinks for 3D bioprinting cartilage. There are strengths to each of the nanocellulose subtypes in terms of printability and biological behaviours, but the blend and crystal variants appear to offer the best balance of printability, chondrogenicity and biocompatibility. The inability of the nanocelluloses used in this current form to be crosslinked have a significantly detrimental impact on mechanical properties compared to pure alginate bioinks and the exploration of crosslinkable nanocelluloses warrants further investigation. Finally, the benefit of enhancing the culture environment for bioengineered nasoseptal cartilage in porous hydrogels is highlighted, indicating the potential benefit of perfusion bioreactor systems, which may be reproduced in a simplified format using controlled orbital shaking integrated into standard tissue culture.

# Chapter 5: Optimisation of Nanocellulose-hyaluronic Acid Bioinks for 3D Bioprinting Cartilage

# Chapter 5: Optimisation of nanocellulose-hyaluronic acid bioinks for 3D bioprinting cartilage

## 5.1 Introduction

### 5.1.1  Background

Hyaluronic acid (HA) is a naturally occurring, anionic and non-sulphated glycosaminoglycan, and one of the main constituents of extracellular matrix. It has a particularly prominent role in cartilage, especially articular cartilage, owing to its biomechanical and physicochemical properties (Gupta *et al.*, 2019). In cartilage, HA conjugates non-covalently with aggrecan: the primary proteoglycan of cartilage tissue through link proteins (Kiani *et al.*, 2002). Specifically, HA possesses high viscoelasticity and hydrophilia, rendering it an ideal lubricant, stabiliser and shock-absorber in joint surfaces (Gupta *et al.*, 2019). At the cellular level, HA confers key roles in cell proliferation, migration, differentiation and tissue morphogenesis (Fallacara *et al.*, 2018). Agglomerations of HA and aggrecan are believed not only to confer many of the structural properties of cartilage, but also mediate chondrocyte-chondrocyte interactions and cell-matrix interactions (Kiani *et al.*, 2002).

Many of these properties render hyaluronic acid an excellent biomaterial for use in biomedical applications, and indeed HA has been successfully translated into clinical uses such as in wound dressings, cosmetics and joint injections (Cooper *et al.*, 2017; Fagien *et al.*, 2019; Graça *et al.*, 2020). In addition to its structural properties and biocompatibility, there are further features of HA that render it a promising material for 3D printing applications.

Specifically, the ability of HA side chains to be structurally modified enables HA hydrogels to be made amenable to crosslinking. Hydroxyl and carboxyl groups are in abundance on HA disaccharide units, and are the most common sites of modification (Khunmanee, Jeong and Park, 2017). Broadly, the modifications enable crosslinking of hyaluronic acid gels by chemical processes (such as Schiff-base crosslinking), physical (such as thermal or UV-mediated crosslinking) or enzymatic processes (Yu *et al.*, 2013; Wu *et al.*, 2016). Two reported approaches commonly used for bioprinting cells within HA is the methacrylation of HA, which enables a covalent crosslinking mediated through exposure to UV

light (Si *et al.*, 2019); and a horseradish peroxidase-mediated covalent oxidation reaction enabled through the introduction of Tyramine residues (Abu-Hakmeh *et al.*, 2016).

Unfortunately, both approaches have the potential for cellular genotoxicity and cytotoxicity when used to crosslink structures post-3D bioprinting, and light intensities of up to 1390 mW/cm$^2$ have been required to evoke successful UV mediated crosslinking (Clark *et al.*, 2019). The advantage of a hydrogen peroxide-mediated crosslinking approach is that the strength of the crosslinking agent could theoretically be diluted to determine a concentration at which the desired structural crosslinking can occur but at a safe, biocompatible dose. Biocompatible doses of hydrogen peroxide have been explored previously for cartilage, and have been deemed to fall in the micromolar concentration range, with evidence of cell damage markers reported at doses as low as 50 µM-100 µM (Asada *et al.*, 2001; Martin *et al.*, 2005; Khan *et al.*, 2008). In other cell lines, the genotoxic effect of hydrogen peroxide is seen at concentrations as low as 7.28 µM, emphasising the importance of discovering a 'tolerance threshold' (Seager *et al.*, 2012).

Other advantages of hyaluronic acid as a bioink are its rheological and structural properties as both a hydrogel and solid. The use of HA as a dermal filler has yielded interest from industry owing to its rheological properties and ease of injection (Fagien *et al.*, 2019). This translates well to extrusion based bioprinting, where shear thinning properties and viscoelasticity are mutually beneficial to both disciplines. Specifically, HA hydrogels have been shown to demonstrate shear thinning properties, and thus suitability for extrusion, but a dominance of viscosity over elasticity owing to its high water content (Petta *et al.*, 2020). This translates to poor shape retention post-printing. This shortcoming has been addressed by structural modification of the HA hydrogels or through blending HA with natural or synthetic polymers to augment its printability (Poldervaart *et al.*, 2017; Petta *et al.*, 2018), with previous candidates including methacrylated gelatin (Duan *et al.*, 2014) and polycaprolactone (Hauptstein *et al.*, 2020).

In Chapter 4, the addition of pulp-derived nanocellulose augmented the printability of alginate in addition to augmenting its chondrogenicity for 3D

bioprinting cartilage. As such, nanocellulose may confer these same benefits to hyaluronic acid bioinks. Gatenholm has considered the combination of hyaluronic acid and pulp-derived nanofibrillated cellulose for 3D bioprinting adipose tissue (70-80% nanocellulose and 20-30% hyaluronic acid) and for bioprinting iPSCs in the hope of chondrogenic differentiation (5% hyaluronic acid and 95% nanocellulose) (Henriksson, Gatenholm and Hägg, 2017; Nguyen *et al.*, 2017). As of yet, no literature reports 3D bioprinting nanocellulose-hyaluronic acid composite bioinks with human chondrocytes.

### 5.1.2  Aims

In light of the sparse evidence to date, validation of a nanocellulose-HA bioink with human chondrocytes is warranted. This specifically needs to address printability characteristics, biocompatibility, chondrogenicity and mechanical suitability for 3D bioprinting cartilage.

To determine the suitability of a composite nanocellulose-hyaluronic acid (NCHA) bioink for 3D bioprinting cartilage, the following objectives will be addressed:

- Producing a range of NCHA composite bioinks ranging from pure HA (100HA) to 20% HA:80% NC (20HA) capable of crosslinking through enzymatic (hydrogen peroxide – horseradish peroxidase) mediated covalent bonding
- Determining the printability characteristics of the composite bioinks and their suitability for extrusion based bioprinting
- Elucidating a safe, biocompatible dose of hydrogen peroxide for crosslinking HA-based bioinks containing human nasoseptal chondrocytes and determine their effect on cell viability, growth and metabolism
- Ensuring that the biocompatible doses of hydrogen peroxide are also suitable mechanically and structurally for crosslinking HA based bioinks
- Determine the chondrogenic potential of different NCHA formulations at the level of gene expression, ECM production and structural integrity

### 5.2 Experimental Protocols

### 5.2.1 Rheological analysis of uncrosslinked biomaterials

Rheological analysis of the materials in their uncrosslinked, hydrogel states was performed in collaboration with Prof Karl Hawkins and Bethan Morgan, College of Engineering, Swansea University. Specifically, parameters relevant to 3D printing such as viscosity, shear thinning, and viscoelasticity were interrogated using an AR-G2 Controlled Stress Rheometer (TA instruments, New Castle, DE, USA). Samples of each hydrogel (100HA, 80HA, 60HA, 40HA and 20HA) were mixed prior to loading 700 µl onto the centre of the lower plate using a 1 ml syringe as described in Section 2.5.6. The rheometer was programmed to record the storage modulus, loss modulus and complex modulus over a frequency range of 0.1 to 10 Hz. The loss tangent (tanδ), is tangent of the phase angle between stress and strain and was calculated as a ratio of loss and storage modulus (tanδ = G"/G'), with values greater than 1 indicating dominance of the viscous component of the complex modulus, whereas values less than 1 indicate a dominance of elasticity. Shear thinning was assessed through logarithmically increasing shear over a range of 0.1 to 100 s$^{1}$ over two minutes, plotting the viscosity of the ink as a product of increasing shear rates.

### 5.2.2 Biocompatibility of hydrogen peroxide crosslinking agent with human nasoseptal chondrocytes

Hydrogen peroxide solutions were produced in PBS as described in Section 2.5.5.4. Specifically, solutions of hydrogen peroxide of 5, 10, 15, 20 and 25 µM were produced through dilution of a 1% stock solution in PBS and compared to positive and negative control solutions of 0.39% hydrogen peroxide solution (115 mM) and PBS alone respectively.

50,000 human nasoseptal chondrocytes were seeded in to each well of a 6 well plate and allowed to adhere for 24 hours. The cells were then exposed to each dose of hydrogen peroxide crosslinker, along with positive and negative controls, each preheated to 37°C, and left for 5 minutes in culture conditions. After 5 minutes, the peroxide solution was discarded and the wells washed gently with PBS three times.

The plates were then processed for live dead assay (Section 2.12.1), Lactate dehydrogenase assays (Section 2.12.2) and alamarBlue (Section 2.7.1) assays.

### 5.2.2.1    Live dead assay

Live dead assays were performed using a cell viability assay kit (Thermofisher Scientific, MA, USA) on each well through the addition of 1 ml of a mixture containing 1:1000 Calcein-AM and 1:500 Ethidium homodimer-1. The solution was protected from light and left for 45 minutes in culture conditions. The live cells were visualised using fluorescence microscopy to detect cells stained with calcein-AM and dead cells with Ethidium homodimer-1 as described in Section 2.12.1. Representative images were acquired from three points taken from three biological repeats at 10x magnification.

### 5.2.2.2    LDH Assay

For LDH assay processing, three media samples were taken immediately after exposure to the hydrogen peroxide reagents from three biological triplicates, after which point, media was reapplied to the wells and left for four hours. One well treated with PBS only was spiked with cell lysis buffer and used as a positive control for cytotoxicity. 50 µl samples from each well were acquired and transferred to a 96 well plate, along with reaction media for 30 minutes. The reaction was terminated at 30 minutes using stop solution and the plates were read immediately at 490 nm and 680 nm as described in Section 2.12.2. The % cytotoxicity was determined using the lysed cells as a positive control, assumed to have 100% lysis, using Equation 11:

$$\% \text{ cytotoxicity} = \frac{\text{Treated LDH activity} - \text{spontaneous LDH activity (cells only)}}{\text{Maximum LDH activity (lysed cells)} - \text{spontaneous LDH activity}} \times 100$$

### 5.2.2.3    alamarBlue assay

The alamarBlue dye (ThermoFisher Scientific, MA, USA) was used to provide an indication of cell proliferation based on metabolism (reduction) of the alamarBlue

reagent. A 10% (v/v) alamarBlue solution was made by adding the solution to chondromedia, of which 500 µl was then added to each well containing cells for 4 hours. The colorimetric change observed was quantified using a plate reader, with triplicates 100 µl samples taken from each well, along with media only controls (no cells), taken after 4 hours and read at 570 nm (reduced form) and 600 nm (oxidised form) wavelengths. A minimum of two separate wells per condition were sampled using three biological repeats. The two wavelength readings for each well were used to calculate the percentage of the alamarBlue solution that had reacted to its reduced form as a marker of cell metabolic activity, calculated as per Section 2.7.1.

### 5.2.2.4 iCELLigence cytotoxicity assay

The iCELLigence apparatus was used to assess for changes in cell adherence and growth following exposure to the different doses of hydrogen peroxide. As described in Section 2.7.2.1, 17,500 human nasoseptal chondrocytes were seeded into the wells of an iCELLigence E8 plate and allowed to adhere and proliferate in standard culture conditions. Two wells were not seeded with cells and instead used as media only controls. Adherence and baseline proliferation were measured over 18 hours, with measurements taken once per minute for the first two hours and then hourly for the remaining 16 hours. At the 18 hour time window, the impedance readings were paused, the media was removed from the cells, and 200 µl of warm PBS or warm hydrogen peroxide was added to each well and left at room temperature for five minutes. The hydrogen peroxide was thereafter discarded and the wells were washed three times with warm PBS, after which fresh 500 µl chondromedia was added to the wells. The experiment was resumed, with measurements taken every minute for two hours to accurately capture the immediate cytotoxic window, and then hourly until a total experimental time of 70 hours was attained.

The change in cellular impedance after exposure to the peroxide was used to calculate a percentage of cell death corrected to the change observed in the PBS control. Growth curves after the addition of peroxide were also monitored and

compared between doses. Technical duplicates were performed on biological triplicates (total n=6 per condition).

### 5.2.3 Mechanical and structural characterisation of crosslinked biomaterials

To ascertain the differences between high (115 mM) and low dose (5 µM) hydrogen peroxide crosslinking from a structural perspective, crosslinked 20HA was tested for Young's modulus, surface topography, porosity and swelling. The porosity and swelling assays were also used to compare the NCHA composite biomaterials, along with biomechanical stress testing and digital measurements of construct size post-crosslinking using digital callipers (Fisher Scientific, MA, USA).

### 5.2.3.1 Atomic force microscopy

AFM was used to characterise the Young's modulus and surface topography of 100 µl discs of 20HA NCHA crosslinked using 100 µl of 5 µM (low dose) or 115 mM (high dose) $H_2O_2$.

The discs were affixed to a glass coverslip using a single droplet of mounting medium (VWR, PA, USA) as described in Section 2.11.1. The materials were characterised using a Bruker Bioscope Catalyst (Bruker, MA, USA) and MikroMasch CSC37 cantilevers (Tallinn, Estonia) as described in Section 2.11.1, applying a maximum force of 4 nN. The elastic (Young's) modulus of each material was calculated using Nanoscope analysis software (v1.50, Bruker, MA, USA) taking at least 50 points per sample (from technical duplicates). Sample topography was captured using PeakForce Quantitative NanoMechanics mode (Bruker, MA, USA).

### 5.2.3.2 Porosity Assay

100 µl discs of 20HA were produced and crosslinked using 100 µl of either high dose (115 mM) or low dose (5 µM) hydrogen peroxide solution. Six repeats of each condition were produced. The discs were transferred to 48 well plates and

left for 24 hours in 1 ml PBS at room temperature. The discs were removed and excess PBS blotted away using tissue paper. Each disc was weighed and the weight recorded. The discs were returned to the 48 well plate and transferred to a non-humid 37°C chamber for 72 hours. The discs were weighed again at the end of this period and recorded. Porosity was calculated using Equation 9:

$$Porosity = \frac{m_{wet} - m_{dry}}{\rho_{PBS} \; x \; V_{pellet}}$$

Where $\rho$ = is the density of PBS at 20°C (1.0723 g/cm$^3$), m = mass and v = volume

This approach was also used to test the different NCHA blend combinations using 5 µM hydrogen peroxide solution as described above, for a total of six replicates.


### 5.2.3.3 Swelling Assay

100 µl discs of 20HA were produced and crosslinked using 100 µl of either high dose (115 mM) or low dose (5 µM) hydrogen peroxide solution. Six repeats of each condition were produced. The discs were transferred to a 48 well plates with 1 ml PBS added to each well. The 48 well plate was transferred to an incubator set at 37°C and 5% $CO_2$ for 24 hours. Fluid excess was removed through blotting with tissue paper and the discs were weighed to attain the wet weight ($m_{wet}$). The PBS was removed from all wells. The 48 well plate was transferred to a no humidity chamber set at 37°C for 72 hours until dry. The discs were weighed again and this was recorded as the $m_{dry}$. The swelling was calculated using Equation 8:

$$Swelling \; \% = \frac{m_{wet} - m_{dry}}{m_{dry}} \; x \; 100$$

This approach was also used to test the different NCHA blend combinations using 5 µM hydrogen peroxide solution as described above using six repeats.


### 5.2.3.4 Changes in construct diameter post-crosslinking

Semispheres of 100 µl of each NCHA composite bioink were measured across three different diameters pre-and post crosslinking using digital callipers. The difference in diameter post-crosslinking was expressed as a percentage change

in diameter for each biomaterial. This was performed in triplicate for each material.

### 5.2.3.5 Biomechanical compression testing

200 µl cylindrical disks of each biomaterial were produced using the 3D printed mould described in Section 2.11.2 to produce equal cylinders of 6mm diameter and 7mm length. The materials were crosslinked within the moulds using 5 µM $H_2O_2$ for five minutes and transferred to the $1^{ST}$ Mechanical Compression Device (Tinius Olsen, Redhill, UK) in PBS for compression testing. Each material was blotted dry with tissue paper and compressed using a 25 N load cell as outlined in Section 2.11.2, to determine the break distance, break force and ultimate compressive strength. These values were used to calculate the ultimate mechanical stress, break stress and strain to failure of each material. Materials were examined without cells (in technical triplicates), and then after culture with cells for 21 days (in technical triplicates) to determine whether the cells and the matrix they produced had any significant effect on the mechanical properties of the material over this time course.

### 5.2.4 Chondrogenicity analysis of NC-HA composite bioinks

Chondrogenicity of each bioink was determined at the level of gene expression through RT-qPCR, and at the level of extracellular matrix production using quantitative hydroxyproline and dimethylmethylene blue (DMMB) assays and through histological staining of glycosaminoglycans with alcian blue, toluidine blue and Safranin O.

### 5.2.4.1 Chondrogenic gene expression analysis

Triplicates of each biomaterial were mixed with 500 µl TRIzol (Invitrogen, Thermofisher) and subsequently degraded with a TissueRuptor II probe for 30 seconds. The lysate was processed using Qiagen QIAshredder and RNeasy Mini Extraction kits (Qiagen, Germany; as described in Section 2.8.2) to yield RNA for reverse transcription. The RNA was quantified and assessed for purity using a Nanodrop Spectrophotometer. The concentrations of RNA in each sample were

diluted with ultrapure nuclease free water across repeats to yield 11 µl samples each containing 450 ng RNA. The RNA was converted to cDNA through reverse transcription as described in Section 2.8.4, and quantified for the expression of COL2A1, SOX9 and ACAN1 relative to housekeeping gene expression (RPL13A and TBP) as per Section 2.8.7. Each material was harvested for RNA extraction and PCR analysis at 4 hours, 24 hours, 7 days, 14 days and 21 days of culture using 3 biological repeats (HN48, HN49, HN50). All relative gene expression values were expressed as fold-changes using the $\Delta\Delta Ct$ method compared to a control value (Section 2.8.8): in this case 100HA at the 4-hour time point. The 21-day time point was repeated for each gene using a total of 6 biological repeats to further elucidate the differences between biomaterials.

### 5.2.4.2 Hydroxyproline assay

10 mg of each cell-laden material was weighed and added to a PTFE-lined screw cap microcentrifugation tube with 100 µl of ultrapure water. The mixture was homogenised and hydrolysed using 12 M hydrochloric acid at 120°C for 3 hours as described in Section 2.9.4. The hydrolysed lysate was mixed and centrifuged at 10,000 g for 3 minutes. 10 µl of the supernatant was transferred to a 96 well plate in triplicate along with one spiked sample and a set of hydroxyproline standards and evaporated at 60°C. 100 µl of Chloramine T and oxidation buffer was added to each well and left for 5 minutes, with a further 100 µl mixture of DMAB reagent diluted in perchloric acid and isopropanol added thereafter for 90 minutes at 60°C. The plates were then read at 560 nm absorbance using a plate reader (POLARstar Omega spectrophotometer, BMG LABTECH, Ortenberg, Germany).

### 5.2.4.3 Dimethylmethylene blue assay

The DMMB assay was used to quantify GAG content in each material at 7 days and 21 days of culture (technical and biological triplicates, n=9). The cell-laden biomaterial semispheres of each bioink were first digested using 300 µl of a 10 mg/ml solution of type I hyaluronidase at 37°C for 1 hour. The remaining tissue was lysed according to Section 2.9.1 to yield protein isolates for GAG

quantification. Isolates were diluted 1 in 50 with distilled water and added to the wells of a 96 well plate in triplicate with 200 µl DMMB reagent. The plates were read immediately at 525 nm compared to a series of chondroitin standards ranging from 0 to 50 µg/ml as outlined in Section 2.9.3.

### 5.2.4.4 Histological analysis of NCHA bioinks

To determine the arrangement of extracellular matrix relative to the cells within the biomaterials, histological analysis was performed. Cell-laden biomaterial semispheres were immersed in 4% paraformaldehyde solution for 30 minutes and then washed three times in PBS (Section 2.10.1). The constructs were then immersed in 1% (w/v) Alcian Blue stain as described in Section 2.10.3.2 for 30 minutes and washed sequentially with hydrochloric acid and distilled water until no further stain was released. Alternatively, constructs were immersed in 0.1% toluidine blue solution as described in Section 2.10.3.3 for 10 minutes and washed until clear. Constructs were also stained with Safranin O as per Section 2.10.3.4 using first Fast green for 20 minutes, washed with acetic acid and stained thereafter with Safranin O stain for 40 minutes. The semispheres were viewed under brightfield microscopy at 4, 10 and 20x magnification with images taken throughout the construct (in x, y and z axes) to ensure the images captured were representative of the whole material (as per Section 2.10.3.5).

### 5.2.5 Statistical analysis

Data sets were assessed for normality (Gaussian distribution) visually and where needed using an Anderson-Darling test. Statistical analysis were thereafter selected accordingly. All data presented is the mean value of technical +/- biological replicates which is presented graphically with error bars depicting standard deviation unless otherwise stated.

For statistical comparisons between two dependent variables, either a t-test (+/- Welch's correction; where standard deviations were not equal) or Mann Whitney test (where data was not normally distributed) was used. In this chapter, the following data sets were analysed using unpaired, two tailed t-tests: comparing

the high and low dose crosslinking agent effects on porosity and swelling (Figure 5.12, Figure 5.13) and where PCR analysis is expressed relative to a control value using the $\Delta\Delta$Ct method (Figure 5.18, Figure 5.19, Figure 5.20). Whereas Mann Whitney tests were used for the Elastic Modulus displayed in Figure 5.10.

For statistically analysing multiple dependent (>2) variables, typically a one-way ANOVA (Brown-Forsythe/Welch ANOVA for unequal SD) was used with a Tukey's post hoc test for multiple comparisons. In this chapter this analysis was to determine significance when comparing mechanical and structural characteristics between the five formulations of NCHA bioink (Figure 5.14, Figure 5.15, Figure 5.16, Figure 5.17), when looking into the cytotoxic effects of increasing doses of crosslinking agent (Figure 5.6, Figure 5.8) and when assessing ECM production in the five bioink formulations (Figure 5.21, Figure 5.22). Where data was acquired across multiple timepoints, such as the iCELLIgence growth curves, a repeated measures ANOVA was performed (Figure 5.7).

A 2-way ANOVA was used when multiple dependent variables (>2) were used across two separate series (such as different time points), with a Tukey's post hoc test. In this chapter, this analysis was used for the following data sets: immediate and delayed LDH assays (Figure 5.5) and biomechanical testing of the different NCHA formulations with or without cells (Figure 5.23, Figure 5.24, Figure 5.25).

## 5.3    Results

In this section, the feasibility of a composite nanocellulose-HA bioink for cartilage bioprinting is explored. Specifically, the printability characteristics are assessed for bioinks of varying proportions of HA and NC, after which the structural and mechanical characteristics are explored. Biologically, the chondrogenic potential of these composite inks is assessed at the level of gene expression and ECM production. Biocompatibility of the crosslinking agent is also examined in the context of the bioink.

### 5.3.1    Rheological analysis of NCHA bioinks

Rheological analysis provides important information about the behaviour of bioinks in their hydrogel states, which can be extrapolated to predicting their suitability for extrusion based bioprinting. Shear rate ramps were performed to determine the flow properties of the different NCHA formulations by measuring the viscosity of the inks as a function of increasing shear rate. All of the material blends demonstrated shear thinning behaviour: a reduction in viscosity with an increase in shear stress, a pseudoplastic behaviour which is characteristic of non-Newtonian fluids such as hydrogels (Figure 5.1).
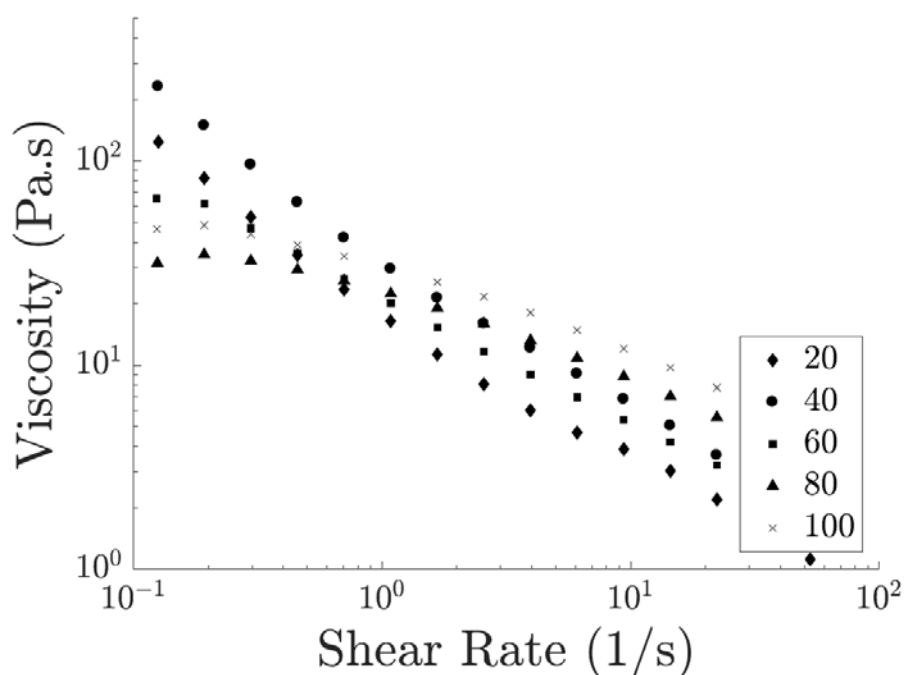
*Figure 5.1: Shear thinning of NCHA composite bioinks. Viscosity in Pa.s is plotted against shear rate for each NCHA bioinks in which 20 =20HA, 40=40HA, 60=60HA, 80=80HA and 100=100HA. Each point represents a mean value of at least 3 separate readings and shear thinning (a reduction in viscosity with increasing shear) can be observed in all bioinks.*

Each bioink was then assessed for their storage (or elastic modulus, G'), loss (or viscous modulus, G") modulus and complex modulus (G*) in the non-crosslinked hydrogel formulations (Figure 5.2).

Of note, the bioinks with a dominance of nanocellulose in their composition (20HA, 40HA) had higher G' than G" moduli, and as a result a higher G* modulus. Furthermore, the loss tangent of the 20HA and 40HA bioinks was consistently less than 1 (Figure 5.3), indicating a dominance of viscoelastic solid type behaviour. This indicates the material should recover when subjected to forces up to the material's yield point. There were no statistically significant differences noted in the storage modulus (p=0.4), complex modulus (p=0.4) or loss tangent (p=0.6) between the 20HA and 40HA materials, but the loss modulus of 40HA was significantly higher than 20HA (p=0.0003).

Conversely, the G' and G" were more closely aligned in 60HA (Figure 5.2), with an overall minor dominance of G' and a loss tangent of less than 1 at the frequencies tested (Figure 5.3), meaning a dominance of elastic over viscous type behaviour was also observed in this bioink. The loss tangent was significantly higher than 20HA (p=0.0006) but not 40HA (p=0.3) meaning a significantly greater degree of viscosity and lesser elasticity was observed compared to 20HA but not 40HA. The complex, storage and loss moduli were significantly different between both 20HA and 40HA with 60HA however.

The inverse of these phenomena was observed in 80HA and 100HA, where a higher G" than G' was observed, and a loss tangent greater than 1 was seen at the majority of the frequencies tested, indicating a prevalence of viscous, liquid-type behaviour. This makes the bioinks more prone to deformation owing to a lack of elasticity relative to viscosity, with implications for bioprinting. The loss tangent of 80HA and 100HA were significantly higher than both 20HA and 40HA (p<0.0001). As such, whilst all ink formulations are printable, 20HA and 40HA are the most suitable for extrusion bioprinting.
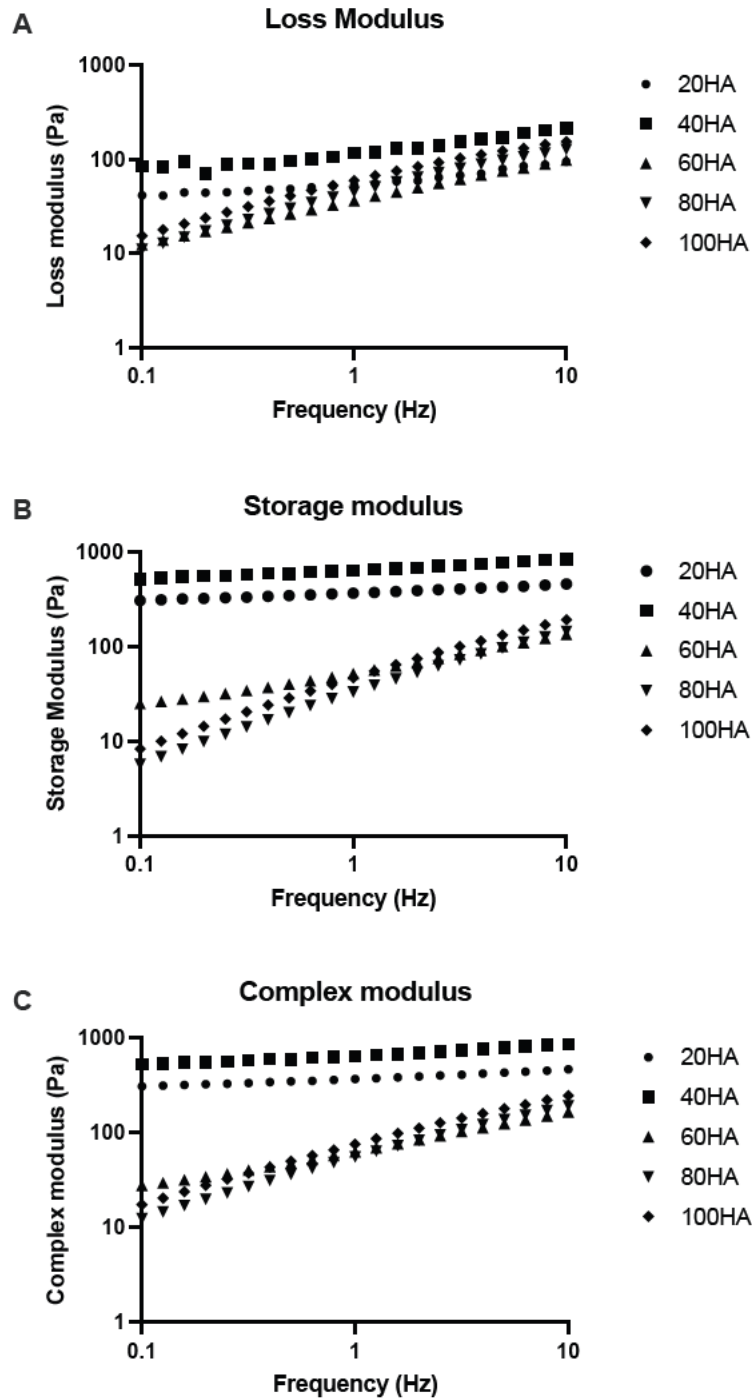
*Figure 5.2: Rheological analysis of NCHA composite bioinks and 100HA. A) Loss modulus (G") is plotted on logarithmic axes as a product of frequency in which a dichotomy between 20-40HA and 60-100HA is highlighted. B) Storage modulus (G') is plotted logarithmically against frequency showing minimal change in G' across the frequency range studies in 20HA and 40HA. C) Complex modulus (G\*) for each NCHA bioink formulation is plotted logarithmically as a function of increasing frequency mirroring the findings of A) and B) in which 20HA and 40HA show minimal change in G\* across the frequency range used. Each data point represents a mean of 3 separate readings.*
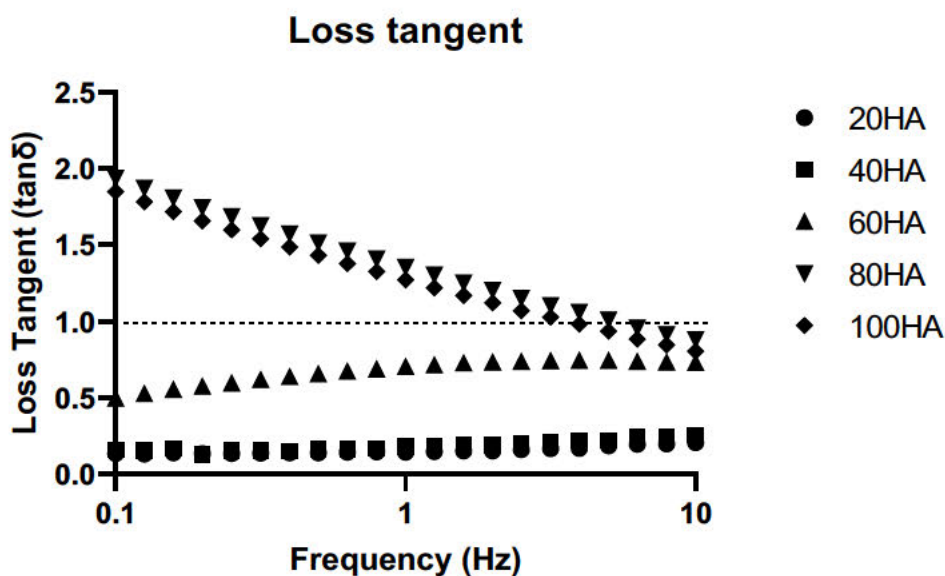
## Loss tangent



*Figure 5.3: Loss Tangent (tanδ) for each NCHA bioink, plotted against increasing frequency. Values below 1 (delineated using the dotted line) indicate a dominance of elastic behaviour, whilst values greater than 1 indicate a dominance of viscosity. Each point represents a mean of three repeat values.*

### 5.3.2 Optimisation of Crosslinking of NCHA bioinks

Post-printing, effective crosslinking must be achievable to allow the shape to hold in the intended design without significant detriment to cells. The Tyramine substitution on the HA chains renders the HA hydrogels capable of covalent crosslinking in the presence of hydrogen peroxide and horseradish peroxidase enzymes. The manufacturer recommendation is that 0.39% hydrogen peroxide is used for optimum crosslinking, which is stated as occurring within a matter of minutes. Higher doses of hydrogen peroxide are likely to have adverse effects on cell viability and potentially induce genotoxicity, as such a range of doses were used including 0 μM, 5 μM, 10 μM, 15 μM, 20 μM and 25 μM, in addition to the recommended dose of 0.39% (w/v) $H_2O_2$ (115 mM).

### 5.3.2.1     Biocompatibility of hydrogen peroxide crosslinking agent

CDCs displayed good immediate viability at doses of 5-25 μM hydrogen peroxide but complete cell death was observed at 115 mM (0.39%) hydrogen peroxide doses (Figure 5.4) using the live:dead assay.

251

To determine the metabolic and proliferative effects of hydrogen peroxide exposure on the cells, further analysis was performed using the LDH cytotoxicity assay and alamarBlue assay, to determine cell death (immediately and at 4 hours) and cellular metabolic activity over a 4-hour period after exposure, respectively.
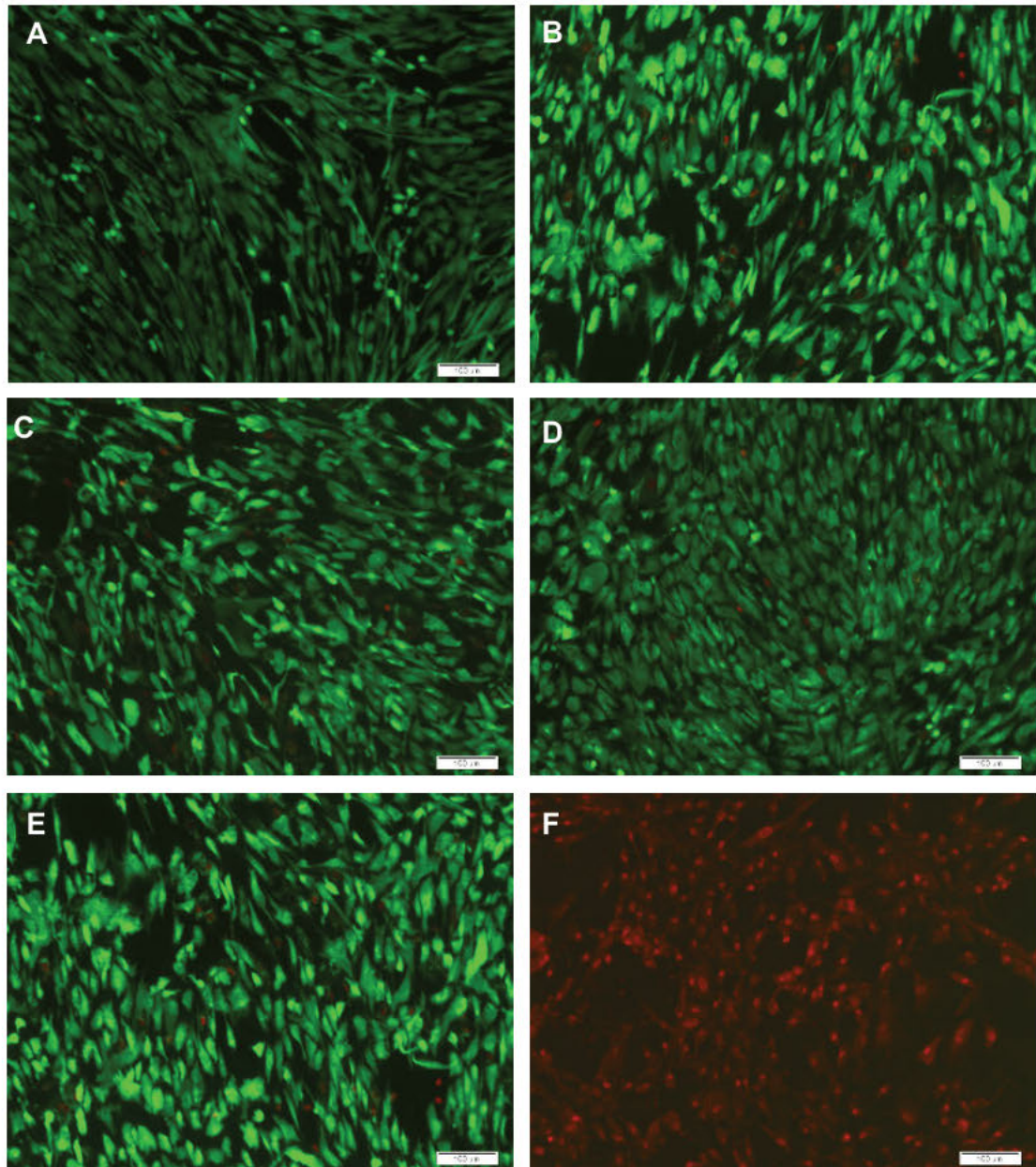


*Figure 5.4: Live-Dead Assay of CDCs exposed to different doses of $H_2O_2$. Live cells are coloured green, dead cells are coloured red. Representative images of 3 repeats taken at 10x magnification are displayed wiuth scale bars depciting 100 µm. A)Live dead assay of CDCs exposed to PBS only (0 µM), universal cell survival is observed. CDCs exposed to 5 µM (B), 10 µM (C), 20 µM (D) and 25 µM (E) $H_2O_2$, demonstrating predominant cell survival but a small number of dead cells. (F) CDCs exposed to 115 mM $H_2O_2$ display universal cell death.*

Statistically significant differences in cytotoxicity were observed between the 115 mM doses and 0 µM (PBS control) immediately (p<0.0001) and at 4 hours after exposure (p<0.0001) and at 20 µM (7.3% immediately; 11.9% at 4 hours; p=0.03). There were no significant differences observed with any other doses of peroxide used (Figure 5.5). Furthermore, there were no significant increases in cytotoxicity seen over the course of 4 hours after exposure for any of the doses analysed.
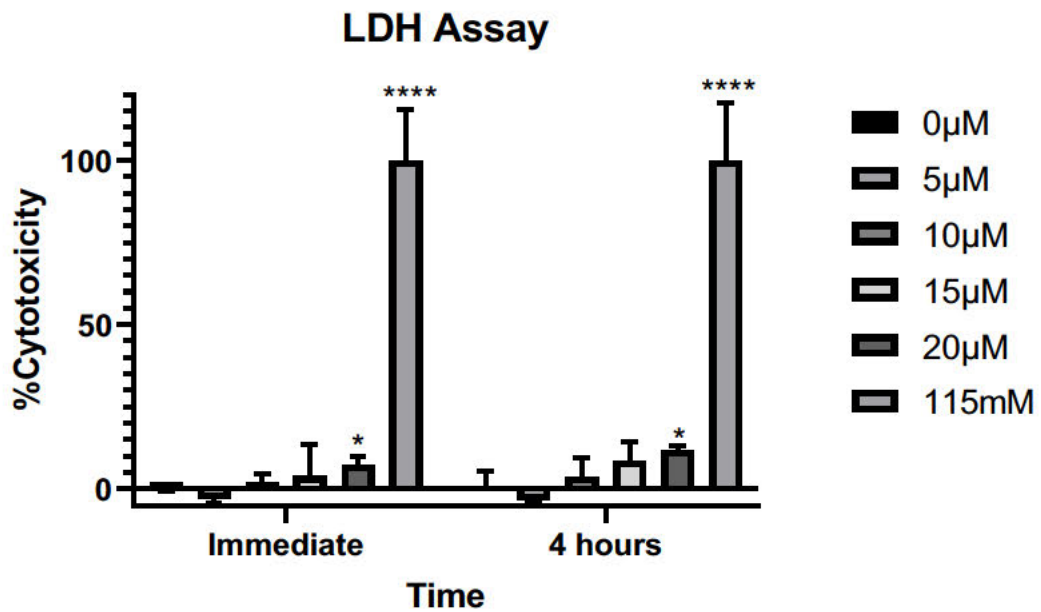


*Figure 5.5: Lactate Dehydrogenase (LDH) Assay of human chondrocytes immediately (left) and 4 hours (right) after exposure to hydrogen peroxide expressed as a percentage of cell death (cytotoxicity). Mean values from 3 biological repeats in technical triplicate are presented + SD. \*= p<0.05; \*\*\*\*=p<0.0001.*
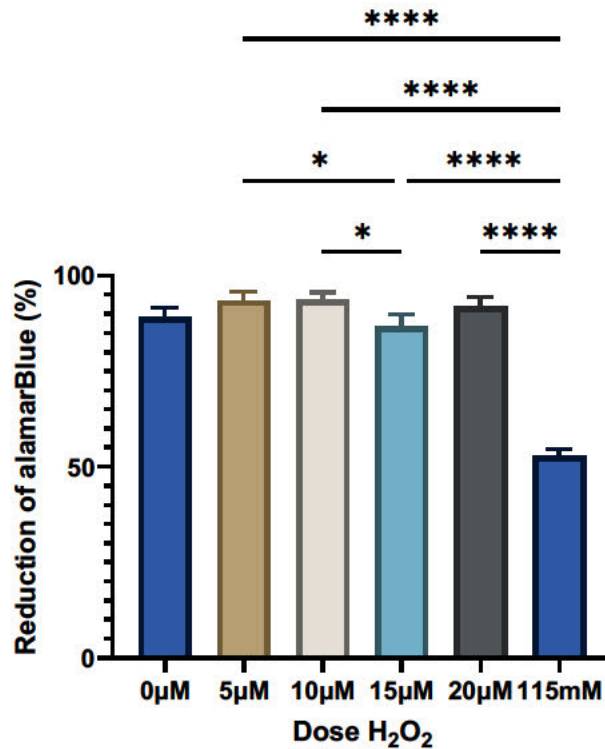
*Figure 5.6: AlamarBlue Assay to show cell viability (expressed as a % of reacted alamarBlue reagent reacted) 4 hours after of exposure to hydrogen peroxide. Mean values of 3 biological repeats + SD are presented. Statistical analysis from a one-way ANOVA is demonstrated. \*=p<0.05; \*\*=p<0.01; \*\*\*=p<0.001; \*\*\*\*=p<0.0001.*

Cellular metabolic activity after exposure to peroxide was examined using the alamarBlue assay (Figure 5.6). Significantly lower metabolic activity was observed over the course of 4 hours in the 0.39% (115 mM) group (52.9%; $p<0.0001$) relative to all other doses used. The 15 µM dose (86.7%) was also significantly lower than 5 (93.5%, $p=0.03$) and 10 µM (93.7%, $p=0.02$) but there were no significant differences seen between the other doses of hydrogen peroxide used.

A further factor which may have been affected by the genotoxic effects of peroxide was cellular proliferation, which has implications for the ability of cells to populate a biomaterial scaffold. As such, the iCELLigence apparatus was used to assess the ability of cells to proliferate after exposure to the tested doses of hydrogen peroxide (Figure 5.7). Over a period of 24 hours, similar growth curves were observed in all wells prior to the addition of hydrogen peroxide. Thereafter, all groups experienced a change in cell impedance with the 0, 5 and 10 µM

254

groups displaying similar trends, but with a more marked drop in cell number seen in the 20 µM and 115 mM groups. The growth curves all demonstrated statistically significant differences when compared across timepoints (p<0.0001).

**Cell Growth Data (24 hours)**
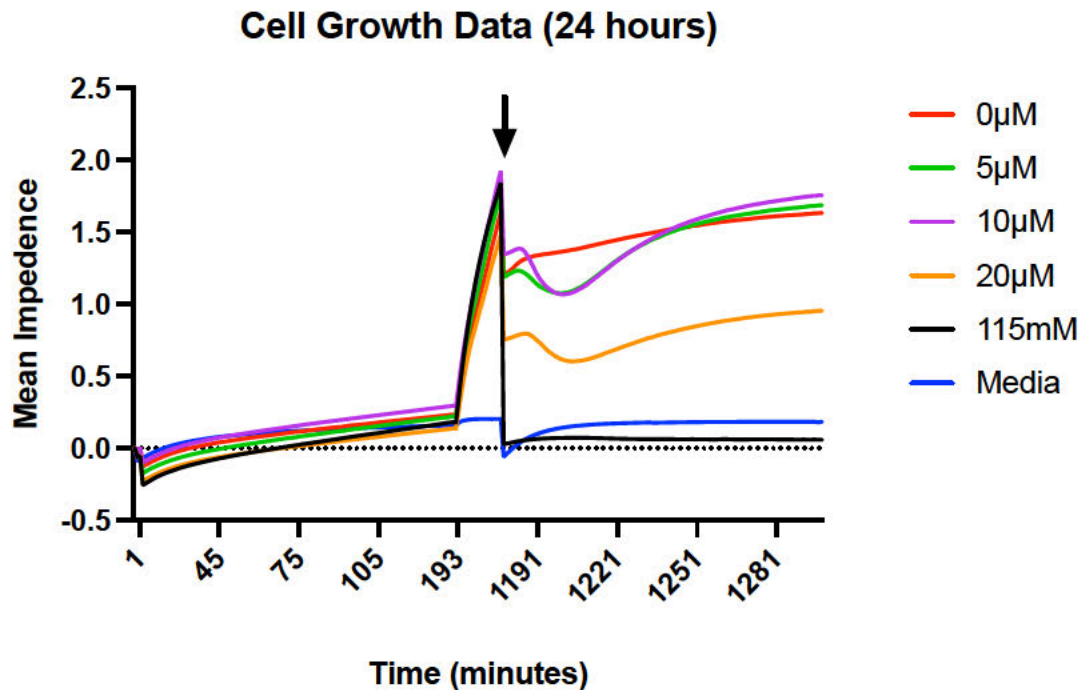


*Figure 5.7: iCELLigence growth curve of cells cultured for 24 hours with the addition of hydrogen peroxide for 5 minutes as denoted by the arrow at 18 hours. Mean values of 3 biological repeats are presented compared to media only control values.*

When focussed specifically on the growth curves around the cytotoxic event, there were no statistically significant differences in the growth curves of 0 µM compared to 5 µM (p=0.06) and 10 µM (p=0.3). The effect of 115 mM was so deleterious to cells that no significant differences were observed between this dose and media only (i.e. no cells detected; p>0.999). 20 µM was also significantly worse than not only the PBS control (0 µM, p<0.0001), but also 5 µM (p=0.0004) and 10 µM (p<0.0001) during the cytotoxic event window.

The reduction in cellular impedance after exposure was used to calculate an estimate of cell detachment and potentially toxicity, corrected for the drop in

impedance following the addition of control 0 µM (warm PBS, Figure 5.8). The estimated cytotoxicity was not significant between the 0, 5 (p=0.24) and 10 µM (p=0.43) doses, but was significantly higher in the 20 µM dosed cells (p<0.0001) and 115 mM dosed cells (p<0.0001).
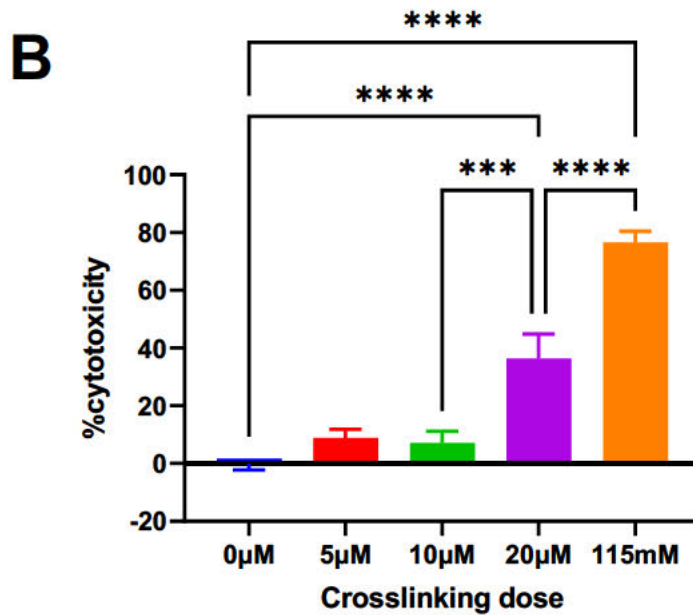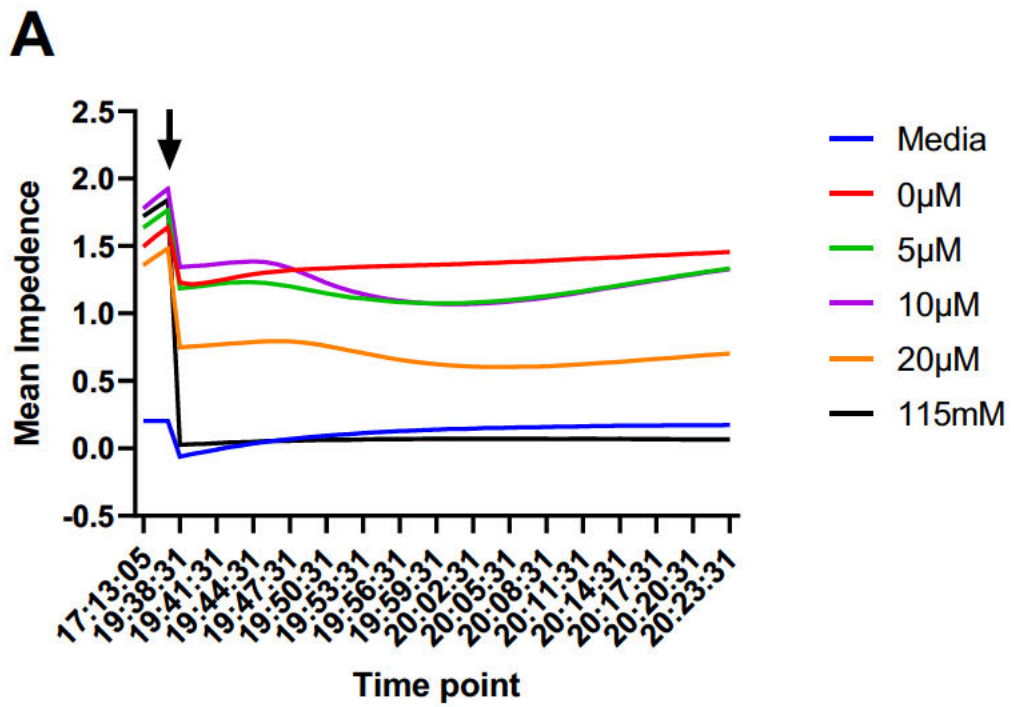
Figure 5.8: A) Cell growth and subsequent changes in cell impedance following exposure to $H_2O_2$ for 5 minutes (point of addition demarcated with arrow). B) Percentage of cytotoxicity based on cell impedance before addition of peroxide and corrected for control (0 μM). ***=p<0.001; ****=p<0.0001.

## 5.3.2.2      Rheological characterisation of crosslinking time

In order to characterise the maximum amount of time for crosslinking changes to occur, the weakest crosslinking combination: 20HA with 5 µM of $H_2O_2$, was used to quantify the change in the material's mechanical properties with time after application of crosslinking agent. In doing so, the aim was to ultimately determine a minimum time period in which satisfactory crosslinking could occur.

At the initial time point, the storage modulus (G') of the bioink was 88.1 Pa (12 seconds), rising at a rate of 1.2 Pa/s to 441.9 Pa by 300 seconds (5 minutes) and continuing to increase at a more linear rate of 0.8 Pa/s to 667.1 Pa by 600 seconds (10 minutes) (Figure 5.9A). The storage modulus did continue to increase until end time point (851.3 Pa), albeit at a lower rate of 0.6Pa/s. The loss modulus (G"; Figure 5.9A) showed a less marked increase to the 300 second mark (39.2 Pa) at a rate of 0.06 Pa/s from the start point of 22.6 Pa, and continued to increase until 600 seconds (41.8 Pa, at a rate of 0.009 Pa/s). Beyond 600 seconds, there was minimal further change in the loss modulus with time (0.01 Pa/s). The loss tangent (tanδ; Figure 5.9B) mirrored the loss modulus, with the steepest rate of change seen between 0-300 seconds. Throughout the time period studied, the loss modulus remained below 1 indicating a dominance of elastic over viscous behaviour, and the reduction of this value (and increase in storage modulus) with time indicates that the material stiffens following exposure to the crosslinking agent.
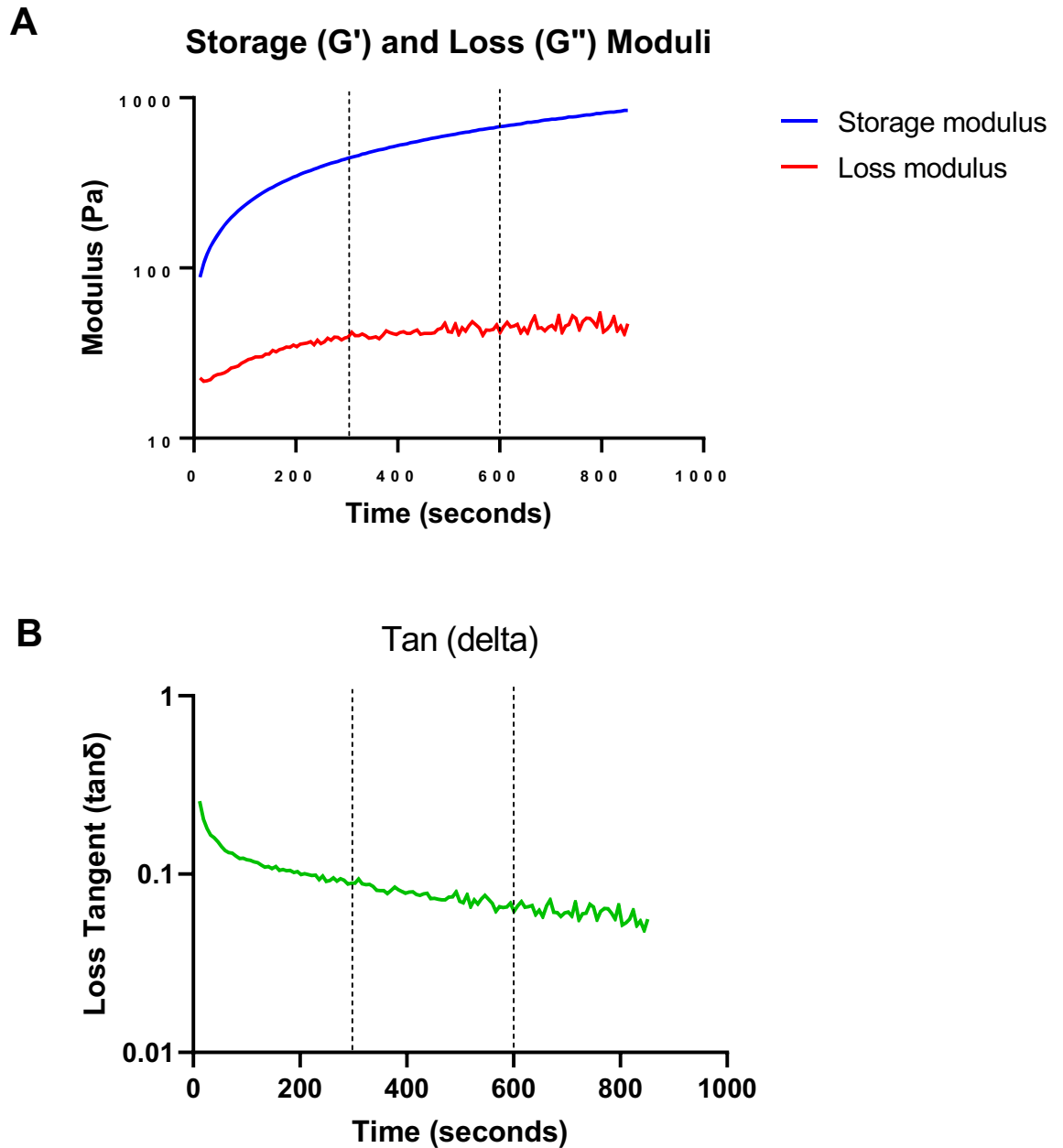
**Figure 5.9: Rheological characterisation of crosslinking time of 20HA with 5 μM $H_2O_2$. A) Loss modulus and storage modulus are plotted logarithmically against time (seconds) with dotted vertical lines indicating the 5 and 10 minutes marks. Evidence of a plateau is seen in the loss modulus as early as 5 minutes and a reduction in the gradient of the storage modulus is seen after both the 5 and 10 minutes marks. B) Loss tangent is plotted logarithmically against time in seconds with dotted vertical lines indicating 5 and 10 minute marks. The curve shows a dominance of elastic over viscous behaviour (tanδ<1) with a minimal change noted after 5 and 10 minutes.**

### 5.3.2.3 Characterisation of topography and elasticity of low dose (5 μM) and high dose (115 mM) crosslinking agents with Atomic Force Microscopy (AFM)

The bioink with the lowest volume of HA, i.e. 20HA, was used in these experiments to determine the minimum structural strength of the NCHA composite bioinks in the presence of low and high doses of crosslinking agent.

Firstly, AFM was used to characterise the surface topography and stiffness of the NCHA in the presence of low and high dose crosslinking agents. A mean elastic (Young's) modulus of 11.8 kPa (median 8.45) in the low dose crosslinked material was observed compared to 23.5 kPa (median 7.65) in the high dose crosslinked material, though this was not a statistically significant difference (p=0.67) (Figure 5.10).

## NCHA crosslinking effects
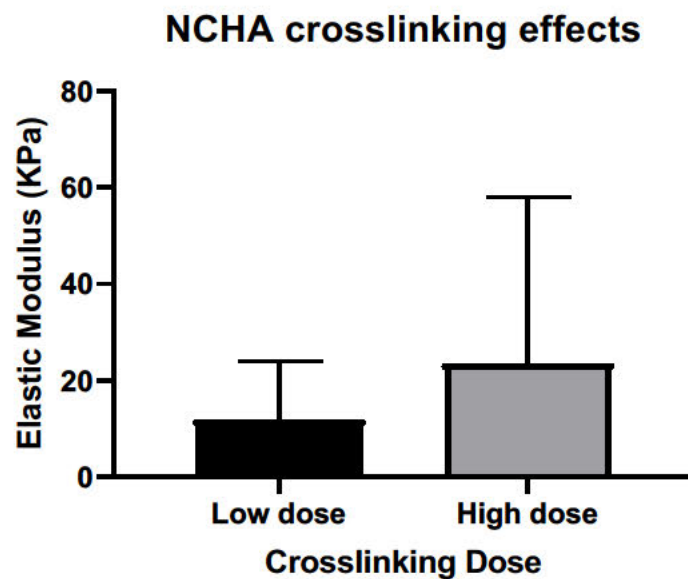


*Figure 5.10: Elastic modulus (kPa) of 20HA crosslinked with low dose (5 μM) or high dose (115 mM) peroxide crosslinking agent. Mean values of 162 measurements from 2 technical replicates are presented with error bars depicting the standard deviation.*

Topographically, a similar arrangement of surface fibres was observed in both crosslinking doses, displaying multidirectionality of fibres and interconnecting pores of variable sizes and depths. There was a degree of surface roughness in the low dose crosslinked material as evidenced in Figure 5.11A, where depths demonstrated a peak of 864nm and trough of -771nm (range of 1.6 microns)

across a representative 15 micron area. Conversely, the higher dose crosslinked material has much greater range of depths, observed across a 15 micron area with a peak height of 2.5µm and trough of -2.3µm (range 4.8µm).
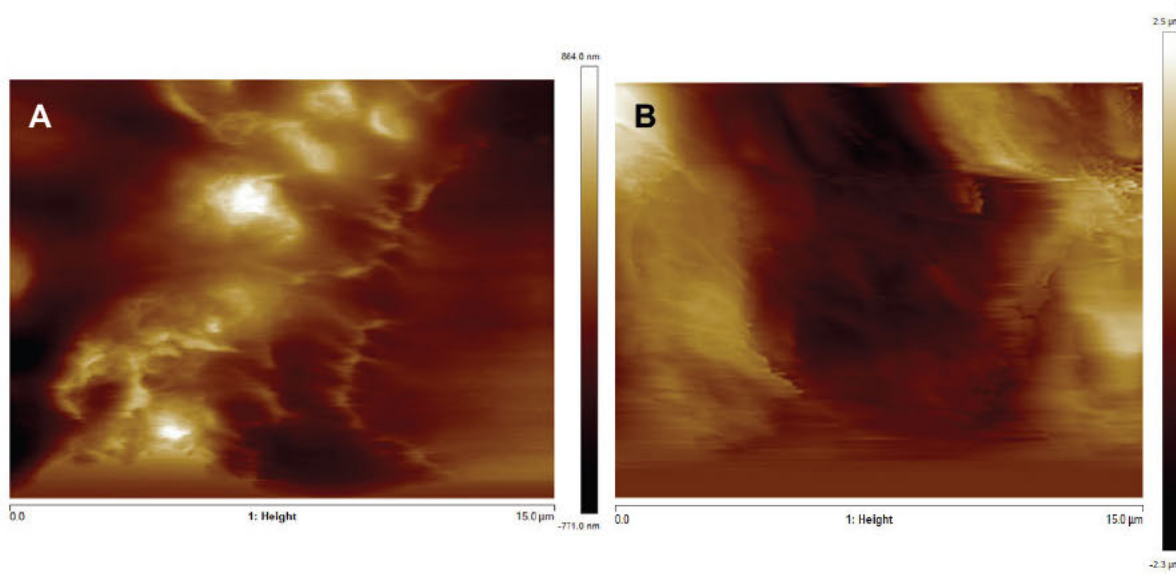


Figure 5.11: Surface topography images of 20HA material acquired with AFM images. representative images are presented from 2 repeats of each condition. A) demonstrates a representative image of the low dose crosslinking agent. Depth is displayed on the scale on the right of each image and a scale bar is present beneath each image (15 microns). Shallow pores of varying sizes are demonstrated (1-10 microns) with a degree of surface roughness evident. B) depicts a representative image of the high dose crosslinking agent in which a greater degree of surface homology is observed but with larger, deeper pore sizes of approximately 10 microns width and 5 microns deep are demonstrated. Moderate surface roughness is also demonstrated.

### 5.3.2.4    Effect of crosslinking agent concentration on porosity and swelling

Porosity and swelling assays were also performed to determine how the effect of different crosslinking strengths affected the volume of the pores forms between the crosslinked bonds and how this affected the amount of liquid content the material accommodates in the form of swelling.

**A**  Porosity
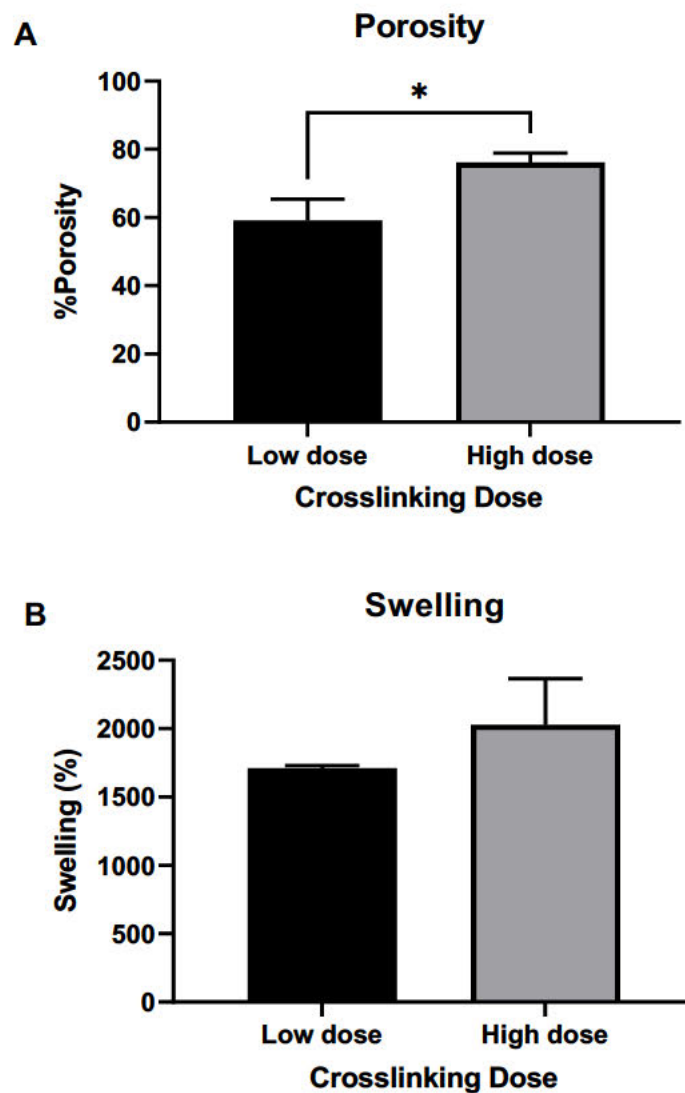
**B**  Swelling

*Figure 5.12: Porosity and Swelling of 20HA in presence of high and low dose crosslinking agent. Mean values of 6 repeats are presented with error bars depicting standard deviation. A) The percentage porosity of low dose and high dose crosslinked 20HA material are presented demonstrating a higher degree of porosity in the high dose crosslinked material. *=p<0.05. B) Swelling of NCHA material in high and low dose crosslinked groups from fully dehydrated state. No significant differences were observed between the two crosslinked states.*

A statistically significant difference in porosity was noted between the high dose and low dose crosslinking agent, with a mean porosity of 59.2% in the low dose crosslinked material and 76.1% in the high dose crosslinked material (p=0.03). Related to this property, is the materials swelling. From their completely dehydrated forms, the crosslinked hydrogel formulations displayed swelling in the

region of 1500 to 2000% indicating a high degree of water content. The degree of swelling was greater in the 20HA crosslinked with high dose peroxide (2028%) compared to the low dose crosslinker (1711%) but this was not significant (p=0.25).

In summary, high dose crosslinking appears to significantly increase the porosity but not the swelling or the elastic modulus of the 20HA bioink.

### 5.3.2.5    Mechanical Strength and Properties of 20HA with high and low dose crosslinker

To further assess the mechanical differences of the bioinks post-crosslinking, the material strength was further characterised using mechanical compression (stress) testing (Figure 5.13, Appendix 2). There was a higher mean strain to failure value in the low dose crosslinked material (64.7%) compared to the high dose material (60.8%), however this was not a statistically significant difference (p>0.999). Similarly, a maximum compressive stress of 388.6 kPa was observed in the low dose group, compared to 421.3 kPa in the high dose group, but again this was not a statistically significant difference (p=0.5). The break force was slightly higher in the high dose crosslinked group at 2.26 N compared to 2.14 N but this was also not significant (p=0.8).

**A**

### Strain to failure



**B**

### Ultimate compressive stress



**C**

### Break force
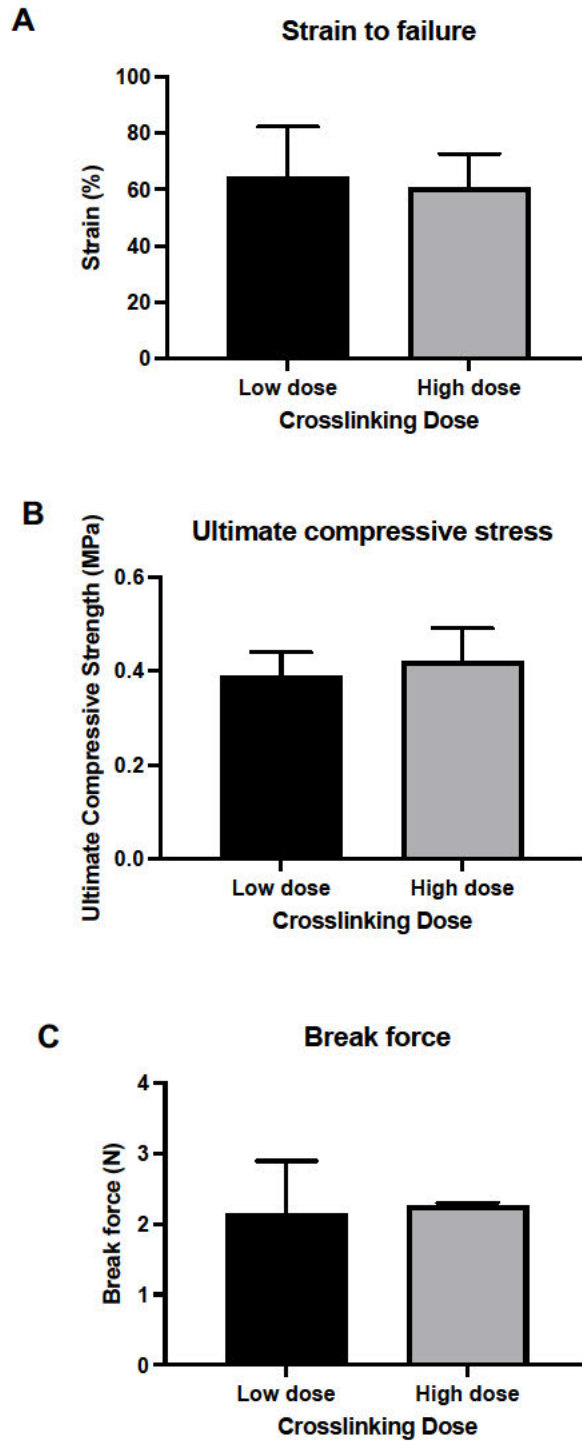


*Figure 5.13: Mechanical compression characteristics of low and high dose crosslinked 20HA bioink. Mean values of three technical repeats with standard deviation are presented. A) Strain to failure under compression is expressed as a mean percentage. No significant differences were observed between the two conditions. B) Mean maximum compressive stress is expressed in MPa. No significant differences were observed between the two conditions. C) The mean break force is presented in Newtons and demonstrated no significant differences between conditions.*

It is therefore noticeable that despite the detrimental cytotoxic effects of the high dose crosslinking agent, there is minimal structural or mechanical benefit to using this dose. In light of these findings, a dose of 5μM $H_2O_2$ was used hereafter.

### 5.3.3 Structural and mechanical characterisation of crosslinked NCHA bioinks

After 3D printing 100 μl semispheres of the NCHA biomaterials, each was crosslinked in 5 μl $H_2O_2$ for 5 minutes. The change in the diameter of the semispheres was calculated as a percentage change in diameter as seen in Figure 5.14. The highest change in diameter was observed in the 20HA material (-6.2%), which was a significantly greater change than 100HA (-5.8%; p=0.001) and 80HA (-5.9%; p=0.008). Statistically significant differences were also observed between 40HA (-6.1%) and 100HA (p=0.006). Of note there were no statistically significant differences between the change in diameter post-crosslinking with 20HA, 40HA and 60HA (-6.0%).

**Change in diameter post-crosslinking**
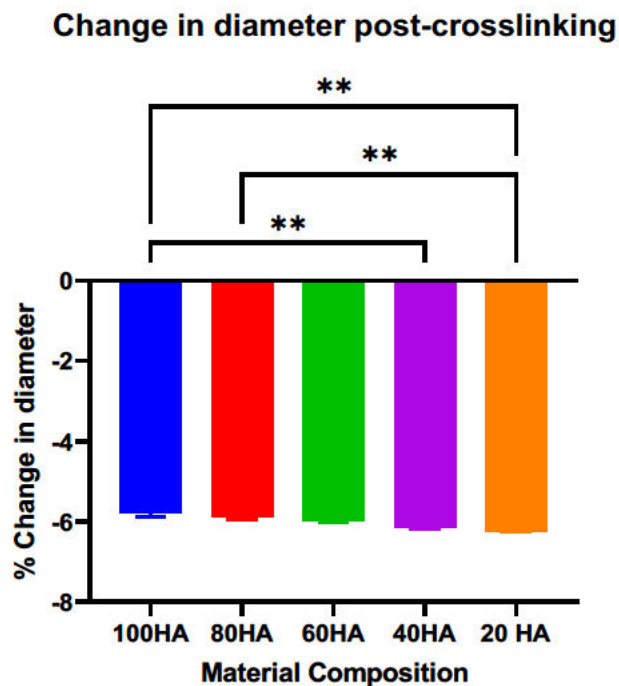


Figure 5.14: Change in diameter of NCHA semispheres following immersion in crosslinking agent. Mean values as a % change in diameter +SD are expressed for 3 repeats. **=p<0.01.

Porosity and swelling assays were undertaken to determine the water retention and pore sizes of the different NCHA formulations. The crosslinked hydrogels were noted to hold a significant amount water content, enabling swelling of up to 2000% in the 100HA (2016%) and 20HA (1954%) materials. Of note, there was lesser swelling noted in the 80HA (141%), 60HA (172%) and 40HA (548%) materials, of which 80HA and 60HA were significantly lower than 20HA (p=0.0007, p=0.0001 respectively). The lower degree of swelling in these materials may be a reflection of the increased heterogeneity of the material composition.
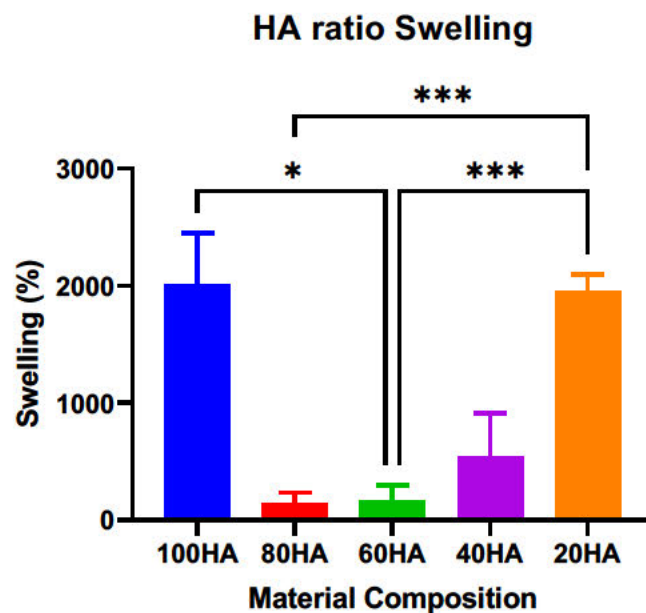


*Figure 5.15: Swelling of crosslinked NCHA bioinks. Values represent the mean of 6 repeats, expressed as a percentage from dry to fully hydrated mass + standard deviation. \*=p<0.05; \*\*\*=p<0.001*

## HA ratio Porosity
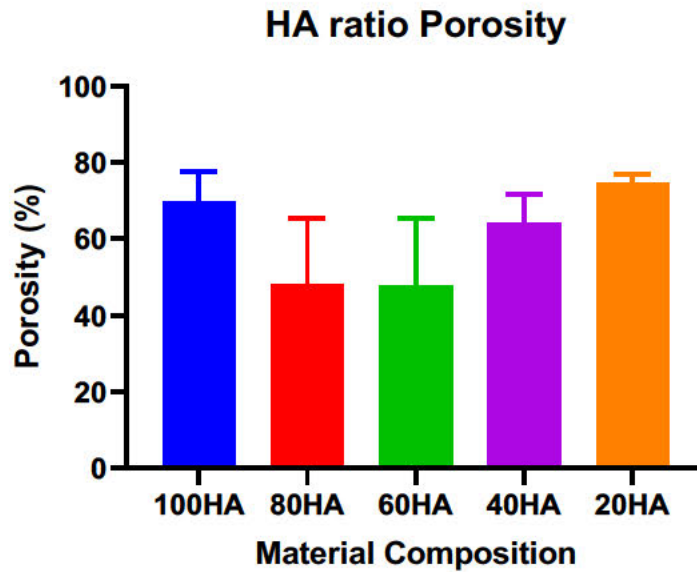


*Figure 5.16: Porosity of crosslinked NCHA bioinks. Values represent a mean of 6 repeats + standard deviation expressed as a percentage of the total material. No significant differences were observed between material composition porosities.*

Mirroring the swelling is the porosity of these materials, in which 20HA and 100HA showed the greatest percentage porosities of 74.7% and 69.6% respectively (Figure 5.16). 80HA (48.0%) and 60HA (47.9%) had lower porosities, mirroring the lower swelling values noted in Figure 5.15. Despite there being discrepancies in the mean porosity of these crosslinked NCHA materials, these were not statistically significant.

Porosity and swelling characteristics may influence the ultimate strength of the biomaterials and their ability to withstand compression under force. As such, the ultimate strength (stress), break force (force required to completely fracture the material) and the ultimate amount of strain (deformation as a result of stress) were determined using mechanical compression testing (Figure 5.17, Appendix 2).
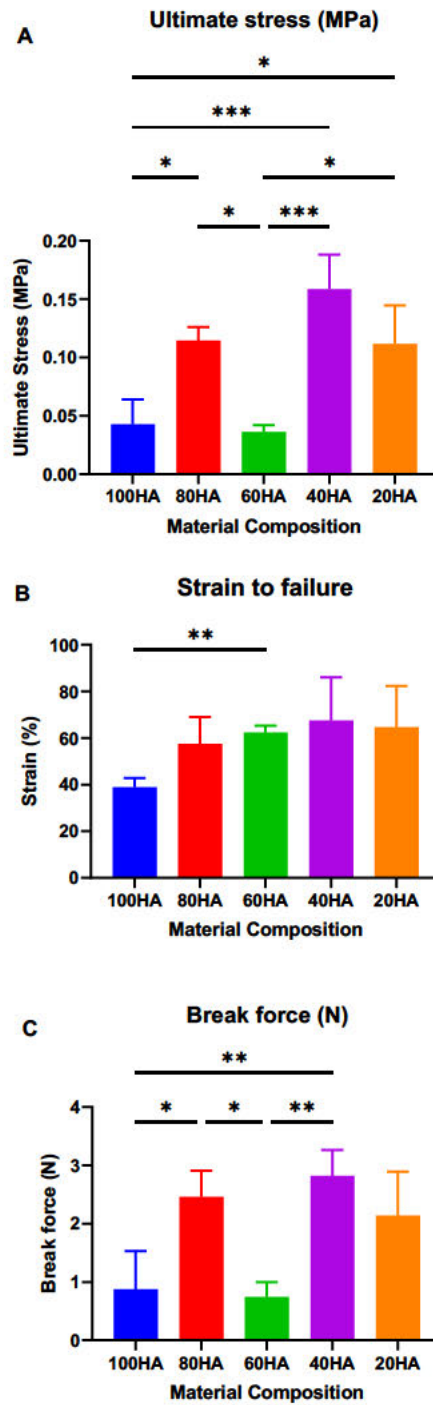
*Figure 5.17: Mechanical compression characteristics of NCHA bioinks. The mean values + SD are presented for 4 repeats per condition. A) Ultimate compressive stress (MPa) is presented graphically demonstrating the highest compressive strength in 40HA, 20HA and 80HA relative to the 100HA and 60HA formulations. B) Strain to failure (expressed as a percentage) was comparable between all NCHA composite inks but significantly lower in the 100HA formulation relative to 60HA. C) The break force of each material is presented in Newtons and demonstrates the highest break force in the 40HA and 80HA materials. \*=p<0.05; \*\*=p<0.01, \*\*\*=p<0.001*

The ultimate stress reflects the highest amount of force exerted on the material per unit of cross-sectional surface area and is a useful measure of the material's ultimate strength. Of all the materials tested, the 40HA appeared to have the highest ultimate stress value of 0.498 Mpa, which was significantly stronger than 60HA (0.116Mpa, p=0.0001) and 100HA (0.134Mpa, p=0.0002). 20HA (0.389Mpa) was also stronger than these two materials (vs 60HA, p=0.0049; vs 100HA p=0.009) but not statistically different in strength to 40HA (p=0.5). Of all the NCHA materials, 100HA was subjected to the least ultimate strain under compression, with a value of 39%. This was statistically significant compared to 60HA (62.3%; p=0.007) but not to any other materials. The break force was determined in Newtons, and found to be greatest in the 40HA material (2.8N), which was statistically significant compared to 60HA (0.74N, p=0.0057) and 100HA (0.87N, p=0.0089), but not to 20HA (2.14N, p=0.56) or 80HA (2.46N, p=0.92).

In summary, the most favourable mechanical properties were observed in the materials with at least 40% (v/v) of nanocellulose. However, at higher proportions of nanocellulose (20HA), this was also associated with significantly higher water content (swelling) and a greater degree of contracture post-crosslinking.

### 5.3.4  Chondrogenic Potential of NCHA bioinks

In addition to the mechanical and structural properties, it is paramount to determine the biological characteristics of the NCHA biomaterials for cartilage tissue engineering: specifically, its ability to emulate the native chondrogenic environment and direct chondrocytes into producing extracellular matrix, retaining a chondrocytic phenotype and encouraging proliferation within the biomaterial.

#### 5.3.4.1      Chondrogenic Gene Expression

Firstly, gene expression was explored over a 21-day time period for chondrogenic markers using three separate biological repeats. Specifically, the genes used were SOX9, type II collagen (COL2A1) and aggrecan (ACAN1).

SOX9 gene expression was comparable across all materials at 4 hours (Figure 5.18). All materials except 100HA then demonstrated a fall in SOX9 expression at 24 hours, the sharpest of which was observed in 20HA (0.35, p=0.006). SOX9 expression remained low in 100HA (0.32, p=0.005), 80HA (0.55, p=0.031) and 60HA (0.36, p=0.006) at the 7-day time point, relative to 100HA at 4 hours. At 21 days, 60HA and 40HA gene expression had risen to approximately 1, comparable to baseline values in 100HA. However, SOX9 expression remained lowered in 100HA (0.46, p=0.009) and 80HA (0.65, p=0.04) at 21 days. The only point at which there was a significant increase in SOX9 expression was in 20HA relative to 100HA (1.99-fold increase, p=0.04).

COL2A1 gene expression showed significant increases over the course of 21 days in all bioinks (Figure 5.19). The greatest magnitude of change was observed in 80HA at 14 (370-fold, p<0.0001) and 21 days (502-fold, p<0.0001). The initial expression of COL2A1 was lower at the 4 hour timepoints in 40HA (0.55, p=0.04) and 20HA (0.41, p=0.03) materials and the 60HA at 24 hours (0.29, p=0.008). By Day 7, all materials demonstrated superior COL2A1 expression compared to 100HA at 4 hours, and this continued to rise for 100HA-60HA, but plateaued at 14-21 days in 40HA and 20HA.

Aggrecan gene expression (Figure 5.20) was initially lowest in the 60HA (0.6, p=0.048) and 20HA (0.5, p=0.03) bioinks for the first 4 hours of culture and this remained significantly reduced for up to 24 hours in culture for 20HA (0.5, p=0.02). However, by 7 days of culture, the aggrecan gene expression had risen significantly in all materials, with the most significant rises observed in the 20HA (6.06, p<0.0001) and 40HA (4.20, p<0.0001) materials. Aggrecan gene expression continued to rise over the 21-day course in all biomaterials (except 100HA which subsequently fell at 21 days (6.36, p=0.04) and the highest level was seen at 21 days in the 20HA material (24.16, p=0.0004).
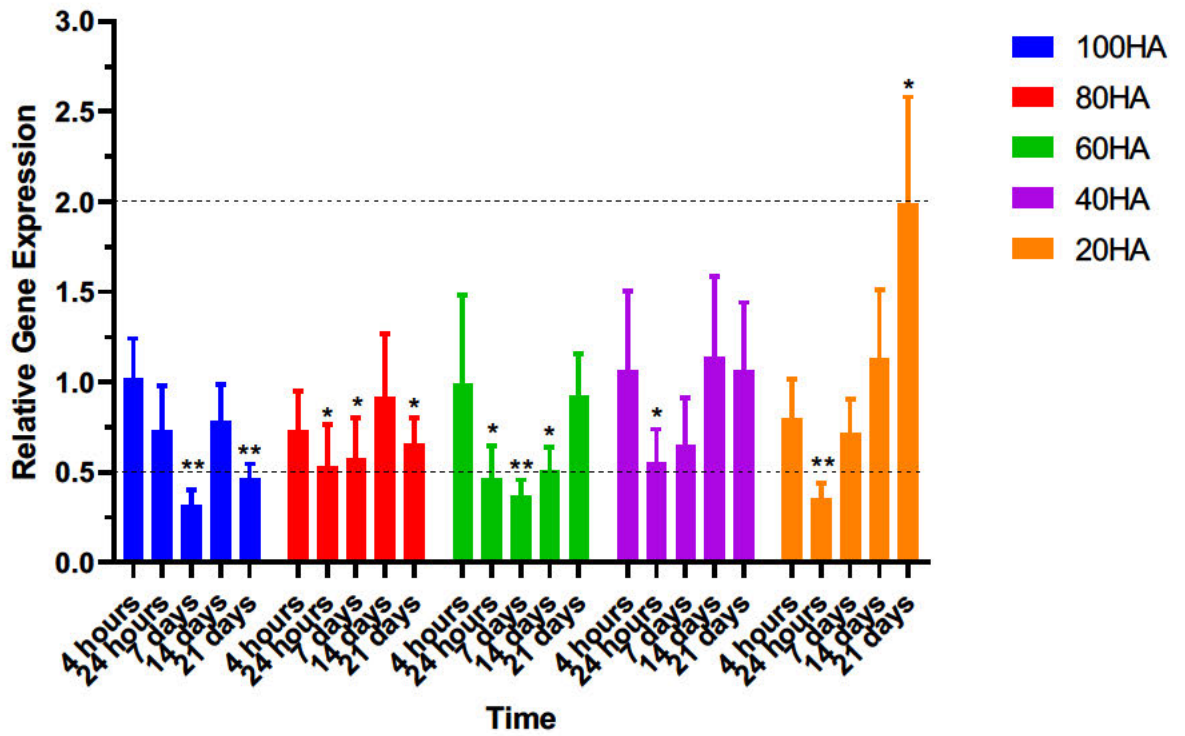
Figure 5.18: Gene expression of SOX9 up to 21 days in culture with NCHA bioinks. All gene expression is relative to 100HA at 4 hours. Mean values of at least 4 technical repeats of 3 separate biological repeats are displayed + SD. Significance is displayed relative to 100HA at 4 hours . *=p<0.05; **=p<0.01; ***=p<0.001; ****=p<0.0001

# COL2A1
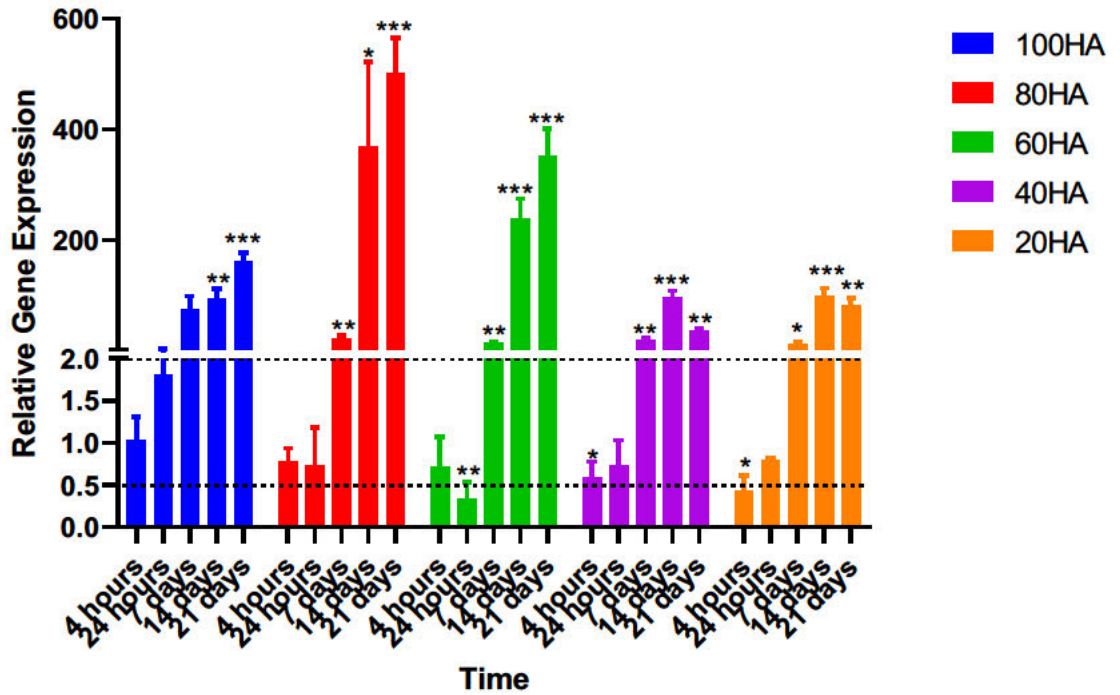


Figure 5.19: Gene expression of COL2A1 up to 21 days in culture with NCHA bioinks. All gene expression is relative to 100HA at 4 hours. Mean values of at least 4 technical repeats of 3 separate biological repeats are displayed + SD. Significance is marked relative to 100HA at 4 hours. *=p<0.05; **=p<0.01; ***=p<0.001; ****=p<0.0001
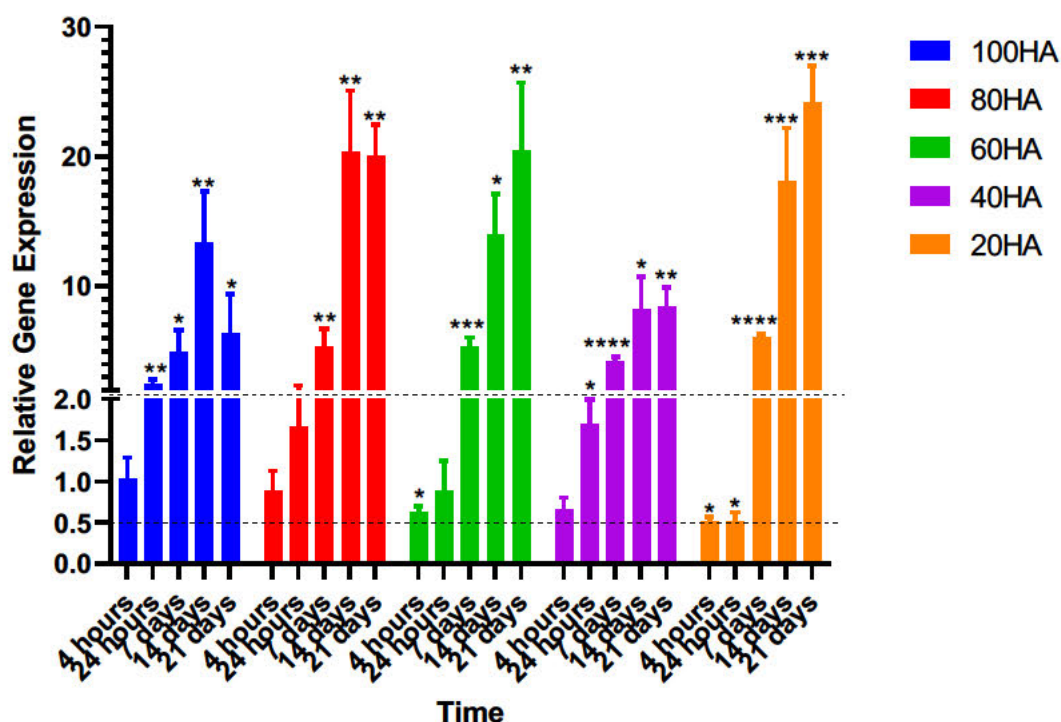
Figure 5.20: Gene expression of ACAN1 up to 21 days in culture with NCHA bioinks. All gene expression is relative to 100HA at 4 hours. Mean values of at least 4 technical repeats of 3 separate biological repeats are displayed + SD. Significance is marked across timepoints (above), and relative to 100HA at 4 hours (below). *=p<0.05; **=p<0.01; ***=p<0.001; ****=p<0.0001

To further elucidate the differences in materials, a biological repeat of 6 was collected at 21 day timepoints of gene expression of SOX9, ACAN1 and COL2A1 (Figure 5.21).

Aggrecan expression relative to 100HA demonstrated a more linear relationship with a higher number of biological repeats (Figure 5.21A), indicating that the increase in nanocellulose content appeared to correlate with the expression of ACAN1 at 21 days. Indeed, 20HA was significantly higher than not only 100HA (p<0.0001) but also 80HA (p=0.0003) and 60HA (p=0.0007) when analysed using a one way ANOVA with Tukey's multiple comparisons test. 20HA was noted to be 6.5-fold higher than 100HA at 21 days across the 6 biological repeats (p<0.0001), 40HA was 3.5-fold higher than 100HA on average (p<0.0001).

Collagen 2 expression demonstrated a similar trend across the biological repeats (Figure 5.21B), with 20HA demonstrating the highest COL2 expression at 21 days (10.5-fold higher than 100HA): a level significantly higher than all other materials (vs 40HA p=0.04, vs 60HA p=0.0002, vs 80HA p=0.0003). Similarly to ACAN1 expression, only 40HA (4.8-fold difference, p=0.02) and 20HA (10.5-fold difference, p<0.0001) were significantly different to 100HA.

SOX9 expression was over 2-fold higher in all NCHA composite biomaterials (Figure 5.21C) and statistically significantly higher in 60HA (2.5-fold, p=0.03), 40HA (4.1-fold, p=0.01) and 20HA (2.8-fold, p=0.01). No significant differences were observed between the NCHA composite biomaterials using Tukey's multiple comparison test.

In summary, all NCHA bioinks show an increase in chondrogenicity over the course of 21 days, however the greatest chondrogenic potential at the level of gene expression is observed in the 20HA and 40HA bioinks.
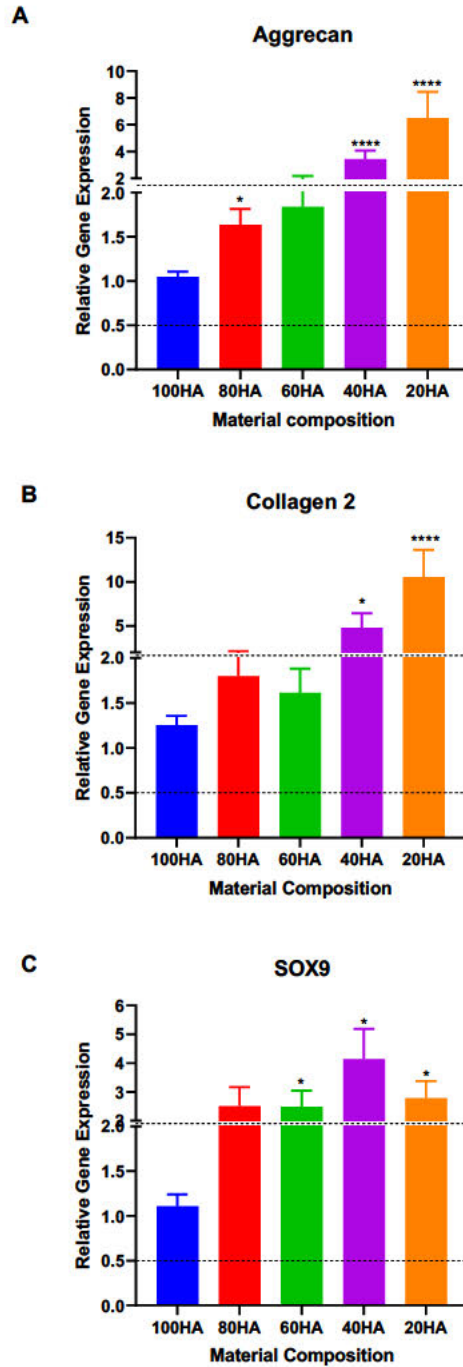
*Figure 5.21: Gene expression profiles at 21 days are displayed showing the mean values of 6 biological repeats presented with standard error, relative to 100HA. Dotted lines indicate thresholds of biological significance (<0.5-fold and >2-fold). A) Relative gene expression of ACAN1 demonstrating biologically and statistically significant gene expression in 20HA and 40HA relative to 100HA. B) Relative gene expression of COL2A1 demonstrating biologically and statistically significant gene expression in 20HA and 40HA relative to 100HA. C) Relative gene expression of SOX9 demonstrating biologically and statistically significant gene expression in 20HA, 40HA and 60HA relative to 100HA. *=p<0.05; **=p<0.01; ****=p<0.0001.*

275

### 5.3.4.2 Extracellular matrix production in NCHA materials

The extracellular matrix production in each biomaterial was assessed at 21 days using a hydroxyproline assay (for collagen production) and DMMB assay for glycosaminoglycan content (Figure 5.22). Mean hydroxyproline content was highest in the 20HA (24.3 ng/ml) and 40HA (24.1 ng/ml) materials: a level that was significantly higher than both 80HA (17.5 ng/ml; $p<0.0001$) and 100HA (19.8 ng/ml vs 40HA $p=0.002$, vs 20HA $p=0.002$). The mean hydroxyproline content in 60HA (21.9 ng/ml) was also significantly higher than 80HA ($p=0.002$) but not 100HA. No significant differences were noted between 60HA, 40HA and 20HA.

Mean glycosaminoglycan content displayed a similar trend, in which content was highest in the 20HA (427.6 µg/ml) and 40HA (430.2 µg/ml) materials relative to 100HA (183.3 µg/ml, $p<0.0001$), 80HA (259.8 µg/ml, $p=0.002$) and in this case also 60HA (230.4 µg/ml, $p=0.0001$). No significant differences were observed between the 40HA and 20HA materials, or between 60HA, 80HA and 100HA.

As such, the levels of cartilage extracellular matrix components mirrors the pattern of gene expression: 20HA and 40HA are similarly the most chondrogenic formulations of this bioink.
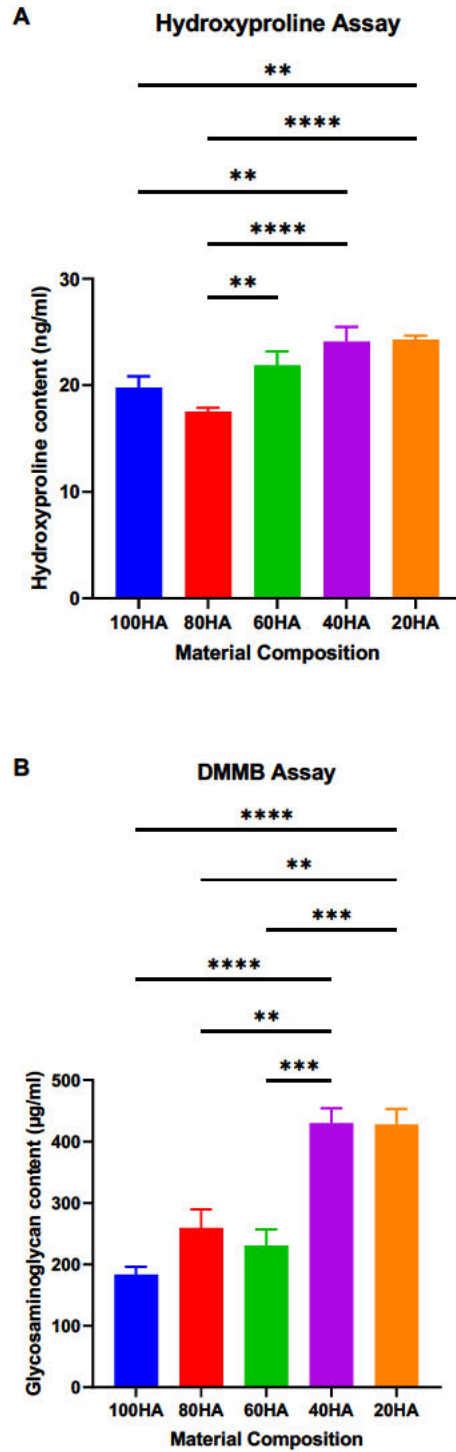
Figure 5.22: assays to quantify extracellular matrix within the NCHA biomaterials. A) The mean levels of hydroxyproline of three biological repeats conducted in technical triplicates is presented with standard deviation. 20HA and 40HA demonstrate statistically significant increases in collagen content compared to 100HA and 80HA. B) Dimethylmethylene Blue assay in which the mean of three biological repeats conducted in technical triplicates is presented with standard deviation. 20HA and 40HA demonstrate statistically greater levels of sulphated glycosaminoglycans than 100HA, 80HA and 60HA. *=p<0.05; **=p<0.01; ***=p<0.001; ****=p<0.0001

### 5.3.4.3 Biomechanical properties of NCHA bioinks following culture with human chondrocytes

Of the material blends studied, the 100HA (0.13Mpa) and 60HA (0.10Mpa) had the lowest ultimate compressive stress without cells (Figure 5.23). These values were significantly lower than 80HA (0.36Mpa, vs 100HA p=0.02, vs 60HA p=0.01) 40HA (0.50Mpa, vs 100HA p=0.0002, vs 60HA p=0.0001) and 20HA (0.39Mpa, vs 100HA p=0.009, vs 60HA p=0.005).

The 40HA material with cells (0.5MPa) was significantly stronger than the 100HA (0.10Mpa, p<0.0001), 80HA (0.25Mpa, p=0.009) and 60HA (0.15Mpa, p=0.0003) materials. The 20HA (0.32Mpa) was also significantly stronger than the 100HA (p=0.02). There were no significant differences between the 60HA, 80HA and 100HA materials after culturing with cells. The presence of cells did not appear to have a significant effect on the ultimate compressive stress of the biomaterials.

The strain to failure on the biomaterials was relatively low without cells, with the lowest value reported in the 100HA material (39.0%), though no significant differences were observed between materials. There was an increase in the mean ultimate strain of each biomaterial after co-culture with cells but this was not a significant increase for any material blend.

## Ultimate Compressive Stress
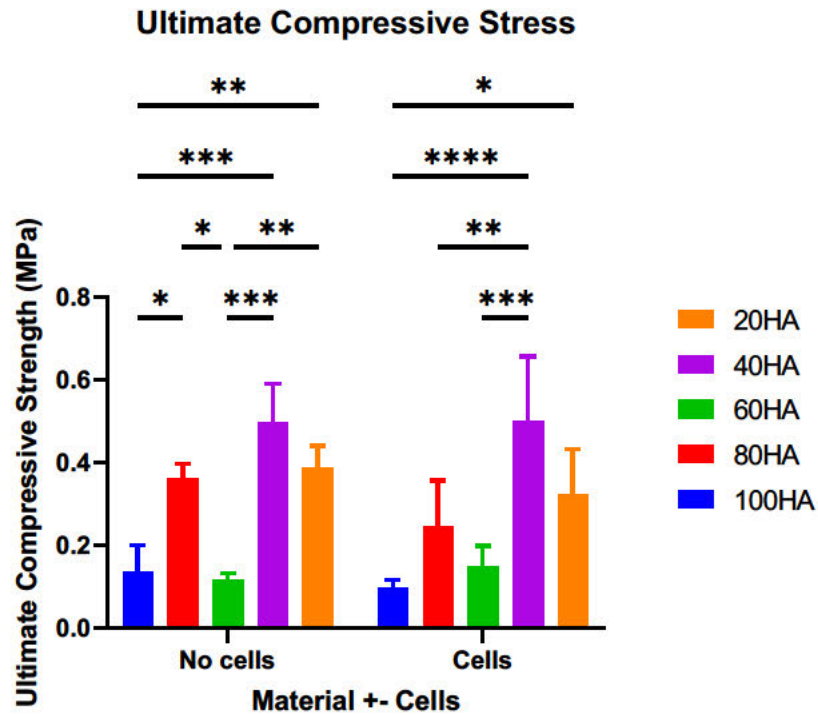


*Figure 5.23: Biomechanical Compression Testing of NCHA bioinks. The ultimate compressive strength (in MPa) is presented with and without cells using 4 replicates. Statistical analysis using a 2-way ANOVA is presented to compare differences between materials with and without cells. \*=p<0.05; \*\*=p<0.01; \*\*\*=p<0.001; \*\*\*\*=p<0.0001*
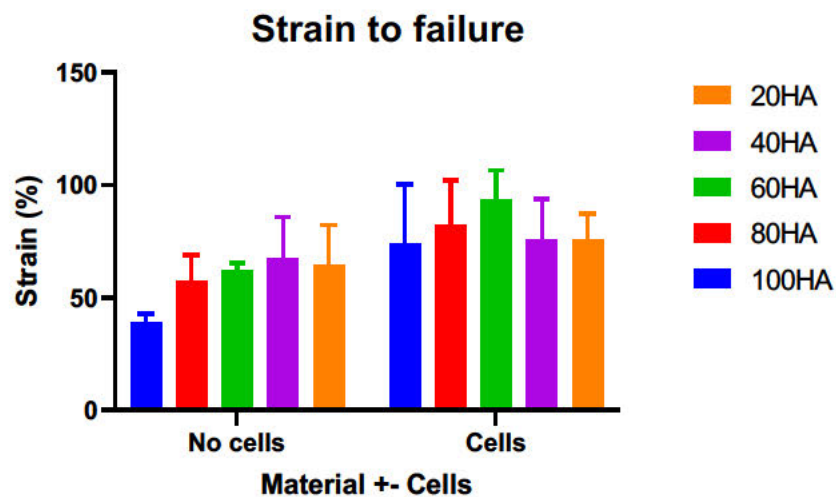
## Strain to failure



*Figure 5.24: Biomechanical Compression Testing of NCHA bioinks. The strain to failure experienced by each biomaterial is presented with and without cells as a percentage value with standard deviation. Statistical analysis using a 2-way ANOVA is presented and to compare the effects of cells cultured in the materials for 21 days using 4 replicates.*

The break force of each material was examined after co-culture with cells. The 40HA had the highest break force (2.7N), which was significantly higher than 100HA (0.68N, p=0.004) and 60HA (0.83N, p=0.008) materials. There was no significant difference in break force noted between any materials before and after culture with cells.

In summary, the most mechanically robust of the NCHA bioinks is the 40HA bioink, both before and after the addition of cells.
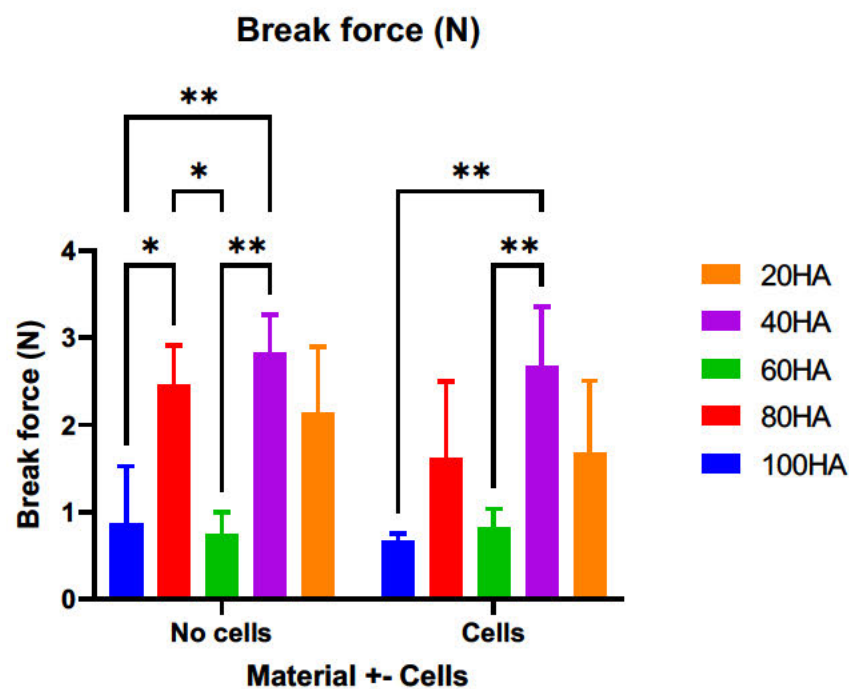


*Figure 5.25: Biomechanical Compression Testing of NCHA bioinks. The mean break force in Newtons is presented with and without cells with standard deviation from 4 replicates. Statistical analysis using a 2-way ANOVA is presented to compare the effects of cells cultured in the different materials for 21 days. *=p<0.05; **=p<0.01*

### 5.3.4.4    Histological analysis of chondrogenic potential of NCHA bioinks

Toluidine Blue, Alcian Blue and Safranin-O stains were performed to visualise cellular distribution and the presence and arrangement of ECM Figure 5.26. Each material contained some HA and as such would be expected to stain in the presence of these stains.

Safranin O-fast green stain demonstrated a universally red stain was applied in each biomaterial, irrespective of the amount of HA within the material. Of note, there was evidence of more intense staining in the 100HA material itself (owing to this material comprising pure glycosaminoglycan) but very intense staining was noted around all cells, to a greater degree than the material, indicating a higher concentration of GAG located in a pericellular location. The fast green component did not appear to prevail in any of the stain, indicating a lack of bone mineralisation. The staining also demonstrated that clusters of cells were visible within the material, surrounded by intense stain indicative of lacunae being formed within the material.

Alcian blue stain similarly binds to sulphated glycosaminoglycans and as such would be expected to stain the biomaterials containing HA. This was noted in all materials with 40HA and 100HA in particular demonstrating this phenomenon. As with Safranin-O staining, there was a higher staining density in the pericellular locations and this is particularly well demonstrated in the 20HA, 60HA and 80HA images.

Toluidine blue is a proteoglycan stain, of which the predominant proteoglycan in cartilage is aggrecan. A violaceous stain is observed in each material, particularly around the cells indicating the production of aggrecan. As this stain has a lower affinity for the biomaterial itself, it is stark to notice that the whilst the cells themselves appear to be heavily stained with toluidine blue, there are cavities of lower amounts of staining around each cell which may be a depiction of lacunae forming around the cells. This is most clearly demonstrated in the 100HA material but seen across all materials studied in this chapter.
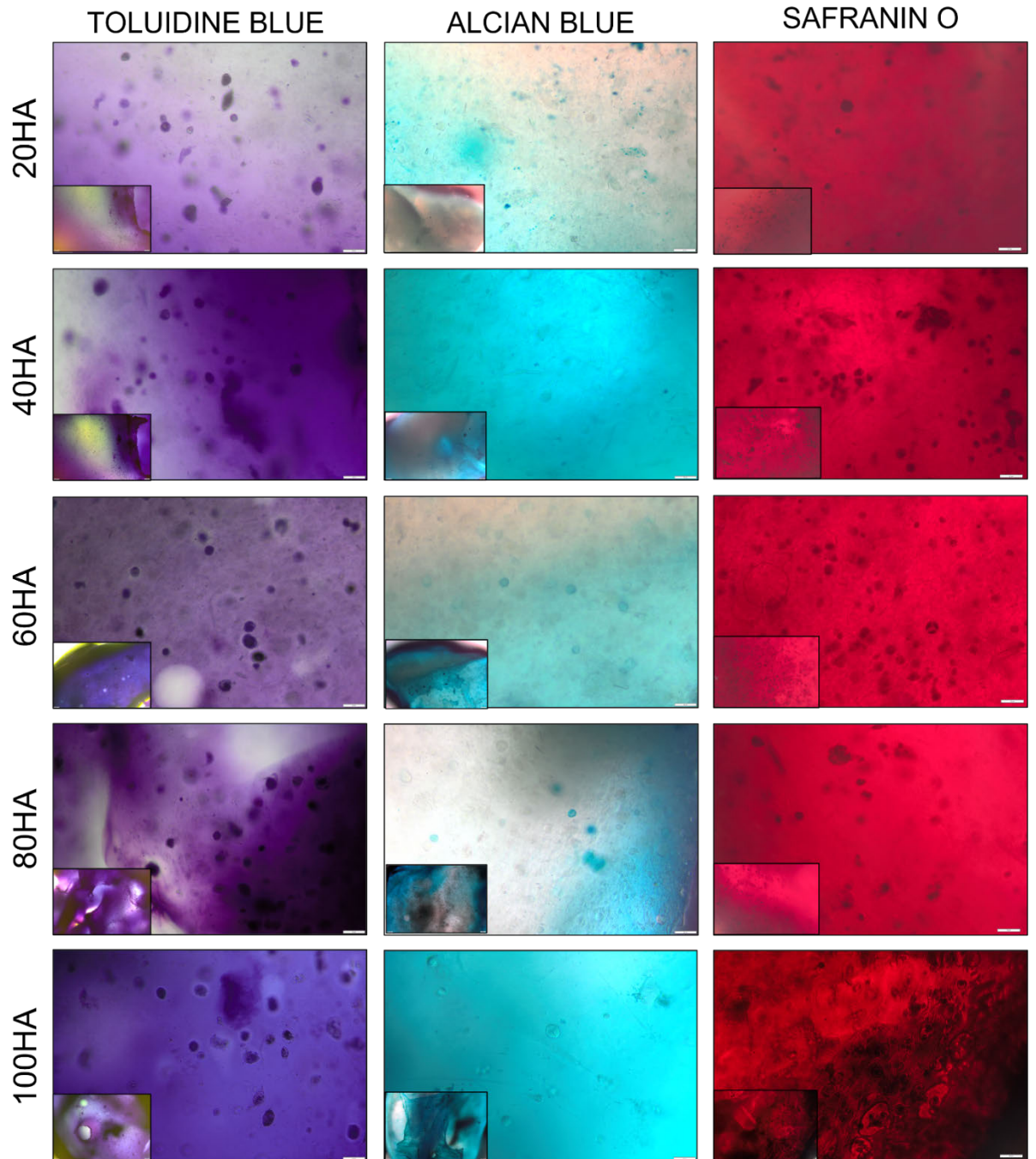
*Figure 5.26: Histological stains for extracellular matrix in intact NCHA bioinks. Each material is presented at 4x (small image) and 20x (large image) magnification stained with Toluidine Blue (left) and Alcian Blue (middle) and Safranin O (right). Intense uptake of stains is seen in a pericellular location in all biomaterials, indicative of extracellular matrix production. The cells can also be seen to be forming lacunae in a number of the stained specimens. Scale bars (bottom right of the 20x magnification images) depict 50 microns.*

## 5.4    Discussion:

### 5.4.1  NCHA bioinks have suitable rheological properties for 3D bioprinting cartilage

In this study, each variant of HA and NCHA bioink demonstrated shear thinning behaviour over the range of frequencies studied. Shear thinning is a time-independent non-Newtonian fluid phenomenon observed in some hydrogels, where the viscosity of the material decreases with increasing shear stress. This is especially important in the context of extrusion-based 3D bioprinting as it means that under the pressure of the extrusion mechanism (usually air), the hydrogel viscosity drops sufficiently to enable the hydrogel to flow through the printer nozzle (Smith *et al.*, 2018).

The viscoelastic properties of the bioinks are also of paramount importance: the viscoelasticity of the materials influence how the material surmounts surface tension and enables uniform, continuous filament extrusion thereafter. The ink must 'recover' after being printed at high shear in order to acquire the necessary fidelity for printing (Petta *et al.*, 2020). It has been reported that viscosity values under 100 Pa.s are inadequate (too runny) for effective post-printing shape retention and that inks with viscosities in excess of $10^4$ Pa.s may not deposit smoothly (Duan *et al.*, 2014). All the bioinks tested in this chapter had viscosities at or below the range of 100 Pa.s which may facilitate extrusion but at the expense of post-printing fidelity. Where the most significant differences existed with the HA and NCHA composite inks is in their viscoelastic properties. The storage modulus is the amount of energy elastically stored in the material during deformation, relates to the number of crosslinks or entanglements within the material, and as such is associated with elastic shape fidelity (Schwab *et al.*, 2020). The bioinks studied in this chapter with the higher levels of HA behaved as a viscoelastic liquid, whereas the materials in which nanocellulose was dominant, adopted a viscoelastic solid behaviour. Viscoelastic liquids display weaker interconnecting networks between nanostructures and have a tendency towards poorer post-printing shape fidelity. Furthermore, the loss tangent of 60HA, 40HA and 20HA was consistently below 1, whereas the 80HA and 100HA remained higher than 1, this indicates that the bioink formulations with higher nanocellulose content had a dominance of the storage modulus over the loss

modulus, which translates to greater elasticity and superior post-printing shape fidelity.

Previous studies have demonstrated that the inclusion of nanocellulose into bioinks can enhance the viscosity, elasticity and ultimately the printability of bioinks (Markstedt *et al.*, 2015a; Jessop *et al.*, 2019b; Sonnleitner *et al.*, 2021). With regard to nanocellulose and alginate, the inclusion of nanocellulose fibrils, crystals and blend variants each augmented the storage modulus of alginate in the magnitude of approximately 60-fold (Jessop *et al.*, 2019b) which is comparable to the difference in storage modulus between 100HA and 20HA/40HA seen at the lower frequencies in this study. Similarly, Markstedt *et al* noted that NC-alginate composite bioinks started to become significantly less viscous at a combination of 60% nanocellulose fibrils and 40% alginate (3% w/v), which is comparable to the rheological findings in this chapter (Markstedt *et al.*, 2015a). HA as a bioink constituent has been suggested to improve yield strength and thereby improve filament formation and construct stiffness (Ouyang *et al.*, 2016). There are a number of factors which influence the rheology of HA hydrogels: the concentration, molecular weight and temperature of the hydrogels all influence its viscoelasticity and subsequent printability (Rebenda *et al.*, 2020). Previous studies have indicated a loss tangent of 0.4-0.6 were ideal for maximum shape fidelity (Petta *et al.*, 2018a; Petta *et al.*, 2018b), which is in the region of the 60-20HA bioinks in this study but considerably lower than the 80HA and 100HA that had loss tangents in excess of 1 for the range of frequencies studied. This may indicate that although the concentration (30 mg/ml) of the HA hydrogel in this study appears promising from a shear thinning perspective, without the addition of nanocellulose blend, the concentration is perhaps too low for reliable post-printing shape fidelity.

### 5.4.2 Using biocompatible doses of the hydrogen peroxide crosslinking agent do not impair the structural properties of the crosslinked biomaterial

The HA bioink contains a tyramine substitution (HA-Tyr) that enables covalent crosslinking through a horseradish peroxidase-mediated oxidation reaction in the presence of hydrogen peroxide. As part of the reaction process, reactive oxygen species (free radicals) are produced, which may have deleterious effects on cell integrity, genetic stability and cellular homeostasis (Djordjević, 2004). The generation of free radicals occurs naturally from physiological processes such as aerobic respiration, and is balanced by antioxidants such as vitamin E and antioxidant enzymes such as superoxide dismutase (Fang, Yang and Wu, 2002). As such, cells have a tolerance threshold of exposure to free radicals, which is a product of the cell type, concentration of the oxidative agent and duration of exposure, and this has been investigated in a variety of cells types spanning lymphoblastic to chondrocytic lineages (Khan *et al.*, 2008; Loo and Halliwell, 2012; Seager *et al.*, 2012). In this chapter, human nasoseptal chondrocytes were exposed to hydrogen peroxide solution for five minutes at a maximum dose of 115 mM and a minimum dose of 5 µM. The HA hydrogel manufacturers (LifeCore Biomed, MN, USA) recommend an optimum crosslinking dose of 0.39% $H_2O_2$, which is approximately 115 mM. This chapter highlights this dose of crosslinking agent is unsuitable for use with cells, causing complete cytotoxicity of chondrocytes in the live-dead and LDH assays and evidenced through a total and immediate loss of cell impedance on iCELLigence, which did not recover over the subsequent 54 hours. Previous studies using HA-Tyr have used crosslinking doses of approximately 300 µM and reported satisfactory cell viability immediately after crosslinking for 5 minutes through live-dead assays (Henriksson, Gatenholm and Hägg, 2017; Nguyen *et al.*, 2017). This chapter highlights that the cytotoxic effect on human nasoseptal chondrocytes is likely to be lower than this: significant reductions in cell viability, proliferation and attachment were observed immediately and at 4 hours using the LDH assay and iCELLigence apparatus. The reasons for the lower cytotoxic threshold seen in this study may relate firstly to the fact that primary human cells rather than cell lines were used in this thesis and secondly, that the cells in this chapter were

directly exposed to hydrogen peroxide without the protection of being embedding within a hydrogel. Moreover, the hydrogels in Henriksson's and Nguyen's studies comprised only 20-30% HA (v/v) with the remainder being nanocellulose, the latter of which is not involved in the peroxidation reaction (Henriksson, Gatenholm and Hägg, 2017; Nguyen *et al.*, 2017). In order to translate this process clinically, the patient's own primary cells would be used to populate a scaffold and cells located on the surface of the biomaterial would receive the greatest exposure to the peroxide, which warrants testing the cytotoxicity in a biomaterial-free environment in the first instance.

In fact, the cytotoxic threshold of hydrogen peroxide in this study (between 10 and 20 µM) more closely aligns to the doses shown to exert a biologically significant effect on cell viability in Seager *et al*'s study of lymphoblastic cells, in which the threshold was found to be 7.28 µM (Seager *et al.*, 2012), and studies of articular cartilage in which doses as low as 50-100 µM evoked markers of impaired cellular viability and function (Asada *et al.*, 2001; Martin *et al.*, 2005; Khan *et al.*, 2008). The differences between the manufacturers recommended dose and the biocompatible doses of 5-10 µM differ by a factor of 23,000, which naturally presents concerns as to whether such a diluted dose of peroxide would be capable of satisfactory crosslinking. Fortunately, it was found that even the lowest crosslinking doses of 5 µM in the bioink containing the lowest amount of HA (20HA) were capable of crosslinking at this dose within 5 minutes. Indeed, when characterised with rheology, the most rapid crosslinking rates were observed within the first 5 minutes and reduced in rate after 10 minutes. Furthermore, significant differences were not observed between the 5 µM and 115 mM crosslinked 20HA as far as elastic modulus, swelling, maximum compressive strength, break force or strain to failure are concerned. There was a significant difference in porosity, however, which may reflect a greater number of covalent bonds forming within the hydrogel in the higher dose group in the crosslinking window. Given that 20HA comprises only 20% HA (responsible for the crosslinking) and 80% NC (which will not itself be crosslinked by the peroxide), it is possible that significant differences may have been observed in the two crosslinking doses with a pure 100HA material. However, the aim of this study was a proof of concept: that the material containing the lowest amount of

286

crosslinking material and the weakest crosslinking dose was still a valid option for 3D bioprinting purposes.

### 5.4.3 The proportion of nanocellulose and hyaluronic acid influences biomechanical properties of the crosslinked bioink

Rheologically, it has already been noted that in their uncrosslinked forms, the nanocellulose and HA differ in their viscoelastic properties which would be expected to translate to the crosslinked forms. There were significant differences in the change in construct size after the addition of crosslinking agent. All the bioinks decreased in size after the addition of crosslinking agent, and this appeared to be a greater degree of contraction in the 20HA and 40HA inks relative to 100HA and 80HA. As the HA is responsible for the crosslinking, this is not an unexpected finding: the crosslinkable Tyramine residues are more dispersed in a 20-40HA ink and upon bonding may evoke a greater degree of contraction on the uncrosslinked, elastic nanocellulose structures. It was interesting that this linear change in size post-crosslinking did not translate to a linear relationship in porosity and swelling. In fact the relationship was more concave, displaying a positive quadratic association, with 100HA and 20HA exhibiting the highest degrees of swelling and 80-60HA having the lowest swelling. Although the porosity did not demonstrate any significant differences between materials, the trend appeared to expectedly mirror the swelling pattern. Hydrogels such as HA and NC, comprise networks of hydrophilic polymers and possess very high water content in their hydrated forms, as evidenced by the high degree of swelling. Hydrogels containing polyelectrolytes have a tendency to swell more owing to charge repulsion between polymer chains (Holback, Yeo and Park, 2011). The nanocellulose used in this thesis has been characterised previously, and is known to have a negative zeta potential (surface charge) of approximately -23.3 mV (Kyle *et al.*, 2018). HA is also known to carry a net negative charge owing to the abundance of carboxylic groups (Horkay *et al.*, 2009). However, when conjugated with Tyramine, these negatively charged carboxylic groups are replaced with amines (Loebel *et al.*, 2015), which carry a positive charge at physiological pH (Berry *et al.*, 2016). This hypothetical

neutralisation of surface charges may explain why the more heterogeneous of the material combinations have lower degrees of swelling: the dielectric moieties evoke less polymeric repulsion, are potentially less hydrophilic and as such draw in less water. This could be further explored through an analysis of the zeta potentials of the different materials pre- and post-crosslinking and a deeper characterisation of pore geometry using a method such as scanning electron microscopy.

Mechanical compression analysis of the crosslinked materials revealed that the 100HA and 60HA were markedly weaker than the 80HA, 40HA and 20HA materials, as evidenced by lower break forces and lower maximum compressive strengths. The 100HA material appeared to display more brittle behaviour under compression than the other biomaterials, which is a recognised phenomenon where high levels of crosslinking have occurred (Peppas *et al.*, 2000). It is not readily apparent why the 60HA was also significantly weaker than the other composite materials, but this may reflect the degree of heterogeneity in the material composition. The compressive strength of the HA materials was comparable to the values reported in other studies of crosslinked HA hydrogels, in the region of 50-100 kPa (Pérez-Madrigal *et al.*, 2019; Wang *et al.*, 2020).

### 5.4.4 Higher nanocellulose content increases the chondrogenic potential of nanocellulose-HA composite bioinks

Plant derived nanocellulose has been demonstrated to augment the printability and chondrogenicity of alginate in this thesis (Chapter 4) and previously published literature (Martínez Ávila *et al.*, 2016; Jessop *et al.*, 2019b). The combination of hyaluronic acid and nanocellulose is less widely reported however.

The findings of this chapter indicate that all materials have inherent chondrogenic potential as evidenced by rising relative gene expression of ACAN1 and COL2A1 over the course of 21 days, indicating the nanocellulose and HA materials produce an environment conducive of extracellular matrix formation. This was supported at the level of extracellular matrix content, where collagen (hydroxyproline) and non-sulphated glycosaminoglycans were detectible in all

material combinations. There was a trend observed at the 21 day time point indicating that the 40HA and 20HA materials evoked the greatest response in chondrogenic, extracellular matrix gene expression (COL2A1 and ACAN1), which aligns to these materials having the greatest hydroxyproline and non-sulphated GAG content at 21 days. These two molecules are key components of nasoseptal cartilage extracellular matrix (Neuman *et al.*, 2013), and to have a sustained elevation of their gene expression indicates that appropriate environmental cues are being provided for sustained cartilage formation. Nanocellulose fibrils and crystals are believed to have structural mimicry to collagen fibres and extracellular matrix ground substance respectively, which may contribute to the augmented gene expression profiles observed in this chapter.

SOX9 gene expression rose most significantly in the 20HA material, which as a upstream mediator of chondrogenicity, secures differentiation down the chondrocyte lineage, promotes cell survival and is a transcriptional activator of ACAN1 and COL2A1 (Lefebvre and Dvir-Ginzberg, 2017), which is likely to underpin the high levels of these genes being expressed in this material combination. The cartilage tissue arrangement within the NCHA and HA bioink formulations appears to emulate native cartilage (as seen in Chapter 3) in which chondrocytes adopting a round morphology exist in lacunae of 1 cell or a small cluster of cells, surrounded by dense extracellular matrix. At a biomechanical level, the production of the extracellular matrix did not appear to have a significant effect on the compressive strength or break force of any of the materials studied in the 21-day period. However, the histological evidence, with gene and ECM expression indicates that these materials offer a suitable mimicry of the nasoseptal cartilage tissue for bioengineering purposes.

### 5.4.5  Summary

Hyaluronic acid–nanocellulose composite bioinks demonstrate promising properties for 3D bioprinting cartilage as evidenced in this chapter. From a rheological perspective, all formulations have the capacity to be printed via extrusion based bioprinting mechanisms however the dominance of elasticity in

nanocellulose-dominant bioinks offer the most promise for superior post printing shape fidelity. The nanocellulose-dominant bioinks also offer the best chondrogenicity profile of all composite inks studied, had superior biomechanical properties prior to the addition of cells, and resulted in the greatest formation of extracellular matrix components. Crucially this novel bioink has the capacity to be crosslinked at a low dose of 5 µM $H_2O_2$, without detriment to its structural properties or cell viability.

# Chapter 6: A Comparative Analysis of Candidate Bioinks For 3D Bioprinting Cartilage

# Chapter 6: A comparative analysis of candidate bioinks for 3D bioprinting cartilage

## 6.1 Introduction

### 6.1.1 Background

This thesis has so far demonstrated that alginate can be augmented biologically and in terms of printability, through the addition of plant-derived nanocellulose. Furthermore, the printability profile of nanocellulose and its enhanced chondrogenicity, have proven advantageous in combination with hyaluronic acid, rendering a novel NCHA composite bioink for 3D bioprinting cartilage.

Cartilage extracellular matrix is a complex, heterogeneous substance, comprising a mixture of collagens, proteoglycans and glycoproteins, with each offering a biological and mechanical role to the tissues and cells into which it is deposited (Eyre, 2004; Han, Grodzinsky and Ortiz, 2011; Gao *et al.*, 2014). In order to achieve biological mimicry, composite bioinks: bioinks containing greater than one material, might best mirror this heterogeneity if like-for-like replacement is the ultimate goal of 3D bioprinting (Heid and Boccaccini, 2020). Furthermore, it is unlikely that a single material scaffold alone is able to offer desirable properties for printing, shape fidelity, bioactivity and compatibility specific to the intended target tissue type. In this thesis, the printability of nanocellulose complements the crosslinking ability of alginate and HA hydrogels to yield bioinks with structural and biological features that render it capable of enhanced chondrogenesis.

A side-by-side comparison of NCHA and NCA bioinks for tissue engineering has only been reported in the context of adipose tissue engineering (Henriksson, Gatenholm and Hägg, 2017) and iPSC proliferation and differentiation into chondrogenic lineages (Nguyen *et al.*, 2017). Whilst NCHA composite bioinks offered superior adipogenesis compared to nanocellulose-alginate, (Henriksson, Gatenholm and Hägg, 2017), alginate was superior to HA in maintaining the pluripotency of iPSCs in culture when blended with nanocellulose fibrils, and led to superior chondrogenic differentiation after five weeks of culture (Nguyen *et al.*, 2017). The relative printability and chondrogenic potential of these materials remains to be investigated in the context of facial cartilage tissue engineering.

In addition to the bioink and associated crosslinking agents, the entire process of bioprinting must be deemed biocompatible in order to be a viable *in vivo* solution. Extrusion based bioprinting operates through pneumatic or hydraulic driven mechanisms used to extrude bioink through a printer nozzle in a continuous filament (Kyle *et al.*, 2017). The printer usually has a cartridge connected to a straight or conical nozzle in order to enable precise deposition of filament, but depending on the viscosity of the bioink, high printing pressures may be warranted to enable continuous extrusion, often at the expense of cell viability (Rutz, Lewis and Shah, 2017). The process of extrusion 3D bioprinting also involves the conversion of extrusion pressure to shear stress. The printer nozzle is one factor that may influence the degree of shear experienced by cells in bioinks. Nozzle geometry: shape, length and diameter, each influence the degree of shear and may additionally influence cell viability (Billiet *et al.*, 2014). In addition to having an impact on viability, some cells and tissues are mechanosensitive, and even at non-cytotoxic levels of shear, the shear experienced through the extrusion bioprinting process may be sufficient to evoke a cellular response. Mesenchymal stem cells for example, are known to respond to biologically relevant levels of shear stress with an increase in osteogenic differentiation (Yourek *et al.*, 2010). Naturally, phenotypic retention in the intended tissue type is paramount for 3D bioprinting processes and divergence into unintended lineages may have adverse effects for the quality of the tissue that is produced.

### 6.1.2 Aims

Whilst in previous chapters, this thesis has demonstrated that nanocellulose augments HA and alginate hydrogels for 3D bioprinting, what remains unclear is which of these novel composites offers the best printability, chondrogenicity and biocompatibility profile for progressing towards 3D bioprinting cartilage for clinical use. As such, this chapter proceeds to determine the biological and mechanical differences between the NCHA and NCA bioinks and indicate whether either of these materials are potentially appropriate for clinical translation and which offers greater promise for the future of 3D bioprinting cartilage.

In order to determine the relative suitability of these bioinks for clinical use, the following objectives will be addressed:

- To determine the suitability of NCA, HA and NCHA bioinks for 3D bioprinting and to compare their printability profiles
- To compare the structural properties of each material in their crosslinked forms both without and with cells
- To ascertain whether the biomaterials offer chondrogenic potential in the form of gene expression, protein expression and extracellular matrix production
- To verify suitable biocompatibility of the HA based materials in their crosslinked states and following extrusion-based bioprinting

## 6.2 Experimental Protocols

### 6.2.1 Bioink preparation

HA powder with a 5% tyramine substitution was acquired from Lifecore Biomedical (Chaska, MN, USA) and hydrated using horseradish peroxidase solution in PBS (10U/ml) to yield a 30mg/ml hydrogel as described in Section 2.5.4. The material was delivered in a sealed, sterile formulation and hydrated in a Class II cabinet to prevent contamination. The resulting formulation was kept as pure HA (HA) for subsequent experiments.

A 2.5% (w/v) alginate solution was produced using UV sterilised sodium alginate powder dissolved in sterile tissue culture grade water as described in Section 2.5.3.

Nanocellulose blend (as described in Section 2.5.1) was neutralised, sterilised and rehydrated in tissue culture grade distilled water as previously described (Section 2.5.2). The nanocellulose was then mixed in a 75:25 volume:volume ratio with either the alginate or the HA hydrogel to yield NCA and NCHA composite bioinks respectively, each comprising 75% nanocellulose blend. All bioinks were maintained at 4°C until use and allowed to equilibrate to 37°C for 20 minutes in a water bath prior to mixing with cells.

### 6.2.2 Printability Assays

A CELLINK INKREDIBLE extrusion-based bioprinter was used to assess the printability of each candidate bioink. The minimum extrusion pressure of each material was determined by gradually increasing the extrusion pressure from 0 kPa until the minimum pressure at which the bioink was deposited continuously through a 22 G nozzle. Each printhead was thereafter left open until the bioink was extruded for approximately three seconds. After extrusion, the filaments were observed for continuity as per the filament drop test described in Section 2.6.5. Each bioink was then printed using the line resolution assay, in which three parallel straight lines of 1 mm thickness were printed as described in Section 2.6.3.1. These lines were visualised under light microscopy at 4x magnification and their width was measured at three equally spaced points using CellSens software (Olympus, Tokyo, Japan). Next, each material was tested for its ability to print a grid structure as described in Section 2.6.3.2. The spaces between intersecting lines within the grids were measured using digital callipers and visualised under 4x magnification. The intersecting angles between filaments was measured using CellSens software (angle resolution), and the areas of the spaces between four intersecting lines were measured from a minimum of three spaces per grid structure (grid resolution). Finally, an STL file of a human auricle was used to print a 3D ear in each of the candidate bioinks and compared to a control auricle of the same design printed in PLA using an Ultimaker 3 Printer (Ultimaker, Utrecht, NL).

### 6.2.3 Atomic force microscopy (AFM)

AFM was used to characterise the Young's modulus and surface topography of the different material combinations after crosslinking with the optimised doses in the previous chapters. 100 µl discs of NCHA, HA and NCA material were produced and crosslinked using either 100 µl of 5 µM $H_2O_2$ or 0.5 M $CaCl_2$.

The discs were affixed to a glass coverslip using a single droplet of mounting medium (VWR, PA, USA) as described in Section 2.11.1. The materials were characterised using a Bruker Bioscope Catalyst (Bruker, MA, USA) and MikroMasch CSC37 cantilevers (Tallinn, Estonia) as described in Section 2.11.1,

applying a maximum force of 4 nN. The elastic (Young's) modulus of each material was calculated using Nanoscope analysis software (v1.50, Bruker, MA, USA) taking at least 50 points per sample. Sample topography was captured using PeakForce Quantitative NanoMechanics mode (Bruker, MA, USA).

The above process was repeated using the same batch of materials, albeit on this occasion encapsulated with 300,000 human nasoseptal chondrocytes (CDCs) per 100 µl disc of biomaterial. The discs were cultured for 21 days in standard culture conditions and thereafter removed from culture medium, washed with PBS and affixed to coverslips as described above. The data acquired from each set of experiments was compared to observe for changes in material properties after 21 days of co-culture with chondrocytes.

### 6.2.4  Chondrogenic and osteogenic gene expression analysis

Triplicates of each biomaterial were mixed with 500 µl TRIzol (Invitrogen, Thermofisher) and subsequently degraded with a TissueRuptor II probe for 30 seconds. The lysate was processed using Qiagen QIAshredder and Rneasy Mini Extraction kits (Qiagen, Germany; as described in Sections 2.8.2) to yield RNA for reverse transcription. The RNA was quantified and assessed for purity using a Nanodrop Spectrophotometer. The concentrations of RNA in each sample were diluted with ultrapure nuclease free water across repeats to yield 11 µl samples each containing 250 ng RNA. The RNA was converted to cDNA through reverse transcription as described in Section 2.8.4, and quantified for the expression of COL2A1, SOX9 and ACAN1 relative to housekeeping gene expression (RPL13A and TBP) as per Section 2.8.7. Each material was harvested for RNA extraction and PCR analysis at 4 hours, 24 hours, 7 days, 14 days and 21 days of culture using 3 biological repeats. All relative gene expression values were expressed as fold-changes using the ΔΔCt method compared to a control value (Section 2.8.8): in this case NCA at the 4-hour time point. The gene expression of each material at each timepoint was compared statistically to the NCA 4-hour value for the same gene using an unpaired, two-tailed t-test. The 21-day time point was repeated for each chondrogenic gene, and also osteogenic gene markers: ALP,

OCN and RUNX2, using a total of 6 biological repeats to further elucidate the differences between biomaterials.

### 6.2.5 Analysis of extracellular matrix production

### 6.2.5.1      Hydroxyproline assay

10 mg of each cell-laden material was weighed and added to a PTFE-lined screw cap microcentrifugation tube with 100 μl of ultrapure water. The mixture was homogenised and hydrolysed using 12M hydrochloric acid at 120°C for 3 hours as described in Section 2.9.4. The hydrolysed lysate was mixed and centrifuged at 10,000 g for 3 minutes. 10 μl of the supernatant was transferred to a 96 well plate in triplicate along with one spiked sample and a set of hydroxyproline standards and evaporated at 60°C. 100 μl of Chloramine T and oxidation buffer was added to each well and left for 5 minutes, with a further 100 μl mixture of DMAB reagent diluted in perchloric acid and isopropanol added thereafter for 90 minutes at 60°C. The plates were then read at 560nm absorbance and analysed as per Section 2.9.4.

### 6.2.5.2      Dimethylmethylene Blue Assay

The DMMB assay was used to quantify glycosaminoglycan (GAG) content in each material at 7 days and 21 days of culture. The cell-laden biomaterial semispheres of each bioink were first digested using 300 μl of a 10 mg/ml solution of type I hyaluronidase at 37°C for 1 hour. The remaining tissue was lysed according to Section 2.9.1 to yield protein isolates for GAG quantification. Isolates were diluted 1 in 50 with distilled water and added to the wells of a 96 well plate in triplicate with 200 μl DMMB reagent. The plates were read immediately at 525 nm compared to a series of chondroitin standards ranging from 0 to 50 μg/ml as outlined in Section 2.9.3.

### 6.2.5.3      Histological analysis of candidate bioinks

To determine the arrangement of extracellular matrix relative to the cells within the biomaterials, histological analysis was performed. Cell-laden biomaterial

semispheres were immersed in 4% paraformaldehyde solution for 30 minutes and then washed three times in PBS (Section 2.10.1). The constructs were then immersed in 1% (w/v) Alcian Blue stain as described in Section 2.10.3.2 for 30 minutes and washed sequentially with hydrochloric acid and distilled water until no further stain was 298eleaseed. Alternatively, constructs were immersed in 0.1% toluidine blue solution as described in Section 2.10.3.3 for 10 minutes and washed until clear. Constructs were also stained with Safranin O as per Section 2.10.3.4 using first Fast green for 20 minutes, washed with acetic acid and stained thereafter with Safranin O stain for 40 minutes. The semispheres were viewed under brightfield microscopy at 4, 10 and 20x magnification with images taken throughout the construct (in x, y and z axes) to ensure the images captured were representative of the whole material (as per Section 2.10.3.5).

### 6.2.6  Porosity, swelling and crosslinking assays

100 μl discs of each biomaterial were produced and crosslinked using 100 μl of either 0.5 M $CaCl_2$ or 5 μM hydrogen peroxide solution. 6 repeats of each condition were produced and assessed for porosity and swelling as described in Sections 2.11.3-2.11.4. The discs were transferred to 48 well plates and left either left for 24 hours in 1 ml PBS at room temperature (porosity) or added to an incubator set at 37°C. The discs were removed and excess PBS blotted away using tissue paper. Each disc was weighed and the wet weight recorded. The discs were returned to the 48 well plate and transferred to a non-humid 37°C chamber for 72 hours. The discs were weighed again at the end of this period (dry weight) and recorded. Porosity and swelling were calculated from the formulae outlined in Sections 2.11.4 and 2.11.3.

To calculate change in crosslinking diameter, discs were measured using digital callipers prior to, and after the completion of, crosslinking as described in Section 2.11.5. The change in disc diameter was expressed as a mean percentage change in diameter based on three readings per disc with discs produced in triplicate.

### 6.2.7  Biomechanical compression testing

200 µl cylindrical disks of each biomaterial were produced using the 3D printed mould described in Section 2.11.2 to produce equal cylinders of 6 mm diameter and 7 mm length. The materials were crosslinked within the moulds using 5 µM $H_2O_2$ for 5 minutes or 0.5 M $CaCl_2$ and transferred to the $1^{ST}$ Mechanical Compression Device (Tinius Olsen, Redhill, UK) in PBS for compression testing. Each material was blotted dry with tissue paper and compressed using a 25 N load cell as outlined in Section 2.11.2, to determine the break distance, break force and ultimate compressive force. These values were used to calculate the ultimate mechanical stress, break stress and strain to failure of each material. Materials were examined without cells, and then after culture with cells for 21 days to determine whether the cells and the matrix they produced had any significant effect on the mechanical properties of the material over this time course.

### 6.2.8  Biocompatibility analysis of candidate biomaterials

300,000 cells were added to 100 µl of each material as per Section 2.5.6 and crosslinked with either 5 µM $H_2O_2$ or 0.5 M $CaCl_2$. The viability of the cells in the biomaterials was assessed using alamarBlue assays, live dead assays and LDH assays. A minimum of three replicates per condition and timepoint was performed.

### 6.2.8.1     LDH Assay

Cells seeded into each of the crosslinked biomaterials were immersed in media along with cell only and media only controls. One of the cell-only controls was subjected to lysis buffer as a positive control. The cell-laden biomaterials were incubated in standard culture conditions for 4 hours, after which 50 µl of media surrounding each sample were acquired and transferred to a 96 well plate, along with reaction media for 30 minutes. The reaction was terminated at 30 minutes using stop solution and the plates were read immediately at 490 nm and 680 nm

as described in Section 2.12.2. The % cytotoxicity was determined using the lysed cells as a positive control, assumed to have 100% lysis, using **Equation 11**:

$$\% \text{ cytotoxicity} = \frac{\text{Treated LDH activity} - \text{spontaneous LDH activity (cells only)}}{\text{Maximum LDH activity (lysed cells)} - \text{spontaneous LDH activity}} \times 100$$

For each condition, samples were taken in triplicate from 3 separate wells, giving a total of 9 replicates per condition.

### 6.2.8.2    Live dead assay

Live dead assays were performed using a mammalian live-dead cell viability assay kit (Thermofisher Scientific, MA, USA). 1 ml of a mixture containing 1:1000 Calcein-AM and 1:500 Ethidium homodimer-1 was applied to a sample of each of the cell-laden biomaterials each well after 24 hours of standard culture. The solution was protected from light and left for 45 minutes in culture conditions. The live cells were visualised using fluorescence microscopy to detect cells stained with calcein-AM and dead cells with Ethidium homodimer-1 as described in Section 2.12.1. Representative images were acquired from 3 points taken from 3 repeats at 10x magnification and repeated at 7 and 21 days for each material.

### 6.2.8.3    AlamarBlue Assay

AlamarBlue dye (ThermoFisher Scientific, MA, USA) was used to provide an indication of cell number and metabolic activity. 1 ml of 10% (v/v) AlamarBlue solution was added to each well containing the cell-laden biomaterials for 4 hours. The colorimetric change was quantified as described in Section 2.6.1 with 100 µl samples taken from each well, along with media only controls (no cells), taken after 4 hours and read at 570 nm (reduced form) and 600 nm (oxidised form) wavelengths. The two wavelength readings for each well were used to calculate the percentage of the alamarBlue solution that had reacted to its reduced form as a marker of cell metabolic activity, calculated as per Section 2.7.1. Readings

were taken in triplicate from three biological repeats at timepoints of 4 hours, 7 days, 14 days and 21 days.

### 6.2.9 Computational modelling of shear stress

Computational fluid dynamics was used in collaboration with Dr Feihu Zhao and Josh Roberts (Swansea University College of Engineering) to model the amount of shear stress the cells experience during the 3D printing process at the pressure and nozzle size used for 3D printing. The nozzle (22G) and syringe used in the CELLINK INKREDIBLE printer, were measured using digital callipers and from the Product Information Sheet as described in Section 2.6.10. These measurements were translated into a 3D model of the nozzles and syringes used in SolidWorks software (MA, USA) which were subsequently exported as a .stl file to TetGen software (Berlin, Germany) to undergo mesh mapping for modelling purposes. The boundary conditions of the internal surface of the nozzle were set as non-slip walls with the outlet pressure set at atmospheric values (zero fluid dilatation). A range of extrusion pressures from 20 to 40 kPa were used to model the fluid velocity and shear stress within the bioink at these printing pressures, plotted against increasing extrusion time. To determine the effect of the predicted fluid velocity and shear stresses on chondrocyte behaviour, 100 μl semispheres of NCHA bioink were produced using a printing pressure of 30 kPa, and cell viability was determined immediately, and at either 4, 18 or 24 hours using a combination of alamarBlue, LDH and live-dead assays (as described in 6.2.8) alongside gene expression analysis for chondrogenic and osteogenic markers as outlined in 6.2.4 at 4 hours and 72 hours post-printing. As a control population, 100 μl semispheres of NCHA bioink were produced manually with a comparable volume, seeding density and geometry using a 1 ml syringe (no nozzle attached) rather than through bioprinting.

### 6.2.10 Statistical analysis

Data sets were assessed for normality (Gaussian distribution) visually and where needed using an Anderson-Darling test. Statistical analysis were thereafter selected accordingly. All data presented is the mean value of technical +/-

biological replicates which is presented graphically with error bars depicting standard deviation unless otherwise stated.

For statistical comparisons between two dependent variables, either a t-test (+/- Welch's correction; where standard deviations were not equal) or Mann Whitney test (where data was not normally distributed) was used. In this chapter, the following data sets were analysed using unpaired, two tailed t-tests: PCR data, where expressed relative to an initial, control time point (Figure 6.8, Figure 6.9, Figure 6.10, Figure 6.26); Live dead assays post-printing (Figure 6.24). Whereas Mann Whitney tests were used for: Angle and grid assay resolution tests (Figure 6.2) and LDH assays in printed and unprinted cells (Figure 6.25).

For statistically analysing multiple dependent (>2) variables, typically a one-way ANOVA was used with a Tukey's post hoc test for multiple comparisons. In this chapter this analysis was used for: Line fidelity assays (Figure 6.1); Porosity, swelling and crosslinking changes (Figure 6.7); 21 day gene expression data (Figure 6.11, Figure 6.12). Where data was abnormally distributed, a Kruskal Wallis ANOVA with Dunn's post hoc test was used. In this chapter this includes: Young's modulus (Figure 6.5).

A 2-way ANOVA was used when multiple dependent variables (>2) were used across two separate series (such as different time points), with a Tukey's post hoc test. In this chapter, this analysis was used for the following data sets: Biomechanical compression and AFM data with/ without cells (Figure 6.15, Figure 6.16, Figure 6.17, Figure 6.18) and AlamarBlue Assays (Figure 6.22, Figure 6.25).

## 6.3 Results

In order to make a valid comparison between the NCA and NCHA bioinks, their printability, structural and mechanical characteristics are directly compared along with a direct comparison of chondrogenesis at the level of gene expression and ECM production. This is contextualised with biocompatibility assessments including in the environment of cell-laden bioinks in the 3D bioprinting apparatus.

### 6.3.1  Printability assays of candidate bioinks

As an initial marker of bioink printability, the ability of the bioinks to be printed into straight lines and grid shapes was assessed using the assays described in Section 6.2.2. The diameter of each straight line was measured and expressed in microns from 9 separate measurements. An accurate and reproducible bioink would have a line diameter close to 1000 microns (1 mm) with low variability between measurements. Of the lines printed (Figure 6.1); the NCHA had the closest mean to 1000 microns with a mean of 1004±48. The mean values for alginate were 1642±263.3; for NCA 1123 ± 147.6 and for HA only 984.4 ±116.7. The range was greatest for HA at 888, followed by alginate (802), NCA (371) and NCHA (120). The NCA (p=0.01), HA (p=0.0005) and NCHA (p=0.0003) were all significantly closer to 1 mm than alginate but no significant differences were observed between these three materials.
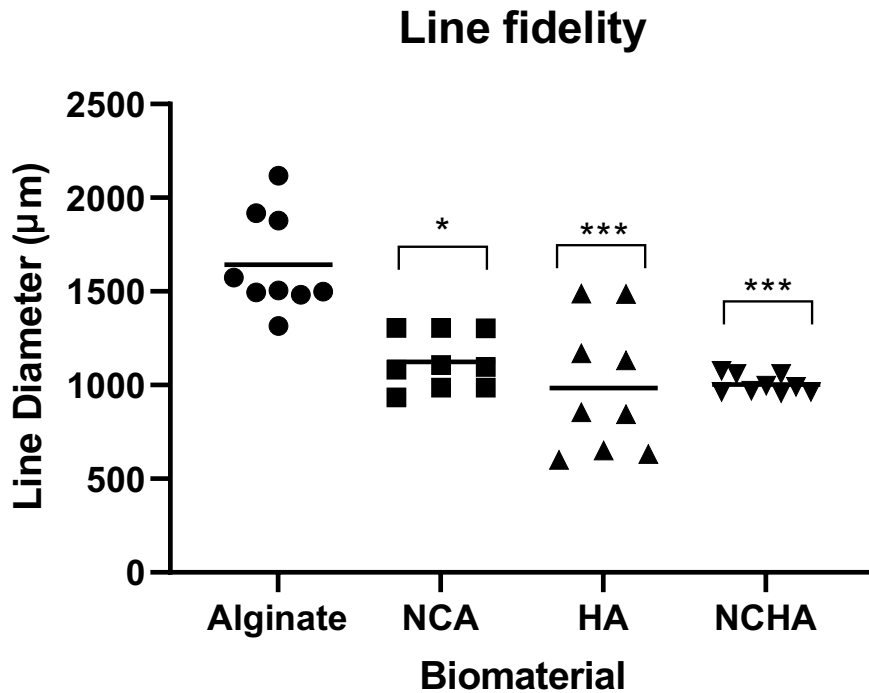
# Line fidelity



*Figure 6.1: Line fidelity test of candidate bioinks. Each repeat measurement is plotted for each bioink with the mean value depicted by horizontal bars. The range of the line diameters is therefore demonstrated by the spread of datapoints in which NCHA demonstrates the lowest range (and thus highest consistency). Statistical significance of each material relative to alginate is expressed . \*=p<0.05; \*\*\*=p<0.001*

The 3D printing of a grid was then attempted using each of the materials in turn (Figure 6.2). Both alginate and HA could not be printed into a recognisable grid and as such, it was not possible to generate measurements for comparison. Both NCA and NCHA were printed successfully into grids and the resolution of angles at crosspoints (90°) and the areas of the square spaces between gridlines were measured. Both the nanocellulose-based bioinks demonstrated angles in excess of 90° at the junctions of gridlines (Figure 6.2A+B), perhaps owing to the drag of the dispersing nozzle over the existing gridline with mean angle values of 94.17± 4.6 in NCA and 95.8± 3.6 in NCHA. This difference was not statistically significant between materials (p=0.7). Similarly, there were no significant differences between the mean area of the spaces between gridlines (p=0.4) with values of 141.4 for NCA and 142.8 for NCHA (Figure 6.2C+D).

A — Angle Resolution Accuracy

B

C — Grid Assay resolution

D
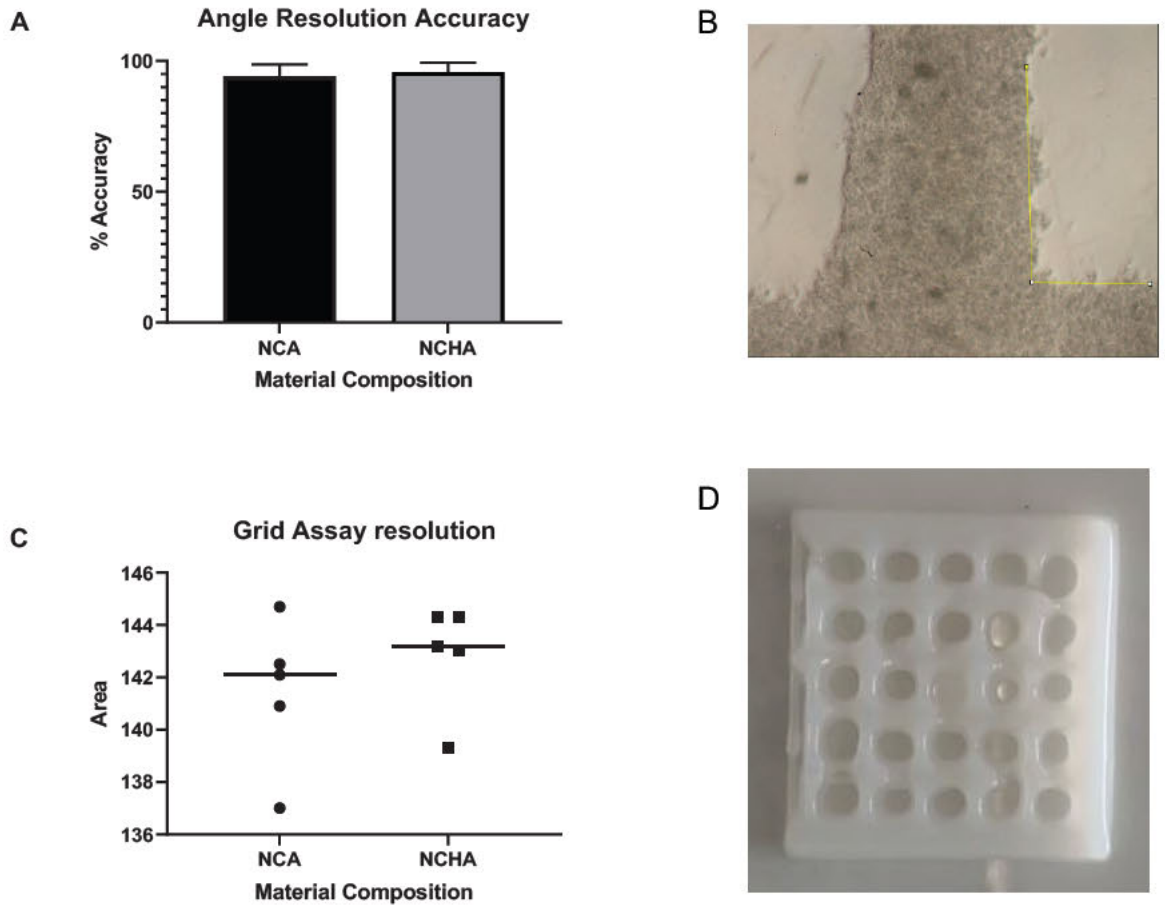
*Figure 6.2: Resolution tests of candidate bioinks in which NCA and NCHA were compared for resolution and accuracy. The angles between gridline crossing points were viewed under 4x magnification and measured using ImageJ (B) and expressed as a percentage relative to 90º (A). The spaces between gridlines (an example grid is demonstrated in D) were compared between bioinks and depicted graphically in (C) where each data point is plotted alongside a horizontal bar to demonstrate the mean.*

HA        Alginate        NCA
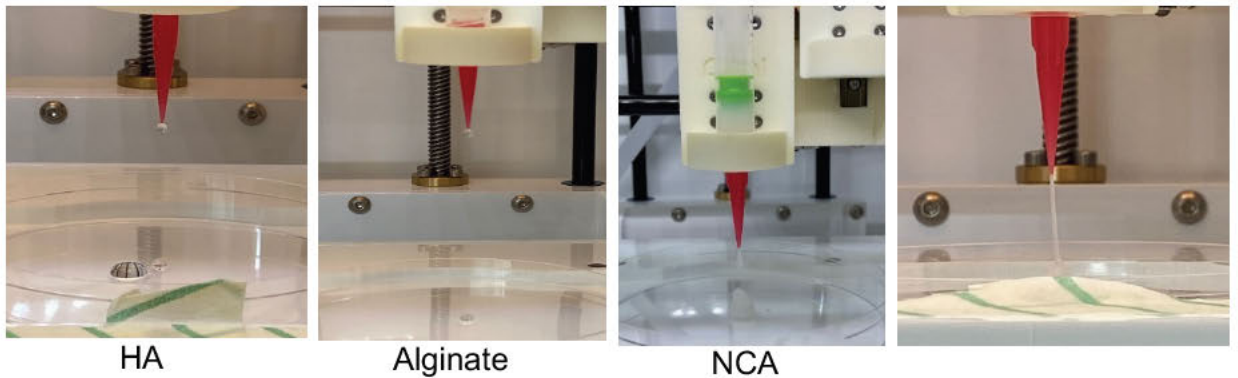
*Figure 6.3: Filament drop tests of candidate bioinks using the CELLINK INKREDIBLE printer. Continuous filaments were not achievable in the HA or Alginate bioinks indicating undergelation. Both NCA and NCHA were able to produce continuous filaments however this was more pronounced in the NCHA than the NCA.*

An additional test of biomaterial suitability for printing is the filament drop test, which involves extruding a filament into air. A weak filament will form a droplet at the nozzle tip and be unable to form 3D structures once printed, a correctly gelled bioink will form a smooth uniform, continuous filament and an overgelled filament will distort upon extrusion in a non-uniform manner, also unsuitable for providing the accuracy of 3D printing. Here, the HA and alginate materials alone were unsuitable for 3D printing at the concentrations used, forming droplets at the end of the extrusion nozzle indicating under-gelation in their uncrosslinked forms. NCA and NCHA however both extruded well in a smooth uniform filament initially, with a longer filament being produced in the NCHA bioink (Figure 6.3).

As a proof of concept, the bioinks were next 3D printed into an entire human auricle to determine its comparability to the complex 3D geometry of this anatomical structure, with the same auricle printed in PLA as a control (Figure 6.4).
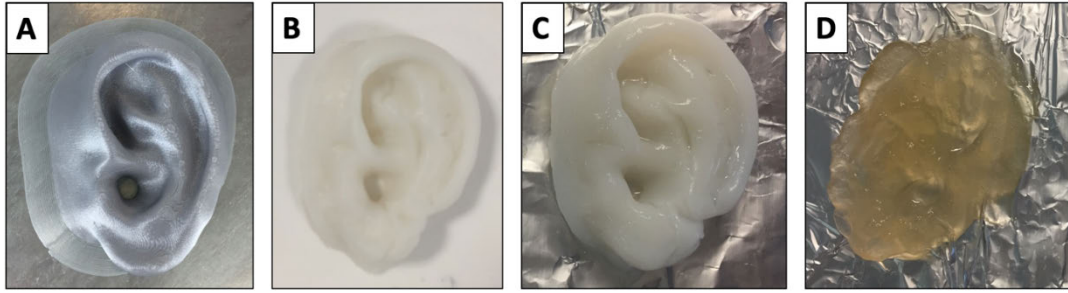
*Figure 6.4: Digital photographs of human auricles printed in A) Polylactic acid (using an Ultimaker 3 Printer) as a control B) NCA crosslinked with 0.5M CaCl$_2$ C) NCHA crosslinked with 5µM H$_2$O$_2$ D) Alginate crosslinked with 0.5M CaCl$_2$. The biomaterials were printed using the CELLINK INKREDIBLE printer. HA was unsuccessfully printed (not shown).*

Each of the nanocellulose-based materials were able to reproduce the structure of a human auricle with good resolution and fidelity. This was not the case with the alginate or HA bioinks that, despite crosslinking, were unable to retain the fidelity of a human auricle.

### 6.3.2    Mechanical characterisation of candidate bioinks

AFM was used to test the crosslinked biomaterials for their elastic (or Young's) modulus as a measure of their ability to withstand compressive stress (Figure 6.5). The HA material appeared to have the greatest Young's modulus with a mean of 30.4 kPa ± 14.8, the NCHA had a mean of 11.84± 12.15 and NCA had a mean Young's modulus of 22.1 kPa±19.2. The greatest range of values was observed in the NCHA bioink, of 112.8 compared to 71.51 in HA and 117.2 in NCA. The differences between the Young's moduli of the biomaterials without cells was highly significant (p<0.0001) for all comparisons.

## Acellular materials
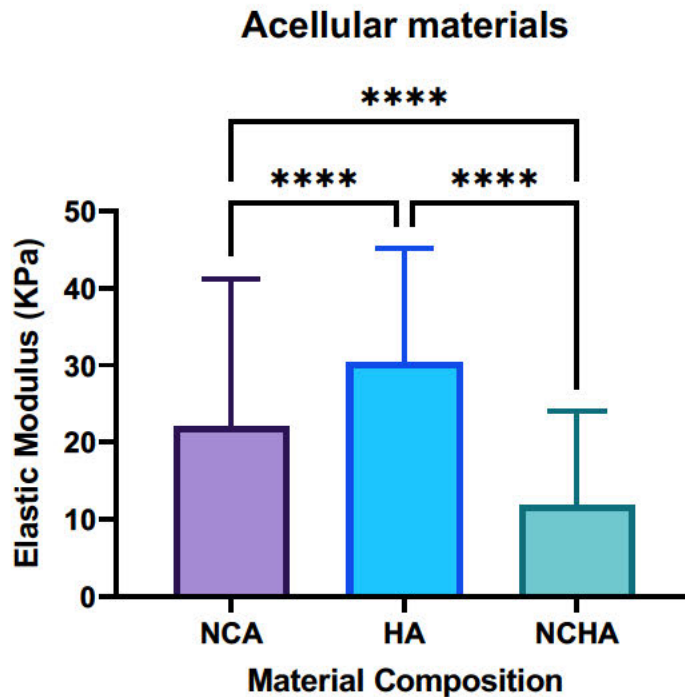


*Figure 6.5: Young's (elastic) modulus of candidate biomaterials after crosslinking using AFM. Mean values from at least 50 separate data points are presented with SD, statistical significance from a Kruskal Wallis ANOVA is presented in which HA demonstrates the highest elastic modulus of all the bioinks tested. ****=p<0.0001*

Surface topography was imaged using the AFM apparatus (Figure 6.6) after crosslinking to determine fibril arrangement and pore geometry. Each of the materials demonstrated a degree of surface roughness with an extensive network of pores and fissures visible on the material surface. The NCA material demonstrated a series of small (<1micron) deep pores (Figure 6.6C) which were much more pronounced than on the NCHA material. The HA material demonstrated numerous small pores (<1 micron diameter) but also wider pores of approximately 3 microns diameter on the material surface (Figure 6.6B). On the surface of the NCHA material at higher magnification (Figure 6.6A) interspersed entanglements of nanocellulose fibrils appeared to be visible on the material surface.
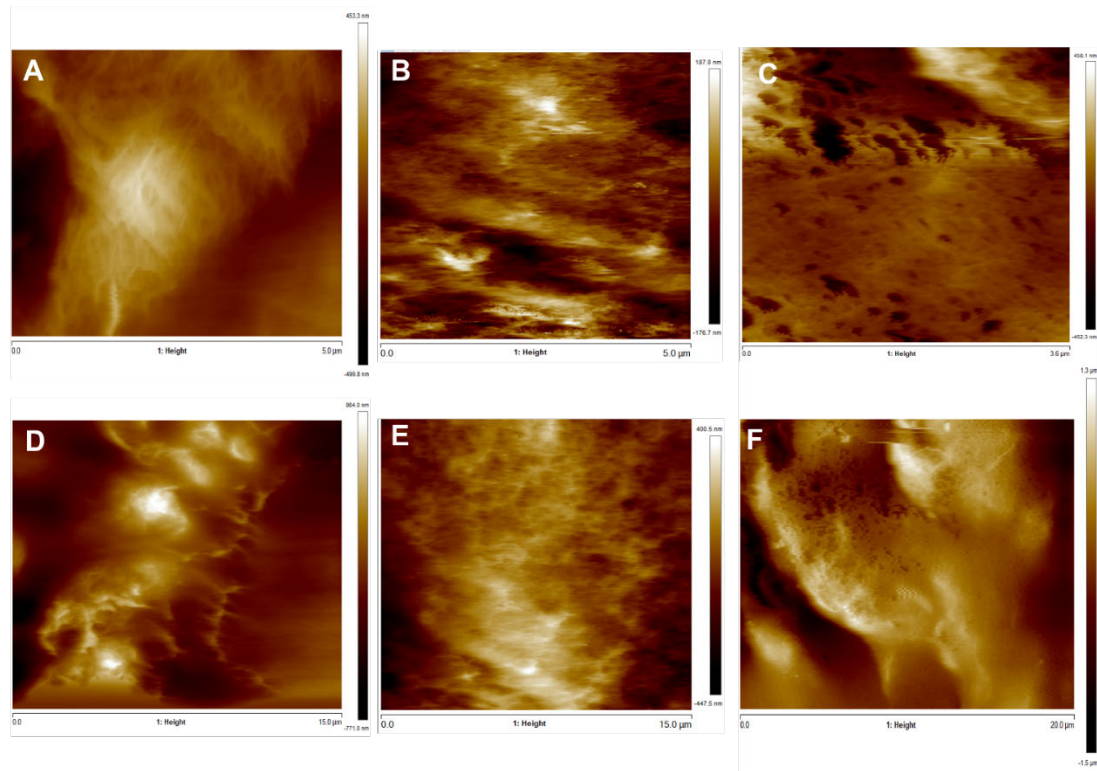
*Figure 6.6: AFM surface topographic images of crosslinked biomaterials in which two representative images are presented per material. A) and D) are images of NCHA taken at windows of 5 micron (A) and 15 microns (D). Surface topography demonstrates a range of pores from peaks of 864 nm to troughs of -771 nm. B) and E) demonstrate surface topography of HA with higher degrees of porosity across windows of 5 microns (B) and 15 microns (E) in which maximum peaks of 400.5nm and troughs of -447.5 nm were observed. C) and F) depict NCA taken at windows of 3.6 microns (C) and 20 microns (F), in which surface roughness spanned peaks of 1.3 microns to troughs of -1.5 microns.*

The biomechanical properties of the candidate biomaterials were tested for porosity, swelling and changes in diameter after crosslinking (Figure 6.7). Although the mean values of porosity differed between materials, no significant differences were noted. Though the highest porosity value was seen in the NCA bioink of 78.9%, HA (53.0%) and NCHA (59.2%) had lower mean porosities but this was not significant (HA 53.0% p=0.07, NCHA 59.2% p=0.2). With regard to swelling, after 24 hours in culture conditions, the NCA had the greatest mean swelling of 16.5%, which was significantly higher than NCHA (2.19%, p= 0.02). HA was also higher than NCHA with a mean swelling of 11.1% (p=0.0006). The change in diameter post-crosslinking was also noted to be a positive change in NCA (indicative of swelling during the crosslinking process) with a mean increase

of 6.6% in diameter. This was significantly different to HA (-5.8%,) and NCHA (-2.0%) both of which reduced in diameter post-crosslinking. The change in diameter of HA post-crosslinking was also significantly different to NCHA (p<0.0001).
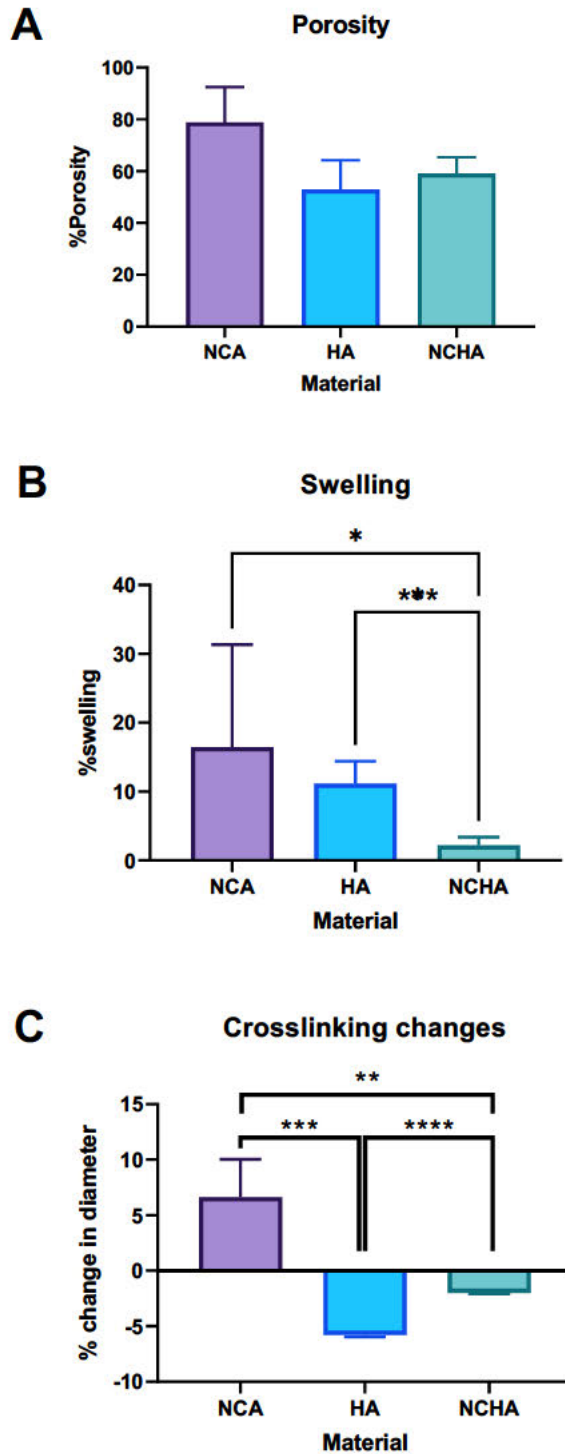
*Figure 6.7: Biomechanical properties of candidate bioinks. A) Porosity of candidate biomaterials expressed as a mean percentage of total material with standard deviation, n=4. B) Mean % swelling from post-crosslinking to fully hydrated hydrogel for each biomaterial with standard deviation, n=4. C) Change in biomaterial semisphere diameter following completion of crosslinking, n=4. \*=p<0.05, \*\*=p<0.01; \*\*\*=p<0.001; \*\*\*\*=p<0.0001*

### 6.3.3  Chondrogenic potential of bioinks

#### 6.3.3.1      Chondrogenic gene expression

In order to determine the relative chondrogenic potential of each bioink, gene expression profiles for each material were characterised over a 21-day time period for the chondrogenic genes SOX9, ACAN1 and COL2A1. The expression of aggrecan was noted to increase significantly in each biomaterial over the course of 21 days (Figure 6.8), relative to expression in NCA at 4 hours. Within the NCA material itself the gene expression of ACAN1 was 7.5-fold higher at 21 days than 4 hours ($p<0.0001$) but not significantly higher at any earlier timepoints. In the HA material, aggrecan expression was significantly higher than NCA at 4 hours from the earlier timepoint of 7 days (2.8-fold higher; $p=0.004$) and continued to rise, as seen at 21 days (4.4-fold higher, $p<0.0001$). The NCHA bioink also demonstrated a statistically significant rise in gene expression at 7 (3.4-fold higher, $p<0.0001$) and 21 days (13.4-fold higher, $p<0.0001$). The differences in gene expression levels at the 21-day time point were statistically different ($p<0.0001$) when compared across this timepoint. The relative gene expression at 7 days was also significantly higher than NCA in the NCHA ($p=0.001$) and HA ($p=0.04$) biomaterials.
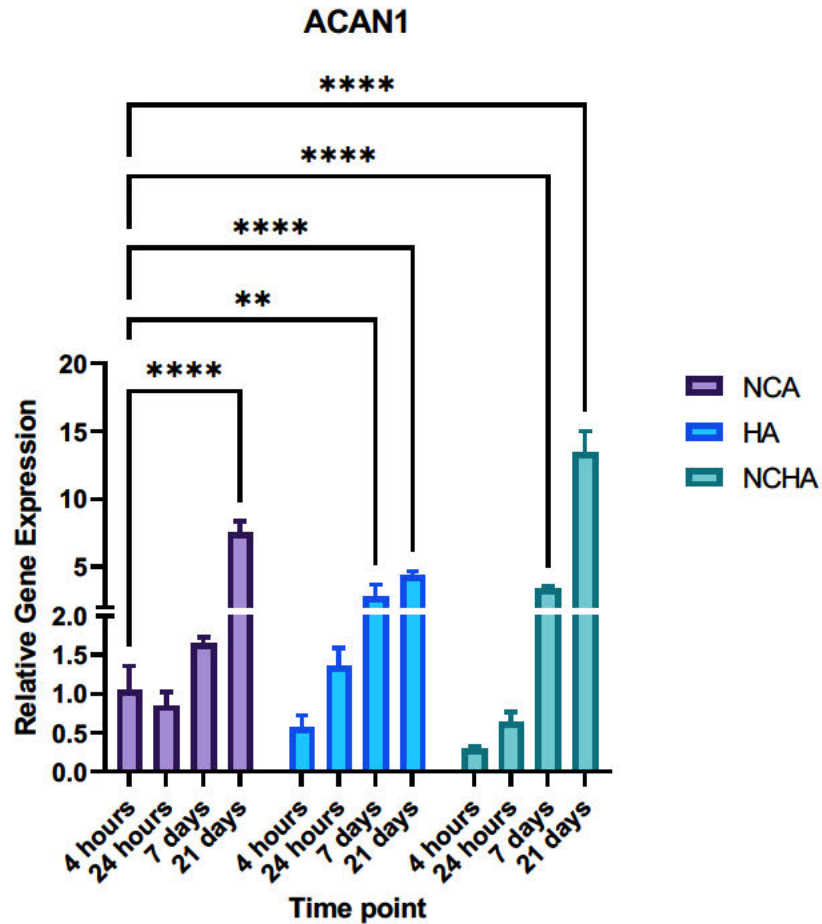
*Figure 6.8: Aggrecan gene expression profile of different biomaterials (NCA, HA and NCHA) over a 21-day course. All relative gene expression values are presented as a mean of three biological repeats (in technical triplicate) with standard deviation relative to NCA at 4 hours. Statistical analysis from unpaired t-tests with the reference population (NCA 4 hours) is presented. \*\*=p<0.01; \*\*\*\*=p<0.0001.*

Type II collagen demonstrated a similar temporal pattern to that observed for ACAN1 over the 21-day time course, with statistically significant increases in COL2A1 expression seen in NCA (57.9-fold increase, $p < 0.0001$), HA (20.0-fold increase, $p < 0.0001$) and NCHA (43.3-fold increase, $p < 0.0001$) at day 21 relative to NCA at 4 hours (Figure 6.9). The expression of COL2A1 was markedly lower at 4 and 24 hours in the HA and NCHA materials relative to NCA with gene expression levels less than 0.5-fold of NCA at 4 hours, however these were not statistically significant differences. Between the materials, no statistically significant differences were observed until 21 days, where the relative gene

expression of COL2A1 was significantly higher in NCA (p<0.0001) than NCHA and HA. NCHA was also significantly higher than HA at this time point (p<0.0001).
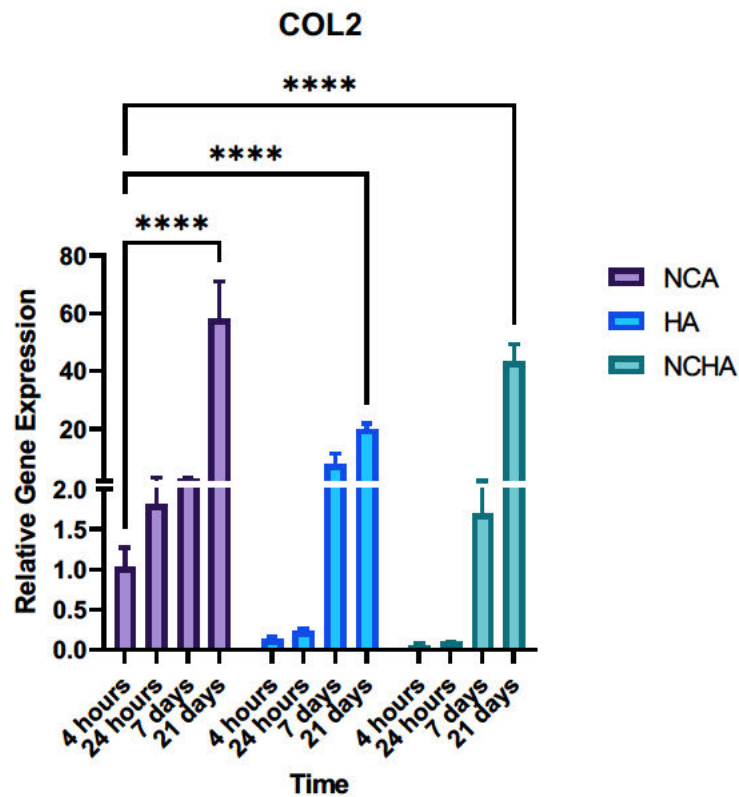


*Figure 6.9: Type 2 collagen gene expression profile of different biomaterials (NCA, HA and NCHA) over a 21-day course. All relative gene expression values are presented as a mean of three biological repeats (in technical triplicate) with standard deviation relative to NCA at 4 hours. Statistical analysis from unpaired t-tests with the reference population (NCA 4 hours) is presented.. ****=p<0.0001.*

SOX9 gene expression demonstrated a less linear pattern over the 21 day time course than the other genes studied (Figure 6.10). In NCA, the levels of SOX9 fluctuated across the 21 days, with no statistically significant differences observed relative to 4 hours. The gene expression levels at 24 hours and 21 days were greater than double that seen at 4 hours however. In HA, the chondrocytes demonstrated a significantly higher expression of SOX9 at the earlier timepoints of 4 (11.9-fold higher, p=0.0001) and 24 hours (8.6-fold higher, p=0.0106), but the expression then started to decline relative to NCA at 4 hours in the later timepoints of 7 and 21 days (3.7- and 5.4-fold respectively; not significantly different to NCA at 4 hours). NCHA however, demonstrated a sustained elevation

in relative gene expression over 21 days, which had an upwards trajectory when compared to NCA at 4 hours. Relative gene expression at 4 hours (9.3-fold, p=0.004), 7 days (8.4-fold, p=0.014) and 21 days (20.1-fold, p<0.0001) were all significantly higher than the NCA 4-hour time point. At 21 days, the relative gene expression in NCHA was significantly higher than both NCA and HA (p<0.0001) using Tukey's multiple comparison test.
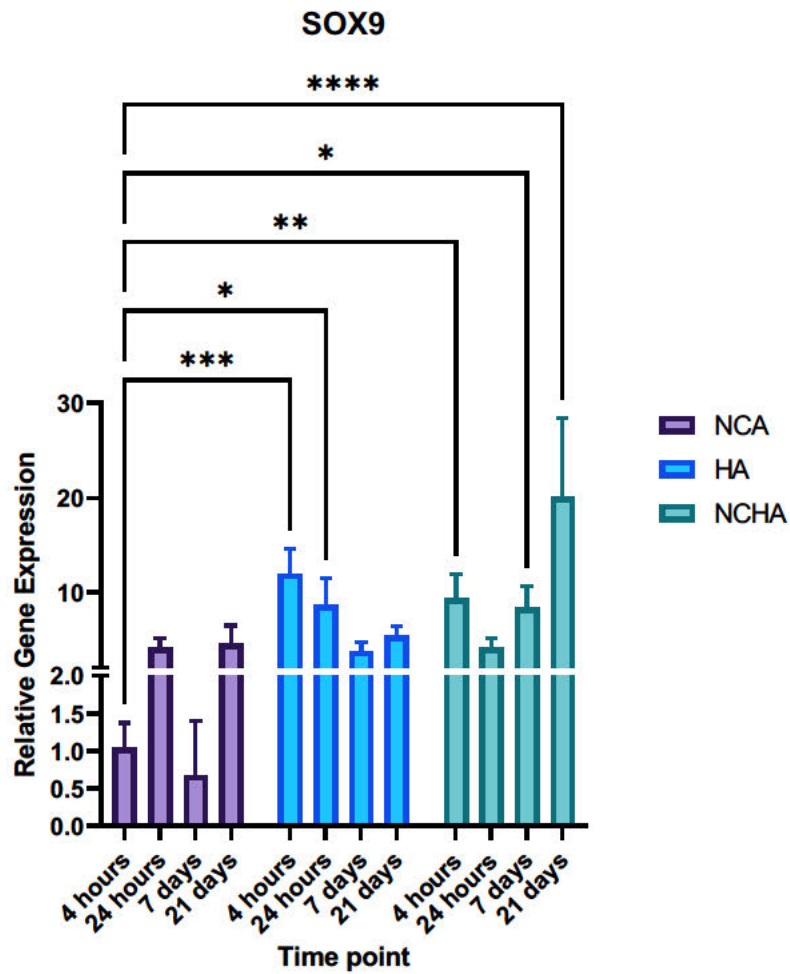


*Figure 6.10: SOX9 gene expression profile of different biomaterials (NCA, HA and NCHA) over a 21-day course. All relative gene expression values are presented as a mean of three biological repeats (in technical triplicate) with standard deviation relative to NCA at 4 hours. Statistical analysis from unpaired t-tests with the reference population (NCA 4 hours) is presented. \*=p<0.05, \*\*=p<0.01; \*\*\*=p<0.001; \*\*\*\*=p<0.0001.*

In summary, each of the candidate biomaterials appeared to show an increase in chondrogenic gene expression with time. However, the HA-containing bioinks showed greater levels of SOX9 expression, whereas the NC-containing inks promoted greater ACAN1 and COL2A1 expression.

### 6.3.3.2 Chondrogenic and osteogenic gene expression in long term culture

The most significant differences in gene expression were seen across the materials at the end-point of 21 days. As such, further biological repeats were conducted at 21 days to confirm the trends seen across the timepoint series (Figure 6.11) and as calcification and ossification appears to be a late manifestation of tissue engineered cartilage, to enable a comparison with osteogenic gene expression at this time point (Figure 6.12).

At 21 days, chondrogenic gene expression was comparable in HA and NCA across all genes analysed, whereas cells in NCHA demonstrated higher relative gene expression (compared to NCA at the 21 day time point) in all genes: ACAN1 (3.5-fold higher, $p<0.0001$), SOX9 (3.1-fold higher, $p=0.0009$) and COL2A1 (3.8-fold higher, not statistically significant). There was a large amount of heterogeneity in the gene expression of COL2A1 across biological repeats which may have influenced the statistical significance of this gene's expression at 21 days.
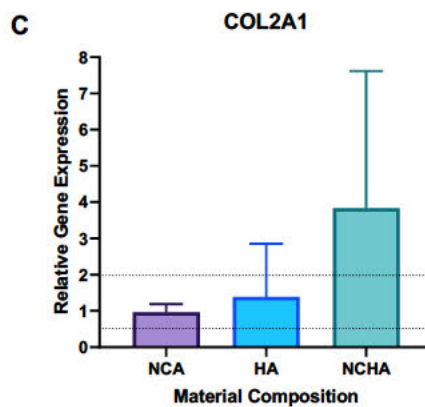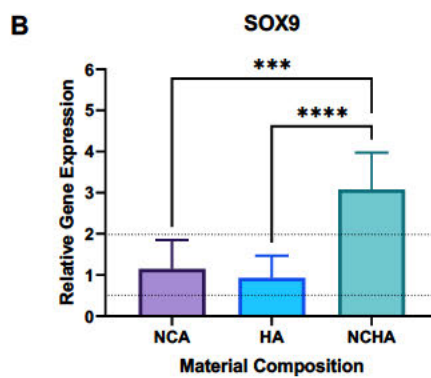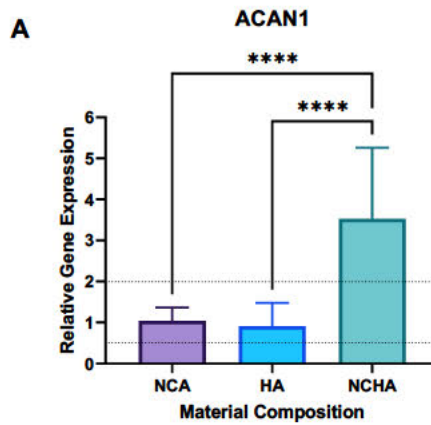
*Figure 6.11: Relative gene expression of NCA, HA and NCHA bioinks at 21 days of culture, expressed relative to NCA. Mean relative gene expression values from 6 biological repeats are presented with standard deviation. A) ACAN1 gene expression at 21 days is presented in HA and NCHA relative to NCA, demonstrating highest gene expression in the NCHA material. B) SOX9 gene expression is presented mirroring ACAN1 in which chondrocytes cultured in NCHA express SOX9 at significantly higher levels than HA and NCA. C) COL2A1 expression in HA and NCHA is presented relative to NCA, in which biologically significant differences in COL2A1 are seen in NCHA but this is not significant. *** = p<0.001; **** = p<0.0001*

The osteogenic gene expression profiles of NCA, HA and NCHA were compared at the 21 day timepoint (Figure 6.12) and demonstrated the inverse relationship to chondrogenic gene markers at 21 days. Specifically, gene expression of ALP, osteocalcin (OCN) and osteoblast differentiation marker RUN Family Transcription Factor 2 (RUNX2) were examined. Relative to chondrocytes in NCA, the expression of ALP was markedly lower at 21 days in the NCHA material (0.22-fold compared to NCA, p=0.0003) but not in HA alone (0.52-fold, p=0.29). This was a similar trend with regard to OCN: the expression was lowest in HA (0.1-fold, p=0.0003) but also significantly lower in NCHA (0.4-fold, p=0.004) compared to NCA at 21 days. RUNX2 was comparably lower in both HA (0.14-fold, p=0.003) and NCHA (0.17-fold, p=0.004) than NCA. The biologically and significantly different gene expression values of these osteogenic markers, coupled with the chondrogenic gene profiles indicate that the HA-based materials encourage retention of a chondrogenic phenotype and direct cells away from osteogenesis and mineralisation. This was more notable in NCHA, in which there was also the greatest level of chondrogenic gene expression.
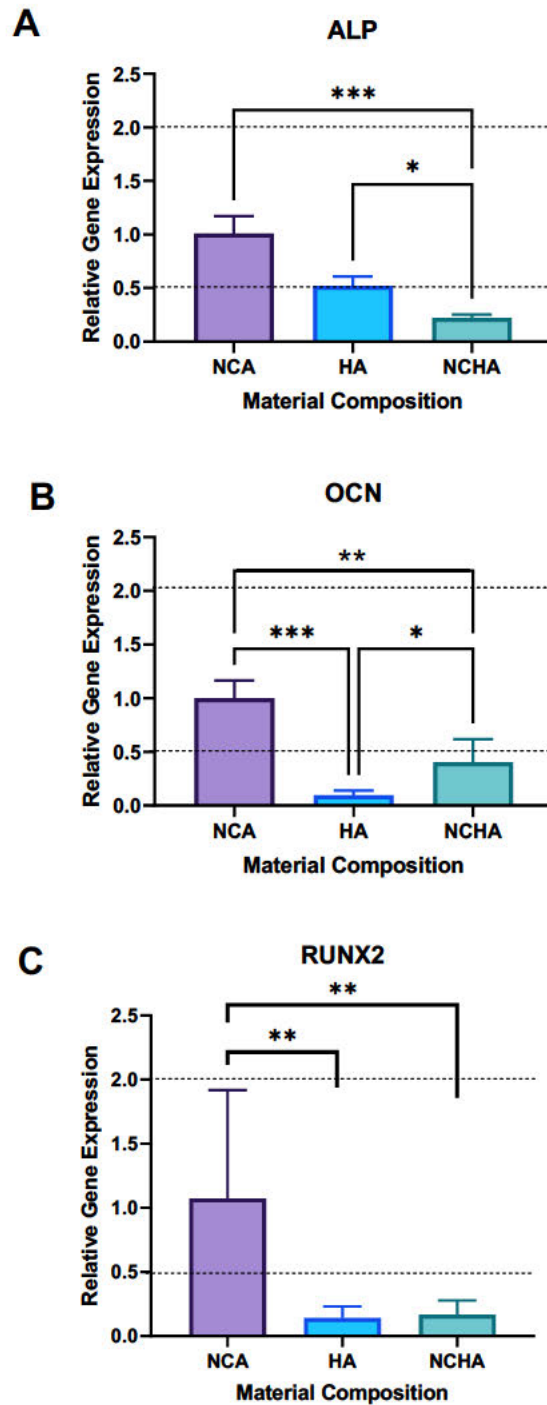
*Figure 6.12: Osteogenic gene expression of human chondrocytes at day 21 in candidate biomaterials. All gene expression values presented are a mean of triplicate repeats with standard deviation, relative to NCA at 21 days. Statistical significance from a One-Way ANOVA is presented. A) ALP gene expression at 21 days is presented, demonstrating biologically and statistically significant differences in NCHA relative to NCA and HA. B) OCN gene expression at 21 days is demonstrated in which significant reductions in gene expression are noted particularly in HA but also NCHA relative to NCA. C) RUNX2 gene expression is presented and significantly lower in NCHA and HA than NCA at 21 days. \*=p<0.05, \*\*=p<0.01; \*\*\*=p<0.001.*

### 6.3.3.3 Extracellular matrix production in candidate biomaterials

In order to assess whether these differences observed at the level of mRNA expression were mirrored at the level of ECM production, quantitative and qualitative assessments of extracellular matrix were performed. A hydroxyproline assay was performed on each material at 21 days, and as demonstrated in Figure 6.13A, revealed that there was almost triple the collagen content in the NCHA bioink (22.3 ng/μl) compared to the NCA bioink (8.8 ng/μl, p=0.002). The collagen content in the HA material (18.1 ng/μl) was over double that of NCA (p=0.002). There were no significant differences between the HA and NCHA materials observed at 21 days (p=0.2).


With regard to sulphated glycosaminoglycan content, similar trends were observed (Figure 6.13B). Specifically, significantly greater amounts of GAG content were noted in the HA (215.1 μg/ml, p<0.0001) and NCHA (268.4 μg/ml, p=0.009) materials compared to the NCA (46.8 μg/ml) material, despite treatment of all samples with hyalase digestion prior to analysis. There were no significant differences noted between the HA and NCHA materials (p=0.47).

**A**
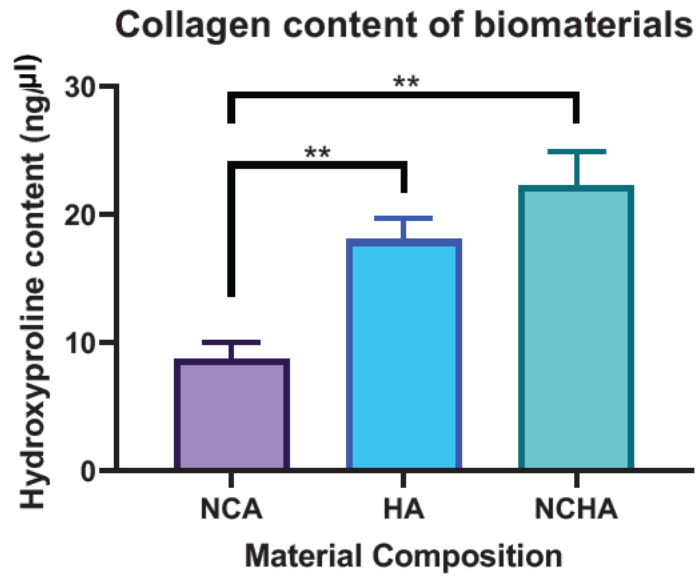


**B**
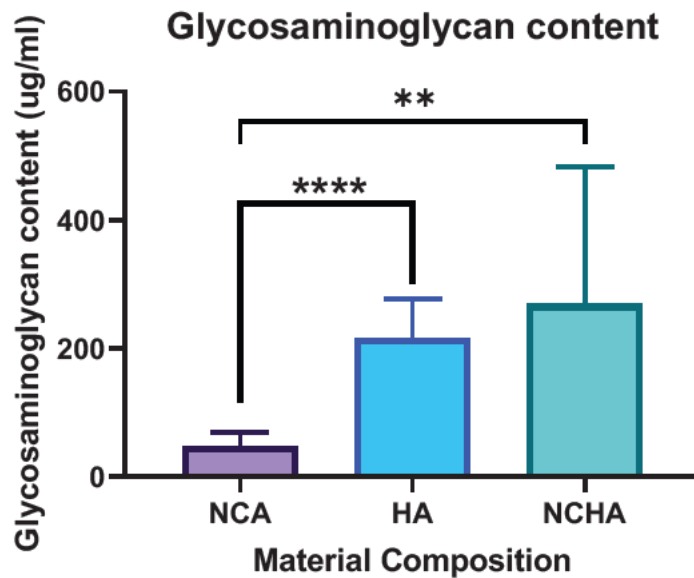


*Figure 6.13: A) Hydroxyproline assay to quantify collagen content in different biomaterials after 21 days of culture with human chondrocytes. Mean values of three biological repeats with standard deviation are presented. B) Glycosaminoglycan content of candidate biomaterials after 21 days of culture with human chondrocytes. NB all samples were treated with hyalase prior to analysis to eliminate confounding from the HA content of bioinks. **=p<0.01, ****=p<0.001*

Cartilaginous extracellular matrix components were stained using Toluidine blue, Alcian blue and Safranin O stains (Figure 6.14). Prominent pericellular stains were noted around the chondrocytes within the HA and NCHA bioinks, indicative of proteoglycan production. Although evidence of some uptake of stain was noticed in NCA, the cells were harder to visualise but did appear to similarly show more intense staining than the adjacent material. Alcian blue stains for glycosaminoglycans showed the most intense background material stain with the HA as expected but cells in all materials demonstrated some evidence of pericellular staining, this is most clearly demonstrated in the NCA material and NCHA material (Figure 6.14). The Safranin O stain did not show any evidence of Fast Green uptake to indicate mineralised bone matrix, but copious red staining indicative of proteoglycan content which was pronounced in the pericellular areas and their lacunae, demonstrated most clearly in the HA material (Figure 6.14) and additionally the NCHA and NCA materials.

From this section it is clear that the observed changes in gene expression do translate to, and mirror, the amount of cartilaginous extracellular matrix deposited into the biomaterial by chondrocytes over a 21-day period. Histologically it would appear that this is more greatly concentrated around the pericellular location in all materials studied, mirroring *in vivo* physiological conditions.
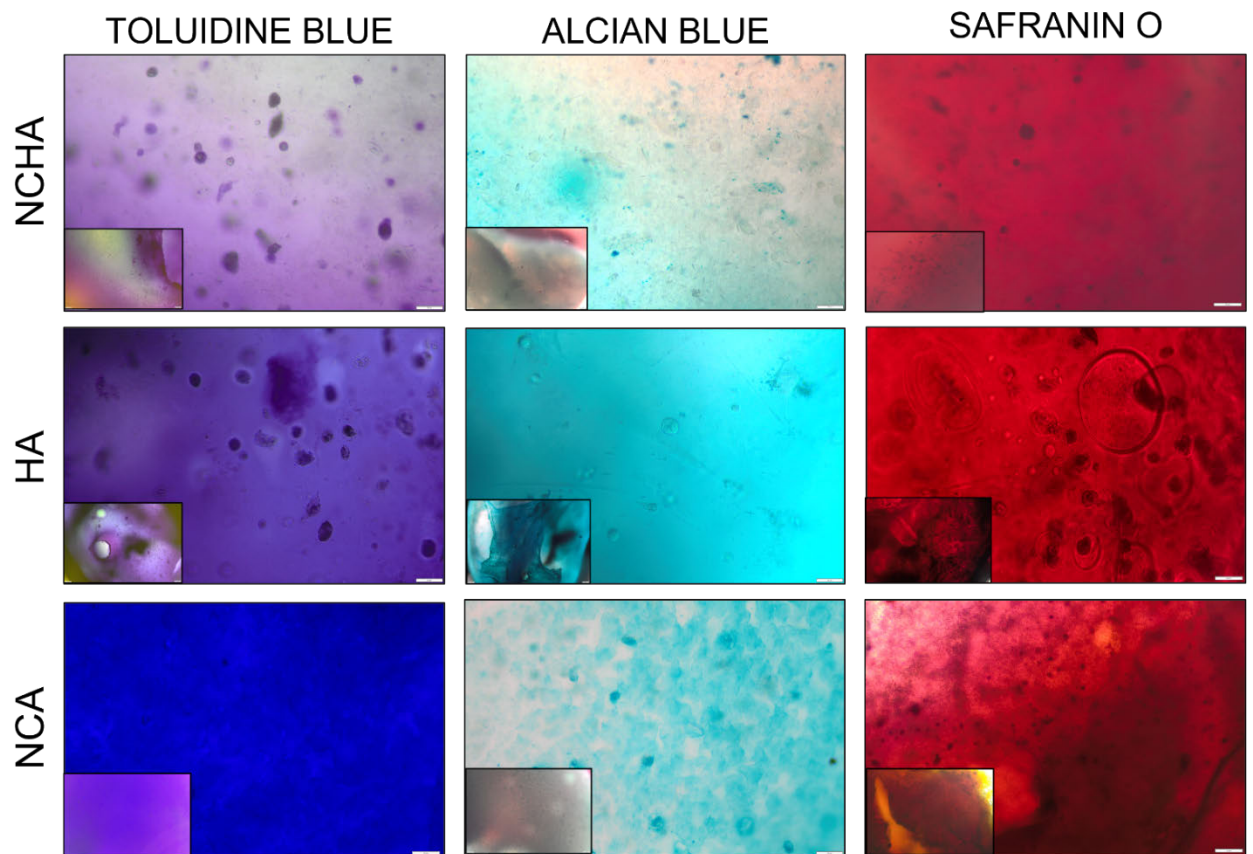
*Figure 6.14: Histological stains of NCHA, HA and NCA with toluidine blue (left), alcian blue (middle column) and Safranin O stains (right column). Intense staining is observed around cells in the NCHA and HA materials with toluidine blue and in all materials with alcian blue and safranin O. No evidence of mineralisation was seen with fast green staining in the safranin O stained specimens (right). Images are displayed at 4x magnification (bottom left image) and 20x magnification (main image) for each material. Scale bars (bottom right of image) depict 50 microns.*

### 6.3.4 Biomechanical properties of candidate bioinks after culture with chondrocytes

The compressive stress of each material was compared without cells and after culture for 21 days with cells (Figure 6.15, Appendix 2). There were no significant differences in the NCHA and NCA either with (p=0.11) or without cells (p=0.40), however the HA material had a lower compressive strength (0.10 MPa) than both the NCHA (0.39 MPa, p=0.002) and the NCA (0.53, p<0.0001) with cells, and the NCHA without cells (0.32 MPa, p=0.03). Only the NCA increased in compressive strength after co-culture with chondrocytes (by 0.29 MPa, p=0.001). This

indicates that nanocellulose confers compressive strength to the HA biomaterial that persists through culture with chondrocytes, but that unlike NCA, co-culture with chondrocytes does not significantly alter the material's compressive strength over the time period studied.
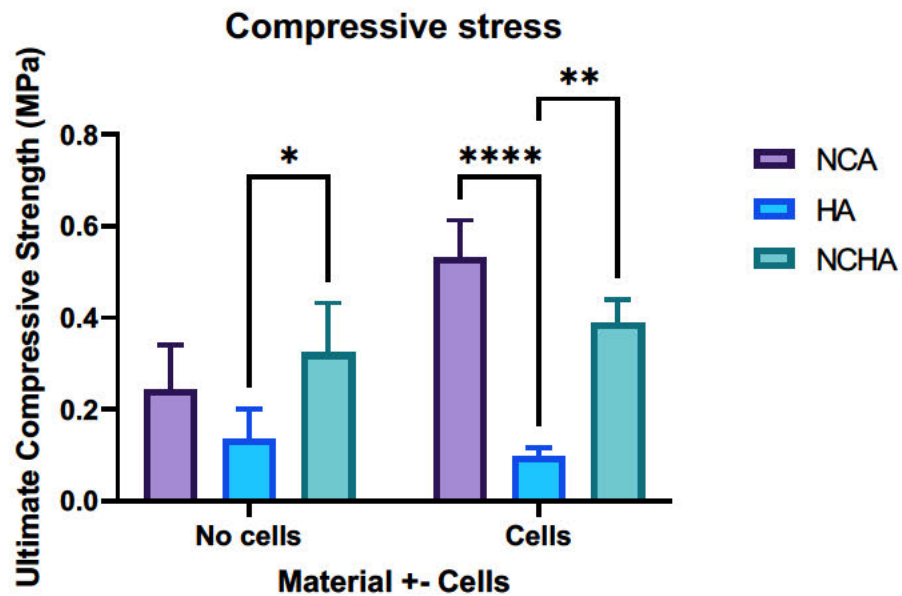


*Figure 6.15: Ultimate compressive stress of biomaterials with and without cells (after 21 days of culture). Materials are compared pre- and post-addition of cells with mean values from four technical repeats with standard deviation presented. \*=p<0.05, \*\*=p<0.01; \*\*\*\*=p<0.0001*

The strain to failure in the biomaterials (Figure 6.16) was not significantly different after culture with chondrocytes in any of the materials studied. However, prior to the addition of cells, the ultimate strain was significantly lower in the HA (39.0%) than NCA (78.7%, p=0.009) and NCHA (75.6%, p=0.02). Though NCHA and NCA were not significantly different in either condition, the strain in the HA material was significantly higher after culture with cells compared to without cells (p=0.03).
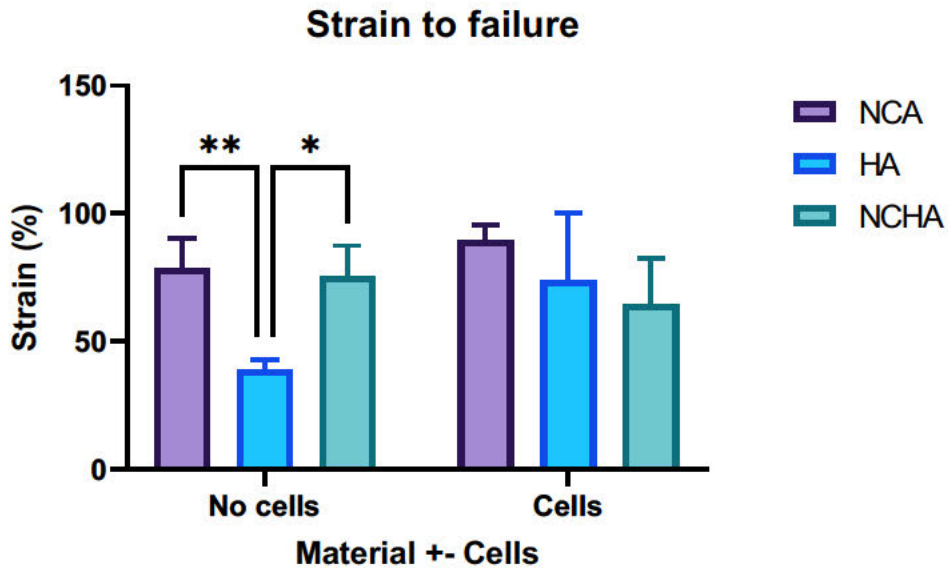
## Strain to failure



*Figure 6.16: Strain to failure experienced by biomaterials without and with the addition of cells cultured for 21 days. Materials are compared in their acellular and cellular states with a mean value from four repeats presented with standard deviation. \*=p<0.05, \*\*=p<0.01.*

The break force of the materials was analysed pre- and post-culture with chondrocytes (Figure 6.17). There were no significant differences when each material was tested with or without cells, indicating that the presence of cells neither significantly strengthened nor weakened the force needed to irreversibly break the materials. However, differences were noted between the NCHA and HA without cells (HA: 1.1 N, NCHA 2.3 N; p=0.005) and with cells (HA: 0.7 N, NCHA 2.0 N; p=0.04).
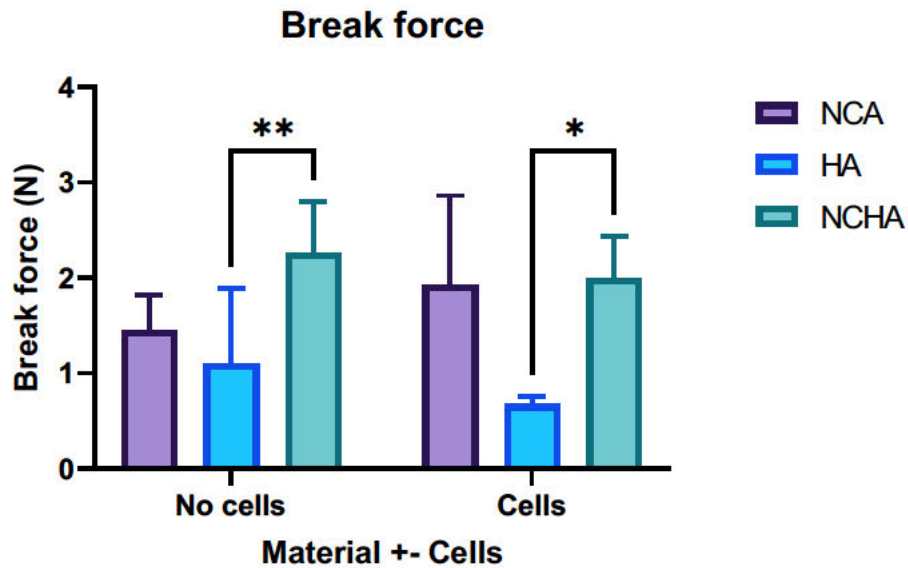
*Figure 6.17: Break force of each candidate material. Materials are compared in their pre- and post-addition of cells. Mean values derived using four technical repeats are presented with standard deviation. \*=p<0.05, \*\*=p<0.01; \*\*\*=p<0.001; \*\*\*\*=p<0.0001*

Further characterisation of mechanical properties of the materials with and without cells was determined using AFM to calculate Young's modulus (Figure 6.18). The HA based materials differed significantly in their elastic modulus after culture with cells for 21 days (Figure 6.18). Specifically, the HA material demonstrated a reduction in Young's modulus with cells from 30.4 kPa to 16.0 kPa (p<0.0001) whereas the NCHA demonstrated an increase in Young's modulus with cells from 11.8 kPa to 26.4 kPa (p<0.0001) (Figure 6.18A). The NCA did not differ significantly between the two conditions (p=0.15).

The elastic moduli of each material with cells also differed significantly, with the lowest elastic modulus seen in the HA with cells (16.0 kPa): significantly lower than NCA (29.5 kPa, p<0.0001) and NCHA (26.4 kPa, p=0.0004) (Figure 6.18B). This relationship differs to that observed prior to the addition of cells, in which HA had a significantly higher Young's modulus than both NCA and NCHA, indicating a softening of the HA biomaterial in culture conditions.
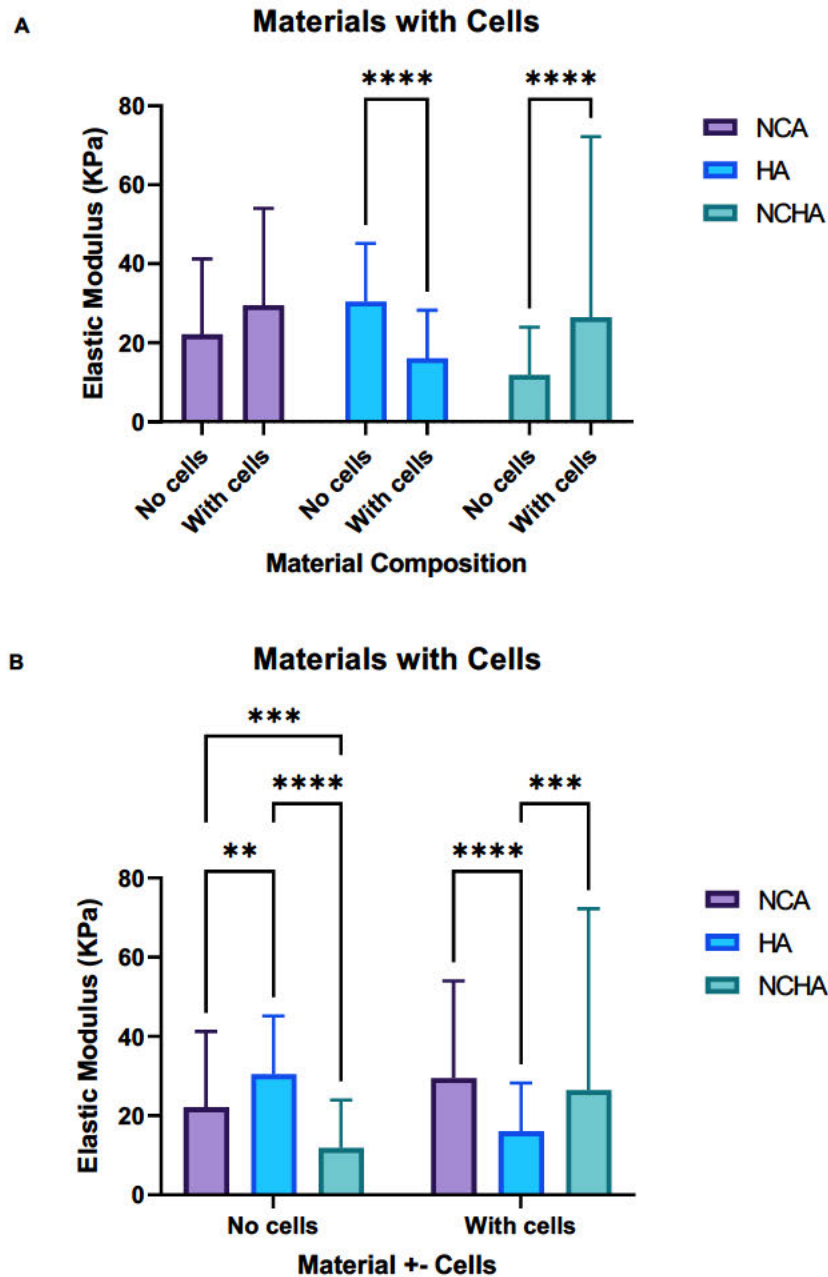
*Figure 6.18: Elastic (Young's) modulus of candidate biomaterials with and without cells as determined by AFM. A) Young's modulus of each material is presented before and after the addition of cells with mean values of four replicates presented plus standard deviation. Statistical analysis of a 2-way ANOVA is presented, showing significant increases in elastic modulus in the NCHA material. B) Young's modulus is presented from 4 technical replicates with standard deviation and pairwise comparisons from a 2 way ANOVA. NCHA appears to have a lower elastic modulus without cells than NCA and HA but is comparable to NCA after coculture with cells. \*=p<0.05, \*\*=p<0.01; \*\*\*=p<0.001; \*\*\*\*=p<0.0001*

Topographic analysis was attempted on each biomaterial prior to and after culture with chondrocytes for 21 days. In the NCHA material, the surface topography appeared much smoother after the period of incubation with cells, though grooves and sulci remained prominent features of the topography. In HA, the porosity of the material initially was stark and more uniform than the porosity observed in NCA or NCHA. NCA appeared to retain its surface roughness after culture with cells though the pore depth appeared to be less deep than without cells.
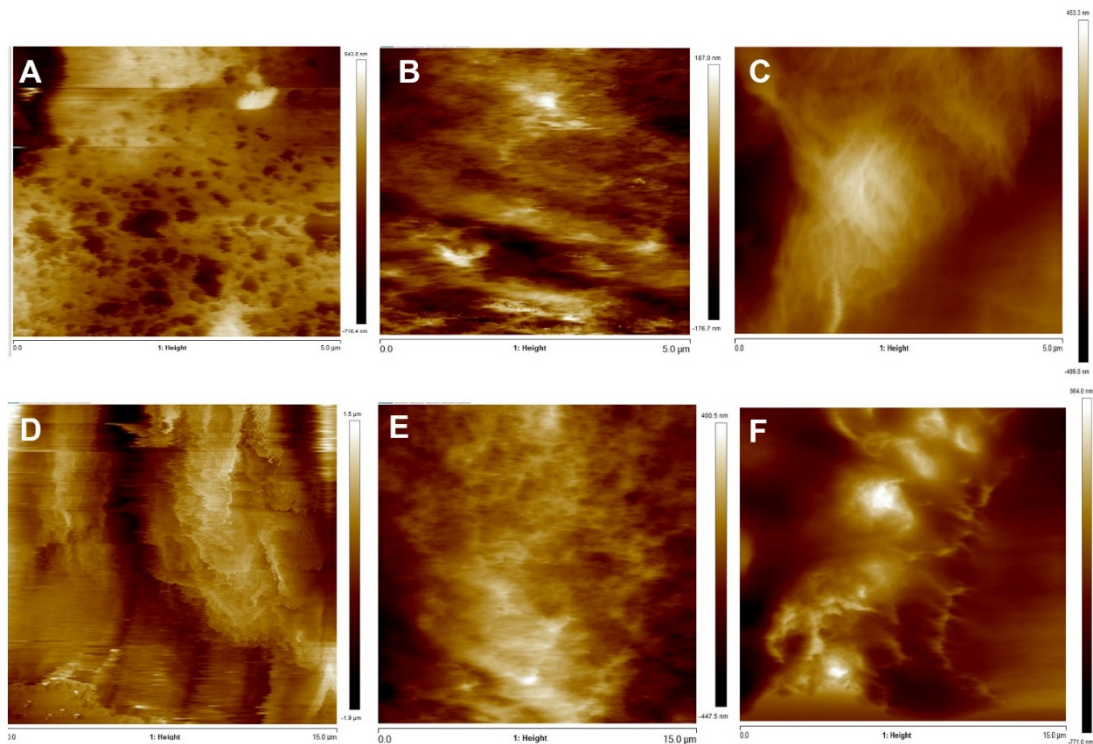


*Figure 6.19: AFM images of candidate biomaterials acquired without cells (A-C) at a height of 5 microns and with cells (D-F) at a height of 15 microns. Topograms are presented for each biomaterial: NCA (A+D), HA (B+E) and NCHA (C+F). A) Surface topography of NCA without cells is displayed in which grooves and sulci are demonstrated with small pores (approximately 1 micron wide) are detected. B) HA without cells demonstrates a high degree of surface roughness with extensive pores <1 micron and larger grooves of 2 microns wide are visible. C) NCHA demonstrates an interconnected fibrillar surface topography with sulci of up to 500nm depth detected. D) Nano- and micro- porosity is evident in the NCA with cells indicative of surface roughness. E) Extensive porosity in demonstrated in the HA with cells which appear to be smaller in size than the NCA (D) and NCHA (F). F) NCHA topography showing large network of interconnecting pores.*

### 6.3.5 Biocompatibility of candidate biomaterials with human chondrocytes

The toxicity profile of the materials with cells was determined immediately using an LDH assay as a marker of cell lysis, compared to a control population of cells only and over longer time courses (up to 21 days) using a live-dead assay. Baseline cytotoxicity on the LDH assay for cells only was 12.7%, 7.6% for cells in NCHA, 2.5% for cells in HA and 28.8% for cells in NCA. The NCA was significantly higher than all other conditions ($p < 0.0001$), and the HA cell cytotoxicity was significantly lower than NCHA and cells alone ($p < 0.0001$). The NCHA did not differ significantly from cells alone, indicating there was no significant cell lysis from the NCHA or crosslinking reaction compared to controls.
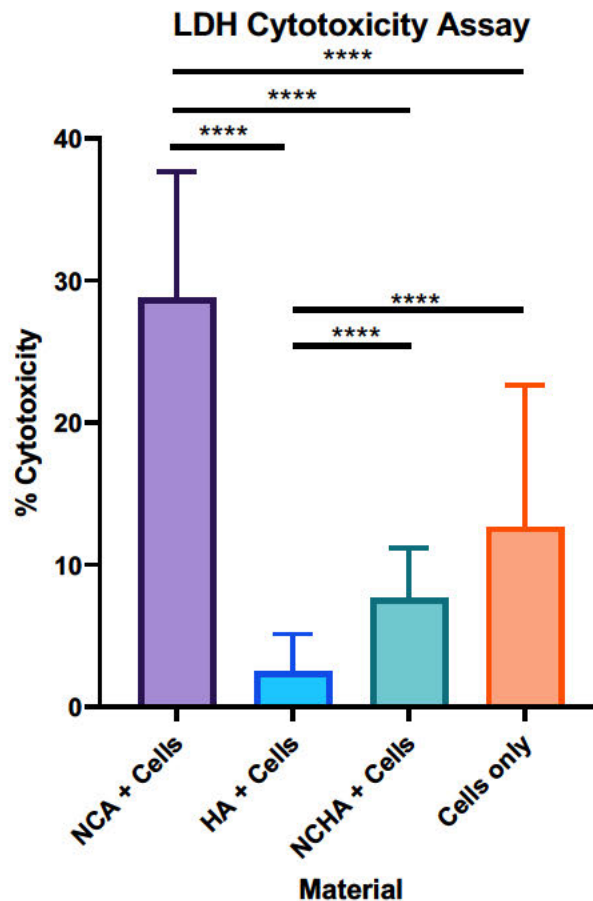


*Figure 6.20: LDH Cytotoxicity assay of cells in biomaterials taken at 4 hours. Mean values from 9 repeats are presented with standard deviation. Statistical analysis from a one way ANOVA is presented, with cells only (not embedded within a biomaterial) presented for reference. \*=p<0.05, \*\*=p<0.01; \*\*\*=p<0.001; \*\*\*\*=p<0.0001*

Over the 21 day time period, CDCs demonstrated excellent cell viability within all of the biomaterials, and an increase in cell number was clear across timepoints as indicated in a higher number of live cells (indicated in green in Figure 6.21). In the NCHA, cells appeared to form clusters at 21 days indicating proliferation and communication of cells within this biomaterial (Figure 6.21). This was evident to a lesser extent in the NCA. Higher cell viability was maintained in the biomaterials compared to cell only controls, and a rounded spheroidal morphology was more obvious compared to the spindle shaped morphology that dominated the cell only condition particularly at later time points.

This increase in cell number observed in the live dead assay was supported by the alamarBlue data taken from NCHA biomaterials seeded with either 50,000, 300,000 or 500,000 cells per 100 μl semisphere. Significant increases in metabolic activity were seen across all seeding denisities between 0 and 21 days. A sharper increase in metabolic activity was observed in the 500,000 cells between 0 (13.2%) and 7 (21.1%) days (p=0.019) which was not observed in the other seeding densities. The highest levels were seen in the 300,000 (37.4%) and 500,000 (36.9%) cell semispheres at 21 days, and these levels were not significantly different from each other (p>0.999), but significantly higher than 50,000 cells (<0.0001 vs 300,000 cells; 0.003 vs 500,000 cells).
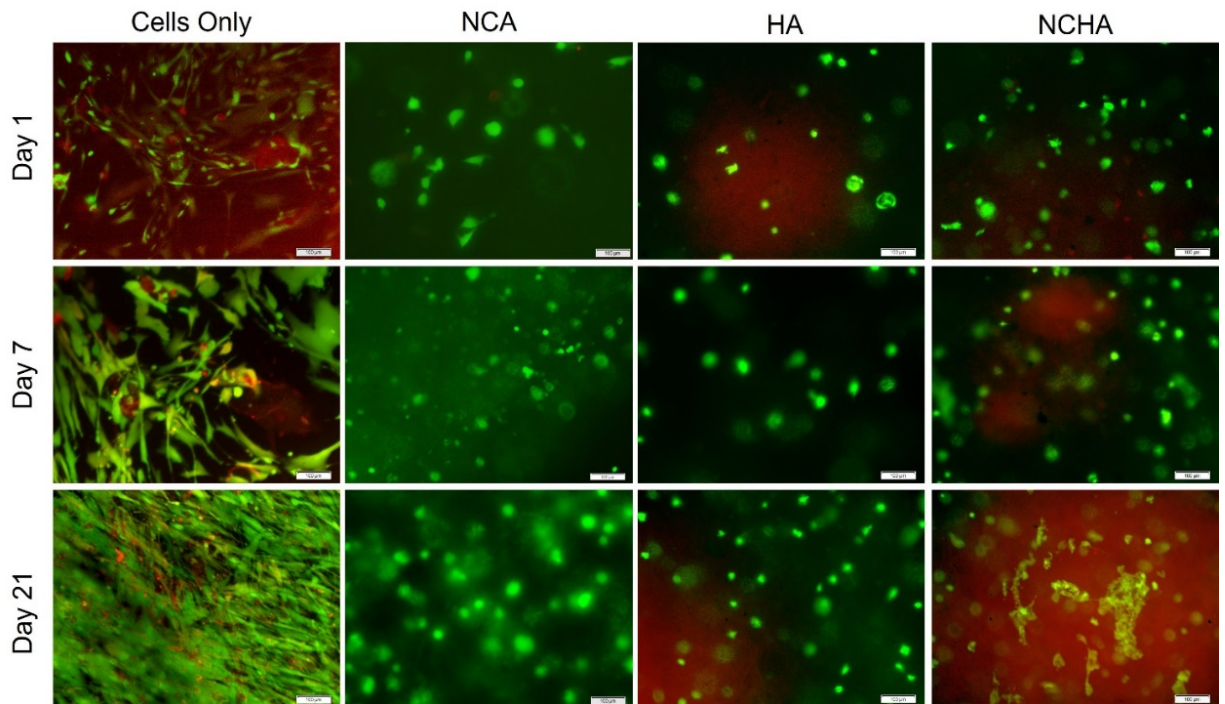
*Figure 6.21: Live dead assay of candidate biomaterials at Day 1 (top row), Day 7 (middle row) and Day 21 (bottom row) of culture containing human nasoseptal chondrocytes for NCA, HA and NCHA. Materials are compared to 'cells only' (left column) for each time point. Morphologically the cells maintained a rounded appearance in the 3D culture conditions relative to cell only conditions and appear to have fewer dead cell signals detectable at each time point. Live cells are stained with Calcein AM, detected on the FITC channel and coloured green in these images, whereas dead cells stained with Ethidium homodimer were detected on the TRITC channel and have been coloured red for illustrative purposes. All images are acquired at 20x magnification with scale bars depicting 100 microns.*

## AlamarBlue Assay
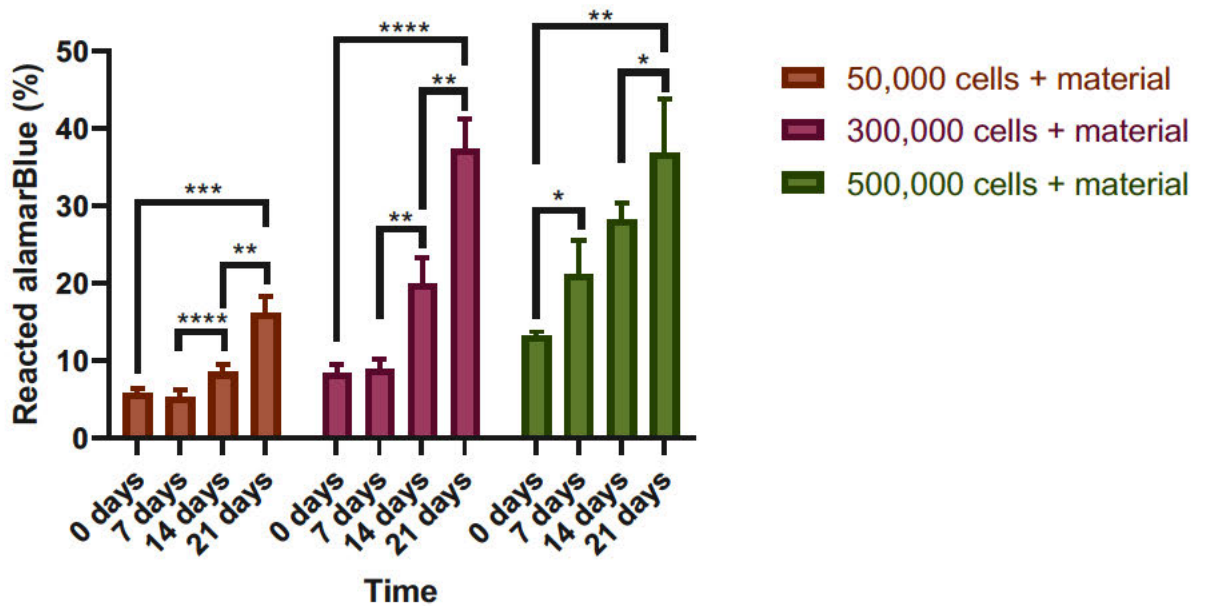


*Figure 6.22: AlamarBlue assay of different seeding densities in NCHA bioink acquired at day 0, 7, 14 and 21 across three seeding densities (50,000; 300,000 and 500,000 cells per 100 µl semisphere). Increases in metabolic activity cell number were observed in all biomaterials. Mean values of 6 replicates are presented with standard deviation. Results from a one-way ANOVA and Tukey's post hoc test are presented. \*=p<0.05, \*\*=p<0.01; \*\*\*=p<0.001; \*\*\*\*=p<0.0001*

### 6.3.6 Biocompatibility of the bioprinting process

### 6.3.6.1    Computational modelling of bioink velocity and shear stress

The computational modelling approach demonstrated that 3D bioprinting using the NCHA bioink and a range of printing pressures from 20 to 40 kPa, translated to a range of shear stress (180-400 Pa) and fluid velocity (7-19 mm/s) when using the CELLINK INKREDIBLE 3D bioprinter (Figure 6.23). The cells within the biomaterial would be subjected to the shear stresses mentioned during their journey through the printer cartridge and conical 22 G nozzle. Of note, irrespective of printing pressure, the plateau in shear and velocity occurred at the same time point, with a period of approximately 1 second (1.08 seconds) until this point was achieved. In these experiments, 30 kPa was used to print the cell-laden NCHA bioink, meaning the cells experienced a maximum shear stress of 292 Pa and maximum fluid velocity of 13.4 mm/s.
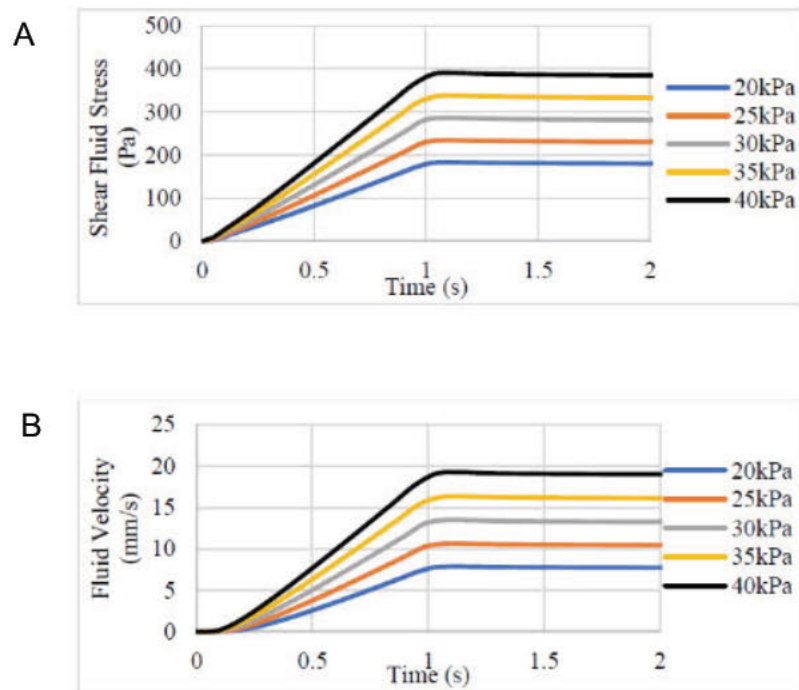
*Figure 6.23: Computational modelling of fluid shear stress and velocity during the extrusion bioprinting process performed in collaboration with Dr Feihu Zhao. A) Shear fluid stress (in Pa) as a product of inlet pressure variation (kPa) is presented temporally as the ink flows through a 22 G conical nozzle over the course of 2 seconds demonstrating increases in shear stress with increasing inlet pressures. B) Fluid velocity (in mm/s) is expressed as a product of inlet pressure variation using a 22G 3D printing nozzle. With increasing inlet pressures, higher levels of fluid velocity are expectedly observed within the bioink.*

Biologically, this translated to a reduction in cell viability as determined with the live-dead assay (Figure 6.24). Cells appeared largely viable in the printed and unprinted samples at 1 hour post-printing (Figure 6.24A) and statistically, there was no immediate difference in cell viability post-printing (Figure 6.24B). However by 24 hours, noticeable differences in the number of dead cells were visible in the printed samples (Figure 6.24A). Relative to the live cells, this was a significant reduction in cell viability in the printed constructs (61%) compared to the unprinted constructs (79.6%, p=0.047) and the constructs tested immediately post-printing (81.9%, p=0.042) (Figure 6.24B). This indicates that cell death from the shear stress of bioprinting is not an immediate, but a delayed phenomenon.
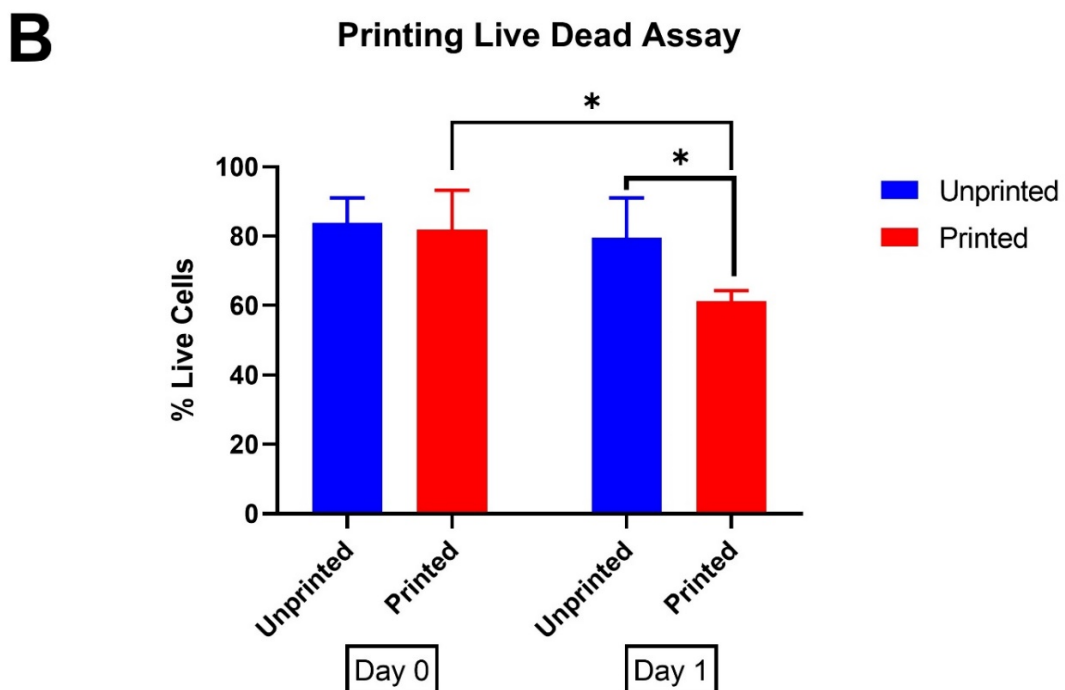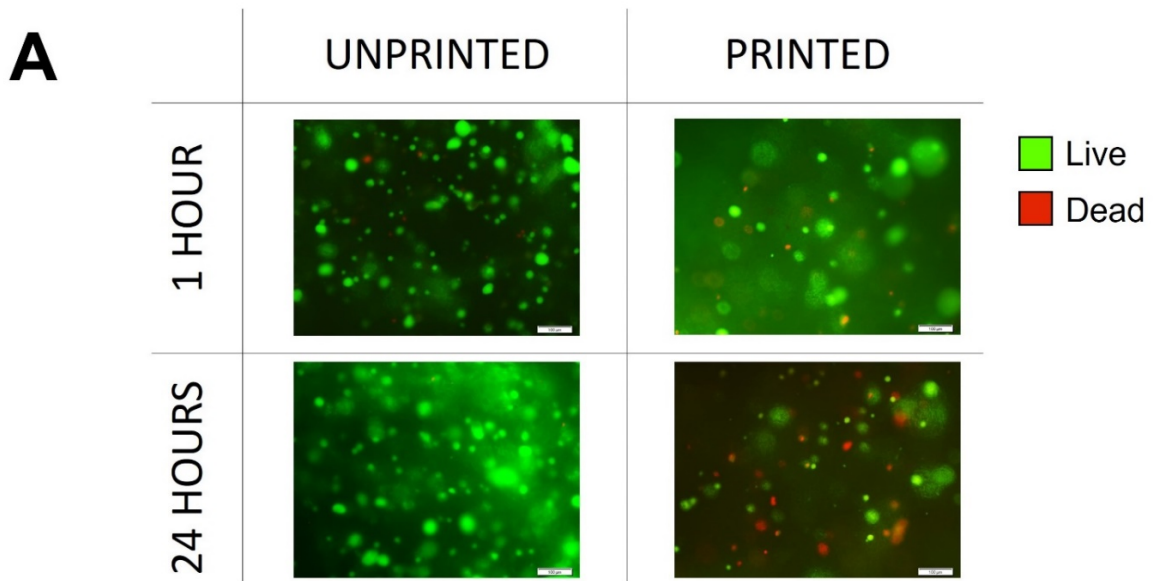
Figure 6.24: Live Dead Assay of CDCs after printing at 1 hour (Day 0) and 24 hours (Day 1) compared to unprinted controls. A) Viability of cells in 3D printed and unprinted conditions within first hour of printing (demonstrated on the top row) appears comparable in viable cells (coloured green) at the initial timepoint but after 24 hours (bottom row), a marked increase in non-viable cells (coloured red) is evident in the printed condition. B) Live dead cell counts of viable cells as a percentage of total cells counted in 3 different areas of printed and unprinted crosslinked materials. Mean values are presented with pairwise comparisons from two-tailed t-tests. No significant differences were seen immediately post-printing but a larger amount of non-viable cells were visualised after 24 hours. *=p<0.05.

These initial findings immediately post-printing were explored further using LDH and alamarBlue assays (Figure 6.25). Using the LDH assay, no significant differences were seen in cell lysis between the printed and unprinted cells immediately post-printing (Figure 6.25A), which translated to comparable amounts of metabolic activity (p=0.5) (Figure 6.25B) . After 24 hours of printing, there were additionally no significant differences in the metabolic activity of the cells in the printed or unprinted constructs using the alamarBlue assay (p=0.9), however both these conditions were noted to be significantly lower than cells only at this time point (p<0.0001). This indicates that post-printing there is no biologically relevant cell lysis evoked by the shear stress of cells and biomaterial passing through the printer nozzle at the printing pressures used, however a delayed cell death pathway such as apoptosis may have been activated in response to the shear stress experienced in these conditions.
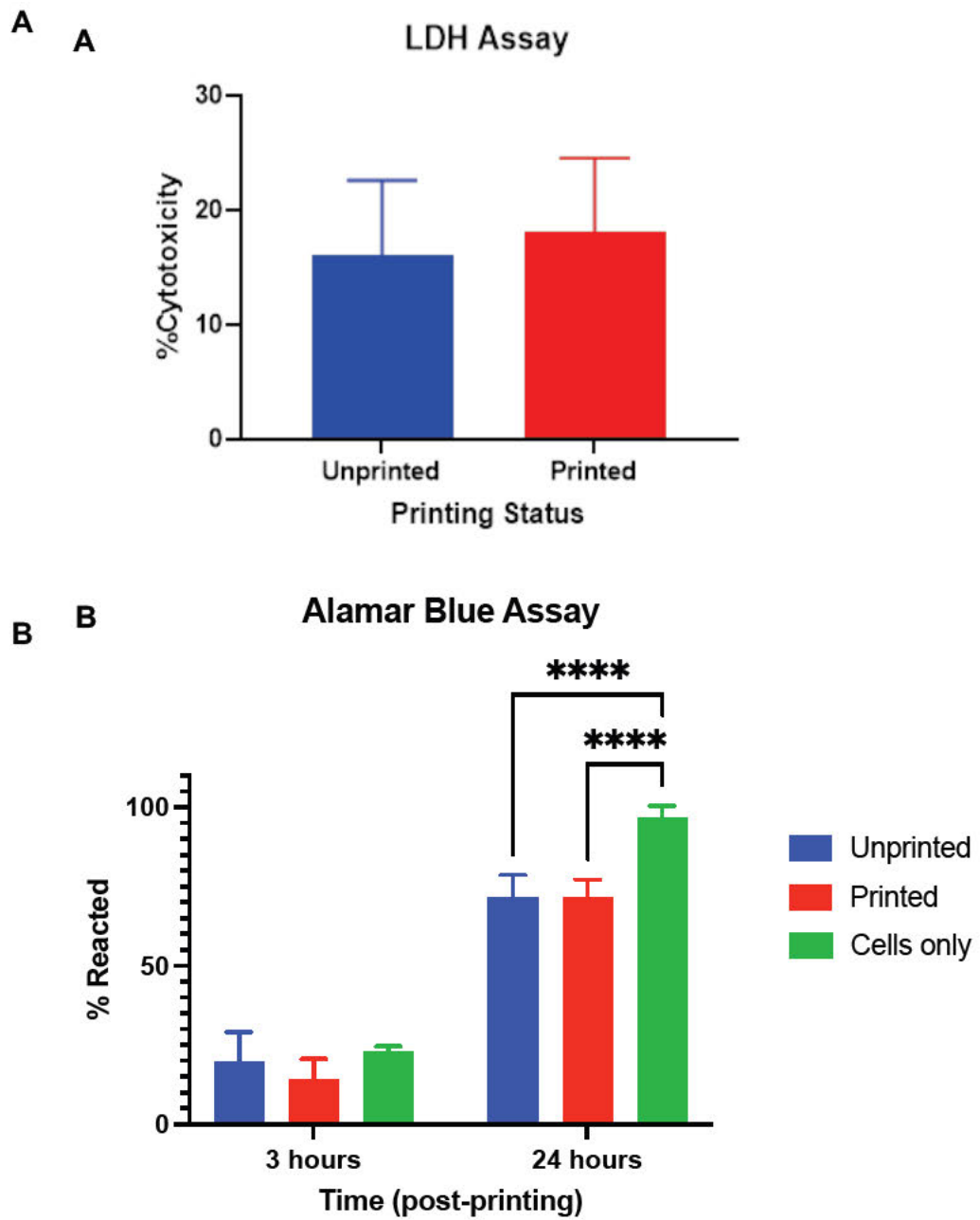
*Figure 6.25: Assessments of cell lysis and metabolism in printed and unprinted cells in NCHA biomaterial. A) An LDH assay of degree of cell cytotoxicity in biomaterials printed through 3D printer versus unprinted cells in biomaterial. No significant evidence of cell lysis in the printed constructs was observed immediately post-printing compared to the unprinted cells. B) AlamarBlue Assay of cells only, cells in biomaterial and cells in printed biomaterials at 3 hours post-printing and at 24 hours post-printing.*
*\*\*\*\*=p<0.0001*

### 6.3.6.2    Gene expression analysis following 3D bioprinting process

An additional finding of interest was in relation to gene expression changes noted as a result of the printing process. The printing process evoked an immediate increase in SOX9 (8.2-fold rise, p=0.049), ALP (4.4-fold increase, p=0.006) and aggrecan (2.9-fold increase, p=0.018) detectable 4 hours after printing compared to the unprinted CDCs. However, by 72 hours, there was a more comparable gene expression profile in the printed and unprinted cells (Aggrecan – p=0.9; SOX9- p=0.2; ALP – p=0.1) with the exception of Type II collagen expression, which had fallen significantly in the printed cohort (0.05-fold change, p=0.0005). Gene expression of osteocalcin and RUNX2 were also tested but were at undetectable levels in all conditions and timepoints tested. This study indicates that both transient and delayed effects on gene expression are evoked following shear stress exerted through the 3D bioprinting process, and in the instance of COL2A1 expression, this may have deleterious effects on long term chondrogenesis.
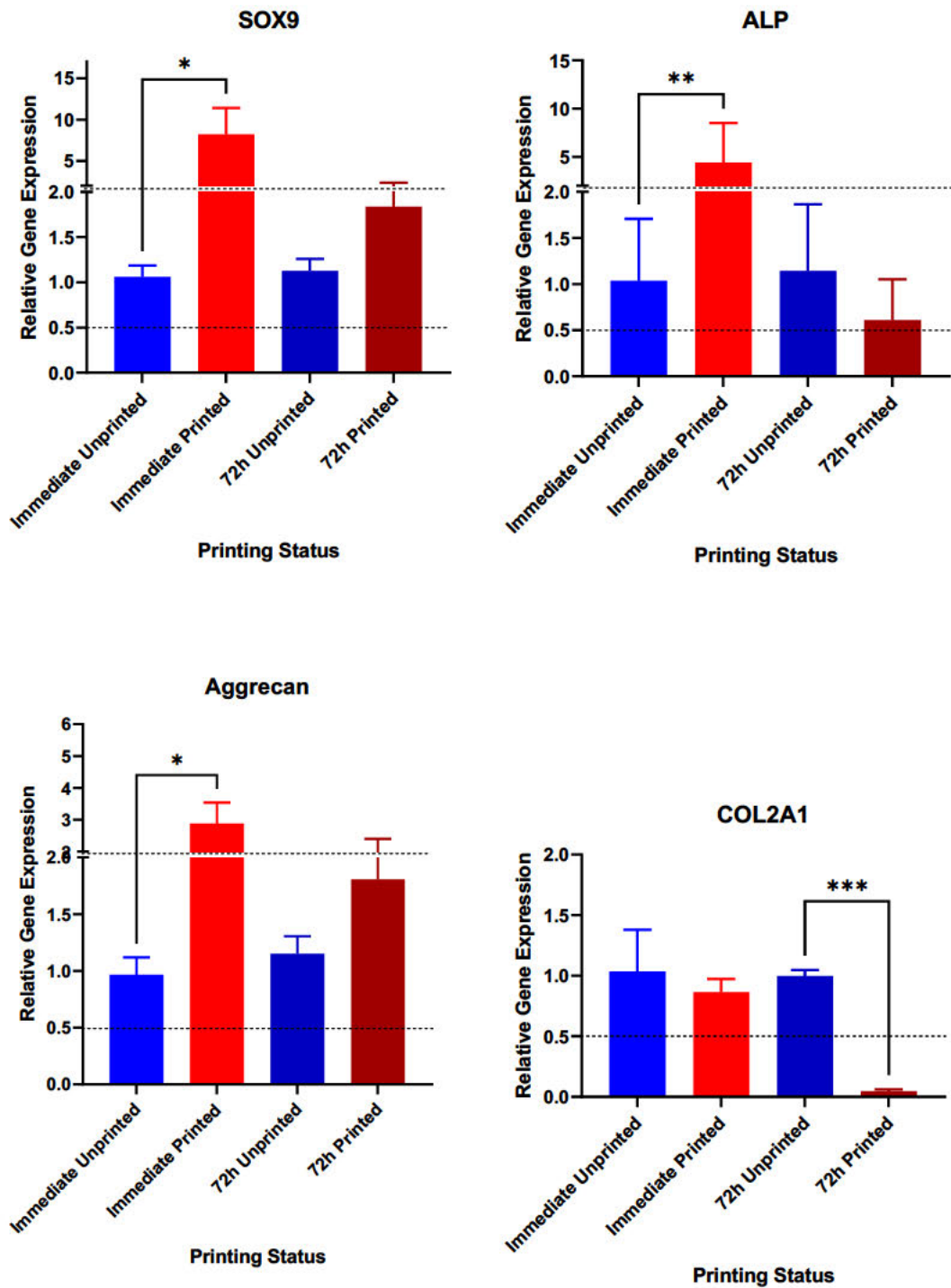
*Figure 6.26: Gene expression changes immediately (4 hours) after printing in NCHA bioink and 72 hours after printing. Chondrogenic genes SOX9, Aggrecan and COL2A1 are presented with ALP as a marker of osteogenesis. Mean values from 4 replicates of three biological samples are presented giving a total of 12 replicates per condition presented with standard deviation. Pairwise comparisons of the printed compared to the unprinted condition are presented at each timepoint with statistical significance from unpaired t-tests. *=p<0.05, **=p<0.01; ***=p<0.001; ****=p<0.0001*

## 6.4 Discussion

### 6.4.1 Nanocellulose augments printability of both HA and alginate based bioinks

As with nanocellulose-alginate composite bioinks (Chapter 4), the addition of nanocellulose to hyaluronic acid improved the printability of the bioink. The tensile strength of the bioinks were compared firstly through the use of a filament drop assay, in which only the nanocellulose-containing bioinks demonstrated the ability to be extruded as a continuous filament. Furthermore, the alginate and HA alone were largely unprintable, failing to maintain shape fidelity in straight lines and grids. This behaviour of HA was predicted to an extent by the rheological characterisation of HA in the preceding chapter, where the viscous component dominated over the elastic component of the HA hydrogel, in contrast to 20HA (NCHA).

With regard to NCHA compared to NCA bioinks, as both materials comprise a similar proportion of nanocellulose blend, their printability characteristics were also, unsurprisingly, similar. There were some differences however, specifically, in regard to line fidelity, the NCHA was the closest to the intended line diameter of 1 mm and demonstrated superiority in consistency compared to the other bioinks studied. This mirrors the filament drop test and indicates that the greatest filament strength and subsequent shape fidelity is achieved with the NCHA bioink. It is likely that the dominance of elasticity, and its behaviour as a viscoelastic solid in this bioink rheologically underpins its superior post-printing resolution and fidelity. Side by side comparisons of NCA and NCHA printability have not been investigated, however, one study has evaluated the addition of hyaluronic acid into a nanocellulose-alginate bioink (Lafuente-Merchan *et al.*, 2021). This study produced NCA bioinks consisting of 80:20 NC:Alginate (v/v), comprising a 10% alginate (w/v) solution. An NC-Alg-HA bioink was also produced in which the 20% (v/v) alginate component also contained 5% (w/v) HA. These inks were printed in a range of 20-22 kPa for NC-Alg and 24-26 kPa for NC-Alg-HA. Rheologically, the HA was found to enhance bioink viscosity, and also led to better angle fidelity in the grid assay, mirroring the findings of this chapter (Lafuente-Merchan *et al.*, 2021).

To fix the materials post-printing in their intended shape, crosslinking is essential. However, this can influence the dimensions of the material owing to the formation of ionic and covalent intermolecular bonds within the hydrogel. In this chapter, after crosslinking there was an increase in diameter with the NCA bioinks, whereas a reduction in diameter was seen with the HA-based bioinks. Of all the materials, the smallest change in diameter was seen in the NCHA bioink after crosslinking, translating to it also being the most suitable for post-crosslinking shape fidelity. This discrepancy may reflect the porosity and swelling properties of the NCA, which were noted to be higher than both the NCHA and HA materials. Hydrogel swelling is believed to reflect the density of the material, with denser bioinks having a lower swelling ratio post-crosslinking (Yu *et al.*, 2014). As NCHA had a lower mean porosity and swelling than NCA, this theory would be concordant with the discrepancies in diameter changes between the bioinks.

### 6.4.2 NCHA displays superior chondrogenicity to NCA and HA bioinks and lower osteogenic potential

In this chapter, a direct comparison of the chondrogenicity of NCA relative to HA and NCHA bioinks was undertaken, demonstrating statistically significant increases in SOX9 and ACAN1 expression in NCHA relative to NCA and HA at 21 days, and biologically significant increases in COL2A1 expression. This translated to changes seen in the extracellular matrix composition, with significantly higher levels of collagen (hydroxyproline) and sulphated GAGs in the NCHA biomaterials at 21 days of culture. Remarkably, this increase in ECM production appeared to translate further into the biomechanical strength of the material, with the NCHA formulation being the only bioink to increase in elastic modulus after culture with cells: a phenomenon observed in the absence of any additional growth factors or supplements to enhance chondrogenic differentiation or proliferation. The likely explanation for this change is that the increased production of extracellular matrix components by chondrocytes embedded in the NCHA material increased the elasticity of the material. Although NCHA demonstrated the highest levels of chondrogenicity, there was evidence of increases in chondrogenic gene expression over time in each of the biomaterials.

There were discrepancies in the onset of certain genes however, with the HA based materials demonstrating a higher initial surge in SOX9 expression and relative suppression of COL2A1 and ACAN1 compared to NCA, which resulted in a delayed surge in the ECM genes (COL2A1 and ACAN1). As SOX9 regulates the expression of COL2A1 and ACAN1, this chronological effect seen in the 21-day PCR data reflects a recognised gene expression sequence (Bell *et al.*, 1997; Bar Oz *et al.*, 2016) (Section 1.6.2.3), however the effect is believed to have the potential to be bifunctional, with overexpression of SOX9 causing an attenuation of COL2A1 expression (Kypriotou *et al.*, 2003). There was no evidence to suggest that overexpression of SOX9 was occurring over this 21 day period however, as COL2A1 continued to rise throughout the study period. NCHA was the only material to show a sustained elevation in SOX9 throughout the 21 day period. It would be of interest to see whether this sustained elevation in SOX9 expression continued to translate to higher ECM gene expression beyond the 21 day culture period.

In addition to regulating cartilage extracellular matrix production, SOX9 is responsible for maintaining a chondrogenic phenotype, protecting against chondrocyte hypertrophy and osteogenic differentiation (Quintana, Zur Nieden and Semino, 2009; Lefebvre, Angelozzi and Haseeb, 2019). It is interesting to note that whilst SOX9 expression was highest in NCHA and HA materials relative to NCA, osteogenic gene markers were conversely lower in these materials: in particular RUNX2, which promotes hypertrophy of chondrocytes and differentiation into osteoblasts (Lefebvre, Angelozzi and Haseeb, 2019). The other bone-specific genes, OCN and ALP were also lower in the HA-based materials. Bone tissue has lower levels of glycosaminoglycans than cartilage, specifically comprising small leucine rich proteoglycans such as biglycan, decorin and asporin, although hyaluronic acid is present in small quantities (Lin *et al.*, 2020). It is interesting therefore to note that the materials containing hyaluronic acid had higher SOX9 expression and were less prone to osteogenic gene expression, indicating the inclusion of HA in bioinks may promote retention of a chondrocytic phenotype. SOX9 (and COL2) expression was also noted to be higher in iPSCs cultured in NCHA than NCA in Nguyen et al's study of nanocellulose-based bioinks for cartilage tissue engineering (Nguyen *et al.*,

2017). This is an important finding, as many previous efforts to bioengineer cartilage tissue have led to ossified and calcified cartilage that would be unsuitable for its intended clinical applications (Jessop *et al.*, 2016).

Unlike HA, alginate is not a native component of cartilage tissue, or indeed any animal tissue. In addition to enhancing chondrogenesis, HA was also noted to increase the adipogenesis of mesenchymal stem cells in a 70:30 or 80:20 NC:HA blend in Henriksson *et al*'s study compared to NCA, leading to increased cell proliferation, spreading and adipogenesis (Henriksson, Gatenholm and Hägg, 2017).

It has been reported that alginate may negatively impede cellular migration and differentiation owing to its encapsulation of cells (Schütz *et al.*, 2017), which was felt to underpin the limited proliferation and spreading of adipocytes in Henriksson *et al* (Henriksson, Gatenholm and Hägg, 2017). Whilst this may have a significant effect for adipogenesis, confluence of cells is less pivotal to cartilage tissue engineering, as chondrocytes often exist in singular cell silos or chondrons (Poole, 1997). However, should the NCHA in this study convey the same advantages as that of Henriksson's NCHA composite bioink, the ability of cells to migrate within the NCHA bioink may have advantageous effects for biomimicry, enabling cells to spread through the scaffold and organise into lacunae surrounded by their own pericellular matrix.

Another feature believed to facilitate cell migration is pore geometry: pores in the nano-scale (<100nm) play important roles in facilitating ECM and collagen production, whereas macropores (100um-1mm) play important roles in cell distribution and migration (Bružauskaitė *et al.*, 2016). Both the NCHA and the NCA used in this study use the NCB formulation of nanocellulose which exhibits a high range of pore sizes spanning from 55 nm to 12 μm, meaning it falls primarily into the nano- and microporosity range of pore sizes, facilitating ECM deposition and cell migration respectively (Bružauskaitė *et al.*, 2016; Kyle *et al.*, 2018). When mixed with alginate, NCB demonstrated good cell integration within the pores visualised with scanning electron microscopy (SEM) imaging, with a large variation in pore sizes primarily in the micro range (Jessop *et al.*, 2019b). Whereas alginate alone exhibited very small pore sizes and cell encapsulation

within the material (Jessop *et al.*, 2019b). It would be of interest to further characterise the pore geometry of the NCHA bioinks using cryo-SEM to determine whether there are differences in pore geometry that may underpin the structural and chondrogenic differences between NCA and NCHA. It has been shown in other materials that HA reduced pore sizes when added to collagen scaffolds, with beneficial effects noted for both cell migration and chondrogenic gene expression (Matsiko *et al.*, 2012).

### 6.4.3 Nanocellulose and HA convey advantageous, albeit different, structural strengths to composite bioinks

Structurally, when visualised under SEM, both NC with alginate and HA demonstrate porous internal structures with channel like arrangements to facilitate oxygen and nutrient permeation through the scaffold (Lafuente-Merchan *et al.*, 2021). Yet, the biomechanical properties of the bioinks were found to differ, with advantages of each of alginate, hyaluronic acid and nanocellulose noted in this thesis.

When initially tested with AFM, HA demonstrated the greatest elasticity using nanoindentation, with an Elastic Modulus of approximately 30 kPa. The HA alone was the only material to weaken after culture with cells for 21 days however, which may be attributable to material degradation in culture: the HA appears to be more hydrophilic than NCHA as evidenced by a greater degree of swelling in culture conditions (Figure 6.7). The nanocellulose based materials both increased in mean elastic modulus over 21 days, albeit only the NCHA was significant. Due to the composite nature of the nanocellulose-based materials, there was a large range of nanoelasticity reported. The nanocellulose based inks also had higher break force and ultimate compressive strength compared to the HA alone, indicating the nanocellulose confers structural strength and resilience to the material, which is important for clinical translation. Native nasoseptal cartilage has a Young's modulus of 2-4 MPa, so further work on strengthening the materials is warranted in the first instance, either through prolonged or enhanced culture conditions or material structural modification (Griffin *et al.*, 2016b).

### 6.4.4 NCHA bioinks demonstrate satisfactory biocompatibility but the printing process may influence cell viability and behaviour

All cells encapsulated in the bioinks demonstrated evidence of increasing cell number and good viability over the course of 21 days in culture. Furthermore, cells embedded in the NCHA exposed to the low dose (5 µM) hydrogen peroxide crosslinking agent appeared to have minimal cytotoxicity, especially in comparison to the 0.5 M calcium chloride (as previously optimised (Al-Sabah *et al.*, 2019)) used to crosslink NCA. In addition to visualising increased cell density with the live-dead assays, evidence of increasing cell number in NCHA was implied with the alamarBlue assay, in which increased metabolic activity was seen across seeding densities of $5x10^5$ to $5x10^6$ cells per ml of biomaterial and over the course of 21 days. HA generally is perceived to have good biocompatibility: enhanced cell viability and proliferation has been observed in other studies when added to NC-alginate inks (Lafuente-Merchan *et al.*, 2021) and for culturing adipocytes in which an immediate viability of 64% increased to 95% at 7 days of culture (Henriksson, Gatenholm and Hägg, 2017).

Whilst the NCHA and crosslinking appeared to have limited adverse effects on cell viability, the same cannot be reported for the bioprinting process. At the viscosity of the bioink used, the high printing pressures needed for extrusion with a 22G nozzle evoked high levels of shear stress (292 Pa) that correlated with reduced cell viability. It was interesting that the adverse effect on cell viability was not immediately apparent on the live-dead assay, with a stark reduction in viable cell number noted only after 24 hours. This is likely to reflect a number of cells that die of apoptosis secondary to shear damage: a recognised pathway in response to shear (Sharifi and Gharravi, 2019) that may take hours to days (Green, 2005). In previous studies *in vitro*, exposure of chondrocytes to shear as low as 1.6 Pa (albeit over 24 hours) led to an increase in nitric oxide release, elevation in nucleosomal DNA fragments and reduction in BCL-2 expression: markers of apoptotic activation (Smith, Carter and Schurman, 2004). In fact, necrosis did not appear to be a major component of the cell death pathway evoked by 3D bioprinting: the live dead, alamarBlue and LDH assays had

comparable immediate viabilities between the printed and unprinted conditions. Cell viability post extrusion printing is typically reported in the region of 70-90% (Rutz, Lewis and Shah, 2017), so an immediate post-printing viability of 80% aligns to this value, however the 24 hour viability of 65% is lower than many reported extrusion bioprinting studies, emphasising the importance of timepoint selection in providing a reflective overview of cell death pathways. Given the good biocompatibility of NCHA as a bioink, further work in optimising printing parameters such as nozzle geometry and extrusion pressures is warranted: even reducing the extrusion pressure by 10 kPa is expected to reduce the shear stress by approximately 1/3 in the computational modelling (Figure 6.23).

Mediating shear stress is also pivotal in ensuring lineage retention and appropriate gene expression profiles (Yourek *et al.*, 2010). The shear stress the cells experienced in the 3D bioprinting process (roughly 290 Pa) appears to have surpassed a mechanotransductive threshold in which both chondrogenic (ACAN1, SOX9) but also osteogenic gene expression (ALP) has been activated. In articular cartilage, high shear stress is believed to underpin osteoarthritic changes, whereas low levels of shear stress are believed to contribute to normal homeostatic mechanisms (Lane Smith *et al.*, 2000). This shear stress response is mediated through the pericellular matrix, primary cilium and stretch activated calcium channels on the surface membrane, with TGFβ1 implicated in degenerative changes (Zhao *et al.*, 2020). The threshold of gene activation in nasoseptal and auricular cartilages is unknown, with the focus so far on understanding mechanotransduction primarily on load-bearing articular cartilage. However, shear stress has been reported to evoke osteogenic differentiation of mesenchymal stem cells, at levels as low as 1 Pa (Yourek *et al.*, 2010; Yue *et al.*, 2019). The gene expression effect appears to be transient with regard to bone markers, but had a latent effect on COL2 expression, which was significantly attenuated at 72 hours, consistent with other studies of the biological effects of shear on chondrocytes (Smith, Carter and Schurman, 2004).

### 6.4.5 Summary

The aim of this chapter was to perform a robust comparison of the suitability of NCA and NCHA bioinks: the two previously optimised bioinks in the preceding chapters. Whilst nanocellulose augments both alginate and HA printability, structural changes in the NCA and NCHA materials that occur post-crosslinking render NCHA superior in terms of shape fidelity. These advantageous printing and crosslinking characteristics are enhanced further by the superior biocompatibility of NCHA, evoking SOX9-driven increases in chondrogenic differentiation, cell proliferation and ECM production to yield constructs that not only populate with chondrocytes but stiffen with extracellular matrix deposition, holding great promise for clinical translation. The printing process itself presents limitations on the biocompatibility of 3D bioprinting NCHA for cartilage tissue engineering, with further parameter refinement warranted to optimise cell viability and retention of a chondrogenic phenotype.

# Chapter 7: Discussion

## Chapter 7: Discussion

### 7.1 Tissue engineering cartilage for facial reconstructive surgery

The ability to tissue engineer cartilage would create a paradigm shift in reconstructive surgery. Contemporary facial reconstruction involving the replacement of deficient cartilage involves the use of cartilaginous grafts with donor site morbidity or alloplastic materials which are prone to infection or extrusion (Jovic *et al.*, 2020). Although replacement of elastic nasal or auricular cartilage with rigid costal cartilage can yield good aesthetic results in expert hands, the framework is prone to ossification, involves donor site morbidity, and requires staged, lengthy and highly specialised operations (Jessop *et al.*, 2015, 2016; Jovic *et al.*, 2020).

3D bioprinting is an attractive alternative to current surgical approaches to reconstruct the ear, obviating the needs for donor sites and presenting the advantages of personalisation, customisation and biomimicry to yield bioengineered cartilage in an identical morphology to the intended tissue (Jovic *et al.*, 2018). Efforts to tissue engineer cartilage for reconstructive surgery have led to a paucity of clinically applicable successes, and the controversy surrounding some of these attempts is undeniable (Macchiarini *et al.*, 2008; Yanaga *et al.*, 2009; Delaere, 2013; Gonfiotti *et al.*, 2014; Zhou *et al.*, 2018b). Successful tissue engineering *in vitro* is attributable to an optimum selection of cells, scaffold and environment: the 'holy trinity' of bioengineering (Vinatier *et al.*, 2009). Whilst the focus of this thesis was the design of a novel, natural and composite biomaterial for bioprinting facial cartilage, attention has been drawn to the essential nature of all components of successful tissue engineering. The main findings from each component covered in this thesis are discussed in the context of the existing literature. Through addressing each of these components in synergy, and where identified unanswered gaps in knowledge, it is the hope that research in this domain can progress along the trajectory to clinical translation.

### 7.2 The importance of cell selection for 3D bioprinting cartilage tissue

Approaches to bioengineering cartilage to date demonstrate enormous heterogeneity in cell selection, ranging from tissue specific sources

(chondroprogenitor cells and chondrocytes) to ADSCs, BMSCs and iPSCs (Jessop *et al.*, 2017). The discovery of a population of tissue specific chondroprogenitor cells in articular cartilage heralded the advent of a new era in cartilage tissue engineering (Williams, Ilyas M. Khan, *et al.*, 2010), and these were believed to have been identified thereafter in nasoseptal cartilage in 2020 (Jessop *et al.*, 2020). Whilst the promise of tissue-specific stem cells in cartilage would offer the benefits of expansion within a biomaterial and directed chondrogenic lineage differentiation to maximise extracellular matrix production, this thesis adds to the already controversial body of evidence surrounding chondroprogenitor cell isolation, characterisation and expansion. Although the aim of this thesis is to 3D bioprint auricular structures, nasoseptal cells have been used owing to their availability from septal surgeries but also as the tissue they produce is stiffer than elastic auricular cartilage (Griffin, Premakumar, Seifalian, Szarko and Butler, 2016; Griffin, Premakumar, Seifalian, Szarko and Butler, 2016b). It is the feeling of experienced ear reconstruction specialists that this might address some of the mechanical shortcomings of auricular cartilage tissue engineering, especially when the considerably stiffer costal cartilages are the current gold standard of reconstruction (Thomas H Jovic *et al.*, 2020). In ear reconstruction surgery, the skin pocket is often limited in surface area, which when coupled to the unpliable solid base of the mastoid bone and posterior auricular area, could render auricular elastic cartilage prone to deformation if a direct 'like for like' replacement was used.

It has been increasingly argued that chondroprogenitor cells are a type of mesenchymal stem cell, capable of trilineage differentiation, expressing key stem cell surface markers and demonstrating plastic adherence (Dominici *et al.*, 2006; Karlsson *et al.*, 2009; Williams, Ilyas M. Khan, *et al.*, 2010; Jessop *et al.*, 2020). Published approaches to isolate these cells include flow assisted cell sorting, isolation on the basis of migration, and adhesion to fibronectin. Fibronectin adhesion is the most popular and simple means of isolating these cells from cartilage tissue (Jessop *et al.*, 2019). This thesis has demonstrated that where nasoseptal cartilage is concerned, the majority of cells isolated from tissue digests demonstrate adherence to fibronectin, making it an unsuitable assay for isolating chondroprogenitor cells. Indeed, other recently published literature has

questioned the validity of this assay and its reliance on CD49e expression as potentially flawed methodology for isolating chondroprogenitors in articular cartilage (Kachroo, Ramasamy and Vinod, 2020; Vinod *et al.*, 2021). In standard culture conditions, all cells isolated from nasoseptal cartilage begin to demonstrate features consistent with mesenchymal stem cell-like behaviour: plastic adherence, the presence of mesenchymal stem cell markers and trilineage differentiation potential. In this thesis, these changes were observed as early as first passage, and as such, this acquired, dedifferentiated phenotype might explain how researchers using different isolation methods have yielded cell populations that demonstrate similar behaviours and cell markers. Indeed, where dedifferentiation has been considered, studies have struggled to phenotypically distinguish the two proposed cell populations (Khan *et al.*, 2009; Vinod, Boopalan and Sathishkumar, 2018; Vinod *et al.*, 2019, 2020), relying primarily on differences in gene expression to distinguish one population from another. This thesis demonstrates that whilst cells that adhere to fibronectin may express higher chondrogenic markers, this is insufficient grounds to declare a distinct population has been isolated, as fibronectin is known to evoke chondrogenic gene expression (Singh and Schwarzbauer, 2014; Casanova *et al.*, 2020), leading to a potential to confound cause and effect. As with other studies, the homology in cell phenotype was not found to not be a phenomenon exclusively attributable to 2D monolayer conditions (Vinod *et al.*, 2019).

Another significant consideration is whether or not combining stem cells and chondrocytes in optimised ratios can yield preferable behaviours for tissue engineering and bioprinting purposes. In both monoculture and 3D culture, this thesis demonstrated no advantage to combining cell populations separated out by fibronectin adherence, in terms of extracellular matrix production, chondrogenic gene expression or growth profiles. This mirrors a recent finding in articular cartilage in which combining articular chondroprogenitors with chondrocytes yielded similar findings (Vinod *et al.*, 2019). The evidence from this thesis, supported by recent studies of articular cartilage, is that current methods of isolating, defining and retaining chondroprogenitor cells are inadequate. In order to maximise the potential of tissue specific progenitor cells, further research efforts must be diverted to ensuring that firstly, true chondroprogenitor cell

populations have been isolated distinctly from chondrocytes that have dedifferentiated. Secondly, that a standardised and reproducible means of isolating these cells can be formulated and ideally applied to cartilage cells from all types of hyaline cartilage. Thirdly, that chondrocyte culture conditions can be optimised in a way that enables both expansion and phenotypic retention so that more reliable co-culture experiments of chondrocytes and chondroprogenitors can be undertaken for exploitation in tissue engineering applications.

### 7.3 Bioink design and fabrication for 3D bioprinting facial cartilage

### 7.3.1   Biological properties of bioinks for 3D printing cartilage tissue

The ideal bioink for cartilage tissue engineering should possess the following biological properties: excellent biocompatibility, encouragement of cartilage phenotypic retention/differentiation, promote cell adhesion, chondrogenic gene expression and ECM production (Han *et al.*, 2021).

In this thesis, we firstly demonstrated that both nanocellulose and alginate are suitable biological materials for enhancing a chondrogenic environment for cartilage tissue engineering. This was evidenced by increases in cell number, chondrogenic gene expression and cartilage ECM production, consistent with previously published literature using a similar combination of biomaterials (Markstedt *et al.*, 2015; Martínez Ávila *et al.*, 2015; Müller *et al.*, 2017; Jessop *et al.*, 2019). What this thesis adds to the body of knowledge surrounding nanocellulose-alginate bioinks is a comparison of pulp-derived nanocellulose structural subtypes and objective evidence that nanocellulose possesses greater chondrogenicity than alginate bioinks alone. The literature on pulp-derived nanocelluloses for cartilage bioprinting typically report use of the fibrillar type, owing to its perceived mimicry of collagen fibres (Markstedt *et al.*, 2015a; Martínez Ávila *et al.*, 2015; Nguyen *et al.*, 2017). Previous work in our group involving the characterisation of nanocellulose crystals, fibrils and blend materials has demonstrated significant structural and rheological differences that would be expected to translate to differences in cell behaviour and printability (Kyle *et al.*, 2018). Whilst the fibrils demonstrate the best properties for 3D printing, the crystals appear to promote the highest levels of chondrogenic gene expression,

meaning structural mimicry of collagen fibrils alone is insufficient to nurture a chondrogenic environment. Based on structural analyses, pore sizes are more likely to have influenced these differences (Kyle *et al.*, 2018; Al-Sabah *et al.*, 2019). The nanocellulose blend variant is unique to our research group but appears to offer a balance between the superior printability of the fibrils and the biocompatibility of the crystals.

Whilst heavily used in 3D bioprinting, especially of mesenchymal tissues such as cartilage and bone (Tarassoli *et al.*, 2021), alginate has poor printability characteristics and is believed to encapsulate cells (Schütz *et al.*, 2017). The latter hinders essential cellular processes such as migration and proliferation upon which tissue engineering heavily depends. In order to further enhance the suitability of the nanocellulose based bioink for 3D bioprinting cartilage, a crosslinkable chondrogenic hydrogel was sought to replace the alginate component of the bioink. Hyaluronic acid, as a native, extrudable and biocompatible natural component of cartilage extracellular matrix, was felt to complement the "collagen-like" structure of pulp-derived nanocellulose biologically whilst retaining a printable bioink as proven in studies of 3D printing adipose tissue (Henriksson, Gatenholm and Hägg, 2017).

Although a plethora of crosslinking approaches have been described for hyaluronic acid hydrogels, hydrogen peroxide induced peroxidation offers a greater control of the exposure of chondrocytes to the crosslinking agent than physical crosslinking modalities such as ultraviolet radiation and thermal gelation (Khunmanee, Jeong and Park, 2017). This has also been found to support greater cell distribution, greater focal adhesion length and lessen traction stress in HA hydrogels (Loebel *et al.*, 2017). Furthermore, previous in vitro studies have indicated a cytocompatible dose of hydrogen peroxide in the micromolar range may be permissive of crosslinking whilst preserving cell viability and genetic stability (Asada *et al.*, 2001; Martin *et al.*, 2005; Khan *et al.*, 2008; Röhner *et al.*, 2011; Seager *et al.*, 2012). Human nasoseptal chondrocytes appeared to tolerate transient exposure to 5 to 10µM $H_2O_2$ without effect to viability or proliferation, and structurally this dose of crosslinking agent appeared to be adequate for

crosslinking when left *in situ* for five minutes, with comparable mechanical properties to the recommended crosslinking doses of 115 mM.

In optimising the nanocellulose-hyaluronic acid bioinks for cartilage bioprinting, it was apparent that bioinks with higher percentages of nanocellulose (20HA and 40HA) possessed superior rheological, structural and chondrogenic properties, consistent with previously published combinations of nanocellulose-alginate and nanocellulose-HA (Markstedt *et al.*, 2015; Henriksson, Gatenholm and Hägg, 2017; Nguyen *et al.*, 2017; Jessop *et al.*, 2019). Cartilage derived cells thrived in all HA, NCA and NCHA biomaterials studied, showing sustained increases in chondrogenic gene expression and increases cell number over 21 days, rendering them each valid biomaterials for cartilage tissue engineering. As hypothesised, replacing the alginate with hyaluronic acid further augmented the chondrogenicity of the bioink, as evidenced by gene expression of COL2, ACAN1 and SOX9, increased extracellular matrix protein and glycosaminoglycan production and attenuated osteogenic gene expression.

The previously optimised crosslinking doses for NCA ($0.5M$ $CaCl_2$ (Al-Sabah *et al.*, 2019a; Jessop *et al.*, 2019a)) and NCHA ($5\mu M$ $H_2O_2$) also demonstrated that the biocompatibility of the crosslinked NCHA material was not only superior to crosslinked NCA, but no different than control populations (cells without biomaterial). These promising findings merit further investigation of biocompatibility prior to use in vivo. Specifically, although biocompatibility of 5-$10\mu M$ $H_2O_2$ was demonstrated in this thesis, a more detailed assessment of DNA damage following exposure to this agent is warranted, as this may not be reflected in cell viability assessments (Low *et al.*, 2008; Seager *et al.*, 2012). It is important to note that peroxide itself is a cellular signalling mechanism that may attenuate expression of type II collagen and aggrecan in chondrocytes (Martin *et al.*, 2005). Though expression of these genes was not directly explored in chondrocytes exposed to hydrogen peroxide, no inhibitive effects appeared to prevail in the chondrocytes cultured in NCHA or HA bioinks studied in this thesis.

### 7.3.2 Mechanical properties of bioinks for 3D printing cartilage tissue

The design of bioinks comprised of natural and plant-derived materials classically have shortcomings in their structural and mechanical properties compared to synthetic materials (Chimene *et al.*, 2016).

All the hydrogels studied in this thesis demonstrated the ability to be extruded through a printer nozzle for 3D printing, with all nanocellulose and HA-based formulations additionally offering shear thinning behaviours. Divergence from the ideal properties for printability became apparent rheologically where HA-dominant bioinks exhibited a dominance of viscous over elastic behaviour, reflected in a poor post-printing shape fidelity that mean HA alone is essentially unprintable (in the concentrations and parameters used for this thesis). Nanocellulose augmented all aspects of printability, producing a bioink that possessed superior shear thinning and post-printing shape fidelity. The printability of nanocellulose mirrors the ordered and disordered regions of nanocellulose particles that confer stiffness yet flexibility respectively and can disentangle to enable alignment in the direction of flow for extrusion (Lin and Dufresne, 2014). The extent to which NCHA is suitable for 3D bioprinting cartilage tissue is demonstrated in its ability to successfully print an entire human auricle: a testament to the post printing shape fidelity and print resolution needed to emulate this complex 3D geometry.

Post-printing, an ideal bioink should change minimally in the presence of crosslinking agents and under culture conditions (Schwab *et al.*, 2020). Of all the bioinks studied, NCHA had the lowest swelling and crosslinking changes, despite maintaining a reasonable porosity of approximately 60%. NCA in contrast, exhibited large amounts of swelling in culture and post-crosslinking, which would need to be factored into prints using this material combination.

Native auricular cartilage tissue has an elastic modulus of approximately 1.4-2.1MPa (Griffin, Premakumar, Seifalian, Szarko and Butler, 2016a), whereas nasoseptal cartilage has an even higher elastic modulus of 2.7MPa (Griffin, Premakumar, Seifalian, Szarko and Butler, 2016b). Bioinks seeking to emulate this tissue would ideally surpass these values in order to withstand the soft tissue coverage and scarring associated with reconstruction. The crosslinked

biomaterials in this thesis had elastic moduli in the region of 10-30 kPa, meaning they fall short of the target tissues by approximately 100-fold. HA, despite its covalent crosslinking, was brittle under compressive forces, and softened further under culture conditions with cells: a property that has been previously described as a limitation of HA bioinks (Antich *et al.*, 2020). These limitations restrict its suitability for use alone as a bioink for cartilage tissue engineering. Greater promise was conferred by the combination of nanocellulose and hyaluronic acid, where increases in the elastic modulus were observed after culture with cells. Whilst this was still an elastic modulus far lower than that of native auricular cartilage, the fact that the cells were contributing matrix that stiffened the material holds promise for achieving a durable material for *in vivo* use. In order to enhance the strength of the NCHA material, exploitation of the available hydroxyl groups on pulp-derived nanocellulose to yield a crosslinkable domain holds promise (Kyle *et al.*, 2018). Previous reports of TEMPO-mediated oxidation reactions have been described in which a functionalised carboxyl group is introduced into the nanocellulose molecule to enable ionic crosslinking using divalent cations such as with alginate (Lin, Bruzzese and Dufresne, 2012; Rees *et al.*, 2015; Levanič *et al.*, 2020). Modification of nanocellulose in this manner was found to significantly enhance the strength of nanocellulose-alginate sponges by almost 3-fold (Lin, Bruzzese and Dufresne, 2012). Whilst this approach warrants further investigation in the context of strengthening NCHA bioinks, increasing the degree of crosslinking may influence pore geometry and chondrogenic capabilities which would require further exploration in parallel to the changes in mechanical properties. Pore geometry in the crosslinked biomaterial warrants further investigation using techniques such as SEM to interrogate pore sizes and distribution in the NCHA material to complete the essential characterisation for this bioink, which has been previously completed with success in the NCA bioinks used in this thesis (Kyle *et al.*, 2018; Al-Sabah *et al.*, 2019; Jessop *et al.*, 2019). Another limitation of TEMPO oxidation of nanocellulose may be accelerated degradation, as oxidated forms are more easily hydrolysed *in vivo* (Lin and Dufresne, 2014). This degradation in physiological conditions is also problematic of alginate based gels, which are prone to degradation and mechanical instability

in ionic solutions (such as culture medium) unless the crosslinking is repeated periodically (Matyash *et al.*, 2014).

## 7.4 Optimisation of environmental factors in cartilage bioprinting

The final consideration for 3D bioprinted cartilage is the conditions of culture post-printing. Whilst the combination of cells and bioink are essential, this thesis emphasises that printing processes and culture conditions will have profound impacts on how the cells proceed to populate the scaffold and produce extracellular matrix that more closely resembles cartilage tissue, and that the key to this is ensuring the correct balance of mechanical stimuli are achieved.

### 7.4.1 The printing process

This thesis has explored the development of a computational model that can be used to correlate nozzle geometry and printing pressures with cell viability and gene expression. Currently, a typical printing pressure of 30KPa enables consistent extrusion of NCHA bioink through a 22G nozzle, which itself offers high printing resolution and accurate, controlled deposition. The caveat to achieving such detail is shear stress, which in this model comprises values of almost 300Pa to enable this ink to be extruded: values that are deleterious to optimal cell survival and behaviour (Smith, Carter and Schurman, 2004; Webb and Doyle, 2017). The salient observations in this thesis were that the cell damage incurred by this process were not immediately apparent, and only manifested after 24 hours of culture, indicative that apoptotic pathways had been activated by the shear stress evoked by the printing process, but that the shear was insufficient to cause overt cell necrosis or lysis as would be detected at the earlier timepoints and in the LDH assay (Green, 2005; Sharifi and Gharravi, 2019). Whilst the literature generally cites viability post-printing with hydrogels to be in the region of 70-90% (Rutz, Lewis and Shah, 2017), it is important to consider the timepoints at which these values were taken and the cellular signalling pathways that may be evoked.

Whilst optimising cell viability is paramount, an apparently overlooked phenomenon is the effect that shear stress during 3D printing has on the behaviour of chondrocytes that survive the 3D printing process. Connective tissues such as cartilage and bone are known to be mechanically sensitive tissues, responding to these extrinsic signals to guide gene expression and matrix formation (Millward-Sadler and Salter, 2004; Stewart *et al.*, 2020; Zhao *et al.*, 2020). The estimated values of 300Pa in this study appear to be sufficient to not only transiently upregulate chondrogenic genes (SOX9 and ACAN1), but a threshold for osteogenesis was also activated, as evidenced by an early increase in ALP expression. Whilst most of these effects were only transient in relation to the printing process, others were long lasting: specifically the stark downregulation of COL2A1 expression. In articular cartilage, high shear is believed to accelerate osteoarthritic changes: reduced collagen II deposition and increased calcification of cartilage matrix (Lane Smith *et al.*, 2000; Smith, Carter and Schurman, 2004; Yue *et al.*, 2019; Zhao *et al.*, 2020). It is significant that these processes can be evoked through 3D printing and that the effects may endure as long as 72 hours (if not longer) after the transient printing process. Using the computational model, the next stages of this research are to further characterise the levels of shear stress that have acceptable long term cell viability and retention of chondrogenic gene expression profiles. This could be achieved through modulating nozzle geometry, bioink viscosity and printing pressures and correlating the predicted levels of shear with immediate and delayed markers of cell death and osteogenic gene expression. Alternatively, methods to enhance cellular protection could be explored.

### 7.4.2 Dynamic culture conditions

Whilst the last two decades have seen extensive research efforts into developing novel bioinks; printing technologies, crosslinking processes (Pedroza-González *et al.*, 2021) and optimisation of bioreactor technology is predicted to dominate the field of cartilage tissue engineering research in future years (Fu *et al.*, 2021). The aim of the culture period post-printing is to optimise the population of the scaffold with chondrocytes and to guide cellular differentiation into a

chondrogenic, matrix producing phenotype. Bioreactors can facilitate and augment this process by increasing perfusion (nutrient delivery, waste removal), better regulation of physicochemical conditions such as pH and temperature and the use of mechanical forces to mimic physiological conditions (Mabvuure, Hindocha and S. Khan, 2012).

The types of forces that could be generated in bioreactors include perfusion pressure, shear stress, hydrostatic pressure, tension and compression, modelled on the basis of the types of stresses that the articular cartilage of a joint such as the knee might undergo physiologically (K. Li *et al.*, 2017). Whilst many of these may indeed enhance articular cartilage formation, this myriad of forces is unlikely to be encountered by the nasal septum or auricle physiologically, and as such it is difficult to predict how these cells might respond. Limited data in the field has indicated that, like articular cartilage, nasoseptal cartilage may respond to intermittent compressive force, mimicking the extrinsic forces of craniofacial growth (Takano-Yamamoto *et al.*, 1991).

In order to enhance culture conditions *in vitro*, in this thesis a simple perfusion bioreactor set up was designed in which 48 well plates containing tissue engineered cartilage were subjected to orbital shaking during 14 days of culture. Using computational modelling, the fluid velocity, pressure gradient and shear stresses of this set up exerted much lower forces than the threshold that has been shown previously to evoke a biologically relevant mechanotransduction signal in articular cartilage (Gemmiti and Guldberg, 2009; Fahy, Alini and Stoddart, 2018). However, augmenting flow rates has been shown to enhance cell proliferation and chondrogenicity at rates as low as 1µm/s in other studies (Pazzano *et al.*, 2000). This thesis achieved flow rates of 3µm/s with subsequent sustained increases in chondrogenic gene expression observed over a 14 day time period, demonstrating the impact of augmented scaffold perfusion on cartilage tissue chondrogenesis *in vitro*. Further work is warranted to better characterise the mechanical stimuli that augment chondrogenesis of the facial cartilages and to determine whether these forces can be emulated in a bioreactor set up using anatomically sized constructs to further enhance chondrogenesis.

### 7.4.3 Cell culture medium

The culture medium used in this thesis was deliberately minimalistic to be able to assess the effect of being embedded in a crosslinked bioink, and the influence on chondrogenicity to eliminate the confounding effects of differential growth factor supplementation. An array of cytokines and growth factors are believed to augment chondrogenic differentiation in culture conditions, including TGF-β, Fibroblast growth factor-2 and interleukin 1β (Heng, Cao and Lee, 2004) in addition to non-proteinaceous factors such as ascorbic acid and dexamethasone (Farquharson *et al.*, 1998; Johnstone *et al.*, 1998; Mackay *et al.*, 1998). In order to maximise cellular expansion, maturation and matrix production in 3D printed tissue, exploring the ideal combination of these growth factors for nasoseptal chondrocytes is warranted. Given the increase in elastic modulus seen after 21 days of co-culturing NCHA and nasoseptal chondrocytes without growth factor supplementation, the inclusion of these additives may further enhance the mechanical properties of the cell-laden 3D bioprinted constructs.

## 7.5 Next steps and future directions

Whilst this thesis has identified a novel and promising combination of biomaterials for bioprinting cartilage, our findings, have highlighted there is the potential to optimise cell source, biomechanical characteristics of the scaffold and further enhance environmental components of the tissue engineering process.

Owing to limitations of equipment availability, of which the coronavirus pandemic has had a major influence, there are some essential components of the material characterisation that remain to be investigated. Specifically, methods such as SEM of the NCHA bioinks would be essential to enable a better understanding of how the different combinations of NC and HA, and the different strengths of the crosslinking agent, influence the pore sizes. With this information, greater correlation of these important structural findings with the biological behaviours can be used to guide future cartilage tissue engineering efforts. Further optimisation of printing parameters is also required to ensure the most suitable conditions for viability and chondrogenicity are implemented at the beginning of the tissue engineering trajectory, and that negative effects of shear stress do not

outweigh the benefits of developing a chondrogenic bioink and culture environment. Ultimately, the best test of chondrogenic potential, biocompatibility and durability of NCHA bioinks is to trial these constructs *in vivo*, and funding has been secured by the Reconstructive Surgery & Regenerative Medicine Research Group to perform animal models at Harvard University in the United States (AAPS/EURAPS Scholarship (Iain Whitaker) and Scar Free Foundation Programme Grant (Iain Whitaker)). *In vivo* more rapid deposition of ECM and material stiffening is anticipated based on previous studies of *in vivo* implantation of bioprinted cartilage tissue using nanocellulose (Apelgren *et al.*, 2017; Möller *et al.*, 2017). As discussed in Sections 7.1 to 7.4, the additional refinements that warrant exploration based on the findings of this thesis are as follows:

- Reliably isolating and expanding chondroprogenitor cells
- Exploring the use of crosslinkable nanocelluloses to enhance material strength
- Optimising printing parameters to protect cell phenotype and viability
- Refining post-printing culture conditions to maximise cartilage production and maturation with a focus on media supplementation and mechanical stimulation

## 7.6 Concluding remarks

The aim of this thesis was to develop a novel, natural printable biomaterial with the ultimate aim of producing tissue specific 3D printed cartilage constructs for facial reconstructive purposes. Nanocellulose has a proven record of excellent printability and chondrogenicity properties. It holds tremendous promise for bioprinting cartilage tissue, augmented further by the addition of hyaluronic acid as a chondrogenic and biocompatible additive. This material blend is readily printable into complex anatomical structures including auricular subunits, and promotes the expansion and differentiation of chondrocytes to encourage the formation of tissue that mimics native cartilage tissue. With further refinement, the foundation of work in this thesis provides a platform for developing novel approaches for personalised 3D bioprinted auricular reconstruction options for patients. It has been a privilege to contribute to the body of knowledge in this

rapidly evolving field of research, and I hope that some of the data generated in this thesis may one day contribute to helping transform the lives of those affected by facial disfigurement.

## Appendix 1: Compensation Matrix
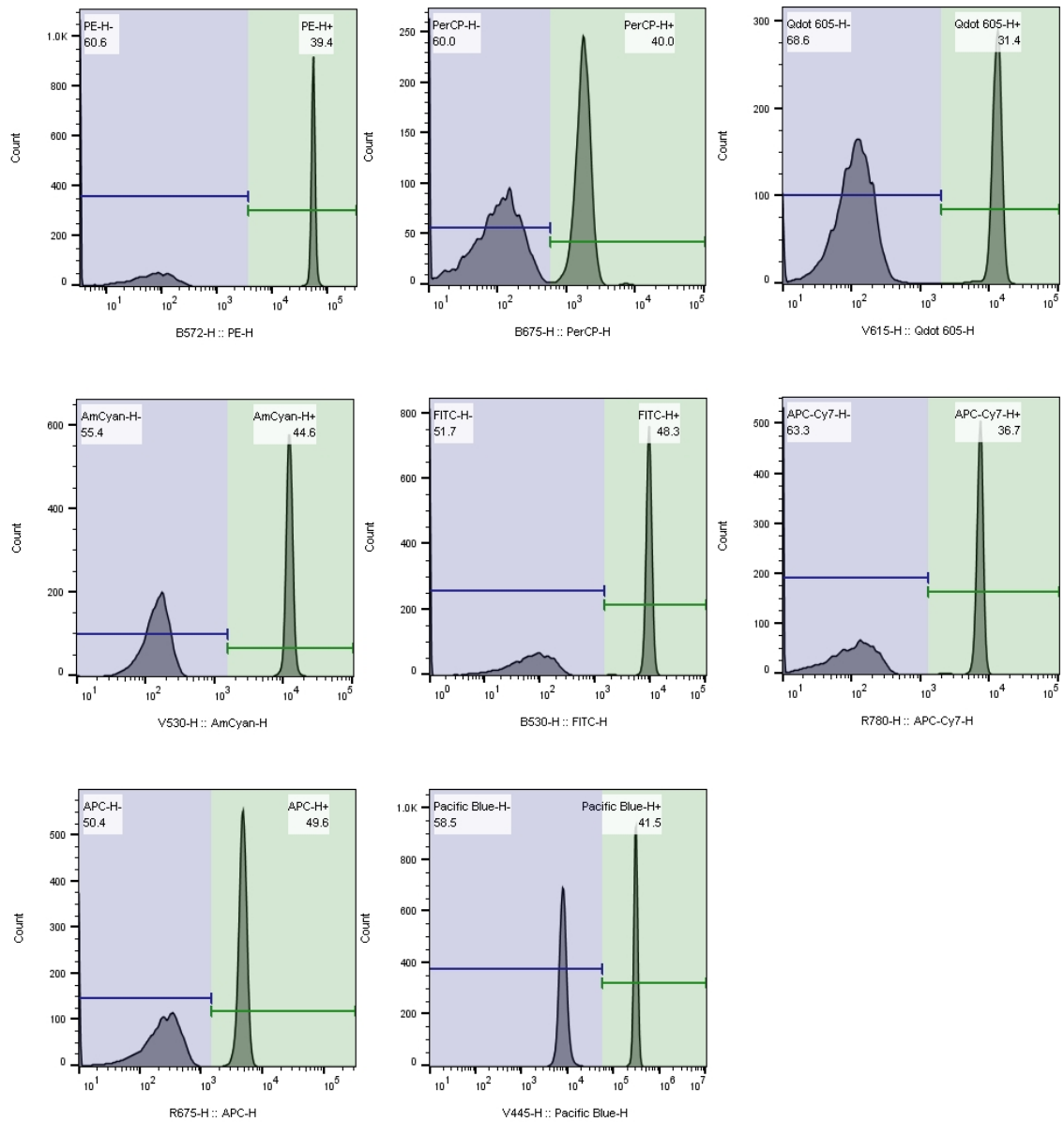


*Appendix 1: Compensation controls for each fluorophore used in the flow cytometric analysis of cell populations. Each compensation bead affixes the fluorophore to provide a positive (green) and negative (blue) peak to distinguish true positive and negative values which can be applied as a compensation matrix to subsequent analyses to correct for non-specific fluorescence.*

# Appendix 2: Stress Strain Curves

**A**

### Alginate



**B**

### NCB



**C**

### NCC



**D**

### NCF



**E**

### HA



**F**
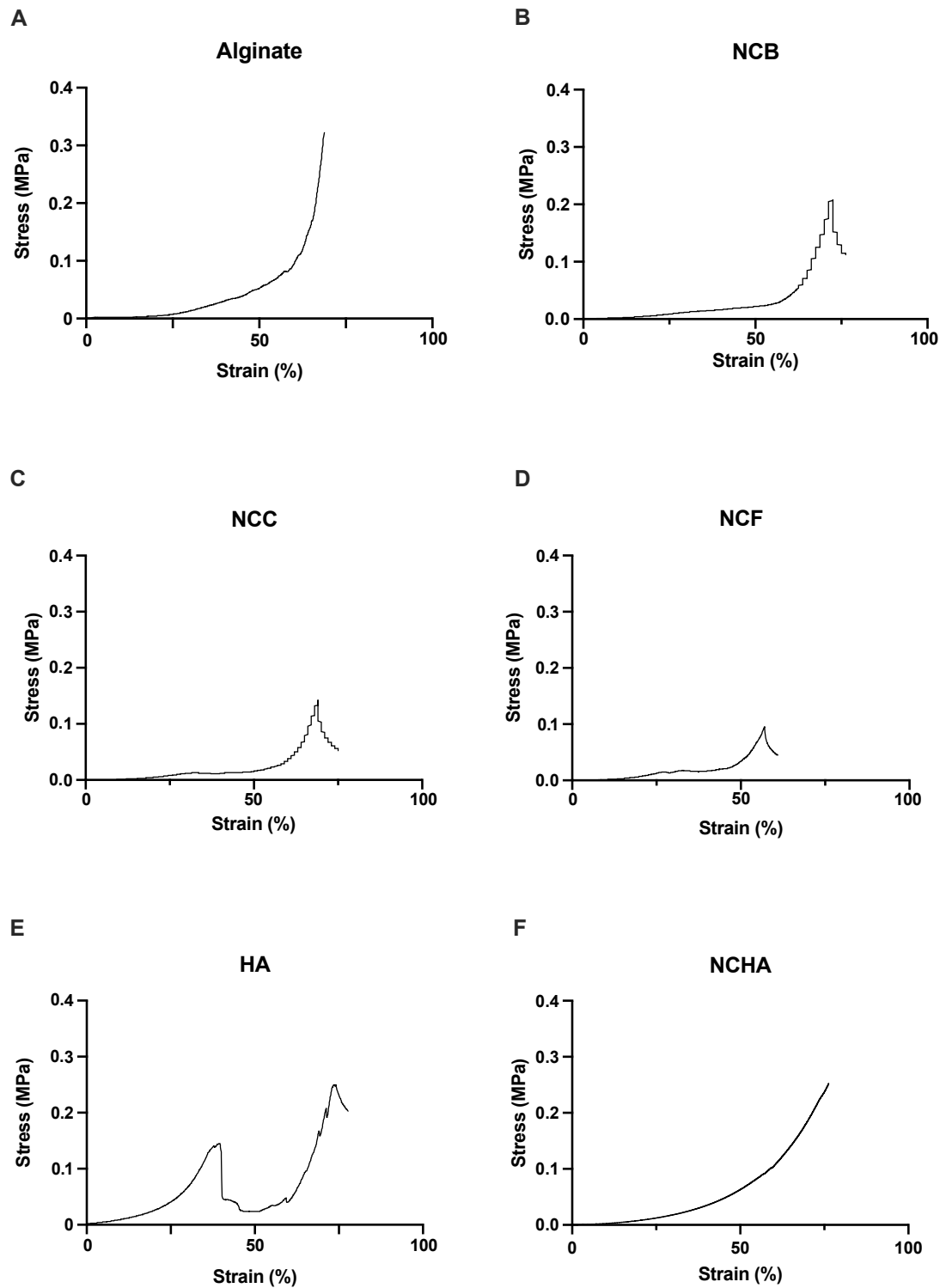
### NCHA



*Appendix 2: Exemplar stress-strain curves for each biomaterial A) Alginate, B) NCB, C) NCC, D) NCF, E) HA and F) NCHA generated using compression testing. Strain to failure is plotted against Stress in MPa to generate each curve.*

## Bibliography

Aarstad, O. *et al.* (2017) 'Mechanical properties of composite hydrogels of alginate and cellulose nanofibrils', *Polymers*. Polymers (Basel), 9(8). doi: 10.3390/polym9080378.

Abu-Hakmeh, A. *et al.* (2016) 'Sequential gelation of tyramine-substituted hyaluronic acid hydrogels enhances mechanical integrity and cell viability', *Medical & biological engineering & computing*. Med Biol Eng Comput, 54(12), pp. 1893–1902. doi: 10.1007/S11517-016-1474-0.

Adams, A. M., Arruda, E. M. and Larkin, L. M. (2012) 'Use of adipose-derived stem cells to fabricate scaffoldless tissue-engineered neural conduits in vitro', *Neuroscience*, 201, pp. 349–356. doi: 10.1016/j.neuroscience.2011.11.004.

Afizah, H. *et al.* (2007) 'A Comparison Between the Chondrogenic Potential of Human Bone Marrow Stem Cells (BMSCs) and Adipose-Derived Stem Cells (ADSCs) Taken from the Same Donors', *https://home.liebertpub.com/ten*. Mary Ann Liebert, Inc. 140 Huguenot Street, 3rd Floor New Rochelle, NY 10801 USA , 13(4), pp. 659–666. doi: 10.1089/TEN.2006.0118.

Agarwal, S. *et al.* (2020) 'Current Developments in 3D Bioprinting for Tissue and Organ Regeneration–A Review', *Frontiers in Mechanical Engineering*. Frontiers, 0, p. 90. doi: 10.3389/FMECH.2020.589171.

Ahearne, M. *et al.* (2005) 'Characterizing the viscoelastic properties of thin hydrogel-based constructs for tissue engineering applications.', *Journal of the Royal Society, Interface*. The Royal Society, 2(5), pp. 455–63. doi: 10.1098/rsif.2005.0065.

Al-Himdani, S. *et al.* (2017) 'Tissue-Engineered Solutions in Plastic and Reconstructive Surgery: Principles and Practice', *Frontiers in Surgery*, 4, p. 4. doi: 10.3389/fsurg.2017.00004.

Al-Sabah, A. *et al.* (2019) 'Structural and mechanical characterization of crosslinked and sterilised nanocellulose-based hydrogels for cartilage tissue engineering', *Carbohydrate Polymers*, 212, pp. 242–251. doi: 10.1016/j.carbpol.2019.02.057.

Alderson, D. (2019) 'The future of surgery', *British Journal of Surgery*. John Wiley and Sons Ltd, 106(1), pp. 9–10. doi: 10.1002/bjs.11086.

Aljohani, W. *et al.* (2018) 'Bioprinting and its applications in tissue engineering and regenerative medicine', *International Journal of Biological Macromolecules*, 107(Pt A), pp. 261–275. doi: 10.1016/j.ijbiomac.2017.08.171.

Almouemen, N., Kelly, H. M. and O'Leary, C. (2019) 'Tissue Engineering: Understanding the Role of Biomaterials and Biophysical Forces on Cell Functionality Through Computational and Structural Biotechnology Analytical Methods', *Computational and Structural Biotechnology Journal*. Research Network of Computational and Structural Biotechnology, 17, p. 591. doi: 10.1016/J.CSBJ.2019.04.008.

Anderson, D. E. *et al.* (2018) 'Physioxia Promotes the Articular Chondrocyte-Like Phenotype in Human Chondroprogenitor-Derived Self-Organized Tissue', *Tissue engineering. Part A*. Tissue Eng Part A, 24(3–4), pp. 264–274. doi: 10.1089/TEN.TEA.2016.0510.

Ansari, S. *et al.* (2016) 'Muscle Tissue Engineering Using Gingival Mesenchymal Stem Cells Encapsulated in Alginate Hydrogels Containing Multiple Growth Factors', *Annals of Biomedical Engineering*, 44(6), pp. 1908–1920. doi: 10.1007/s10439-016-1594-6.

Anthwal, N. and Thompson, H. (2016) 'The development of the mammalian outer and middle ear', *Journal of Anatomy*. Wiley-Blackwell, 228(2), p. 217. doi: 10.1111/JOA.12344.

Antich, C. *et al.* (2020) 'Bio-inspired hydrogel composed of hyaluronic acid and alginate as a potential bioink for 3D bioprinting of articular cartilage engineering constructs', *Acta Biomaterialia*. Elsevier, 106, pp. 114–123. doi: 10.1016/J.ACTBIO.2020.01.046.

Ao, C. *et al.* (2017) 'Fabrication and characterization of electrospun cellulose/nano-hydroxyapatite nanofibers for bone tissue engineering', *International Journal of Biological Macromolecules*. Elsevier, 97, pp. 568–573. doi: 10.1016/J.IJBIOMAC.2016.12.091.

Apelgren, P. *et al.* (2017) 'Chondrocytes and stem cells in 3D-bioprinted structures create human cartilage in vivo', *PloS one*. PLoS One, 12(12). doi: 10.1371/JOURNAL.PONE.0189428.

Arora, A. *et al.* (2017) 'Co-culture of infrapatellar fat pad–derived mesenchymal stromal cells and articular chondrocytes in plasma clot for cartilage tissue engineering', *Cytotherapy*. Elsevier, 19(7), pp. 881–894. doi: 10.1016/J.JCYT.2017.04.003.

Asada, S. *et al.* (2001) 'Hydrogen peroxide induces apoptosis of chondrocytes; involvement of calcium ion and extracellular signal-regulated protein kinase', *Inflammation Research 2001 50:1*. Springer, 50(1), pp. 19–23. doi: 10.1007/S000110050719.

Athanasiou, K. A., Niederauer, G. G. and Agrawal, C. M. (1996) 'Sterilization, toxicity, biocompatibility and clinical applications of polylactic acid/ polyglycolic acid copolymers', *Biomaterials*. Elsevier, 17(2), pp. 93–102. doi: 10.1016/0142-9612(96)85754-1.

Aurich, M. *et al.* (2018) 'Induced Redifferentiation of Human Chondrocytes from Articular Cartilage Lesion in Alginate Bead Culture After Monolayer Dedifferentiation: An Alternative Cell Source for Cell-Based Therapies?', *Tissue engineering. Part A*. Tissue Eng Part A, 24(3–4), pp. 275–286. doi: 10.1089/TEN.TEA.2016.0505.

Axpe, E. and Oyen, M. L. (2016) 'Applications of Alginate-Based Bioinks in 3D Bioprinting.', *International journal of molecular sciences*. Multidisciplinary Digital Publishing Institute (MDPI), 17(12). doi: 10.3390/ijms17121976.

Bächinger, H. P. *et al.* (2010) 'Collagen Formation and Structure', *Comprehensive Natural Products II: Chemistry and Biology*. Elsevier, 5, pp. 469–530. doi: 10.1016/B978-008045382-8.00698-5.

Bäckdahl, H. *et al.* (2006) 'Mechanical properties of bacterial cellulose and interactions with smooth muscle cells', *Biomaterials*. Elsevier, 27(9), pp. 2141–2149. doi: 10.1016/J.BIOMATERIALS.2005.10.026.

Bakarich, S. E. *et al.* (2014) 'Printed ionic-covalent entanglement hydrogels from

carrageenan and an epoxy amine', *RSC Advances*. The Royal Society of Chemistry, 4(72), pp. 38088–38092. doi: 10.1039/C4RA07109C.

Balgude, A. P. *et al.* (2001) 'Agarose gel stiffness determines rate of DRG neurite extension in 3D cultures', *Biomaterials*. Elsevier, 22(10), pp. 1077–1084. doi: 10.1016/S0142-9612(00)00350-1.

Baptista, L. S. *et al.* (2013) 'Bioengineered Cartilage in a Scaffold-Free Method by Human Cartilage-Derived Progenitor Cells: A Comparison With Human Adipose-Derived Mesenchymal Stromal Cells', *Artificial Organs*. John Wiley & Sons, Ltd, 37(12), pp. 1068–1075. doi: 10.1111/AOR.12121.

Bar Oz, M. *et al.* (2016) 'Acetylation reduces SOX9 nuclear entry and ACAN gene transactivation in human chondrocytes', *Aging Cell*. Wiley-Blackwell, 15(3), p. 499. doi: 10.1111/ACEL.12456.

Barret, J. P. *et al.* (2011) 'Full face transplant: the first case report.', *Annals of surgery*, 254(2), pp. 252–6. doi: 10.1097/SLA.0b013e318226a607.

Beck, J. C. (1925) 'The anatomy, psychology, diagnosis and treatment of congenital malformation and absence of the ear', *Laryngoscope*, 35(Nov), pp. 813–831.

Bell, D. M. *et al.* (1997) 'SOX9 directly regulates the type-II collagen gene', *Nature genetics*. Nat Genet, 16(2), pp. 174–178. doi: 10.1038/NG0697-174.

Benning, L. *et al.* (2018) 'Assessment of hydrogels for bioprinting of endothelial cells', *Journal of Biomedical Materials Research Part A*. John Wiley & Sons, Ltd, 106(4), pp. 935–947. doi: 10.1002/jbm.a.36291.

Berghaus, A. and Toplak, F. (1986) 'Surgical Concepts for Reconstruction of the Auricle: History and Current State of the Art', *Archives of Otolaryngology--Head and Neck Surgery*, 112(4), pp. 388–397. doi: 10.1001/archotol.1986.03780040028007.

Berry, M. D. *et al.* (2016) 'Pharmacological characterization of a high-affinity p-tyramine transporter in rat brain synaptosomes', *Scientific Reports 2016 6:1*. Nature Publishing Group, 6(1), pp. 1–13. doi: 10.1038/srep38006.

Bertassoni, L. E. *et al.* (2014) 'Direct-write bioprinting of cell-laden methacrylated gelatin hydrogels', *Biofabrication*, 6(2), p. 024105. doi: 10.1088/1758-5082/6/2/024105.

Bhatnagar, D., Simon, M. and Rafailovich, M. H. (2016) 'Hydrogels for Regenerative Medicine', in *Recent Advances in Biopolymers*. InTech. doi: 10.5772/62044.

Bhattacharya, M. *et al.* (2012) 'Nanofibrillar cellulose hydrogel promotes three-dimensional liver cell culture', *Journal of Controlled Release*. Elsevier, 164(3), pp. 291–298. doi: 10.1016/J.JCONREL.2012.06.039.

Bichara, D. A. *et al.* (2012) 'The tissue-engineered auricle: past, present, and future.', *Tissue engineering. Part B, Reviews*, 18(1), pp. 51–61. doi: 10.1089/ten.TEB.2011.0326.

Billiet, T. *et al.* (2014) 'The 3D printing of gelatin methacrylamide cell-laden tissue-engineered constructs with high cell viability', *Biomaterials*. Biomaterials, 35(1), pp. 49–62. doi: 10.1016/J.BIOMATERIALS.2013.09.078.

Bleuel, J. *et al.* (2015) 'Effects of cyclic tensile strain on chondrocyte metabolism: a systematic review', *PloS one*. PLoS One, 10(3). doi: 10.1371/JOURNAL.PONE.0119816.

Bos, E. J. *et al.* (2018) 'Structural and mechanical comparison of human ear, alar, and septal cartilage', *Plastic and Reconstructive Surgery - Global Open*. Lippincott Williams and Wilkins, 6(1). doi: 10.1097/GOX.0000000000001610.

Brent, B. *et al.* (1992) 'Auricular repair with autogenous rib cartilage grafts: Two decades of experience with 600 cases', *Plastic and Reconstructive Surgery*, 90(3), pp. 375–376. doi: 10.1097/00006534-199209000-00002.

Browne, R. *et al.* (2021) 'Botched Botox Injections: A Transatlantic Epidemic', *Plastic and reconstructive surgery*, 147(2). doi: 10.1097/PRS.0000000000007571.

Bružauskaitė, I. *et al.* (2016) 'Scaffolds and cells for tissue regeneration: different scaffold pore sizes—different cell effects', *Cytotechnology*. Springer, 68(3), p. 355. doi: 10.1007/S10616-015-9895-4.

Bulstrode, N., Stewart, K. and Moffat, C. (2015) 'What age to offer ear reconstruction?', *Journal of plastic, reconstructive & aesthetic surgery : JPRAS*, 68(9), pp. 1322–1323. Available at: https://pubmed.ncbi.nlm.nih.gov/26066848/ (Accessed: 5 June 2020).

Campbell, G. (1983) 'Otoplasty: something old, something new. Reconstruction of the external ear using fresh cadaver homograft ear cartilage and a sternomastoid myocutaneous flap', *British Journal of Plastic Surgery*, 36(2), pp. 262–266. doi: 10.1016/0007-1226(83)90105-4.

Cao, Y. *et al.* (1997) 'Transplantation of chondrocytes utilizing a polymer-cell construct to produce tissue-engineered cartilage in the shape of a human ear', *Plastic and Reconstructive Surgery*, 100(2), pp. 297–304. doi: 10.1097/00006534-199708000-00001.

Cao, Y. *et al.* (1998) 'Comparative study of the use of poly(glycolic acid), calcium alginate and pluronics in the engineering of autologous porcine cartilage', *Journal of Biomaterials Science, Polymer Edition*, 9(5), pp. 475–487. doi: 10.1163/156856298X00578.

Caron, M. M. J. *et al.* (2012) 'Redifferentiation of dedifferentiated human articular chondrocytes: comparison of 2D and 3D cultures', *Osteoarthritis and Cartilage*. W.B. Saunders, 20(10), pp. 1170–1178. doi: 10.1016/J.JOCA.2012.06.016.

Carvalho, M., Martins, A. P. and Sepodes, B. (2019) 'Hurdles in gene therapy regulatory approval : a retrospective analysis of European Marketing Authorization Applications', *Drug Discovery Today*. Elsevier Ltd, 24(3), pp. 823–828. doi: 10.1016/j.drudis.2018.12.007.

Casale, J. and Crane, J. S. (2021) 'Biochemistry, Glycosaminoglycans', *StatPearls*. StatPearls Publishing. Available at: https://www.ncbi.nlm.nih.gov/books/NBK544295/ (Accessed: 12 January 2022).

Casanova, M. R. *et al.* (2020) 'Fibronectin Bound to a Fibrous Substrate Has Chondrogenic Induction Properties', *Biomacromolecules*. American Chemical Society, 21(4), pp. 1368–1378. doi: 10.1021/ACS.BIOMAC.9B01546.

Catros, S. *et al.* (2010) 'Effect of laser energy, substrate film thickness and bioink

viscosity on viability of endothelial cells printed by Laser-Assisted Bioprinting', *Applied Surface Science*, 257, pp. 5142–5147. doi: 10.1016/j.apsusc.2010.11.049.

Chang, Q., Cui, W. D. and Fan, W. M. (2011) 'Co-culture of chondrocytes and bone marrow mesenchymal stem cells in vitro enhances the expression of cartilaginous extracellular matrix components', *Brazilian Journal of Medical and Biological Research*. Associação Brasileira de Divulgação Científica, 44(4), pp. 303–310. doi: 10.1590/S0100-879X2011007500026.

Changing Faces (2019) *My Visible Difference*, *Changing Faces: My Visible Differences*. Available at: https://www.changingfaces.org.uk/wp-content/uploads/2021/01/CHANGING-FACES-Report-My-Visible-Difference.pdf (Accessed: 16 June 2022).

Check Hayden, E. (2011) 'Stem cells: The growing pains of pluripotency', *Nature*. Nature, 473(7347), pp. 272–274. doi: 10.1038/473272A.

Chen, H. *et al.* (2019) 'Effect of rheological properties of potato, rice and corn starches on their hot-extrusion 3D printing behaviors', *Journal of Food Engineering*. Elsevier, 244, pp. 150–158. doi: 10.1016/J.JFOODENG.2018.09.011.

Chen, P. *et al.* (1991) 'Stimulation of chondrogenesis in limb bud mesoderm cells by recombinant human bone morphogenetic protein 2B (BMP-2B) and modulation by transforming growth factor beta 1 and beta 2', *Experimental cell research*. Exp Cell Res, 195(2), pp. 509–515. doi: 10.1016/0014-4827(91)90403-H.

Chen, Q., Suki, B. and An, K.-N. (2003) *DYNAMIC MECHANICAL PROPERTIES OF AGAROSE GEL BY A FRACTIONAL DERIVATIVE MODEL*. Available at: https://pdfs.semanticscholar.org/ecfb/27677cc4ba385fa67b547c9c41ae796edd97.pdf (Accessed: 26 February 2019).

Chimene, D. *et al.* (2016) 'Advanced Bioinks for 3D Printing: A Materials Science Perspective', *Annals of Biomedical Engineering*, 44(6), pp. 2090–2102. doi: 10.1007/s10439-016-1638-y.

Clark, C. C. *et al.* (2019) 'A mechanically robust thixotropic collagen and hyaluronic acid bioink supplemented with gelatin nanoparticles', *Bioprinting*. Elsevier, 16, p. e00058. doi: 10.1016/J.BPRINT.2019.E00058.

Cohen, B. P. *et al.* (2018) 'Tissue engineering the human auricle by auricular chondrocyte-mesenchymal stem cell co-implantation', *PLOS ONE*. Public Library of Science, 13(10), p. e0202356. doi: 10.1371/JOURNAL.PONE.0202356.

Coimbra, P. *et al.* (2011) 'Preparation and chemical and biological characterization of a pectin/chitosan polyelectrolyte complex scaffold for possible bone tissue engineering applications', *International Journal of Biological Macromolecules*. Elsevier, 48(1), pp. 112–118. doi: 10.1016/J.IJBIOMAC.2010.10.006.

Concaro, S., Gustavson, F. and Gatenholm, P. (2009) 'Bioreactors for tissue engineering of cartilage', *Advances in biochemical engineering/biotechnology*. Adv Biochem Eng Biotechnol, 112, pp. 125–143. doi: 10.1007/978-3-540-69357-4 6.

Constantine, K. K. *et al.* (2014) 'Comparison of Microtia reconstruction outcomes using rib cartilage vs porous polyethylene implant', *JAMA Facial Plastic Surgery*, 16(4), pp. 240–244. doi: 10.1001/jamafacial.2014.30.

Cooper, C. *et al.* (2017) 'Use of Intraarticular Hyaluronic Acid in the Management of Knee Osteoarthritis in Clinical Practice', *Arthritis care & research*. Arthritis Care Res (Hoboken), 69(9), pp. 1287–1296. doi: 10.1002/ACR.23204.

Correro-Shahgaldian, M. R. *et al.* (2016) 'Properties and Mechanobiological Behavior of Bovine Nasal Septum Cartilage', *Annals of Biomedical Engineering*, 44(5), pp. 1821–1831. doi: 10.1007/s10439-015-1481-6.

Cotin, G. *et al.* (1983) '[1-stage operation in major aplasias of the ear. Value of combined plastic and functional intervention].', *Annales d'oto-laryngologie et de chirurgie cervico faciale : bulletin de la Societe d'oto-laryngologie des hopitaux de Paris*, 100(4), pp. 293–7. Available at: http://www.ncbi.nlm.nih.gov/pubmed/6881817 (Accessed: 25 October 2019).

Cunha, L. and Grenha, A. (2016) 'Sulfated Seaweed Polysaccharides as

Multifunctional Materials in Drug Delivery Applications.', *Marine drugs*. Multidisciplinary Digital Publishing Institute (MDPI), 14(3). doi: 10.3390/md14030042.

Daly, A. C. *et al.* (2016) '3D Bioprinting of Developmentally Inspired Templates for Whole Bone Organ Engineering', *Advanced Healthcare Materials*, 5(18), pp. 2353–2362. doi: 10.1002/adhm.201600182.

Darling, E. M. and Athanasiou, K. A. (2005) 'Rapid phenotypic changes in passaged articular chondrocyte subpopulations', *Journal of orthopaedic research : official publication of the Orthopaedic Research Society*. J Orthop Res, 23(2), pp. 425–432. doi: 10.1016/J.ORTHRES.2004.08.008.

Das, R. H. J. *et al.* (2008) 'In vitro expansion affects the response of chondrocytes to mechanical stimulation', *Osteoarthritis and Cartilage*. W.B. Saunders, 16(3), pp. 385–391. doi: 10.1016/J.JOCA.2007.07.014.

Dashtdar, H. *et al.* (2016) 'Ultra-structural changes and expression of chondrogenic and hypertrophic genes during chondrogenic differentiation of mesenchymal stromal cells in alginate beads', *PeerJ*. PeerJ Inc., 2016(3). doi: 10.7717/PEERJ.1650/SUPP-1.

Al Dayeh, A. A. and Herring, S. W. (2014) 'Compressive and tensile mechanical properties of the porcine nasal septum', *Journal of biomechanics*. NIH Public Access, 47(1), p. 154. doi: 10.1016/J.JBIOMECH.2013.09.026.

Delaere, P. R. (2013) 'Stem-cell-based, tissue-engineered tracheal replacement in a child', *The Lancet*, 381(9861), p. 113. doi: 10.1016/S0140-6736(13)60043-4.

Derakhshanfar, S. *et al.* (2018) '3D bioprinting for biomedical devices and tissue engineering: A review of recent trends and advances', *Bioactive Materials*. Elsevier, 3(2), pp. 144–156. doi: 10.1016/J.BIOACTMAT.2017.11.008.

Diañez, I. *et al.* (2019) '3D printing in situ gelification of κ-carrageenan solutions: Effect of printing variables on the rheological response', *Food Hydrocolloids*. Elsevier, 87, pp. 321–330. doi: 10.1016/J.FOODHYD.2018.08.010.

Diaz-Romero, J. *et al.* (2005) 'Immunophenotypic analysis of human articular chondrocytes: changes in surface markers associated with cell expansion in

monolayer culture', *Journal of cellular physiology*. J Cell Physiol, 202(3), pp. 731–742. doi: 10.1002/JCP.20164.

Diaz-Romero, J. *et al.* (2008) 'Immunophenotypic changes of human articular chondrocytes during monolayer culture reflect bona fide dedifferentiation rather than amplification of progenitor cells', *Journal of cellular physiology*. J Cell Physiol, 214(1), pp. 75–83. doi: 10.1002/JCP.21161.

Diaz-Siso, J. R. *et al.* (2018) 'Vascularized Composite Allotransplantation: Alternatives and Catch-22s.', *Plastic and reconstructive surgery*, 142(5), pp. 1320–1326. doi: 10.1097/PRS.0000000000004855.

Diekman, B. O. *et al.* (2010) 'Chondrogenesis of adult stem cells from adipose tissue and bone marrow: induction by growth factors and cartilage-derived matrix', *Tissue engineering. Part A*. Tissue Eng Part A, 16(2), pp. 523–533. doi: 10.1089/TEN.TEA.2009.0398.

Djordjević, V. B. (2004) 'Free radicals in cell biology', *International review of cytology*. Int Rev Cytol, 237, pp. 57–89. doi: 10.1016/S0074-7696(04)37002-6.

Dolati, F. *et al.* (2014) 'In vitro evaluation of carbon-nanotube-reinforced bioprintable vascular conduits.', *Nanotechnology*. NIH Public Access, 25(14), p. 145101. doi: 10.1088/0957-4484/25/14/145101.

Dominici, M. *et al.* (2006) 'Minimal criteria for defining multipotent mesenchymal stromal cells. The International Society for Cellular Therapy position statement', *Cytotherapy*. Cytotherapy, 8(4), pp. 315–317. doi: 10.1080/14653240600855905.

Dowthwaite, G. P. *et al.* (2004) 'The surface of articular cartilage contains a progenitor cell population', *Journal of cell science*. J Cell Sci, 117(Pt 6), pp. 889–897. doi: 10.1242/JCS.00912.

Drury, J. L. and Mooney, D. J. (2003) 'Hydrogels for tissue engineering: scaffold design variables and applications', *Biomaterials*. Elsevier, 24(24), pp. 4337–4351. doi: 10.1016/S0142-9612(03)00340-5.

Duan, B. *et al.* (2013) '3D bioprinting of heterogeneous aortic valve conduits with alginate/gelatin hydrogels.', *Journal of biomedical materials research. Part A*. NIH

Public Access, 101(5), pp. 1255–64. doi: 10.1002/jbm.a.34420.

Duan, B. *et al.* (2014) 'Three-dimensional printed trileaflet valve conduits using biological hydrogels and human valve interstitial cells', *Acta Biomaterialia*. Elsevier, 10(5), pp. 1836–1846. doi: 10.1016/J.ACTBIO.2013.12.005.

Elder, B. D. and Athanasiou, K. A. (2009) 'Hydrostatic Pressure in Articular Cartilage Tissue Engineering: From Chondrocytes to Tissue Regeneration', *Tissue Engineering. Part B, Reviews*. Mary Ann Liebert, Inc., 15(1), p. 43. doi: 10.1089/TEN.TEB.2008.0435.

Elsaesser, A. F. *et al.* (2016) 'Characterization of a migrative subpopulation of adult human nasoseptal chondrocytes with progenitor cell features and their potential for in vivo cartilage regeneration strategies', *Cell & Bioscience 2016 6:1*. BioMed Central, 6(1), pp. 1–15. doi: 10.1186/S13578-016-0078-6.

European Commission (2007) 'REGULATION (EC) No 1394/2007 OF THE EUROPEAN PARLIAMENT AND OF THE COUNCIL of 13 November 2007 on advanced therapy medicinal products and amending Directive 2001/83/EC and Regulation (EC) No 726/2004', *Official Journal of the European Union*.

European Commission (2013) *Eight Great Technologies European Commission*. Available at: https://rio.jrc.ec.europa.eu/en/library/eight-great-technologies (Accessed: 28 October 2019).

European Medicines Agency (2016) 'The European regulatory system for medicines The EU regulatory system for medicines', pp. 1–6.

Ewa-Choy, Y. W. *et al.* (2017) 'Effect of alginate concentration on chondrogenesis of co-cultured human adipose-derived stem cells and nasal chondrocytes: a biological study', *Biomaterials Research*. BioMed Central, 21(1). doi: 10.1186/S40824-017-0105-7.

Eyre, D. (2002) 'Collagen of articular cartilage', *Arthritis research*. Arthritis Res, 4(1), pp. 30–35. doi: 10.1186/AR380.

Eyre, D. R. (2004) 'Collagens and cartilage matrix homeostasis', *Clinical orthopaedics and related research*. Clin Orthop Relat Res, 427(427 Suppl). doi: 10.1097/01.BLO.0000144855.48640.B9.

Fagien, S. *et al.* (2019) 'Rheologic and Physicochemical Properties Used to Differentiate Injectable Hyaluronic Acid Filler Products', *Plastic and reconstructive surgery*. Plast Reconstr Surg, 143(4), pp. 707e-720e. doi: 10.1097/PRS.0000000000005429.

Fahy, N., Alini, M. and Stoddart, M. J. (2018) 'Mechanical stimulation of mesenchymal stem cells: Implications for cartilage tissue engineering', *Journal of Orthopaedic Research®*. John Wiley & Sons, Ltd, 36(1), pp. 52–63. doi: 10.1002/JOR.23670.

Fallacara, A. *et al.* (2018) 'Hyaluronic Acid in the Third Millennium', *Polymers*. Polymers (Basel), 10(7). doi: 10.3390/POLYM10070701.

Fan, R. *et al.* (2016) 'Bio-printing cell-laden Matrigel–agarose constructs', *Journal of Biomaterials Applications*. SAGE PublicationsSage UK: London, England, 31(5), pp. 684–692. doi: 10.1177/0885328216669238.

Fang, Y. Z., Yang, S. and Wu, G. (2002) 'Free radicals, antioxidants, and nutrition', *Nutrition (Burbank, Los Angeles County, Calif.)*. Nutrition, 18(10), pp. 872–879. doi: 10.1016/S0899-9007(02)00916-4.

Farquharson, C. *et al.* (1998) 'Ascorbic acid-induced chondrocyte terminal differentiation: the role of the extracellular matrix and 1,25-dihydroxyvitamin D', *European journal of cell biology*. Eur J Cell Biol, 76(2), pp. 110–118. doi: 10.1016/S0171-9335(98)80023-X.

Fawzy, M. A. *et al.* (2017) 'Optimization of alginate alkaline extraction technology from Sargassum latifolium and its potential antioxidant and emulsifying properties', *Carbohydrate Polymers*, 157, pp. 1903–1912. doi: 10.1016/j.carbpol.2016.11.077.

Feng, W. *et al.* (2017) 'Effects of Short-Range Order on the Magnetic and Mechanical Properties of FeCoNi(AlSi)x High Entropy Alloys', *Metals*. Multidisciplinary Digital Publishing Institute, 7(11), p. 482. doi: 10.3390/met7110482.

Ferreira, M. M. *et al.* (2017) 'Clinical Development and Commercialization of Advanced Therapy Medicinal Products ( ATMPs ) in EU : how are the product

pipeline and regulatory framework evolving?', *Human gene therapy clinical development*, 28(3), pp. 126–135. doi: 10.1089/humc.2016.193.

Fink, H. P. *et al.* (1997) 'Investigation of the supramolecular structure of never dried bacterial cellulose', *Macromolecular Symposia*. John Wiley & Sons, Ltd, 120(1), pp. 207–217. doi: 10.1002/MASY.19971200121.

Firmin, F. (2010) 'State-of-the-art autogenous ear reconstruction in cases of microtia.', *Advances in oto-rhino-laryngology*, 68, pp. 25–52. doi: 10.1159/000314561.

Forget, A. *et al.* (2017) 'Mechanically Tunable Bioink for 3D Bioprinting of Human Cells', *Advanced Healthcare Materials*. John Wiley & Sons, Ltd, 6(20), p. 1700255. doi: 10.1002/adhm.201700255.

Fortier, L. A., Nixon, A. J. and Lust, G. (2002) 'Phenotypic expression of equine articular chondrocytes grown in three-dimensional cultures supplemented with supraphysiologic concentrations of insulin-like growth factor-1', *American journal of veterinary research*. Am J Vet Res, 63(2), pp. 301–305. doi: 10.2460/AJVR.2002.63.301.

Freeman, F. E. and Kelly, D. J. (2017) 'Tuning Alginate Bioink Stiffness and Composition for Controlled Growth Factor Delivery and to Spatially Direct MSC Fate within Bioprinted Tissues', *Scientific Reports 2017 7:1*. Nature Publishing Group, 7(1), pp. 1–12. doi: 10.1038/s41598-017-17286-1.

Fu, L. *et al.* (2021) 'The Application of Bioreactors for Cartilage Tissue Engineering: Advances, Limitations, and Future Perspectives', *Stem Cells International*. Hindawi Limited, 2021. doi: 10.1155/2021/6621806.

Fung, Y. C. (1981) 'Biomechanics'. New York, NY: Springer New York. doi: 10.1007/978-1-4757-1752-5.

Gao, Y. *et al.* (2014) 'The ECM-cell interaction of cartilage extracellular matrix on chondrocytes', *BioMed Research International*. Hindawi Publishing Corporation, 2014. doi: 10.1155/2014/648459.

Gardner, J. *et al.* (2017) 'Promissory identities: Sociotechnical representations &amp; innovation in regenerative medicine.', *Social science & medicine (1982)*,

174, pp. 70–78. doi: 10.1016/j.socscimed.2016.12.018.

Gardner, J. and Webster, A. (2016) 'The social management of biomedical novelty: Facilitating translation in regenerative medicine', *Social Science & Medicine*. Pergamon, 156, pp. 90–97. doi: 10.1016/J.SOCSCIMED.2016.03.025.

Gardner, J., Webster, A. and Barry, J. (2018) 'Anticipating the clinical adoption of regenerative medicine: building institutional readiness in the UK', *Regenerative Medicine*, 13(1), pp. 29–39. doi: 10.2217/rme-2017-0121.

Gasques, J. A. L., Pereira de Godoy, J. M. and Cruz, E. M. T. N. (2008) 'Psychosocial effects of otoplasty in children with prominent ears.', *Aesthetic plastic surgery*, 32(6), pp. 910–4. doi: 10.1007/s00266-008-9179-x.

Gelse, K., Pöschl, E. and Aigner, T. (2003) 'Collagens--structure, function, and biosynthesis', *Advanced drug delivery reviews*. Adv Drug Deliv Rev, 55(12), pp. 1531–1546. doi: 10.1016/J.ADDR.2003.08.002.

Gemmiti, C. V. and Guldberg, R. E. (2009) 'Shear Stress Magnitude and Duration Modulates Matrix Composition and Tensile Mechanical Properties in Engineered Cartilaginous Tissue', *Biotechnology and bioengineering*. NIH Public Access, 104(4), p. 809. doi: 10.1002/BIT.22440.

Gershlak, J. R. *et al.* (2017) 'Crossing kingdoms: Using decellularized plants as perfusable tissue engineering scaffolds', *Biomaterials*. Elsevier, 125, pp. 13–22. doi: 10.1016/J.BIOMATERIALS.2017.02.011.

Gilbert, F. *et al.* (2018) 'Print Me an Organ? Ethical and Regulatory Issues Emerging from 3D Bioprinting in Medicine', *Science and Engineering Ethics*. Springer Netherlands, 24(1), pp. 73–91. doi: 10.1007/s11948-017-9874-6.

Gillies, H. (1937) 'Reconstruction of the external ear with special reference to the use of maternal ear cartilage as the supporting structure', *Rev Chir Struct.*, (7), pp. 169–79.

Gomes, M. . *et al.* (2002) 'Alternative tissue engineering scaffolds based on starch: processing methodologies, morphology, degradation and mechanical properties', *Materials Science and Engineering: C*. Elsevier, 20(1–2), pp. 19–26. doi: 10.1016/S0928-4931(02)00008-5.

Gonfiotti, A. *et al.* (2014) 'The first tissue-engineered airway transplantation: 5-year follow-up results.', *Lancet (London, England)*, 383(9913), pp. 238–44. doi: 10.1016/S0140-6736(13)62033-4.

Gorecka, J. *et al.* (2019) 'The potential and limitations of induced pluripotent stem cells to achieve wound healing', *Stem Cell Research and Therapy*. BioMed Central Ltd., 10(1), pp. 1–10. doi: 10.1186/S13287-019-1185-1/TABLES/3.

Gorgieva, S., Girandon, L. and Kokol, V. (2017) 'Mineralization potential of cellulose-nanofibrils reinforced gelatine scaffolds for promoted calcium deposition by mesenchymal stem cells', *Materials Science and Engineering: C*. Elsevier, 73, pp. 478–489. doi: 10.1016/J.MSEC.2016.12.092.

Graça, M. F. P. *et al.* (2020) 'Hyaluronic acid-Based wound dressings: A review', *Carbohydrate polymers*. Carbohydr Polym, 241. doi: 10.1016/J.CARBPOL.2020.116364.

Graham, H. B. (1927) 'THE RECONSTRUCTION OF A COMPLETELY DESTROYED AURICLE: CASE REPORT.', *California and western medicine*, 27(4), pp. 518–9. Available at: http://www.ncbi.nlm.nih.gov/pubmed/18740492 (Accessed: 28 October 2019).

Granéli, C. *et al.* (2014) 'Novel markers of osteogenic and adipogenic differentiation of human bone marrow stromal cells identified using a quantitative proteomics approach', *Stem Cell Research*. Elsevier, 12(1), pp. 153–165. doi: 10.1016/J.SCR.2013.09.009.

Green, D. R. (2005) 'Apoptotic Pathways: Ten Minutes to Dead', *Cell*. Cell Press, 121(5), pp. 671–674. doi: 10.1016/J.CELL.2005.05.019.

Griffin, M. F. *et al.* (2016a) 'Biomechanical Characterisation of the Human Auricular Cartilages; Implications for Tissue Engineering', *Annals of Biomedical Engineering*. Ann Biomed Eng, 44(12), pp. 3460–3467. doi: 10.1007/s10439-016-1688-1.

Griffin, M. F. *et al.* (2016b) 'Biomechanical characterisation of the human nasal cartilages; implications for tissue engineering', *Journal of Materials Science: Materials in Medicine*. J Mater Sci Mater Med, 27(1), pp. 1–6. doi:

10.1007/s10856-015-5619-8.

Griffin, M. F. *et al.* (2020) 'Comparison of the compressive mechanical properties of auricular and costal cartilage from patients with microtia', *Journal of biomechanics*. J Biomech, 103. doi: 10.1016/J.JBIOMECH.2020.109688.

Grigoryan, B. *et al.* (2021) 'Development, characterization, and applications of multi-material stereolithography bioprinting', *Scientific Reports 2021 11:1*. Nature Publishing Group, 11(1), pp. 1–13. doi: 10.1038/s41598-021-82102-w.

Grogan, S. P. *et al.* (2007) 'Identification of markers to characterize and sort human articular chondrocytes with enhanced in vitro chondrogenic capacity', *Arthritis & Rheumatism*. John Wiley & Sons, Ltd, 56(2), pp. 586–595. doi: 10.1002/ART.22408.

Grogan, S. P. *et al.* (2009) 'Mesenchymal progenitor cell markers in human articular cartilage: normal distribution and changes in osteoarthritis', *Arthritis research & therapy*. Arthritis Res Ther, 11(3). doi: 10.1186/AR2719.

Groll, J. *et al.* (2016) 'Biofabrication: reappraising the definition of an evolving field.', *Biofabrication*, 8(1), p. 013001. doi: 10.1088/1758-5090/8/1/013001.

Gu, Q. *et al.* (2016) 'Functional 3D Neural Mini-Tissues from Printed Gel-Based Bioink and Human Neural Stem Cells', *Advanced Healthcare Materials*. John Wiley & Sons, Ltd, 5(12), pp. 1429–1438. doi: 10.1002/adhm.201600095.

Gumrah Dumanli, A. (2017) 'Nanocellulose and its Composites for Biomedical Applications', *Current Medicinal Chemistry*, 24(5), pp. 512–528. doi: 10.2174/0929867323666161014124008.

Gungor-Ozkerim, P. S. *et al.* (2018) 'Bioinks for 3D bioprinting: An overview', *Biomaterials Science*. Royal Society of Chemistry, pp. 915–946. doi: 10.1039/c7bm00765e.

Gupta, R. C. *et al.* (2019) 'Hyaluronic Acid: Molecular Mechanisms and Therapeutic Trajectory', *Frontiers in Veterinary Science*. Frontiers Media SA, 6(JUN), p. 192. doi: 10.3389/FVETS.2019.00192.

Guyot, Y. *et al.* (2015) 'A three-dimensional computational fluid dynamics model

of shear stress distribution during neotissue growth in a perfusion bioreactor', *Biotechnology and Bioengineering*, 112(12), pp. 2591–2600. doi: 10.1002/bit.25672.

Guyuron, B. and DeLuca, L. (1997) 'Ear projection and the posterior auricular muscle insertion', *Plastic and reconstructive surgery*. Plast Reconstr Surg, 100(2), pp. 457–460. doi: 10.1097/00006534-199708000-00030.

Hacker, V. H. (1901) *Fälle aus der chirurgischen Klinik: Sitzung vom Jan 19, 1901*. Wien Klin Wochenschr.

Hall, A. C. (2019) 'The Role of Chondrocyte Morphology and Volume in Controlling Phenotype—Implications for Osteoarthritis, Cartilage Repair, and Cartilage Engineering', *Current Rheumatology Reports*. Springer, 21(8). doi: 10.1007/S11926-019-0837-6.

Hamada, T. *et al.* (2013) 'SURFACE MARKERS AND GENE EXPRESSION TO CHARACTERIZE THE DIFFERENTIATION OF MONOLAYER EXPANDED HUMAN ARTICULAR CHONDROCYTES', *Nagoya Journal of Medical Science*. Nagoya University School of Medicine/Graduate School of Medicine, 75(1–2), p. 101. doi: 10.18999/nagjms.75.1-2.101.

Han, L., Grodzinsky, A. J. and Ortiz, C. (2011) 'Nanomechanics of the Cartilage Extracellular Matrix', *Annual review of materials research*. NIH Public Access, 41, p. 133. doi: 10.1146/ANNUREV-MATSCI-062910-100431.

Han, X. *et al.* (2021) 'Advances of Hydrogel-Based Bioprinting for Cartilage Tissue Engineering', *Frontiers in Bioengineering and Biotechnology*. Frontiers Media S.A., 9, p. 816. doi: 10.3389/FBIOE.2021.746564/BIBTEX.

Hardingham, T. E., Oldershaw, R. A. and Tew, S. R. (2006) 'Cartilage, SOX9 and Notch signals in chondrogenesis', *Journal of Anatomy*. Wiley-Blackwell, 209(4), p. 469. doi: 10.1111/J.1469-7580.2006.00630.X.

Hattori, S., Oxford, C. and Reddi, A. H. (2007) 'Identification of superficial zone articular chondrocyte stem/progenitor cells', *Biochemical and biophysical research communications*. Biochem Biophys Res Commun, 358(1), pp. 99–103. doi: 10.1016/J.BBRC.2007.04.142.

Hauptstein, J. *et al.* (2020) 'Hyaluronic Acid-Based Bioink Composition Enabling 3D Bioprinting and Improving Quality of Deposited Cartilaginous Extracellular Matrix', *Advanced Healthcare Materials*. John Wiley & Sons, Ltd, 9(15), p. 2000737. doi: 10.1002/ADHM.202000737.

Havaldar, R., Pilli, S. C. and Putti, B. B. (2014) 'Insights into the effects of tensile and compressive loadings on human femur bone.', *Advanced biomedical research*. Wolters Kluwer -- Medknow Publications, 3, p. 101. doi: 10.4103/2277-9175.129375.

Hazur, J. *et al.* (2020) 'Improving alginate printability for biofabrication: establishment of a universal and homogeneous pre-crosslinking technique', *Biofabrication*. IOP Publishing, 12(4), p. 045004. doi: 10.1088/1758-5090/AB98E5.

He, Y. *et al.* (2016) 'Research on the printability of hydrogels in 3D bioprinting.', *Scientific reports*. Nature Publishing Group, 6, p. 29977. doi: 10.1038/srep29977.

Heath, C. A. (2000) 'The Effects of Physical Forces on Cartilage Tissue Engineering', *Biotechnology and Genetic Engineering Reviews*, 17(1), pp. 533–552. doi: 10.1080/02648725.2000.10648004.

Heid, S. and Boccaccini, A. R. (2020) 'Advancing bioinks for 3D bioprinting using reactive fillers: A review', *Acta Biomaterialia*. Elsevier, 113, pp. 1–22. doi: 10.1016/J.ACTBIO.2020.06.040.

Helwany, M. and Tadi, P. (2021) 'Embryology, Ear', *StatPearls*. StatPearls Publishing. Available at: https://www.ncbi.nlm.nih.gov/books/NBK557588/ (Accessed: 10 January 2022).

Heng, B. C., Cao, T. and Lee, E. H. (2004) 'Directing Stem Cell Differentiation into the Chondrogenic Lineage In Vitro', *STEM CELLS*. John Wiley & Sons, Ltd, 22(7), pp. 1152–1167. doi: 10.1634/STEMCELLS.2004-0062.

Henriksson, I., Gatenholm, P. and Hägg, D. A. (2017) 'Increased lipid accumulation and adipogenic gene expression of adipocytes in 3D bioprinted nanocellulose scaffolds', *Biofabrication*, 9(1), p. 015022. doi: 10.1088/1758-5090/aa5c1c.

Holback, H., Yeo, Y. and Park, K. (2011) 'Hydrogel swelling behavior and its biomedical applications', *Biomedical Hydrogels*. Woodhead Publishing, pp. 3–24. doi: 10.1533/9780857091383.1.3.

Hölzl, K. *et al.* (2016) 'Bioink properties before, during and after 3D bioprinting', *Biofabrication*, 8(3), p. 032002. doi: 10.1088/1758-5090/8/3/032002.

Homicz, M. R. *et al.* (2003) 'A Compositional Analysis of Human Nasal Septal Cartilage', *https://doi.org/10.1001/archfaci.5.1.53*.  Mary Ann Liebert, Inc., publishers  140 Huguenot Street, 3rd Floor New Rochelle, NY 10801 USA , 5(1), pp. 53–58. doi: 10.1001/ARCHFACI.5.1.53.

Van Hoorick, J. *et al.* (2019) '(Photo-)crosslinkable gelatin derivatives for biofabrication applications', *Acta biomaterialia*. Acta Biomater, 97, pp. 46–73. doi: 10.1016/J.ACTBIO.2019.07.035.

Hopp, B. *et al.* (2012) 'Femtosecond laser printing of living cells using absorbing film-assisted laser-induced forward transfer', *Optical Engineering*. International Society for Optics and Photonics, 51(1), p. 014302. doi: 10.1117/1.OE.51.1.014302.

Horkay, F. *et al.* (2009) 'Ions in hyaluronic acid solutions', *The Journal of Chemical Physics*. American Institute of Physics, 131(18). doi: 10.1063/1.3262308.

Hu, W. *et al.* (2019) 'Advances in crosslinking strategies of biomedical hydrogels', *Biomaterials Science*. The Royal Society of Chemistry, 7(3), pp. 843–855. doi: 10.1039/C8BM01246F.

Huang, M. *et al.* (2020) 'High-Performance, UV-Curable Crosslinked Films via Grafting of Hydroxyethyl Methacrylate Methylene Malonate', *Industrial & engineering chemistry research*. NIH Public Access, 59(10), p. 4542. doi: 10.1021/ACS.IECR.9B06618.

Hunziker, E. B. *et al.* (2015) 'An educational review of cartilage repair: precepts & practice--myths & misconceptions--progress & prospects', *Osteoarthritis and cartilage*. Osteoarthritis Cartilage, 23(3), pp. 334–350. doi: 10.1016/J.JOCA.2014.12.011.

Hunziker, E. B., Quinn, T. M. and Häuselmann, H. J. (2002) 'Quantitative structural organization of normal adult human articular cartilage', *Osteoarthritis and cartilage*. Osteoarthritis Cartilage, 10(7), pp. 564–572. doi: 10.1053/JOCA.2002.0814.

Hynes, R. O. (1992) 'Integrins: Versatility, modulation, and signaling in cell adhesion', *Cell*. Cell, pp. 11–25. doi: 10.1016/0092-8674(92)90115-S.

Iglauer, S. *et al.* (2011) 'Dilute iota- and kappa-Carrageenan solutions with high viscosities in high salinity brines', *Journal of Petroleum Science and Engineering*. Elsevier, 75(3–4), pp. 304–311. doi: 10.1016/J.PETROL.2010.11.025.

In, E., Naguib, H. and Haider, M. (2014) 'Mechanical stability analysis of carrageenan-based polymer gel for magnetic resonance imaging liver phantom with lesion particles.', *Journal of medical imaging (Bellingham, Wash.)*. Society of Photo-Optical Instrumentation Engineers, 1(3), p. 035502. doi: 10.1117/1.JMI.1.3.035502.

Iwasaki, M. *et al.* (1993) 'Transforming growth factor-beta 1 stimulates chondrogenesis and inhibits osteogenesis in high density culture of periosteum-derived cells', *Endocrinology*. Endocrinology, 132(4), pp. 1603–1608. doi: 10.1210/ENDO.132.4.8462458.

Jabr, F. (2012) 'In the Flesh: The Embedded Dangers of Untested Stem Cell Cosmetics - Scientific American', *Scientific American*. Available at: https://www.scientificamerican.com/article/stem-cell-cosmetics/ (Accessed: 4 January 2019).

Jaffe, B. F. (1969) 'The incidence of ear diseases in the navajo indians', *Laryngoscope*. Laryngoscope, 79(12), pp. 2126–2134. doi: 10.1288/00005537-196912000-00007.

Jakab, K. *et al.* (2008) 'Tissue Engineering by Self-Assembly of Cells Printed into Topologically Defined Structures', *Tissue Engineering Part A*. Mary Ann Liebert, Inc. 140 Huguenot Street, 3rd Floor New Rochelle, NY 10801 USA , 14(3), pp. 413–421. doi: 10.1089/tea.2007.0173.

Jeong, H.-S., Venkatesan, J. and Kim, S.-K. (2013) 'Hydroxyapatite-fucoidan

nanocomposites for bone tissue engineering', *International Journal of Biological Macromolecules*. Elsevier, 57, pp. 138–141. doi: 10.1016/J.IJBIOMAC.2013.03.011.

Jessop, Z. M. *et al.* (2015) 'The Challenge for Reconstructive Surgeons in the Twenty-First Century: Manufacturing Tissue-Engineered Solutions', *Frontiers in Surgery*, p. 52. doi: 10.3389/fsurg.2015.00052.

Jessop, Z. M. *et al.* (2016) 'Combining regenerative medicine strategies to provide durable reconstructive options: auricular cartilage tissue engineering', *Stem Cell Research & Therapy*, 7(1), p. 19. doi: 10.1186/s13287-015-0273-0.

Jessop, Z. M. *et al.* (2017) '3D bioprinting for reconstructive surgery: Principles, applications and challenges.', *Journal of plastic, reconstructive & aesthetic surgery : JPRAS*, 70(9), pp. 1155–1170. doi: 10.1016/j.bjps.2017.06.001.

Jessop, Zita M *et al.* (2019) 'Printability of pulp derived crystal, fibril and blend nanocellulose-alginate bioinks for extrusion 3D bioprinting', *Biofabrication*, 11(4), p. 045006. doi: 10.1088/1758-5090/ab0631.

Jessop, Zita M. *et al.* (2019) 'Tissue specific stem/progenitor cells for cartilage tissue engineering: A systematic review of the literature', *Applied Physics Reviews*. American Institute of Physics Inc. doi: 10.1063/1.5050814.

Jessop, Z. M. *et al.* (2020) 'Isolation and characterisation of nasoseptal cartilage stem/progenitor cells and their role in the chondrogenic niche', *Stem Cell Research and Therapy*. BioMed Central Ltd., 11(1), pp. 1–13. doi: 10.1186/S13287-020-01663-1/FIGURES/6.

Jiamei, D. *et al.* (2008) 'An investigation of psychological profiles and risk factors in congenital microtia patients', *Journal of plastic, reconstructive & aesthetic surgery : JPRAS*. J Plast Reconstr Aesthet Surg, 61 Suppl 1(SUPPL. 1). doi: 10.1016/J.BJPS.2007.09.002.

Johns, A. L., Im, D. D. and Lewin, S. L. (2018) 'Early Familial Experiences With Microtia: Psychosocial Implications for Pediatric Providers', *Clinical Pediatrics*. SAGE Publications Inc., 57(7), pp. 775–782. doi: 10.1177/0009922817734358.

Johnstone, B. *et al.* (1998) 'In vitro chondrogenesis of bone marrow-derived

mesenchymal progenitor cells', *Experimental cell research*. Exp Cell Res, 238(1), pp. 265–272. doi: 10.1006/EXCR.1997.3858.

Jones, J. W. *et al.* (2000) 'Successful hand transplantation. One-year follow-up. Louisville Hand Transplant Team.', *The New England journal of medicine*, 343(7), pp. 468–73. doi: 10.1056/NEJM200008173430704.

Jorfi, M. and Foster, E. J. (2015) 'Recent advances in nanocellulose for biomedical applications', *Journal of Applied Polymer Science*. John Wiley & Sons, Ltd, 132(14), p. n/a-n/a. doi: 10.1002/app.41719.

Joseph, J. (1916) 'Die Verwendung rhinoplastischer Methoden zur Deckung von Lippen-, Kinn-, Wangen- und Ohrdefekten', *Kriegsverletzungen der Kiefer und der angrenzenden Teile*, pp. 601–14.

Joseph, J. (1931) *Nasenplastik und sonstige Gesichtsplastik*. pt 3. Leipzig, C Kabitzsch.

Jovic, T. H. *et al.* (2018) 'The clinical need for 3D printed tissue in reconstructive surgery', *3D Bioprinting for Reconstructive Surgery*. Woodhead Publishing, pp. 235–244. doi: 10.1016/B978-0-08-101103-4.00002-8.

Jovic, T. H. *et al.* (2019) 'Plant-Derived Biomaterials: A Review of 3D Bioprinting and Biomedical Applications', *Frontiers in Mechanical Engineering*. Frontiers Media SA. doi: 10.3389/fmech.2019.00019.

Jovic, Thomas H. *et al.* (2020) '3D Bioprinting and the Future of Surgery', *Frontiers in Surgery*. Frontiers Media SA, 7, p. 609836. doi: 10.3389/fsurg.2020.609836.

Jovic, Thomas H *et al.* (2020) '"Auricular reconstruction: A sociocultural, surgical and scientific perspective"', *Journal of Plastic, Reconstructive and Aesthetic Surgery*. Elsevier BV, 73(8), pp. 1424–1433. doi: 10.1016/j.bjps.2020.03.025.

Jovic, T. H. *et al.* (2021) 'Microtia: A Data Linkage Study of Epidemiology and Implications for Service Delivery', *Frontiers in Pediatrics*. Frontiers Media S.A., 9, p. 218. doi: 10.3389/FPED.2021.630036/BIBTEX.

Julio Nazer, H., Guillermo Lay-Son, R. and Lucía Cifuentes, O. (2006)

'Prevalencia de nacimiento de microtia-anotia. Maternidad del Hospital Clínico de la Universidad de Chile, período 1983-2005', *Revista Medica de Chile*. Rev Med Chil, pp. 1295–1301. doi: 10.4067/s0034-98872006001000012.

Jung, S. *et al.* (2012) 'A Review of Microvascular Ear Replantation', *Journal of Reconstructive Microsurgery*, 29(03), pp. 181–188. doi: 10.1055/s-0032-1331150.

Kachroo, U., Ramasamy, B. and Vinod, E. (2020) 'Evaluation of CD49e as a distinguishing marker for human articular cartilage derived chondroprogenitors', *Knee*. Knee, 27(3), pp. 833–837. doi: 10.1016/j.knee.2020.04.002.

Karlsson, C. *et al.* (2009) 'Identification of a stem cell niche in the zone of Ranvier within the knee joint', *Journal of anatomy*. J Anat, 215(3), pp. 355–363. doi: 10.1111/J.1469-7580.2009.01115.X.

Kelder, C. *et al.* (2018) 'The 3D Printing of Calcium Phosphate with K-Carrageenan under Conditions Permitting the Incorporation of Biological Components—A Method', *Journal of Functional Biomaterials*, 9(4), p. 57. doi: 10.3390/jfb9040057.

Kerin, A. J., Wisnom, M. R. and Adams, M. A. (1998) 'The compressive strength of articular cartilage', *Proceedings of the Institution of Mechanical Engineers. Part H, Journal of engineering in medicine*. Proc Inst Mech Eng H, 212(4), pp. 273–280. doi: 10.1243/0954411981534051.

Khan, I. M. *et al.* (2008) 'Oxidative stress induces expression of osteoarthritis markers procollagen IIA and 3B3(−) in adult bovine articular cartilage', *Osteoarthritis and Cartilage*. W.B. Saunders, 16(6), pp. 698–707. doi: 10.1016/J.JOCA.2007.10.004.

Khan, I. M. *et al.* (2009) 'Clonal chondroprogenitors maintain telomerase activity and Sox9 expression during extended monolayer culture and retain chondrogenic potential', *Osteoarthritis and Cartilage*, 17(4), pp. 518–528. doi: 10.1016/j.joca.2008.08.002.

Khatiwala, C. *et al.* (2013) '3D CELL BIOPRINTING FOR REGENERATIVE MEDICINE RESEARCH AND THERAPIES',

*http://dx.doi.org/10.1142/S1568558611000301*. World Scientific Publishing Company , 7(1). doi: 10.1142/S1568558611000301.

Khunmanee, S., Jeong, Y. and Park, H. (2017) 'Crosslinking method of hyaluronic-based hydrogel for biomedical applications.', *Journal of tissue engineering*. SAGE Publications, 8, p. 2041731417726464. doi: 10.1177/2041731417726464.

Kiani, C. *et al.* (2002) 'Structure and function of aggrecan', *Cell Research 2002 12:1*. Nature Publishing Group, 12(1), pp. 19–32. doi: 10.1038/sj.cr.7290106.

Kimbrel, E. A. and Lanza, R. (2015) 'Current status of pluripotent stem cells: moving the first therapies to the clinic', *Nature Reviews Drug Discovery*. Nature Publishing Group, 14(10), pp. 681–692. doi: 10.1038/nrd4738.

Kirkham, H. L. D. (1940) 'THE USE OF PRESERVED CARTILAGE IN EAR RECONSTRUCTION', *Annals of Surgery*. Ovid Technologies (Wolters Kluwer Health), 111(5), pp. 896–902. doi: 10.1097/00000658-194005000-00019.

Kisiday, J. D. (2019) 'Expansion of Chondrocytes for Cartilage Tissue Engineering: A Review of Chondrocyte Dedifferentiation and Redifferentiation as a Function of Growth in Expansion Culture', *Regenerative Medicine Frontiers*. Hapres, 2(1), p. e20002. doi: 10.20900/rmf20200002.

Koelling, S. *et al.* (2009) 'Migratory chondrogenic progenitor cells from repair tissue during the later stages of human osteoarthritis', *Cell stem cell*. Cell Stem Cell, 4(4), pp. 324–335. doi: 10.1016/J.STEM.2009.01.015.

Koga, H. *et al.* (2008) 'Comparison of mesenchymal tissues-derived stem cells for in vivo chondrogenesis: Suitable conditions for cell therapy of cartilage defects in rabbit', *Cell and Tissue Research*. Springer, 333(2), pp. 207–215. doi: 10.1007/S00441-008-0633-5/FIGURES/6.

Korte, W. (1905) 'Fall von Ohrenplastik: Sitzung am Nov 13, 1905', *Verh Fr Verein Chir Berlins*, 18, pp. 91–92.

Kubosch, E. J. *et al.* (2016) 'The trans-well coculture of human synovial mesenchymal stem cells with chondrocytes leads to self-organization, chondrogenic differentiation, and secretion of TGFβ', *Stem cell research &*

*therapy*. Stem Cell Res Ther, 7(1). doi: 10.1186/S13287-016-0322-3.

Kundu, J. *et al.* (2015) 'An additive manufacturing-based PCL-alginate-chondrocyte bioprinted scaffold for cartilage tissue engineering', *Journal of Tissue Engineering and Regenerative Medicine*, 9(11), pp. 1286–1297. doi: 10.1002/term.1682.

Kuo, C. K. *et al.* (2006) 'Cartilage tissue engineering: Its potential and uses', *Current Opinion in Rheumatology*. Lippincott Williams and Wilkins, 18(1), pp. 64–73. doi: 10.1097/01.BOR.0000198005.88568.DF.

Kusuhara, H. *et al.* (2009) 'Tissue engineering a model for the human ear: assessment of size, shape, morphology, and gene expression following seeding of different chondrocytes', *Wound repair and regeneration : official publication of the Wound Healing Society [and] the European Tissue Repair Society*. Wound Repair Regen, 17(1), pp. 136–146. doi: 10.1111/J.1524-475X.2008.00451.X.

Kuzmenko, V. *et al.* (2018) 'Tailor-made conductive inks from cellulose nanofibrils for 3D printing of neural guidelines', *Carbohydrate Polymers*. Elsevier, 189, pp. 22–30. doi: 10.1016/J.CARBPOL.2018.01.097.

Kyle, S. *et al.* (2017) '"Printability'' of Candidate Biomaterials for Extrusion Based 3D Printing: State-of-the-Art"', *Advanced Healthcare Materials*, 6(16), p. 1700264. doi: 10.1002/adhm.201700264.

Kyle, S. *et al.* (2018) 'Characterization of pulp derived nanocellulose hydrogels using AVAP® technology', *Carbohydrate Polymers*. Elsevier, 198, pp. 270–280. Available at: http://www.ncbi.nlm.nih.gov/pubmed/30093000 (Accessed: 21 November 2018).

Kypriotou, M. *et al.* (2003) 'SOX9 exerts a bifunctional effect on type II collagen gene (COL2A1) expression in chondrocytes depending on the differentiation state', *DNA and cell biology*. DNA Cell Biol, 22(2), pp. 119–129. doi: 10.1089/104454903321515922.

Lafuente-Merchan, M. *et al.* (2021) 'Development, characterization and sterilisation of Nanocellulose-alginate-(hyaluronic acid)- bioinks and 3D bioprinted scaffolds for tissue engineering', *Materials Science and Engineering:*

*C*. Elsevier, 126, p. 112160. doi: 10.1016/J.MSEC.2021.112160.

Landers, R. *et al.* (2002) 'Rapid prototyping of scaffolds derived from thermoreversible hydrogels and tailored for applications in tissue engineering', *Biomaterials*. Elsevier, 23(23), pp. 4437–4447. doi: 10.1016/S0142-9612(02)00139-4.

Lane Smith, R. *et al.* (2000) 'Effects of shear stress on articular chondrocyte metabolism.', *Biorheology*, 37(1–2), pp. 95–107. Available at: https://europepmc.org/article/med/10912182 (Accessed: 18 January 2022).

Langer, R. and Vacanti, J. P. (1993) 'Tissue engineering.', *Science (New York, N.Y.)*, 260(5110), pp. 920–6. Available at: http://www.ncbi.nlm.nih.gov/pubmed/8493529 (Accessed: 21 November 2018).

Lee, K. Y. and Mooney, D. J. (2012) 'Alginate: properties and biomedical applications.', *Progress in polymer science*. NIH Public Access, 37(1), pp. 106–126. doi: 10.1016/j.progpolymsci.2011.06.003.

Lee, W. *et al.* (2014) 'Synergy between Piezo1 and Piezo2 channels confers high-strain mechanosensitivity to articular cartilage', *Proceedings of the National Academy of Sciences of the United States of America*. Proc Natl Acad Sci U S A, 111(47), pp. E5114–E5122. doi: 10.1073/PNAS.1414298111.

Lefebvre, V., Angelozzi, M. and Haseeb, A. (2019) 'SOX9 in cartilage development and disease', *Current Opinion in Cell Biology*. Elsevier Current Trends, 61, pp. 39–47. doi: 10.1016/J.CEB.2019.07.008.

Lefebvre, V. and Dvir-Ginzberg, M. (2017) 'SOX9 and the many facets of its regulation in the chondrocyte lineage', *Connective tissue research*. NIH Public Access, 58(1), p. 2. doi: 10.1080/03008207.2016.1183667.

Levanič, J. *et al.* (2020) 'Stable nanocellulose gels prepared by crosslinking of surface charged cellulose nanofibrils with di- and triiodoalkanes', *Cellulose*. Springer, 27(4), pp. 2053–2068. doi: 10.1007/S10570-019-02947-3/TABLES/4.

Lewin, S. (2015) 'Complications after Total Porous Implant Ear Reconstruction and Their Management', *Facial plastic surgery : FPS*. Facial Plast Surg, 31(6), pp. 617–625. doi: 10.1055/S-0035-1567890.

Lewitus, D. Y. *et al.* (2011) 'Biohybrid Carbon Nanotube/Agarose Fibers for Neural Tissue Engineering', *Advanced Functional Materials*. John Wiley & Sons, Ltd, 21(14), pp. 2624–2632. doi: 10.1002/adfm.201002429.

Li, C. *et al.* (2017) 'Applications of Three-Dimensional Printing in Surgery', *Surgical Innovation*, 24(1), pp. 82–88. doi: 10.1177/1553350616681889.

Li, D. *et al.* (2010) 'Psychosocial outcomes among microtia patients of different ages and genders before ear reconstruction', *Aesthetic Plastic Surgery*. Aesthetic Plast Surg, 34(5), pp. 570–576. Available at: https://pubmed.ncbi.nlm.nih.gov/20397014/ (Accessed: 28 May 2020).

Li, J. *et al.* (2015) '*Iota* -carrageenan/chitosan/gelatin scaffold for the osteogenic differentiation of adipose-derived MSCs *in vitro*', *Journal of Biomedical Materials Research Part B: Applied Biomaterials*. John Wiley & Sons, Ltd, 103(7), pp. 1498–1510. doi: 10.1002/jbm.b.33339.

Li, K. *et al.* (2017) 'Advances in Application of Mechanical Stimuli in Bioreactors for Cartilage Tissue Engineering.', *Tissue engineering. Part B, Reviews*, 23(4), pp. 399–411. doi: 10.1089/ten.TEB.2016.0427.

Li, S. *et al.* (2019) 'Chitosans for Tissue Repair and Organ Three-Dimensional (3D) Bioprinting', *Micromachines*. Multidisciplinary Digital Publishing Institute (MDPI), 10(11). doi: 10.3390/MI10110765.

Li, Weichang *et al.* (2015) '*In vitro and in vivo* evaluation of a novel collagen/cellulose nanocrystals scaffold for achieving the sustained release of basic fibroblast growth factor', *Journal of Biomaterials Applications*. SAGE PublicationsSage UK: London, England, 29(6), pp. 882–893. doi: 10.1177/0885328214547091.

Li, Wenyan *et al.* (2015) 'The Effect of Layer-by-Layer Assembly Coating on the Proliferation and Differentiation of Neural Stem Cells', *ACS Applied Materials & Interfaces*, 7(5), pp. 3018–3029. doi: 10.1021/am504456t.

Limraksasin, P. *et al.* (2020) 'Shaking culture enhances chondrogenic differentiation of mouse induced pluripotent stem cell constructs', *Scientific Reports 2020 10:1*. Nature Publishing Group, 10(1), pp. 1–15. doi:

10.1038/s41598-020-72038-y.

Lin, N., Bruzzese, C. and Dufresne, A. (2012) 'TEMPO-Oxidized Nanocellulose Participating as Crosslinking Aid for Alginate-Based Sponges', *ACS Applied Materials and Interfaces*. American Chemical Society, 4(9), pp. 4948–4959. doi: 10.1021/AM301325R.

Lin, N. and Dufresne, A. (2014) 'Nanocellulose in biomedicine: Current status and future prospect', *European Polymer Journal*. Pergamon, 59, pp. 302–325. doi: 10.1016/J.EURPOLYMJ.2014.07.025.

Lin, X. *et al.* (2020) 'The Bone Extracellular Matrix in Bone Formation and Regeneration', *Frontiers in Pharmacology*. Frontiers Media SA, 11. doi: 10.3389/FPHAR.2020.00757.

Liu, N. *et al.* (2016) '3D bioprinting matrices with controlled pore structure and release function guide in vitro self-organization of sweat gland', *Scientific Reports 2016 6:1*. Nature Publishing Group, 6(1), pp. 1–8. doi: 10.1038/srep34410.

Livak, K. J. and Schmittgen, T. D. (2001) 'Analysis of relative gene expression data using real-time quantitative PCR and the 2-ΔΔCT method', *Methods*. Methods, 25(4), pp. 402–408. doi: 10.1006/meth.2001.1262.

Loebel, C. *et al.* (2015) 'Precise tailoring of tyramine-based hyaluronan hydrogel properties using DMTMM conjugation', *Carbohydrate Polymers*. Elsevier, 115, pp. 325–333. doi: 10.1016/J.CARBPOL.2014.08.097.

Loebel, C. *et al.* (2017) 'Cross-Linking Chemistry of Tyramine-Modified Hyaluronan Hydrogels Alters Mesenchymal Stem Cell Early Attachment and Behavior', *Biomacromolecules*. Biomacromolecules, 18(3), pp. 855–864. doi: 10.1021/ACS.BIOMAC.6B01740.

Loo, A. E. K. and Halliwell, B. (2012) 'Effects of hydrogen peroxide in a keratinocyte-fibroblast co-culture model of wound healing', *Biochemical and Biophysical Research Communications*, 423(2), pp. 253–258. doi: 10.1016/j.bbrc.2012.05.100.

Lou, Y.-R. *et al.* (2014) 'The Use of Nanofibrillar Cellulose Hydrogel As a Flexible Three-Dimensional Model to Culture Human Pluripotent Stem Cells', *Stem Cells*

*and Development*. Mary Ann Liebert, Inc. 140 Huguenot Street, 3rd Floor New Rochelle, NY 10801 USA , 23(4), pp. 380–392. doi: 10.1089/scd.2013.0314.

Loukas, M. *et al.* (2010) 'Anatomy in ancient India: A focus on the Susruta Samhita', *Journal of Anatomy*, 217(6), pp. 646–650. doi: 10.1111/j.1469-7580.2010.01294.x.

Low, G. K. M. *et al.* (2008) 'Oxidative damage induced genotoxic effects in human fibroblasts from Xeroderma Pigmentosum group A patients', *The international journal of biochemistry & cell biology*. Int J Biochem Cell Biol, 40(11), pp. 2583–2595. doi: 10.1016/J.BIOCEL.2008.05.009.

Lowdell, M. W. and Thomas, A. (2017) 'The expanding role of the clinical haematologist in the new world of advanced therapy medicinal products.', *British journal of haematology*, 176(1), pp. 9–15. doi: 10.1111/bjh.14384.

Luquetti, D. V. *et al.* (2012) 'Microtia: Epidemiology and genetics', *American Journal of Medical Genetics, Part A*. NIH Public Access, pp. 124–139. doi: 10.1002/ajmg.a.34352.

Luquetti, D. V., Leoncini, E. and Mastroiacovo, P. (2011) 'Microtia-anotia: A global review of prevalence rates', *Birth Defects Research Part A - Clinical and Molecular Teratology*. Birth Defects Res A Clin Mol Teratol, 91(9), pp. 813–822. doi: 10.1002/bdra.20836.

Ma, X. *et al.* (2019) 'Correlation between mandible and external ear in patients with Treacher-Collins syndrome', *Journal of Craniofacial Surgery*. Lippincott Williams and Wilkins, 30(4), pp. 975–979. doi: 10.1097/SCS.0000000000005216.

Mabvuure, N., Hindocha, S. and S. Khan, W. (2012) 'The Role of Bioreactors in Cartilage Tissue Engineering', *Current Stem Cell Research & Therapy*. Bentham Science Publishers, 7(4), pp. 287–292. doi: 10.2174/157488812800793018.

Macchiarini, P. *et al.* (2008) 'Clinical transplantation of a tissue-engineered airway', *The Lancet*, 372(9655), pp. 2023–2030. doi: 10.1016/S0140-6736(08)61598-6.

Mackay, A. M. *et al.* (1998) 'Chondrogenic differentiation of cultured human

mesenchymal stem cells from marrow', *Tissue engineering*. Tissue Eng, 4(4), pp. 415–428. doi: 10.1089/TEN.1998.4.415.

Maki, K. *et al.* (2021) 'Hydrostatic pressure prevents chondrocyte differentiation through heterochromatin remodeling', *Journal of Cell Science*. Company of Biologists Ltd, 134(2). doi: 10.1242/JCS.247643/VIDEO-2.

Malda, J. *et al.* (2013) '25th Anniversary Article: Engineering Hydrogels for Biofabrication', *Advanced Materials*, 25(36), pp. 5011–5028. doi: 10.1002/adma.201302042.

Malinen, M. M. *et al.* (2014) 'Differentiation of liver progenitor cell line to functional organotypic cultures in 3D nanofibrillar cellulose and hyaluronan-gelatin hydrogels', *Biomaterials*. Elsevier, 35(19), pp. 5110–5121. doi: 10.1016/J.BIOMATERIALS.2014.03.020.

Malkoc, V. (2018) 'Challenges and the future of 3D bioprinting.', *Journal of Biomedical Imaging and Bioengineering*, 1(3), pp. 62–63. Available at: http://www.alliedacademies.org/biomedical-imaging-and-bioengineering/ (Accessed: 31 December 2018).

Mandrycky, C. *et al.* (2016) 'Research review paper 3D bioprinting for engineering complex tissues', *Biotechnology Advances*, 34, pp. 422–434. doi: 10.1016/j.biotechadv.2015.12.011.

Mankins, J. C. (1995) *TECHNOLOGY READINESS LEVELS A White Paper*. Available at: https://aiaa.kavi.com/apps/group public/download.php/2212/TRLs Mankins Paper 1995.pdf (Accessed: 4 January 2019).

Marcus, P. *et al.* (2014) 'Articular Chondroprogenitor Cells Maintain Chondrogenic Potential but Fail to Form a Functional Matrix When Implanted Into Muscles of SCID Mice', *Cartilage*. SAGE Publications Inc., 5(4), pp. 231–240. doi: 10.1177/1947603514541274.

Markov, P. A. *et al.* (2017) 'Mechanical properties, structure, bioadhesion, and biocompatibility of pectin hydrogels.', *Journal of biomedical materials research. Part A*, 105(9), pp. 2572–2581. doi: 10.1002/jbm.a.36116.

Markstedt, K. *et al.* (2015a) '3D Bioprinting Human Chondrocytes with Nanocellulose-Alginate Bioink for Cartilage Tissue Engineering Applications.', *Biomacromolecules*, 16(5), pp. 1489–96. doi: 10.1021/acs.biomac.5b00188.

Markstedt, K. *et al.* (2015b) '3D Bioprinting Human Chondrocytes with Nanocellulose–Alginate Bioink for Cartilage Tissue Engineering Applications', *Biomacromolecules*, 16(5), pp. 1489–1496. doi: 10.1021/acs.biomac.5b00188.

Martin, G. *et al.* (2005) 'Comparative effects of IL-1β and hydrogen peroxide (H2O2) on catabolic and anabolic gene expression in juvenile bovine chondrocytes', *Osteoarthritis and Cartilage*. W.B. Saunders, 13(10), pp. 915–924. doi: 10.1016/J.JOCA.2005.03.009.

Martin, I. *et al.* (1999) 'Mammalian chondrocytes expanded in the presence of fibroblast growth factor 2 maintain the ability to differentiate and regenerate three-dimensional cartilaginous tissue', *Experimental cell research*. Exp Cell Res, 253(2), pp. 681–688. doi: 10.1006/EXCR.1999.4708.

Martin, I., Wendt, D. and Heberer, M. (2004) 'The role of bioreactors in tissue engineering', *Trends in Biotechnology*. Elsevier Current Trends, 22(2), pp. 80–86. doi: 10.1016/J.TIBTECH.2003.12.001.

Martínez Ávila, H. *et al.* (2015) 'Novel bilayer bacterial nanocellulose scaffold supports neocartilage formation in vitro and in vivo', *Biomaterials*. Elsevier, 44, pp. 122–133. doi: 10.1016/J.BIOMATERIALS.2014.12.025.

Martínez Ávila, H. *et al.* (2016) '3D bioprinting of human chondrocyte-laden nanocellulose hydrogels for patient-specific auricular cartilage regeneration', *Bioprinting*. Elsevier, 1–2, pp. 22–35. doi: 10.1016/J.BPRINT.2016.08.003.

Martins, A. *et al.* (2009) 'Hierarchical starch-based fibrous scaffold for bone tissue engineering applications', *Journal of Tissue Engineering and Regenerative Medicine*. John Wiley & Sons, Ltd, 3(1), pp. 37–42. doi: 10.1002/term.132.

Matsiko, A. *et al.* (2012) 'Addition of hyaluronic acid improves cellular infiltration and promotes early-stage chondrogenesis in a collagen-based scaffold for cartilage tissue engineering', *Journal of the mechanical behavior of biomedical materials*. J Mech Behav Biomed Mater, 11, pp. 41–52. doi:

10.1016/J.JMBBM.2011.11.012.

Mattox, J. M. (2013) 'Additive Manufacturing and its Implications for Military Ethics', *Journal of Military Ethics*. Routledge, 12(3), pp. 225–234. doi: 10.1080/15027570.2013.847534.

Matyash, M. *et al.* (2014) 'Swelling and mechanical properties of alginate hydrogels with respect to promotion of neural growth.', *Tissue engineering. Part C, Methods*, 20(5), pp. 401–11. doi: 10.1089/ten.TEC.2013.0252.

Le May, I., Lappi, V. G. and White, W. E. (1975) 'Materials for biomedical applications', *Polymer Engineering and Science*. John Wiley & Sons, Ltd, 15(11), pp. 789–794. doi: 10.1002/pen.760151105.

McCormick, W. F. (1980) 'Mineralization of the costal cartilages as an indicator of age: preliminary observations.', *Journal of forensic sciences*. ASTM International, 25(4), p. 11287J. doi: 10.1520/JFS11287J.

McKim, J. M. (2014) 'Food additive carrageenan: Part I: A critical review of carrageenan in vitro studies, potential pitfalls, and implications for human health and safety', *Critical reviews in toxicology*. Crit Rev Toxicol, 44(3), pp. 211–243. doi: 10.3109/10408444.2013.861797.

Medvedev, S. P., Shevchenko, A. I. and Zakian, S. M. (2010) 'Induced Pluripotent Stem Cells: Problems and Advantages when Applying them in Regenerative Medicine', *Acta Naturae*. National Research University Higher School of Economics, 2(2), p. 18. doi: 10.32607/20758251-2010-2-2-18-27.

Millward-Sadler, S. J. and Salter, D. M. (2004) 'Integrin-Dependent Signal Cascades in Chondrocyte Mechanotransduction', *Annals of Biomedical Engineering 2004 32:3*. Springer, 32(3), pp. 435–446. doi: 10.1023/B:ABME.0000017538.72511.48.

Mishra, R. K., Datt, M. and Banthia, A. K. (2008) 'Synthesis and Characterization of Pectin/PVP Hydrogel Membranes for Drug Delivery System', *AAPS PharmSciTech*, 9(2), pp. 395–403. doi: 10.1208/s12249-008-9048-6.

Miyamoto, M. *et al.* (2003) 'Simultaneous stimulation of EP2 and EP4 is essential to the effect of prostaglandin E2 in chondrocyte differentiation', *Osteoarthritis and*

*cartilage*. Osteoarthritis Cartilage, 11(9), pp. 644–652. doi: 10.1016/S1063-4584(03)00118-3.

Moberg, T. *et al.* (2017) 'Rheological properties of nanocellulose suspensions: effects of fibril/particle dimensions and surface characteristics', *Cellulose*. Springer Netherlands, 24(6), pp. 2499–2510. doi: 10.1007/s10570-017-1283-0.

Möller, T. *et al.* (2017) 'In Vivo Chondrogenesis in 3D Bioprinted Human Cell-laden Hydrogel Constructs', *Plastic and Reconstructive Surgery - Global Open*, 5(2), p. e1227. doi: 10.1097/GOX.0000000000001227.

Mollon, B. *et al.* (2013) 'The clinical status of cartilage tissue regeneration in humans', *Osteoarthritis and Cartilage*. W.B. Saunders, 21(12), pp. 1824–1833. doi: 10.1016/J.JOCA.2013.08.024.

Monsur, H. A. *et al.* (2016) 'International Journal of Food Properties Chemical structure of sulfated polysaccharides from brown seaweed (Turbinaria turbinata) Chemical structure of sulfated polysaccharides from brown seaweed (Turbinaria turbinata)', *International Journal of Food Properties*, 20(7), pp. 1457–1469. doi: 10.1080/10942912.2016.1211144.

de Moraes, J. O., Müller, C. M. O. and Laurindo, J. B. (2012) 'Influence of the simultaneous addition of bentonite and cellulose fibers on the mechanical and barrier properties of starch composite-films', *Food Science and Technology International*, 18(1), pp. 35–45. doi: 10.1177/1082013211427622.

Moreira Teixeira, L. S. *et al.* (2012) 'Enzyme-catalyzed crosslinkable hydrogels: emerging strategies for tissue engineering', *Biomaterials*. Biomaterials, 33(5), pp. 1281–1290. doi: 10.1016/J.BIOMATERIALS.2011.10.067.

Müller, M. *et al.* (2017) 'Alginate Sulfate–Nanocellulose Bioinks for Cartilage Bioprinting Applications', *Annals of Biomedical Engineering*. Ann Biomed Eng, 45(1), pp. 210–223. doi: 10.1007/s10439-016-1704-5.

Murphy, S. V and Atala, A. (2014) '3D bioprinting of tissues and organs', *Nature Biotechnology*, 32(8), pp. 773–785. doi: 10.1038/nbt.2958.

Myres, J. L. (1933) 'THE EDWIN SMITH SURGICAL PAPYRUS: published in facsimile and hieroglyphic transliteration with translation and commentary, in two

volumes. By James Henry Breasted. University of Chicago Oriental Institute Publications, vols. III–IV. Chicago, 1930. 2 vols. £4 10s.', *Antiquity*. Cambridge University Press, 7(26), pp. 244–246. doi: 10.1017/S0003598X00008073.

Nabovati, A., Llewellin, E. W. and Sousa, A. C. M. (2009) 'A general model for the permeability of fibrous porous media based on fluid flow simulations using the lattice Boltzmann method', *Composites Part A: Applied Science and Manufacturing*. Elsevier Ltd, 40(6–7), pp. 860–869. doi: 10.1016/j.compositesa.2009.04.009.

Nagata, S. (1994a) 'Modification of the stages in total reconstruction of the auricle: Part III. Grafting the three-dimensional costal cartilage framework for small concha-type microtia.', *Plastic and reconstructive surgery*, 93(2), pp. 243–53; discussion 267-8. Available at: http://www.ncbi.nlm.nih.gov/pubmed/8310016 (Accessed: 25 October 2019).

Nagata, S. (1994b) 'Modification of the stages in total reconstruction of the auricle: Part IV. Ear elevation for the constructed auricle.', *Plastic and reconstructive surgery*, 93(2), pp. 254–66; discussion 267-8. Available at: http://www.ncbi.nlm.nih.gov/pubmed/8310017 (Accessed: 25 October 2019).

Naghieh, S. *et al.* (2018) 'Influence of crosslinking on the mechanical behavior of 3D printed alginate scaffolds: Experimental and numerical approaches', *Journal of the Mechanical Behavior of Biomedical Materials*. Elsevier, 80, pp. 111–118. doi: 10.1016/J.JMBBM.2018.01.034.

Nakano-Okuno, M., Borah, B. R. and Nakano, I. (2014) 'Ethics of iPSC-Based Clinical Research for Age-Related Macular Degeneration: Patient-Centered Risk-Benefit Analysis', *Stem Cell Reviews and Reports*. Springer US, 10(6), pp. 743–752. doi: 10.1007/s12015-014-9536-x.

Nazarian, R. and Eshraghi, A. A. (2011) 'Otoplasty for the protruded ear.', *Seminars in plastic surgery*, 25(4), pp. 288–94. doi: 10.1055/s-0031-1288921.

Neely, E. L. (2016) 'The Risks of Revolution: Ethical Dilemmas in 3D Printing from a US Perspective', *Science and Engineering Ethics*. Springer Netherlands, 22(5), pp. 1285–1297. doi: 10.1007/s11948-015-9707-4.

Nelson, K. and Restina, T. (2014) 'Innovative nanocellulose process breaks the cost barrier', *TAPPI Journal*, 13(5), pp. 19–23. doi: 10.32964/TJ13.5.19.

Neuman, M. K. *et al.* (2013) 'A compositional analysis of cadaveric human nasal septal cartilage', *The Laryngoscope*. Laryngoscope, 123(9), pp. 2120–2124. doi: 10.1002/LARY.23727.

Nguyen, D. *et al.* (2017) 'Cartilage Tissue Engineering by the 3D Bioprinting of iPS Cells in a Nanocellulose/Alginate Bioink', *Scientific Reports 2017 7:1*. Nature Publishing Group, 7(1), pp. 1–10. doi: 10.1038/s41598-017-00690-y.

Niemelä, B. J. *et al.* (2008) 'Prominent ears: The effect of reconstructive surgery on self-esteem and social interaction in children with a minor defect compared to children with a major orthopedic defect', *Plastic and Reconstructive Surgery*, 122(5), pp. 1390–1398. doi: 10.1097/PRS.0b013e3181881fb0.

Nishimura, K. *et al.* (2018) 'Formation of Branched and Chained Alginate Microfibers Using Theta-Glass Capillaries', *Micromachines*, 9(6), p. 303. doi: 10.3390/mi9060303.

O'Brien, F. J. (2011) 'Biomaterials &amp; scaffolds for tissue engineering', *Materials Today*. Elsevier, 14(3), pp. 88–95. doi: 10.1016/S1369-7021(11)70058-X.

Ogueta, S. *et al.* (2002) 'Prolactin is a component of the human synovial liquid and modulates the growth and chondrogenic differentiation of bone marrow-derived mesenchymal stem cells', *Molecular and cellular endocrinology*. Mol Cell Endocrinol, 190(1–2), pp. 51–63. doi: 10.1016/S0303-7207(02)00013-8.

Ohara, K., Nakamura, K. and Ohta, E. (1997) 'Chest wall deformities and thoracic scoliosis after costal cartilage graft harvesting', *Plastic and Reconstructive Surgery*, 99(4), pp. 1030–1036. doi: 10.1097/00006534-199704000-00017.

Orlando, G. *et al.* (2013) 'Will Regenerative Medicine Replace Transplantation?', *Cold Spring Harbor Perspectives in Medicine*, 3(8), pp. a015693–a015693. doi: 10.1101/cshperspect.a015693.

Osidak, E. O. *et al.* (2020) 'Collagen as Bioink for Bioprinting: A Comprehensive Review', *International Journal of Bioprinting*. Whioce Publishing Pte. Ltd., 6(3),

pp. 1–10. doi: 10.18063/IJB.V6I3.270.

Otto, I. A. *et al.* (2018) 'Progenitor cells in auricular cartilage demonstrate cartilage-forming capacity in 3D hydrogel culture.', *European cells & materials*, 35, pp. 132–150. doi: 10.22203/eCM.v035a10.

Ouyang, L. *et al.* (2016) '3D Printing of Shear-Thinning Hyaluronic Acid Hydrogels with Secondary Cross-Linking', *ACS Biomaterials Science and Engineering*. American Chemical Society, 2(10), pp. 1743–1751. doi: 10.1021/ACSBIOMATERIALS.6B00158/SUPPL FILE/AB6B00158 SI 001.PD F.

Pääkko, M. *et al.* (2007) 'Enzymatic hydrolysis combined with mechanical shearing and high-pressure homogenization for nanoscale cellulose fibrils and strong gels', *Biomacromolecules*. American Chemical Society, 8(6), pp. 1934–1941. doi: 10.1021/bm061215p.

Pankov, R. and Yamada, K. M. (2002) 'Fibronectin at a glance', *Journal of Cell Science*. The Company of Biologists, 115(20), pp. 3861–3863. doi: 10.1242/JCS.00059.

Papacharalampous, G. *et al.* (2007) 'Surgical correction of pinna malformations.', *Journal of plastic, reconstructive & aesthetic surgery : JPRAS*, 60(6), pp. 659–62. doi: 10.1016/j.bjps.2006.11.013.

Parel, S. M. *et al.* (1986) 'Osseointegration in maxillofacial prosthetics. Part II: Extraoral applications.', *The Journal of prosthetic dentistry*, 55(5), pp. 600–606.

Park, I. K. and Cho, C. S. (2010) 'Stem Cell-assisted Approaches for Cartilage Tissue Engineering', *International Journal of Stem Cells*. Korean Society for Stem Cell Research, 3(2), p. 96. doi: 10.15283/IJSC.2010.3.2.96.

Park, S. *et al.* (2012) 'The Sulfated Polysaccharide Fucoidan Stimulates Osteogenic Differentiation of Human Adipose-Derived Stem Cells', *Stem Cells and Development*.  Mary Ann Liebert, Inc.  140 Huguenot Street, 3rd Floor New Rochelle, NY 10801 USA  , 21(12), pp. 2204–2211. doi: 10.1089/scd.2011.0521.

Park, S. Y. *et al.* (2018) 'Physical and Mechanical Properties of Alginate-Based Hydrogel Film as Carrier for Release of Acetylthiocholine', *INTERNATIONAL*

*JOURNAL OF PRECISION ENGINEERING AND MANUFACTURING*, 19(1), p. 129. doi: 10.1007/s12541-018-0015-1.

Paxton, N. *et al.* (2017) 'Proposal to assess printability of bioinks for extrusion-based bioprinting and evaluation of rheological properties governing bioprintability', *Biofabrication*. IOP Publishing, 9(4), p. 044107. doi: 10.1088/1758-5090/AA8DD8.

Pazzano, D. *et al.* (2000) 'Comparison of Chondrogensis in Static and Perfused Bioreactor Culture', *Biotechnology Progress*. American Chemical Society (ACS), 16(5), pp. 893–896. doi: 10.1021/BP000082V.

Pedroza-González, S. C. *et al.* (2021) 'Bioinks for 3D Bioprinting: A Scientometric Analysis of Two Decades of Progress', *International Journal of Bioprinting*. Whioce Publishing Pte. Ltd., 7(2), pp. 68–91. doi: 10.18063/IJB.V7I2.337.

Peet, E. W. (1971) 'Congenital absence of the ear', *British Journal of Surgery*. Wiley, 58(8), pp. 638–638. doi: 10.1002/bjs.1800580836.

Peppas, N. A. *et al.* (2000) 'Hydrogels in pharmaceutical formulations', *European Journal of Pharmaceutics and Biopharmaceutics*. Elsevier, 50(1), pp. 27–46. doi: 10.1016/S0939-6411(00)00090-4.

Pereira, R. F., Sousa, A., *et al.* (2018) 'A single-component hydrogel bioink for bioprinting of bioengineered 3D constructs for dermal tissue engineering', *Materials Horizons*. The Royal Society of Chemistry, 5(6), pp. 1100–1111. doi: 10.1039/C8MH00525G.

Pereira, R. F., Barrias, C. C., *et al.* (2018) 'Cell-instructive pectin hydrogels crosslinked via thiol-norbornene photo-click chemistry for skin tissue engineering', *Acta Biomaterialia*, 66, pp. 282–293. doi: 10.1016/j.actbio.2017.11.016.

Perera, J. R., Jaiswal, P. K. and Khan, W. S. (2012) 'The Potential Therapeutic Use of Stem Cells in Cartilage Repair', *Current Stem Cell Research & Therapy*. Curr Stem Cell Res Ther, 7(2), pp. 149–156. doi: 10.2174/157488812799219054.

Pérez-Madrigal, M. M. *et al.* (2019) 'Robust alginate/hyaluronic acid thiol–yne click-hydrogel scaffolds with superior mechanical performance and stability for

load-bearing soft tissue engineering', *Biomaterials Science*. Royal Society of Chemistry, 8(1), pp. 405–412. doi: 10.1039/C9BM01494B.

Petta, D. *et al.* (2018) '3D bioprinting of a hyaluronan bioink through enzymatic- and visible light-crosslinking', *Biofabrication*. IOP Publishing, 10(4), p. 044104. doi: 10.1088/1758-5090/AADF58.

Petta, Dalila *et al.* (2018) 'Three-Dimensional Printing of a Tyramine Hyaluronan Derivative with Double Gelation Mechanism for Independent Tuning of Shear Thinning and Postprinting Curing', *ACS Biomaterials Science and Engineering*. American Chemical Society, 4(8), pp. 3088–3098. doi: 10.1021/ACSBIOMATERIALS.8B00416/SUPPL FILE/AB8B00416 SI 007.PD F.

Petta, D. *et al.* (2020) 'Hyaluronic acid as a bioink for extrusion-based 3D printing', *Biofabrication*. IOP Publishing, 12(3), p. 032001. doi: 10.1088/1758-5090/AB8752.

Phanthong, P. *et al.* (2018) 'Nanocellulose: Extraction and application', *Carbon Resources Conversion*. Elsevier, 1(1), pp. 32–43. doi: 10.1016/J.CRCON.2018.05.004.

Piras, C. C. and Smith, D. K. (2020) 'Multicomponent polysaccharide alginate-based bioinks', *Journal of Materials Chemistry B*. Royal Society of Chemistry, pp. 8171–8188. doi: 10.1039/d0tb01005g.

Pitsillides, A. A. and Beier, F. (2011) 'Cartilage biology in osteoarthritis--lessons from developmental biology', *Nature reviews. Rheumatology*. Nat Rev Rheumatol, 7(11), pp. 654–663. doi: 10.1038/NRRHEUM.2011.129.

Pitts-Taylor, V. (2008) *Cultural encyclopedia of the body*. Greenwood Press.

Poldervaart, M. T. *et al.* (2017) '3D bioprinting of methacrylated hyaluronic acid (MeHA) hydrogel with intrinsic osteogenicity', *PLOS ONE*. Public Library of Science, 12(6), p. e0177628. doi: 10.1371/JOURNAL.PONE.0177628.

Poole, C. A. (1997) 'Review. Articular cartilage chondrons: form, function and failure', *Journal of Anatomy*. J Anat, 191(1), pp. 1–13. doi: 10.1046/j.1469-7580.1997.19110001.x.

Popa, E. G. *et al.* (2015) 'Chondrogenic potential of injectable *κ* -carrageenan hydrogel with encapsulated adipose stem cells for cartilage tissue-engineering applications', *Journal of Tissue Engineering and Regenerative Medicine*. John Wiley & Sons, Ltd, 9(5), pp. 550–563. doi: 10.1002/term.1683.

Presbítero-Espinosa, G. *et al.* (2021) 'Characterization of Sodium Alginate Hydrogels Reinforced with Nanoparticles of Hydroxyapatite for Biomedical Applications', *Polymers 2021, Vol. 13, Page 2927*. Multidisciplinary Digital Publishing Institute, 13(17), p. 2927. doi: 10.3390/POLYM13172927.

Probst, F. A. *et al.* (2010) '[Calvarial reconstruction by customized bioactive implant].', *Handchirurgie, Mikrochirurgie, plastische Chirurgie : Organ der Deutschsprachigen Arbeitsgemeinschaft fur Handchirurgie : Organ der Deutschsprachigen Arbeitsgemeinschaft fur Mikrochirurgie der Peripheren Nerven und Gefasse : Organ der V...*, 42(6), pp. 369–73. doi: 10.1055/s-0030-1248310.

Prockop, D. J. and Kivirikko, K. I. (1995) 'Collagens: molecular biology, diseases, and potentials for therapy', *Annual review of biochemistry*. Annu Rev Biochem, 64, pp. 403–434. doi: 10.1146/ANNUREV.BI.64.070195.002155.

Purkait, R. and Singh, P. (2008) 'A test of individuality of human external ear pattern: Its application in the field of personal identification', *Forensic Science International*, 178(2–3), pp. 112–118. doi: 10.1016/j.forsciint.2008.02.009.

Quarto, R. *et al.* (1997) 'Modulation of commitment, proliferation, and differentiation of chondrogenic cells in defined culture medium', *Endocrinology*. Endocrinology, 138(11), pp. 4966–4976. doi: 10.1210/ENDO.138.11.5522.

Quintana, L., Zur Nieden, N. I. and Semino, C. E. (2009) 'Morphogenetic and regulatory mechanisms during developmental chondrogenesis: new paradigms for cartilage tissue engineering', *Tissue engineering. Part B, Reviews*. Tissue Eng Part B Rev, 15(1), pp. 29–41. doi: 10.1089/TEN.TEB.2008.0329.

Raghunath, J. *et al.* (2005) 'Advancing cartilage tissue engineering: the application of stem cell technology', *Current Opinion in Biotechnology*. Elsevier Current Trends, 16(5), pp. 503–509. doi: 10.1016/J.COPBIO.2005.08.004.

Rana, D., Kumar, T. S. S. and Ramalingam, M. (2017) 'Impact of Nanotechnology on 3D Bioprinting', *Journal of Bionanoscience*, 11(1), pp. 1–6. doi: 10.1166/jbns.2017.1417.

Randall, B. A. (1893) 'An attempt to replace an auricle bitten off in childhood.', *Arch Otology*, (22), pp. 163–165.

Rebenda, D. *et al.* (2020) 'On the Dependence of Rheology of Hyaluronic Acid Solutions and Frictional Behavior of Articular Cartilage', *Materials 2020, Vol. 13, Page 2659*. Multidisciplinary Digital Publishing Institute, 13(11), p. 2659. doi: 10.3390/MA13112659.

Reddy, N., Reddy, R. and Jiang, Q. (2015) 'Crosslinking biopolymers for biomedical applications', *Trends in Biotechnology*. Elsevier Current Trends, 33(6), pp. 362–369. doi: 10.1016/J.TIBTECH.2015.03.008.

Rees, A. *et al.* (2015) '3D Bioprinting of Carboxymethylated-Periodate Oxidized Nanocellulose Constructs for Wound Dressing Applications.', *BioMed research international*. Hindawi, 2015, p. 925757. doi: 10.1155/2015/925757.

Reinisch, J. F. and Lewin, S. (2009) 'Ear reconstruction using a porous polyethylene framework and temporoparietal fascia flap.', *Facial plastic surgery : FPS*, 25(3), pp. 181–9. doi: 10.1055/s-0029-1239448.

Reinisch, J. and Tahiri, Y. (2018) 'Polyethylene Ear Reconstruction: A State-of-the-Art Surgical Journey.', *Plastic and reconstructive surgery*, 141(2), pp. 461–470. doi: 10.1097/PRS.0000000000004088.

Rhim, J.-W. (2012) 'Physical-Mechanical Properties of Agar/κ-Carrageenan Blend Film and Derived Clay Nanocomposite Film', *Journal of Food Science*, 77(12), pp. N66–N73. doi: 10.1111/j.1750-3841.2012.02988.x.

Risbud, M. V. and Shapiro, I. M. (2011) 'Notochordal cells in the adult intervertebral disc: new perspective on an old question', *Critical reviews in eukaryotic gene expression*. Crit Rev Eukaryot Gene Expr, 21(1), pp. 29–41. doi: 10.1615/CRITREVEUKARGENEEXPR.V21.I1.30.

de River, J. P. (1927) 'RESTORATION OF THE AURICLE.', *California and western medicine*, 26(5), pp. 654–6. Available at:

http://www.ncbi.nlm.nih.gov/pubmed/18740337 (Accessed: 25 October 2019).

Röhner, E. *et al.* (2011) 'Toxicity of polyhexanide and hydrogen peroxide on human chondrocytes in vitro', *Orthopedics*, 34(7), pp. e290-4. doi: 10.3928/01477447-20110526-02.

Roots Analysis Private Limited (2017) *3D Bioprinting: Technologies, Products and Key Application Areas, (2nd Edition), 2018-2035*. Available at: https://www.rootsanalysis.com/reports/view document/3d-bioprinting-technologies-products-and-key-application-areas-2nd-edition-2018-2035/182.html (Accessed: 3 January 2019).

Rosadi, I. *et al.* (2019) 'In vitro study of cartilage tissue engineering using human adipose-derived stem cells induced by platelet-rich plasma and cultured on silk fibroin scaffold', *Stem Cell Research and Therapy*. BioMed Central Ltd., 10(1), pp. 1–15. doi: 10.1186/S13287-019-1443-2/FIGURES/8.

Rutz, A. L., Lewis, P. L. and Shah, R. N. (2017) 'Toward next-generation bioinks: Tuning material properties pre- and post-printing to optimize cell viability', *MRS Bulletin*. Cambridge University Press, 42(8), pp. 563–570. doi: 10.1557/MRS.2017.162.

Salek, M. M., Sattari, P. and Martinuzzi, R. J. (2012) 'Analysis of fluid flow and wall shear stress patterns inside partially filled agitated culture well plates', *Annals of Biomedical Engineering*, 40(3), pp. 707–728. doi: 10.1007/s10439-011-0444-9.

Salgado, A. J., Coutinho, O. P. and Reis, R. L. (2004) 'Novel Starch-Based Scaffolds for Bone Tissue Engineering: Cytotoxicity, Cell Culture, and Protein Expression', *Tissue Engineering*. Mary Ann Liebert, Inc. , 10(3–4), pp. 465–474. doi: 10.1089/107632704323061825.

Sarig, A. *et al.* (1982) 'Reconstruction of the auricle in microtia by bipedicled postauricular tubed flap', *Annals of Plastic Surgery*, 8(3), pp. 221–223. doi: 10.1097/00000637-198203000-00009.

Sarkar, K., Xue, Y. and Sant, S. (2017) 'Host Response to Synthetic Versus Natural Biomaterials', in *The Immune Response to Implanted Materials and*

*Devices*. Cham: Springer International Publishing, pp. 81–105. doi: 10.1007/978-3-319-45433-7_5.

Schanz, F. (1890) 'Wiederersatz einer verlorengegangenen Ohrmuschel.', *Korrespondenz-Blatter des allgemeinen Arztl Vereins von Thuringen*, 19, pp. 288–93.

Schütz, K. *et al.* (2017) 'Three-dimensional plotting of a cell-laden alginate/methylcellulose blend: towards biofabrication of tissue engineering constructs with clinically relevant dimensions', *Journal of Tissue Engineering and Regenerative Medicine*. John Wiley & Sons, Ltd, 11(5), pp. 1574–1587. doi: 10.1002/TERM.2058.

Schuurman, W. *et al.* (2013) 'Gelatin-Methacrylamide Hydrogels as Potential Biomaterials for Fabrication of Tissue-Engineered Cartilage Constructs', *Macromolecular Bioscience*, 13(5), pp. 551–561. doi: 10.1002/mabi.201200471.

Schwab, A. *et al.* (2020) 'Printability and Shape Fidelity of Bioinks in 3D Bioprinting', *Chemical Reviews*. American Chemical Society, 120(19), pp. 11028–11055. doi: 10.1021/ACS.CHEMREV.0C00084.

Seager, A. L. *et al.* (2012) 'Pro-oxidant Induced DNA Damage in Human Lymphoblastoid Cells: Homeostatic Mechanisms of Genotoxic Tolerance', *Toxicological Sciences*, 128(2), pp. 387–397. doi: 10.1093/toxsci/kfs152.

Seol, D. *et al.* (2012) 'Chondrogenic progenitor cells respond to cartilage injury', *Arthritis and rheumatism*. Arthritis Rheum, 64(11), pp. 3626–3637. doi: 10.1002/ART.34613.

Shahin, K. and Doran, P. M. (2015) 'Shear and Compression Bioreactor for Cartilage Synthesis', in *Methods in molecular biology (Clifton, N.J.)*, pp. 221–233. doi: 10.1007/978-1-4939-2938-2_16.

Sharifi, N. and Gharravi, A. M. (2019) 'Shear bioreactors stimulating chondrocyte regeneration, a systematic review', *Inflammation and Regeneration*. BioMed Central Ltd., 39(1), pp. 1–8. doi: 10.1186/S41232-019-0105-1/TABLES/8.

Shoichet, M. S. *et al.* (1996) 'Stability of hydrogels used in cell encapsulation: An in vitro comparison of alginate and agarose', *Biotechnology and Bioengineering*.

John Wiley & Sons, Ltd, 50(4), pp. 374–381. doi: 10.1002/(SICI)1097-0290(19960520)50:4<374::AID-BIT4>3.0.CO;2-I.

Shpichka, A. *et al.* (2020) 'Fibrin-based Bioinks: New Tricks from an Old Dog', *International Journal of Bioprinting*. Whioce Publishing Pte. Ltd., 6(3), pp. 1–14. doi: 10.18063/IJB.V6I3.269.

Si, H. *et al.* (2019) '3D Bioprinting of the Sustained Drug Release Wound Dressing with Double-Crosslinked Hyaluronic-Acid-Based Hydrogels', *Polymers 2019, Vol. 11, Page 1584*. Multidisciplinary Digital Publishing Institute, 11(10), p. 1584. doi: 10.3390/POLYM11101584.

Singh, P. and Schwarzbauer, J. E. (2014) 'Fibronectin matrix assembly is essential for cell condensation during chondrogenesis', *Journal of Cell Science*. Company of Biologists Ltd, 127(20), pp. 4420–4428. doi: 10.1242/JCS.150276/-/DC1.

Siqueira, P. *et al.* (2019) 'Three-Dimensional Stable Alginate-Nanocellulose Gels for Biomedical Applications: Towards Tunable Mechanical Properties and Cell Growing', *Nanomaterials*. Multidisciplinary Digital Publishing Institute (MDPI), 9(1). doi: 10.3390/NANO9010078.

Smith, C. M. *et al.* (2004) 'Three-Dimensional BioAssembly Tool for Generating Viable Tissue-Engineered Constructs', *Tissue Engineering*, 10(9–10), pp. 1566–1576. doi: 10.1089/ten.2004.10.1566.

Smith, I. O. *et al.* (2009) 'Nanostructured polymer scaffolds for tissue engineering and regenerative medicine', *Wiley Interdisciplinary Reviews: Nanomedicine and Nanobiotechnology*. John Wiley & Sons, Ltd, 1(2), pp. 226–236. doi: 10.1002/WNAN.26.

Smith, P. T. *et al.* (2018) 'Chemical modification and printability of shear-thinning hydrogel inks for direct-write 3D printing', *Polymer*. Elsevier, 152, pp. 42–50. doi: 10.1016/J.POLYMER.2018.01.070.

Smith, R. L., Carter, D. R. and Schurman, D. J. (2004) 'Pressure and shear differentially alter human articular chondrocyte metabolism: a review.', *Clinical Orthopaedics and Related Research*. Lippincott Williams and Wilkins, 427(427

Suppl), pp. S89-95. Available at: https://europepmc.org/article/med/15480081 (Accessed: 18 January 2022).

Solchaga, L. A., Penick, K. J. and Welter, J. F. (2011) 'Chondrogenic Differentiation of Bone Marrow-Derived Mesenchymal Stem Cells: Tips and Tricks', *Methods in molecular biology (Clifton, N.J.)*. NIH Public Access, 698, p. 253. doi: 10.1007/978-1-60761-999-4_20.

Solovieva, E. V *et al.* (2018) 'Fibrinogen-modified sodium alginate as a scaffold material for skin tissue engineering', *Biomedical Materials*, 13(2), p. 025007. doi: 10.1088/1748-605X/aa9089.

Songu, M. and Kutlu, A. (2014) 'Long-term psychosocial impact of otoplasty performed on children with prominent ears', *Journal of Laryngology and Otology*. Cambridge University Press, 128(9), pp. 768–771. doi: 10.1017/S0022215114001662.

Sonnleitner, D. *et al.* (2021) 'Correlating rheology and printing performance of fiber-reinforced bioinks to assess predictive modelling for biofabrication', *Journal of Materials Research*. Springer Nature, 36(19), pp. 3821–3832. doi: 10.1557/S43578-021-00276-5/FIGURES/7.

Stewart, K. and Wikström, S.-O. (2008) 'Autologous ear reconstruction - celebrating 50 years.', *Journal of plastic, reconstructive & aesthetic surgery : JPRAS*, 61 Suppl 1, pp. S2-4. doi: 10.1016/j.bjps.2008.09.014.

Stewart, S. *et al.* (2020) 'Mechanotransduction in osteogenesis', *Bone and Joint Research*. British Editorial Society of Bone and Joint Surgery, 9(1), pp. 1–14. doi: 10.1302/2046-3758.91.BJR-2019-0043.R2/ASSET/IMAGES/LARGE/2046-3758.91.BJR-2019-0043.R2-FIG5.JPEG.

Stößlein, S. *et al.* (2019) 'In-situ determination of time-dependent alginate-hydrogel formation by mechanical texture analysis', *Carbohydrate Polymers*, 205, pp. 287–294. doi: 10.1016/j.carbpol.2018.10.056.

von Szymanowski, J. (1870) 'Ohrbildung, Otoplastik', in *Handbuch der operativen Chirurgie*, p. 303.

Szymanski, A. and Bhimji, S. S. (2021) 'Anatomy, Head and Neck, Ear',

*StatPearls*. StatPearls Publishing. Available at: https://www.ncbi.nlm.nih.gov/books/NBK470359/ (Accessed: 10 January 2022).

Takano-Yamamoto, T. *et al.* (1991) 'Comparison of the effects of hydrostatic compressive force on glycosaminoglycan synthesis and proliferation in rabbit chondrocytes from mandibular condylar cartilage, nasal septum, and spheno-occipital synchondrosis in vitro', *American Journal of Orthodontics and Dentofacial Orthopedics*. Mosby, 99(5), pp. 448–455. doi: 10.1016/S0889-5406(05)81578-1.

Takeda, Y. *et al.* (2021) 'Compressive mechanical stress enhances susceptibility to interleukin-1 by increasing interleukin-1 receptor expression in 3D-cultured ATDC5 cells', *BMC Musculoskeletal Disorders*. BioMed Central Ltd, 22(1), pp. 1–13. doi: 10.1186/S12891-021-04095-X/FIGURES/7.

Tanzer, R. C. (1983) 'Total reconstruction of the external ear', *Annals of Plastic Surgery*, 10(1), pp. 76–85. doi: 10.1097/00000637-198301000-00012.

Tarassoli, S. P. *et al.* (2021) 'Candidate Bioinks for Extrusion 3D Bioprinting—A Systematic Review of the Literature', *Frontiers in Bioengineering and Biotechnology*. Frontiers, 0, p. 383. doi: 10.3389/FBIOE.2021.616753.

Taylor, M. S. *et al.* (1994) 'Six bioabsorbable polymers: In vitro acute toxicity of accumulated degradation products', *Journal of applied biomaterials*. J Appl Biomater, 5(2), pp. 151–157. doi: 10.1002/jab.770050208.

Thébaud, N.-B. *et al.* (2007) 'Human endothelial progenitor cell attachment to polysaccharide-based hydrogels: A pre-requisite for vascular tissue engineering', *Journal of Materials Science: Materials in Medicine*. Kluwer Academic Publishers, 18(2), pp. 339–345. doi: 10.1007/s10856-006-0698-1.

Thirabanjasak, D., Tantiwongse, K. and Thorner, P. S. (2010) 'Angiomyeloproliferative lesions following autologous stem cell therapy.', *Journal of the American Society of Nephrology : JASN*. American Society of Nephrology, 21(7), pp. 1218–22. doi: 10.1681/ASN.2009111156.

Thomas, D. J., Jessop, Z. M. and Whitaker, I. S. (2018) *3D bioprinting for reconstructive surgery : techniques and applications*. Woodhead Publishing, an

imprint of Elsevier.

Thomas, P. *et al.* (2020) 'Comprehensive review on nanocellulose: Recent developments, challenges and future prospects', *Journal of the mechanical behavior of biomedical materials*. J Mech Behav Biomed Mater, 110. doi: 10.1016/J.JMBBM.2020.103884.

Thorne, C. H. *et al.* (2001) 'Auricular reconstruction: Indications for autogenous and prosthetic techniques', *Plastic and Reconstructive Surgery*, 107(5), pp. 1241–1252. doi: 10.1097/00006534-200104150-00025.

Tibbitt, M. W. and Anseth, K. S. (2009) 'Hydrogels as extracellular matrix mimics for 3D cell culture', *Biotechnology and Bioengineering*. John Wiley & Sons, Ltd, 103(4), pp. 655–663. doi: 10.1002/BIT.22361.

Toivonen, S. *et al.* (2016) 'Regulation of Human Pluripotent Stem Cell-Derived Hepatic Cell Phenotype by Three-Dimensional Hydrogel Models', *Tissue Engineering Part A*.  Mary Ann Liebert, Inc.  140 Huguenot Street, 3rd Floor New Rochelle,   NY   10801   USA    ,   22(13–14),   pp.   971–984.   doi: 10.1089/ten.tea.2016.0127.

Tonon, R. and D'Andrea, P. (2000) 'Interleukin-1beta increases the functional expression of connexin 43 in articular chondrocytes: evidence for a Ca2+-dependent mechanism', *Journal of bone and mineral research : the official journal of the American Society for Bone and Mineral Research*. J Bone Miner Res, 15(9), pp. 1669–1677. doi: 10.1359/JBMR.2000.15.9.1669.

Torres-Rendon, J. G. *et al.* (2015) 'Bioactive Gyroid Scaffolds Formed by Sacrificial Templating of Nanocellulose and Nanochitin Hydrogels as Instructive Platforms for Biomimetic Tissue Engineering', *Advanced Materials*. John Wiley & Sons, Ltd, 27(19), pp. 2989–2995. doi: 10.1002/adma.201405873.

Truong, T. and Maricevich, R. (2017) 'Ear Reconstruction', *Seminars in Plastic Surgery*, 31(03), pp. 125–126. doi: 10.1055/s-0037-1604242.

Tsonis, P. A. (1991) '1,25-Dihydroxyvitamin D3 stimulates chondrogenesis of the chick limb bud mesenchymal cells', *Developmental biology*. Dev Biol, 143(1), pp. 130–134. doi: 10.1016/0012-1606(91)90060-G.

Tuan, R. S., Chen, A. F. and Klatt, B. A. (2013) 'Cartilage Regeneration', *The Journal of the American Academy of Orthopaedic Surgeons*. NIH Public Access, 21(5), p. 303. doi: 10.5435/JAAOS-21-05-303.

Türkkan, S. *et al.* (2018) 'Fabrication of functionalized citrus pectin/silk fibroin scaffolds for skin tissue engineering', *Journal of Biomedical Materials Research Part B: Applied Biomaterials*, 106(7), pp. 2625–2635. doi: 10.1002/jbm.b.34079.

Venkatesan, J., Bhatnagar, I. and Kim, S.-K. (2014) 'Chitosan-Alginate Biocomposite Containing Fucoidan for Bone Tissue Engineering', *Marine Drugs*, 12(1), pp. 300–316. doi: 10.3390/md12010300.

Veronesi, F. *et al.* (2014) 'Adipose-derived mesenchymal stem cells for cartilage tissue engineering: state-of-the-art in in vivo studies', *Journal of biomedical materials research. Part A*. J Biomed Mater Res A, 102(7), pp. 2448–2466. doi: 10.1002/JBM.A.34896.

Vinatier, C. *et al.* (2009) 'Cartilage engineering: a crucial combination of cells, biomaterials and biofactors', *Trends in biotechnology*. Trends Biotechnol, 27(5), pp. 307–314. doi: 10.1016/J.TIBTECH.2009.02.005.

Vinatier, C. and Guicheux, J. (2016) 'Cartilage tissue engineering: From biomaterials and stem cells to osteoarthritis treatments', *Annals of physical and rehabilitation medicine*. Ann Phys Rehabil Med, 59(3), pp. 139–144. doi: 10.1016/J.REHAB.2016.03.002.

Vinod, E. *et al.* (2019) 'Comparison of human articular chondrocyte and chondroprogenitor cocultures and monocultures: To assess chondrogenic potential and markers of hypertrophy', *Tissue and Cell*. Churchill Livingstone, 57, pp. 42–48. doi: 10.1016/J.TICE.2019.01.007.

Vinod, E. *et al.* (2020) 'Comparative analysis of fresh chondrocytes, cultured chondrocytes and chondroprogenitors derived from human articular cartilage', *Acta Histochemica*. Urban & Fischer, 122(1), p. 151462. doi: 10.1016/J.ACTHIS.2019.151462.

Vinod, E. *et al.* (2021) 'Migratory chondroprogenitors retain superior intrinsic chondrogenic potential for regenerative cartilage repair as compared to human

fibronectin derived chondroprogenitors', *Scientific Reports 2021 11:1*. Nature Publishing Group, 11(1), pp. 1–13. doi: 10.1038/s41598-021-03082-5.

Vinod, E., Boopalan, P. R. J. V. C. and Sathishkumar, S. (2018) 'Reserve or Resident Progenitors in Cartilage? Comparative Analysis of Chondrocytes versus Chondroprogenitors and Their Role in Cartilage Repair', *Cartilage*. SAGE Publications Inc., 9(2), pp. 171–182. doi: 10.1177/1947603517736108.

Walker, J. M. *et al.* (2011) 'Nondestructive evaluation of hydrogel mechanical properties using ultrasound.', *Annals of biomedical engineering*. NIH Public Access, 39(10), pp. 2521–30. doi: 10.1007/s10439-011-0351-0.

Wallace, C. G. *et al.* (2014) 'Three-dimensional computed tomography reveals different donor-site deformities in adult and growing microtia patients despite total subperichondrial costal cartilage harvest and donor-site reconstruction', *Plastic and Reconstructive Surgery*, 133(3), pp. 640–651. doi: 10.1097/01.prs.0000438052.14011.0a.

Wang, L. *et al.* (2020) 'Fabrication of Injectable, Porous Hyaluronic Acid Hydrogel Based on an In-Situ Bubble-Forming Hydrogel Entrapment Process', *Polymers 2020, Vol. 12, Page 1138*. Multidisciplinary Digital Publishing Institute, 12(5), p. 1138. doi: 10.3390/POLYM12051138.

Wang, X. *et al.* (2016) '3D Bioprinting Technologies for Hard Tissue and Organ Engineering.', *Materials (Basel, Switzerland)*. Multidisciplinary Digital Publishing Institute (MDPI), 9(10). doi: 10.3390/ma9100802.

Wang, X., Wang, Q. and Xu, C. (2020) 'Nanocellulose-Based Inks for 3D Bioprinting: Key Aspects in Research Development and Challenging Perspectives in Applications-A Mini Review', *Bioengineering (Basel, Switzerland)*. Bioengineering (Basel), 7(2). doi: 10.3390/BIOENGINEERING7020040.

Webb, B. and Doyle, B. J. (2017) 'Parameter optimization for 3D bioprinting of hydrogels', *Bioprinting*. Elsevier, 8, pp. 8–12. doi: 10.1016/J.BPRINT.2017.09.001.

Wee and Gombotz (1998) 'Protein release from alginate matrices.', *Advanced*

*drug delivery reviews*, 31(3), pp. 267–285. Available at: http://www.ncbi.nlm.nih.gov/pubmed/10837629 (Accessed: 28 December 2018).

Whitaker, I. S. *et al.* (2008) 'Composite tissue allotransplantation: a review of relevant immunological issues for plastic surgeons.', *Journal of plastic, reconstructive & aesthetic surgery : JPRAS*, 61(5), pp. 481–92. doi: 10.1016/j.bjps.2007.11.019.

Williams, R., Khan, Ilyas M, *et al.* (2010) 'Identification and clonal characterisation of a progenitor cell sub-population in normal human articular cartilage.', *PloS one*. Edited by S. Agarwal, 5(10), p. e13246. doi: 10.1371/journal.pone.0013246.

Williams, R., Khan, Ilyas M., *et al.* (2010) 'Identification and Clonal Characterisation of a Progenitor Cell Sub-Population in Normal Human Articular Cartilage', *PLoS ONE*. Public Library of Science, 5(10). doi: 10.1371/JOURNAL.PONE.0013246.

Wilson, S. A. *et al.* (2017) 'Shear-Thinning and Thermo-Reversible Nanoengineered Inks for 3D Bioprinting.', *ACS applied materials & interfaces*, 9(50), pp. 43449–43458. doi: 10.1021/acsami.7b13602.

Wu, X. *et al.* (2016) 'Synergistic therapeutic effects of Schiff's base cross-linked injectable hydrogels for local co-delivery of metformin and 5-fluorouracil in a mouse colon carcinoma model', *Biomaterials*. Biomaterials, 75, pp. 148–162. doi: 10.1016/J.BIOMATERIALS.2015.10.016.

Xie, X. *et al.* (2012) 'Comparative evaluation of MSCs from bone marrow and adipose tissue seeded in PRP-derived scaffold for cartilage regeneration', *Biomaterials*, 33(29), pp. 7008–7018. doi: 10.1016/j.biomaterials.2012.06.058.

Xiong, Z. *et al.* (2002) 'Fabrication of porous scaffolds for bone tissue engineering via low-temperature deposition', *Scripta Materialia*. Pergamon, 46(11), pp. 771–776. doi: 10.1016/S1359-6462(02)00071-4.

Yamasaki, S. *et al.* (2014) 'Cartilage Repair With Autologous Bone Marrow Mesenchymal Stem Cell Transplantation: Review of Preclinical and Clinical Studies', *Cartilage*. SAGE Publications, 5(4), p. 196. doi: 10.1177/1947603514534681.

Yamashita, A. *et al.* (2013) 'Cartilage tissue engineering identifies abnormal human induced pluripotent stem cells', *Scientific Reports 2013 3:1*. Nature Publishing Group, 3(1), pp. 1–6. doi: 10.1038/srep01978.

Yanaga, H. *et al.* (2009) 'Generating ears from cultured autologous auricular chondrocytes by using two-stage implantation in treatment of microtia', *Plastic and Reconstructive Surgery*, 124(3), pp. 817–825. doi: 10.1097/PRS.0b013e3181b17c0e.

Yang, I. H. *et al.* (2004) 'Comparison of phenotypic characterization between "alginate bead" and "pellet" culture systems as chondrogenic differentiation models for human mesenchymal stem cells', *Yonsei medical journal*. Yonsei Med J, 45(5), pp. 891–900. doi: 10.3349/YMJ.2004.45.5.891.

Ye, J. R. *et al.* (2014) 'Turning the chitosan surface from hydrophilic to hydrophobic by layer-by-layer electro-assembly', *RSC Advances*. The Royal Society of Chemistry, 4(102), pp. 58200–58203. doi: 10.1039/C4RA10327K.

Yegappan, R. *et al.* (2018) 'Carrageenan based hydrogels for drug delivery, tissue engineering and wound healing', *Carbohydrate Polymers*. Elsevier, 198, pp. 385–400. doi: 10.1016/J.CARBPOL.2018.06.086.

Yi, S. W. *et al.* (2018) 'Gene expression profiling of chondrogenic differentiation by dexamethasone-conjugated polyethyleneimine with SOX trio genes in stem cells', *Stem Cell Research and Therapy*. BioMed Central Ltd., 9(1), pp. 1–13. doi: 10.1186/S13287-018-0998-7/FIGURES/7.

Yoon, J. K. *et al.* (2015) 'Distribution of Porcine Endogenous Retrovirus in Different Organs of the Hybrid of a Landrace and a Jeju Domestic Pig in Korea', *Transplantation Proceedings*, 47(6), pp. 2067–2071. doi: 10.1016/j.transproceed.2015.05.023.

Young, I. C. *et al.* (2017) 'A novel compressive stress-based osteoarthritis-like chondrocyte system', *Experimental biology and medicine (Maywood, N.J.)*. Exp Biol Med (Maywood), 242(10), pp. 1062–1071. doi: 10.1177/1535370217699534.

Yourek, G. *et al.* (2010) 'Shear stress induces osteogenic differentiation of human mesenchymal stem cells', *Regenerative medicine*. NIH Public Access, 5(5), p.

713. doi: 10.2217/RME.10.60.

Yu, F. *et al.* (2013) 'An injectable hyaluronic acid/PEG hydrogel for cartilage tissue engineering formed by integrating enzymatic crosslinking and Diels–Alder "click chemistry"', *Polymer Chemistry*. The Royal Society of Chemistry, 5(3), pp. 1082–1090. doi: 10.1039/C3PY00869J.

Yu, F. *et al.* (2014) 'Diels–Alder crosslinked HA/PEG hydrogels with high elasticity and fatigue resistance for cell encapsulation and articular cartilage tissue repair', *Polymer Chemistry*. The Royal Society of Chemistry, 5(17), pp. 5116–5123. doi: 10.1039/C4PY00473F.

Yuan, X. and Yang, S. (2015) 'Deletion of IFT80 Impairs Epiphyseal and Articular Cartilage Formation Due to Disruption of Chondrocyte Differentiation', *PloS one*. PLoS One, 10(6). doi: 10.1371/JOURNAL.PONE.0130618.

Yue, D. *et al.* (2019) 'The rate of fluid shear stress is a potent regulator for the differentiation of mesenchymal stem cells', *Journal of cellular physiology*. J Cell Physiol, 234(9), pp. 16312–16319. doi: 10.1002/JCP.28296.

Zambrano, N. Z. *et al.* (1982) 'Collagen arrangement in cartilages', *Acta anatomica*. Acta Anat (Basel), 113(1), pp. 26–38. doi: 10.1159/000145534.

Zarrintaj, P. *et al.* (2018) 'Agarose-based biomaterials for tissue engineering', *Carbohydrate Polymers*. Elsevier, 187, pp. 66–84. doi: 10.1016/J.CARBPOL.2018.01.060.

Zhang, M. *et al.* (2008) 'Crosstalk between integrin and G protein pathways involved in mechanotransduction in mandibular condylar chondrocytes under pressure', *Archives of biochemistry and biophysics*. Arch Biochem Biophys, 474(1), pp. 102–108. doi: 10.1016/J.ABB.2008.03.010.

Zhang, Y. *et al.* (2015) 'In vitro study of directly bioprinted perfusable vasculature conduits', *Biomaterials Science*, 3(1), pp. 134–143. doi: 10.1039/C4BM00234B.

Zhang, Z. *et al.* (1993) 'The αvβ1 integrin functions as a fibronectin receptor but does not support fibronectin matrix assembly and cell migration on fibronectin', *Journal of Cell Biology*. J Cell Biol, 122(1), pp. 235–242. doi: 10.1083/jcb.122.1.235.

Zhao, T. *et al.* (2011) 'Immunogenicity of induced pluripotent stem cells', *Nature*. Nature, 474(7350), pp. 212–216. doi: 10.1038/NATURE10135.

Zhao, Z. Z. *et al.* (2020) 'Mechanotransduction pathways in the regulation of cartilage chondrocyte homoeostasis', *Journal of cellular and molecular medicine*, 24(10), pp. 5408–5419. doi: 10.1111/JCMM.15204.

Zhong, D. *et al.* (2018) 'Excessive tensile strain induced the change in chondrocyte phenotype', *Acta of Bioengineering and Biomechanics Original paper*, 20(2). doi: 10.5277/ABB-01133-2018-02.

Zhou, G. *et al.* (2018a) 'In Vitro Regeneration of Patient-specific Ear-shaped Cartilage and Its First Clinical Application for Auricular Reconstruction.', *EBioMedicine*, 28, pp. 287–302. doi: 10.1016/j.ebiom.2018.01.011.

Zhou, G. *et al.* (2018b) 'In Vitro Regeneration of Patient-specific Ear-shaped Cartilage and Its First Clinical Application for Auricular Reconstruction', *EBioMedicine*. Elsevier B.V., 28, pp. 287–302. doi: 10.1016/j.ebiom.2018.01.011.

Zhu, K. *et al.* (2018) 'A General Strategy for Extrusion Bioprinting of Bio-Macromolecular Bioinks through Alginate-Templated Dual-Stage Crosslinking', *Macromolecular Bioscience*, 18(9), p. 1800127. doi: 10.1002/mabi.201800127.